Eugene G. Morozov

Oceanic Internal Tides: Observations, Analysis and Modeling

A Global View

Springer

Oceanic Internal Tides: Observations, Analysis and Modeling

Eugene G. Morozov

Oceanic Internal Tides: Observations, Analysis and Modeling

A Global View

Springer

Eugene G. Morozov
Physical Department
Shirshov Institute of Oceanology,
 Russian Academy of Sciences
Moscow
Russia

© Springer International Publishing AG 2018
This work is subject to copyright. All rights are reserved by the Publisher, whether the whole or part of the material is concerned, specifically the rights of translation, reprinting, reuse of illustrations, recitation, broadcasting, reproduction on microfilms or in any other physical way, and transmission or information storage and retrieval, electronic adaptation, computer software, or by similar or dissimilar methodology now known or hereafter developed.
The use of general descriptive names, registered names, trademarks, service marks, etc. in this publication does not imply, even in the absence of a specific statement, that such names are exempt from the relevant protective laws and regulations and therefore free for general use.
The publisher, the authors and the editors are safe to assume that the advice and information in this book are believed to be true and accurate at the date of publication. Neither the publisher nor the authors or the editors give a warranty, express or implied, with respect to the material contained herein or for any errors or omissions that may have been made. The publisher remains neutral with regard to jurisdictional claims in published maps and institutional affiliations.

Cover photo: Plastic Buoyancy holding a wire with instruments. (Courtesy of T. Demidova)

Printed on acid-free paper

Preface

This book presents the author's study of the properties of internal tides. The experimental data that were used in this research were collected during experiments aimed at studying other physical processes in the ocean, for example the general circulation or mesoscale eddies. To date, special experiments designed to study internal tides have been very rare. Since the horizontal size of mesoscale eddies and internal tide wavelengths have almost the same length, it was possible to interpret the data in light of the phenomena related to internal tides. In the experiments aimed at studying mesoscale eddies, additional instruments were sometimes set on the moorings and additional moorings were deployed with the goal of better understanding of the internal tides.

This book is the result of 50 years of scientific research carried out by the author since 1967. Internal waves are investigated across a wide range of frequencies with special emphasis on internal tides. The research is based on the statistical analysis of temperature and velocity measurements in different regions of the World Ocean. Systematic studies of internal waves presented in Krauss (1966), Miropolsky (2001), Vlasenko et al. (2005), Gerkema and Zimmerman (2008) are generally related to theoretical studies. A summary of the experimental studies is presented in Roberts (1975), Morozov (1985), Konyaev and Sabinin (1992). This book focuses mainly on the experimental studies of internal waves. It is a progressive study of the research presented by Morozov (1985). The data of measurements in the ocean are interpreted in light of the modern concepts and models of oceanic internal waves.

Surface waves are familiar to everybody. Waves similar to surface waves can appear at the density interface between fluids of different density or over the continuous stratification of fluid. If a perturbation displaces the water particles from the state of equilibrium, oscillations will appear under the influence of the buoyancy forces and forces returning the particles to the equilibrium. Since the water particles are interconnected, spatial oscillations will develop, which are known as gravity waves. The density differences within the fluid are smaller than at the surface between water and air; hence, the returning forces are weaker, and the wave periods are longer than the periods of surface waves. In oceanic conditions, the amplitudes

of waves can be as large as several tens or even hundreds of meters as reported in early publications (Bockel 1962; Perry and Schimke 1965; Niiler 1968; Osborne and Burch 1980).

The measurements show that internal gravity waves are found everywhere in the ocean where positive density stratification of water exists. Upon the discovery that this phenomenon is global, studies of oceanic internal waves became one of the leading research fields of oceanography in the second half of the twentieth century. Internal waves play an important role in all dynamical processes in the ocean, especially in the energy transfer from the surface to the ocean interior and in the mixing of water layers. Internal waves exist everywhere in the ocean; they are the main mechanism by which wind energy is transferred from the ocean surface to the depths. In addition to the important influence of internal waves on ocean dynamics as a whole, they are important in the practical sense for underwater navigation, marine biology, sedimentation, acoustics, and optics of the ocean.

Cold dense water masses are formed in the polar regions of the Earth and descend to the deep layers in all oceans. The Sun warms only the upper ocean layer. Since the density distribution is generally stationary in the ocean, which is significantly different from two-layer stratification, we can conclude that the existing stratification is a result of the long mixing processes.

Munk and Wunsch (1998) discussed the problem of mixing in the ocean and the formation of the existing stratification. According to their estimates, the flow of Antarctic Bottom Water formed over the continental slope of Antarctica is approximately equal to 25–30 Sv. Approximately one-third of this amount of water flows to the north. Without internal mixing, a layer of warm water would be located in the upper part of the ocean, and cold waters would fill the entire depths of the ocean. According to the estimates of Munk and Wunsch, such a structure could be formed in approximately 3000 years. However, mixing induces an upward buoyancy water flow, and the cold waters mix with the overlying layers. The current estimates of vertical diffusivity in the abyssal depths of the ocean are 10^{-5} m²/s. This is not sufficient to perform the necessary mixing. Hence, "hot points" of mixing exist, in which the vertical diffusivity is much greater, and intense mixing occurs exactly at these points. Such regions are characterized by sharp changes in the bottom topography: submarine ridges, continental slopes, seamounts, and abyssal channels and fractures.

Mixing in the ocean is generally determined by the energy transferred from wind and tides. The role of internal tides in the vertical and horizontal exchange dominates over that of other types of internal waves. In the theoretical paper by Müller (1976), internal wave packets are compared with gas molecules. A quantitative estimate of the role of internal waves in the transport of energy, momentum, and mass, the influence of internal waves on the mixing processes in the ocean, and the study of the generation, propagation, instability, and breaking of internal waves are among the main problems of modern physics of the ocean. The understanding of internal wave dynamics is important for the study of circulation in the ocean and its thermohaline structure.

Density stratification is a necessary condition for the existence of internal waves. Internal waves occupy a wide frequency band from the Brunt–Väisälä frequency to the inertial frequency. Tidal oscillations and partly turbulent pulsations also belong to this frequency range. The problem of the physical mechanism of perturbations of physical fields in the ocean can be solved jointly by experimental field measurements, theoretical studies, and numerical and laboratory modeling. Experimental research can verify the theoretical conclusions and put forward the questions that need theoretical interpretation.

The study of internal wave properties and their relation to the mean state of the ocean is key to understanding many processes in the ocean. The influence of the mean ocean state on the internal wave regime, revealing the mechanisms of the generation and breaking of internal waves, the influence of tide and wind on internal wave parameters, the investigation of the energy exchange between waves of different frequency ranges and between waves and mean motion are the most pressing problems of internal wave research.

In this book, we consider the characteristics of internal waves and determine their relation to the mean state of the ocean and other oceanic processes. The analysis is based on the application of statistical methods in the processing of large amounts of field data on temperature and currents measured on moorings in various regions of the ocean. The main focus was on the temperature measurements and the analysis of temperature fluctuations because these data reflect the vertical displacements of water caused by internal waves.

This book is the result of more than 50 years of research. Over these years, the oceanographers of the world have come to a better understanding of the important role of internal waves in ocean dynamics. Our knowledge of internal waves has increased rapidly. During this time period, the oceanographic concept has changed. New instruments for measuring in the ocean have been developed and applied in the research. The theory of ocean physics has also progressed.

The author would have been unable to accomplish such a vast amount of work including the development of the database, without the help of other scientists from the Shirshov Institute of Oceanology and colleagues from other oceanographic institutes around the world.

Moscow, Russia   Eugene G. Morozov

References

Bockel M (1962) Travaux oceanographiques de l' "Origny" a Gibraltar. Cah Oceanogr 14: 325–329

Gerkema T, Zimmerman JTF (2008) An introduction to internal waves. Lect notes, Royal NIOZ. Texel. http://imis.nioz.nl/imis.php?module=ref&refid=289938. Accesed in October 2017

Konyaev KV, Sabinin KD (1992) Waves inside the ocean. Gidrometeoizdat, S.-Petersburg, p 272

Krauss W (1966) Interne Wellen. Gebrüder Borntraeger, Berlin–Nikolasee

Miropolsky YZ (2001) In: Shishkina O (ed) Dynamics of internal gravity waves in the ocean, Springer

Morozov EG (1985) Oceanic internal waves. Russian, Nauka, Moscow, p 151

Müller P (1976) On the diffusion of momentum and mass by internal gravity waves. J Fluid Mech 77(4):789–823

Munk WH, Wunsch C (1998) Abyssal recipes II: energetics of tidal and wind mixing. Deep-Sea Res 45:1977–2010

Niiler PP (1968) On the internal tidal motions in the Florida straits. Deep-Sea Res 15(1):113–123

Osborne AR, Burch TL (1980) Internal solitons in the Andaman sea. Science 208(4443):451–459

Perry RB, Schimke GR (1965) Large amplitude internal waves observed off the north-west coast of Sumatra. J Geophys Res 70(10):2319–2324

Roberts J (1975) Internal gravity waves in the ocean. Marcel Dekker, NY

Vlasenko V, Stashchuk N, Hutter K (2005) Baroclinic tides: theoretical modeling and observational evidence. Cambridge Univ. Press, Cambridge, p 351

Acknowledgements

Contents

About the Author

Eugene G. Morozov is the Head of the Laboratory of Hydrological Processes at the Shirshov Institute of Oceanology in Moscow, Russia. He has been working at this institute after graduating from the Moscow Institute of Physics and Technology in 1970. He never changed his place of work.

His research is focused on oceanic internal waves and large-scale circulation of the ocean. He is a field oceanographer and a specialist in the observations in the open ocean. He works on data acquisition, data processing, interpretations, and partly numerical modeling. Since 2002, he has been interested in the abyssal flows in the Atlantic Ocean and abyssal circulation, especially in the flows in deep fractures. Since 2008, he has been also working on the problems of arctic oceanography in cooperation with scientists from the University Centre in Svalbard. His interests lies in the interaction of the ocean water and glaciers descending to the fjords.

During his oceanographic career, he participated in 47 long oceanic cruises in all oceans of the globe and in 15 coastal expeditions. His field work is related to internal tides and currents in the ocean such as the Gulf Stream, Kuroshio and their rings, Antarctic Circumpolar Current, Falkland Current, California Current, equatorial countercurrents in the Indian and Atlantic oceans.

He was a Guest Scientist at Woods Hole Oceanographic Institution, USA; Universidad Complutense de Madrid, Spain; Royal Netherlands Institute of Sea Research; the University Centre in Svalbard, Norway; Universidad de Buenos Aires, Argentina; Universidad de Montevideo, Uruguay; Arizona State University, USA; Florida State University, USA; University of Victoria, Canada; and University of Cape Town, South Africa.

In 1999, he became a member of the Executive Committee of the International Association for the Physical Sciences of the Oceans (IAPSO). From 2011 to 2015, he was the President of this Association. He was also a member of the Executive Committee of the International Union of Geodesy and Geophysics (IUGG) and a member of the Executive Committee of the Scientific Committee on Oceanic Research (SCOR).

Abbreviations

AABW	Antarctic Bottom Water
ADCP	Acoustic Doppler current profiler
ADOX	Antarctic Deep Outflow Experiment
AVP	Absolute velocity profiler
AWI	Alfred Wegener Institute
BEST	Benguela Source and Transport Experiment
CMDAC	Current Meter Data Assembly Center
COARE	Coupled Ocean–Atmosphere Research Experiment
CONSLEX	Continental Slope Experiment
CSIRO	Commonwealth Scientific and Industrial Research Organisation
CTD	Conductivity temperature depth profiler
DESOTO	DESOTO experiment in 1997 (near the De Soto Canyon)
DOMES	Deep Ocean Mining Environmental Study
EBC	Eastern Boundary Current Experiment
EPOCS	Equatorial Pacific Ocean Climate Studies
ESTOC	European Station for Time Series in the Ocean
FASINEX	Frontal Air-Sea Interaction Experiment
FOCI	Fisheries-Oceanography Coordinated Investigations
FZ	Fracture zone
GARP	Global Atmospheric Research Program
GARS	Gulf of Alaska Recirculation Study
GATE	GARP Atlantic Tropical Experiment
GM	Garrett–Munk model (Garrett and Munk 1972, 1975)
GMPO	Gulf of Mexico Physical Oceanography Program
GW	Gigawatts
HOME	Hawaii Ocean Mixing Experiment
IBCAO	International Bathymetric Chart of the Arctic Ocean
IWEX	Internal wave experiment
KERE	Kuroshio Extension Regional Experiment

LADCP	Lowered acoustic Doppler current profiler
LDE	Local dynamic experiment
LLWODP	Low Level Waste Ocean Dumping Program
MANOP	Manganese Nodule Program
MAPCOWS	Abyssal Boundary Current Studies in the Atlantic Ocean
MAPKIWI	Abyssal Boundary Current Studies in the Pacific Ocean
MAPSOON	Abyssal Boundary Current Studies in the Indian Ocean
MASAR	Mid-Atlantic Slope and Rise Experiment
MILDEX	Mixed Layer Dynamics Experiment
MODE	Mid-Ocean Dynamics Experiment
MORENA	Multidisciplinary Oceanographic Research in the Eastern Boundary of the North Atlantic project
MOVE	Meridional Overturning Variability Experiment
NASA	National Aeronautics and Space Administration
NEADS	North-East Atlantic Dynamic Study
NIO	National Institute of Oceanography, India
NIOZ	Netherlands Institute of Sea Research
NOAA	National Oceanic and Atmospheric Administration
NPBC	North Pacific boundary current experiment
OMEX	Ocean Margin Exchange Project
OPTOMA	Ocean Prediction Through Observations Modeling and Analysis
OTIS	Oregon State University (OSU) Tidal Inversion Software
PEQUOD	Pacific Equatorial Ocean Dynamics Experiment
PIRATA	Pilot Research Moored Array in the Tropical Atlantic changed to Prediction and Research Moored Array in the Tropical Atlantic
POLYMODE	Joint Russian Polygon and USA Mid-Ocean Dynamics Experiment
POM	Princeton Ocean Model
ROMS	Regional Ocean Modeling System
SAZ	Sub-Antarctic Zone Experiment
SeaWiFS	Sea-viewing Wide Field-of-view Sensor
SEQUAL	Seasonal Equatorial Atlantic Experiment
SOGLOBEC	Southern Ocean experiment of the Global Ocean Ecosystems Dynamics
SWINDEX	Southwest Indian Ocean Experiment
SYNOP	Synoptic Ocean Prediction Experiment
TOGA	Tropical Ocean Global Atmosphere Experiment
TOPEX/POSEIDON	TOPography EXperiment and the Greek god of the ocean Poseidon
TW	Terawatts
WBUC	West Boundary Undercurrent experiment
WHOI	Woods Hole Oceanographic Institution
WOCE ACM	WOCE Atlantic current meter program

WOCE ICM	WOCE Indian Ocean current meter program
WOCE PCM	WOCE Pacific current meter program
WOCE SCM	WOCE Southern Ocean current meter program
WODB	World Ocean Database
XBT	Expandable bathythermographs

Abstract

This book is dedicated to the study of the structure and variability of internal tides and their geographical distribution in the ocean.

The work is mainly the result of the experimental analysis of oceanic measurements combined with numerical modeling, and it gives a comprehensive presentation of internal wave processes on the globe. In particular, it is based on the observations from moored buoys in many regions of the global ocean (Atlantic, Pacific, Indian, Arctic, and Southern) that have been carried out over 40 years within many oceanographic programs, including WOCE and CLIVAR, by many researchers from different countries. However, a significant part of the data was collected by the author who is a field oceanographer. These data were processed and interpreted within the concept of the modern knowledge of internal wave motion. The properties of internal waves are analyzed in relation to the bottom topography and mean state of the ocean in specific regions.

Internal waves play an important role in the formation of the existing stratification of seawater and are responsible for important processes of ocean dynamics, such as energy transfer and mixing. One of the most important ideas presented in this book is the strong generation of internal tides over submarine ridges. Energy fluxes from submarine ridges related to tidal internal waves exceed by many times the fluxes from continental slopes. Submarine ridges form an obstacle to the propagation of tidal currents that can cause the generation of large amplitude internal tides. The energy fluxes from these submarine ridges account for approximately one-fourth of the total energy dissipation of barotropic tides. Combined model simulations and moored measurements result in a map of the global distribution of internal tide amplitudes.

Chapter 1
Modern Concepts About Oceanic Internal Waves

Abstract This chapter describes the modern concepts about oceanic internal waves. It presents the mathematical formulation of the internal motion in the ocean. Since the book is mainly the result of the experimental analysis of oceanic measurements the processing tools for the measurements of field data are presented here together with the description of the Vlasenko numerical model for the generation, propagation, and dissipation of internal tides. The Garrett and Munk spectral background model is also described because this is important for understanding the internal motion despite the fact that it does not describe internal tides. Mechanisms of internal tide generation are analyzed and general notes on internal wave motion are presented.

1.1 Main Relations

Let us consider a continuously stratified ocean. We use a right-handed coordinate system with axis z directed downwards. We consider only adiabatic processes and consider that water is incompressible. We write an equation system neglecting the friction and diffusion terms. We limit our consideration to free internal waves (Krauss 1966; Tareev 1966; LeBlond and Mysak 1978). We write the following equations of motion:

$$
\begin{aligned}
\frac{du}{dt} - fv &= -\left(\frac{1}{\rho}\right)\frac{\partial p}{\partial x}, \\
\frac{dv}{dt} + fu &= -\left(\frac{1}{\rho}\right)\frac{\partial p}{\partial y}, \\
\frac{dw}{dt} &= -\left(\frac{1}{\rho}\right)\frac{\partial p}{\partial z} + g;
\end{aligned}
\tag{1.1}
$$

continuity equation:

$$\frac{\partial u}{\partial x} + \frac{\partial v}{\partial y} + \frac{\partial w}{\partial z} = 0; \qquad (1.2)$$

and incompressibility equation:

$$\frac{d\rho}{dt} = 0. \qquad (1.3)$$

Here, f is the Coriolis parameter considering that the presentation of the vector of the angular velocity of the Earth is traditional:

$$f = \left\{ \begin{array}{c} 0 \\ 0 \\ 2\Omega_z \end{array} \right\}; \quad \Omega_x = 0, \quad \Omega_y = 0, \quad 2\Omega_z = -f; \qquad (1.4)$$

where, u, v, w are velocity components; ρ is density; and p is pressure.

We assume that the mean motion is zero. Let us introduce small perturbations and present the fluctuations as small perturbations relative to the mean state. Then, each of the five variables u, v, w, ρ, p can be presented as:

$$M = M_0(x, y, z, t) + M'(x, y, z, t).$$

We shall consider that the unperturbed field of characteristics denoted with subscript $_0$ is known. It does not depend on perturbations and satisfies the main equation system. The equations can be significantly simplified if there is zero mean motion and the hydrostatic equation is satisfied:

$$\frac{\partial p_0}{\partial z} + g\rho_0 = 0. \qquad (1.5)$$

In order to linearize the equations we can neglect convective acceleration compared to the local acceleration because the latter is much greater:

$$|\frac{\partial v}{\partial t}| \gg |v\nabla v|, \quad |\frac{\partial \rho}{\partial t}| \gg |v\nabla \rho|. \qquad (1.6)$$

We can also consider that $\frac{1}{(\rho_0 + \rho')} \approx \frac{1}{\rho_0}$, and the Coriolis parameter does not change with latitude. Then, we obtain an equation system for perturbations. We shall write it omitting the primes at variables:

$$\frac{\partial u}{\partial t} - fv = -\left(\frac{1}{\rho_0}\right)\frac{\partial p}{\partial x},$$

$$\frac{\partial v}{\partial t} + fu = -\left(\frac{1}{\rho_0}\right)\frac{\partial p}{\partial y}, \tag{1.7}$$

$$\frac{\partial w}{\partial t} = -\left(\frac{1}{\rho_0}\right)\frac{\partial p}{\partial z} + g\frac{\rho}{\rho_0};$$

$$\frac{\partial u}{\partial x} + \frac{\partial v}{\partial y} + \frac{\partial w}{\partial z} = 0;$$

$$\frac{\partial \rho}{\partial t} + w\frac{\partial \rho_0}{\partial z} = 0.$$

Let us consider seawater density as a function of pressure. We assume zero friction, zero heat fluxes, and zero salt diffusion. Thus:

$$\frac{d\rho}{dt} = \left(\frac{\partial \rho}{\partial P}\right)\frac{dP}{dt} = \frac{1}{c^2}\frac{dP}{dt}. \tag{1.8}$$

We assume small horizontal gradients of pressure and write:

$$\frac{dP}{dt} = \frac{\partial P}{\partial t} + w\frac{dP}{dz}; \tag{1.9}$$

term $\frac{\partial P}{\partial t}$ in the right part of this equation is small, then:

$$\frac{d\rho}{dt} = \frac{1}{c^2}\frac{dP}{dt} = \frac{1}{c^2}w\frac{dP}{dz} = \frac{1}{c^2}wg\rho_0. \tag{1.10}$$

On the other hand:

$$\frac{d\rho}{dt} = \frac{\partial \rho}{\partial t} + w\frac{d\rho_0}{dz} = \frac{g\rho_0 w}{c^2}. \tag{1.11}$$

We rewrite Eq. (1.11) taking into account the following expression for N (the Brunt-Väisälä frequency):

$$N^2 = \frac{g}{\rho_0}\frac{d\rho_0}{dz} - \frac{g^2}{c^2} \tag{1.12}$$

and get:

$$\frac{\partial \rho}{\partial t} + \frac{\rho_0}{g} N^2(z) w = 0. \tag{1.13}$$

Let us consider the physical sense of the Brunt-Väisälä frequency. We trace a water particle in a stratified environment with a given vertical distribution of density $\rho_0(z)$. We adiabatically displace the particle from the equilibrium position. We assume that vertical displacement of the particle ζ is small. The buoyancy force returns the particle to the equilibrium position. The joint forcing of the buoyancy and inertial forces induces the oscillation motion of the particle. We assume that the density of the medium at the equilibrium position of the particle is $\rho_0(z)$, and at the point of the maximum displacement the density is $\rho_0(z+\zeta)$. We extend the buoyancy force in a series with respect to ζ and take the second decomposition term (the first term is zero) to get the linear component of the return force:

$$-g\frac{d\rho_0}{dz}\zeta,$$

which is balanced by the inertia force:

$$\rho_0\frac{d^2\zeta}{dt^2}.$$

Thus, we obtain an equation for oscillations:

$$\rho_0\frac{d^2\zeta}{dt^2} = -g\frac{d\rho_0}{dz}\zeta. \tag{1.14}$$

The particle oscillation is described by equation:

$$\zeta = \zeta_0 e^{i\sqrt{N^2}\,t}, \tag{1.15}$$

where, N is the frequency of oscillations:

$$N^2 = \frac{g}{\rho_0}\frac{d\rho_0}{dz}. \tag{1.16}$$

Here, we accept the expression for the Brunt-Väisälä frequency without the second term in (1.12). We differentiate the first equation of system (1.7) with respect to z, and the third with respect to x and subtract one from the other; then we differentiate the second equation with respect to z, and the third with respect to y and subtract. Finally, we get:

$$\frac{\partial}{\partial t}\left(\frac{\partial u}{\partial z}-\frac{\partial w}{\partial x}\right)-f\frac{\partial v}{\partial z}=-\frac{g}{\rho_0}\frac{\partial \rho}{\partial x}$$

$$\frac{\partial}{\partial t}\left(\frac{\partial v}{\partial z}-\frac{\partial w}{\partial y}\right)+f\frac{\partial u}{\partial z}=-\frac{g}{\rho_0}\frac{\partial \rho}{\partial y}. \tag{1.17}$$

We differentiate both Eq. (1.17) with respect to time and substitute

$$\frac{\partial \rho}{\partial t}=-\frac{\rho_0}{g}N^2 w. \tag{1.18}$$

The dimension of N is frequency; it is called the Brunt-Väisälä frequency. Usually, this frequency is written as:

$$N=\sqrt{\frac{g}{\rho_0}\frac{d\rho_0}{dz}}.$$

In addition to this definition of the Brunt-Väisälä frequency (Eq. 1.16) the authors of some publications add the second term to this frequency (Eq. 1.12):

$$N^2=\frac{g}{\rho_0}\frac{d\rho_0}{dz}-\frac{g^2}{c^2}, \tag{1.19}$$

where the second term is the adiabatic correction if we take into account compressibility of water, and c is the sound velocity:

$$\frac{1}{c^2}=\frac{\partial \rho}{\partial p}. \tag{1.20}$$

This correction is small and can be neglected. We shall consider its physical sense below.

After differentiating (1.17) with respect to time we get:

$$\frac{\partial^2}{\partial t^2}\left(\frac{\partial u}{\partial z}-\frac{\partial w}{\partial x}\right)-f\frac{\partial^2 v}{\partial z\partial t}=N^2\frac{\partial w}{\partial x}$$

$$\frac{\partial^2}{\partial t^2}\left(\frac{\partial v}{\partial z}-\frac{\partial w}{\partial y}\right)+f\frac{\partial^2 u}{\partial z\partial t}=N^2\frac{\partial w}{\partial y}. \tag{1.21}$$

We differentiate the first equation of system (1.21) by x and the second by y and summarize:

$$\frac{\partial^2}{\partial t^2}\left[\frac{\partial}{\partial z}\left(\frac{\partial u}{\partial x}+\frac{\partial v}{\partial y}\right)-\left(\frac{\partial^2 w}{\partial x^2}+\frac{\partial^2 w}{\partial y^2}\right)\right]+f\left[\frac{\partial^3 u}{\partial t\,\partial z\,\partial y}-\frac{\partial^3 v}{\partial t\,\partial z\,\partial x}\right]$$
$$=N^2\left(\frac{\partial^2 w}{\partial x^2}+\frac{\partial^2 w}{\partial y^2}\right). \tag{1.22}$$

Taking into account the continuity equation from system (1.7) we get:

$$\frac{\partial^2}{\partial t^2}\Delta w-f^2\frac{\partial^2 w}{\partial z^2}=N^2\left(\frac{\partial^2 w}{\partial x^2}+\frac{\partial^2 w}{\partial y^2}\right). \tag{1.23}$$

Term $f^2\frac{\partial^2 w}{\partial z^2}$ was obtained as follows:

We differentiate the first equation of system (1.7) by y and the second by x and get the following after subtraction:

$$\frac{\partial}{\partial t}\left(\frac{\partial u}{\partial y}-\frac{\partial v}{\partial x}\right)+f\frac{\partial w}{\partial z}=0. \tag{1.24}$$

Then, we can reduce the system to one equation for the vertical velocity:

$$\Delta\frac{\partial^2 w}{\partial t^2}+N^2\Delta_h w+f^2\frac{\partial^2 w}{\partial z^2}+(N^2/g)\left(\frac{\partial^3 w}{\partial z\partial t^2}+f^2\frac{\partial w}{\partial z}\right)=0, \tag{1.25}$$

where Δ is the Laplacian, Δ_h is the horizontal Laplacian.

The last term in the left part of the equation is small and usually neglected.

Let us formulate the boundary conditions. Zero boundary condition at the bottom is obviously $w = 0$. Boundary conditions at the surface are determined from condition $\frac{dp}{dt}=0$. We linearize this equation and exclude pressure using the equations of motion:

$$\left(\frac{\partial}{\partial z}\right)\left(\frac{\partial^2 w}{\partial t^2}+f^2 w\right)+g\Delta_h w=0. \tag{1.26}$$

It is known from practice that this condition almost does not differ from the "rigid lid" condition because internal waves at the surface are almost not manifested.

The main equation system and the equation for the vertical velocity are invariant with respect to the shifts of the horizontal coordinate axes and time; hence the following solution in the form of plane waves always exists:

$$w = W(z)\ \exp\ i(k_x x+k_y y-\omega t),\quad k=\sqrt{k_x^2+k_y^2}, \tag{1.27}$$

where k is the wavenumber, $W(z)$ is the amplitude function, ω is the angular velocity. We substitute this solution to the equation for vertical velocity and get the equation for the amplitude function:

$$\frac{d^2W(z)}{dz^2} + \frac{N^2(z)}{g}\frac{dW(z)}{dz} + \frac{N^2(z) - \omega^2}{\omega^2 - f^2}k^2W(z) = 0. \qquad (1.28)$$

We write the boundary conditions for this equation in a simplified form as the "rigid lid":

$$W = 0 \text{ at } z = 0 \text{ and } z = H. \qquad (1.29)$$

It is easy to show that term $\frac{N^2(z)}{g}\frac{dW(z)}{dz}$ is small. It is neglected in some papers because if the Boussinesq approximation is used this term does not appear. This term determines the decay of vertical velocity with depth. In the case if $\frac{N^2(z)-\omega^2}{\omega^2-f^2} > 0$, which is usually observed in the ocean, we get an eigen-value problem. Usually in the real ocean $N > f$, then the condition for internal wave existence is determined by the frequency range $f < \omega < N$, in which wave solutions exist.

The solution of Eq. (1.28) is an eigen-value problem. Each eigen-value k_m corresponds to amplitude function $W_m(z)$, which is a solution of Eq. (1.28) with boundary conditions (1.29). Internal waves characterized by eigen-values k_m (wavenumber) and eigen-functions $W_m(z)$ are considered internal waves of mode m with respect to depth. Thus, a standing wave over depth is formed together with a running wave in the horizontal plane. Equation (1.28) is linear and homogeneous; hence any sum of modes $\sum_m A_m W_m(z)$ is also a solution of this equation.

Let us consider a simple case when the Brunt-Väisälä frequency does not depend on depth. This corresponds to the exponential increase in density with depth and roughly approximates realistic density distribution in the major part of the ocean. It is easy to show that solution $W_m(z) = A_m \sin(k_z z)$ satisfies Eq. (1.28). Vertical wavenumber k_z can be found from the boundary condition at the bottom ($z = H$). It is equal to $\pi m/H$, where m is the mode number. We substitute this solution to Eq. (1.28) and obtain the dispersion relation for the condition of the constant Brunt-Väisälä frequency with depth:

$$\omega^2 = \frac{f^2 k_z^2 + N^2 k^2}{k^2 + k_z^2}. \qquad (1.30)$$

Let us consider some limiting cases.

1. $\omega = f$ corresponds to pure inertial oscillations, $k = 0$.
2. $k_z \gg k$ corresponds to the condition of long waves: $L \gg H$.

If the mode structure has been formed in the case $f \ll N$,

we get $\omega = \frac{Nk}{k_z}$. The phase velocity of such waves is

$$c = \frac{\omega}{k} = \frac{NH}{\pi m}. \tag{1.31}$$

This does not depend on the wavelength, which means that long internal waves similar to long surface waves are characterized by zero dispersion.

3. $k_z \ll k$ corresponds to short waves. If $f \ll N$, we get in the limiting case $\omega = N$.

The boundary conditions have only a slight influence on the wave, and we can write dispersion relation in the following form $\omega = \frac{Nk}{(k_z^2 + k^2)^{1/2}} = N \cos \theta$, where θ is the angle between the direction of the wave vector and surface; here $k^2 = k_x^2 + k_y^2$. Thus, the wave packets propagate along sloping trajectories. The physical sense of this phenomenon is as follows: if a particle is displaced not strictly in the vertical direction, the returning buoyancy force would be smaller, and the frequency of oscillations would decrease. This idea is the basis of the dispersion relation in unlimited fluid in the book by Phillips (1977) in the case that we do not accept the approximation of the small Coriolis parameter:

$$\omega^2 = \frac{N^2 k^2 + f^2 k_z^2}{k^2 + k_z^2} = N^2 \cos^2 \theta + f^2 \sin^2 \theta. \tag{1.32}$$

Thus, this expression establishes the relation between the frequency of oscillations and the inclination of the wave vector, which is the direction of internal wave propagation relative to the horizontal plane. The wave frequency depends only on the inclination of the wave vector. The wave frequency does not depend on the absolute value of the vector. When the frequency is close to the inertial frequency the water motion is almost horizontal and the orbits are close to circular. In the Northern Hemisphere, the velocity vector rotates in a clockwise direction. When the wave frequency increases, the orbit takes the form of an ellipse and inclines. In the limiting case when $\omega = N$ the oscillations become vertical (Fig. 1.1).

Fig. 1.1 Wave vectors $\bar{k}$, group velocities c_g, and hodographs of the particle velocities (ellipses) near the inertial frequency (left) and Brunt-Väisälä frequency (right); θ is the angle between the wave vector and the horizontal plane
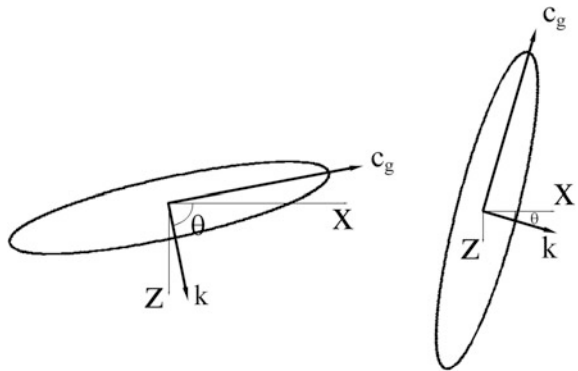
The orbits of the particle motion caused by internal waves are in the plane normal to the wave vector. The particle orbits of high-frequency waves close to the Brunt-Väisälä frequency become close to a linear segment normal to the wave vector. The motion is in the vertical plane. The particle orbits of low-frequency waves with a frequency close to the Coriolis parameter are close to horizontal circles. The ratio of the ellipse axes is equal to f/ω. The sine of the ellipse inclination to the horizontal plane is determined by the ratio of the vertical and horizontal wavenumbers, which follows from expression (1.32):

$$\frac{k_z}{k} = \sqrt{\frac{(N^2 - \omega^2)}{(\omega^2 - f^2)}}. \tag{1.33}$$

The greater deviation of particle trajectory from the vertical the smaller the frequency of oscillations. As the frequency decreases up to the inertial frequency the orbits transfer to horizontal circles and the returning buoyancy forces decrease. However, the Coriolis force exists on the rotating Earth, which turns the trajectories into circles. The centrifugal force is balanced by the Coriolis force, and if we write an equation for both accelerations we get:

$$\frac{v^2}{r} = fv.$$

Here, v is the horizontal velocity, r is the radius of the orbit. From this relation one can easily find the radius of the orbit of inertial oscillations if the velocity and Coriolis parameter, which depends on the latitude, are known. The inertial period is calculated from the inertial frequency as $T = \frac{2\pi}{f}$. The Coriolis parameter is calculated as $f = 2\Omega \sin \varphi$, where Ω is the angular velocity of the Earth's rotation. If we consider a region at a latitude of 30° and velocity of inertial currents, for example, equal to 10 cm/s the radius of the orbits would be equal to 1375 m. Inertial frequency f at 30° latitude is equal to 7.27×10^{-5} s^{-1} ($\Omega = 0.261$ h^{-1}).

We assume that the Brunt-Väisälä frequency variations over the wave length are small, and wave frequency ω is between N and f far from each of the limiting frequencies. The group velocity $c_g = \frac{d\omega}{dk} = \left\{ \frac{\partial\omega}{\partial k_x}, \frac{\partial\omega}{\partial k_y}, \frac{\partial\omega}{\partial k_z} \right\} = \left\{ \frac{\partial\omega}{\partial k}, \frac{\partial\omega}{\partial k_z} \right\} = \frac{kk_z(N^2 - f^2)}{\omega(k^2 + k_z^2)^2}(k_z, -k), k^2 = k_x^2 + k_y^2$ is normal to wave vector $\overline{k}$. The inclination of the group velocity vector $c_g = \frac{d\omega}{dk}$ is written as $\theta = arctg\sqrt{\frac{\omega^2 - f^2}{N^2 - \omega^2}}$. Thus, for the greater wave periods (smaller frequencies) the group velocity vector would be directed closer to the horizontal plane. Group velocity $c_g = \frac{d\omega}{dk}$ is normal to phase velocity $c_{ph} = \frac{\omega}{k}$; hence, their projections on the vertical have different signs. In the upward directed wave packet the waves propagate downwards; hence the direction of the energy propagation in the vertical direction is opposite to the wave phase

propagation. The closer the wave frequency to the Brunt-Väisälä frequency, the closer the group velocity vector to the vertical.

When the waves reflect from the surface or bottom, the wave conserves its angle to the horizontal but not to the sloping bottom. The principle of equality of the incident and reflection angles is not true for internal waves (Garrett and Munk 1979). This property is a sequence of the conservation of dispersion relation, which in this case is the conservation of the wave frequency. When the wave enters the region, in which the Brunt-Väisälä frequency decreases to the wave frequency, the wave reflects from the boundary and the group velocity vector in the vicinity of the point where $N = \omega$ tends to zero and to the vertical direction. Many laboratory experiments confirm this. It is likely that the first experiments were the works by Mowbray and Rarity (1967) and Stevenson (1968).

The waves propagating upwards reflect from the surface, and downward propagating waves reflect from the ocean bottom. Thus, a vertical standing wave (or a set of modes) is formed. If the entire ocean is not a waveguide, the waves reflect from the layers, in which $N < \omega$. Thus, a waveguide for high-frequency waves can be formed in the thermocline.

1.2   The Garrett and Munk Spectral Background Model

Moored measurements in the ocean show that spectra of oscillations of various measured properties (velocity, temperature, conductivity) are continuous in the entire frequency band without energetic peaks excluding the peaks at the tidal and inertial frequencies. The level of spectral densities decreases with frequency approximately by a power law with the exponent ranging from −1 to −4, while the majority of measurements show that the range is from −2 to −3. Lack of stable peaks excluding the previously mentioned frequencies indicates that a large set of oscillations with random phases and amplitudes exists in the ocean. Internal waves are responsible for quite a wide range of recorded fluctuations, especially those which are related to the vertical fluctuations of water particles, in particular, the temperature fluctuations.

Spectra of velocity based on moored measurements are characterized by almost the same features as the temperature spectra. One-dimensional spatial spectra of vertical displacements or temperature obtained by towed instruments usually do not have clearly manifested reliable peaks. The level of spectral density decays with the wavenumber according to a power law with exponent ranging from −1 to −4.

Garrett and Munk (1972a) analyzed field data in the ocean and contrived a model of the background energy spectra in a wide range of internal wave scales. They assumed that the wave field in different locations of the ocean is approximately the same at any time; hence a universal climatic spectrum of internal waves exists in the ocean. Therefore, numerous experiments carried out in different regions of the ocean measure one and the same universal wave field. Perturbations in individual time periods and at individual locations appear over this background state. Various

one-dimensional (frequency and spatial) spectra, which result from these measurements, are derivatives of one and the same spatiotemporal energy spectrum depending on frequency and wavenumber $E(k_x, k_y, k_z, \omega)$. This assumption, which is generally very strong, makes all ocean regions similar, but it does not take into account the local sources of energy and differences in the conditions of wave propagation. The further analysis of numerous results of field measurement showed that this assumption is generally correct if we consider waves far from the ocean surface and other regions of the energy supply. The authors, Garrett and Munk (1972a) limited their model to the middle layer of the ocean excluding the upper and bottom layers approximately 500–700 m thick, so that the field data would not contradict their model. They also excluded high and equatorial latitudes, and excluded the tidal frequencies, at which significant energy input to the internal wave frequency range occurs. There is no doubt that the advantages of the assumptions made the authors strongly simplify the spectrum model.

The authors assumed that all fluctuations of oceanographic characteristics in the frequency range of internal waves are determined only by internal waves, while the other processes do not influence these fluctuations. Internal waves are presented by superposition of free linear waves with random amplitudes and phases. The energy of internal waves is continuously distributed in the frequency-wavenumber space (the continuum equivalent to a set of modes). The wave field is horizontally isotropic but has vertical symmetry, i.e. the upward and downward internal wave energy fluxes are equal.

The authors constructed a model of dimensionless energy spectra; they introduced the corresponding scales of spatial wavenumbers $\hat{M} = 0.122$ cyc/km and frequency $\hat{N} = 3$ cph. Due to the fact that the interpretation of internal waves as oscillations with a small number of lower modes does not satisfy the rapid decay of coherence between sensors divided vertically by tens or even hundreds of meters, the authors selected a multi-modal model with a number of modes equal to 20.

The discrete set of modes is substituted by equivalent continuum; thus, the energy appears distributed between the horizontal and vertical wavenumbers but not related to the specific wavenumbers corresponding to modes. This assumption seemed less doubtful than the presentation of internal waves by a set of discrete modes because high modes can hardly develop in the ocean without rapid decay. The assumption about the vertical symmetry of the internal wave field, or in other words about equal upward and downward energy fluxes, presents the possibility for us to make the transition from a four-dimensional spectrum to three-dimensional $E(k_x, k_y, \omega)$ and consider the spectral density of energy in a unit vertical water column from the surface to the bottom. The authors introduced horizontal isotropy of solutions. Three-wave resonant nonlinear interactions facilitate this; however experimental evidences of wave anisotropy exist especially in the band of the low and tidal frequencies. However, the authors introduced this simplification by excluding tidal internal waves from the model. This allowed them to reduce the model to a two-dimensional one.

The authors tried to construct the energy spectrum as function of frequency and three components of wave vector. They introduced many simplifications, which will eventually result in a universal spectrum for the entire ocean. More exactly, it will solve the problem for the part of the ocean in which this spectrum would be valid. This later became known to the oceanographic community as spectrum GM72.

The solutions are limited by the lower frequency equal to the local Coriolis parameter. No solutions exist with the wavenumbers smaller than the wavenumber of the lower mode $\tilde{k} = \tilde{k}^{(1)}(\omega)$. The tilde hereinafter denotes dimensionless variables. At depth $\tilde{z}$ no solutions exist at the frequencies greater than $\tilde{n} = e^{-\tilde{z}}$, because these solutions are below the turning point. The Brunt-Väisälä frequency deeper than this point is lower than the frequencies of internal waves; hence the solutions are negligibly small.

We write vertical displacements $\tilde{\zeta}$ in internal waves as:

$$\tilde{\zeta} = \frac{\tilde{Z}(\tilde{z})\hat{q}}{2\pi\hat{N}}\sin\left(\tilde{k}_x\,\tilde{x} + \tilde{k}_y\,\tilde{y} - \tilde{\omega}\,\tilde{t}\right),$$

where $\tilde{Z}(\tilde{z})$ is the dimensionless eigen wave function for the vertical displacements. It is equal to:

$$\tilde{Z}(\tilde{z}) = \frac{\tilde{k}}{\tilde{a}}J_{\tilde{a}}(\tilde{k})L(\tilde{\omega}, \tilde{k}),$$

where $L(\tilde{\omega}, \tilde{k})$ is the normalizing function, $J_{\tilde{a}}(\tilde{k})$ is the Bessel function of the order $\tilde{a}$, $\hat{q}$ is the dimensional coefficient (dimension of velocity),

$$\tilde{a} = \tilde{k}\left(\frac{\tilde{\omega^2} - \tilde{f^2}}{\tilde{\omega^2}}\right)^{-1/2}.$$

We average $\tilde{Z}(\tilde{z})$ over depth to the turning depths, at which wave frequency $\tilde{\omega}$ is equal to the Brunt-Väisälä frequency $\tilde{n}$, and get:

$$\overline{\tilde{Z}^2} = \frac{1}{\tilde{n}}\frac{\tilde{\omega^2} - \tilde{f^2}}{\tilde{\omega^2}}.$$

We denote $\tilde{E}$ as dimensionless internal wave energy in a unit water column, where $E = (\tilde{k}, \tilde{\omega})$ is the spectral density of dimensionless energy. Then:

$$\tilde{E} = \int \int E(\tilde{k}, \tilde{\omega}) d\tilde{k}\, d\tilde{\omega}.$$

We write dimensional energy in a unit water column as:

$$\hat{E} = (\overset{\wedge}{N^2}/2\pi \overset{\wedge}{M^3})\, \tilde{E}.$$

Here, we use cyclic wavenumbers normalized by $\hat{M}$, and the distance and inverse wavenumbers normalized by the buoyancy scale or stratification depth $\hat{b}$:

$$\hat{b} = \frac{1}{2\pi \hat{M}} = 1300\,m,\ \tilde{y} = y/\hat{b}.$$

Garrett and Munk introduce the notion of moored spectra, which are the spectra calculated from the data of instruments installed on moorings, towed spectra from towed measurements, and dropped spectra obtained from the instruments lowered from ships, for example, CTD profilers.

Consequently, the three types of dimensionless spectra would be written as:

$$MS_\zeta(\tilde{\omega}) = \int \tilde{\overline{Z}}^2(\tilde{\omega})\, \tilde{E}(\tilde{k}, \tilde{\omega}) d\tilde{k}$$

$$TS_\zeta(\tilde{k_x}) = \iint \tilde{\overline{Z}}^2(\tilde{\omega})\, \tilde{E}(\tilde{k_x}, \tilde{k_y}, \tilde{\omega}) d\tilde{k_y}\, d\tilde{\omega}$$

$$DS_\zeta(\tilde{k_z}) = \int \tilde{\overline{Z}}^2(\tilde{\omega})\, \tilde{E}(\tilde{k_z}, \tilde{\omega}) d\tilde{\omega}.$$

The dimensional spectrum of fluctuations of horizontal velocity and vertical displacements $\hat{F}_{u,v,\zeta}(\tilde{\omega})$ for the moored measurements at one point based on the dimensionless energy spectrum is written as:

$$\hat{F}_{u,v,\zeta}(\tilde{\omega}) = \hat{M}^{-2} \hat{N} \left[\tilde{\overline{U}}^2, \tilde{\overline{V}}^2, (2\pi \hat{N})^{-2} \tilde{\overline{Z}}^2 \right] \int_0^\infty E(\tilde{k}, \tilde{\omega})\, d\tilde{k},$$

where $\tilde{\overline{U}}, \tilde{\overline{V}}, \tilde{\overline{Z}}$ are eigen functions of the main equation system as functions of depth.

Spectrum of vertical displacements $\hat{F}_\zeta(\tilde{k_x})$ for towed measurements in direction x ($\tilde{k_x}$ is the horizontal component of wavenumber along the x-axis) with a velocity

much greater than the horizontal phase velocity of the wave $\tilde{\omega}/\tilde{k}_x$ would be written as:

$$\hat{F}_{\zeta}(\tilde{k}_x) = \frac{\hat{M}^{-3}}{2\pi^3} \int\limits_{\tilde{f}}^{1} d\,\tilde{\omega}\ \overline{\tilde{Z}}^2 \int\limits_{\tilde{k}_x}^{\infty} d\,\tilde{k} \left(\tilde{k}^2 - k_x^2\right)^{-1/2} \tilde{E}(\tilde{k},\tilde{\omega}).$$

The problem is reduced to finding energy spectrum $E = (\tilde{k},\tilde{\omega})$, which could be presented as a product of the function of wavenumber and function of frequency. However, experiments show that the range of wavenumbers for the fluctuations at fixed frequency is a function of this frequency $\mu(\tilde{\omega})$. Therefore, the authors introduce an additional function to the expression of the spectrum. The authors also assumed self-similarity of the dimensionless energy spectrum $E = (\tilde{k},\tilde{\omega})$. This means that $E = (\tilde{k},\tilde{\omega})$ is a function of dimensionless wavenumber $\tilde{k}$ and it is proportional to $\mu(\tilde{\omega})$, but the shape of the spectrum does not change:

$$E = (\tilde{k},\tilde{\omega}) = C\mu^{-1}(\omega)A(\lambda)\Omega(\omega),$$

where $\lambda = \tilde{k}/\mu$, and $A(\lambda) = 0$ at $\lambda < \lambda^{(1)} = \tilde{k}^{(1)}/\mu$, $\lambda^{(1)}$ is sufficiently small, and it is usually assumed equal to zero.

It is convenient to select a power law for the frequency coefficient:

$$\Omega(\tilde{\omega}) = \tilde{\omega}^{-p+2s}(\tilde{\omega}^2 - \tilde{f}^2)^{-s}.$$

Far from $\tilde{f}$ this law takes a form of $\tilde{\omega}^{-p}$. We consider for definiteness that $s = 1/2$, however, the value of s can range from 0 to 1 for the convergence of integral $\int_f^1 \Omega(s)d\omega$. The simplest form was selected for function $A(\lambda)$: $A = 1$ for $0 \leq \lambda \leq 1$, and $A = 0$ for $\lambda > 1$. The power law was also selected for function $\mu(\omega)$:

$$\mu(\tilde{\omega}) = j_i\pi(\tilde{\omega}/\tilde{f})^{r-1}(\tilde{\omega}^2 - \tilde{f}^2)^{1/2} \sim \tilde{\omega}^r),$$

where j_i is the equivalent number of modes of inertial oscillations.

Based on the experimental facts Garrett and Munk selected the multiplicative constant of the energy spectrum C equal to $2\tilde{f}E/\pi$, $p = 2$, $q = 2$, $r = 1$; however, this selection can be doubted. The spectrum of dimensionless energy would be written as:

$$E(\tilde{k}, \tilde{\omega}) = \frac{2}{\pi} E \frac{\tilde{f} \, (\tilde{\omega}^2 - \tilde{f}^2)^{-1/2}}{\mu(\tilde{\omega}) \, \tilde{\omega}} \text{ at } \tilde{k}^{(1)} \le \tilde{k} \le \mu,$$

where $\mu(\tilde{\omega}) = j_i \pi (\tilde{\omega}^2 - \tilde{f}^2)^{1/2}$,

or $E(\tilde{k}, \tilde{\omega}) = 2E\tilde{f} \, / [j_i \pi \, \tilde{\omega}(\tilde{\omega}^2 - \tilde{f}^2)]$.

The authors recommend the following selection of constants: $E = 2\pi10^{-5}$, $j_i = 20$, thus assuming that the number of equivalent modes is 20. Then, the total energy of internal waves in a unit column would be:

$$\hat{E} = 0.38 \text{ J cm}^{-2}.$$

After integration we get an expression for the spectrum of vertical displacements based on moored measurements:

$$F_\zeta(\tilde{\omega}) = \frac{E\tilde{f} \, \omega^{-3}(\tilde{\omega}^2 - \tilde{f}^2)^{1/2}}{2\pi^3 \hat{M}^2 N(z)}.$$

The spectrum of horizontal velocity for moored measurements would be written as:

$$F_u(\tilde{\omega}) = \frac{2N(z)E\tilde{f} \, \omega^{-3}(\tilde{\omega}^2 + \tilde{f}^2)(\tilde{\omega}^2 - \tilde{f}^2)^{-1/2}}{\pi \hat{M}^2}.$$

Here, $N(z) = \frac{1}{2\pi} \sqrt{\frac{g}{\rho_0} \frac{\partial \rho}{\partial z}}$ is the dimensional Brunt-Väisälä frequency, $\tilde{f} = \frac{f}{\hat{N}}$, f is the dimensional inertial frequency equal to 0.042 cph at a latitude of 30°.

We remember that: $E = 2\pi10^{-5}$, $j_i = 20$, $\hat{M} = 0.122$ cycle/km, and frequency $\hat{N} = 3$ cph.

We get the following for the spectrum values:

$$F_\zeta(\omega) = \frac{E\hat{N}f \, \omega^{-3}(\omega^2 - f^2)^{1/2}}{2\pi^3 \hat{M}^2 N(z)} = 204 \cdot \frac{f\omega^{-3}(\omega^2 - f^2)^{1/2}}{N(z)} \text{ m}^2\text{h},$$

$$F_u(\omega) = \frac{2\hat{N}N(z)Ef \, \omega^{-3}(\omega^2 + f^2)(\omega^2 - f^2)^{-1/2}}{\pi \hat{M}^2}$$
$$= 8062 \cdot N(z)f(\omega^2 + f^2)(\omega^2 - f^2)^{-1/2} \, \omega^{-3} \text{ m}^2/\text{h}.$$

We write the towed spectrum for dimensionless variables as:

$$F_\zeta(\widetilde{k}) = \frac{E \widetilde{f} \ \widehat{N} \int_{\widetilde{\omega}_\mu}^{\widetilde{n}} \omega^{-3} \cos h^{-1}\left(\frac{\mu}{k}\right) d\omega}{N(z) j \pi^5 \widehat{M}^3} \approx \frac{jE \widetilde{f} \ \widehat{N} \widetilde{k}^{-2}}{2N(z)\pi^3 \widehat{M}^3} \ \text{for} \ \widetilde{f} \leq \widetilde{\omega}_\mu \leq \widetilde{n} \ .$$

A transition to dimensional values results in:

$$F_\zeta(k) = \frac{jEf\,k^{-2}}{2N(z)\pi^3 M^3} = 0.167 \frac{f}{N(z)} k^{-2} \ \text{m}^3.$$

Since this expression is well satisfied in the frequency range

$$f \ll \omega \ll N(z),$$

it is applicable to the wavenumbers of medium range

$$\widetilde{k} \ \sim j\pi\,\widetilde{\omega}, \text{which is } k \sim j\pi \frac{\omega}{\widehat{N}} \widehat{M} \ \sim 1 \, \text{cycle/km}.$$

Decay of spectrum for smaller k is less, while rapid decay is observed for greater k. At very small k, the expression transforms in the limiting case to:

$$F_\zeta(0) = \frac{0.08 \, E \widehat{N}}{N(z)\pi^5 f \widehat{M}^3}.$$

The numerical value for this expression is $F_\zeta(k = 0.04 \ \text{cycle/km}) = \frac{1}{2} F(0)$.

It appears that if we consider realistic spectra in this range, processes other than internal waves (for example, crossing of fronts) play an important role, and the spectra obtain the corresponding form.

The Garrett-Munk spectrum (GM-72) models background characteristics of internal waves in the range of mid-latitudes in deep ocean layers far from the surface and bottom. This model has been confirmed by numerous experiments. However, each specific experimental spectrum differs from the model one. The differences are in the existence of several not very reliable spectral peaks and deviation of the decay law from the model one.

The model does not work near generation sources of internal waves, for example in the regions of strong currents or topographic features. The energy levels near the sources are higher, and higher coherences are observed between measurements at different points because the energy of fluctuations is higher than the background energy level. At low latitudes, observers report a higher level of energy that can be one order of magnitude greater (Sabinin and Serikov 1974; Desaubies 1976;

Kushnir and Andryushchenko 1977; Johnson and Sanford 1980; Sabinin 1982; Konyaev and Serebryany 1983).

A review of the experimental confirmations of the GM-72 model is given, for example by Wunsch and Webb (1979). A progressive model was developed in a later paper by the authors Garrett and Munk (1975) (model GM-75). In the modified model, the authors change the form of the initial dimensionless energy spectrum. Previously they presented the spectrum as:

$$E(\widetilde{k}, \widetilde{\omega}) \sim A(\lambda)B(\widetilde{\omega})\mu(\widetilde{\omega}),$$

where function $B(\widetilde{\omega}) \equiv \Omega(\widetilde{\omega})$ characterizes the dependence of the spectrum on frequency; function $A(\widetilde{k}, \widetilde{\omega}) \equiv A(\lambda) = A\left(\frac{\widetilde{k}}{\mu}\right)$ characterizes the dependence of the spectrum on wavenumber at fixed frequency. In the GM-75 model, the authors rejected a simple form of function $A\left(\frac{\widetilde{k}}{\mu}\right) = 1$. Function $\mu(\widetilde{\omega})$, which is the bandwidth of the wavenumbers at fixed frequency, was introduced into function $A(\lambda)$.

If the sensors are separated over vertical by the scales equal to the inverse bandwidth, the influence of different wavenumbers is significant; hence, coherence decreases. However, only a slight dependence of vertical coherence on frequency was found. These facts indicate that the bandwidth depends on frequency: $\mu = \mu(\widetilde{\omega})$.

In the GM-75 model, the authors introduced a scale of the mode number j_* and the corresponding wavenumbers:

$$\widetilde{k_*} = j_*\pi(\omega^2 - f^2)^{1/2}, \widetilde{k_{z_*}} = j_*\pi\, \widetilde{n}\,(z)$$

conserving the dependence of $\widetilde{k}$ on $\widetilde{\omega}$, which is the dispersion relation:

$$\widetilde{k} = j\pi(\widetilde{\omega^2} - \widetilde{f^2})^{1/2}.$$

Lowest modes with wavenumbers $\widetilde{k_*}$ and $\widetilde{k_{z_*}}$ have the greatest energy; the authors select j_* equal to 6.

They suggest the following form for function $A(k, \omega)$: $\frac{\widetilde{A(\lambda)}}{\widetilde{k_*}}$,

$$A(\lambda) = \frac{(t-1)}{(1+\lambda)^t}, \quad \text{where } \lambda = \frac{\widetilde{k}}{\widetilde{k_*}} = \frac{\widetilde{k_z}}{\widetilde{k_{z_*}}}.$$

Parameter t is selected equal to 2.5; it determines the spectrum decay for large wavenumbers.

The authors suggest the following expression for function $B\left(\widetilde{\omega}\right)$:

$$B(\widetilde{\omega}) = \frac{2}{\pi} \frac{f}{\widetilde{\omega}(\widetilde{\omega^2} - \widetilde{f^2})^{1/2}}.$$

Then, the dimensionless energy spectrum would be written as:

$$E(\widetilde{k}, \widetilde{\omega}) = EA(\lambda)\frac{B(\widetilde{\omega})}{\widetilde{k_*}} = \frac{2E\widetilde{f}\,A(\lambda)}{\pi\,\widetilde{\omega}\,\widetilde{k_*}(\widetilde{\omega^2} - \widetilde{f^2})^{1/2}}.$$

This form of the model spectrum gives a better approximation of the experimental spectrum than the previous one.

The expression for the moored spectrum of vertical displacements in this version of the model remains unchanged. The expression for the towed spectra is very cumbersome. It is given in a number of works, for example by Katz and Briscoe (1979). The development of the GM models generally occurred in the 10 years after they were published: Cairns and Williams (1976); Desaubies (1976); Bell (1976); Müller et al. (1978); Sabinin and Shulepov (1981); Samodurov (1982).

Desaubies (1976) suggests an analytical expression for the frequency spectrum (model GM-76). He suggests the following expression for function $A(\lambda)$:

$$A(\lambda) = \frac{2}{\pi}(1 + \lambda^2)^{-1}.$$

In this case, it is possible to obtain analytical expressions for the spectra of measured values. The moored spectrum is written as:

$$MS_\zeta(\omega) = \int_0^\infty E(k, \omega)\overline{Z^2}dk = \frac{2}{\pi} r \frac{f}{N(z)} \frac{(\omega^2 - f^2)^{1/2}}{\omega^3} = \frac{2}{\pi} \frac{E\,\overset{\wedge}{b^2}\hat{N}f(\omega^2 - f^2)^{1/2}}{N(z)\omega^3}.$$

The expression for the towed spectrum is:

$$TS_\zeta(k) = \frac{2}{\pi} \int_f^N \overline{Z^2 d\omega} \int_k^\infty E(k, \omega)(k' - k)dk' = \left(\frac{2}{\pi}\right)^3 rt \frac{f}{N(z)} \left(\ln\frac{N(z)}{f} - \frac{N^2(z) - f^2}{2N^2(z)}\right)k^{-2}$$

$$= \left(\frac{2}{\pi}\right)^3 \frac{E\,\hat{b}j}{2} \frac{f}{N(z)} \left(\ln\frac{N(z)}{f} - \frac{N^2(z) - f^2}{2N^2(z)}\right)k^{-2}.$$

These expressions depend on two parameters $t = \frac{j}{2\hat{N}\hat{b}}$ and $r = \hat{N}E\overset{\wedge}{b^2}$. One can vary these parameters and tune the model spectrum for different conditions. The

sense of these parameters is approximately the same as E and j, respectively. No restrictions are needed for the exponential character of the vertical profile of the Brunt-Väisälä frequency as the GM-72 model requires. This model has the advantage that it is needed to specify the values of E and j. In some regions of the ocean, for example, in the Sargasso Sea the values of $\hat{N}$ and $\hat{b}$ cannot be determined because the vertical profile of the Brunt-Väisälä frequency cannot be approximated by an exponent. In 1973, the Internal Wave Experiment (IWEX) was carried out in the Sargasso Sea. This was a three-mooring deployment forming a tetrahedron 6 km wide. The apex was located at a depth of 600 m. It made possible the calculation of 38 spectra and 1406 cross-spectra on different scales. On this basis Müller, Olbers, and Willebrand (1978) constructed a model similar to GM-72, but this model allowed a slight anisotropy. They found that 20 modes were excited at low frequencies, and their number gradually decreased to 10 at high frequencies. The decay laws were slightly different, and greater concentration of energy was found at the inertial frequency than suggested in the GM-72 model.

The characteristic features of all models of the frequency spectra are energy increase near the inertial frequency, decay of spectra proportional to ω^{-2}, and sharp decay at the Brunt-Väisälä frequency. The main disadvantage of these models is the lack of the peak at the tidal frequency.

A peculiarity exists in the high-frequency spectrum range, which not all models describe. This is an increase in the energy level at frequencies slightly lower than the Brunt-Väisälä frequency compared to the decay proportional to ω^{-2} (Munk 1980; Sabinin and Shulepov 1981; Cairns 1975; van Haren 2005b). This occurs due to the peculiarities of internal wave behavior near the turning point where $\omega = N(z)$. Desaubies (1973, 1975) showed that if we present the solution as Airy functions, this behavior can be explained by the phase coincidence of the incident and reflected waves near the layer where the wave frequency becomes equal to the Brunt-Väisälä frequency. Munk (1980) showed that intense wave interaction occurs here; hence the energy and coherence increase.

Internal wave spectrum in the ocean based on the measurements is quasi-stationary in time and space. The state of perturbation induced by internal waves in the ocean is much more stable than the surface perturbations induced by surface waves. This is clear, because the wind being a strong and variable energy source is active over the surface. All models of the background state of the spectrum characterize the mean state of the ocean perturbed by internal waves. However, they do not suggest any mechanism forming the universal spectrum of internal waves. The existence of such a spectrum without the assumptions of the GM models is doubtful.

Numerous investigations show that tidal interactions and wind are the main sources of internal wave generation (Garrett and Kunze 2007; Munk 1966; Munk and Wunsch 1998). Both forcing factors do not generate short-period internal waves directly. First, internal tides and inertial oscillations are generated and then packets of short-period waves appear after the transfer of energy over the cascade of scales to high-frequency range. In the frequency range of internal waves

background waves are generated, which are described by the Garrett-Munk spectrum. It was shown on the basis of numerical experiments by Sugiyama et al. (2009) that the Garrett-Munk spectrum is maintained only under the condition that energy is transferred to the ocean from wind at frequencies close to the inertial and from tidal forcing at tidal frequencies. If both energy sources exist, nonlinear interactions between internal waves lead to the fact that the resulting spectrum appears close to the Garrett-Munk spectrum. The ratio of energies transferred at the inertial and tidal frequencies is not very important. If one of the sources is lacking, the level of the resulting spectrum would be lower than the GM spectrum. This actually happens in tideless seas and under ice cover (Ivanov and Serebryany 1982; Morozov et al. 2007; Morozov and Marchenko 2012).

Internal waves observed in the upper layer of the ocean significantly differ from those in the deep layers (Garrett and Munk 1979). The Garrett-Munk model does not correlate well with the experimental spectra in the upper layer due to sharp vertical variations in the Brunt-Väisälä frequency and the existence of energy sources due to interaction with the atmosphere. The wave field cannot be stationary and homogeneous because the mean state of the upper ocean is not stationary and homogeneous. There is a strong interaction between waves in the upper layer. A strong energy supply from the surface excludes the hypothesis about wave anisotropy. A model was suggested by Roth et al. (1981), in which the energy of internal waves in the upper ocean consists of the energy of the basic state described by the Garrett-Munk model and the energy from additional sources at the surface. It is likely that direct excitation of internal waves by wind is low (Levine 1983). However, internal waves in the upper layer are quite intense. This was reported for the first time by Pinkel (1975) based on the data of measurements from the *Flip* vessel. Pinkel noted that internal waves in the upper layer are more energetic and narrow-band.

The measurements of Sabinin (Sabinin 1973; Brekhovskikh et al. 1975) showed that high-frequency internal waves in the upper ocean layer are non-stationary and anisotropic. The modal structure of such waves is simpler than in the deep layers, because low modes dominate. This occurs because during the generation of internal waves in a narrow seasonal thermocline standing vertical waves appear more easily than in the thick deep thermocline.

The main objective of internal wave research is the construction of a model spectra formed as a result of the energy supply from external perturbations, energy transfer over the spectrum, and dissipation. Much has been done already, but as yet we do not have any complete description of all the interactions. A method to solve this problem was suggested by McComas and Müller (1981). They studied the evolution of the Garrett-Munk spectrum under the influence of resonant interactions and their model explains many of the details. However a dynamic description of the background spectrum is needed. It is important to describe the mechanisms forming the background spectra and to determine the contributions of different processes to the dynamic of internal waves. In this sense, modeling reported by Sugiyama et al. (2009) is very interesting. The problem is difficult because internal waves exist for quite a long time compared with the time they propagate through homogeneous

regions of the environment. When the waves propagate to regions with changing background conditions their properties change. The waves slowly get energy from external sources and compensate dissipation. Therefore, it is difficult to link external influence and the dynamic response of the system.

Observations on the fluctuations of temperature, velocity, and energy, the analysis of which was performed without comparison with the Garrett-Munk model, in particular, Konyaev (1975a), Navrotsky and Filyushkin (1969), Halpern (1971), Fofonoff (1969), Voorhis (1968), Miropolskiy and Neiman (1974) show that irregular peaks appear over the general decay of spectra with frequencies in the range from the inertial to the Brunt-Väisälä frequency, if we exclude tidal frequencies. The confidence level of such peaks is low. The peaks are not stable in time and space (Morozov 1985). Vertical and horizontal correlation between fluctuations is low and changes over time (Ivanov and Morozov 1983; Siedler 1974).

When packets of internal wave perturbations appear their energy can increase by one order of magnitude. The duration of the wave packets and the periods of waves in the packets are different. The duration of wave packets can be as long as a few hours, while the dominating peaks in the packets range from tens of minutes to one or two hours. Very frequently wave packets appear in specific phases of long-period perturbations (Ziegenbein 1969, 1970). Internal tides are typical long-period perturbations that can break and decompose into packets of intense short-period waves (Haury et al. 1979; Osborne and Burch 1980; Perry and Schimke 1965). A model of the generation of internal lee wave packets when a current overflows a topographic obstacle was suggested by Maxworthy (1979). Breaking inertial oscillations can be another source of short-period waves. Short-period internal waves in intense wave packets are characterized by low-modal structure, narrow bandwidth and anisotropy (Konyaev and Sabinin 1973, 1992).

1.3   Generation of Internal Waves

Any perturbation that displaces water particles from the equilibrium generally generates internal waves. Therefore, the internal wave spectrum is wide and continuous. If displaced from the equilibrium the stratified water medium responds to the perturbation by the generation of free internal waves. The initial amplitudes of such waves are close to the amplitude of the perturbing force, while the phase velocities are determined by the parameters of the environment. Various processes can generate initial amplitudes of internal waves. The ocean and the atmosphere interact at the water surface. The energy is transferred to the ocean by winds, the heating of the surface, and moving regions of high and low pressure (anticyclones and cyclones). The barotropic tide is a powerful generator of internal waves.

The interaction between the barotropic tide and bottom topography is one of the most important sources of internal wave generation in the ocean. The currents of the

barotropic tide flow over the slopes of the bottom topography and obtain a vertical component that displaces the water particles, thus generating an internal wave.

Short-period internal waves are observed everywhere in the ocean. No evident sources of short-period internal waves exist. There are no clearly pronounced narrow-band peaks on the spectra of fluctuations of temperature and velocity in the ocean in the frequency range of short-period internal waves. On the other hand, any perturbation in stratified fluid generates internal waves in a wide range of frequencies. Frequently, the sources of internal waves are stratified flows that become unstable if small perturbations appear. The currents caused by long-period internal waves (including internal tides) can be considered as stratified flows, which can generate shorter internal waves.

The wind generates wind waves that induce vertical displacements of water. The divergence and convergence of wind leads to the vertical motions causing internal displacements of water particles. Heat flows propagate through the ocean surface. The surface warms and cools under the influence of solar irradiance, evaporation, and precipitation. Part of this energy is transferred to internal waves.

The problem of internal wave generation by atmospheric perturbations is very wide. Internal waves can be generated by a region of atmospheric pressure moving at a low speed similarly to the internal waves of smaller size that appear after a moving vessel (Borisenko 1975; Voit 1959; Magaard 1974; Dotsenko 1976; Cherkesov 1976). The major part of approaches to the generation of internal waves by atmospheric processes is based on resonance effects. A more general approach to this problem was suggested by Leonov and Miropolsky (1973). The field of generated internal waves in their model is a function of the atmospheric pressure spectrum.

A smaller number of publications consider the generation of internal waves by wind (Benilov et al. 1978; Miropolsky 1975a; Krauss 1976). It is likely that the direct generation of internal waves by wind does not occur (Levine 1983). Tomczak (1967) showed that internal waves can be generated by wind divergence causing vertical motions. Another mechanism was suggested by Thorpe (1975): an internal wave field appears due to the vertical velocities at the lower boundary of the upper boundary layer of the ocean under wind forcing. Internal waves can be generated by the fluctuations caused by the variations in the buoyancy flux. Magaard (1973) showed that if the sea surface temperature changes, variations of pressure appear at the lower boundary of the Ekman layer that generate internal waves.

Theoretical studies indicate that there is a possibility of internal wave (iw) generation by the nonlinear interaction of two surface waves (1 and 2). The following conditions should be observed:

$$k_{iw} = k_1 - k_2; \ \omega_{iw} = \omega_1 - \omega_2,$$

where k and ω are wavenumbers and frequencies of the corresponding waves.

The theory of such interactions was developed in Brekhovskikh et al. (1972), Nesterov (1970), Olbers and Eden (1990), but a practical confirmation can be found only in laboratory experiments (Joyce 1974). The opinions of different authors on

the reality of such internal wave generation are contradictory. Olbers and Herterich (1979) consider that the energy proportion obtained by internal waves through this mechanism is negligible.

Internal waves can be also generated at the ocean bottom. The motions of the ocean bottom caused by seismicity induce perturbations that can generate internal waves (Fedosenko and Cherkesov 1968). Such motions are not characteristic of the ocean as a whole and their contribution to the energetic balance is negligible, although individual seismic events causing tsunami waves can also generate internal waves of low intensity. Internal waves can be also generated by the tides of the solid Earth (Bogdanov and Sebekin 1976).

In the bottom layer, internal tides are generated due to the flow of stratified tidal currents over irregularities of the bottom topography. The generation of internal tides will be discussed below, but we note that the estimates of Tareev (1965) and Bell (1975) show that wave drag at the bottom is of the same order of magnitude as the wind stress at the ocean surface. It is likely that Zeilon (1911) was the first to demonstrate in laboratory experiments that currents overflowing bottom topography slopes generate baroclinic oscillations.

In addition to the generation of internal waves near the surface and bottom, their generation in the water column is very likely. Internal waves can be generated owing to the instability of large-scale currents or mesoscale eddies (Belyayev and Gezentsvey 1978; Voronovich and Goncharov 1982; Miropolsky 1975b; Frankignoul 1976; Morozov et al. 1998; Kunze and Boss 1998). However, the estimates presented by Rhines (1973) show that there is no significant energy flux between these scales. Thorpe (1975) presents an impressive picture-scheme of internal wave generation by various processes.

Internal waves can be generated as a result of the interaction between two other internal waves if the following condition is satisfied:

$$k_1 \pm k_2 \pm k_3 = 0; \quad \omega_1 \pm \omega_2 \pm \omega_3 = 0.$$

Energy transfer between waves can occur due to this effect (Voronovich 1975; Miropolsky 2001; Martin et al. 1972; McEwan 1971; Olbers 1976; Thorpe 1966).

The breaking of large-scale internal waves (tidal and inertial) can be an important source of smaller wave generation (Sawyer 1983). Wave breaking can have different causes. Waves of one mode can break in the stratified flow of another wave. It was shown by Orlanski and Bryan (1969) that instability leading to wave breaking can appear in places where the orbital velocity of water particles exceeds the phase velocity of the wave. After breaking, the wave energy can transfer to turbulent kinetic energy, to the potential energy of the wave column after mixing, or to the energy of waves of smaller scale generated during breaking. This phenomenon was reported by Garrett and Munk (1972b). Polzin et al. (1997) analyzed turbulent mixing in the Brazil Basin and found that it is small over abyssal plains and increases significantly over the slopes of the Mid-Atlantic Ridge. The authors associate it with the breaking of internal waves generated over the steep slopes. High-amplitude internal waves over steep underwater slopes were reported by

Sabinin et al. (1987), Sabinin and Serebryany (2005) and Vlasenko and Morozov (1993).

The waves can break due to the shear instability of stratified currents of the wave motion. The mean flow shear needed for breaking is estimated from the Richardson number (decreasing of the Richardson number below 1/4). The Richardson number $Ri = \frac{N^2(z)}{(du/dz)^2}$ shows the relative contribution of stratification and velocity shear to stability, which is described by the Taylor–Goldstein equation for modeling Kelvin–Helmholtz instability caused by the shear flow of a stratified flow. If the Richardson numbers are small, velocity shear overwhelms the stability of stratified fluid; thus wave breaking, mixing, and the generation of small-scale internal waves occurs. Unstable stratified currents of a larger-scale internal wave can generate smaller waves. If the Richardson numbers are large, stratification usually suppresses turbulence (Miles 1961; Garrett 1968; Turner 1973).

A decrease in the Richardson number may appear at the moments when velocity shear caused by the superposition of many waves results in the critical shear. This condition may appear at random spatial locations, but it needs to be maintained for some time for instability to develop (Garrett and Munk 1972b).

Thus, as a result of larger wave breaking its energy is transferred to waves of smaller scale and other smaller scale processes, in particular, to turbulence. The cascade energy transfer from greater scales to smaller scales has not been well studied. Olbers and Pomphrey (1981) showed theoretically that resonance three-wave interaction and scattering over bottom irregularities are insignificant in the energy balance of internal waves in the ocean.

Müller and Olbers (Müller 1976; Müller and Olbers 1975) suggested considering internal waves as energy sink from the energy of mesoscale motions. Large-scale vertical velocity shear in a stratified flow feeds internal waves with energy and maintains their energy balance. The internal wave field is similar to viscosity, against which large-scale motion works, for example, mesoscale eddies. Energy from breaking eddies is transferred to internal waves (Brown and Owens 1981; Morozov et al. 1998). There are contradictions among researches about the importance of this mechanism (Frankignoul 1976; Frankignoul and Joyce 1979). Internal waves may be produced directly by mesoscale eddies, along with the submesoscale eddies in the same spatial-temporal scales range (McWilliams 2016). It is likely that this effect can be observed if the energy of eddies is sufficiently high. Experimental attempts to find this effect statistically failed (Ruddick and Joyce 1979).

Moving sea ice may also generate internal waves, especially in summer when a fresh and warm upper layer exists. Internal waves change air-ocean drag, and their instability leads to enhanced turbulent mixing in the mixed layer (McPhee and Kantha 1989).

1.4   Some Mathematical Tools of Data Processing and Modeling

1.4.1   Vlasenko Numerical Model

We use the fully nonlinear non-hydrostatic model of baroclinic tides developed by Vlasenko (1992). In its complete form this model is presented in Vlasenko et al. (2002, 2005).

   We consider a two-dimensional (x, z) flow in a continuously stratified rotating ocean of variable depth. Then, internal waves are described by the following set of equations:

$$\Omega_t + J(\Omega, \Psi) - fV_z = \frac{g\rho_x}{\rho_0} + K(x)\Omega_{xx} + K\Omega_{zz} + (K\Psi_{zz})_z$$

$$V_t + J(V, \Psi) + f\,\Psi_z = K(x)V_{xx} + (KV_z)_z \qquad (1.34)$$

$$\rho_t + J(\rho, \Psi) + \frac{\rho_0 N^2(z)}{g}\Psi_x = R(x)\rho_{xx} + (R\rho_z)_z + (R\rho_{0_z})_z$$

where Ψ is the stream function $(\Psi_z = u; \Psi_x = -w)$, $\Omega = \Psi_{xx} + \Psi_{zz}$ is the vorticity, (U, V, W) is the velocity vector, N is the Brunt-Väisälä frequency, ρ is the density disturbance due to the wave motion, ρ_0 is the mean density, f is the Coriolis parameter, K, $K(x)$, R, and $R(x)$ are the vertical and horizontal coefficients of turbulent viscosity and mass diffusivity, J is the Jacobian and g is the acceleration due to gravity.

   Although the model is two-dimensional, we introduce the equation for the V-component of velocity normal to the x, z plane to account for the effects of rotation. However, the V-component is considered constant. For convenience, the equation of density diffusion has been used instead of the equations of heat and salt diffusion.

   The boundary conditions at the surface located at z = 0 are:

$$\rho_z = 0, \ \Omega = 0, \ \ \Psi = 0 \qquad (1.35)$$

and hence, no tangential stresses are considered. We also consider zero vertical motion and no heat and salt transport through the surface.

   At the bottom, no heat, salt, and mass transports exist:

$$\text{at } z = -H(x), \ \partial\rho/\partial n = 0, \ \Psi = \Psi_0 \sin \omega t \qquad (1.36)$$

where ω is the tidal frequency, n denotes the unit vector normal to the bottom and Ψ_0 is the amplitude of the mass transport in a barotropic tidal current. The boundary condition for vorticity at the bottom is calculated using equation $\Omega = \Delta\Psi$ with the value of the Ψ field obtained at the previous time step.

The wave perturbations of vorticity, stream function, and density are assumed zero at the lateral boundaries located far from the bottom irregularities at the submarine ridge. We stop the calculations when the wave perturbations reach the lateral boundaries. The phase velocity of the perturbations does not exceed 2–3 m/s, which allows us to continue the calculations for a suitable number of time steps.

The calculations start from a state of rest when the fluid at the bottom is motionless, and the isopycnals are horizontal; hence: at $t = 0$: $\Omega = 0$, $\rho = 0$, $\Psi = 0$.

The bottom topography was introduced in the model from the data of navigation charts and from the digital databases of bottom topography. Continuous stratification was specified with the values of the Brunt-Väisälä frequency in each of the layers calculated on the basis of CTD-profiling.

The vertical step in the model varies with depth but the number of levels remains equal to the initial value (20–40), and it does not change with the changing depth. The thickness of the layers is reduced in the depth intervals with strong stratification; it is increased, where the stratification is weak, by introducing a new variable:

$$z_1 = \int_0^z N(s)ds / \int_0^{-H(x)} N(s)ds, \qquad (1.37)$$

where z_1 is a new variable describing depth, z is the old depth variable, $N(s)$ is the depth dependent Brunt-Väisälä frequency, s is a dummy variable for differentiating by the vertical to the current depth level, and $H(x)$ is the depth of the ocean. This transformation allows us to convert a curvilinear grid, caused by irregular bottom topography to a rectangular one (the new coordinates are termed σ-coordinates). After the end of calculations we make a back transformation to present the results in the usual form.

A semi-implicit numerical scheme utilizes a rectangular grid with second order approximations of the spatial derivatives and first order approximations of the temporal derivatives in every temporal semi-layer. At each time step, the implicit system, which is a tri-diagonal matrix, is solved using standard techniques.

We specify a density field unperturbed by internal waves corresponding to the vertical distribution of the Brunt-Väisälä frequency $N(z)$ from observations. We model the following physical phenomenon. A long barotropic tidal wave propagates from the open ocean to the continental slope or submarine ridge. The tidal currents flow over the topographic obstacles and obtain a vertical component. Periodically oscillating vertical components with a tidal period displace water particles; thus a tidal internal wave is generated. The input parameters of the model are stratification, bottom topography, and stream function of the tidal current. The model outputs the fields of density and velocity over the domain of calculations. See Sects. 2.1, 6.1, 6.3, 7.6, 7.8 as examples.

1.4.2   Spatiotemporal Spectrum

We used the method developed for seismological problems and applied by Barber to ocean waves to estimate the wavelength and direction of internal tides (Barber 1963). We assume that the sensors are located randomly over the study sites.

The method is based on the calculation of the cross-spectra for each pair of the possible combinations of sensors with further convolution at the frequency of the waves under study. The spectra are calculated using the Fourier transformation of the correlation function as described by Blackman and Tukey (1958). The amplitude and phase cross-characteristics of the oscillation are used to calculate the spatiotemporal spectra at the wave frequency and estimate the components of the horizontal wavenumber.

The method basically accounts for the statistical phase difference between each pair of wave sensors. In the estimates presented in this book, we used the temperature sensors, which reflect the vertical motion induced by internal waves assuming that the vertical gradients of temperature are significant. It is important that the distance between the moorings should be comparable with the wavelength of the oscillations under study. Otherwise uncertainty appears in the interpretation of the phase differences if the distance between the sensors is too large. If the distance between the sensors is too small and the span of the array of sensors is smaller than the wavelength due to a limited number of sensors it is impossible to resolve the wavelength correctly.

If moored temperature measurements are available at the same depth at several points in the ocean, we can calculate cross-spectra of fluctuations P and Q (co-spectrum and quadratic spectrum). Next, we perform a transformation for the M_2 semidiurnal tidal frequency f_0 to determine the distribution of the mutual spectral energy at this frequency with respect to wavenumbers K_x and K_y.

So far we do not have a continuous spectrum of distances, but instead, we have a finite set of definite distances corresponding to the distances between the moored stations; the calculation of a spatial spectrum at f_0 frequency was carried out using the following formula:

$$E(k_x, k_y, f_0) = 2 \sum_{i=1}^{n-1} \sum_{j=i+1}^{n} [P_{ij}(f_0) \cos 2\pi(k_x x_{ij} + k_y y_{ij}) - Q_{ij}(f_0) \sin 2\pi(k_x x_{ij} + k_y y_{ij})],$$

$$(1.38)$$

where $k_x^2 + k_y^2 = k^2$ is the spatial wavenumber, while the wavelength L is: $L = 1/k$; i, j are the sequential numbers of the sensors, n is the total number of the sensors; P_{ij} and Q_{ij} are the real and imaginary parts of the cross-spectrum between the sensors with numbers i and j; $x_{ij} = X_i - X_j$ and $y_{ij} = Y_i - Y_j$ are the projections of the distances between the sensors on the horizontal axes x and y.

Usually, the number of sensors is small. Each sensor is installed on a mooring. The number of moorings deployed in the study sites rarely exceeds 10. Hence the

shape of the spectral peak is not a delta-function but has a finite width. Usually, the spatiotemporal spectra of internal tides with semidiurnal frequency (or possibly, other frequencies) are presented as contour lines of percentage normalized by the maximum value.

1.4.3 Dispersion Relation

We can estimate the wavelength of internal tide on the basis of the dispersion relation. We assume that these calculations are valid if the bottom is flat and no forcing exists beyond the slopes of the bottom topography. We can estimate the wavelength of the internal tide by numerical integration of the equation for vertical velocity (*w*) caused by internal waves with zero boundary conditions for vertical velocity at the surface and bottom (LeBlond and Mysak 1978, see Sect. 1.1, Eq. 1.28):

$$\frac{d^2 w}{dz^2} + \frac{N^2(z)}{g}\frac{dw}{dz} + \frac{N^2(z) - \omega^2}{\omega^2 - f^2} w k^2 = 0, \qquad (1.39)$$

where $N^2(z)$ is the squared Brunt-Väisälä frequency based on the CTD data; ω is the semidiurnal frequency, f is the Coriolis parameter, and k is the horizontal wavenumber. We usually integrate this equation with a vertical step of 10 m at the given ocean stratification. The wavenumbers obtained in the solution of this eigen function problem correspond to the modes of internal tides. We can judge the mode number by the number of zero crossings of the eigen function. Mode one has no zero crossings (only zero values at the bottom and surface), mode two has one zero crossing, etc.

1.5 General Notes on Internal Tides

Oceanic internal tides are usual internal waves of high amplitude and energy with quasi-tidal periodicity. Their frequency is equal to the frequency of the corresponding barotropic tide. Actually, internal tides are not tidal waves, which are directly generated by the gravity forces of the Moon and Sun. They are generated in the ocean when the currents of the barotropic tide flow over the slopes of bottom topography and obtain a vertical component. However, internal tides occupy a special place among the other internal waves owing to their high energy and some other very important properties.

The first description of internal waves was given by B. Franklin. He described the waves at the interface between oil and water in a ship's lantern. In 1762, he wrote: "… looking on the lamp, I remarked that tho' the surface of the oil was perfectly tranquil, and duly preserved its position and distance with regard to the

brim of the glass, the water under the oil was in great commotion, rising and falling in irregular waves."

The first observations of internal tides in the ocean were performed by F. Nansen (Helland-Hansen and Nansen 1909; Nansen 1902) using observations with water sampling bottles. The results of the observations were described by Pettersson (1908). A few years later observations with Nansen water bottles and bathythermographs revealed internal tidal waves in various regions of the ocean. After the discovery of the internal tides, the observations have been continuing for tens of years. Thus, it was shown and proved that this phenomenon exists almost everywhere in the ocean (Defant 1932; Fjelstad 1933; Rudnic and Cochrane 1951; Emery 1956; Reid 1956; La Fond 1961; Summers and Emery 1963; Lee and Cox 1966; Weston and Reay 1969; Rooth and Düing 1971).

Detailed research of this phenomenon and estimates of the scales and parameters required special measurements and observations. Further measurements of temperature and currents in the ocean on moored buoys confirmed the existence of strong oscillations at tidal periods (Cairns and La Fond 1966; Halpern 1971; Maeda 1971; Schott 1971; Wunsch and Hendry 1972; Wunsch and Dahlen 1974; Gulev and Bolshakov 1979; Matygin et al. 1982; Bolshakov and Sabinin 1983). Reviews of publications and their analysis were published by Wunsch (1975a, b) and Schott (1977). The calculation of spectra of temperature and velocity fluctuations in various regions of the ocean at different depths showed that clearly manifested peaks at the semidiurnal and diurnal frequencies are found everywhere. As a rule, the semidiurnal peak is higher. These fluctuations (vertical displacements of water particles) are maximal in the middle of the water column and significantly exceed the fluctuations of the sea surface height. The estimates show that approximately one third of all vertical displacements associated with internal waves are related to internal tides (Gregg and Briscoe 1979).

Internal tidal waves appear to be one of the main mechanisms of barotropic tide dissipation, which leads to mixing in the ocean. Internal tides cause vertical displacements of isopycnals that are usually of the order of a few tens of meters, but sometimes exceed one hundred meters. A typical amplitude of the internal tide is within 10–20 m. Internal tides influence engineering constructions in the ocean such as oil platforms and pipelines (Osborne and Burch 1980); they also influence the propagation of acoustic signals (Dushaw 2006) and transport sediments at the ocean bottom (Cacchione et al. 2002; McPhee-Shaw 2006). They can influence the motion of submarine vessels. Internal waves influence the mean state of the ocean. Before applying the field CTD data for numerical modeling, the data of quasi-synchronous CTD surveys of study sites in the ocean should be averaged to minimize the distortions induced by internal waves that displace isopycnal surfaces. The shear of horizontal currents related to internal waves leads to the generation of short-period internal wave packets; this causes variations in the mean state of the ocean and the generation of turbulence. One of the main roles of internal waves in the ocean is the transport of energy in the vertical direction from the surface and the redistribution of energy in the horizontal plane.

Garrett and Kunze (2007) suggested three key dimensionless parameters governing the generation of internal tides: the ratio of tidal excursion of water particles to the scale of the topography, the ratio of the bottom slope to the angle, at which rays of internal waves of tidal frequency propagate, and the ratio of the height of the topography to the depth of the ocean. Beams of internal tides are observed close to the generation region. As the distance from the sources increases, the higher modes lose their energy, which concentrates in the first modes; then, the propagation of internal tides in the form of beams is gradually displaced by the lower modes.

Tidal currents can generate internal waves not only with the tidal periods. For example, tidal currents over topographic obstacles can cause lee waves with periods shorter than the tidal period and shorter wavelengths. The small horizontal scale of underwater obstacles is an important condition for such generation. The scale should be smaller than the length of the major axis of the tidal oscillation of water particles.

Internal waves of tidal periods can rapidly degenerate into smaller scale waves. The period of the appearance of packets of short-period waves is equal to the tidal period. The effect of the generation of short-period waves is especially strong in the coastal regions of the ocean (Haury et al. 1979; Holloway 1987, 1996; Holloway et al. 1997; Klymak and Gregg 2004; Lamb 1994; Matsuura and Hibiya 1990; Rippeth and Inall 2002; Sandström and Elliott 1984; Vlasenko et al. 2005). The generation of short-period packets decreases in the deep ocean where the tidal currents are not as strong as in the coastal regions. Generally the periods of tidal internal waves have the same frequencies as the barotropic tides determined by astronomical processes.

The theory of internal tide generation was developed in the 1960s and 1970s (Cox and Sandström 1962; Rattray 1960; Prinsenberg and Rattray 1975; Prinsenberg et al. 1974; Baines 1973; Bell 1975). The generation of internal tides was summarized in reviews (Wunsch 1975a, b; Baines 1982; Schott 1977). The modern concepts about the problems of internal tide generation were later summarized by Garrett and Kunze (2007).

The most intense generation of internal tides occurs over submarine slopes when their inclination is close to the inclination of internal tide characteristics $\left(s = \sqrt{\frac{\omega^2 - f^2}{N^2 - \omega^2}} \right)$ (Baines 1982; Holloway and Merrifield 1999; Johnston and Merrifield 2003). Usually this happens in the upper parts of submarine ridges and in the region of the shelf break (Hibiya 2004). Vertical shear increases this effect (Hibiya 1990). Elongated bottom features increase the resulting energy flux compared to seamounts (Holloway and Merrifield 1999). The barotropic flow tends to go around symmetric seamounts producing only a weak internal tide. If the barotropic flow crosses an elongated ridge it is forced across isobaths, generating an energetic internal tide. Changing the horizontal aspect ratio of the topography from 1:1 (a seamount) to 3:1 (a ridge) increases the resulting baroclinic energy flux by nearly an order of magnitude (Holloway and Merrifield 1999). The effect of the Earth's rotation even in the straits is important (Katsumata and Hibiya 2002).

In the earlier publications (Bell 1975) it was estimated that approximately 10% of the energy losses of the barotropic tide in the deep ocean transfers to internal waves. However, many authors considered that even this 10% was an important contribution to the mixing in the deep ocean (Garrett and Munk 1979; Wunsch 1975a). In addition, Wunsch (1975a) considered that this estimate was too low. The later publications of Sjöberg and Stigebrandt (1992) and Morozov (1995) increased the energy dissipation of the barotropic tide over submarine ridges to 25% of the total losses. The review papers by Munk and Wunsch (1998) and Garrett (2003) emphasize the role of mid-oceanic ridges in the generation of internal tides. The mapping of the tidal elevation over the entire World Ocean by Egbert and Ray (2000, 2001) resulted in the estimates of the total rate of tidal energy dissipation at 2.5 TW (1 TW = 10^{12} W) for the lunar semidiurnal tide M_2, 3.2 TW for all lunar tides, and 3.7 TW if solar tides are included. Only a small portion of this energy (0.2 TW) is dissipated in the atmosphere and solid Earth (Egbert and Ray 2001). Later estimates reported by Egbert and Ray (2003) indicate that the total dissipation of the M_2 tide is 2.43 TW, of which 1.65 TW dissipates in the shallow seas and 0.78 TW in the deep ocean. Kantha and Tierney (1997) suggest on the basis of altimetric observations that the total energy of the M_2 baroclinic tide is 50 PJ, while the dissipation is 360 GW (3.6×10^{11} W).

The increased interest in deep-ocean internal tides coincided with the increased interest in ocean mixing in the 1990s and 2000s (Samelson 1998; Wunsch and Ferrari 2004). This interest was furthered by the possibility of mapping tidal elevation using satellite altimetry. These observations strongly supported the theory of the generation of internal tides over submarine ridges and their propagation from the regions of generation over long distances. For example, the propagation of internal tides from the Hawaiian Ridge is clearly shown by Ray and Mitchum (1997).

Research on the generation of internal tides is ongoing. Garrett and Kunze (2007) come to the conclusion that low modes dominate in the radiated energy flux from large steep mid-ocean ridges and island chains. The height of bottom topography features has a greater influence on the energy flux than the details of the bottom slope. Regions of the critical slope are sources of intense beams of internal tide energy, and their contribution to the low modes is greater than to the high modes. If lower modes encounter topographic obstacles, for example, islands, deep slopes, or rough sea floor their energy can be transferred to higher modes again (Johnston et al. 2003; Johnston and Merrifield 2003; St. Laurent and Garrett 2002). Their energy can be transferred to smaller-scale internal waves in the ocean interior (MacKinnon and Winters 2005; Polzin 2004; St. Laurent and Garrett 2002; van Haren 2005b). Radiating beams can become nonlinear as they encounter strong near-surface stratification, leading directly to turbulence (Althaus et al. 2003) or breaking up into groups of higher frequency, short wavelength, nonlinear internal waves far from the original source (Gerkema 2001; New and da Silva 2002).

Continental slopes may be significant sinks rather than just sources of internal tide energy. Some of the internal tide energy flux from large topographic features in

mid-ocean propagates across ocean basins and later breaks on distant continental slopes (Nash et al. 2004).

Many more publications discuss the generation of internal tides and suggest models and mechanisms of internal tide generation. A theoretical work by Khatiwala (2003) shows that the presence of an upper reflecting surface can significantly reduce the rate of transfer of the barotropic tidal energy to the internal wave field. This reduction is particularly large for extended topographic features. Numerical experiments by Mohri et al. (2010) on tidal interactions with small-scale topographic features show that the stratified fluid response over abyssal bottom topography can be categorized into four dynamical regimes depending on two dimensionless parameters related to tidal advection and buoyancy. Steady internal tide waves are generated during a short interval of the maximum tidal flow. The effect of non-hydrostatic barotropic flow was considered by Garrett and Gerkema (2007). The effect is slight for internal tides but can be significant for higher frequency motions. The analysis of surface tide/internal tide decomposition from pressure and velocity measurements was reported by Kelly et al. (2010). This method makes possible a more exact calculation of the depth structure of internal tide energy flux.

Numerical experiments reported by Legg (2004a, b) show that the internal tides generated at the shelf break by cross-slope barotropic tidal currents can generate high vertical wavenumber structure in the velocity field in the presence of a corrugated bottom oriented so that ridges and valleys run up and down the slope. This high-wavenumber structure cannot exist if the Coriolis force is ignored.

An increasing number of models have appeared that numerically analyze the generation of internal tides. The authors vary topographic width, amplitude of the barotropic tide, and stratification (Qian et al. 2010). The results show that a large amount of energy is converted from the barotropic tide to the baroclinic wave when the slope coincides with the wave slope. Internal wave generation is most efficient in the presence of strong upper-ocean stratification over a steep tall ridge. Interaction between remotely generating shoaling internal tides and surface tide velocities can generate or destroy internal tides. The theory of this mechanism and measurements confirming it on the New Jersey shelf were reported by Kelly and Nash (2010). Sometimes internal tides are not related to local forcing. Episodic increases in internal tide energy and energy flux appear intermittently in 3–5 day bursts. The generation of internal tides in the deep ocean beneath turning depths, which exist in some very deep regions of the ocean, was discussed by Paoletti et al. (2014). Internal waves become evanescent but still the generation of weak internal tides occurs.

A model developed by Chuang and Wang (1981) deals with the effects of a density front on the generation of internal waves on a continental margin. The authors consider the horizontal stratification that maintains a geostrophic current. The influence of the density front on the generation of internal tides is particularly strong when the front is located above the continental slope. In this case the topographic effect is reduced.

Fluctuations of ocean currents at tidal frequencies are caused by the joint influence of the barotropic tide and internal waves. The barotropic tide contribution to the temperature and salinity fluctuations at tidal frequencies is very small. Therefore, analysis of temperature fluctuations is more demonstrative in the research of internal tides and other internal waves.

Observations of internal tides in the open ocean are hampered by the fact that the ratio of their amplitude to noise is frequently low. The measured signal from the waves of close frequencies may block the signal of internal tides. Processes of lower frequencies (mesoscale eddies) of high energy may displace the frequency of internal tides to the neighboring frequencies due to the Doppler effect, and a weak signal would not be discerned.

Internal tides are found practically everywhere in the ocean. Observations show that their energy is not constant in time. This fact is not related to the properties of internal waves only, because the existence of alternating energy in time may be caused by the presence or absence of other signals or by the influence of the mean state of the ocean (stratification, currents, vorticity, etc.).

When we measure temperature fluctuations, we can be quite sure that the main contribution to the temperature fluctuations with the tidal periods is made by the internal tides. As to the measurements of horizontal velocities, differentiation between the barotropic tide and internal tide is difficult. Separation of these processes requires a set of measurements over one vertical line. Since phase velocity of internal tides is not high (it is of the order of 1 m/s) they are subjected to the influence of the Doppler effect. This leads to the diffusion of the energy of internal tides around the exact frequency of the tide. Variations in the mean state of the ocean in the region of generation and over the pathway of its propagation lead to the same effects.

Many authors of publications on tidal internal waves share the viewpoint that low modes dominate. This property of internal tides makes them different from the rest of the frequency range of internal waves, which is described by the Garrett-Munk model (1972a). Many other properties of internal tides, for example, anisotropy do not satisfy the concepts of this model. Contradictions with the model are not surprising. The authors did not take into account the source of internal tides in the frequency range considered in the model, and excluded them from the model.

The problem of the mode structure of semidiurnal internal waves has yet to be solved so far. There is no common agreement among researchers about the mode structure. In a number of papers the authors interpret the data so that several lower modes dominate (Makshtas and Sabinin 1972; Tareev 1965; Sabinin 1982; Sabinin et al. 1977; Bukatov et al. 1978). The opposite point of view is that mode structure does not always satisfactorily describe the real wave structure especially near the source of generation and it is more correct to use the beam interpretation (Regal and Wunsch 1973; Torgrimson and Hickey 1979; Lyashenko and Sabinin 1979; Matygin et al. 1982; Barbee et al. 1975; Serebryaniy 1985).

Let us consider the problem of internal tide generation from the point of view of scales. The length of an internal tidal wave is of the order of 100 km. The horizontal scale of the forcing tidal mass force is $2\pi R \cos\varphi/p$, where R is the radius of

the Earth, φ is latitude, p is a parameter equal either to 1 or 2 for the diurnal and semidiurnal tide. The ratio of the horizontal scales of these two processes is of the order of 10^2–10^3. The ratio of the differences in the densities of layers for the barotropic tide is 1 (between air and water), while the ratio for the internal tide is 10^{-3}. The difference in the scales of phenomena indicates that direct interaction between internal waves and tidal forcing is low. An exception can probably occur at the latitudes where the frequency of tidal oscillations is close to the inertial frequency; hence, the generation of waves is possible in the case of resonance over shallow depths (Foux 1982).

Internal tides are the oceanic response to the forced oscillations of isopycnals by the vertical components of the barotropic tide, which appear over underwater slopes. A numerical model of internal tide generation over the shelf was published by Prinsenberg et al. (1974) and Rattray et al. (1969). Propagation of the barotropic tide over the slopes of the bottom topography generates a "beam" of energy radiated from the shelf break. These numerical models are further developments of the analytical model by Rattray (1960) on internal wave generation over the shelf.

Cox and Sandström (1962) estimated the influence of small variations in the bottom topography on the energy transfer from the barotropic tide to internal tides. This model was further developed in Mork (1968), Hendershott (1973), Blackford (1978) and Bell (1975). In some works, the authors made an attempt to measure internal tides in the regions where the bottom topography should facilitate the intense generation of internal tides (Magaard and McKee 1973; Regal and Wunsch 1973; Schott and Willebrand 1973; Wunsch and Hendry 1972). Their hypotheses were correct. Internal tides in these regions appeared strong. Gould and McKee (1973) showed that according to the theory of Baines (1974, 1982) the maximum generation of the M_2 and S_2 internal tides over the continental slope in Biscay Bay does not occur at the same locations.

Investigations at the end of the 20th century proved that the interaction of tidal currents with various inhomogeneities of the mean ocean state (not only with the slopes of the bottom topography) can lead to the generation of internal tides. Such inhomogeneities should have a significant horizontal scale to produce this effect. For example, elevations of isopycnals in mesoscale eddies can play the role of such inhomogeneities of the mean ocean state. Their horizontal scale is comparable with the wavelength of the internal tide (Golubev et al. 1979).

The problem of internal tide generation is important for the understanding of ocean dynamics and its energetic balance. The transformation of barotropic tide energy to the energy of the internal tide is still a problem in the global balance of tidal energy (Cartwright 1977; Hendershott 1973; Munk 1997; Munk and Wunsch 1998). This problem is being solved step by step. Early estimates of the dissipation of tidal energy in shallow seas indicate that it is of the order of 1.4–1.7 $\times 10^{12}$ W (Miller 1966). It is approximately one third of the tidal energy dissipation 4.3–5.0 $\times 10^{12}$ W (Cartwright 1977; Olbers 1983). Later estimates result in a smaller value of the barotropic tide dissipation (Munk and Wunsch 1998). According to the estimates by Egbert (1997) and Egbert and Ray (2000) the energy dissipation is 1.6–2.0 $\times 10^{12}$ W, while 0.6–0.8 $\times 10^{12}$ W dissipate in the deep ocean. The energy transfer from the

barotropic tide to internal waves occurs over inhomogeneities of the bottom topography. Baines (1982) estimated the energy dissipation of the barotropic tide over continental slopes, which in total results in approximately 1% of the barotropic tide energy dissipation. Bell (1975) estimated the dissipation of the barotropic tide energy over rough topography of the deep ocean as 10% of its total energy dissipation. Sjöberg and Stigebrandt (1992) and Morozov (1995) reported that the energy dissipation of the barotropic tide to internal tide over submarine ridges is approximately 25% of the total losses. The commonly accepted balance of the barotropic tide energy does not exist. The problem requires further investigation.

Since the internal tide is generated by the currents of the barotropic tide it should inherit the property of the spring-neap variability with a period of 14 days. In addition, the diurnal and semidiurnal internal tides should separate into a set of waves as the barotropic tide does. These problems are understudied. The authors of a few publications conclude that the internal tide inherited these properties from the barotropic tide (Gould and McKee 1973). These problems require detailed research.

1.6   Observations of Internal Tides in Different Regions of the Ocean

We shall consider properties of internal tides in different regions of the ocean. Semidiurnal internal tides are observed in almost all regions of the ocean. Their amplitude is always significantly greater than the background internal waves characterized by the Garrett-Munk (1972a) model. Numerous measurements of internal waves in the ocean, theoretical researches, satellite observations, and numerical modeling have given us such an understanding of the process that it has become possible to study the mechanisms responsible for the distribution of the energy of internal tides over oceanic basins.

We assume that the regions of submarine ridges and continental slopes are generators of internal tides. We shall consider the properties of internal tides in each region with respect to the location of the region relative to the nearest submarine ridge, continental slopes, or other features of the bottom topography. In addition to the analysis of the spectra of temperature fluctuations and amplitudes of vertical displacements characteristic of each region of measurements we shall consider variations of spectra over the scale of the study region and vertical and horizontal coherences of temperature fluctuations and where possible two-dimensional spatiotemporal spectra at the semidiurnal frequency.

According to the theoretical conclusions (Baines 1982; Rattray et al. 1969), internal perturbations are initially generated in the form of beams directed to the bottom and surface. Then, after reflections from the surface and bottom they gradually fill the entire water column and form the mode structure of waves. The vertical wave vectors in different packets (propagating upwards and downwards) compensate each other leading to the formation of vertically standing waves.
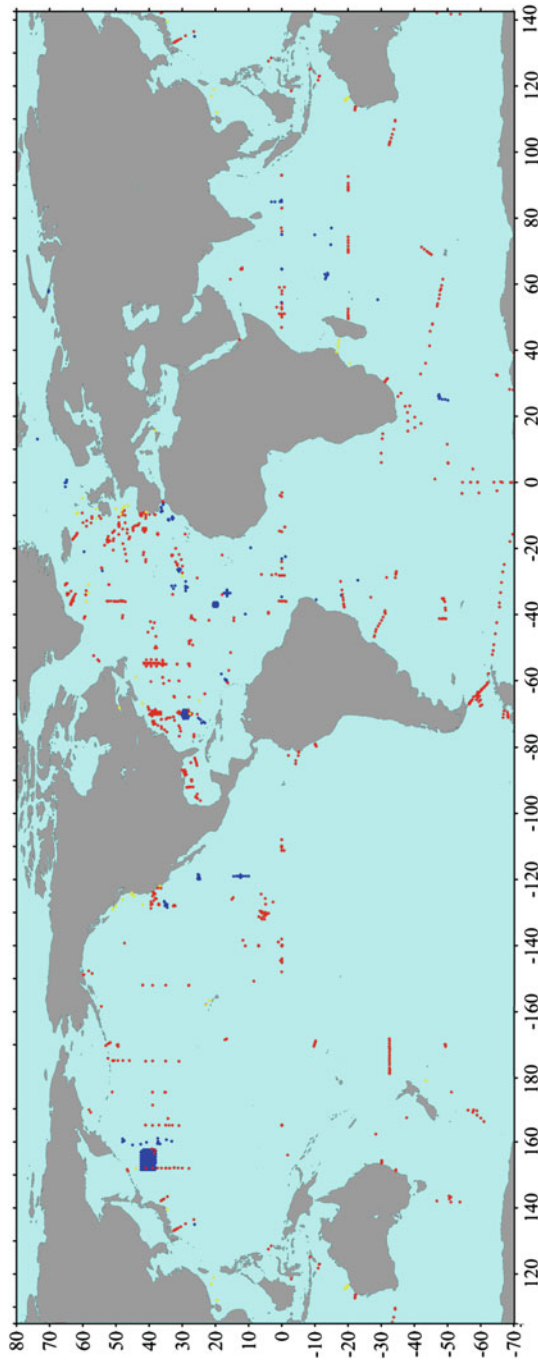
Fig. 1.2 Locations of moorings in the World Ocean, the data from which were used in our research. Locations of measurements collected and analyzed with the participation of the author are shown with blue dots. Locations of measurements only analyzed by the author are shown with red dots. Locations of measurements reported in the literature and reviewed here are shown with yellow dots
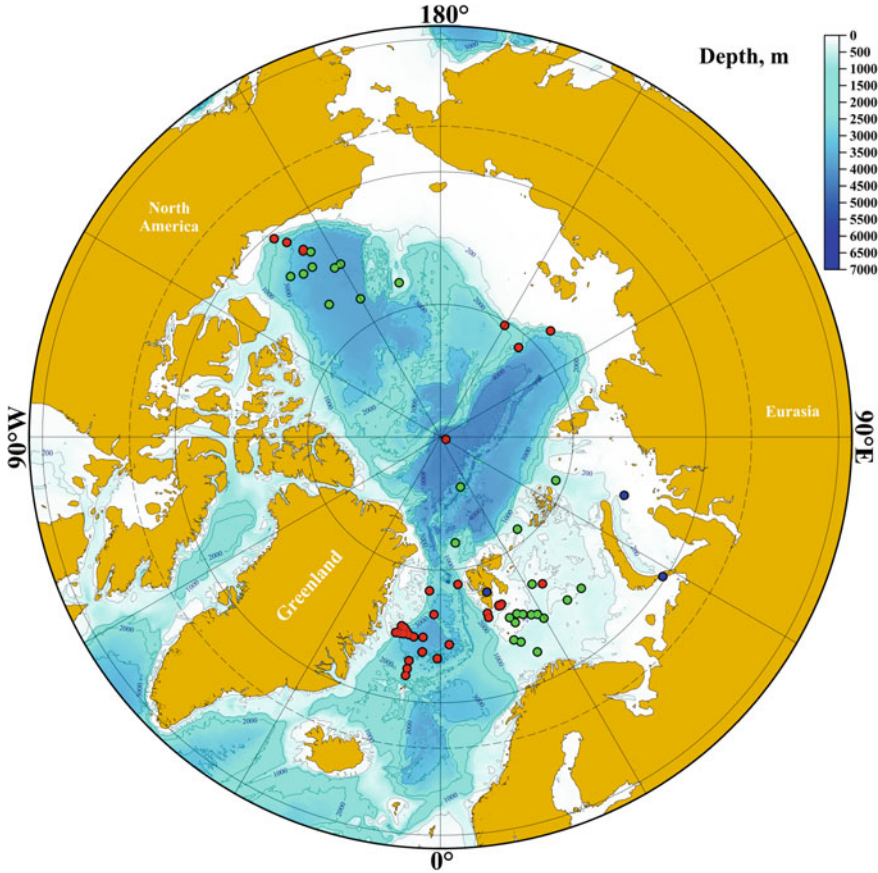
Fig. 1.3 Locations of moorings in the Arctic Ocean. Locations of measurements collected and analyzed with the participation of the author are shown with blue dots. Locations of measurements only analyzed by the author are shown with red dots. Locations of measurements reported in the literature and reviewed here are shown with green dots

The main generation source of internal fluctuations is usually located approximately at the highest point of the continental slope where the shelf break starts or at the top of submarine ridges or seamounts (Baines 1982). The intensity of generated oscillation increases if the depth of the sharp vertical gradients of temperature and density in the seasonal pycnocline is close to the point of the sharp depth increase. Two types of waves are generated. A wave similar to the surface wave is generated in the layer of the seasonal pycnocline. Under the interface layer, packets of waves appear that propagate over sloping trajectories (Baines 1982); these are beams of internal waves. One beam is directed along the slope of the bottom topography downwards and the other propagates to the ocean surface.

Below, we shall consider observations in different research sites of the World Ocean. A chart of locations of moorings in the ocean analyzed in this research is

shown in Fig. 1.2. A separate chart of locations of moorings in the Arctic Ocean is shown in Fig. 1.3. The data of many moorings were downloaded from the WOCE Current Meter Data Assembly Center (CMDAC) operated by Oregon State University (OSU). The CMDAC dataset consists both of current meter records gathered as part of WOCE and historical records.

References

Althaus AM, Kunze E, Sanford TB (2003) Internal tide radiation from Mendocino Escarpment. J Phys Oceanogr 33:1510–1527

Baines PG (1973) The generation of internal tides by flat-bump topography. Deep-Sea Res 20:179–205

Baines PG (1974) The generation of internal tides over steep continental slopes. Phil Trans Roy Soc London Ser A 277:27–58

Baines PG (1982) On internal tide generation models. Deep-Sea Res 29(3):307–338

Barbee WB, Dworski JG, Irish JB, Larsen LN, Rattray M (1975) Measurements of internal waves of tidal frequency near a continental boundary. J Geophys Res 80(15):1965–1974

Barber NF (1963) The directional resolving power of an array of wave detectors. In: Ocean wave spectra. Prentice Hall, Engelwood Cliffs, NJ, pp 137–150

Bell TH (1975) Topographically generated internal waves in the open ocean. J Geophys Res 80 (3):320–327

Bell TH (1976) The structure of internal wave spectra as determined from towed thermistor chain measurements. J Geophys Res 81(21):3709–3714

Belyayev VS, Gezentsvey AN (1978) Shear instability of internal waves in the ocean, Izv. Acad. Sci. USSR, Ser. Atmosph Oceanic Phys 14(6):459–463

Benilov AY, Solntseva NI, Filyushkin BN (1978) Relationship between the variability of the wind field and internal waves. Oceanology 18(3):257–266

Blackford BL (1978) On the generation of internal waves by tidal flow over a sill—a possible nonlinear mechanism. J Mar Res 36(3):529–549

Blackman RB, Tukey JW (1958) The measurements of power spectra from the point of view of communications engineering. Dover, NY

Bogdanov KT, Sebekin BI (1976) Generation of internal tides and the influence of Earth's tides on tidal motions in the ocean, Izv. Acad. Sci. USSR, Ser. Atmosph Oceanic Phys 12(5):326–329

Bolshakov VN, Sabinin KD (1983) Mean characteristics of semidiurnal tidal currents in Polygon-70 and their variability. Izv. Acad. Sci. USSR, Ser. Atmosph Oceanic Phys. 19(1):51–56

Borisenko YD (1975) Generation of internal waves in a two-layer fluid by a travelling pressure system. Izv. Acad. Sci. USSR, Ser. Atmosph Oceanic Phys 11(6):411–413

Brekhovskikh LM, Goncharov VV, Kurtepov VM, Naugolnykh KA (1972) Resonant excitation of internal waves by nonlinear interaction of surface waves. Izv. Acad. Sci. USSR, Ser. Atmosph Oceanic Phys 11(6):411–413

Brekhovskikh LM, Konjaev KV, Sabinin KD, Serikov AN (1975) Short-period internal waves in the sea. J Geophys Res 80(3):856–864

Brown ED, Owens B (1981) Observations of the horizontal interactions between the internal wave field and the mesoscale flow. J Phys Oceanogr 11(11):1474–1480

Bukatov AE, Kushnir VM, Smirnov GV (1978) Tidal-period internal waves in the equatorial zone of the Indian Ocean. Oceanology 18(5):514–519

Cacchione DA, Pratson LF, Ogston AS (2002) The shaping of continental slopes by internal tides. Science 296:724–727

Cairns JL (1975) Internal wave measurements from a mid-water float. J Geophys Res 80(C3):299–306

Cairns JL, La Fond EC (1966) Periodic motions of the seasonal thermocline along the southern California coast. J Geophys Res 71(16):903–3916

Cairns JL, Williams GO (1976) Internal wave observations from a mid-water float. J Geophys Res 81(C12):1943–1950

Cartwright DE (1977) Oceanic tides. Rep Prog Phys 40:665–708

Cherkesov LV (1976) Hydrodynamics of surface and internal waves. Naukova Dumka Publishers, Kiev, p 363 (in Russian)

Chuang W-S, Wang D-P (1981) Effects of a density front on the generation and propagation of internal tides. J Phys Oceanogr 11(10):1357–1374

Cox CS, Sandström H (1962) Coupling of internal and surface waves in water of variable depth. J Oceanogr Soc Jpn 20th anniversary volume, 499–513

Defant A (1932) Die Gezeiten und inheren Gezeiten-wellen des Atlantischen Ozeans. Wiss. Ergebn. Dt. Atlant. Exoed. "Meteor" 1925–1927. Bd. 7. H. 1. 313 s

Desaubies YJF (1973) Internal waves near the turning point. Geophys Fluid Dyn 5(1):143–154

Desaubies YJF (1975) A linear theory of internal wave spectra and coherences near the Väisälä frequency. J Geophys Res 80:895–899

Desaubies YJF (1976) Analytical representation of internal wave spectra. J Phys Oceanogr 6 (6):976–981

Dotsenko SF (1976) Non-stationary internal waves generated by periodical pressure forcing. Proc Marine Hydrophys Inst 2(73):48–60

Dushaw BD (2006) Mode-1 internal tides in the western North Atlantic Ocean. Deep-Sea Res 53 (3):449–473

Egbert GD (1997) Tidal data inversion: interpolation and inference. Prog Oceanogr 40:53–80

Egbert GD, Ray RD (2000) Significant dissipation of tidal energy in the deep ocean inferred from satellite altimeter data. Nature 405:775–778

Egbert GD, Ray RD (2001) Estimates of M_2 tidal energy dissipation from TOPEX/Poseidon altimeter data. J Geophys Res 106:22475–22502

Egbert GD, Ray RD (2003) Semidiurnal and diurnal tidal dissipation from TOPEX/Poseidon altimetry. Geophys Res Lett 30(17):1907. https://doi.org/10.1029/2003GL017676

Emery KO (1956) Deep standing internal waves in California basins. Limnol Oceanogr 1(1):35–41

Fedosenko VS, Cherkesov LV (1968) Internal waves generated by underwater earthquakes. Izv. Acad. Sci. USSR, Ser. Atmosph Oceanic Phys 4(11):1197–1203

Fjelstad JE (1933) Interne Wellen. Geophys Publication, Oslo

Fofonoff NP (1969) Spectral characteristics of internal waves in the ocean. Deep-Sea Res 16 (Suppl.):58–71

Foux VR (1982) An introduction to the theory of wave motions in the ocean. Leningrad State University Publishing House, Leningrad, p 199 (in Russian)

Frankignoul C (1976) Observed interaction between oceanic internal waves and mesoscale eddies. Deep-Sea Res 23(9):805–820

Frankignoul C, Joyce TM (1979) On the internal wave variability during the internal wave experiment (IWEX). J Geophys Res 84(C2):769–776

Garrett C (1968) On the interaction between internal gravity waves and a shear flow. J Fluid Mech 34:711–720

Garrett C (2003) Internal tides and ocean mixing. Science 301:1858–1859

Garrett C, Gerkema T (2007) On the body-force term in internal-tide generation. J Phys Oceanogr 37(8):2172–2175

Garrett C, Kunze E (2007) Internal tide generation in the deep ocean. Annual Rev Fluid Mech 39:57–87

Garrett CJR, Munk WH (1972a) Space-time scales of internal waves. Geophys Fluid Dyn 3 (3):225–264

Garrett C, Munk W (1972b) Oceanic mixing by breaking internal waves. Deep-Sea Res 19 (12):823–832

Garrett C, Munk W (1975) Space-time scales of internal waves: a progress report. J Geophys Res 80(3):291–297

Garrett C, Munk W (1979) Internal waves in the ocean. Ann Rev Fluid Mech 11:339–369

Gerkema T (2001) Internal and interfacial tides: beam scattering and local generation of solitary waves. J Marine Res 59:227–255

Golubev YN, Ivanov VF, Cherkesov LV (1979) Generation of internal tides by the interaction of a barotropic wave with an elevation of isopycnal surface. In: Surface and internal waves. Sebastopol, pp 195–203 (in Russian)

Gould WJ, McKee WD (1973) Observations of the vertical structure of semidiurnal tidal currents in the Bay of Biscay. Nature 224:88–91

Gregg MC, Briscoe MG (1979) Internal waves, finestructure, microstructure, and mixing in the ocean. Rev Geophys Space Phys 17(7):1524–1547

Gulev SK, Bolshakov VN (1979) Study of internal tide field isotropy, Vestnik. MGU. Geogr Ser 5:8–11

Halpern D (1971) Observations on short-period internal waves in Massachusetts Bay. J Mar Res 29(2):116–132

Haury LR, Briscoe MG, Orr MH (1979) Tidally generated internal wave packets in Massachusetts Bay. Nature 278:312–317

Helland-Hansen B, Nansen F (1909) The Norwegian Sea. Rep Norw Fish Marine Invest 2(1/2):1–64

Hendershott MC (1973) Inertial oscillations of tidal period. Prog Oceanogr 6:1–27

Hibiya T (1990) Generation mechanism of internal waves by a vertically sheared tidal flow over a sill. J Geophys Res 95:1757–1764. https://doi.org/10.1029/JC095iC02p01757

Hibiya T (2004) Internal wave generation by tidal flow over a continental shelf slope. J Oceanogr 60(3):637–643

Holloway PE (1987) Internal hydraulic jumps and solitons at a shelf break region on the Australian North West shelf. J Geophys Res 92(C5):5405–5416

Holloway PE (1996) A numerical model of internal tides with application to the Australian North West shelf. J Phys Oceanogr 26(1):21–37

Holloway PE, Merrifield MA (1999) Internal tide generation by seamounts, ridges, and islands. J Geophys Res 104(C11):25937–25951

Holloway PE, Pelinovsky EN, Talipova TG, Barnes B (1997) A nonlinear model of internal tide transformation on the Australian North West shelf. J Phys Oceanogr 27:871–896

Ivanov YA, Morozov EG (1983) Investigations of temperature fluctuations at tidal and inertial periods. In: Atlantic Hydrophysical Polygon-70. Amerind Co. Oxonian Press Ltd., New Delhi, pp 289–299

Ivanov VA, Serebryany AN (1982) Frequency spectra of shortperiod internal waves in a nontidal sea. Izv. Acad. Sci. USSR, Ser. Atmosph Oceanic Phys 18(6):527–529

Johnson WR, Sanford TB (1980) Anomalous behavior of internal gravity waves near Bermuda. J Phys Oceanogr 10(2):2021–2034

Johnston TMS, Merrifield MA (2003) Internal tide scattering at seamounts, ridges, and islands. J Geophys Res 108(C6):3180. https://doi.org/10.1029/2002JC001528

Johnston TMS, Merrifield MA, Holloway PE (2003) Internal tide scattering at the Line Islands Ridge. J Geophys Res 108(C11):3365. https://doi.org/10.1029/2003JC001844

Joyce TM (1974) Nonlinear interactions among standing surface and internal gravity waves. J Fluid Mech 63(4):801–825

Kantha LH, Tierney CC (1997) Global baroclinic tides. Prog Oceanog 40:163–178. https://doi.org/10.1016/S0079-6611(97)00028-1

Katsumata K, Hibiya T (2002) Internal wave generation by tidal flow over a sill in a rotating channel. J Geophys Res 107(C10):3176. https://doi.org/10.1029/2001JC001096

Katz EJ, Briscoe MG (1979) Vertical coherence of the internal wave field from towed sensors. J Phys Oceanogr 9(3):518–530

Kelly SM, Nash JD (2010) Internal-tide generation and destruction by shoaling internal tides. Geophys Res Lett 37:L23611. https://doi.org/10.1029/2010GL045598

Kelly SM, Nash JD, Kunze E (2010) Internal-tide energy over topography. J Geophys Res 115: C06014. https://doi.org/10.1029/2009JC005618

Khatiwala S (2003) Generation of internal tides in an ocean of finite depth: analytical and numerical calculations. Deep-Sea Res 50(1):3–21

Klymak JM, Gregg MC (2004) Tidally generated turbulence over the Knight Inlet sill. J Phys Oceanogr 34(5):1135–1151

Konyaev KV (1975a) An experimental study of short-period internal sea waves. Izv. Acad. Sci. USSR, Ser. Atmosph Oceanic Phys 11(3):170–176

Konyaev KV, Sabinin KD (1973) New data on internal waves in the sea measured using distributed temperature sensors. Dokl Akad Nauk SSSR 209(1):86–89

Konyaev KV, Sabinin KD (1992) Waves inside the ocean. Gidrometeoizdat, Saint Petersburg, p 272 (in Russian)

Konyaev KV, Serebryany AN (1983) Internal waves in the shelf zone of the sea during a storm. Oceanology 23(4):421–423

Krauss W (1966) Interne Wellen. Gebrüder Borntraeger, Berlin-Nikolasee

Krauss W (1976) On currents, internal, and inertial in a stratified ocean due to variable winds. Dt Hyrdogr Ztschr 29(3):87–96

Kunze E, Boss E (1998) A model for vortex-trapped internal waves. J Phys Oceanogr 28 (10):2104–2115

Kushnir VM, Andryushchenko EG (1977) Nonstationary characteristics of short-period internal gravity waves in the ocean. Izv. Acad. Sci. USSR, Ser. Atmosph Oceanic Phys 13(11):844–845

La Fond EC (1961) Isotherm follower. J Mar Res 19(1):33–39

Lamb KG (1994) Numerical experiments of internal wave generation by strong tidal flow across a finite amplitude bank edge. J Geophys Res 99:843–864

St. Laurent LS, Garrett C (2002) The role of internal tides in mixing the deep ocean. J Phys Oceanogr 32(10):2882–2899

LeBlond PH, Mysak LA (1978) Waves in the ocean. Elsevier oceanographic series. Elsevier, Amsterdam, p 602

Lee WH, Cox CS (1966) Time variation of ocean temperature and its relation to internal waves and oceanic heat flow measurements. J Geophys Res 71(8):2101–2111

Legg S (2004a) Internal tides generated on a corrugated continental slope. Part I: cross-slope barotropic forcing. J Phys Oceanogr 34(1):156–173

Legg S (2004b) Internal tides generated on a corrugated continental slope. Part II: along-slope barotropic forcing. J Phys Oceanogr 34(8):1824–1838

Leonov AI, Miropolsky YZ (1973) Resonant excitation of internal gravity waves in the ocean by atmospheric pressure fluctuations. Izv. Acad. Sci. USSR, Ser. Atmosph Oceanic Phys 9 (8):480–485

Levine MD (1983) Internal waves in the ocean. Rev Geophys Space Phys 21(5):1206–1216

Lyashenko AF, Sabinin KD (1979) On the spatial structure of the internal tides on the 1970 hydrophysical test range in the Atlantic. Izv. Acad. Sci. USSR, Ser. Atmosph Oceanic Phys 15 (8):595–601

MacKinnon JA, Winters KB (2005) Subtropical catastrophe: significant loss of low-mode tidal energy at 28.9°. Geophys Res Lett 32(15):L15605. https://doi.org/10.1029/2005GL023376

Maeda A (1971) Phase velocity of semidiurnal internal waves at ocean weather station T. J Oceanogr Soc Jpn 27(4):163–174

Magaard L (1973) On the generation of internal gravity waves by a fluctuating buoyancy flux at the sea surface. Geophys Fluid Dyn 5(2):101–111

Magaard L (1974) On the generation of internal gravity waves by meteorological forces. Mem Soc Roy Sci Liege 6:79–84

Magaard L, McKee WD (1973) Semidiurnal tidal current at "site D". Deep-Sea Res 20(11):993–1010

Makshtas AP, Sabinin KD (1972) Relation of the oscillations of sound scattering depth with internal waves in the ocean. Oceanology 12(4):746–749

Martin S, Simmins W, Wunsch C (1972) The excitation of resonant triads by single internal wave. J Fluid Mech 53(1):17–44

Matsuura T, Hibiya T (1990) An experimental and numerical study of the internal wave generation by tide-topography interaction. J Phys Oceanogr 20(4):506–521

Matygin AS, Sabinin KD, Filonov AE (1982) Average spatial spectra of internal tides on the 1970 Atlantic hydrophysical test range. Izv. Acad. Sci. USSR, Ser. Atmosph Oceanic Phys 18(2): 129–133

Maxworthy T (1979) A note on the internal solitary waves produced by tidal flow over a three-dimensional ridge. J Geophys Res 84(C1):338–342

McComas CH, Müller P (1981) Time scales of resonant interactions among oceanic internal waves. J Phys Oceanogr 11(8):970–986

McEwan A (1971) Generation of resonantly excited standing internal gravity waves. J Fluid Mech 50(3):431–448

McPhee MG, Kantha LH (1989) Generation of internal waves by sea ice. J Geophys Res 94 (C3):3287–3302

McPhee-Shaw E (2006) Boundary–interior exchange: reviewing the idea that internal-wave mixing enhances lateral dispersal near continental margins. Deep-Sea Res II 53(1–2):42–59

McWilliams JC (2016) Submesoscale currents in the ocean. Proc Roy Soc London A 472:20160117. http://dx.doi.org/10.1098/rspa.2016.0117. Last accessed Oct 2017

Miles JW (1961) On the stability of a heterogeneous shear flow. J Fluid Mech 10(4):495–509

Miller G (1966) The flux of tidal energy out of the deep oceans. J Geophys Res 71(10):2485–2489

Miropolskiy YZ (1975b) Influence of shear flow on the generation of short-period internal waves in the ocean. Izv. Acad. Sci. USSR, Ser. Atmosph Oceanic Phys 11(9):585–589

Miropolskiy YZ, Neiman VG (1974) Internal waves and temperature microstructure in the Timor Sea. Izv. Acad. Sci. USSR, Ser. Atmosph Oceanic Phys 10(11):730–736

Miropolsky YZ (1975a) Generation of internal waves in the ocean by the wind field. Oceanology 15(5):519–532

Miropolsky YZ (2001) Dynamics of internal gravity waves in the ocean. In: Shishkina O (ed) Springer, Berlin

Mohri K, Hibiya T, Iwamae N (2010) Revisiting internal wave generation by tide-topography interaction. J Geophys Res 115:C11001. https://doi.org/10.1029/2009JC005908

Mork M (1968) On the formation of internal waves caused by tidal flow over a bottom irregularity. Rep Geophys Inst Univ, Bergen, Norway, p 28

Morozov EG (1985) Oceanic internal waves. Nauka, Moscow, p 151 (in Russian)

Morozov EG (1995) Semidiurnal internal wave global field. Deep-Sea Res 42(1):135–148

Morozov EG, Marchenko AV (2012) Short-period internal waves in an Arctic fjord (Spitsbergen). Izvestiya Atmos Ocean Phys 48(4):401–408. https://doi.org/10.1134/S0001433812040123

Morozov EG, Pelinovsky EN, Talipova TG (1998) Exceedance frequency for internal waves during the Mesopolygon-85 experiment in the Atlantic. Oceanology 38(4):521–527

Morozov EG, Shchuka SA, Zapotyl'ko VS (2007) Towed spectra of internal waves in the pycnocline of the Baltic Sea. Dokl. Earth Sci 412(1):151–153. https://doi.org/10.1134/S1028334X07010357

Mowbray DE, Rarity BSH (1967) Theoretical and experimental investigation of the phase configuration of internal waves of small amplitude in a density stratified liquid. J Fluid Mech 28(1):1–16

Müller P (1976) On the diffusion of momentum and mass by internal gravity waves. J Fluid Mech 77(4):789–823

Müller P, Olbers DJ (1975) On the dynamics of internal waves in the deep ocean. J Geophys Res 80(27):3848–3860

Müller P, Olbers DJ, Willebrand J (1978) The IWEX spectrum. J Geophys Res 83(C1):479–500

Munk WH (1966) Abyssal recipes. Deep-Sea Res 13:207–230

Munk WH (1980) Internal wave spectra at the buoyant and inertial frequencies. J Phys Oceanogr 10:1718–1728

Munk WH (1997) Once again: once again—tidal friction. Prog Oceanogr 40:7–35

Munk WH, Wunsch C (1998) Abyssal recipes II: energetics of tidal and wind mixing. Deep-Sea Res 45:1977–2010

Nansen F (1902) Oceanography of the North Pole basin: Norwegian North Pole expedition, 1893–1896. Scientific results. Longmans and Green, Toronto, pp 1–427

Nash JD, Kunze E, Toole JM, Schmitt RW (2004) Internal tide reflection and turbulent mixing on the continental slope. J Phys Oceanogr 34(5):1117–1134

Navrotsky VV, Filyushkin BN (1969) Statistical analysis of time fluctuations of temperature in the surface layer of the sea. Izv. Acad. Sci. USSR, Ser. Atmosph Oceanic Phys 5(7):408–412

Nesterov SV (1970) Resonance generation of internal waves. Izv. Acad. Sci. USSR, Ser. Atmosph Oceanic Phys 6(7):437–441

New AL, da Silva JCB (2002) Remote-sensing evidence for the local generation of internal soliton packets in the central Bay of Biscay. Deep-Sea Res 49:915–934

Olbers DJ (1976) Nonlinear energy transfer and the energy balance of the internal wave field in the deep ocean. J Fluid Mech 74(2):375–398

Olbers DJ (1983) Models of the oceanic internal wave field. Rev Geophys Space Phys 21 (7):1567–1606

Olbers D, Eden C (1990) Revisiting the generation of internal waves by resonant interaction with surface waves. J Phys Oceanogr 20(8):2335–2350

Olbers DJ, Herterich K (1979) The spectral energy transfer from surface waves to internal waves in the ocean. J Fluid Mech 92(2):349–380

Olbers DJ, Pomphrey N (1981) Disqualifying two candidates for the energy balance of oceanic internal waves. J Phys Oceanogr 11(10):1423–1425

Orlanski I, Bryan K (1969) Formation of the thermocline step-structure by large amplitude internal gravity waves. J Geophys Res 74(28):6975–6983

Osborne AR, Burch TL (1980) Internal solitons in the Andaman Sea. Science 208(4443):451–459

Paoletti MS, Drake M, Swinney HL (2014) Internal tide generation in non-uniformly stratified deep oceans. J Geophys Res 119:1943–1956. https://doi.org/10.1002/2013JC009469

Perry RB, Schimke GR (1965) Large amplitude internal waves observed off the north-west coast of Sumatra. J Geophys Res 70(10):2319–2324

Pettersson O (1908) Strömstudier vid Östersjönsportar. Sven Hydrogr Biol Komm Skr 3:13–37

Phillips OM (1977) The dynamics of the Upper Ocean, 2nd edn. Cambridge University Press, NY, p 336

Pinkel R (1975) Upper ocean internal wave observations. J Geophys Res 80(27):3892–3910

Polzin K (2004) Idealized solutions for the energy balance of the finescale internal wave field. J Phys Oceanogr 34:231–246

Polzin KL, Toole JM, Ledwell JR, Schmitt RW (1997) Spatial variability of turbulent mixing in the abyssal ocean. Science 276:93–96

Prinsenberg S, Rattray M (1975) Effects of continental slope and variable Brunt-Väisälä frequency on the coastal generation of internal tides. Deep-Sea Res 22:251–263

Prinsenberg SJ, Wilmot WL, Rattray M (1974) Generation and dissipation of coastal internal tides. Deep-Sea Res 21(4):263–281

Qian H, Shaw P-T, Ko DS (2010) Generation of internal waves by barotropic tidal flow over a steep ridge. Deep-Sea Res 57(12):1521–1531

Rattray M (1960) On the coastal generation of internal tides. Tellus 12:54–62

Rattray M, Dworsky J, Kovala P (1969) Generation of long internal waves at the continental slope. Deep-Sea Res 16(Suppl.):179–195

Ray RD, Mitchum GT (1997) Surface manifestation of internal tides in deep ocean: observations from altimetry and island gauges. Prog Oceanogr 40:135–162

Regal R, Wunsch C (1973) M_2-tidal currents in the western North Atlantic. Deep-Sea Res 20 (5):493–502

Reid JL (1956) Observations of internal tides in October 1950. Trans Am Geophys Union 37 (3):15–20

Rhines P (1973) Observation of the energy containing ocean eddies and theoretical models of waves and turbulence. Boundary Layer Meteorol 4(10):345–360

Rippeth TP, Inall ME (2002) Observations of the internal tide and associated mixing across the Malin Shelf. J Geophys Res 107(C4):3028. https://doi.org/10.1029/2000JC000761

Rooth C, Düing W (1971) On the detection of inertial waves with pycnocline followers. J Phys Oceanogr 1(1):12–16

Roth MW, Briscoe MG, McComas CH (1981) Internal waves in the upper ocean. J Phys Oceanogr 11(9):1234–1247

Ruddick BR, Joyce TM (1979) Observations of interactions between the internal wave field and low frequency flows in the North Atlantic. J Phys Oceanogr 9(3):498–517

Rudnic P, Cochrane JD (1951) Diurnal fluctuations in bathythermograms. J Mar Res 3:257–261

Sabinin KD (1973) Certain features of short-period internal waves in the ocean, Izv. Acad. Sci. USSR, Ser. Atmosph Oceanic Phys 9(1):32–36

Sabinin KD (1982) High frequency internal wave spectra in the equatorial Indian Ocean. Oceanology 22(6):672–683

Sabinin KD, Serebryany AN (2005) Intense internal waves in the ocean. J Mar Res 59:327–353. https://doi.org/10.1357/002224001762842235

Sabinin KD, Serikov AN (1974) Results from the measurements of the space-time characteristics of short-period internal waves in the tropical Atlantic. Izv. Acad. Sci. USSR, Ser. Atmosph Oceanic Phys 10(10):650–657

Sabinin KD, Shulepov VA (1981) Model of the frequency spectrum of internal waves in the ocean, Izv. Acad. Sci. USSR, Ser. Atmosph Oceanic Phys 17(1):48–54

Sabinin KD, Shulepov VA, Filonov AE (1977) Spatial characteristics of tidal internal waves in the Iberian Basin. Izv. Acad. Sci. USSR, Ser. Atmosph Oceanic Phys 13(8):588–593

Sabinin KD, Nazarov AA, Serikov AN (1987) Study of high amplitude internal waves near steep bottom rises, Izv. Acad. Sci. USSR, Ser. Atmosph Oceanic Phys 23(11):879–886

Samelson RM (1998) Large-scale circulation with locally enhanced vertical mixing. J Phys Oceanogr 28:712–726

Samodurov AS (1982) Model of the climatic spectrum of internal waves in the ocean. Oceanology 22(2):130–133

Sandström H, Elliott JA (1984) Internal tide and solitons on the Scotian Shelf: a nutrient pump at work. J Geophys Res 89(C4):6415–6426. https://doi.org/10.1029/JC089iC04p06415

Sawyer C (1983) Tidal phase of internal wave generation. J Geophys Res 88(4):2642–2648

Schott F (1971) On the horizontal coherence and internal wave propagation in the North Sea. Deep-Sea Res 18(3):291–308

Schott F (1977) On the energetics of baroclinic tides in the North Atlantic. Ann Geophys 33:41–62

Schott F, Willebrand J (1973) On the determination of internal wave directional spectra from moored instruments. J Mar Res 31(2):116–134

Serebryaniy AN (1985) Internal waves in the coastal zone of a tidal sea. Oceanology 25(5):574–578

Siedler G (1974) Observations of internal wave coherence in the deep ocean. Deep-Sea Res 21 (8):597–610

Sjöberg B, Stigebrandt A (1992) Computations of the geographical distribution of the energy flux to mixing process via internal tides and the associated vertical circulation in the ocean. Deep-Sea Res 39:269–291

Stevenson TN (1968) Some two-dimensional internal waves in a stratified fluid. J Fluid Mech 33 (4):715–720

Sugiyama Y, Niwa Y, Hibiya T (2009) Numerically reproduced internal wave spectra in the deep ocean. Geophys Res Lett 36:L07601

Summers HJ, Emery KO (1963) Internal waves of tidal period off Southern California. J Geophys Res 68(3):827–840

Tareev BA (1965) Baroclinic internal waves induced during overflow of bottom irregularities and their influence on sedimentation in the ocean. Oceanology 5(1):45–52

Tareev BA (1966) Dynamics of internal gravity waves in a continuously stratified ocean. Izv. Acad. Sci. USSR, Ser. Atmosph Oceanic Phys 2(10):1064–1075

Thorpe SA (1966) On wave interactions in a stratified fluid. J Fluid Mech 24(4):737–751

Thorpe SA (1975) The excitation, dissipation, and interaction of internal waves in the deep ocean. J Geophys Res 80(3):328–338

Tomczak M (1967) Uber den Einfluss fluktulerender Windfelder auf ein stetig geschichtetes Meer. Dt Hydrogr Ztschr 20(3):101–129

Torgrimson GM, Hickey BM (1979) Barotropic and baroclinic tides over the continental slope and shelf off Oregon. J Phys Oceanogr 9:945–961

Turner JS (1973) Buoyancy effects in fluids. Cambridge, Cambridge University Press

van Haren H (2005b) Internal waves near the buoyancy frequency in a narrow wave-guide. Deep-Sea Res 53:121–129

Vlasenko VI (1992) Nonlinear model for the generation of baroclinic tides over extensive inhomogeneities of bottom topography. Phys Oceanogr (Morskoy gidrofizicheskiy zhurnal) 3:417–424

Vlasenko VI, Morozov EG (1993) Generation of semidiurnal internal waves near a submarine ridge. Oceanology 33(3):282–286

Vlasenko V, Stashchuk N, Hutter K (2002) Water exchange in fjords induced by tidally generated internal lee waves. Dyn Atmosph Oceans 35(1):63–83

Vlasenko V, Stashchuk N, Hutter K (2005) Baroclinic tides: theoretical modeling and observational evidence. Cambridge, Cambridge University Press, p 351

Voit SS (1959) Waves at the interface between two fluids generated by a travelling pressure system. Proc Marine Hydrophysical Inst 17:33–40 [in Russian]

Voorhis AD (1968) Measurements of vertical motion and partition of energy in the New England slope water. Deep-Sea Res 15(5):599–608

Voronovich AG (1975) Resonance, three-wave interaction between internal waves. Oceanology 15(5):773–780

Voronovich AG, Goncharov VV (1982) Influence of large-scale motions on the propagation of short internal waves. Izv. Acad. Sci. USSR, Ser. Atmosph Oceanic Phys 18(1):55–60

Weston DE, Reay WW (1969) Tidal-period internal waves in a tidal stream. Deep-Sea Res 16 (5):473–478

Wunsch C (1975a) Deep ocean internal waves: what do we really know? J Geophys Res 80 (3):339–343

Wunsch C (1975b) Internal tides in the ocean. Rev Geophys Space Phys 13(1):167–182

Wunsch C, Dahlen J (1974) A moored temperature and pressure recorder. Deep-Sea Res 21:145–154

Wunsch C, Ferrari R (2004) Vertical mixing, energy, and the general circulation of the oceans. Ann Rev Fluid Mech 36:281–314. https://doi.org/10.1146/annurev.fluid.36.050802.122121

Wunsch C, Hendry R (1972) Array measurements of the bottom boundary layer and internal wave field on the continental slope. Geophys Fluid Dyn 4(2):101–145

Wunsch C, Webb S (1979) The climatology of deep ocean internal waves. J Phys Oceanogr 9 (2):235–243

Zeilon N (1911) On tidal boundary waves and related hydrodynamical problems. Kgl sven vetenskapsakad handl 47(4):1–46

Ziegenbein J (1969) Short internal waves in the Strait of Gibraltar. Deep-Sea Res 16(5):479–488

Ziegenbein J (1970) Spatial observations of short internal waves in the Strait of Gibraltar. Deep-Sea Res 17(5):867–876

Chapter 2
Observations of Internal Tides
in the Atlantic Ocean

Abstract This chapter describes the measurements of internal tides in the Atlantic Ocean and in the Mediterranean Sea together with modeling of the generation and propagation of internal tides in some important regions of the Atlantic Ocean. The generation of internal tides is associated with the interaction of the currents of the barotropic tide with the slopes of the bottom topography. One of the most important ideas presented here is the strong generation of internal tides over submarine ridges. The generation and propagation of internal tides in the Strait of Gibraltar where the strongest internal tides on the globe exist are described. The generation of internal tides over the Mid-Atlantic Ridge in the South Atlantic is demonstrated on the basis of measurements in several regions near the ridge. The measurements reveal strong internal tides in Biscay Bay. Weaker internal tides are found in the Sargasso Sea. Measurements of internal tides on mooring clusters confirm the well known fact that internal tides are generated over the bottom slopes.

2.1 Gibraltar Strait

The Strait of Gibraltar (Fig. 2.1) is the only connection between the Atlantic Ocean and the Mediterranean Sea. The flow in the strait is characterized by a two-layer system of opposite currents that exists due to the difference in sea level and water density between the Atlantic Ocean and the Mediterranean Sea. Intense evaporation in the Mediterranean, which is estimated at 50 cm of water column per year, is compensated by a strong surface current of relatively fresher water from the Atlantic Ocean. The velocities of this flow reach 40 cm/s. The flow changes its direction at a depth of approximately 100 m. A deep-water current of more saline Mediterranean Water flows into the ocean owing to the difference in water density. The velocities of the lower current are even greater and reach 85 cm/s. The velocity maximum is close to the bottom. A barotropic tidal wave with mean velocities in the range 70–80 cm/s propagates through the strait. A profile of vertical velocity based on ADCP data is shown in the inset of Fig. 2.1.
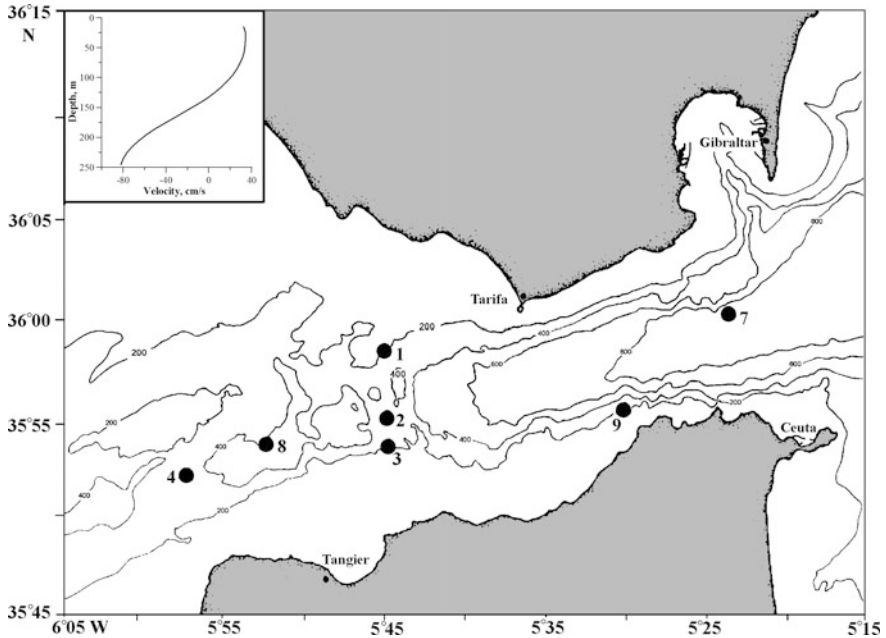
Fig. 2.1 Bottom topography (meters) in the Strait of Gibraltar. Depth contour lines are shown at depths of 200, 400, 600, and 800 m. Locations of moorings (with their numbers) during the Gibraltar experiment in 1985–1986 are shown with black dots. Land is shown with gray color. Velocity profile based on averaged ADCP measurements moored at the bottom is shown in the inset. Reproduced from Morozov et al. (2002). © American Meteorological Society. Used with permission

The barotropic tide generates an internal tidal wave when the tidal currents flow over uneven topography in the strait, especially over the Camarinal Sill located in the middle of the Strait of Gibraltar (Armi and Farmer 1988; Bryden et al. 1994). Our analysis (Morozov et al. 2002) shows that extreme tidal internal waves are observed only over the Camarinal Sill. A strong internal bore is observed in the eastern part of the strait caused by the interaction of the internal tide with the currents. The mixing caused by the decay of internal waves makes the interface between the inflowing and outflowing waters in the western part of the strait thicker than in its eastern part.

The measurements of Boyce (1975) and Bockel (1962) over the Camarinal Sill revealed that the vertical displacements caused by the internal tides may exceed 200 m. Wave packets of internal waves are recorded in the eastern part of the strait; their surface manifestations are clearly seen at the surface (Oceanography from the Space Shuttle 1996). Such packets can be seen at almost every tidal cycle. Reviews of publications about such packets are given by Watson and Robinson (1990) and Watson (1994). The period of waves is approximately 10–20 min; the width of the packet is 10–15 km. The wave heights from the foot to the crest reach 60 m.

Ziegenbein (1969, 1970) recorded a tidal bore using lines of thermistors. The largest waves break and form the microstructure (Wesson and Gregg 1988). A model suggested by Brandt et al. (1996) describes the breaking of internal tides into packets of short-period waves.

In 1986–1986, an experiment with moorings was carried out in the Strait of Gibraltar to study the flows between the Atlantic Ocean and the Mediterranean Sea. This experiment was organized by the Woods Hole Oceanographic Institution (USA). A scheme of the locations of moorings is shown in Fig. 2.1. The data from buoy 2 deployed close to the Camarinal Sill were used to study the vertical structure of the internal tidal oscillations. The instruments measuring velocity and temperature were located at nominal depths: 91, 112, 135, 182, 235, and 302 m. Due to the strong currents in the strait the instruments were subjected to large vertical displacements exceeding 60 m. The instruments were supplied with pressure sensors. This made it possible to calculate the real location of the isotherms at each time moment of measurements.

The analysis shows that the displacement of the 13 °C isotherm gives the best illustration pattern because this isotherm always remains within the depth interval of measurements on the mooring. The vertical displacement of this isotherm ranges from 100 to 300 m. Superposition of the diurnal and semidiurnal tidal components based on the data from July 2 to July 31, 1986, is clearly seen in Fig. 2.2.

We used an elliptic band filter (Parks and Burrus 1987) to separate four tidal components, which form the semidiurnal and diurnal internal oscillations over the sill shown by the displacement of the 13 °C isotherm. The filter for the M_2 frequency was tuned to allow the frequencies from 1/12.37 to 1/12.47 h^{-1} with a central frequency of 1/12.42 h^{-1}. The filters for the other tidal components (O_1, K_1, and S_2) were similar. The graphs of calculations with the frequencies of the main tidal components are shown in Fig. 2.3. The mean amplitudes of internal fluctuations are equal to 17.7, 21.9, 68.8, and 12.7 m for the components of internal tide O_1 (25.82 h), K_1 (23.93 h), M_2 (12.42 h), and S_2 (12.00 h), respectively. The

Fig. 2.2 Depth variation of the 13 °C isotherm over the Camarinal Sill from July 2 to July 31, 1986. Reproduced from Morozov et al. (2002). © American Meteorological Society. Used with permission
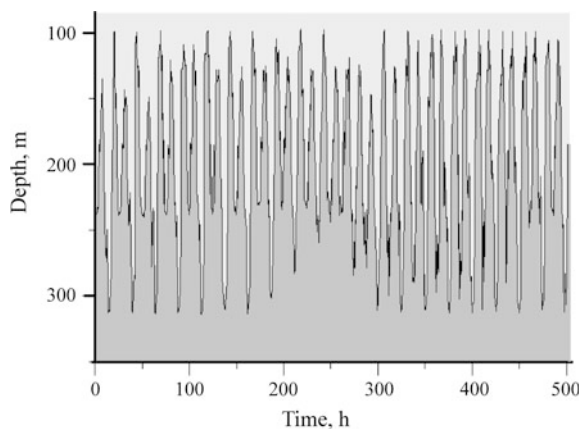
internal tidal oscillations are observed over the sill exactly at the source of their generation; hence we conclude that these waves are forced internal oscillations, which transform into free propagating waves east and west of the sill. Internal tidal waves rapidly lose their energy and at a distance of approximately 50 km from the sill their amplitude becomes three times smaller.

We used the antenna method (Barber 1963) (see Sect. 1.4.2) developed for the arbitrary position of the sensors to estimate the wavelength of the semidiurnal internal tide. Assuming that the main generation of the tidal internal waves occurs at the Camarinal Sill, the moorings in the strait were divided into two groups: buoys 1, 2, 3, 4, 8 for the internal tide propagating to the west of the sill and buoys 1, 2, 3, 9, 7 (Fig. 2.1) for the easterly propagating internal tide.

The wavelength was calculated on the basis of 10 different combinations of the time series duration for the western group. The resulting wavelength ranged from
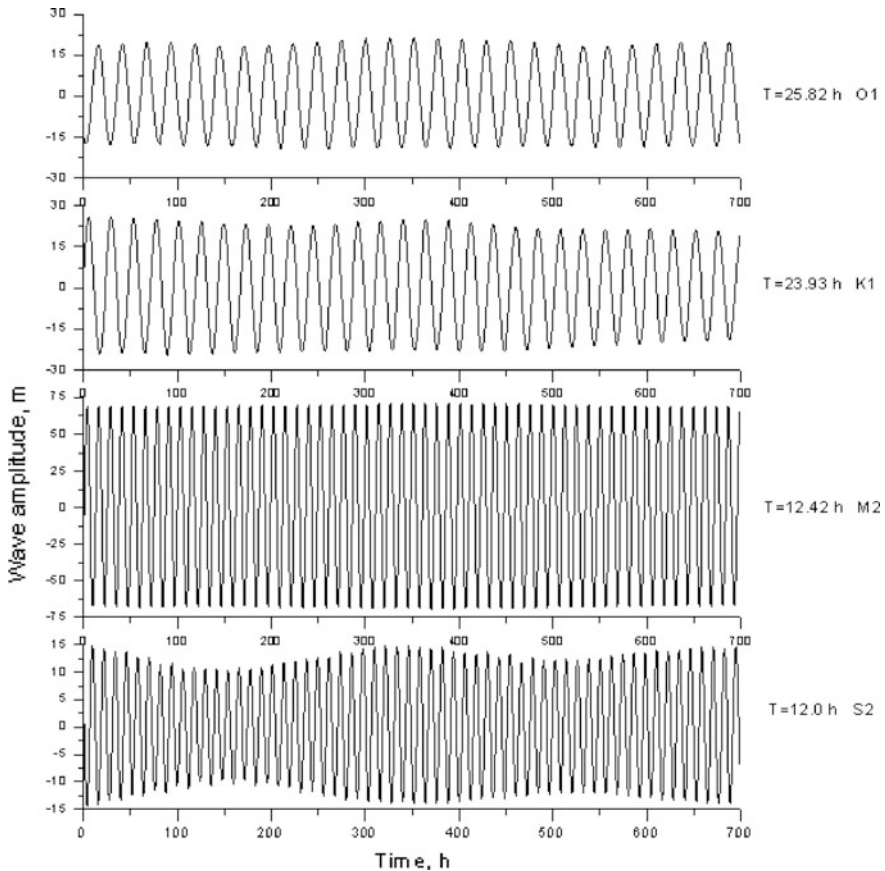

Fig. 2.3 Graphs of vertical displacements with the frequencies of the main tidal components O_1, K_1, M_2, S_2 from July 2 to July 31, 1986, after band filtering. Reproduced from Morozov et al. (2002). © American Meteorological Society. Used with permission

45 to 60 km, and the direction of the wave varied from 210° to 280°. The wavelength of the internal tide propagating to the east was estimated from 16 different combinations of moorings. The wavelength ranged from 90 to 140 km, while the direction of propagation varied between 90° and 120°.

The wavelength of the internal tide propagating in the eastern direction was greater and the difference is not surprising because the depths east of the Camarinal Sill are greater than in the western part of the strait. The wavelength of the internal tide estimated on the basis of the dispersion relation east of the sill was 94 km, and west of the sill the wavelength was equal to 59 km. We assumed the mean depth east of the sill equal to 800 m, and that west of the sill equal to 500 m.

Publications of the model simulations describe the generation of internal tides over the sill (Hibiya 1990; Longo et al. 1992; Wang 1993). The approach of Brandt et al. (1996) is related to the interface displacement. They describe the generation and evolution of the tidal internal wave in the Strait of Gibraltar and its transformation into a series of internal waves with shorter periods. Wang (1993) uses a model with continuous stratification, but the resolution of the model is not enough to analyze the propagation of short period wave packets. The numerical model by Longo et al. (1992) is a nonlinear two-layer model. The stratification is specified as two layers of varying thickness, while internal tide waves are generated at the interface between the layers.

We applied a nonlinear numerical model to analyze the water motion in a continuously stratified rotating ocean of variable depth (Vlasenko 1992) (see Sect. 1.4.1). The domain for calculations was 300 km long with a horizontal step of 200 m and 20 vertical levels. The time step was equal to 7 s. This modeling was aimed at studying the influence of the currents on internal tide propagation in the Strait of Gibraltar. In the first approximation of the model calculation there was no mean current. We introduced only a periodical barotropic tidal flow by periodically increasing and decreasing the stream function. The periodical changes in the horizontal flow with an amplitude of 80 cm/s induce internal waves propagating in both directions from the Camarinal Sill located in the middle of the computation domain. The fluctuations of the density field are not symmetrical with respect to the position of the Camarinal Sill because the bottom topography east and west of the sill is different. An internal bore is formed on the trailing edge of the wave, which is steeper than the leading edge. A packet of shorter internal waves follows the bore.

In the next step of the calculation we introduced a steady westward current in the entire water column of the strait. The velocity of the mean current was 30 cm/s. Similar to the first version of calculations we superimposed a periodical barotropic tidal current on the mean current. The westward flow changes the internal wave field. In the eastern part, where the internal tide propagates opposite to the current, we observed a well pronounced internal bore followed by a train of short-period internal waves. The mean current opposite to the wave makes the wavelength shorter. The slopes of the internal tide are steeper, which leads to wave breaking and the formation of a packet of shorter internal waves. In the case of a uniform westerly current the bore is observed in the entire water column.

In the third step of the model calculation, we analyzed the internal tide developing in the strait with two opposite currents modeling the real situation. The eastward flow with mean velocities of 50 cm/s was specified in the upper 250–300 m layer and the lower current with a vertically average velocity of 25 cm/s occupied the rest of the water column. These two opposing flows result in a strong shear at 250 m depth.

The results of the calculation after four tidal periods presented as perturbations of the density field induced by the propagating internal tide are shown in Fig. 2.4. Numerical calculations of isopycnal fluctuations in the main thermocline show the propagation of an internal bore. The regime of internal waves propagating to the west (in the same direction as the outflowing current) and those propagating to the east differs significantly. Internal waves propagating eastward have greater amplitude. The waves propagating to the east opposite to the currents, which occupy a layer from 200 m to the bottom, are strongly nonlinear. Their length is 74 km. They propagate as a periodical pulse of internal tidal perturbations, which rapidly increases its amplitude and then breaks into a packet of shorter internal waves. Initially, the amplitude of the vertical displacements caused by internal waves exceeds 100 m. The amplitude decreases while the wave propagates from the sill and small-scale internal waves developing at the steep slopes of isopycnals associated with undular internal bores are generated. These short internal waves with a wavelength of about 7–8 km develop on the trailing edge of the propagating tidal internal wave.

The westerly propagating wave is shorter. Its wavelength is 58 km, as the depth west of the Camarinal Sill is shallower. The structure of the wave is approximately the same except for the fact that the internal bore propagating to the west is less pronounced in the western part than in the eastern part of the basin. The presence of the two opposing currents with a shear intensifies the internal bore in the upper
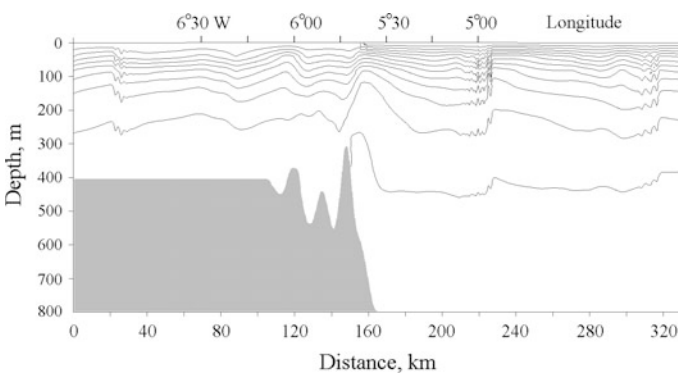

Fig. 2.4 Model calculations of perturbations of the density field induced by internal tide. The contour lines are shown with an interval of 0.00025 g/cm^3. The perturbations develop on the background of oppositely directed inflowing and outflowing currents. Reproduced from Morozov et al. (2002). © American Meteorological Society. Used with permission

Table 2.1 Wavelength of the semidiurnal tide determined using different methods

	Western part (km)	Eastern part (km)
Moored measurements	45–60	90–140
Dispersion relation	59	94
Numerical modeling	58	74

layer at depths of 100–200 m, while in the deeper water it becomes less apparent. The speed of the leading edge changes from 0.8 to 1.6 m/s depending on the relative velocity of the barotropic flow.

Model simulations show that if the mean current is uniform over depth the internal bore develops at approximately mid-depth. If we introduce a shear current as it is actually observed in the strait the internal bore and internal wave packets concentrate near the depth of the shear at a depth of 0–100 m; hence their manifestation at the surface is clearly seen on radar images and even visually from the shore and ships. Comparison of wavelengths calculated on the basis of mooring arrays, dispersion relation, and numerical modeling is given in Table 2.1.

The event of the surface manifestation of strong internal waves, which looks like boiling water, was analyzed by Alonso del Rosario et al. (2003) and Bruno et al. (2002). This event occurs during neap tides when a favorable combination of the stratification, vertical profile of horizontal background velocity, and bottom topography determines its generation. When this phenomenon occurs, the manifestation of high-amplitude internal waves is observed at the sea surface as high-frequency chaotic oscillations, named in Spanish as "hervideros" (boiling water).

2.2 Messina Strait

The Strait of Messina is located between continental Italy and the island of Sicily (Fig. 2.5). This narrow channel is a region of strong currents. Beginning with Greek and Roman mythology, many legends have risen around this strait. Homer (800 BC) thought that the currents in the strait were caused by the monsters Scylla and Charybdis. Five hundred years later, Aristotle thought that the currents were caused by the hollows in the sea bottom and by winds. In the 20th century it became possible to observe the surface manifestation of this phenomenon from space (Alpers and Salusti 1983).

The mean depth of the strait is about 120 m. The depth of the sill, which crosses the strait, is about 80 m. In the narrowest part of the strait the distance between the coasts is about 3 km. The northern slope is much steeper than the southern one but shallower (Bignami and Salusti 1990).

It was only in the second half of the 20th century that oceanographers discovered that the strong currents are induced by the tide. This fact is surprising because the
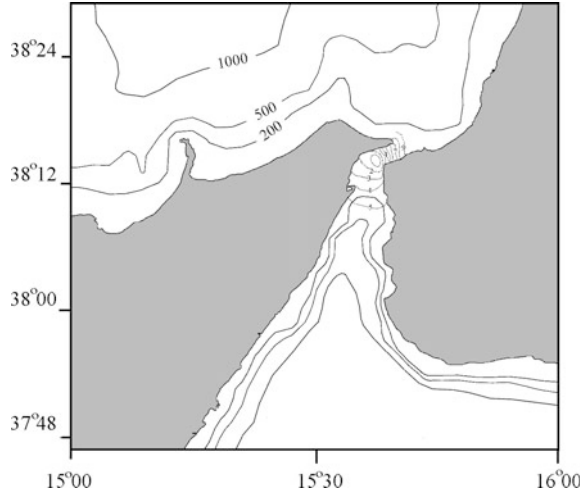
amplitude of the tide in the Mediterranean Sea is only about 10 cm. An amphidromic point for the M_2 tides in the two adjoining basins, the Tyrrhenian and the Ionian seas is located exactly at the shallowest point of the strait. Two equal Kelvin waves with opposite directions of propagation result in an amphidrome. The phase of the tide changes abruptly over 10 km within 5 h. Therefore, the M_2 tidal currents with velocities of 2–3 m/s can be observed (Defant 1961). The difference in the water properties of the two basins is very significant. The sill depth (80–100 m) is shallower than the interface layer below the Surface Tyrrhenian Water (150 m) in the adjacent basins. The alternating tidal flow is formed of different water masses. Surface Tyrrhenian Water flowing southward can be observed during six hours and Intermediate Levantine Water flowing northward can be observed during the next six hours (Hopkins et al. 1984). Therefore, the Strait of Messina differs from the Strait of Gibraltar where both Atlantic and Mediterranean water circulations occur at the same time.

In the Strait of Messina, a large gradient of tidal amplitude is formed because the tides in the basins north and south of the strait have a phase shift of about 5 h. This yields a difference in the amplitudes of 10 cm over a distance of 10 km. Thus, in the Strait of Messina the main forcing of currents is due to the periodic difference in the sea level caused by tides. The currents accelerate in the narrows and induce internal waves over the sill. Due to the phase difference of the tides and due to the topographic constrictions, the current velocities in the Strait of Messina can attain values as high as 3.0 m/s in the sill region. Modeling of tides in the strait was presented by Androsov et al. (1993, 2002).

The forms of internal displacements vary considerably. This results from strong turbulence that was recorded north of the sill. Their most famous manifestations are the terrifying vortices of Scylla and Charybdis known from the ancient legends. Surface manifestations of internal waves are clearly seen in the satellite images (Fig. 2.6).

Fig. 2.6 Satellite photo of surface manifestations of internal waves propagating south of the Messina Strait. NASA image on August 11, 2003 (http://earthobservatory.nasa.gov/IOTD/view.php?id=7630; last accessed in October 2017)
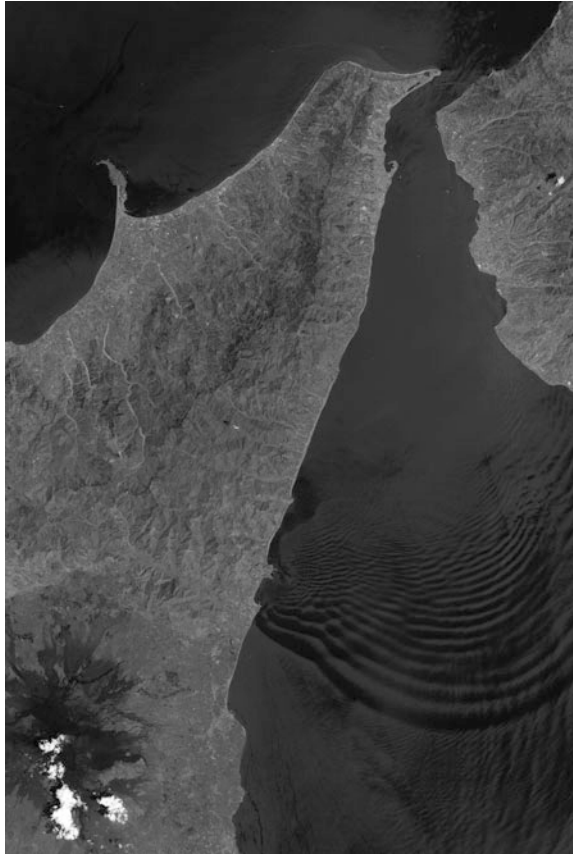
Usually, the interface between different water masses is located at a depth of
150 m. Strong tidal currents interacting with bottom topography induce strong
internal waves of tidal period (Di Sarra et al. 1987; Griffa et al. 1986). The estimates
of the internal tide amplitude in the strait on the basis of measurements and modeling
are within 30–50 m. It was reported by Hopkins et al. (1984) that the vertical
displacements over the slopes associated with the internal tides can be as high as
100 m. During the tidal flow, the surface waters spread as a subsurface jet intruding
at a depth of about 100 m. The jets form an internal bore, which develops into trains
of internal solitary waves (Brandt et al. 1997, 1999; Sapia and Salusti 1987).

2.3   Canary Basin, Gambia Abyssal Plain

This region is known as the Gambia Abyssal Plain, Canary Basin, or Cabo Verde
Basin. The Mid-Atlantic Ridge is the western boundary of the region. The other
topographic features in the region are the Great Meteor Banks, Azores Islands,

Canary Islands, Madeira Islands, and Cabo Verde Islands. Many experiments have been carried out in this region. Internal tides near the Great Meteor Banks and Mid-Atlantic Ridge are well pronounced. Figure 2.7 shows a spectrum based on the data of the Subduction Experiment (1991–1993).

In November 1989, the Shirshov Institute of Oceanology carried out moored measurements east of the Cruiser, Irving, and Meteor banks. It was planned to record strong internal tides in the region because the amplitudes of the barotropic tide in the region are high and the direction of the barotropic tide currents is almost normal to the line of underwater banks (Gordeev et al. 1974). The flat tops of the banks are located at a depth of 300–400 m, while the mean depth of the basin exceeds 5000 m.

A cluster of five moorings with velocity and temperature meters at depths of 700, 900, 1000, and 1200 m was deployed here. The central mooring (31° 00′N, 26° 30′W) was equipped with additional instruments at 300 and 2000 m. The duration of the experiment was 448 h; the time sampling was 15 m. Bottom topography and locations of moorings are shown in Fig. 2.8.

Semidiurnal internal tides dominate in the region. The mean amplitudes of the semidiurnal temperature fluctuations at depths of 1000 and 1200 m are 0.5 °C, which corresponds to the vertical displacements of 80 m; the maximum wave heights in the spring phase of the tide reached 100 m, while in the neap phase they were close to 60 m. Statistical cross-analysis revealed high vertical coherence (0.65–0.75) at the semidiurnal frequency of temperature fluctuations with a phase shift between various sensors close to 0°.

Spectral cross-analysis between sensors at different moorings revealed high horizontal coherence between temperature time series (0.60–0.75). A decrease in the amplitude of fluctuations from west to east was found. The ratio of spectral

Fig. 2.7 Spectrum of temperature fluctuations based on the data of the ACM-25 Subduction Experiment; the NE mooring at 33° 00′N, 22° 00W′; depth 750 m
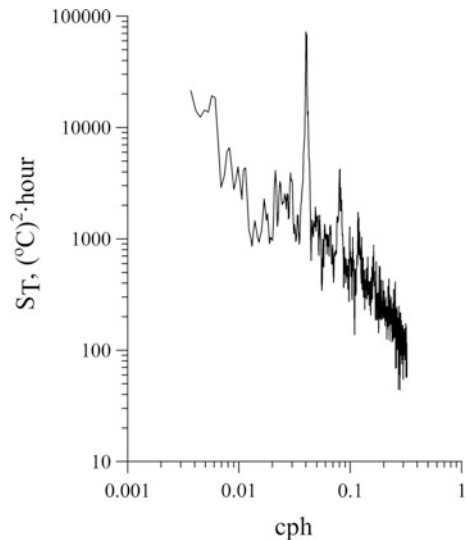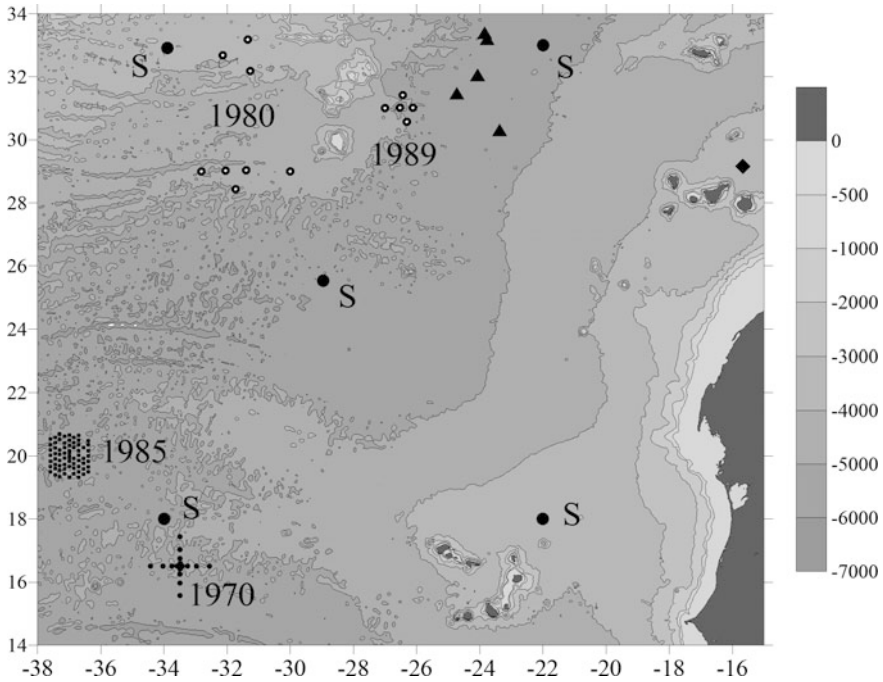
Fig. 2.8 Bottom topography (meters) of the Canary Basin. Depth contour lines are shown at depths of 500, 1000, 2000, 3000, 4000, 5000, and 6000 m. Locations of moorings are shown with black symbols. The following experiments are indicated with different symbols: Polygon-70 (1970, small dots); Mesopolygon-85 (1985, small dots); Subduction (S, large dots); Moorings in 1980 (1980, dots with a white circle in the middle); Moorings in 1989 (1989, dots with a white circle in the middle); ESTOC (rhombs); Standalone miscellaneous moorings (triangles). Land is shown with gray color

densities at the semidiurnal frequency at a depth of 1200 m on moorings 5, 4, and 2 was 9: 6: 1. The moorings were located on the west-east line at a latitude of 31°N and longitudes: 26° 32′, 26° 18′, and 26° 06′W, respectively. This fact indicates that the energy of internal waves decreases from west to east in the direction from the source at the banks.

The estimates of spatiotemporal spectrum were carried out using the Barber's method (see Sect. 1.4.2) (Barber 1963). A spatiotemporal spectrum at the semidiurnal frequency based on the data at a depth of 700 m is shown in Fig. 2.9. Based on these data, the internal tide had a length of 170 km. The direction of propagation was 115°. The estimates at other depths are approximately the same. The direction of propagation ranged between 90° and 120°. These estimates agree with the estimates from the dispersion relation.

The northeastern mooring of the WOCE Subduction experiments ACM-25 and ACM-26 was located in this region (NE: 33° 00′N, 22° 00W). The experiment was organized by the Woods Hole Oceanographic Institution (USA). This mooring was
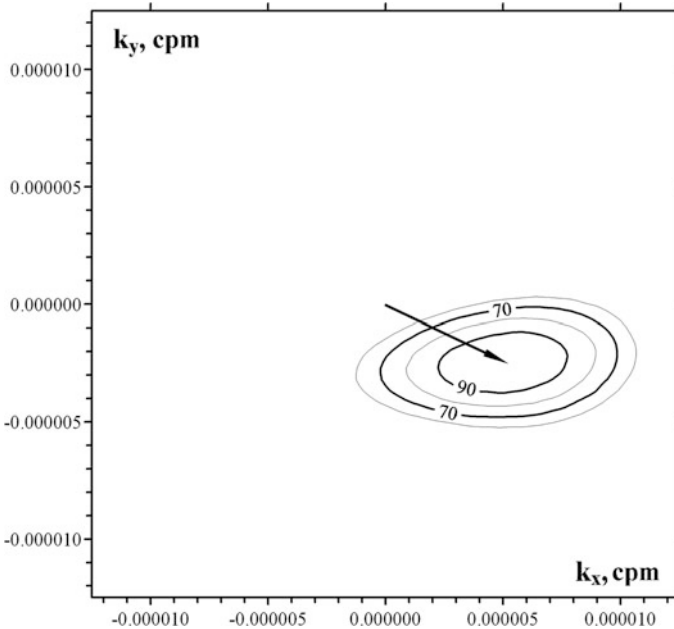
Fig. 2.9 Spatiotemporal spectrum at the semidiurnal frequency in the study site east of Great Meteor Seamount in 1989 at a depth of 700 m. The contour lines correspond to 90, 80, 70, and 60% of the main maximum. The arrow shows the wave vector corresponding to a wavelength of 170 km. The internal tide propagates to the southeast (azimuth 115°)

replaced twice, and the total period of its operation was from June 1991 to June 1993. The amplitude of internal tides at this point at depths of 750 and 1500 was estimated at 50 m.

High amplitudes of semidiurnal internal tides in the region are confirmed by the measurements on a standalone mooring (CMDAC number 795: 31° 29′N, 24° 44′W′; the depth of the instrument was 1016 m) in 1985–1986. The amplitudes of waves were estimated at 50 m. High amplitudes were also recorded on another standalone mooring (CMDAC number 843: 30° 19′N, 23° 22′W; the instruments were at 674 and 1619 m) in 1981–1982. The amplitudes of the semidiurnal internal tides were estimated at 40 m.

Measurements on a standalone mooring at 32° 03′N, 24° 04′W (CMDAC number 8313, 1071 m) in 1984–1986 confirm large amplitudes of internal tides (50 m) east of the Great Meteor Banks. At a greater distance from the banks (moorings at 33° 12′N, 23° 46′W and 33° 24′N, 23° 51′W in 1993), the amplitudes of semidiurnal waves at a depth of 200 m were estimated at 25 m.

Smaller amplitudes of the semidiurnal internal tides were recorded on a standalone mooring at 29° 10′N, 15° 40′W during the ESTOC experiment in 1994–1997. The experiment was organized by the Institute für Meereskunde (Germany). Three repeated deployments of moorings, each one year long, were performed here.

This point was located approximately 1000 km southeast of the study site in 1989; hence, its location was significantly farther from the Great Meteor Banks (100–150 km north of the Canary Islands). The measurements were carried out at 300, 500, 800, 1200, 1600, 2500, and 3500 m. The amplitudes of waves at 1200 m were 25 m.

In May–June 1980, the Russian oceanographic ship *Akademik Kurchatov* (Shirshov Institute of Oceanology) deployed three moorings with velocity and temperature meters at 300, 500, 700, 1500, and 2000 m east of the Mid-Atlantic Ridge, southwest of the Great Meteor Banks at latitudes of 32°–33°N (32° 41′N, 32° 08′W; 33° 11′N, 31° 21′W; 32° 11′N, 31° 16′W). Then, the moorings were replaced and deployed at 29° 00′N, 30° 00′W; 29° 02′N, 31° 24′W; 28° 26′N, 31° 44′W; 29° 01′N, 32° 03′W; 29° 00′N, 32° 49′W. The moorings operated for 23 days. Bottom topography and locations of stations are shown in Fig. 2.8 (Morozov and Nikitin 1984a).

Spectra of temperature fluctuations in this region are characterized by highly reliable peaks at the semidiurnal frequency. Vertical displacements at 700 and 1500 m reached 40 m. Vertical coherences shown in Table 2.2 are high even over large vertical scales.

The horizontal coherences were very high. At a depth of 700 m where the temperature sensors were located, horizontal coherence was always higher than 0.6. The spatiotemporal spectrum was calculated from the time series 180 h long, and also from the time series 86 h to study the temporal variations of the spectral estimates and stability of internal tides.

Let us consider the spatiotemporal spectrum based on the data in 1980. A spatiotemporal spectrum based on the data of four moorings is shown in Fig. 2.10. Two main maxima are distinguished in the spectrum related to the internal tides with a length of 140 km in the direction of 110° and another peak is related to a wavelength of 110 km in the direction of 230°. Calculations of the spectra over parts of the time series show that these two waves dominate in all versions of the calculations. The main features of the spectra remain, while variations are seen only in details.

Comparing the locations of mooring relative to the features of the bottom topography in the region we can conclude that one of the wave systems was

Table 2.2 Coherence between temperature fluctuations at different depths on a mooring deployed south of the Azores Islands

| Depths of measurements (m)	Depths of measurements				
	500 m	700 m	1500 m	2000 m	2500 m
300	0.85	0.82	0.62	0.76	0.68
500		0.95	0.80	0.90	0.70
700			0.87	0.91	0.74
1500				0.73	0.57
2000					0.67
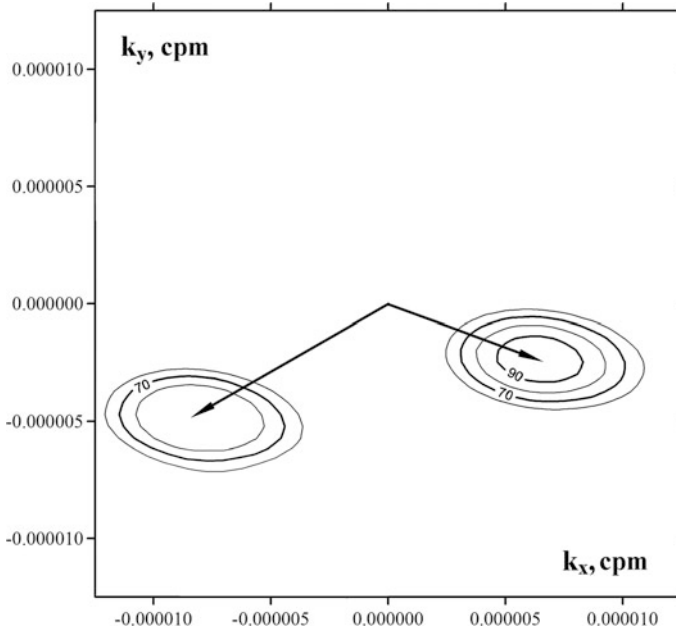
Fig. 2.10 Spatiotemporal spectrum at the semidiurnal frequency in the study site southwest of the Great Meteor Banks in 1980 at a depth of 700 m. The contour lines correspond to 90, 80, 70, and 60% of the main maximum. Two arrows show the wave vectors corresponding to wavelengths of 140 km (direction 110°) and 110 km (direction 230°)

generated near the Mid-Atlantic Ridge and propagated to the southeast (110°); the other was generated at the slopes of the Great Meteor Banks and propagated to the southwest (230°). Stability of spectral functions over the period of measurements indicates that the directions of these internal tides were quasi-stationary.

Rapid changes in stratification on the slopes of the Great Meteor Seamount were studied by van Haren (2005a) on the basis of the ADCP and thermistor string data. Rapid changes in the bottom boundary layer stratification caused by upslope and downslope tidal currents were recorded. A steep front or bore may pass, whose overturning diminishes the local stratification. During the remainder of the tidal period the stratification is gradually reconstituted.

The dynamical pattern of the tidal wave trapping and internal wave generation near the Great Meteor Seamount was presented by Mohn and Beckmann (2002) based on the observations and modeling. The authors reveal tidally induced eddy around the mountain and periodical upward and downward currents that generate the internal tide.

Depth integrated energy flux from the Great Meteor Seamount was estimated by Gerkema and van Haren (2007) at 2.3 kW m^{-1} for the semidiurnal internal tide based on the observations using CTD/LADCP yo-yo casts, while an estimate of 2.6 kW m^{-1} was obtained from the model simulations.

The northwestern and central moorings of the WOCE ACM-25, ACM-26 Subduction experiments were located in the same region (Center: 25° 30′N, 28° 54′W; NW: 32° 54′N, 33° 54′W). These moorings were changed twice; the total period of their operation lasted from June 1991 to June 1993. The measurements in the main thermocline were performed at depths of 750 and 1500 m. The amplitude of the internal tides at the northwestern point of ACM-25 was estimated at 80 m. This point was located between the Great Meteor Banks and the Mid-Atlantic Ridge. The central point of the ACM 26 experiment was located south of the Great Meteor Banks. The amplitude of the internal tides there was estimated at 55 m. Vertical coherence between different time series at depths separated by a few hundred meters exceeded 0.6.

Internal tides in the southern part of the Gambia Abyssal Plain are less intense. Their amplitudes are smaller and the waves are not as stable as in the region close to the Great Meteor Banks. Two Russian experiments were organized here by the Shirshov Institute of Oceanology. The goal of the Polygon-70 experiment was to study mesoscale eddies in the open ocean. The Polygon-70 and the MODE experiments in 1973 were the pioneer experiments with instrumental measurements of the mesoscale eddies using moorings. The Polygon-70 experiment continued the field studies of mesoscale eddies, which were previously recorded by hydrographic surveys in 1967 in the Arabian Sea. In 1985 another experiment, Mesopolygon-85 was organized here to study the mesoscale eddies of smaller scale in the upper ocean and the intra-thermocline Mediterranean lenses in the deep thermocline.

The measurements during the Polygon-70 experiment were carried out from February to September, 1970, in the central tropical Atlantic (central mooring at 16° 30′N, 33° 30′W). The moorings at 17 locations in the form of a cross in the horizontal plane were periodically replaced providing continuous operation of the whole array. The temperature measurements were carried out at 200 m for the entire duration time of the experiment, and the measurements at 1000 m were made only in the first month of the experiment (Atlantic Hydrophysical Polygon-70 1983; Ivanov and Morozov 1983). The bottom topography and locations of moorings are shown in Fig. 2.8.

Spectra of temperature fluctuations were characterized by a stable peak at the semidiurnal frequency. This peak was found at all depths of measurements on all moorings. The heights of semidiurnal waves at 1000 m were approximately 20 m. Vertical coherence between pairs of levels 200–1000 m was usually not high and rarely exceeded the 95% confidence level (0.5). This conclusion was reached also by Bolshakov and Sabinin (1983). We note that the southwestern point of the ACM-25 Subduction experiment was located in approximately the same region in the middle of the Gambia Abyssal Plain (SW mooring at 18°N, 34°W). The amplitudes of tidal internal waves at 1500 m were estimated at 30 m. The southeastern point was located at a distance of 100 km from the Cabo Verde Islands (SE mooring at 18°N, 22°W). The amplitude of internal tides at this point was estimated at 30 m.

The data of the Polygon-70 experiment made it possible to study the horizontal scale of coherence of the semidiurnal temperature fluctuations since very many

cross-spectra were available (Ivanov and Morozov 1983; Morozov and Filatova 1978). Horizontal coherence at a depth of 1000 m appeared significant over all scales of the study site.

At a depth of 200 m, the amount of measurements was significantly greater than at 1000 m. We analyzed the variation of horizontal coherence as a function of the distance between moorings. Coherence was estimated on the basis of 251 pairs of time series 12 days long. Depending on the geometry of the study site we could estimate horizontal coherences over a set of distances from 5 to 115 miles.

The number of coherence estimates at each of the fixed distances ranged from 3 to 17. The results of calculations are plotted in Fig. 2.11. The estimates of horizontal coherence are more or less uniformly distributed in a band of values from 0.30 to 0.75.

The scatter of the horizontal coherence estimates over distances up to 100 miles is significant; it ranges from reliable to low and random values. Such a distribution in this region notably differs from the variations in the horizontal coherence in the other regions, in which coherence is high everywhere. However, in this analysis of the horizontal coherence variations we found that the major part of estimates fluctuates around 0.5. Horizontal coherence remains at this level at different mean conditions. According to Thompson (1979), a coherence of 0.5 at 20 degrees of freedom of the statistical processing indicates that it is non-zero with a probability of 95%.

We selected 10 time intervals of synchronous mooring data to calculate the spatiotemporal spectra. In this case, it was possible to select different versions of antenna consisting of four-seven temperature sensors of different moorings at
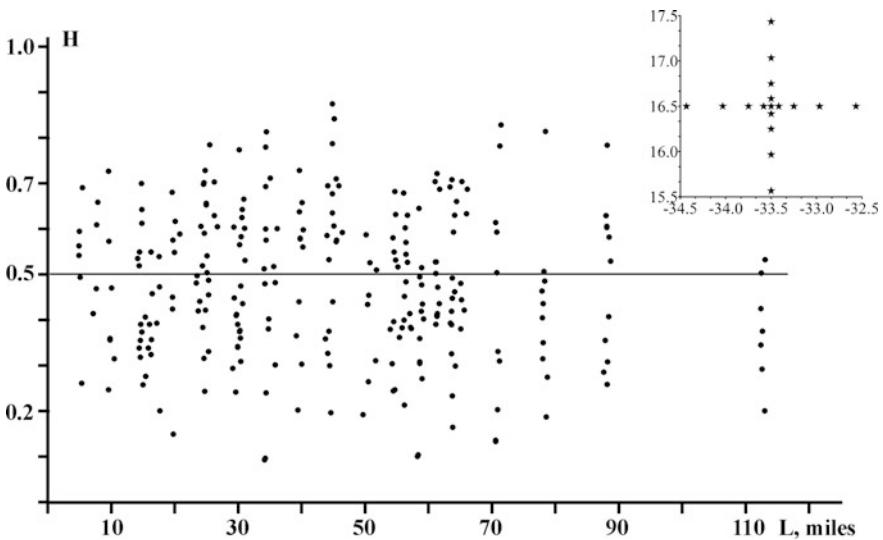

Fig. 2.11 Horizontal coherence of temperature fluctuations at the semidiurnal frequency at a depth of 200 m versus horizontal distance in the Polygon-70 experiment. Line 0.5 shows the 95% confidence level. Scheme of the mooring (stars) locations is shown in the inset

200 m depth (Morozov and Nikitin 1981a). The duration of time series in each of the 10 versions of spectra calculation was 12 days. The wavelengths of internal tides calculated from numerical integration of the equation for vertical velocity (see Sect. 1.4.3) were 113 and 63 km for the first and second modes, respectively.

The typical spatiotemporal spectrum is shown in Fig. 2.12. The most significant peak corresponds to the first mode of internal tides (wavelength 105 km); the direction of the wave propagation was 170°. Two less significant peaks are related to the second mode with wavelengths equal to 50 and 55 km; the directions of these waves were 260° and 160°.

The calculations of the spatiotemporal spectra indicate that one and sometimes two wave systems of different directions exist in this region. The first mode dominates, but sometimes the second mode is also recorded. The direction to the south dominates. This dominating direction of wave propagation was found also by Bolshakov and Sabinin (1983), Golenko (1982), Lyashenko and Sabinin (1979), Matygin et al. (1982), Sabinin and Shulepov (1978).

Two important facts follow from the data analysis. First, the semidiurnal internal tides are determined by the propagation of waves from several sources. The second fact is the stability of wave direction during different periods of measurements. The conclusion about the stability of wave direction to the south was also based on the analysis of phase relations (Ivanov and Morozov 1983).

Field works in the Mesopolygon-85 study site (center at 20° 00′N, 37° 30′W) were carried out in April–May 1985 on 73 moorings (Morozov 1988). The location of the Mesopolygon-85 experiment was selected close to the Polygon-70 (Fig. 2.8). The moorings were deployed over a uniform triangle grid. The distance between moorings was 10 miles.

Fig. 2.12 Spatiotemporal spectrum of fluctuations at the semidiurnal frequency in the Polygon-70 study site at a depth of 200 m. The contour lines correspond to 90, 80, 70, 60, and 50% of the main maximum. The arrows show the wave vectors corresponding to wavelengths of 105 km (direction 170°); 50 km (direction 260°), and 55 km (direction 160°)
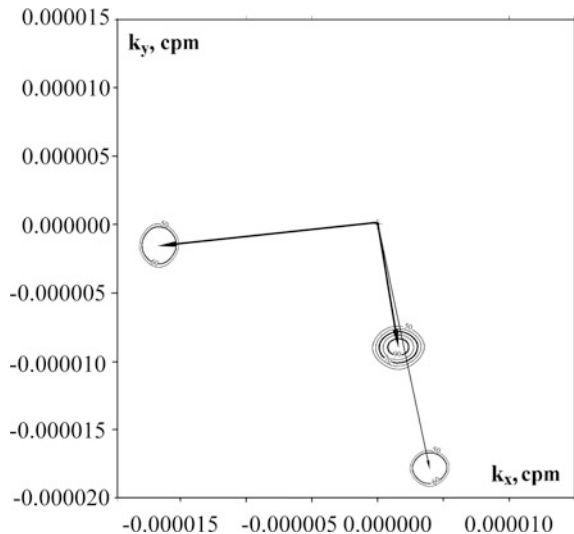
The characteristic features of spectral functions in the Mesopolygon-85 study site are similar to the Polygon-70 spectra. Similar to the Polygon-70, the horizontal coherence at 200 m varied in wide limits from 0.25 to 0.75. Such variation in the horizontal coherence is characteristic of the regions located far from the intense sources of internal tide generation such as submarine ridges or continental slopes. We suppose that in the Polygon-70 and Mesopolygon-85 regions internal tides were generated in the bottom layer due to the interaction of the barotropic tide with the moderately rough bottom topography. Such topographic features are in abundance in the regions of these experiments. Many hills with an elevation over the bottom up to 1000 m are typical for the bottom topography here. These hills are found with an interval of 20–50 miles. Such a corrugated topography (Baines 1973, 2007) distributed over large bottom regions can become a source of the local generation of internal tides. Numerical simulation of internal wave generation over such topography is reported by Zhang et al. (2017).

Internal tides in the Mesopolygon-85 study site are not very stable because they interact with the mesoscale eddies. Instability is most pronounced at the frontal zones between eddies (Morozov et al. 1998). The interaction is not very strong. The spatial scales of these two processes are close (50–100 km), but the time scales are significantly different (12 h and one month). Nevertheless, the mesoscale eddies transform the mean state of the ocean, which causes internal waves to propagate in a horizontally inhomogeneous environment. Frontal zones with high horizontal gradients of temperature and density are formed at the boundaries between eddies. Nonlinear effects can be intensified, and a sharp growth of amplitudes is possible, which is followed by wave breaking.

The existing theoretical models describing the interaction between internal waves and frontal zones indicate that the internal wave field is intensified in frontal zones (Ivanov and Morozov 1974; Badulin et al. 1985; Sabinin et al. 1990). Intensification of internal waves should decrease with increasing wavelength. The data reported by Morozov et al. (1998) support this mechanism of intensification. Model studies by Dunphy and Lamb (2014) show that the propagation of internal tide thorough a mesoscale eddy can form spatial hot and cold spots of the energy flux. The energy flux in the hot spots can exceed twice the incident flux while in the cold spots it can decrease to almost zero.

2.4 Sargasso Sea, POLYMODE, LDE, ARRAY, WOCE ACM-1, LOTUS, LLWODP, FASINEX-86, and IWEX Experiments

Many oceanographic experiments have been carried out in the Sargasso Sea. In 1973, the Internal Wave Experiment (IWEX) and Mid-Ocean Dynamic Experiment (MODE) were organized by US scientists. A 9-month Array-1 experiment was conducted in 1974–1975 by US scientists. This was followed in 1975-1977 by the

Array-2 experiment. Moorings with velocity and temperature meters (four instruments on each mooring) operated over two years. During this period the moorings were changed twice so that three sequential time series were obtained. The joint USSR-USA POLYMODE experiment was organized in 1977–1978. In addition, the Local Dynamic Experiment (LDE) experiment was organized as part of the POLYMODE. In the Russian part of the POLYMODE experiment, the moorings were deployed at 19 locations; they operated over 13 months. Further experiments that were conducted in the region of the Sargasso Sea are: the Low Level Waste Ocean Dumping Program (Oregon State University, LLWODP), WOCE ACM-1 (Miami Rosenstiel School of Marine and Atmospheric Science, RSMAS), Lotus (Woods Hole Oceanographic Institution), Frontal Air-Sea Interaction Experiment (FASINEX-86) (WHOI); and some standalone moorings have also been deployed. The bottom topography and locations of moorings in the experiments in the Sargasso Sea are shown in Fig. 2.13.

First, we shall analyze the results of measurements of the POLYMODE and Array experiments. Spectral functions of velocity and temperature fluctuations are characterized by a stable semidiurnal peak. However, its height over the background spectra and location relative to the frequency axis can change in time and space. The amplitude of semidiurnal waves was not high and rarely exceeded 20 m. We shall consider the relation of spectral functions to the mean state of the ocean and their time variations.

Vertical coherence of temperature fluctuations at the semidiurnal frequency in the Sargasso Sea was low. If the distance between instruments exceeded 200–300 m, coherence rarely reached significant values.

Let us consider spatial spectral cross-analysis of measurements in the Sargasso Sea. The Internal Wave Experiment (IWEX) was conducted in 1973 in the Sargasso Sea at 27° 44′N, 69° 51′W. The three-mooring deployments formed a tetrahedron with a side of 6 km. Its apex was at a depth of 600 m (Brisco 1975; Frankignoul and Joyce 1979). The data analysis of the IWEX experiment presented by Müller et al. (1978) shows that the semidiurnal internal tides propagate from the continental slope of America to the east. We analyzed the data of the POLYMODE and Array-2 experiments located approximately in the same region (Morozov 1983). The spatiotemporal spectra based on these data do not confirm the IWEX results. The peaks of the spatiotemporal spectrum are not stable in time. We think that the internal tides propagating to the east in the IWEX experiment were generated locally over the slopes of the bottom topography west of the experiment. The continental slope is located at a distance of 1000 km west of the IWEX site so that weak internal tides of the Sargasso Sea generated over the continental slope could hardly propagate over such a long distance.

There is another cause for the difference between the results of the IWEX and other experiments. The measurements in the IWEX experiment were carried out for 42 days. The POLYMODE and Array-2 experiments lasted much longer. This can be one of the causes that led to the finding of unstable internal tides in the region, which could have been revealed only from long-term records.
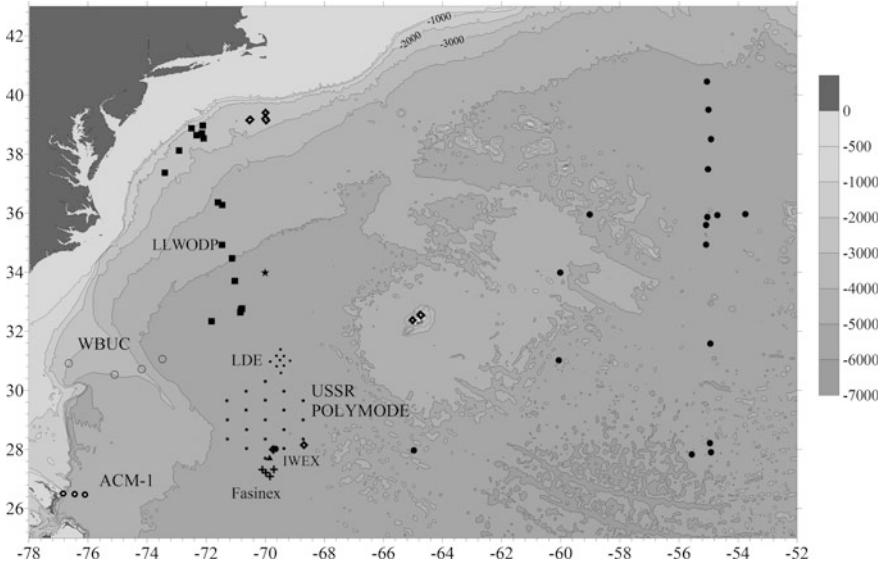
Fig. 2.13 Bottom topography (meters) in the Sargasso Sea and locations of moorings of the Array, IWEX, POLYMODE, LDE, Lotus, WOCE ACM-1, LLWODP, and FASINEX experiments. Depth contour lines are shown at depths of 500, 1000, 2000, 3000, 4000, 5000, and 6000 m. Locations of moorings are shown with black symbols. The following experiments are indicated with different symbols: Array (large dots); ACM-1 (dots with a white circle in the middle); USSR POLYMODE (small dots); LDE (small dots); IWEX (triangle); Lotus (stars); LLWODP (squares); FASINEX (crosses); West boundary undercurrent WBUC (open circles); standalone miscellaneous moorings (diamonds with a white circle in the middle). Land is shown with gray color

Spectra calculation from the Array-2 data allows us to estimate the horizontal coherences over a wide scale of distances between moorings. These calculations also result in the unstable direction of the semidiurnal internal tides in the region. Sometimes, the peaks on the spectra were not very reliable.

Horizontal coherence in the region is low. A graph of its dependence on distance based on the Array-2 data is shown in Fig. 2.14. The location of the moorings relative to the varying position of mesoscale eddies is important for the cross-spectral analysis. The westward motion of eddies influences the spectral functions because the measurements were carried out in the environment of variable currents.

Frequency shifts of the semidiurnal peaks were frequently observed in the POLYMODE region. We assume that a wave with period T_0 and phase velocity C_{ph} propagates in a flow with velocity component u along the direction of the wave. Then, owing to the Doppler effect we measure wave period T_1, which is different from the real period. The relation between them is as follows:

Fig. 2.14 Horizontal coherence of temperature fluctuations at the semidiurnal frequency versus horizontal distance. The Array-2 experiment, depth 1000 m. Line 0.5 shows the 95% confidence level
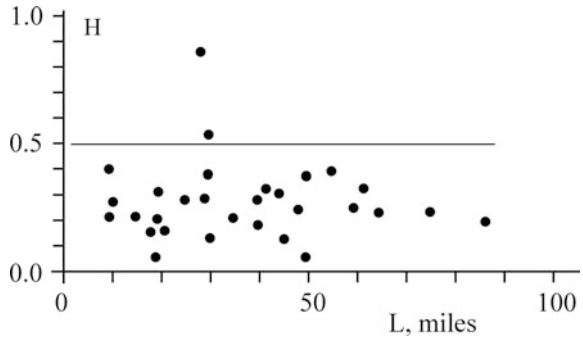
$$T_1 = \frac{T_0}{1 + \frac{u}{C_{ph}}}.$$

Depending on the sign of u the recorded wave period would be either greater or smaller than T_0. The observed velocities in the mesoscale eddies in the Sargasso Sea were of the order of 30 cm/s. Phase velocities of the semidiurnal tides were as high as 360 cm/s. Hence, the variations in the measured periods of the semidiurnal tides due to the Doppler effect range between 13 and 11 h. The horizontal coherence between temperature fluctuations measured on moorings is lower than in many other regions of the World Ocean. This is also related to the eddy activity in the region and high variable velocities of the eddies. The influence of the Doppler effect on the semidiurnal internal tides differs in space depending on the relative position of moorings and eddies. If we calculate the spectral function using time series of 12–20 days long, this effect is much stronger than in the case of very long time series. In the latter case, the influence of the Doppler effect caused by the current of alternating directions is attenuated due to the statistical averaging over a long time period, and no frequency shift is observed.

The regions of the Sargasso Sea, in which the experiments were carried out, are far from submarine ridges and continental slopes. Hence, the energy of internal waves that were generated on the slopes decreases strongly before the waves arrive to the site of the measurements. The ocean bottom in the region of the experiments is relatively flat with gentle slopes and low hills. One should not expect the strong generation of semidiurnal internal tides over deep topography.

In the course of propagation trough variable fields of currents and stratification internal tide changes its properties. Sometimes the changes are very strong so that this process becomes different from the one in the generation region. The existence of strong mesoscale eddies in the Sargasso Sea (Kamenkovich et al. 1986) that change the mean state of the ocean influences the properties of the propagating internal tide. The barotropic tide is relatively weak in the region. All of these factors influence internal tides and lead to the non-stationary and non-homogeneous internal tides in the Sargasso Sea.

The existence of relatively weak internal tides was confirmed by Dushaw (2006). The research was based on an ocean acoustic tomography array deployed in 1991–1992 centered at 25°N, 66°W. It was a pentagonal array, 700-km across for mode-1 internal-tides. The M_2 internal-tide energy flux was estimated at 70 W m^{-1}. Internal tides were radiating from the Caribbean Islands. However, it was found that the decay of internal tides was very weak and the waves retained their coherence over great distances. This finding of weak decay disagrees with the results of many other publications, for example, with the modeling results by Ansong et al. (2015) based on the high resolution model of ocean circulation.

2.5   Southwest Atlantic, Trindadi and Martin Vas Islands, Brazil Basin, Santos Plateau, WOCE ACM-24, ACM-3, ACM-12 Experiments

It is known that the internal tides in the South Atlantic are very intense (Morozov 1995). Tidal currents obtain a significant vertical component in the region of the continental slope and the Mid-Atlantic Ridge. This leads to the generation of progressive internal tides which propagate from the slopes of bottom topography to the ocean.

In 1993-1994, the WOCE ACM-24 experiment was conducted in the South Atlantic. The experiment was organized by Florida State University. Seven moorings were deployed in a line along approximately 18°S (Weatherly et al. 2000; Sandoval and Weatherly 2001). The goal of the experiment was to study the western boundary currents and the northward flow of Antarctic Bottom Water along the continental slope of South America. A scheme of the region, bottom topography, and locations of moorings along a line normal to the continental slope are shown in Fig. 2.15. The length of the mooring array was approximately 500 km. All moorings returned temperature data at 1800 m. Locations of the instruments in relation to the continental slope are shown in Fig. 2.16. Intense internal tides were recorded on the westernmost mooring (18° 44′S, 37° 15′W). A graph of the variations in the internal tide amplitudes at 1800 m is shown in Fig. 2.16. The mean peak to peak temperature variations on the western mooring were 0.25 °C, which corresponds to an amplitude of internal tides equal to 95 m. The amplitudes at the eastern mooring decreased to 19 m. The spectrum of temperature fluctuations calculated from the 18-month time series at 1800 m on the mooring at 18° 44′S, 37° 15′W is shown in Fig. 2.17. The spectrum is characterized by a highly reliable peak at the semidiurnal frequency.

The data of these measurements are supported by the measurements on a standalone Russian mooring (17° 59′S, 32° 36′W) in April 1969 deployed from the R/V *Akademik Kurchatov* 250 km north of the line of shallow banks, among which are the seamounts Davis, Eclaireur, Jaseur, Dogaressa, and Columbia and Trindadi and Martin Vas islands. This mooring was located only 7 miles north of mooring 7 of the
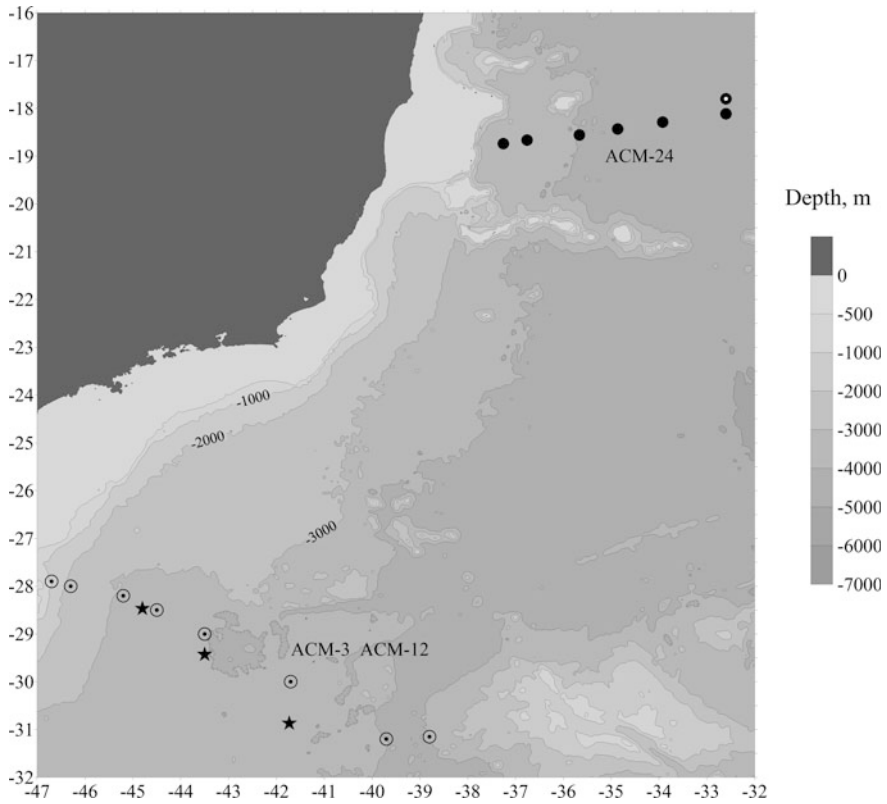
Fig. 2.15 Bottom topography (meters) in the South Atlantic east of Brazil and locations of moorings of the WOCE ACM-3, ACM-12, ACM-24, and other experiments. Depth contour lines are shown at depths of 500, 1000, 2000, 3000, 4000, 5000, and 6000 m. Locations of the ACM-24 moorings are shown by black circles, moorings of the ACM-3 and ACM-12 array are shown by open circles with a black dot in the middle; the moorings of the WHOI experiment in 1991–1992 are shown by stars; the mooring of the USSR experiment in 1969 is shown by a black dot with a white circle in the middle. Land is shown with gray color

ACM 24 experiment. The line of submarine banks and islands extends along approximately 21° S normal to the continent. Temperature measurements at 600 m revealed well pronounced semidiurnal fluctuations with vertical displacements reaching 40 m.

Another moored experiment in the Brazil Basin was conducted in 1991–1992 at 28°–31°S. Three moorings in a line were deployed at 29° 26′S, 43° 30′W; 28° 28′S, 44° 28′W; 30° 52′S, 41° 44′W (CMDAC numbers of moorings: 9072, 9062, 9092). Locations of moorings are shown in Fig. 2.15. The amplitudes of the semidiurnal internal tides at depths of 895, 908, and 914 m, respectively were estimated at approximately 30 m on each of the moorings.

Fig. 2.16 Decay of internal tide amplitudes with the distance from the continental slope based on the ACM-24 experiment. Locations of moorings on the map of bottom topography (top panel); locations of instruments relative to the slope (middle panel); amplitude of the semidiurnal internal tide versus longitude (bottom panel)
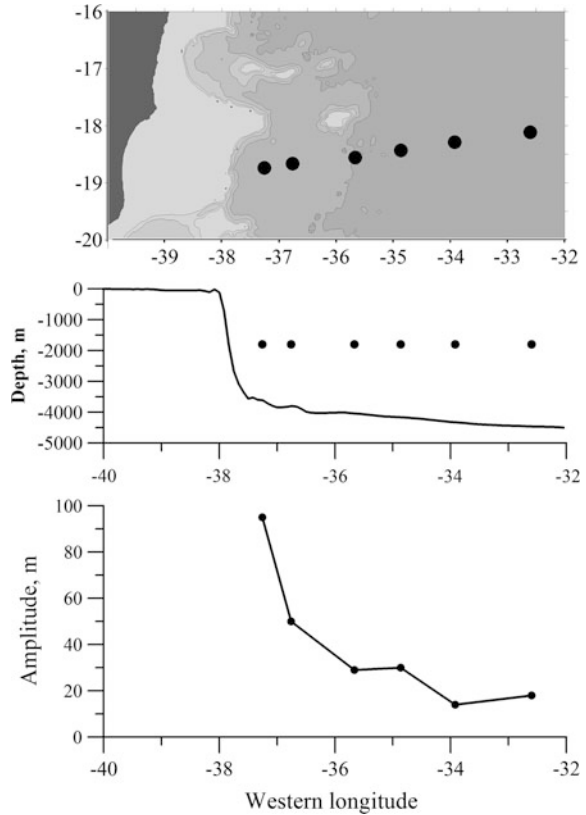
Experiments ACM-3 and ACM-12 (Deep Ocean) of the WOCE Program were dedicated to the investigation of the bottom circulation in the Atlantic in 1991–1992. Scientists from WHOI (USA) and Meereskunde (Germany) deployed 12 moorings in the South Atlantic. The ACM-3 array of moorings was extended almost in a line normal to South America up to the Vema Channel between 28°–31° S and 47°–38°W. The location of moorings is shown in Fig. 2.15. In addition to the deep instruments all moorings had current and temperature meters in the main thermocline. We selected the temperature measurements in the layer 800–1100 m to analyze the variations in the amplitudes of internal tides as function of distance from the continental slope. The locations of instruments over the background of the depth profile are shown in the top panel of Fig. 2.18. The amplitudes of internal tides are shown in the bottom panel. One can see a decrease in the amplitudes up to the Vema Channel as the distance from the continental slope increases. The amplitude of temperature fluctuations associated with the semidiurnal internal tides on the eastern moorings at the depths of 900–1000 m was 0.2 °C, which corresponds to the vertical displacements equal to 20 m.

Fig. 2.17 Spectrum of temperature fluctuations (ACM-24). Measurements at 1800 m on the mooring at 18° 44′S, 37° 15′W
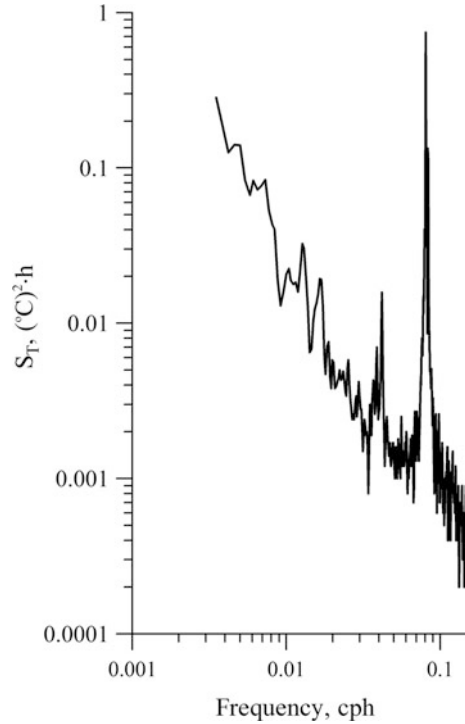
Some publications report the measurements of the internal tides in the region. Measurements of the internal tides in 2001 near Brazil in the region of Cabo Frio (23°S, 42°W) were reported by Pereira and Castro (2007). Analysis of the measurements supported by the model simulations was presented by Pereira et al. (2007). Internal tides are generated over the shelf break and slope. The amplitudes of the semidiurnal internal tides reached 30 m.

Model simulations of internal tide generation in the region of the Mid-Atlantic Ridge over the axis of the ridge between 33° 35′S, 34° 17′S and 13° 40′W, 15° 40′W were performed by Zilberman et al. (2009). Internal tides propagated from the Mid-Atlantic Ridge with peak depth-integrated baroclinic energy fluxes of 1100–1500 W m^{-1}.

2.6   East Equatorial Atlantic, Gulf of Guinea, GATE-77 Experiment

Two clusters of moorings were deployed in the East Equatorial Atlantic during the Global Atmospheric Research Program (GARP) and the GARP Atlantic Tropical Experiment (GATE) in 1977 and 1978. The experiments were organized by the

Fig. 2.18 Decay of the
internal tide amplitudes with
the distance from the
continental slope based on the
WOCE ACM-3 and ACM-12
experiments. Locations of
moorings on the map of
bottom topography (top
panel); locations of
instruments relative to the
slope (middle panel);
amplitude of the semidiurnal
internal tide versus longitude
(bottom panel)
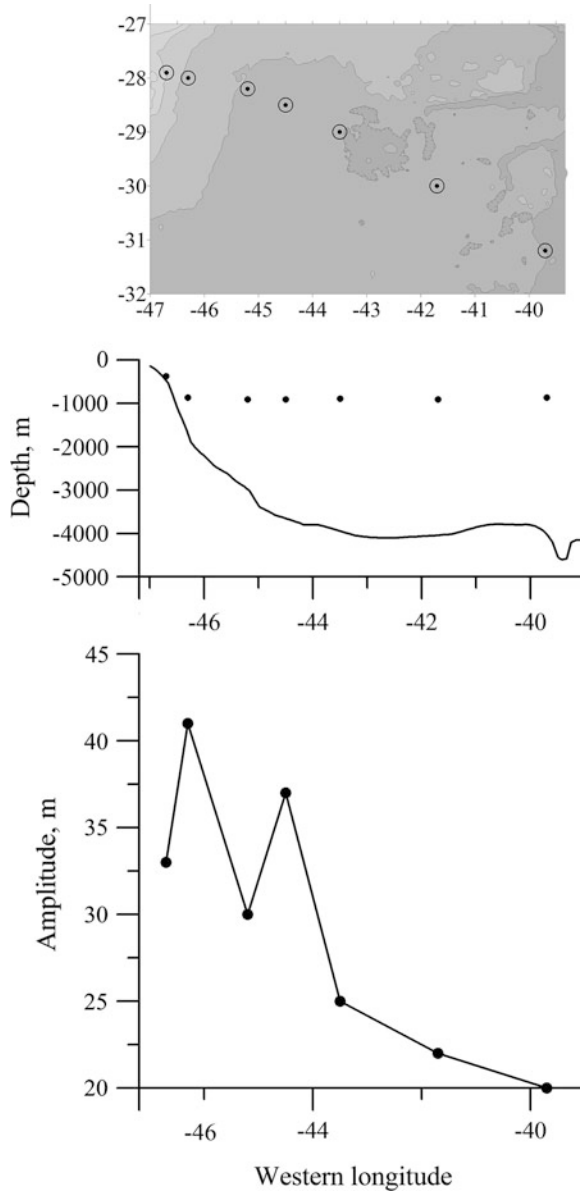
IFREMER Institute (France). The region is located in the Guinea Gulf approximately at the equator at 4°W. The moorings were deployed 250 miles south of the continental slope of Africa (Käse and Clarke 1978; Käse and Olbers 1980) (Fig. 2.19).
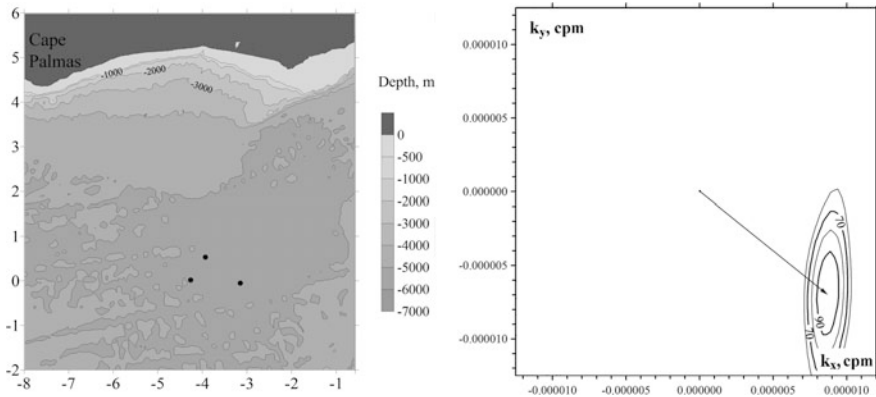
Fig. 2.19 Bottom topography (meters) in the Guinea Gulf and locations of moorings of the GATE-77 experiment. Depth contour lines are shown at depths of 500, 1000, 2000, 3000, 4000, and 5000 m. Land is shown with gray color. Locations of the moorings are shown with black symbols (left panel). Spatiotemporal spectrum at the semidiurnal frequency in the study site GATE-77 south of the Guinea coast at a depth of 600 m (right panel). The contour lines correspond to 90, 80, 70, and 60% of the main maximum. The arrow shows the wave vector corresponding to a wavelength of 91 km

Spectral functions of temperature and velocity fluctuations were characterized by significant peaks at the semidiurnal frequency. The amplitudes of the semidiurnal internal tides at a depth of 900 m were approximately 50 m. Only three moorings were deployed. The low number of moorings decreased the accuracy of estimating the wavelength and direction; the peak of the spatiotemporal spectrum is wide. The estimates of the spatiotemporal spectrum at the semidiurnal frequency from the temperature data at 600 m show a maximum corresponding to a wavelength of 91 km. The waves propagated southeast from the steep African continental slope at Cape Palmas (Fig. 2.19).

2.7   Northwest Atlantic, SYNOP-87, Gulf Stream Extension-79, RISE-74 Experiments

Many moorings were deployed in the Northwest Atlantic. A chart of the mooring locations is shown in Fig. 2.20. The experiments include: SYNOP 1987 (WHOI); Gulf Stream Extension 1979 (WHOI); Rise 1974 (WHOI); Gulf Stream Line W in 2005–2008 (WHOI); Low Level Waste Dumping experiment in 1980–1984 (Oregon State University), Deep Water Dump Experiment Site 106 in 1989–1991 (US Geological Survey); moorings near Cape Hatteras (NC Field, 1992–1993) (US Minerals Management Service); MASAR experiment (1984–1985) (Science Applications International Corp, USA); West Boundary Undercurrent experiment in 1977–1978 (WHOI); and many standalone moorings, for example, moorings

WHOI 506 at 39° 23′N, 69° 59′W and WHOI 507 at 39° 10′N 70° 00′W in 1973–1974. Bottom topography of the region and locations of moorings are shown in Fig. 2.20.

The moorings of the Gulf Stream Extension south of the Newfoundland Bank recorded internal tides with amplitudes up to 40 m at a depth of 1000 m. The waves propagated from the continental slope to the southeast (140°). The wavelength was 100 km (Fig. 2.21).

The spatiotemporal spectrum at the SYNOP study site was calculated on the basis of temperature measurements at 500 m. The spectral peak indicates that internal tides with a wavelength of 100 km propagated from the continental slope to the south (185º) (Fig. 2.21). The wave amplitudes decayed in the southern direction and the signal of measurements on the southern moorings was weak.

The spatiotemporal spectrum based on the measurement from the RISE experiment was calculated from the data at 200 m on six moorings. The spectral peak indicates that internal tides with a wavelength of 100 km propagated to the southeast (135º) from the continental slope (Fig. 2.21).

Five moorings were deployed in a line normal to the continental slope in the Gulfstream Line W experiment. Temperature measurements at 1000 m were carried out on three moorings W2, W4, W5 (39° 13′N, 69° 27′W; 38° 25′N, 68° 54′W;
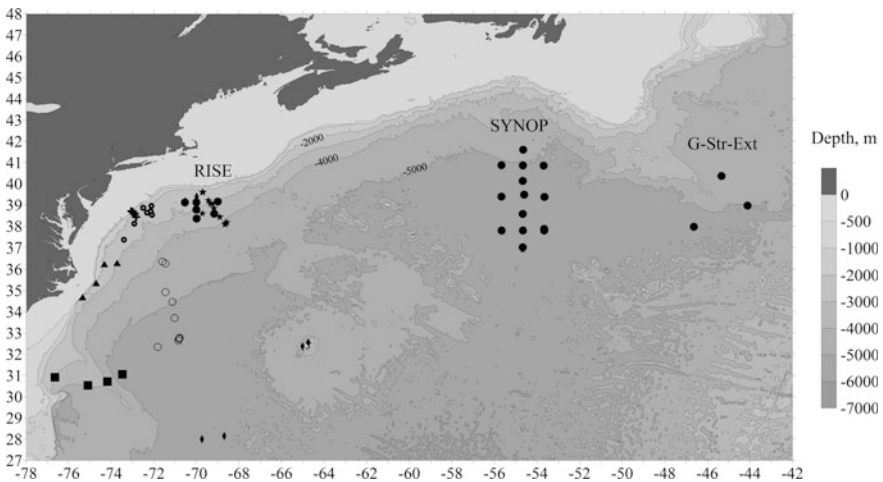
Fig. 2.20 Bottom topography (meters) of the Northwest Atlantic region. Depth contour lines are shown at depths of 500, 1000, 2000, 3000, 4000, 5000, and 6000 m. Locations of moorings are shown with black symbols. The following experiments are indicated with different symbols: RISE, SYNOP, and Gulf Stream Extension (large dots); Deep Water Dump experiment (smaller dots with a white circle in the middle); Gulf Stream Line W (stars); Hatteras (triangles); Low Level Waste Dump (open circles); MASAR (crosses); Standalone miscellaneous moorings (diamonds); West Boundary Undercurrent (squares). Land is shown with gray color
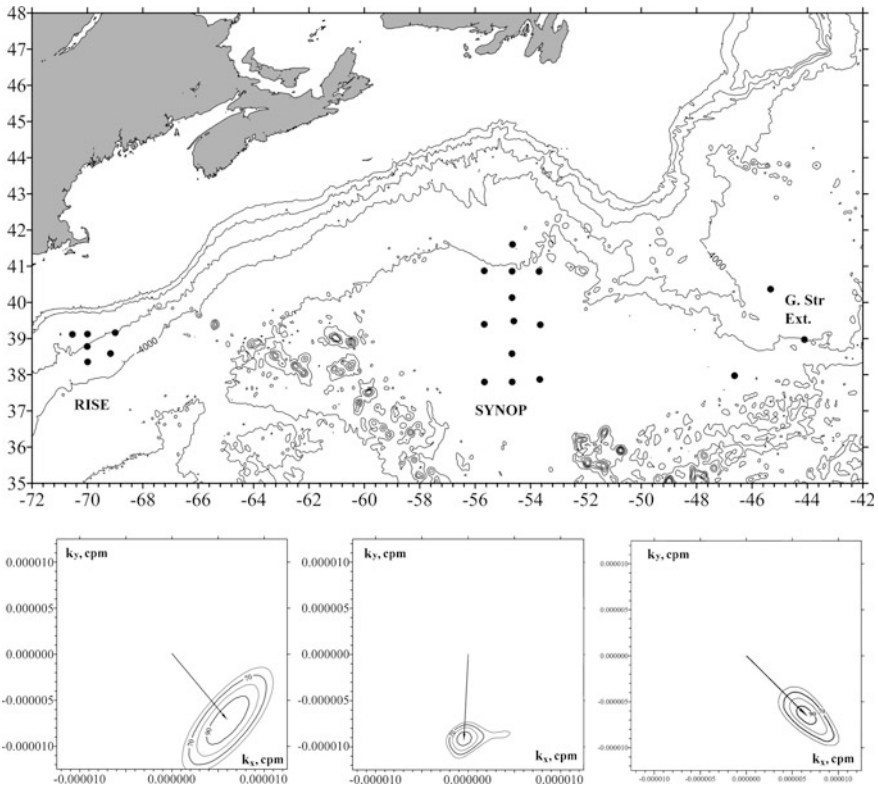
Fig. 2.21 Bottom topography of the Northwest Atlantic in the region of the RISE, SYNOP, and Gulf Stream Extension experiments and locations of moorings. Spatiotemporal spectra at the semidiurnal frequency at each of the three study sites are shown in the lower part of the figure from left to right. The contour lines correspond to 90, 80, 70, and 60% of the main maximum. The arrows show the wave vectors corresponding to a wavelength of 100 km

38° 04′N, 68° 40′W) shown in Fig. 2.20 with stars. The amplitudes of the semidiurnal internal tides at moorings W2, W4, and W5 decreased from the continental slope in the following sequence: 50, 30, and 25 m, respectively.

Four moorings were deployed along 31°N approximately along the line from the continental slope (from 76° 39′W to 73° 29′W) (Figs. 2.13, 2.20) in the West Boundary Undercurrent (WBUC) experiment (1977–1978). The amplitudes of internal tides at 2000 m decreased over 200 km from 30 to 20 m.

All measurements indicate that the internal tides propagated from the continental slope in approximately the normal direction to the slope. The amplitudes decay with the distance from the slope.
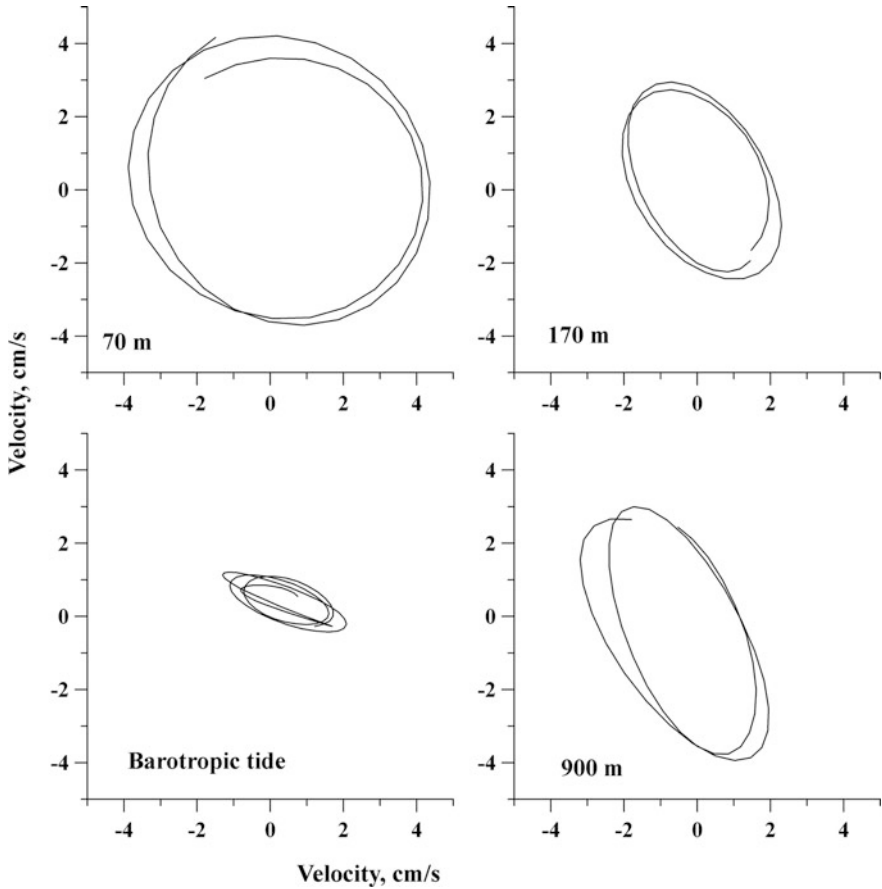
Fig. 2.22 Ellipses of the currents of the barotropic tide and internal tides at 70, 170, and 900 m on the mooring deployed at 38° 40′N, 72° 59′W

Moored measurements in the MASAR experiment in 1984–1985 (locations of moorings are shown in Fig. 2.20) demonstrate vertical variations in the ellipses of tidal currents on the mooring deployed at 38° 40′N, 72° 59′W. The mooring was deployed at a depth of 970 m.

Tidal ellipses of the internal tide were calculated after removing the currents of the barotropic tide. The latter was calculated after band-filtering of the initial time series, and then the measurements at each hour were averaged over the vertical. Tidal currents associated with the internal tide are strong at the surface and at the bottom. The currents are weaker at a depth of 170 m corresponding to the zero of the eigen function for the horizontal velocity associated with internal tides. The ellipses are shown in Fig. 2.22.

2.8 Northwest Atlantic Shelf

In the region of the US eastern coast, the tidal currents generate strong internal tides over the shelf break and continental slope. Intense internal tides propagate in both directions from the slope, while the internal wave front appears approximately parallel to the continental slope. Investigations of internal waves in this region are presented in a number of publications (Vlasenko et al. 1997; Hallock and Field 2005). Depth-integrated, time-averaged fluxes of the energy of high-frequency internal wave packets propagating to the shore in the northwestern direction range from 9 to 24 W m^{-1} based on the ADCP measurements by Hallock and Field (2005).

Provided that the data are available, it is possible to compare the results of field measurements, numerical modeling, and remote observations from space (Bondur et al. 2006a, b). Internal waves cause variations in surface waves (ripples), which are recorded using optical and radar instruments. Many images of surface manifestations of internal waves were obtained recently using radars with synthetic aperture (SAR images) from the ERS-1,2 Radarsat and ENVISAT (Apel et al. 1975; Bondur 1995; Bondur et al. 2005).

Satellite images of the oceanic region near Long Island at the eastern US coast showed that well pronounced surface manifestations of internal waves are observed in the period from May to October when a sharp seasonal thermocline exists due to the summer warming of the surface. In this study we used seven images from the Radarsat-1 satellite (standard beam full resolution, size of the images 100 km 100 km, resolution 26 × 30 m) in the period from June 1997 to August 2002 obtained within the NASAMQ N0361 GB project.

A radar image of the sea surface with manifestations of internal waves superimposed on the bottom topography north of the Hudson Canyon is shown in Fig. 2.23. The waves are formed at the shelf break near the upper part of the continental slope. One wave system propagates to the coast and the other is directed to the open sea. The wave crests are clearly oriented along the isobaths.

The wave propagating to the coast gets a permanent energy supply. This energy supply can compete with dissipation and lead to intensification of the wave and strong nonlinearity. The waves generated at the shelf break that propagate to the ocean almost do not manifest themselves at the surface. In this case the energy of internal tides is distributed over the deep water column and does not concentrate over the shallow shelf as occurs when the waves propagate to the shore.

Usually, intense high-frequency internal waves propagate as packets with a periodicity close to 12 h. We analyze the wave propagation using the numerical model developed by V. Vlasenko (see Sect. 1.4.1) (Vlasenko 1992; Vlasenko et al. 1997; Vlasenko and Alpers 2005). Numerical modeling allows us to obtain internal wave properties in a wide range of oceanic conditions: stratification, parameters of the tide, bottom topography, and also to investigate separately any factor influencing the properties of internal waves, which is impossible in an oceanic field experiment.

Tidal velocities were calculated from the satellite data using the NASA database available at Oregon State University; the method is described by Egbert and Erofeeva (2002). The bottom topography was specified from the ETOPO digital database. Stratification of the ocean (unperturbed state) was taken from the CTD-data in this region (WOD13 2013).

The domain for numerical simulations was 240 km long with a horizontal step of 50 m and 30 vertical levels. The width of the shelf was specified as 100 km. The ocean bottom over the shelf gently deepened to 200 m and then sharply increased over the continental slope. The time step was 2 s. The coefficients of horizontal viscosity and density diffusion over the slope were specified at 20 m^2/s, while beyond the slope they were 3 m^2/s; the corresponding vertical coefficients were 0.0001 m^2/s.

As a result of simulations we obtained a density section for the given tidal phase when the wave propagates opposite to the tidal currents, which cause intensification of the wave. The calculated density field after 5.4 M_2 periods is shown in Fig. 2.24. The selection of this phase is related to the fact that two wave fronts are seen in the

domain of simulations. The figure clearly shows the formation of an internal wave propagating from the shelf break to the open ocean as well as an internal wave propagating to the shore over the shelf.

The wavelength of the wave directed to the shore was close to 25 km, while the wavelength of the oceanic wave was about 120 km. The amplitudes of internal tides over the shelf reached 50 m. High amplitudes of internal tides are confirmed by moored measurements on the continental slope during the MASAR experiment on a mooring (CMDAC number 6871; 38° 43′N, 73° 04′W) at a depth of 130 m over the shelf depth equal to 200 m.

Analysis of the satellite images of the ocean surface showed that intense internal waves are seen at the surface as alternating dark and light bands. The distance between wave crests appeared close to the results of numerical modeling (20 km over the shelf and 120 km in the open ocean). The maximum amplitudes were found in the region where internal tide propagates to the shelf. After further propagation the wave breaks into packets of short-period waves and eventually decays.

Numerical modeling showed that internal perturbations propagate along characteristic surfaces. This is seen in Fig. 2.25. The curves corresponding to the characteristic surfaces are plotted in Fig. 2.25 with thick black lines.

In the other research site, moored measurements were performed in 1983–1984 on the US continental slope deeper than the shelf break at 39° 55′N, 70° 05′W. Moored current meters were installed at 124, 140, 240, 390, and 484 m, over a depth of 491 m. The amplitudes of the semidiurnal internal tides exceeded 100 m. The mooring was located at the point of a wide internal wave beam so that intense oscillations were recorded in the layer 240–390 m. The fluctuations in the upper layer and near the bottom were weak. A scheme of the beam and spectra are shown in Fig. 2.26.

The generation of internal tides over the continental slope in this region was considered by Shroyer et al. (2011). Packets of short-period internal waves appeared with a periodicity of the M_2 internal tide. The amplitudes of internal waves reached 15 m. Internal tides in the regions closer to the coast and in the

Fig. 2.24 Simulated density field over a section normal to the shore in the Long Island region after 5.4 tidal periods of calculation. The density of seawater at the surface was assumed equal to 1.02256 g/cm^3. Density contour lines are plotted with an interval of 0.0002 g/cm^3
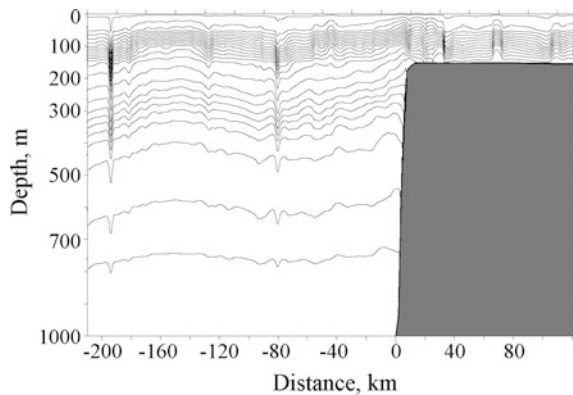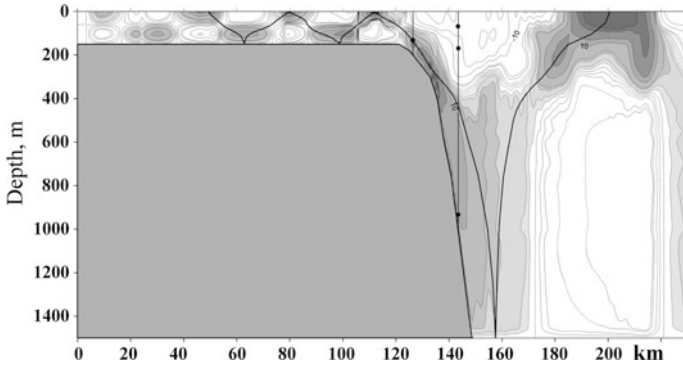
Fig. 2.25 Simulated velocity field (cm/s) over a section normal to the shore in the Long Island region after 5.4 tidal periods of calculation. The characteristic curve is shown with a heavy line. Locations of the MASAR experiment moorings on the continental slope are shown with vertical lines; the dots on the lines indicate instruments
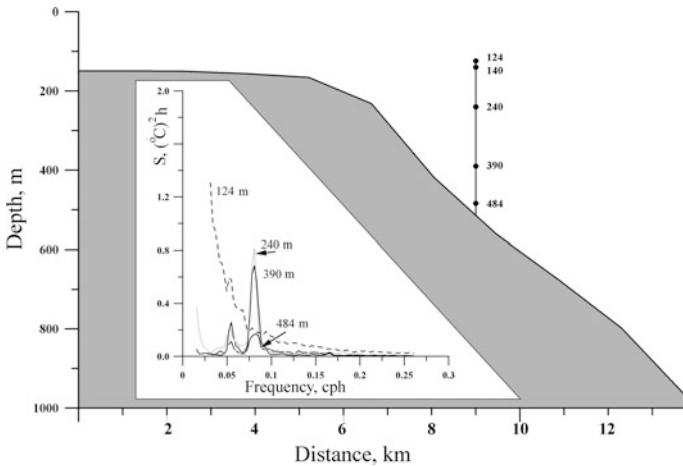
Fig. 2.26 Spectra of temperature fluctuations measured on mooring at 39° 55′N, 70° 05′W at levels of 124, 140, 240, 390, and 484 m, over a depth of 491 m. The spectra show intensification of fluctuations on the beam of internal semidiurnal perturbations at depths of 240–390 m. The gray color shows the profile of the bottom slope

estuaries were analyzed by McCardel et al. (2016). The authors indicate that internal tides result from various causes, for example, tidal straining of the along-channel density gradient modulating stratification and also dissipation of internal waves.

Energy fluxes of internal waves from the shelf-edge of Nova Scotia and Grand Banks were studied by Sandström and Oakey (1995), and by Sandström and Elliott

(1984, 2011). The energy flux from the Nova Scotia shelf was within 1300–4700 W m^{-1}, whereas it was smaller from the Grand Banks (200 W m^{-1}).

Very high internal tides were recorded in the lower St. Lawrence estuary (49°N, 68°W) (Wang et al. 1991). The largest vertical displacement occurred near the sill, which is the generation region. The average amplitude of the internal tide was 40 m, while the maximum values could reach 80 m during the spring tides. The amplitude decreased with the distance from the generation region.

Studies of internal tides on the basis of modeling and moored observations in the region of Georges Bank in the outer Gulf of Maine were reported by Brickman and Loder (1993) based on the measurements with moored thermistors at 42° 00′N, 66° 50′W. This is a region of strong tidal flow. The estimated energy flux was 195 W m^{-1}.

2.9   West of Great Britain, CONSLEX, NEADS Experiments

Moored measurements were carried out in 1978 and 1982 west of Great Britain and Ireland. We analyzed the data of moorings from the Continental Slope Experiment (CONSLEX) and North East Atlantic Dynamic Study (NEADS). The experiments were organized by the Institute of Oceanographic Sciences, Deacon Lab., and the Ministry of Agriculture, Fisheries and Food (MAFF) (UK). A chart of the moorings is shown in Fig. 2.27. Moored measurements reveal strong semidiurnal internal tides. The measurements in 1982–1983 (CONSLEX) on a mooring deployed on the western slope of the Rockall Trough (53° 25′N, 19° 01′W, depth 2495 m) showed that temperature fluctuations at a depth of 1200 m exceed 0.5°C, which corresponds to the vertical displacements in the internal tide exceeding 100 m. High amplitudes of internal tides (100 m) were also found in 1986–1987 at a depth of 600 m on the eastern slope of the Rockall Trough (51° 03′N, 15° 10′W, depth of the ocean is 2978 m).

The amplitudes of internal tides measured in 1991–1992 on a mooring at a distance of 100 km from a steep slope (52° 20′N, 16° 21′W, depth 3510 m) at depths of 510 and 810 m were 35 and 40 m, respectively. The amplitudes of the semidiurnal tide in the southern part of the Rockall Trough (52° 25′N, 17° 45′W, depth 4200 m) at a depth of 1137 m (measurements in 1980–1981) were 30–35 m.

There was no synchronous operation of the moorings in this region; therefore calculation of spatiotemporal spectra is not possible. The direction of waves can be determined from the ellipses of tidal oscillations related to internal waves. The measurements in 1982–1983 on a mooring at 60° 12′N, 9° 14′W were performed at four depths (250, 654, 1055, and 1440 m). The depth at the mooring location is 1463 m. It is possible to separate the baroclinic motion by averaging the semidiurnal fluctuations of currents at four depths (see Sect. 7.5). Four-day ellipses of the barotropic tide and internal wave averaged by vertical are plotted in Fig. 2.28. The direction of the major axes of the ellipses almost normal to the slope indicates that
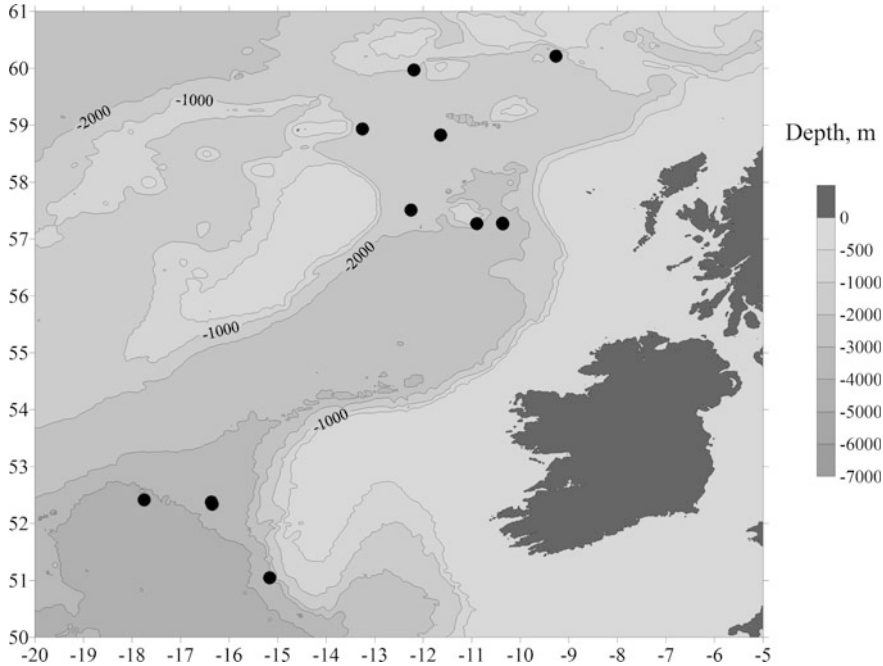
Fig. 2.27 Bottom topography west of Great Britain and Ireland. Depth contour lines are shown at depths of 500, 1000, 2000, 3000, and 4000 m. Locations of moorings are shown with black symbols. Land is shown with gray color

internal tides propagate from the continental slope, while the ellipse for the barotropic tide is extended in the direction of the passage, because the currents of the barotropic tide are governed by the bottom topography.

Internal tides in this region were analyzed by Sherwin (1988). The author calls this region the Malin shelf. The onshore flux of internal wave energy was 104 W m^{-1}. Investigations were also carried out in the Rockall Deep. A numerical model was applied by Sherwin and Taylor (1990) to study internal wave generation over the Malin shelf. The authors indicate that a critical region exists at the shelf break where the bottom depth increases from 200 to 700 m. The energy flux to the ocean was of the order of 20 W·m^{-1}. Moored ADCP measurements reported by Inall et al. (2000) resulted in estimates of vertical diffusivity of the order of 10^{-3} m^2/s. An analytical model was used to study internal tides in the region (Guizien et al. 1999). The results of modeling agree with the observations using thermistor chains and moored ADCP. The amplitude of the displacements of the thermocline was 8 m; the total baroclinic energy was estimated at 3 J/m^3. Detailed modeling studies of internal tides in the region were reported by Xing and Davies (1996). The existence of the energetic internal tide west of Scotland was reported by
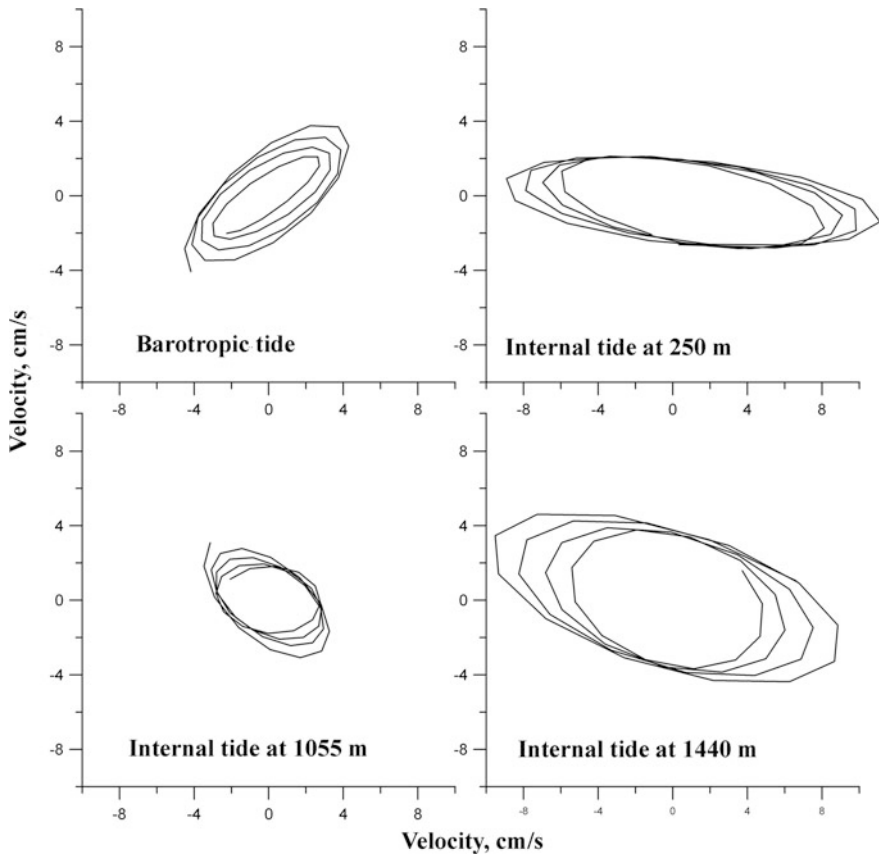
Fig. 2.28 Ellipses of the currents of the barotropic tide and internal tides at 250, 1055, and 1440 m on the mooring deployed at 60° 12′N, 9° 14′W

Rippeth and Inall (2002) based on seabed mounted ADCP and thermistor chain deployed in 1996. The diffusion coefficients were estimated at $1.6–6.1 \times 10^{-4}$ $m^2 s^{-1}$. Beams of internal tide generated at the shelf break disintegrate into packets of short-period internal waves that lose their energy. A model of this process was considered by Vlasenko and Stashchuk (2015).

2.10 Gulf of Mexico

The measurements were carried out in 1985 within the Gulf of Mexico Physical Oceanography Program (GMPO). The experiment was organized by the Science Applications International Corp. (SAIC, USA). A cluster of moorings was deployed in the Gulf of Mexico (24°–26°N, 94°–96°W), which made possible the
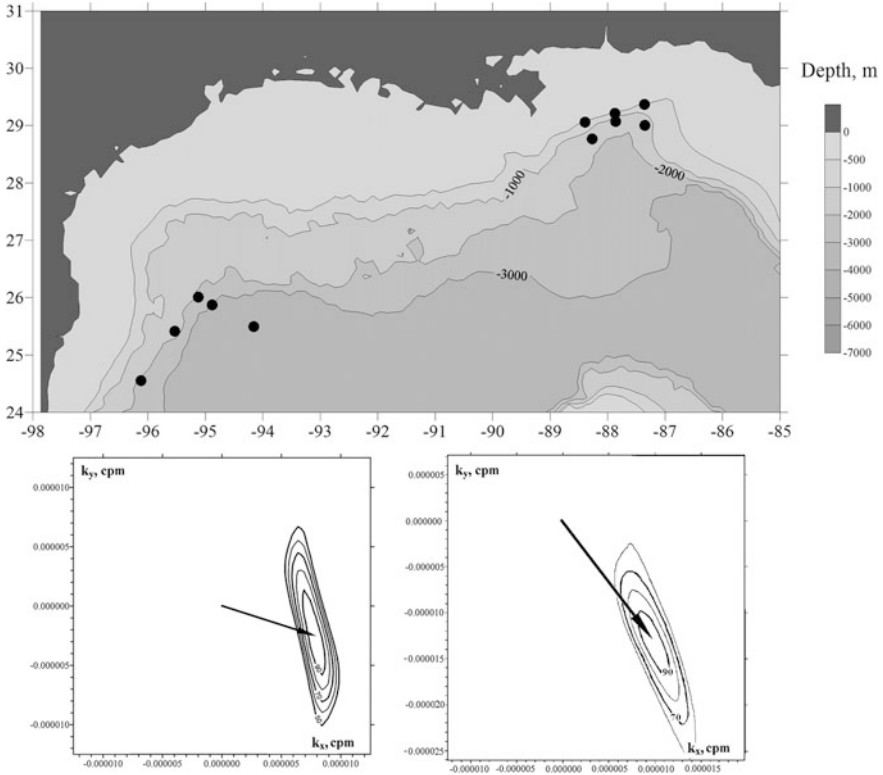
Fig. 2.29 Bottom topography of the Gulf of Mexico. Locations of moorings in the GMPO and DESOTO experiments are shown with black dots. Depth contour lines are shown at depths of 500, 1000, 2000, and 3000 m. Spatiotemporal spectra at the semidiurnal frequency for each of the two study sites are shown in the lower part of the figure from left to right. The contour lines correspond to 90, 80, 70, and 60% of the main maximum. The arrows show the wave vectors corresponding to a wavelength of 120 km (GMPO) and 55 km (DESOTO)

investigation of internal tides generated over the continental slope. A chart of the moorings is shown in Fig. 2.29. Temperature fluctuations at 1000 m at the semidiurnal frequency exceeded 0.5 °C, which corresponds to the vertical displacements larger than 100 m.

The calculation of the spatiotemporal spectrum was performed on the basis of data on five moorings at 300 m. The direction of semidiurnal tide was 110°; the wavelength was 120 km. The direction of the waves almost normal from the continental slope indicates that the waves were generated over the slope.

The DESOTO experiment in 1997 (near the De Soto Canyon) was conducted in another part of the Gulf of Mexico (29°–29° 30′N, 87°–89°W) (Fig. 2.29) (Wang et al. 2003). The experiment was organized by SAIC, USA. The calculation of the

spatiotemporal spectrum was performed on the basis of measurements on four moorings at 500 m. The direction of the semidiurnal internal tides was 150° from the continental slope, and the wavelength was 55 km. The wavelength was shorter than in the GMPO experiment because the depth of the sea here is shallower (approximately 2000 m).

2.11 Falkland Gap, MAPCOWS-86 Experiment

The MAPCOWS cluster of moorings was one of a long series of experiments conducted jointly by Oregon State University and Texas A & M University. The measurements near the Falkland Ridge confirm that the internal tides in the South Atlantic are strong.

The MAPCOWS experiment in 1986 included the deployment of 14 moorings for a time period of 10 months in the region of the Falkland Gap in the Falkland Ridge. Seven of the total 14 moorings were deployed along the 41° 12′W meridian north of the ridge in a line normal to the ridge. A chart of the moorings is shown in Fig. 2.30. The line of moorings was extended along a distance of 224 km. The temperature and salinity meters were located at depths in the range 1500–1750 m and 3300–3600 m and also in the bottom layer. We estimated the amplitude of internal tides close to 50 m with low variations over a distance of 224 km.
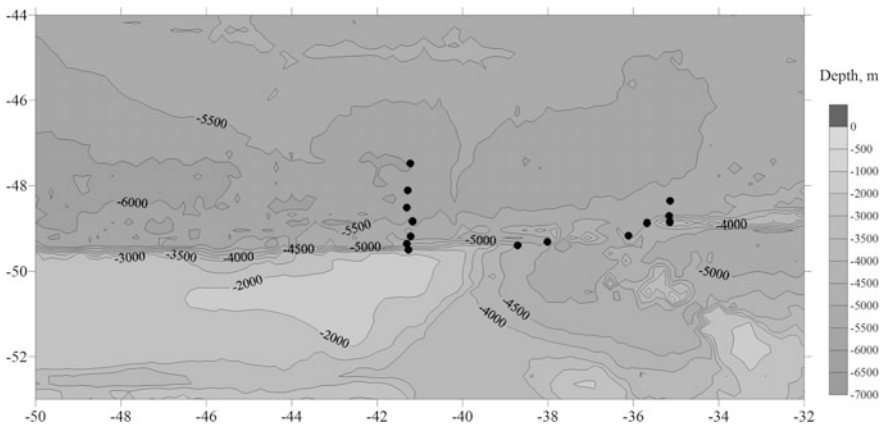
Fig. 2.30 Bottom topography in the region of the Falkland Gap, the MAPCOWS experiment. Depth contour lines are shown at depths of 500, 1000, 2000, 2500, 3000, 3500, 4000, 4500, 5000, 5500, and 6000 m. Locations of moorings are shown with black dots

2.12 Biscay Bay

The Ocean Margin Exchange Project (OMEX) experiment was conducted to support the idea that continental shelves and slopes could be significant sinks for the atmospheric CO_2. The experiment was organized by the Institute für Meereskunde (Germany). The locations of instruments on the moorings and the data collected in this experiment allowed us to estimate the amplitudes of the internal tides. In the OMEX experiment, characteristics of internal tides in Biscay Bay were investigated from the moored temperature data in 1993-1995. Seven moorings were deployed on the northern slope of Biscay Bay. The locations of moorings are shown in Fig. 2.31. The amplitudes of internal tides at depths of 1000–1500 m over the ocean bottom at 2000–3000 m reached 100 m. Pingree and New (New and Pingree 1990a; 1990b; Pingree and New 1991) reported on even greater peak to peak amplitudes, which were as high as 200 m.

Four moorings (black dots with a white circle in the middle in Fig. 2.31) were deployed on the northern slope of Biscay Bay in 1980-1981 at points with coordinates 47°16' N, 9° 58′W; 48° 05′N, 9° 50′W; 48° 08′N, 9° 45′W; 48° 07′N, 9° 17′W. The instruments were located at depths of 800–1000 m, while the ocean bottom increased from 1470 to 4400 m. Such locations of moorings in a cluster allowed us to calculate the spatiotemporal spectrum for the semidiurnal internal tides and estimate the direction of the waves to the southeast from the northwestern part of the continental slope (130°); the wavelength was estimated within
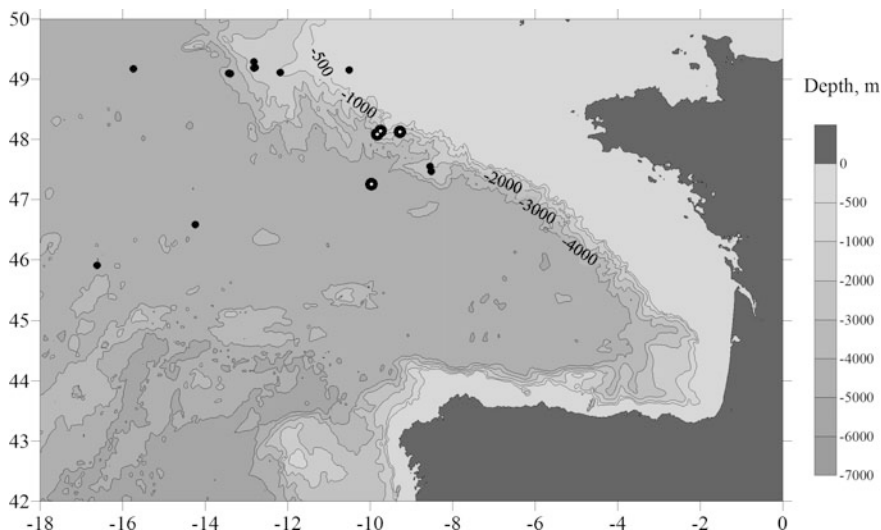
Fig. 2.31 Bottom topography in the region of Biscay Bay. Depth contour lines are shown at depths of 500, 1000, 2000, 3000, 4000 m. Locations of moorings are shown with black dots. The moorings used to calculate the spatiotemporal spectrum are indicated with a white circle in the middle

140–150 km. It is noteworthy that the direction and wavelength remain the same over the entire period of measurements. The amplitude of internal tides was within 70–80 m (Fig. 2.32).

Data of moorings near the northern shelf edge of Bay of Biscay were analyzed by Xie et al. (2015). During the spring tide, strong nonlinear internal tides and large amplitude internal solitary waves were observed. Onshore and seaward traveling internal tides were identified. The signal of internal tide can be observed over a distance of 300 km from the shelf edge (Pingree and New 1995). Beams of internal wave energy were found from the data of moored thermistor chains by Pingree and New (1989). Packets of large-amplitude internal solitons were found at a distance of 150 km from the shelf edge by New and Pingree (1990a). Associated horizontal and vertical velocities were as high as 60 and 16 cm/s, respectively. Moored measurements at the shelf break at 48°N, 8°W on the northern slope of Bay of Biscay by Pichon and Mazé (1990) show that the amplitudes of internal tides can reach 80 m. Strong M_2 internal tides in this region were also reported by van Haren (2007b). The region of Biscay Bay was indicated by Baines (1982) as the region of strong internal tide generation on the continental slope.

Moored measurements reported by Jézéquel et al. (2002) provide evidence of very high amplitudes of internal tide (200 m) on the continental slope at 47° 30′N,
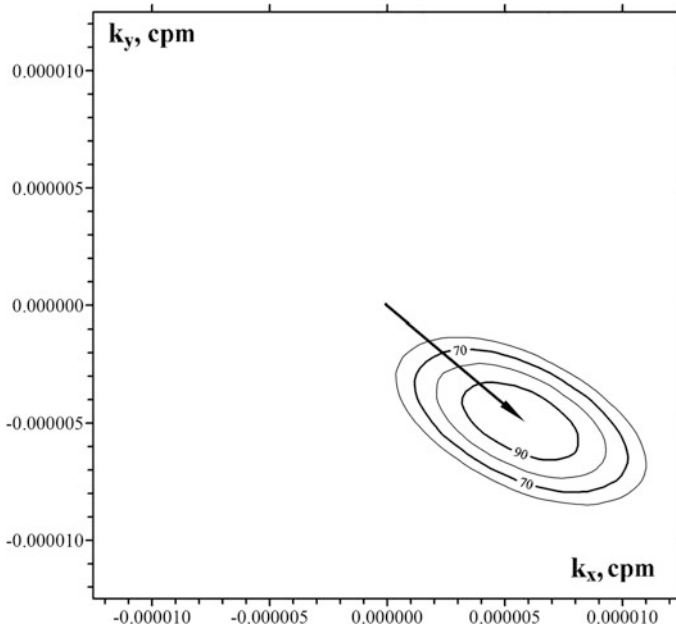
Fig. 2.32 Spatiotemporal spectrum at the semidiurnal frequency based on the data of four moorings shown in Fig. 2.31 by black dots with a white circle in the middle. The contour lines correspond to 90, 80, 70, and 60% of the main maximum. The arrows show the wave vectors corresponding to a wavelength of 145 km

7° 15′W at the depths of the ocean from 400 to 1000 m. Strong internal tides over the Celtic Sea shelf break in the northern part of Biscay Bay, which is a hot spot of tidal energy conversion (Baines 1982), were studied by Vlasenko et al. (2013, 2014). The authors analyze moored measurements in 2008 at 50°N, 8°W over the Jones Bank, and in 2012 at 48° 30′N, 9° 30′W over the shelf break. The time series recorded at a shelf break mooring showed that the semidiurnal internal tides were accompanied by packets of internal solitary waves with maximum amplitudes up to 105 m. The amplitudes of waves near the Jones Bank were as high as 40 m.

2.13   West of the Iberian Peninsula and Gibraltar Strait, MORENA, WOCE ACM-27, ACM-28, Vityaz-88 Experiments

Two lines of moorings were deployed in 1993–1994 on the continental slope of the Iberian Peninsula as part of the Multidisciplinary Oceanographic Research in the Eastern Boundary of the North Atlantic project (MORENA). The experiment was organized by the Instituto Español de Oceanografía (Spain) and Universidade de Lisboa (Portugal). The lines included three WOCE ACM-27 moorings (along 42° 16′N) and four ACM-28 moorings along 41° 00′N from 9° 30′W to 11° 00′W (Fig. 2.33). The eastern mooring was located at a distance of 50 km from the shore on the continental slope at a depth of 1300 m. The line of moorings extended to the depth of 4000 m. The length of the northern line was 100 km and the length of the southern line was 150 km. The amplitude of the semidiurnal internal tides decreased over 150 km from 75 m on the continental slope to 38 m in the deep basin.

In 1988, the Russian R/V *Vityaz* (Shirshov Institute of Oceanology) deployed 19 moorings for a period of 15 days each west of the Strait of Gibraltar to study the formation of Mediterranean lenses of high salinity. The locations of moorings are shown in Fig. 2.33.

These measurements allowed us to estimate the amplitude, wavelength, and direction of internal tides. The amplitudes were within 30–40 m. On a mooring cluster (33°N, 11°W), in which the moorings operated synchronously for 15 days, it was possible to estimate the direction and wavelength of the semidiurnal internal tides. We expected that the waves would propagate from the continental slope in the region of Morocco, but the waves arrived in the direction to the south-southwest (200°) from the southwestern coast of the Iberian Peninsula. The wavelength was 100 km (Fig. 2.34).

Moored measurements west of the Iberian Peninsula were carried out in 1996–1999 within the OMEX Program (CMDAC numbers: 6988–6993 and 7016–7042) on several moorings at: 42° 39′N, 9° 42′W; 42° 37′N, 10° 02′W; 39° 37′N, 9° 44′ W; 41° 22′N; 9° 18′W; 38° 13′N, 9° 47′W; 38° 24′N, 9° 46′W. The experiment
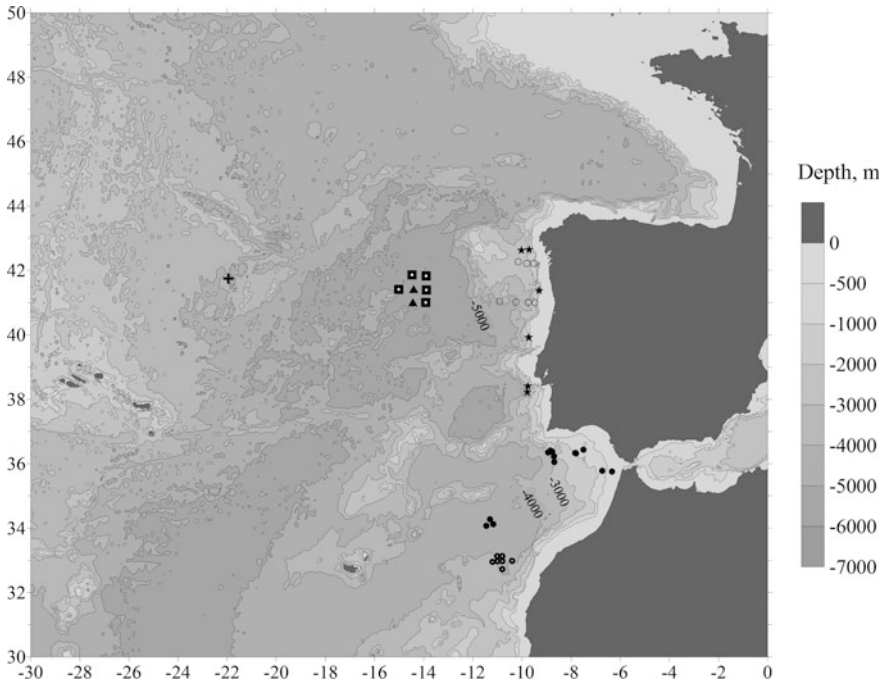
Fig. 2.33 Bottom topography (meters) west of the Iberian Peninsula. Depth contour lines are shown at depths of 500, 1000, 2000, 3000, 4000, and 5000 m. Locations of moorings are shown with black symbols. The moorings from the following experiments are indicated with different symbols: ACM-27, ACM 28 (open circles); Vityaz-88 (black dots, the moorings used to calculate spatiotemporal spectrum have white dots in the middle); OMEX experiment (stars); moorings in 1984–1985 (squares and triangles, the spatiotemporal spectrum was calculated from the data on moorings indicated with a white dot in the middle); standalone mooring (cross). Land is shown with gray color

was organized by the Institute für Meereskunde (Germany). The mean amplitude of the semidiurnal internal tides at depths of 600–1000 m was estimated at 30–40 m.

In 1984–1985 moored measurements were carried out on a cluster located close to 41° 30′N, 15° 00′W. The data were downloaded from the CMDAC database (CMDAC numbers: acc00739–acc00747). Temperature meters were set at depths of 2600–2700 m on five moorings. The mean amplitude at a depth of 2600 m was estimated at 30–40 m, and at a depth of 1500–1600 m the amplitudes were 40–50 m.

The spatiotemporal spectrum based on the data at 2600 m using the Barber's method (Barber 1963) is shown in Fig. 2.35. The wavelength of the semidiurnal internal tides was 105 km. The waves propagated from the northeast from a region of shallower depths less than 850 m at 42°30′N, 12°00′W.
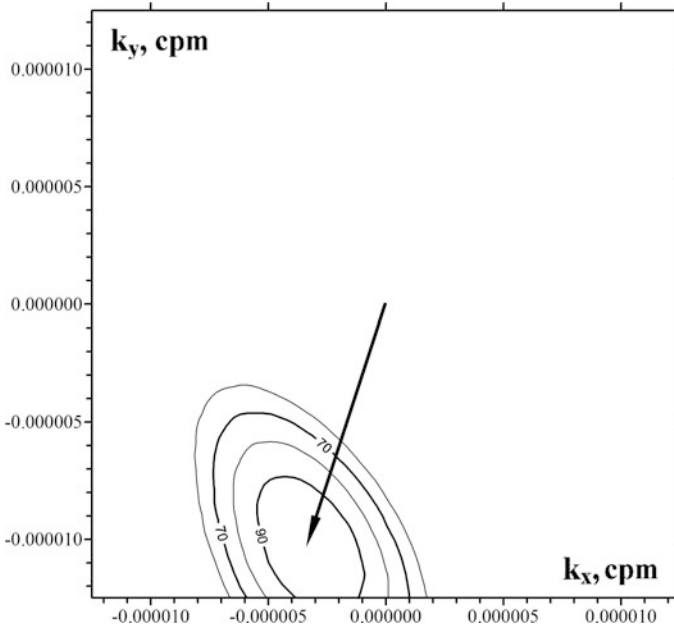
Fig. 2.34 Spatiotemporal spectrum at the semidiurnal frequency based on the data of six moorings shown in Fig. 2.33 (depth 1000 m). The locations are indicated by black dots with a white circle in the middle (Vityaz-88). The contour lines correspond to 90, 80, 70, and 60% of the main maximum. The arrow shows the wave vector corresponding to a wavelength of 100 km

A standalone mooring in the middle of the Iberia Basin at point 41° 45′N, 21° 57′W, which operated in 1980–1981, recorded the amplitudes of internal tides at a depth of 600 m equal to 30 m.

Moored measurements with thermistor chains were carried out by Jeans and Sherwin (2001) on the shelf break west of Portugal at 41°N. The authors recorded high-frequency internal waves generated by internal tide with an amplitude of 45 m. The estimated energy fluxes were 2000 W m^{-1}.

2.14 West Equatorial Atlantic, WOCE ACM-10 Experiment

Moored measurements in this region were carried out within the WOCE ACM-10 Program in 1992–1994. The moorings with instruments were deployed in a line normal to the axis of the deep Equatorial Channel along 36°W. The channel connects the northwestern boundary of the Brazil Basin and the Ceara Abyssal Plain. The experiment was organized by WHOI oceanographers. A total of six mooring
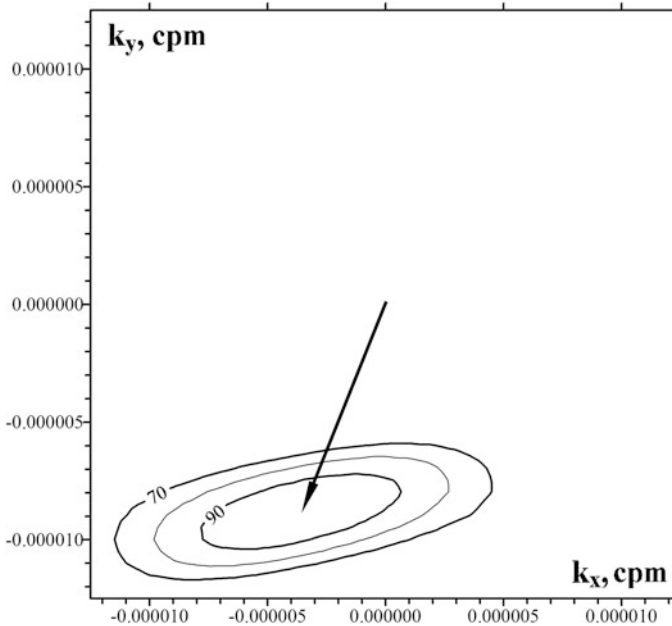
Fig. 2.35 Spatiotemporal spectrum at the semidiurnal frequency based on the data of five moorings shown in Fig. 2.33 (depth 2600 m) as squares with black dots and a white circle in the middle (moorings in 1984–1985). The contour lines correspond to 90, 80, and 70% of the main maximum. The arrow shows the wave vector corresponding to a wavelength of 105 km

were deployed. All instruments were set at depths of 3000 m and deeper. The amplitudes of the internal tides at the depths close to 3000 m were within 20–25 m.

In 1977–1978, two WHOI moorings were deployed in the Equatorial Channel at 4° 03′N, 39° 40′W and 4° 01′N, 39° 19′W. The upper level of measurements was at 4100 m. The amplitudes of internal tides were close to 20 m.

2.15   Romanche and Chain Fracture Zones, WOCE ACM-11 Experiment

The measurements in the equatorial Romanche and Chain fracture zones were carried out in 1992-1994 within the French ROMANCHE Program by scientists of the IFREMER Institute. Four moorings were deployed in each of the fractures across their axes. The distance between the moorings was 2–3 miles. In the Romanche Fracture Zone, the moorings were deployed close to 0° 42′N, 14° 42′W, while in the Chain Fracture Zone they were located near 0° 54′S, 13° 36′W. The experiment was aimed at studying the bottom flow of Antarctic Bottom Water;

therefore no measurements were performed above 1700 m. These moorings recorded intense internal tides with an amplitude of 50–60 m.

A mooring with a line of temperature sensors was deployed in 2013–2014 in the western part of the Romanche Fracture Zone at 01° 05′S, 22° 28′W by the Shirshov Institute of Oceanology and the Royal Netherlands Institute of Sea Research (NIOZ) (van Haren et al. 2014). The sensors in the bottom layer recorded internal tides with an amplitude exceeding 70 m, which generated trains of shorter internal waves.

2.16   Hunter Channel

Moored measurements in the Hunter Channel were carried out in 1992–1994. The Hunter Channel is a wide deep passage east of the Vema Channel connecting the Argentine and Brazil basins. The investigations were carried out by German scientists from the Institute für Meereskunde (Germany) headed by (Zenk et al. 1999). Six moorings were deployed in the channel and two moorings north of the channel. The program was aimed at studying the bottom currents; therefore many moorings had instruments only in the bottom layer. Only two moorings had instruments at 900 m at: 34° 23′S, 27° 43′W and 34° 33′S, 26° 58′W. Another mooring was deployed northwest of the channel at 26° 52′S, 34° 47′W. The amplitude of internal tides over the channel was within 40–50 m; the amplitudes on the northwestern mooring were 25 m.

2.17   Reykjanes Ridge

The moorings near the Reykjanes Ridge were deployed in 1991–1993 at 54° 24′N, 25° 54′W. This research was within the WOCE ACM-8 German Component Program with the assistance of the Ministry of Agriculture, Fisheries and Food (MAFF) (UK). The amplitude of internal tides at a depth of 1040 m over the ocean bottom at 3300 m was estimated at 40 m. In 1989, a similar estimate was obtained on the mooring deployed by the Shirshov Institute of Oceanology (Russia) at 54° 09′N, 26° 44′W at depths of 1000 m and 1500 m over the oceanic depth equal to 3366 m. Long-term moored ADCP measurements organized by the NIOZ Institute (van Haren 2007a) indicate that the M_2 tidal currents are strong in this region and the corresponding shear is also high.

2.18   Central Equatorial Atlantic, SEQUAL, PIRATA Experiments

Several moorings were deployed in the Central Equatorial Atlantic to study the subsurface equatorial undercurrent (the SEQUAL experiment, WHOI). The measurements were only in the upper layer not deeper than 300 m. They were carried out from February to September, 1983 at longitudes 26°–28°W. The amplitudes of the semidiurnal internal tides at a depth of 300 m were estimated at 50 m.

The PIRATA experiment was carried out in 2002 (NOAA/PMEL). The instruments on the mooring at the equator and 23°W were only in the upper layer not deeper than 120 m. The recorded amplitudes did not exceed 20 m.

2.19   Denmark Strait, WOCE ACM-8 Experiment

Twenty-two moorings were deployed in 1986-1999 over the threshold of the Strait of Denmark. The experiment was organized by the Ministry of Agriculture, Fisheries and Food (MAFF) (UK). The main goal of the experiment was to study the overflow of bottom waters from the Arctic to the Atlantic; therefore the major part of the instruments was concentrated in the bottom layer. The estimates of amplitudes of internal tides are not reliable because the temperature fluctuations with the semidiurnal period are small and the vertical temperature gradients are also small. However, the amplitudes were estimated at 30 m.

2.20   Iceland-Faroe Overflow, WOCE ACM-8 Experiment

Seven moorings were deployed in 1990–1991 in a line in the southeastern direction from the continental slope of Iceland. The experiment was organized by the Institute of Oceanographic Sciences (UK). Similar to the mooring program in the Denmark Strait the main goal of the experiment was to study the overflow of bottom waters from the Arctic to the Atlantic; therefore the major part of the instruments was concentrated in the bottom layer. In our research we used the moored temperature measurements on two moorings (at 62° 43′N, 16° 49′W, the depth of the ocean was 1800 m; the instruments were set at 1135 and 1465 m; and at 62° 26′N, 16° 28′W, the depth of the ocean was 2056 m; the instruments were set at 1403 and 1722 m). The amplitude of internal tides was estimated at 40–50 m.

Internal tides in the Faroe-Shetland Channel were studied by Hall et al. (2011). The authors applied moored ADCP and thermistors to study internal tides in the region. The authors also performed numerical modeling. The energy fluxes over the flanks of the Wyville Thomson Ridge were estimated at >5000 W m^{-1}. The nonlinear internal wave energy flux was typically of the order of 10 W m^{-1}. The

maximum model vertical displacement was 33 m, which is close to the 37 m observed by Sherwin (1991). Strong mixing in the channel was reported by Seim and Fer (2011). Tidal currents induce vertical displacement of the mooring with the tidal periodicity as high as 20 m. The speed of the overflow current reached 1.35 m/s. Intensification of tidal currents during increased overflow was analyzed by Perkins et al. (1994). The increase in the tidal currents was accompanied by an increase in the generation of the internal tide.

2.21 North Atlantic, Irminger Basin, WOCE ACM-8 Experiment

Moored measurements in the Irminger Basin west of the Reykjanes Ridge were carried out in 1991–1995 within the WOCE ACM-8 German Component Program. The experiment was organized by the Bundesamt für Seeschifffahrt und Hydrographie (BSH), Hamburg, Germany. The moorings were deployed at points with coordinates 59° 00′N, 32° 49′W; 59° 08′N, 34° 02′W at depths of 2100–2850 m. The amplitudes of the internal tides at depths of 820–880 m were estimated at 30–40 m.

2.22 Benguela Region, WOCE ACM-4 Experiment

The Benguela Source and Transport Experiment (BEST) was conducted in 1992–1993 in the region of the Benguela Current at a latitude of 30° S within the WOCE ACM-4 Program (Garzoli et al. 1999). The experiment was organized by Oregon State University, USA. Four moorings were deployed with current and temperature meters at 200, 500, 3000, and 5000 m. The eastern mooring was deployed on the continental slope and the western one was located at a distance of 150 km from the foot of the Walvis Ridge. A chart of the bottom topography and moorings is shown in Fig. 2.36. The amplitudes of the semidiurnal internal tides at the continental slope (14° 42′E) and at the Walvis Ridge (6° E) were high, reaching 45 and 50 m, respectively. The amplitudes on two other moorings located at a greater distance from the steep topography were 37 m at 8° 50′E and 40 m at 13° 12′E.

Fig. 2.36 Bottom topography (meters) in the Benguela region. Depth contour lines are shown at depths of 500, 1000, 2000, 3000, 4000, and 5000 m. Locations of moorings of the BEST experiment are shown with black symbols (top panel). Locations of instruments relative to the slope (middle panel). Internal tide amplitudes at a depth of 500 m versus longitude (bottom panel)

2.23 Norwegian Sea

In July 1975 four moorings were deployed from the Russian R/V *Akademik Kurchatov* in the Norwegian Sea for 20 days in the region of 65°00–66°00 N, 1° 00 W–1°00 E. This was a joint USSR-USA pre-POLYMODE experiment. Weak internal tides with amplitudes of 20 m were recorded at a depth of 500 m.

In 1994–1995, three moorings were deployed in the region north of Norway (74° 40′N, 13° 06′E) on the continental slope at a depth of 1700–1800 m from the

Russian R/V *Akademik Mstislav Keldysh*. The instruments at a level of 1300 m recorded amplitudes of tidal internal waves exceeding 35 m.

2.24   Mid-Atlantic Ridge (27°N)

Moored measurements at mid-latitudes on the slopes of the Mid-Atlantic Ridge in the region of 27°N were carried out in 1977–1978. Five moorings were deployed east of the ridge near 41°W and three moorings west of the ridge close to 48°W. The data were downloaded from the CMDAC database (CMDAC numbers: 01098–01117). A chart of the bottom topography and locations of moorings are shown in Fig. 2.37. The amplitude of the semidiurnal internal tides at a depth of 1500 m was estimated at 35–40 m. Despite the location of moorings in a cluster on both sides of the Mid-Atlantic Ridge and acceptable distances between the moorings for the calculation of spatiotemporal spectra it was not possible to calculate a reliable estimate of the spectrum. Complex topography in the region and multiple sources of internal tidal perturbations did not allow us to separate the waves generated in different regions of the slope.
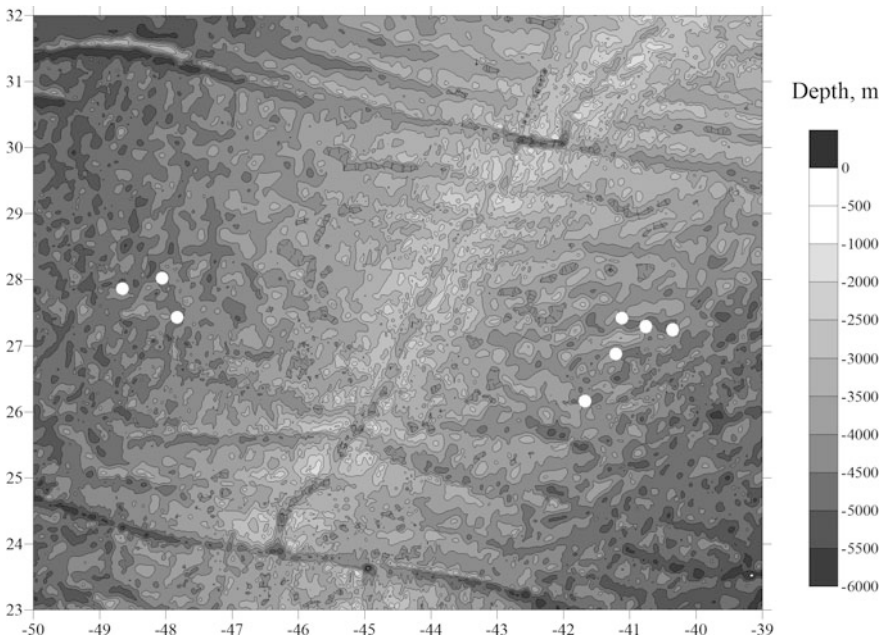
Fig. 2.37 Bottom topography (meters) in the Mid-Atlantic Ridge region. Depth contour lines are shown at depths of 500, 1000, 1500, 2000, 2500, 3000, 3500, 4000, 4500, 5000, 5500, and 6000 m. Locations of moorings of two experiments in 1977–1978 are shown with white dots

2.25 Agulhas Region

Moored measurements on ten moorings in the Agulhas region were carried out in 1985–1987 south of Africa. The eastern moorings are formally related to the Indian Ocean. Eight of them had instruments located in the depth range 700–1800 m. The other instruments were either deeper where the temperature gradient was close to zero or they were in the upper layer. The data were downloaded from the CMDAC database (CMDAC numbers: 1145–1169; WHOI moorings 834–843). Locations of moorings are shown in Fig. 2.38. The amplitudes of the semidiurnal internal tides at depths of 650–850 m were close to 30 m on all moorings. The amplitudes varied significantly over time. The measured temperatures varied in a wide range of time scales of tens of days. It is likely that the instruments were operating in strong temperature fronts associated with eddies and the temperature fluctuations could probably have been caused by horizontal temperature gradients. The largest amplitudes of the internal tides were recorded by the western moorings located close to a seamount with the summit above 2000 m depth at 40° 30′S, 15° 00′E. The moorings closer to the continental slope recorded smaller amplitudes. The amplitudes of internal tides in the depth interval 650–850 m are indicated with numerals on the map.
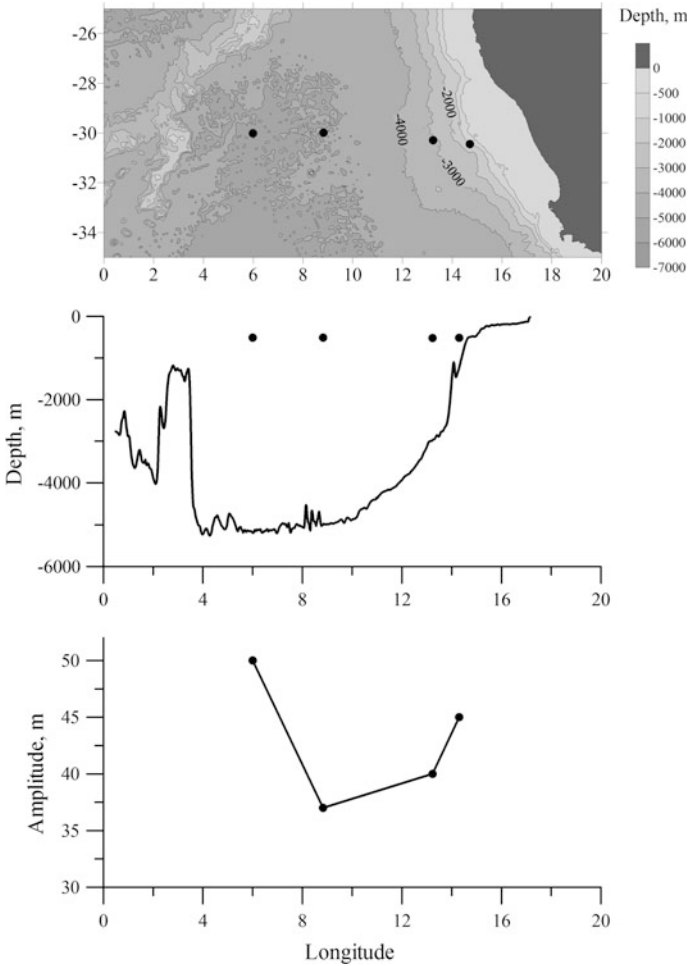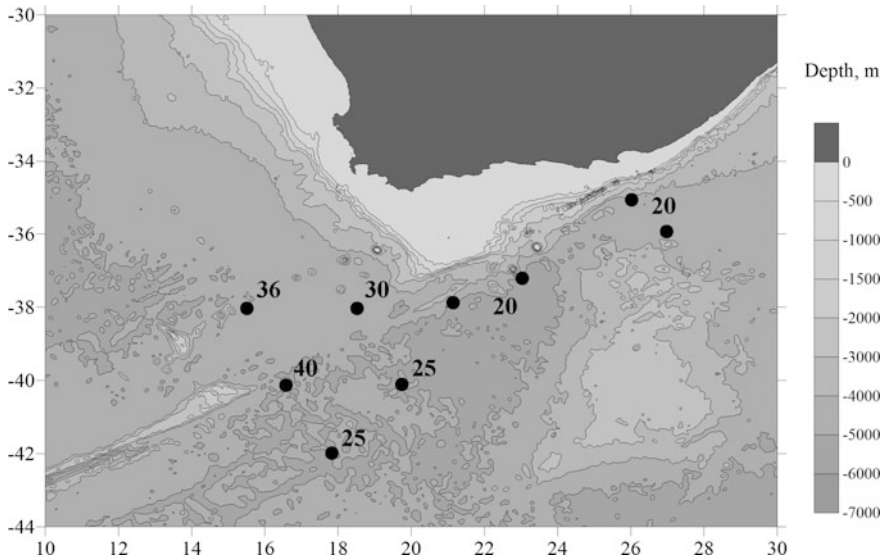

Fig. 2.38 Bottom topography (meters) in the Agulhas region. Depth contour lines are shown at depths of 500, 1000, 1500, 2000, 3000, 4000, 5000, and 6000 m. Locations of moorings of the experiments in 1985–1987 are shown with black dots. The numerals at the mooring locations indicate the amplitude of the internal tide (m)

The generation of internal tides over the shelf near the Cape Point Valley (South Africa) was discussed by Largier (1994). The amplitudes of internal tides were of the order of 10 m and the energy flux to the ocean was low: 40 W m^{-1}.

2.26   West Tropical Atlantic, MOVE Experiment

In 2000, an array of moorings was deployed in the subtropical West Atlantic to monitor the transport of North Atlantic Deep Water. The experiment was named Meridional Overturning Variability Experiment (MOVE). It was organized by the Scripps Institution of Oceanography, USA. Four moorings were deployed between the slope of the Lesser Antilles (Guadeloupe) and the Mid-Atlantic Ridge. The goal of the experiment was to monitor the transport fluctuations across this section. MOVE is also part of the International Ocean SITES Program. The moorings operated from 2000 to 2013.

Strong internal tides with amplitudes up to 70 m were recorded over the slope of the Lesser Antilles close to Guadeloupe Island. Smaller amplitudes were found in the middle of the basin (15 m) and even smaller amplitudes were found closer to the flanks of the Mid-Atlantic Ridge (13 m). Large amplitudes of internal tides up to 40 m were recorded on the mooring at 18° 38′N, 57° 30′W at a depth of 600 m in a cruise of the R/V *Akademik Kurchatov* in 1969.

2.27   Labrador Sea

In 1994-1998 eight moorings were deployed in the Labrador Sea in a line between 52° 26′N, 56° 45′W and 54° 05′N, 55° 07′W. The experiment was organized by the Bedford Institute of Oceanography, Canada. This was the ACM-29 WOCE experiment. The vertical temperature gradients at depths in the range 760–1500 m were very small, which made evaluation of internal tide amplitudes difficult. However, over the continental slope of Labrador they ranged from 20 to 40 m.

References

Alonso del Rosario JJ, Bruno Mejías BM, Vazquez-Lopez-Escobar A (2003) The influence of tidal hydrodynamic conditions on the generation of lee waves at the main sill of the Strait of Gibraltar. Deep-Sea Res 50:1005–1021

Alpers W, Salusti E (1983) Scylla and Charybdis observed from space. J Geophys Res 88 (3):1800–1808

Androsov AA, Voltzinger NE, Kagan BA, Salusti ES (1993) Residual tidal currents in the Strait of Messina. Izv Acad Sci USSR Ser Atmosph Oceanic Phys 29(4):522–531

Androsov AA, Kagan BA, Romanenkov DA, Voltzinger NE (2002) Numerical modeling of barotropic tidal dynamics in the Strait of Messina. Advances Water Resources. 25:401–415

Ansong JK, Arbic BK, Buijsman MC, Richman JG, Shriver JF, Wallcraft AJ (2015) Indirect evidence for substantial damping of low-mode internal tides in the open ocean. J Geophys Res 120:6057–6071. https://doi.org/10.1002/2015JC010998

Apel JR, Byrne HM, Proni JR, Charnell RL (1975) Observations of oceanic internal and surface waves from the earth resources technology satellite. J Geophys Res 80(6):865–881

Armi L, Farmer DM (1988) The flow of Mediterranean water through the Strait of Gibraltar. Farmer DM, Armi L (1988) The flow of Atlantic water through the Strait of Gibraltar. Prog Oceanogr 21:1–105

Atlantic Hydrophysical Polygon-70 (1983) Amerind Co. Oxonian Press, New Delhi

Badulin SI, Shrira VI, Tsimring LS (1985) The trapping and vertical focusing of internal waves in a pycnocline due to the horizontal inhomogeneities of density and currents. J Fluid Mech 158:199–218

Baines PG (1973) The generation of internal tides by flat-bump topography. Deep-Sea Res 20:179–205

Baines PG (1982) On internal tide generation models. Deep-Sea Res 29(3):307–338

Baines PG (2007) Internal tide generation by seamounts. Deep Sea Res 54(9):1486–1508. doi:10.1016 j.dsr.2007.05.009

Barber NF (1963) The directional resolving power of an array of wave detectors. In: Ocean wave spectra. NY, Engelwood Cliffs, Prentice Hall, pp 137–150

Bignami F, Salusti E (1990) Tidal currents and transient phenomena in the Strait of Messina: a review. In: Pratt LJ. (ed) The physical oceanography of sea straits, pp 95–124. Kluwer Academic, The Netherlands

Bockel M (1962) Travaux Oceanographiques de l' "Origny" a Gibraltar. Cah Oceanograph 14:325–329

Bolshakov VN, Sabinin KD (1983) Mean characteristics of semidiurnal tidal currents in Polygon-70 and their variability. Izv Acad Sci USSR Ser Atmosph Oceanic Phys 19(1):51–56

Bondur VG (1995) The principles of monitoring the Earth from space for the need of the ecology and natural resources. Izv Vuzov Geodesy Aerophotography 12:14–38

Bondur V, Keeler R, Gibson C (2005) Optical satellite imagery detection of internal wave effects from a submerged turbulent outfall in the stratified ocean. Geophys Res Lett 32:L12610. https://doi.org/10.1029/2005GL022390

Bondur VG, Morozov EG, Belchansky GI, Grebenyuk YV (2006a) Radar survey and numerical modeling of internal tides in the shelf region, Investigation of the Earth from Space, pp 51–63

Bondur VG, Morozov EG, Grebenyuk YV (2006b) Radar observations and numerical modeling of internal tides in the coastal zone of the North Atlantic region. Investigation of the Ocean from Space. IKI, Moscow, pp 21–29

Boyce FM (1975) Internal waves in the Strait of Gibraltar. Deep Sea Res 22:597–610

Brandt P, Alpers W, Backhaus JO (1996) Study of the generation and propagation of internal waves in the Strait of Gibraltar using a numerical model and synthetic aperture radar images of the European ERS 1 satellite. J Geophys Res 101:14,237–14,252

Brandt P, Rubino A, Alpers W, Backhaus JO (1997) Internal waves in the Strait of Messina studied by a numerical model and synthetic aperture radar Images from the ERS 1/2 Satellites. J Phys Oceanogr 27(5):648–663

Brandt P, Rubino A, Quadfasel D, Alpers W, Sellschopp J, Fiekas H-V (1999) Evidence for the influence of Atlantic-Ionian stream fluctuations on the tidally induced internal dynamics in the Strait of Messina. J Phys Oceanogr 29(5):1071–1080

Brickman D, Loder JW (1993) Energetics of the internal tide on northern Georges Bank. J Phys Oceanogr 23(3):409–424

Brisco MG (1975) Preliminary results from the trimoored internal wave experiment (IWEX). J Geophys Res 80(27):3872–3884

Bruno M, Alonso JJ, Cózar A, Vidal J, Ruiz-Cañavate A, Echevarría F, Ruiz J (2002) The boiling-water phenomena at Camarinal Sill, the Strait of Gibraltar. Deep-Sea Res II 49:4097–4113

Bryden HL, Candela J, Kinder TH (1994) Exchange through the Strait of Gibraltar. Prog Oceanogr 33:201–248

Defant A (1961) Physical oceanography. Pergamon, NY

Di Sarra A, Pace A, Salusti E (1987) Long internal waves and columnar disturbances in the Strait of Messina. J Geophys Res 92:6495–6500

Dunphy M, Lamb KG (2014) Focusing and vertical mode scattering of the first mode internal tide by mesoscale eddy interaction. J Geophys Res 119:523–536. https://doi.org/10.1002/2013JC009293

Dushaw BD (2006) Mode-1 internal tides in the western North Atlantic Ocean. Deep-Sea Res 53 (3):449–473

Egbert GD, Erofeeva S (2002) Efficient inverse modeling of barotropic ocean tides. J Atmos Ocean Tech 19:183–204

Frankignoul C, Joyce TM (1979) On the internal wave variability during the internal wave experiment (IWEX). J Geophys Res 84(C2):769–776

Garzoli SL, Richardson PL, Rae CMD, Fratantoni DM, Goni GJ, Roubicek AJ (1999) Three Agulhas rings observed during the Benguela Current Experiment. J Geophys Res 104 (C9):20971–20985

Gerkema T, van Haren H (2007) Internal tides and energy fluxes over Great Meteor Seamount. Ocean Sci 3:441–449. https://doi.org/10.5194/os-3-441-2007

Golenko NN (1982) Isotropy of inertial and semidiurnal tide motions in the ocean. Oceanology 22 (1):23–31

Gordeev RG, Kagan BA, Rivkind VY (1974) Modeling of semidiurnal tides in the global ocean. Izv Acad Sci USSR Ser Atmosph Oceanic Phys 10(7):497–498

Griffa A, Marullo S, Santolieri R, Viola A (1986) Preliminary observations of large-amplitude tidal internal waves near the Strait of Messina. Contin Shelf Res 6:677–687

Guizien K, Barthdemy E, Inall ME (1999) Internal tide generation at a shelf break by an oblique barotropic tide: observations and analytical modeling. J Geophys Res 104(7):15655–15668

Hall RA, Huthnance JM, Williams RG (2011) Internal tides, nonlinear internal wave trains, and mixing in the Faroe-Shetland Channel. J Geophys Res 116:C03008. https://doi.org/10.1029/2010JC006213

Hallock ZR, Field RL (2005) Internal-wave energy fluxes on the New Jersey shelf. J Phys Oceanogr 35(1):3–12

Hibiya T (1990) Generation mechanism of internal waves by a vertically sheared tidal flow over a sill. J Geophys Res 95:1757–1764. https://doi.org/10.1029/JC095iC02p01757

Hopkins TS, Salusti E, Settimi D (1984) Tidal forcing of the water mass interface in the Strait of Messina. J Geophys Res 89(C2):2013–2024

Inall ME, Ripperth TP, Sherwin TJ (2000) Impact of nonlinear waves on the dissipation of internal tidal energy at a shelf break. J Geophys Res 105(4):8687–8705

Ivanov YA, Morozov EG (1974) Deformation of internal gravity waves by a flow with a horizontal velocity shear. Oceanology 14(3):457–461

Ivanov YA, Morozov EG (1983) Investigations of temperature fluctuations at tidal and inertial periods. In: Atlantic Hydrophysical Polygon-70 (pp 289–299). Amerind Co. Oxonian Press Ltd., New Delhi

Jeans DRG, Sherwin TJ (2001) The evolution and energetics of large amplitude nonlinear internal waves on the Portuguese shelf. J Mar Res 59:327–353. https://doi.org/10.1357/002224001762842235

Jézéquel N, Mazé R, Pichon A (2002) Interaction of semidiurnal tide with a continental slope in a continuously stratified ocean. Deep-Sea Res 49(4):707–734

Kamenkovich VM, Koshlyakov MN, Monin AS (1986) Synoptic Eddies in the Ocean. Springer

Käse RH, Clarke RA (1978) High-frequency internal waves in the upper thermocline during GATE. Deep-Sea Res 25(9):815–825

Käse RH, Olbers D (1980) Wind-driven inertial waves observed during phase III of GATE. Deep-Sea Res Suppl 26:191–216

Largier JL (1994) The internal tide over the shelf inshore of Cape Point Valley South Africa. J Geophys Res 99:10023–10034

Longo A, Manzo M, Pierini S (1992) A model for the generation of nonlinear internal tides in the Strait of Gibraltar. Oceanol Acta 15:233–243

Lyashenko AF, Sabinin KD (1979) On the spatial structure of the internal tides on the 1970 hydrophysical test range in the Atlantic. Izv Acad Sci USSR Ser Atmosph Oceanic Phys 15 (8):595–601

Matygin AS, Sabinin KD, Filonov AE (1982) Average spatial spectra of internal tides on the 1970 Atlantic Hydrophysical test range. Izv Acad Sci USSR Ser Atmosph Oceanic Phys 18(2):129–133

McCardell G, O'Donnell J, Souza AJ, Palmer MR (2016) Internal tides and tidal cycles of vertical mixing in western Long Island Sound. J Geophys Res 121:1063–1084. https://doi.org/10.1002/2015JC010796

Mohn C, Beckmann A (2002) The upper ocean circulation at Great Meteor Seamount. Part I: Structure of density and flow fields. Ocean Dyn 52:179–193. https://doi.org/10.1007/s10236-002-0017-4

Morozov EG, Filatova LP (1978) Horizontal coherence of semidiurnal fluctuations of temperature in the Polygon-70 test area. Izv Acad Sci USSR Ser Atmosph Oceanic Phys 14(3):243–246

Morozov EG, Nikitin SV (1981) Investigation of the direction of internal waves of tidal period in study area 70. Oceanology 21(2):168–171

Morozov EG (1983) Investigation of 9-month temperature and velocity spectra in the Western Atlantic. Izv Acad Sci USSR Ser Atmosph Oceanic Phys 19(10):166–168

Morozov EG, Nikitin SV (1984a) Propagation of semidiurnal internal waves in a region with varying bottom topography. Oceanological Res 36:44–49

Morozov EG (1988) Spatial characteristics of semidiurnal internal waves in the Mesopolygon study region. In: Hydrophysical investigations within the Mesopolygon Program (pp 144–146). Nauka,Moscow

Morozov EG (1995) Semidiurnal internal wave global field. Deep-Sea Res 42(1):135–148

Morozov EG, Pelinovsky EN, Talipova TG (1998) Exceedance frequency for internal waves during the Mesopolygon-85 experiment in the Atlantic. Oceanology 38(4):521–527

Morozov EG, Trulsen K, Velarde MG, Vlasenko VI (2002) Internal tides in the Strait of Gibraltar. J Phys Oceanogr 32:3193–3206

Müller P, Olbers DJ, Willebrand J (1978) The IWEX spectrum. J Geophys Res 83(C1):479–500

New AL, Pingree RD (1990a) Large amplitude internal soliton packets in the central Bay of Biscay. Deep-Sea Res 37:513–524

New AL, Pingree RD (1990b) Evidence for internal tidal mixing near the shelf break in the Bay of Biscay. Deep-Sea Res 37(12):1783–1803

Oceanography from the Space Shuttle (1996) NASA http://geoinfo.amu.edu.pl/wpk/ocean/oss_contents.html. Last accessed in October 2017

Parks TW, Burrus CS (1987) Digital filter design. John Wiley & Sons. Chapter 7, section 7.3.3

Pereira AF, Castro BM (2007) Internal tides in the Southwestern Atlantic off Brazil: observations and numerical modeling. J Phys Oceanogr 37(6):1512–1526

Pereira AF, Castro BM, Calado L, da Silveira ICA (2007) Numerical simulation of M_2 internal tides in the South Brazil Bight and their interaction with the Brazil Current. J Geophys Res 112:C04009. https://doi.org/10.1029/2006JC003673

Perkins H, Sherwin TJ, Hopkins TS (1994) Amplification of tidal currents by overflow on the Iceland-Faeroe Ridge. J Phys Oceanogr 24(4):721–735

Pichon A, Mazé R (1990) Internal tides over a shelf break: analytical model and observations. J Phys Oceanogr 20(5):657–671

Pingree RD, New AL (1989) Downward propagation of internal tidal energy into the Bay of Biscay. Deep-Sea Res 36:735–758

Pingree RD, New AL (1991) Abyssal penetration and bottom reflection of internal tidal energy in the Bay of Biscay. J Phys Oceanogr 21:28–39

Pingree RD, New AL (1995) Structure, seasonal development and sunglint spatial coherence of the internal tide on the Celtic and Armorican shelves and in the Bay of Biscay. Deep-Sea Res 42 (2):245–284

Rippeth TP, Inall ME (2002) Observations of the internal tide and associated mixing across the Malin Shelf. J Geophys Res 107(C4):3028. https://doi.org/10.1029/2000JC000761

Sabinin KD, Shulepov VA (1978) Spatial characteristics of semidiurnal internal waves in the Polygon-70 hydrophysical test area in the Atlantic. Oceanology 18(1):253–264

Sabinin KD, Nazarov AA, Serebryaniy AN (1990) Short-period internal waves and currents in the ocean. Izv Acad Sci USSR Ser Atmosph Oceanic Phys 26(8):621–625

Sandoval FJ, Weatherly GL (2001) Evolution of the deep western boundary current of Antarctic bottom water in the Brazil Basin. J Phys Oceanogr 31(6):1440–1460

Sandström H, Elliott JA (1984) Internal tide and solitons on the Scotian Shelf: a nutrient pump at work. J Geophys Res 89(C4):6415–6426. https://doi.org/10.1029/JC089iC04p06415

Sandström H, Oakey NS (1995) Dissipation in internal tides and solitary waves. J Phys Oceanogr 25(4):604–614

Sandström H, Elliott JA (2011) Production, transformation, and dissipation of energy in internal tides near the continental shelf edge. J Geophys Res 116:C04004. https://doi.org/10.1029/2010JC006296

Sapia A, Salusti E (1987) Observation of nonlinear internal solitary wave trains at the northern and southern mouths of the Strait of Messina. Deep-Sea Res 34:1081–1092

Seim KS, Fer I (2011) Mixing in the stratified interface of the Faroe Bank Channel overflow: the role of transverse circulation and internal waves. J Geophys Res 116:C07022. https://doi.org/10.1029/2010JC006805

Sherwin T (1988) Analysis of an internal tide observed on the Marlin Shelf north of Ireland. J Phys Oceanogr 18:1035–1050

Sherwin TJ, Taylor NK (1990) Numerical investigations of linear internal tide generation in the Rockall Trough. Deep-Sea Res 37(10):1595–1618

Sherwin TJ (1991) Evidence of a deep internal tide in the Faeroe-Shetland channel. In: Parker BB (ed) Tidal hydrodynamics (pp 469–488). Wiley, NY

Shroyer EL, Moum JN, Nash JD (2011) Nonlinear internal waves over New Jersey's continental shelf. J Geophys Res 116:C03022. https://doi.org/10.1029/2010JC006332

Thompson RORY (1979) Coherence significance levels. J Atmospheric Sci 36(10):2020–2021

van Haren H (2005) Details of stratification in a sloping bottom boundary layer of Great Meteor Seamount. Geophys Res Lett 32:L07606. https://doi.org/10.1029/2004GL022298

van Haren H (2007a) Inertial and tidal shear variability above Reykjanes Ridge. Deep-Sea Res 54 (6):856–870

van Haren H (2007b) Unpredictability of internal M_2. Ocean Sci 3:337–344. https://doi.org/10.5194/os-3-337-2007

van Haren H, Gostiaux L, Morozov E, Tarakanov R (2014) Extremely long Kelvin-Helmholtz billow trains in the Romanche Fracture Zone. Geophys Res Lett 41:8445–8451

Vlasenko VI (1992) Nonlinear model for the generation of baroclinic tides over extensive inhomogeneities of bottom topography. Phys Oceanogr (Morskoy gidrofizicheskiy zhurnal) 3:417–424

Vlasenko VI, Golenko NN, Paka VT, Sabinin KD, Chapman R (1997) Study of the dynamics of baroclinic tides in the region of the shelf edge. Oceanology 37(5):599–609

Vlasenko VI, Alpers W (2005) Generation of secondary internal waves by the interaction of an internal solitary wave with an underwater bank. J Geophys Res 110:C02019. https://doi.org/10.1029/2004JC002467

Vlasenko V, Stashchuk N, Palmer MR, Inall ME (2013) Generation of baroclinic tides over an isolated underwater bank. J Geophys Res 118(C9):4395–4408. https://doi.org/10.1002/jgrc.20304

Vlasenko V, Stashchuk N, Inall ME, Hopkins JE (2014) Tidal energy conversion in a global hot spot: on the 3-D dynamics of baroclinic tides at the Celtic Sea shelf break. J Geophys Res 119:3249–3265. doi:10.1002/2013JC009708

Vlasenko V, Stashchuk N (2015) Internal tides near the Celtic Sea shelf break: a new look at a well known problem. Deep-Sea Res 103:24–36

Wang D-P (1993) The Strait of Gibraltar model: Internal tide, diurnal inequality and fortnightly modulation. Deep Sea Res 40:1187–1203

Wang D-P, Oey L-Y, Ezer T, Hamilton P (2003) Near-surface currents in DeSoto Canyon (1997–99): comparison of current meters, satellite observation, and model simulation. J Phys Oceanogr 23(1):313–326

Wang J, Ingram RG, Mysak LA (1991) Variability of internal tides in the Laurentian Channel. J Geophys Res 96:16859–16875. https://doi.org/10.1029/91JC01580

Watson G, Robinson IS (1990) A study of internal wave propagation in the Strait of Gibraltar using shore-based marine radar images. J Phys Oceanogr 20(3):374–395

Watson G (1994) Internal waves in a stratified shear flow: the Strait of Gibraltar. J Phys Oceanogr 24(2):509–517

Weatherly G, Kim YY, Kontar E (2000) Eulerian measurements of the Deep Western Boundary Current of North Atlantic Deep Water at 18°S. J Phys Oceanogr 30:971–986

Wesson JC, Gregg MC (1988) Turbulent dissipation in the Strait of Gibraltar and associated mixing. In: Nihoul JCJ, Jamart BM (eds) Small scale turbulence and mixing in the ocean. Proceedings 19th International Liege Colloquium Ocean Hydrodynamics (pp 201–222). Elsivier, Amsterdam

WOD13 World Ocean Database (2013) Geographically Sorted Data. https://www.nodc.noaa.gov/OC5/WOD/datageo.html. Last updated October 26, 2013; last accessed in October 2017

Xie XH, Cuypers Y, Bouruet-Aubertot P, Pichon A, Lourenço A, Ferron B (2015) Generation and propagation of internal tides and solitary waves at the shelf edge of the Bay of Biscay. J Geophys Res 120:6603–6621. https://doi.org/10.1002/2015JC010827

Xing J, Davies AM (1996) Processes influencing the internal tide, its higher harmonics, and tidally induced mixing on the Malin-Hebrides Shelf. Prog Oceanog 38:155–204

Zenk W, Siedler G, Lenz B, Hogg NG (1999) Antarctic bottom water flow through the hunter channel. J Phys Oceanogr 29(11):2785–2801

Zhang L, Buijsman MC, Comino E, Swinney HL (2017) Internal wave generation by tidal flow over periodically and randomly distributed seamounts. J Geophys Res 122:5073–5084. https://doi.org/10.1002/2017JC012884

Ziegenbein J (1969) Short internal waves in the Strait of Gibraltar. Deep-Sea Res 16(5):479–488

Ziegenbein J (1970) Spatial observations of short internal waves in the Strait of Gibraltar. Deep-Sea Res 17(5):867–876

Zilberman NV, Becker JM, Merrifield MA, Carter GS (2009) Model estimates of M_2 internal tide generation over Mid-Atlantic Ridge topography. J Phys Oceanogr 39(10):2635–2651

Chapter 3
Observations of Internal Tides in the Pacific Ocean

Abstract This chapter describes the measurements of internal tides in the Pacific Ocean together with modeling of the generation and propagation of internal tides in some important regions of the Pacific. The generation of internal tides is associated with the interaction of the currents of the barotropic tide with the slopes of the bottom topography. One of the most important ideas presented here is the strong generation of internal tides over submarine ridges. The generation and propagation of strong internal tides over the Aleutian and Hawaiian ridges and in the South China Sea are described. The generation of internal tides in the regions of internal tides that are of high but still lower energy than those near the Aleutian Islands is revealed over the Kyushu-Palau and Emperor ridges and over the Mendocino Escarpment. Attention is focused on the measurements of internal tides in the Northwest Pacific where the Megapolygon experiment was conducted with 173 moorings. Measurements of internal tides on mooring clusters confirm the well known fact that internal tides are generated over the bottom slopes. The propagation of beams of internal tides from the top of a seamount was found in the East Pacific.

3.1 Henderson Seamount (25°N, 119°W)

Henderson Seamount is located in the region where Russian research work was undertaken on the R/V *Dmitry Mendeleev* in 1986 (25° 20′N, 119° 32′W). This seamount is even shown on the school charts and globes. However, its actual location is 30 miles distant from the place indicated on those charts. The top of this seamount is at a depth of approximately 400 m while the surrounding waters are more than 4000 m deep. Another similar seamount, Fieberling Guyot, is located in the region (32° 25′N, 127° 47′W). The top of the Fieberling Guyot is at 438 m surrounded by waters 4500 m deep (Eriksen 1998).

The conditions of stratification and the position of the summit make us think that mainly sloping internal tidal perturbations should be generated over the slopes of such a seamount (Baines 1982). Several two-dimensional models exist, which simulate the generation of internal tides over sloping bottom topography (Baines

1973, 1974, 1982, 1983; Rattray 1960). The generation of internal tides also occurs on solitary seamounts (Baines 2007). Interaction of the barotropic tide currents with three-dimensional bottom topography should be considered as generation by a point source with further radial propagation of perturbations. A three-dimensional wave should decay proportional to the distance from the seamount.

Let us consider the results of moored temperature measurements at different distances from Henderson Seamount. A scheme of the moorings and bottom topography is shown in Fig. 3.1. The instruments were set at 75, 150, 400, 700, and 1200 m. We shall calculate the beam trajectory from the data of stratification and bottom topography to understand how internal tidal perturbations propagate from the topographic slope. This trajectory is a characteristic line of the hyperbolic equation for velocity in coordinates (x, z) (Turner 1973).

The curve of the characteristic line is determined by the following relation (see relations 1.33; 6.02; 7.03):

$$\frac{dz}{dx} = \pm \left(\frac{\omega^2 - f^2}{N(z)^2 - \omega^2} \right)^{1/2}. \tag{3.1}$$

Here, $N(z)$ is the Brunt-Väisälä frequency, ω is the tidal frequency, and f is the Coriolis parameter. The trajectories of the propagation of perturbations are shown
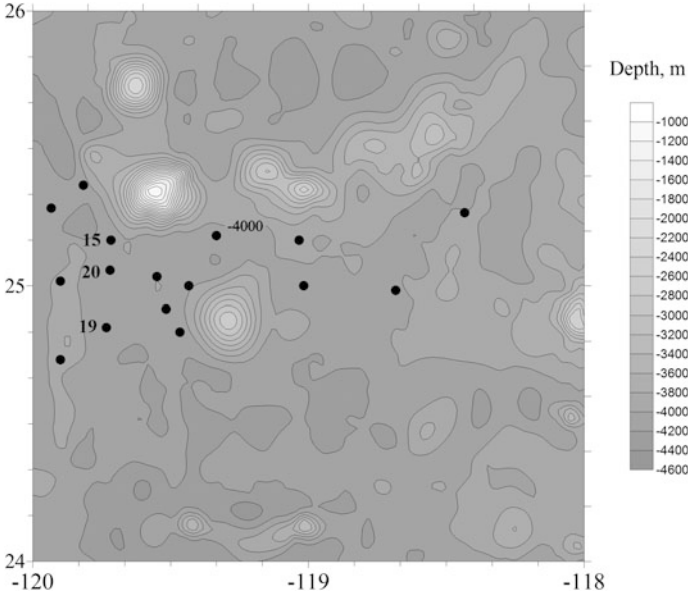
Fig. 3.1 Bottom topography near the Henderson Seamount in the Northeast Pacific. Depth contour lines between 1000 and 4400 m are shown with an interval of 200 m. Locations of moorings are shown with black dots. Moorings 15, 20, and 19 are indicated
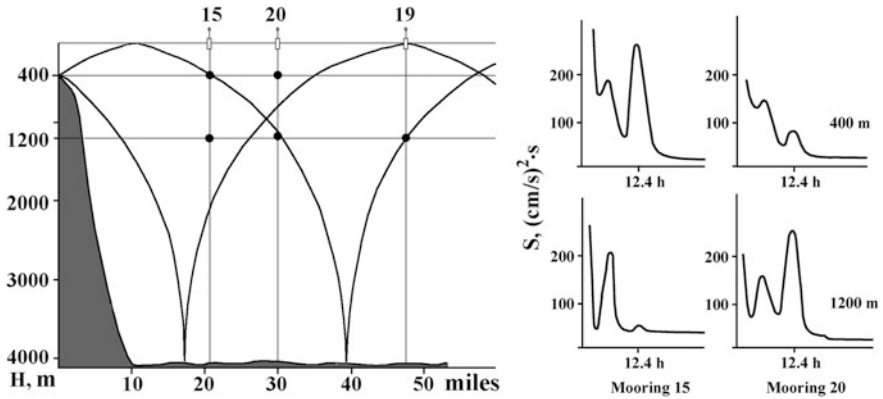
Fig. 3.2 Trajectories of semidiurnal internal wave beams and locations of moorings relative to the seamount in the Northeast Pacific (25° 20′N, 119° 32′E) (left panel). Spectra of velocity fluctuations at moorings 15 and 20 at depths of 400 and 1200 m (right panel). Modified and redrawn from Morozov (1995, 2006)

in Fig. 3.2. Locations of moorings and instruments on moorings, together with the slope of the seamount are also shown in the figure.

We consider variations in the temperature frequency spectra from the mooring data at depths of 400 and 1200 m as functions of distance from the seamount slope. It is important to note whether or not the wave trajectory (characteristic line) passes the location of the instrument. We assume that the width of such a trajectory is approximately 100 m because physically it is not a narrow line as the theory predicts (Morozov et al. 2009).

Spectra of velocity fluctuations at depths of 400 and 1200 m on moorings 15 and 20 are shown in Fig. 3.2. We consider Figs. 3.1 and 3.2 together and note that the semidiurnal peak on mooring 15 at a depth of 400 m is strong. The trajectory passes through the location of the instrument. At the same time, the peak on mooring 15 at a depth of 1200 m is weak because the trajectory bypasses this location. The semidiurnal peak on mooring 20 at a depth of 400 m is strong; it is weak at a depth of 1200 m. We note that if the trajectory of semidiurnal internal perturbation passes through the location of the instrument, semidiurnal fluctuations of velocity are strong.

We calculated the vertical and horizontal coherences between all pairs of the time series on moorings 15 (400 m) and 20 (1200 m). Six possible versions of coherence were calculated. As was expected the highest coherence was between time series mooring 15 (400 m) and mooring 20 (1200 m) along the characteristic line. The value of this slant coherence is 0.74; the coherences between the other pairs of time series are below the 95% confidence level (0.5).

3.2 West of California and Oregon, South of the Mendocino Escarpment, DM-86, Abrupt Topography, LLWODP WEST, OPTOMA, WOCE PCM-2, and EBC Experiments

The Mendocino Escarpment is a zonal transform fault at approximately $40° 30′N$ west of northern California. The ocean is relatively flat south of the escarpment at a depth of 4400 m. In April-May 1986, the moorings were deployed 600–700 km south of the Mendocino Escarpment and 400–500 km from the western coast of USA (the DM-86 experiment on the Russian R/V *Dmitry Mendeleev* to study the currents and internal waves in the northeastern part of the Pacific Ocean). Eight moorings were deployed in the region. Velocity and temperature meters were set at depths of 75, 150, 250, 400, 700, and 1200 m. A chart of the study site is shown in Fig. 3.3. The amplitudes of the semidiurnal internal tides were calculated from the fluctuations of temperature and vertical temperature gradient. The amplitudes were estimated at 25–30 m.

Spectral cross-analysis of temperature measurements at different depths of one mooring and between time series at one depth on different moorings was performed based on the data of the DM-86 experiment. The spectral analysis indicates that the semidiurnal fluctuations are well correlated and the coherence between various pairs of time series exceeds 0.6. Horizontal coherences at 150, 700, and 1200 as functions of distance are shown in Fig. 3.4. Coherences are high everywhere and exceed the 95% confidence level (0.5) at 20 degrees of freedom used in the calculations.

The estimates of spatiotemporal spectrum were carried out using the Barber's method (Barber 1963). A spatiotemporal spectrum for the semidiurnal frequency based on the data at a depth of 700 m is shown in Fig. 3.5. Based on these data, the wavelength of the internal tide was 130 km. The direction of propagation was 175°. The estimates at the other depths were approximately the same. These estimates agree with the estimates from the dispersion relation (see Sect. 1.4.3).

Calculation of the spatiotemporal spectra based on the data of two sequential time series showed that the form of the spectra did not change significantly, which indicates time stability of wavelength and direction. When planning the experiment we expected that the semidiurnal internal tides would propagate from the continental slope of North America. However, this signal from the east was almost negligible.

The generation and propagation of internal tides from the slopes of the bottom topography of the Mendocino Escarpment and continental slope of North America was studied using the numerical model developed by Vlasenko (see Sect. 1.4.1) (Vlasenko 1992; Vlasenko et al. 2005). We used the typical stratification in the region (unperturbed state) from the CTD-data in this region (WOD13 2013) and bottom topography from the digital database (Smith and Sandwell 1997). The tidal velocities were calculated from the satellite data using the NASA database available at Oregon State University and the method described by Egbert and Erofeeva (2002).
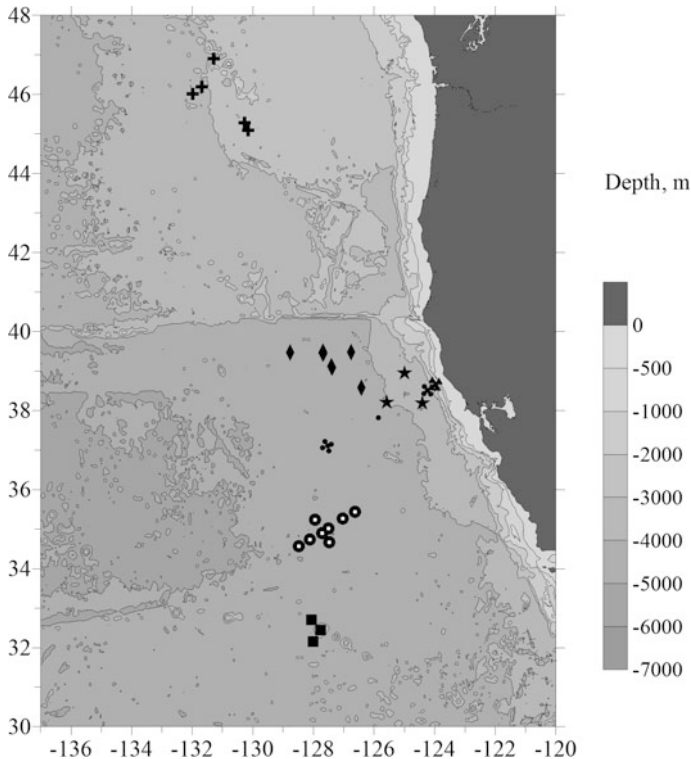
Fig. 3.3 Bottom topography in the study site in the Northeast Pacific and locations of moorings. Depth contour lines are shown at depths of 500, 1000, 2000, 3000, 4000, and 5000 m. Locations of moorings are shown with black symbols. Locations of the DM-86 moorings are shown with black dots and a white circle in the middle; moorings of the abrupt topography experiment are shown with squares; OPTOMA moorings are shown with stars; LLWODP WEST moorings are shown with diamonds; EBC moorings are shown with triangles; WOCE PC-2 moorings are shown with small dots; VENTS moorings are shown with crosses. Land and islands are shown with gray color

We selected a domain for calculations 800 km long with a horizontal step of 1000 m and 34 vertical levels. The time step was 6 s. The coefficients of horizontal viscosity on the slopes were specified equal to 250 m^2/s, while over the flat bottom they decreased to 200 m^2/s. The corresponding vertical diffusivities were specified equal to 0.0001 m^2/s.

The results of numerical simulations show that the wavelength of semidiurnal internal tide propagating from the Mendocino Escarpment was equal to 120–130 km. A similar estimate (120 km) was obtained from the integration of the dispersion relation (see Sect. 1.4.3). The amplitude of the wave at a distance of 600 km from the escarpment was 20–25 m. Immediately at the slopes of the escarpment the amplitude was equal to 50 m.

Fig. 3.4 Horizontal
coherence at 150, 700, and
1200 m versus distance
between moorings based on
the data of the DM-86
experiment. Thin line (0.5)
shows the 95% confidence
level. Scheme of the mooring
(stars) locations is shown in
the inset
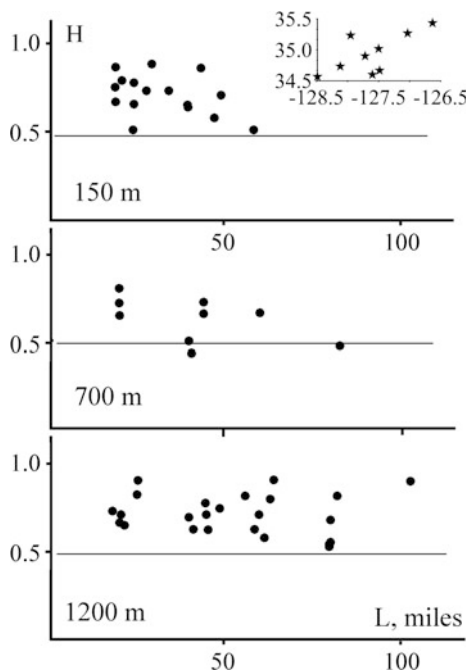
We also performed a numerical simulation of the waves generated at the continental slope of North America. The estimates of the wavelengths were the same (120–130 km), but the amplitudes of the semidiurnal internal tides were of the order of 10 m.

Investigations of internal tides in the Mendocino region were presented by Althaus et al. (2003). The research was based on 115 full-depth profiles of horizontal velocity, temperature, and salinity collected at 21 stations using the Absolute Velocity Profiler (AVP). The authors recorded strong internal perturbations radiating from the escarpment and beam structure of tidal internal waves. They estimated a baroclinic energy flux of 7000 W m^{-1} radiating from the escarpment in packets that emanate from the flanks of the ridge (northward and southward) (Althaus et al. 2003).

The abrupt topography experiment west of California was conducted in 1990–1991. The experiment was organized by the Woods Hole Oceanographic Institution, USA. Two moorings were deployed at 32° 41′N, 128° 04′W and 32° 09′N, 128° 00′W near a submarine slope. The amplitudes of internal tides at depths of 1400–1500 m were 25–30 m. At smaller depths of the ocean at one mooring located at 32° 27′N, 127° 46′W the amplitudes of internal tides at 300 m were 15–25 m.

The Low Level Waste Ocean Dumping experiment (LLWODP WEST) was conducted in 1980–1985 west of California at 40°N, 128°W. The experiment was organized by Oregon State University. Five moorings operated repeatedly 300 km
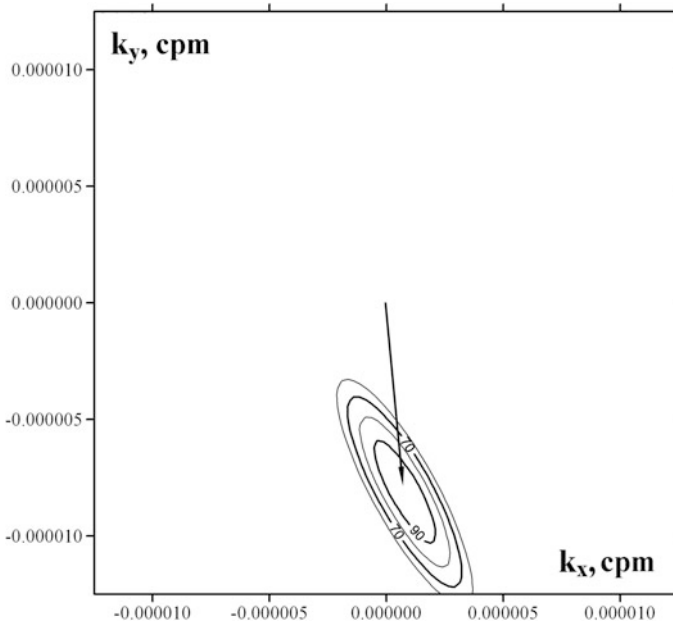
Fig. 3.5 Spatiotemporal spectrum of the semidiurnal temperature fluctuations at 700 m based on the data of study site at 35°N, 128°W in April–May 1986. The contour lines correspond to 90, 80, 70, and 60% of the main maximum. The arrow shows the wave vector corresponding to a wavelength of 130 km. The internal tide propagated to the south from the Mendocino Escarpment (azimuth 175°)

west of the US continental slope. The instruments were set at a depth of 1250 m while the ocean depth was 4200 m. The amplitudes of internal tides were estimated at 25–30 m.

The OPTOMA experiment was conducted in 1984–1985 west of California at 39°N, 125°W. The experiment was organized by Oregon State University. Three moorings operated on the continental slope at a depth of 3000 m at 38° 57′N, 124° 00′W, 38° 12′N, 124° 25′W, 38° 13′N, 125° 35′W. The instruments were set at 800 and 1200 m. The estimate of the spatiotemporal spectrum at a depth of 800 m indicates that the waves of the internal tide were directed from the coast and from the Mendocino Escarpment (Fig. 3.6). The amplitudes were estimated at 30 m.

The WOCE PCM-2 experiment was conducted in 1992–1994 200 km north of the 1986 experiment west of California at 37°N, 127°W. The experiment was organized by the Scripps Institution of Oceanography, USA. The moored measurements were carried out with a time sampling of 3 h. The distance between moorings was only 10 km; the calculated wavelength was approximately 110 km. The distance between moorings was too small to get a reliable estimate of the spatiotemporal spectrum. However, this experiment confirmed the results of 1986
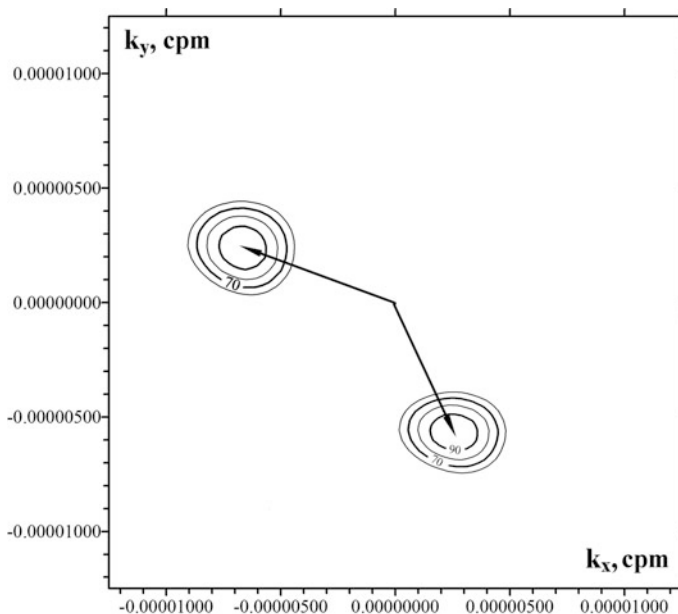
Fig. 3.6 Spatiotemporal spectrum of semidiurnal temperature fluctuations at 800 m based on the data of the OPTOMA experiment study site at 39°N, 124°W. The contour lines correspond to 90, 80, 70, and 60% of the main maximum. The arrows show the wave vectors corresponding to two waves: one propagating from the Mendocino Escarpment with a length of 140 km (azimuth 155°) and the other propagating from the continental slope with a wavelength of 145 km (azimuth 290°)

that the internal tide propagated from the Mendocino Escarpment. The amplitudes of the internal tide at a depth of 600 m were 25 m.

The Eastern Boundary Current experiment (EBC) was conducted at 38° 30′N, 124°W in 1992–1994 over the continental slope of California. The experiment was organized by Oregon State University. Five moorings operated for two years. Time sampling was one hour. The distance between moorings was of the order of 10 km. The wavelength was estimated at 80 km and the amplitude of the internal tides was approximately 25 m.

During the VENTS (hydrodynamic vents) experiment in 1984–2001, repeated deployments of moorings were carried out in the region of 44°N, 130°W. The experiment was organized by the NOAA/PMEL. In some cases, the moorings were organized in clusters, but only the location of moorings in 1989 allowed us to calculate the spatiotemporal spectra and estimate the wavelengths and direction of waves. In the other years, the distances between moorings were either much smaller or much longer than the wavelength. The depths of deployments changed from 1500 to 3600 m. The amplitudes of internal tides at 1300–2000 m were estimated at 25 m. The spatiotemporal spectrum for the semidiurnal waves is shown in Fig. 3.7. The amplitudes of the internal tides west of the US coast during the MILDEX
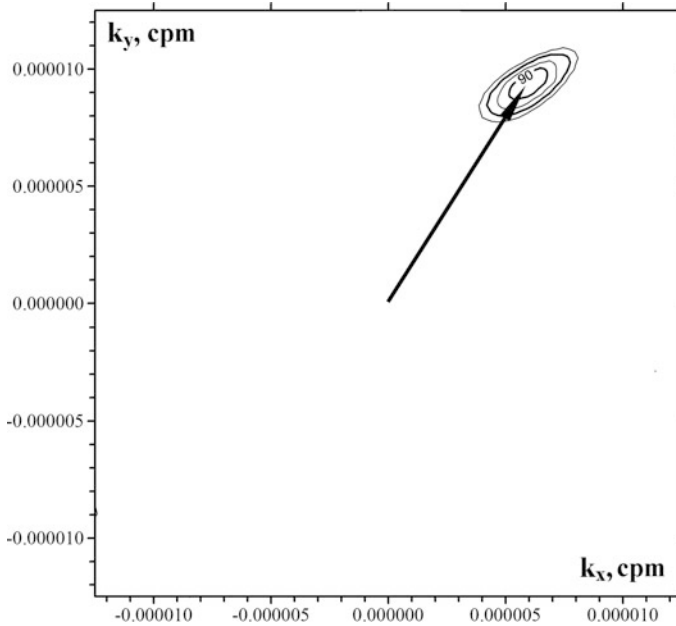
Fig. 3.7 Spatiotemporal spectrum of semidiurnal temperature fluctuations at 2000 m based on the data of the VENTS experiment study site at 44°N, 130°W. The contour lines correspond to 90, 80, 70, and 60% of the main maximum. The arrows show the wave vector corresponding to the wave propagating from the Mendocino Escarpment with a length of 92 km (azimuth 35°)

experiment in 1983 in the upper layer did not exceed 20 m as reported by Levine and Richman (1989).

Many publications report on measurements of internal tide on the Pacific continental shelf of the USA. The generation of an internal tide beam approximately 80 m wide propagating down the continental slope was reported by Torgrimson and Hickey (1979). The beam reflected from the surface and bottom while passing the line of moorings. Dissipation of the baroclinic energy on the outer shelf was estimated at 2.5×10^{-5} W m^{-3}, which gives 5 mW/m^2 if we assume that the shelf depth is 200 m. This coincides exactly with the estimates by Kurapov et al. (2003). They applied a tidal inverse model for assimilation of surface currents from coast-based high-frequency (HF) radars. Measurements of the internal tide and internal bore on a line of five moorings across the continental slope along 43° 12′N were reported by Martini et al. (2011, 2013). The maximum amplitudes of internal tides were as large as 100 m. The authors report on internal tide signals arriving from the south from the Mendocino Escarpment located at a distance of 300–400 km. Internal tides generated high-frequency internal waves propagating over the shelf (Osborne et al. 2011; D'Asaro et al. 2007).

3.3 Northwest Pacific, Megapolygon-87, WP1, and WP2 Experiments

In August-September 1981, moored measurements of temperature and velocity were conducted north of the Kuroshio Current (Morozov and Nikitin 1985) from the Russian R/V *Akademik Kurchatov*. The bottom topography of the larger region and locations of moorings are shown in Fig. 3.8. The instruments were set at depths of 100, 400, 800, and 1300 m. A few moorings had instruments at 5000 m. The synchronous operation of all moorings was 10 days.

The spectra are characterized by a clearly pronounced peak at the semidiurnal frequency. At a depth of 800 m, the mean amplitudes of internal tides were estimated at 25 m. Horizontal coherences between the time series were not always higher than the confidence level. The vertical coherence dropped below the confidence level if the distance between the temperature meters exceeded 400 m.

The bottom topography in the region is characterized by two prominent features: the Shatsky Rise (33°N, 158°E) and the Emperor Ridge located east of the study site. It is likely that the internal tides were generated at several sources and interfered in the region adjusting to the bottom topography.

In 1980–1982, the WestPac-1 and WestPac-2 experiments were conducted in this region by the WHOI. Nine moorings with instruments at a depth of 1200 m
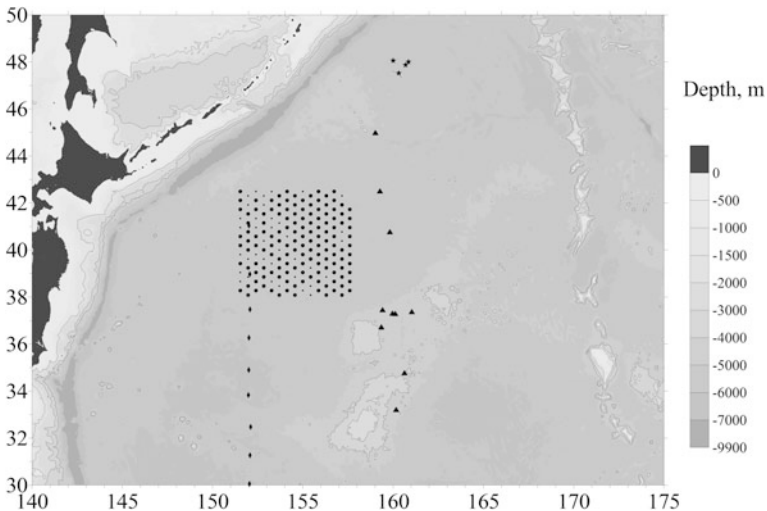
Fig. 3.8 Bottom topography in the study sites in the Northwest Pacific and locations of moorings. Depth contour lines are shown at depths of 500, 1000, 2000, 3000, 4000, 5000, and 6000 m. Locations of moorings are shown with black symbols. Land and islands are shown with gray color. Megapolygon moorings are shown with black dots (planned points are shown with small dots and moorings that returned data are shown with larger dots); Kamchatka experiment moorings are shown with stars; Northwest Pacific moorings in 1981 are shown with triangles; WP-1 and WP-2 moorings are shown with diamonds

were deployed along 152°E from 41°N to 28°N. The amplitudes of internal tides were estimated at 35–45 m. The largest amplitudes (45 m) were recorded at 35°N, which is closer to the Shatsky Rise, while the smallest were at 41°N and 28°N, most distant from the rise.

Publications report on the generation of intense internal tides in the region of the Kuril Islands (Tanaka et al. 2008, 2010). Tidal currents in the Kuril Straits were extremely strong and the transport in the straits was as high as 5 Sv (Nakamura et al. 2000). We shall analyze the measurements of the semidiurnal internal tides southeast of Kamchatka.

In August 1984, four moorings were deployed east of the Kuril Islands at 48°N, 160°E from the Russian R/V *Akademik Mstislav Keldysh* to study the mesoscale eddies and internal waves. The study site was located at a distance of 500 km southeast of the southern Kamchatka cape (Cape Lopatka). The time series of temperature and velocity were obtained from instruments at 100, 150, 200, 300, 500, and 3000 m. The semidiurnal spectral peak at the M_2 frequency corresponded to the internal tide with an amplitude of 20 m at a depth of 500 m. Horizontal and vertical coherences did not always exceed the 95% confidence level. We assume that the generation of internal tides occurred over the slopes of the Kuril Islands.

We used the Barber's method to calculate the spatiotemporal spectrum at the semidiurnal frequency (see Sect. 1.4.2) (Barber 1963). The spatiotemporal spectrum is shown in Fig. 3.9. The internal tide propagated from the slopes of the Kuril Islands to the southeast in the direction 110°–120°. The wavelength was 80–90 km, which corresponds to its estimate using the dispersion relation.

In August–October 1987, the Megapolygon experiment was conducted in the Northwest Pacific (Maximenko et al. 2001) by the Shirshov Institute of Oceanology, Russia. A total of 173 moorings were deployed with velocity and temperature meters at 120 and 1200 m. Some of the moorings had additional instruments at 400 and 4500 m. The locations of moorings and bottom topography are shown in Fig. 3.8. Planned locations of moorings and moorings that returned data are denoted by dots of different sizes (Fig. 3.10).

The time sampling on all instruments was 30 in. The duration of operation of all moorings was two months. The mean amplitude of the semidiurnal internal tides at a depth of 1200 m was estimated at 20 m.

Temperature sensors were set at a depth of 1200 m on the moorings of the northwestern group (13 moorings) and southeastern group (15 moorings) (Fig. 3.10). The period of synchronous operation of these moorings was one month. The spatiotemporal spectra of semidiurnal temperature fluctuations based on the data of the northwestern and southeastern group of moorings are shown in Fig. 3.11 superimposed on the geographical chart of bottom topography.

We calculated different versions of spatiotemporal spectra using temperature and velocity time series from various combinations of moorings (see Sect. 1.4.2) using the Barber's method (Barber 1963). Let us first analyze the spatiotemporal spectra calculated from the temperature data.

The main peaks correspond to the wavenumbers directed to the northwest. The wavelength was approximately 150 km. We suppose that these waves were
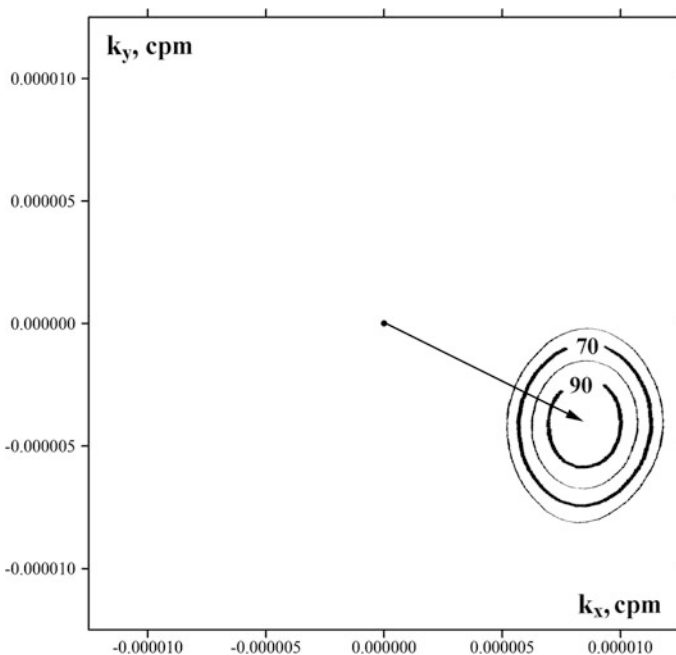
Fig. 3.9 Spatiotemporal spectrum at the semidiurnal frequency in the study site southeast of Kamchatka in 1984 at a depth of 500 m. The contour lines correspond to 90%, 80%, 70%, and 60% of the main maximum. The arrow shows the wave vector corresponding to a wavelength of 90 km. The internal tide propagated to the southeast (azimuth 120°)

generated over the Shatsky Rise (32°N–34°N, 157°E–164°E) or over the Emperor Ridge. The second smaller peak on the northwestern group of moorings corresponds to the waves propagating to the southeast generated on the continental slope of the Kuril Islands. This peak is not seen on the spectra based on the southeastern group of moorings. It is likely that the internal tide became weaker here after propagating longer distance; hence a reliable peak disappears.

Similar peaks were found based on the measurements at 120 m but they are less stable. Reliable peaks are obtained if we make a calculation of densely located moorings. Calculation of the spectrum based on the whole set of measurements at 120 m does not result in a reliable spectrum.

It is interesting to calculate a spatiotemporal spectrum for the semidiurnal internal tide based on the velocity measurements. We selected 51 moorings with synchronous velocity data at 120 m. The duration of their synchronous work was 348 h (Fig. 3.12).

The eigen function for the equation of vertical velocities induced by internal tides has zero values at the surface and at the bottom while the maximum is in the depth range 1000–1500 m over the ocean depths 4000–5000 m. The eigen function for the horizontal velocity has maxima at the surface and bottom and zero in the
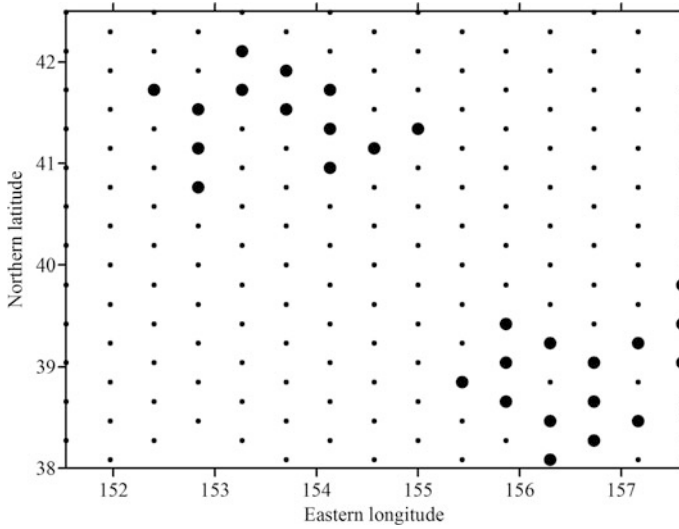
Fig. 3.10 Megapolygon study site. Planned moorings are shown with small dots. Moorings with temperature data at 1200 m in the northwestern and southeastern groups of moorings are shown with larger dots
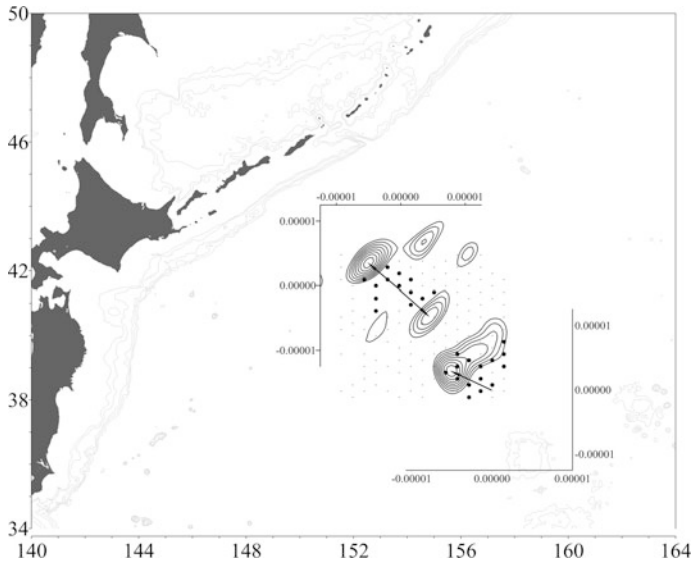
Fig. 3.11 Spatiotemporal spectra for the semidiurnal internal tides based on the temperature data from the moorings in the northwestern and southeastern groups of the Megapolygon experiment are superimposed on the geographical chart of bottom topography (thin gray lines show isobaths) with marked locations of moorings. The contour lines correspond to 90, 80, 70, 60, 50, 40, and 30% of the main maximum. The arrows show the wave vectors corresponding to the waves propagating from the slope of the Kuril Islands and Shatsky Rise
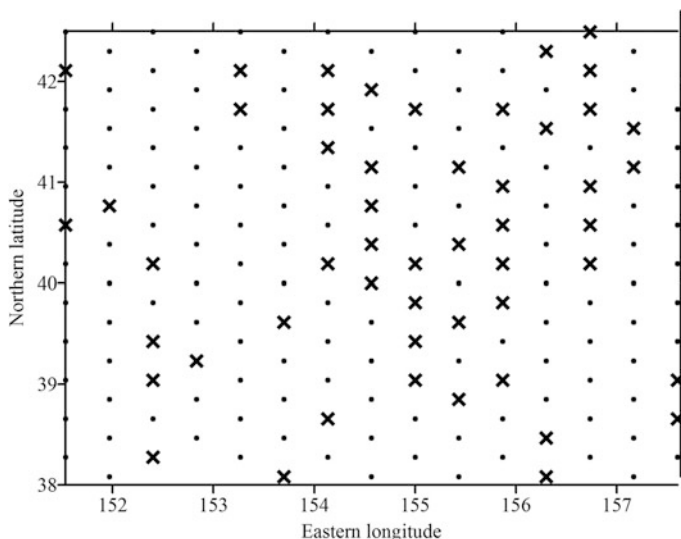
Fig. 3.12 Megapolygon study site. Planned moorings are shown with small dots. Moorings with synchronous velocity data at 200 m used in the calculation of spatiotemporal spectrum are shown with crosses

depth range 1000–1500 m. Therefore, the calculation of spectra based on the data of velocities should be done on the basis of measurements in the upper layer (moored measurements at 120 m in the study site).

However, the velocity data contain the currents induced by the barotropic tide and internal tide. We have to exclude the currents of the barotropic tide from the time series. With this in mind we passed the data of velocity components from each of the 51 moorings through a band filter tuned to the M_2 semidiurnal frequency (12.4 h). After such filtering only the fluctuations with the semidiurnal frequency in the band of periods between 11.4 and 13.4 h remained in the time series. After band filtering each component (u and v) at each mooring, we averaged the 51 time series for every sampling time moment (every 30 min). Thus, we obtained a time series of the barotropic tide currents covering 348 h that corresponds to the spring-neap variability of the semidiurnal tides. Then, we subtracted the barotropic tide components from the filtered time series, thus obtaining the time series of internal tide velocity components.

A topographic chart, locations of all moorings with data (dots) and moorings with synchronous current measurements at 120 m (crosses) are shown in Fig. 3.12.

We followed a similar procedure by averaging four time series over the vertical at one mooring 2019 (38° 49′N, 155° 22′E). The averaging was performed with the corresponding weights after band filtering to separate the barotropic M_2 tidal signal. The measurements were made at 120, 1200, 2600, and 4600 m. The depth of the location was 5800 m. The weight coefficients of averaging were: 0.1 for 120 m, 0.22 for 1200 m, 0.33 for 2600 m, and 0.35 for 4600 m. We considered that the

measurements are related to the following vertical layers: 0–580, 580–1850, 1850–3700, and 3700–5800 m. The difference between this method of averaging and averaging by dividing the sum of four values by four was not significant. The results of averaging the time series and separating the barotropic tide and internal tide on September 25, 1987 (tidal ellipses) are shown in Fig. 3.13.

Thus, we obtained 51 time series of velocities measured on moorings and excluded the signal of the barotropic tide from the time series. A spatiotemporal spectrum was calculated from the data of internal tides at 120 m. The spectrum is shown in Fig. 3.14. The spectrum shows that the semidiurnal internal wave propagated from the east; its length was about 150–160 km.

3.4   Emperor Seamounts

Moored measurements west of the Emperor Ridge were carried out in 1982–1983. The experiment was organized by the University of Washington, USA. One mooring was deployed at 38° 50′N, 171° 06′E at a distance of 50 km from the ridge, the second mooring was deployed at 34° 20′N, 167° 02′E at a distance of 300 km from the ridge (Fig. 3.15). The instruments were set at 940 and 1125 m. The amplitudes of internal tides on the first mooring were 40 m, and 20 m on the second mooring.

In 1983-1985, three moorings operated along 165°E at 31° 02′, 33° 01′, and 41° 07′N. The instruments at 620–670 m recorded internal tides with amplitudes of 30–50 m. The largest amplitudes (35 m) were recorded on WHOI mooring 8012 (41° 06′N, 165° 02′E) at a depth of 669 m. In 1983–1984, two moorings were

Fig. 3.13 Three tidal ellipses on September 25, 1987: ellipse based on the TOPEX/POSEIDON data (thick line) (Egbert and Erofeeva 2002), ellipse based on averaging of 51 mooring data at 120 m (thin line), and ellipse based on vertical averaging of four current meter data at mooring 2019 (38°49′ N, 155°22′ E) (dashed line with dots)
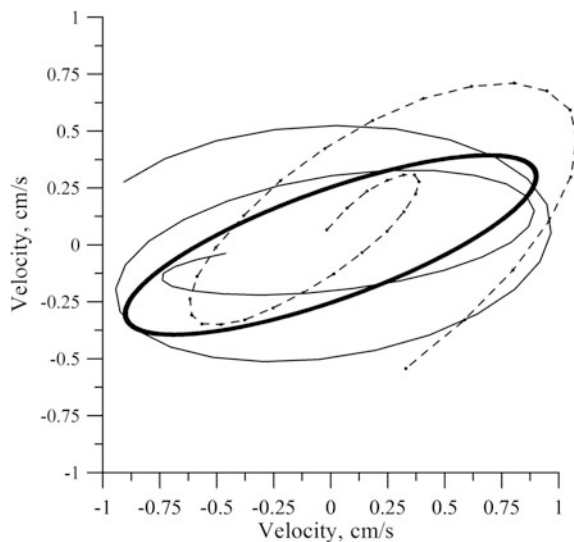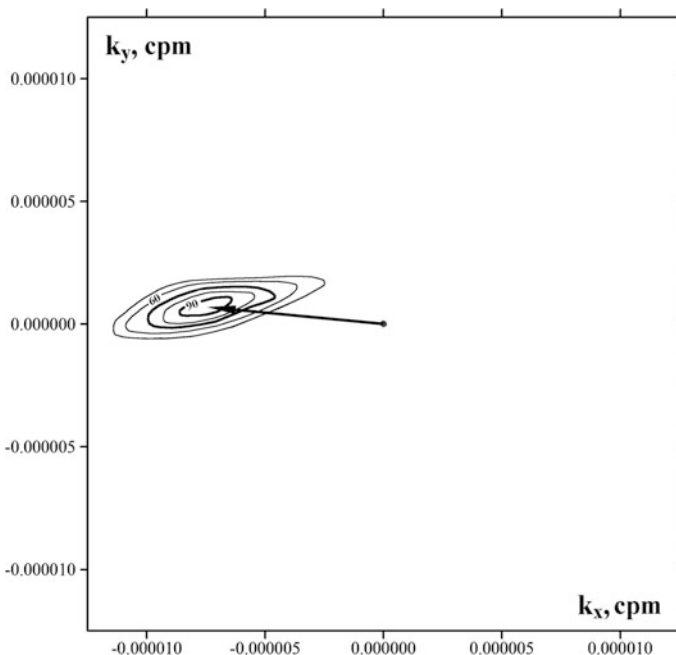
Fig. 3.14 Spatiotemporal spectrum for the semidiurnal internal tides based on the velocity data from 51 Megapolygon moorings at 120 m after removing the barotropic tide component. The contour lines correspond to 90, 80, 70, 60, and 50% of the main maximum. The arrow shows the wave vector

located east of the ridge at 175°E at 39° 00′N and 35° 15′N. The amplitudes of the internal tide at these moorings at depths of 648 and 669 m were estimated at 25 m.

One of the confirmations that strong generation of internal tides occurs over the slopes of the Emperor Ridge is based on the measurements from a moving ship performed with expandable bathythermographs (XBT). According to the classification of Garrett and Munk (1972) spectral characteristics of internal waves obtained using towed instruments are called towed spectra. An unusual approach, which is suggested here, is that nothing is towed by the ship. Only XBT casts are made regularly. Towed measurements are usually obtained by towing a line of sensors or another instrument. The devices that are currently used limit the speed of towing by 5–6 knots, depth of measurement by 200 m, and the length of the tack by 100 km. All the limits are approximate. These limits are only acceptable in the study of high-frequency internal waves. They are not acceptable for investigating internal tides, whose wavelength is usually greater than 100 km. Therefore, only short internal waves are investigated using the towed methods.

Measurements using XBTs are capable to replace towed measurements of internal tides. If the measurements are made repeatedly in two directions it is possible to take into account the Doppler effect. If the length of the tack exceeds the
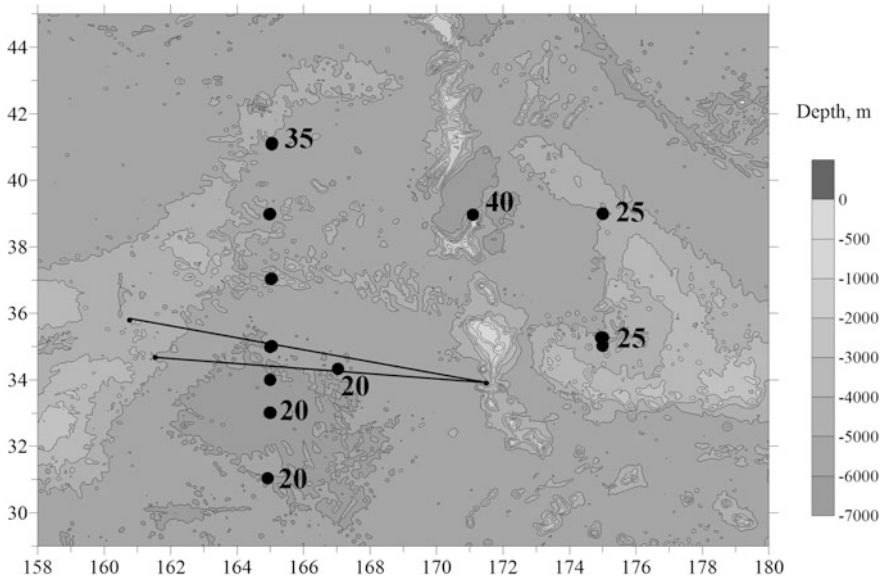
Fig. 3.15 Bottom topography, location of moorings (black dots) and tow tacks (lines) west of the Emperor Ridge. The numerals at several dots indicate the amplitudes of the internal tides

wavelength several times, these data can be used for analyzing internal tides if the XBT launches are made frequently enough. The time needed to complete such a section should be relatively short. It is impossible to tow any instrument from a ship at the needed high speed.

A section performed using expandable bathythermographs that reach the depths of 500–600 m at the full speed of the vessel can be considered as towing according to the Garrett-Munk classification (Melnikov et al. 1985). Since the speed of the ship is relatively fast and the section is made quickly we can consider that long-period oscillations do not change significantly during the time needed to carry out the measurements over the section.

The following experiment was organized in 1981 from the Russian R/V *Akademik Kurchatov*. Two tacks in opposite directions with frequent (one hour interval) casts of XBTs were performed in 1981 from the Shatsky Rise to the Emperor Ridge and back. We obtained the data of profiling by expandable bathythermographs from 35° 48′N, 160° 46′E up to 33° 54′N 171° 29′E and back to 34° 40′N, 161° 32′E (Fig. 3.15). The length of the first tack was 1133 km, and the length of the second tack was 929 km. The tacks were located almost normal to the ridge, which allows us to consider that the first tack was directed almost opposite to the direction of the tidal internal wave propagation, and the opposite tack was made approximately in the direction of the wave. The speed of the ship was about 7.2 m/s, and the approximate phase speed of the wave was $C_{ph} = 3$ m/s. Under the condition of this relation between the speeds, the Doppler shifted

wavelength L_D and period T_D are related to the real wavelength L_0 and period T_0 as:

$$L_D = \frac{L_0}{1 \pm \frac{U}{C_{ph}}}, \quad T_D = \frac{T_0}{1 \pm \frac{U}{C_{ph}}}. \tag{3.2}$$

The plus sign in the denominator of these relations corresponds to the opposite directions of the ship and wave, and the minus sign corresponds to the same directions.

The temperature profiles measured by XBTs reach a depth of 500–600 m, but most reliable records were obtained from the depths of about 300 m. The analog records of temperature profiles with depth were digitized and one-dimensional spatial spectra depending on the horizontal wavenumber were calculated on the basis of these data. The wavelength of an internal wave is approximately 7–9 times shorter than the length of the tack; hence, the statistical reliability of the spectra calculations is not very high. Nevertheless we can give an interpretation of the spectral peaks. The spectra based on the data of the two tacks are shown in Fig. 3.16.

Let us use relation (3.2) to calculate the real wavelengths from the Doppler shifted values of wavenumbers corresponding to the peaks on the spectra. The wavelength taken from the spectra (with a Doppler shift) calculated from the tack directed to the ridge corresponding to a wavenumber of 0.014 cycles/km is equal to 72 km, which corresponds to a real wavelength of 92.7 km. The measurements over the tack directed from the ridge reveal a peak at a wavenumber of 0.0075 cycles/km corresponding to a Doppler wavelength of 137.3 km and to a real

Fig. 3.16 One-dimensional spatial temperature towed spectra at a depth of 300 m based on XBT-section in the direction to the Emperor Ridge (thicker line) and back (thinner line)
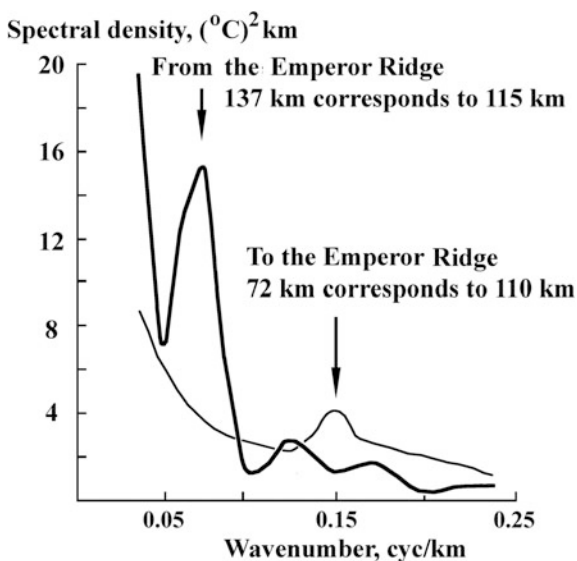
wavelength equal to 96.2 km, respectively. These two values correlate well with one another, but both of them are smaller than the estimates obtained from the measurements on the buoys and by integrating the equation for eigen values. A slight increase in wavelength is possible if we assume that our tacks were not strictly located in the direction of the wave propagation.

If we calculate the spectra as frequency spectra with the data measured with an interval of one hour we obtain that on the first section (tack) the peak is located at a frequency corresponding to the period equal to 2.3 h and on the second section the peak corresponds to a period of 5.3 h. Thus, if the wave and ship move in the opposite directions the tidal period (12.4 h) reduces to 2.3 h (the observer passes one wavelength faster and considers that the wavelength and period are shorter). If the ship and wave propagate in the same direction, the ship overtakes the wave and the observer also considers that the wave and its period are shorter, but not as short as in the case of the opposite motion.

3.5   Kermadec Ridge, MAPKIWI Experiment

Twenty moorings were deployed in 1991–1992 east of the Kermadec Ridge in the Southwest Pacific Ocean along latitude 32° 30′S between 168° and 179°W (Fig. 3.17). The experiment was organized by Oregon State University. The instruments on the moorings were located mostly at depths greater than 2500 m. Sixteen moorings had temperature and current meters at a depth of 2500 m. The energy and amplitudes of internal tides strongly depend on the bottom topography and relative location of underwater slopes. The amplitudes of internal tides varied between 13 and 33 m. The largest energies and amplitudes were found on the moorings close to the Kermadec Ridge and Louisville Seamounts. Graphs of the variation in the energy and amplitude of internal tides versus longitude are shown in Fig. 3.18.

Analysis of the data collected on these moorings was presented by Chiswell and Moore (1999). The authors estimated the energy flux from the Kermadec Ridge and found it quite low: 264 W m^{-1}. Taking into account that the length of the ridge is 2500 km, the total radiated energy was approximately 0.8 GW.

3.6   Equatorial Pacific, TOGA COARE, PEQUOD, Tropical Heat, MANOP, and EPOCS Experiments

During the TOGA COARE experiment, a line of temperature sensors was deployed by the WHOI in 1992–1993 in the upper layer (52–260 m) almost at the equator (1° 45′S, 156°E). The line was supported by a surface buoyancy. The amplitudes of internal tides just below the upper thermocline were estimated at 10–20 m.
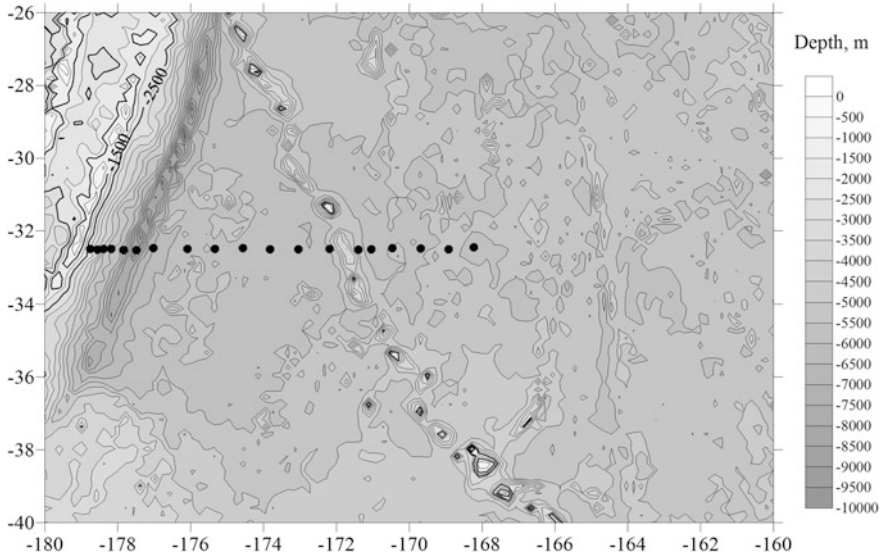
Fig. 3.17 Bottom topography in the study site in the South Pacific near the Kermadec Ridge (179°W) and Louisville Seamounts (172°W). Depth contour lines are shown with an interval of 500 m. Isobaths 1500 and 2500 m are thicker. Locations of moorings are shown with black dots

During the PEQUOD (Oregon State University) experiment (0°, 145°E) (1981–1982), a cluster of 6 moorings was deployed in the Equatorial Pacific. The amplitudes of internal tides at a depth of 1500 m over the ocean depth of 4200–4400 were estimated at 50 m.

Two moorings were deployed in 1984–1985 in the Equatorial Pacific (1°N, 140°W; 1°S, 140°W). The instruments were located only in the upper layer not deeper than 200 m. The amplitudes of internal tides in the upper thermocline did not exceed 20 m.

During the MANOP experiment (Oregon State University) (138°W) (1982–1983) aimed at the study of sediments, several moorings were deployed in the equatorial zone of the Pacific 1°N, 139°W. In the region of submarine slopes, the amplitudes of semidiurnal internal tides at a depth of 1000 were 40 m.

The EPOCS experiment (NOAA/PMEL) was carried out in 1980–1981 at 110°W, 140°W, 165°E at the equator. Most of the measurements were made in the upper layer above 300 m. Only at 140°W, some instruments were at depths of 1000 and 2000 m. At 140°W the amplitudes were 30–40 m. The amplitudes of internal tides at depths close to 300 m at 110°W and 165°E were estimated at 20 m.

A scheme of moorings near the Pacific equator is shown in Fig. 3.19.

Eulerian and Lagrangian measurements of internal waves at the equator at 140°W were reported by Lien et al. (2002). The authors analyzed high-frequency internal waves in the upper layer. The amplitude of internal tides based on their measurements did not exceed 10 m in the layer shallower than 200 m.
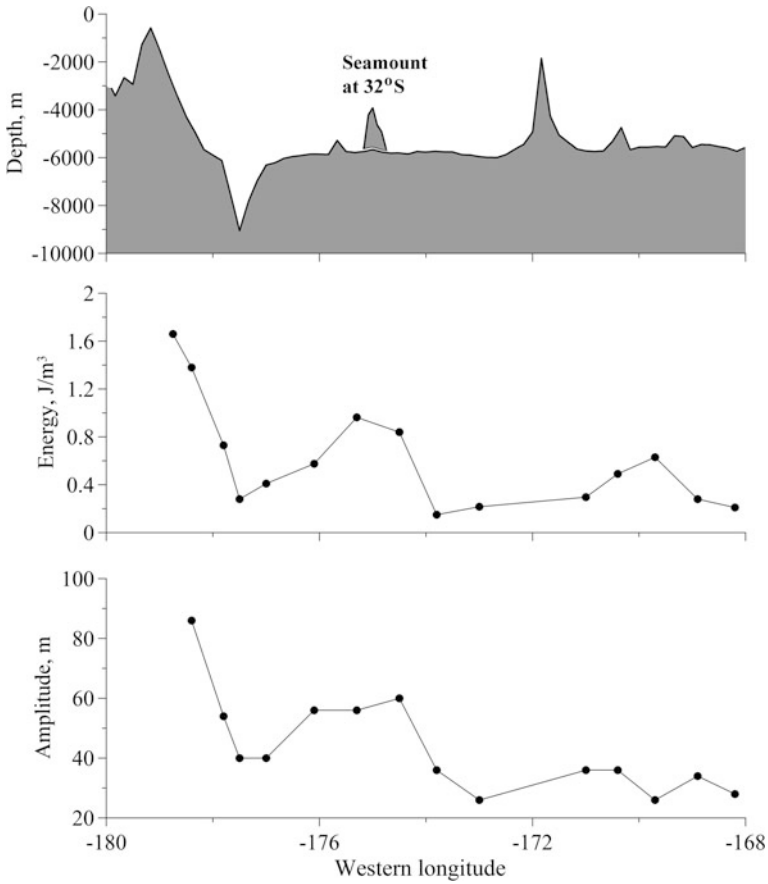
Fig. 3.18 Profile of the bottom topography along the line of moorings (32° 30′S) (top panel). Energy (middle panel) and amplitude of internal tides (bottom panel) versus longitude
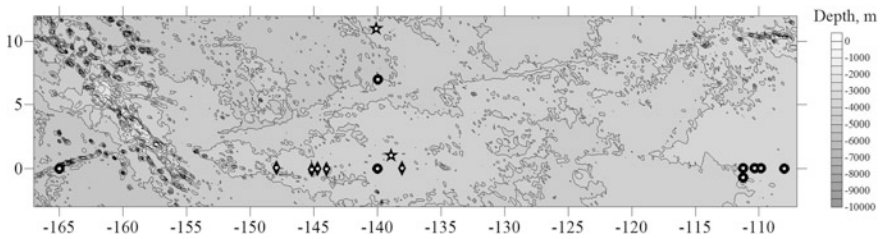
Fig. 3.19 Bottom topography in the Equatorial Pacific. Depth contour lines are shown with an interval of 500 m. Locations of moorings are shown by black symbols with a white dot in the middle. The EPOCS moorings are shown with dots, the MANOP moorings are shown with stars, and the PEQUOD moorings are shown with diamonds

Measurements of internal tides by Gourdeau (1998) on a mooring with 30 temperature sensors deployed at 2°S, 156°E show that the amplitude of the M_2 internal tide was as high as 25 m. The two lower modes were responsible for 70% of the vertical displacement. The internal tide propagated to the northeast from a series of islands.

3.7 East Tropical Pacific, East Pacific Rise, DOMES Experiment

Moored measurements were carried out in the Northeast Pacific in 1990–1991. Three moorings were deployed at 15° 01′N, 126° 00′W; 11° 44′N, 138° 23′W; 8° 27′N, 150° 45′W (NOAA/PMEL). The instruments were set in the upper layer not deeper than 200–300 m. The amplitudes of internal tides were 20–25 m.

Moored measurements near the East Pacific Rise were analyzed by Liang (2014). Five moorings were deployed in the region 9° 30′N, 104° 00′W. The distances between the nearby stations were about 30 km. The study is based only on the measurements of currents. The baroclinic semidiurnal tidal currents dominated over the ridge crest. The magnitude of the semidiurnal baroclinic currents decreased away from the ridge crest. The baroclinic semidiurnal tidal currents were coherent over vertical separations of a few hundred meters near the seafloor.

3.8 Kyushu-Palau Ridge

A standalone mooring was deployed in this region at 26° 20′N, 134° 58′E from the Russian R/V *Vityaz* in November 1987 assuming that intense internal tides should be generated here as it followed from the model (Morozov 1995, see Chap. 8). By this time the model estimates described in Chap. 8 were completed; the region of the Kyushu-Palau Ridge was characterized as a region of intense internal tides. The mooring was deployed at a distance of 80 km from the ridge. The measurements continued for only four days. Repeated CTD casts were carried out during the operation of the mooring. The measurements recorded internal tides with amplitudes exceeding 60 m at a depth of 800 m.

The internal tides in the southern part of the Sea of Japan were studied by Park and Watts (2006) on the basis of measurements with inverted echo-sounders and a numerical model. Beams of the semidiurnal internal tides were observed propagating into the open basin. The generation of beams occurred at a depth of 200 m over the slope, where the slope of bottom topography coincided with the wave characteristics, and where the semidiurnal barotropic cross-slope tidal currents were the strongest. The maximum vertical displacement of the thermocline was 25 m.

3.9   Aleutian Ridge, FOCI (52°N, 170°W); GARS (59°N, 148°W), North Pacific Boundary Current (46°–51°N, 175°W) Experiments

The internal tides radiated from the Aleutian Ridge were studied by Cummins et al. (2001) using satellite altimetry and modeling. Altimetry observations show coherent southward propagation of the semidiurnal internal tides over a distance of at least 1100 km. The model results show that the strongest energy fluxes occur in the vicinity of the Amukta Pass (52°N, 172°W). The model results also suggest that the net rate of conversion of barotropic to baroclinic energy is about 1.8 GW in the vicinity of the Amukta Pass.

The GARS experiment was conducted in 1986–1988 over the continental slopes of Alaska and the Aleutian Islands. The experiment was organized by the University of Alaska. The moorings were deployed at 57° 13′N, 148° 28′W at a depth of 5040 m and at 54° 27′N, 158° 28′W at a depth of 2150 m on the slope. The amplitude of internal tides at a depth of 1000 m was estimated at 70 m, while at a distance of 100 km from the slope the amplitude was 50 m. Locations of moorings are shown in Fig. 3.20.
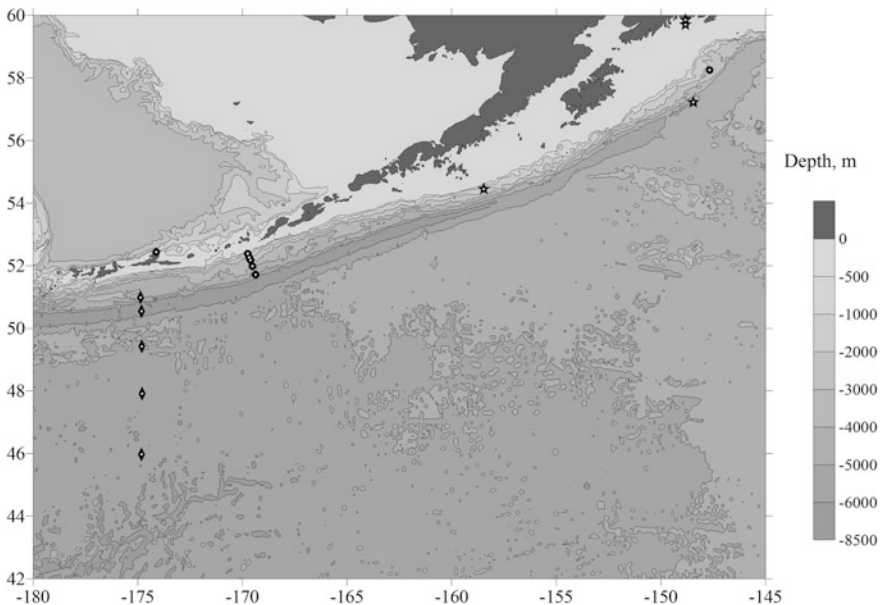
Fig. 3.20 Bottom topography in the study site near the Aleutian Ridge and locations of moorings. Depth contour lines are shown at depths of 500, 1000, 2000, 3000, 4000, 5000, and 6000 m. Land and islands are shown with gray color. Locations of moorings are shown with black symbols with a white dot in the middle. The FOCI moorings are shown with dots, the GARS moorings are shown with stars, and the NPBC moorings are shown with diamonds

During the FOCI experiment in 2001 (NOAA/PMEL), one mooring was deployed in the Bering Sea north of the Aleutian Ridge at 58° 15′N, 147° 41′W. The amplitudes of the internal tides at a depth of 600 m were low and did not exceed 20 m.

A mooring at 52° 24′N, 169° 45′W deployed on the southern slope of the Aleutian Islands over a depth of 1050 m recorded the amplitudes of internal tides exceeding 150 m at a depth of 560 m. The records from another mooring over a depth of 2000 m showed amplitudes in the range 150–200 m. Over a depth of 3000 m the amplitudes decreased to 70–80 m and over a depth of 6000 m the amplitudes dropped to 25 m. A strong tidal flow propagated through the passes between the islands generating intense internal tides. Two moorings were deployed at 173–174° W on both sides of the Aleutian Ridge on the slopes of the islands. The amplitudes of the semidiurnal internal tides at depths of 500–700 m over the ocean depths of 1000–1200 m exceeded 100 m (Fig. 3.21). We performed a procedure for estimating the energy density of the internal tide similar to that used by Lozovatsky et al. (2003). Decay of the semidiurnal internal tide energy and amplitudes with distance is shown in Fig. 3.22. The graph shows that the energy decay with distance is similar in two different regions of the oceans.

During the North Pacific Boundary Current (NPBC) experiment in 1981–1982, five moorings were deployed in a line normal to the Aleutian Ridge from its southern side from 51°N to 46°N along 175°W (CMDAC numbers: 3202, 3207, 3210, 3214, 3219). The experiment was organized by the Woods Hole Oceanographic Institution, USA. A graph of the variation in the amplitudes of internal tides with distance at 2000 m is combined with the results of internal tides
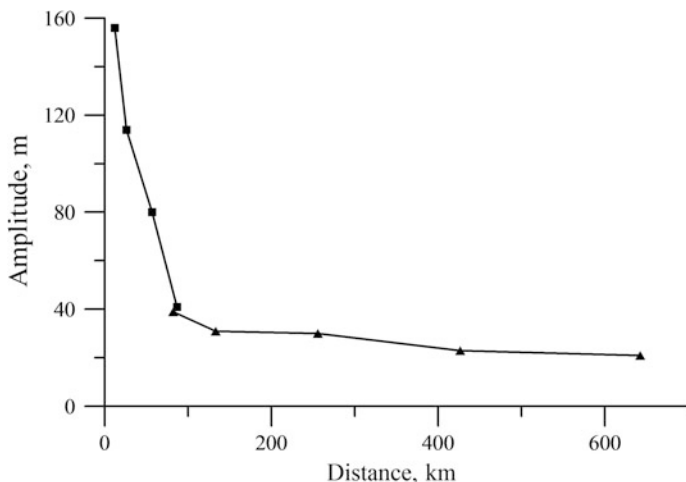
Fig. 3.21 Combined graph of the semidiurnal internal tide amplitude decay with the distance from the Aleutian Islands based on the data of the FOCI experiment (squares) and NPBC experiment (triangles)
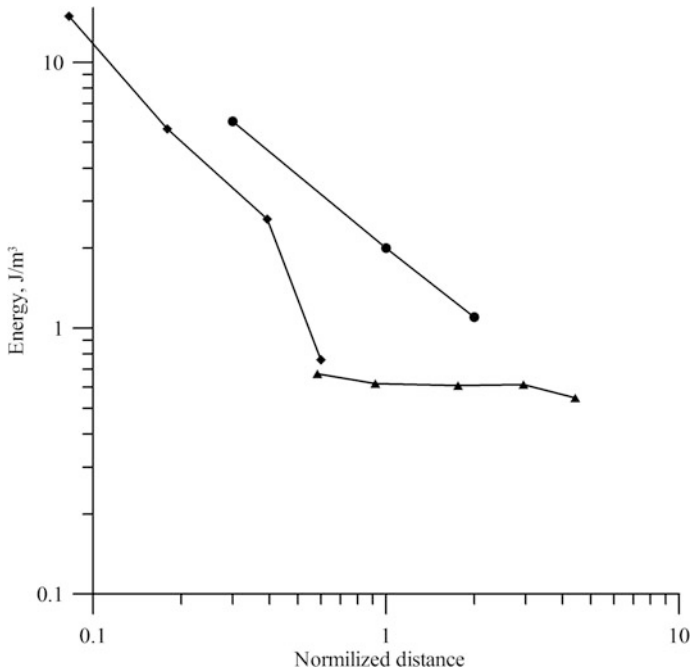
Fig. 3.22 Combined graph of the semidiurnal internal tide energy decay with the distance from the Aleutian Islands based on the data of the FOCI experiment (squares) and NPBC experiment (triangles). Decay of the internal tide energy based on the measurements near the Mascarene Ridge in the Indian Ocean (dots) (Lozovatsky et al. 2003) is shown for comparison

recorded in 2001 (CMDAC numbers: 5014, 5018, 5023). Decay of the semidiurnal internal tide amplitudes with distance is shown in Fig. 3.21.

Decay of the amplitudes in the FOCI experiment within 87 km from the slope of the islands is much stronger than in the NPBC experiment (distance range 82–142 km). The energy decay is similar. The energy decay is also similar to the decay in the experiment near the Mascarene Ridge (Sects. 4.1 and 7.7), which is close to the power law. Energy decay near the Aleutian Islands is of the same order of magnitude, but possibly the errors are higher in the region of smaller vertical temperature gradients.

The generation of the internal tide in the Gulf of Alaska was analyzed by Bracher and Flatté (1997) on the basis of acoustic experiments in the Central Pacific at 32°–33°N. They studied the effect of the plane first mode M_2 internal tide by ray tracing and found that the internal tide arrives from the Gulf of Alaska after propagating over more than 3000 km. The maximum energy flux was estimated at 7000 W m^{-1}.

3.10   Hawaii Islands

Intensive studies of internal waves and mixing were carried out during the Hawaii Ocean Mixing Experiment (HOME) in the early 2000s. The goals of the HOME experiment were to quantify the rate of tidal energy conversion to mixing at the Hawaiian Ridge, and to identify the mechanisms by which the energy transformation occurs. By the end of the 20th century it became clear that strong mixing in the ocean occurs near topographic slopes. The experiment was aimed at studying the topographic mixing through an integrated program of observations and modeling. The investigations were focused on tidally forced mixing as the global mixing energy supply. The Hawaiian Ridge was selected as a study site knowing that this is the region of strong interaction between the barotropic tide and bottom topography (Pinkel et al. 2000).

Field experiments were aimed at identifying "hot spots" of enhanced mixing and barotropic to baroclinic conversion. The Near-field program of research was aimed at identifying the mechanisms responsible for topographic mixing, and the Far-field program was aimed at studying radiation of baroclinic waves. Field works were planned from 2000 to 2002, and the data analysis extended to 2006. It is clear that strong mixing is associated with tidally forced internal waves.

A special issue of the *Journal of Physical Oceanography* (Vol. 36, no. 6, 2006) was dedicated to the HOME results. Guest editors Rob Pinkel and Dan Rudnick wrote in the editorial that internal tides exceeding 100-m amplitude were found on the deep flanks of the ridge. Low-mode radiated energy fluxes agree with model predictions. Diffusivities exceed 10^{-3} m^2 s^{-1}.

Much data on internal tides in the Hawaii region comes from satellite observations supported by tide gauges. It was reported by Ray and Mitchum (1996, 1997) that there is a persistent component of internal tides that remains phase-locked to the barotropic tide over a period of three years. It is manifested by a modulation at the surface by 5 cm. This phase-locked component remains spatially coherent over great distances exceeding 1000 km. Propagation of the internal tides over even greater distances up to 2000 km was reported by Dushaw et al. (1995) based on satellite altimetry.

The studies of internal tides before the beginning of the HOME experiment indicated that strong internal tides exist in the region of the Hawaiian Ridge. Internal tide generation occurs due to the interaction between the tidal currents and slopes of the ridge. The most intense generation occurs between the Kauai and Oahu islands in the Kauai Channel over the Kaena Ridge. Tidal velocities of the barotropic tide estimated from the satellite altimetry and moored ADCP in the channel prove this (Chavanne et al. 2010).

Internal tides 100 km north of Oahu Island were studied by Chiswell (1994) at the ALOHA deep-water station (22° 45′N, 158° 00′W), which was visited by ships on a monthly basis. Internal tides with amplitudes up to 30 m were recorded. Chiswell (2002) reported that the measurements using inverted echo sounders at the ALOHA station made it possible to estimate the semidiurnal energy flux equal to

4400 W m^{-1}. Estimates of the internal tide energy flux were made in the Near-field region of Hawaii using velocity and density profilers from the R/V *Flip* moored in the channel between the Kauai and Oahu islands at a depth of 1100 m (21° 39′N, 158° 38′W). The measurements in the Far-field region were made 450 km offshore south of the Kaena Ridge. Energetic beams of internal tides were observed over the slopes of the Kaena Ridge in the Near-field. In the Far-field the internal tide was mostly presented by the first-mode semidiurnal internal waves. The depth average semidiurnal energy flux in the Far-field was estimated at 1700 W m^{-1} in the southern direction. Energetic beams were also found in Near-field using velocity and density profiles by Nash et al. (2006). Observed overturns correlate with tide. Energetic internal tides cause overturns, which were as high as 24 m (Levine and Boyd 2006).

Modeling studies support the role of the Hawaiian Ridge in generating internal tides. One of the first modeling studies of internal tide generation over the Hawaiian Ridge was reported by Holloway and Merrifield (1999). Their study was aimed at determining which topographic features characteristic of the Hawaiian Ridge facilitate strong internal tide generation. They also modeled general features of the beam propagation of the radiated internal tide energy. A long (two-dimensional) ridge produces an internal tide with an energy flux 40 times larger than that found over a seamount of the same height and slope. The maximum conversion of barotropic to baroclinic energy occurred over the 500 m submerged ridge with baroclinic energy fluxes reaching 1200 W m^{-1}. They found a rapid decay of the energy flux. After propagating one wavelength, the energy flux reduces to 300 W m^{-1}. Model studies by Holloway and Merrifield (2003) revealed spring-neap variability of the internal tide at the Hawaiian Ridge. The energy fluxes were directed northward and southward from the ridge. In the regions of the most intense internal tide generation in the Kauai Channel between Oahu and Kauai islands, the energy fluxes of the semidiurnal internal tide from the ridge ranged between 13,700 and 2600 W m^{-1}.

Horizontal propagation of the internal tides from the Hawaiian Ridge and some other locations of strong internal tide generation were studied by Rainville and Pinkel (2006b). The authors developed a ray model to quantify the effects of spatially variable topography, stratification, and vorticity on the propagation of internal gravity waves. They found that mesoscale variability is sufficient to cause coherence losses of the M_2 internal tide generated at the Hawaiian Ridge as it propagates southward. The internal tide propagating northward from the ridge should experience less mesoscale variability. The pathway of mode-1 internal tide is subjected to notable rotation due to the changes in the bottom topography, stratification, and vorticity in the course of its propagation.

Velocity and density profiles along the 3000-m isobath were analyzed by Lee et al. (2006). Baroclinic energy fluxes radiating from different regions of the Hawaiian Ridge ranged from 21,000 to 13,000 W m^{-1}. The authors estimated the dissipative length scales of internal tides at 1000 km. Model simulations reveal a tide loss of 15 GW. Egbert and Ray (2001) estimated tidal losses at the ridge at 20 GW. Model simulations of Niwa and Hibiya (2001) result in 15 GW for the M_2

internal tide, and Morozov (1995) gives an estimate of 8 GW based on the Baines model (1982). This estimate increased from 8 GW up to 12 GW after recalculation to be reported in this book. In the model suggested by St. Laurent et al. (2003), the estimates of the tidal losses were 22 GW. An estimate of 6 GW along the entire ridge was given by Ray and Cartwright (2001). This energy radiated away in mode-1 based on satellite altimetry.

The Doppler sonar survey was used to study internal tides in the upper ocean around the Hawaii Islands. The results were reported by Martin et al. (2006). Within 150 km of the ridge, the energy density of internal tide over the slopes exceeded 10 times the open-ocean values. Doppler sonar measurements showed that beams of the internal tide originate at the edge of the ridge peak and terminate at the ocean surface about 30–40 km south of the ridge peak. Modeling by Merrifield et al. (2001) supports the conclusion that the beams of internal tides exist in the Near-field zone of the Hawaiian Ridge.

Model estimates of the M_2 internal tide energetics at the Hawaiian Ridge were performed by Merrifield and Holloway (2002) on the basis of the POM model. The internal tide accounts for 9.7 GW of radiated energy away from the ridge in the northeastern and southwestern directions. The strongest generation occurs at three sites where enhanced barotropic currents flow across elongated topographic features. The depth integrated baroclinic energy flux and energy densities at these sites are of the order of 10,000 W m^{-1}.

Model estimates of internal tides supported by moored measurements in Mamala Bay on the southern coast of Oahu Island were reported by Eich et al. (2004). The steady M_2 component of the internal tide was characterized by vertical displacements as high as 35 m over the continental slope. Seasonal changes in amplitude and phase were observed.

Variability of the internal tide near Oahu Island was discussed by Bondur et al. (2008) on the basis of the ADCP data and thermistor strings deployed at the shelf break in 2003 and 2004. The orbits of the internal tide motions were highly variable. The authors explain such motion as the interference of the waves arriving from both sides of Oahu Island. Due to the supercritical slopes of the bottom local generation of internal tide occurs only sporadically when the density stratification becomes weaker.

In 2005–2006, measurements were performed by the Woods Hole Oceanographic Institution from three moorings of the WHOI Hawaii Ocean Timeseries Site (WHOTS) in the upper layer (10–155 m) at 23°N, 158°W. The amplitudes of internal tides in the upper layer were estimated at 15–20 m.

Internal-tide energy fluxes of the order of 10,000 W m^{-1} were found at various locations of the Hawaiian Ridge (Rainville and Pinkel 2006a, b; Nash et al. 2006). The total loss of barotropic tidal energy, for all the tidal constituents together, along the Hawaiian Ridge was estimated at 25 GW by Zaron and Egbert (2006).

The coherence of internal tide was studied by Mitchum and Chiswell (2000) on the basis of long time series of sea level from tide gauges and time series of dynamic heights inferred from inverted echo sounders moored approximately at 22° 45′N, 158° 00′W north of the Hawaiian Ridge. The variations in amplitudes

and phases of the M_2 tidal components correlate at low frequencies with the internal tide. The low-frequency variability is correlated with low-frequency depth oscillations of the pycnocline. These modulations are coherent over long distances along the Hawaiian Ridge.

Variations in tidal energy conversion to internal tides were analyzed by Zilberman et al. (2011) on the basis of moored current, temperature, and conductivity measurements in the region of the Kaena Ridge. The energy conversion from the barotropic to baroclinic tide measured near the ridge crest varied by a factor of two over the 6-month period of measurements. The authors suggest that such variations are caused by the influence of mesoscale eddies that passed through the region.

Modeling of internal tides over the Hawaiian Ridge was reported by Kang et al. (2000). The M_2 baroclinic energy flux exceeded 10,000 W m^{-1} for the strongest energy beam propagating to the northeast. The tidal energy was transformed into the internal tides that propagated in both directions from the ridge over distances exceeding 1000 km. The authors assume that on average 2700 W m^{-1} was radiated from the ridge in both directions; thus a total of 5.4 GW was radiated from the 2000 km long Hawaiian Ridge.

Modeling of semidiurnal M_2 tidal energy conversion over the Hawaiian Ridge was performed by Carter et al. (2008) using a high-resolution primitive equation model over a region of the Hawaiian Ridge from Niihau to Maui approximately 800 km long. This region includes the Kaena Ridge, one of the three main internal tide generation sites along the Hawaiian Ridge. The M_2 barotropic tide loses 2.7 GW of energy over the study region. The major part of this energy (2.3 GW) is converted into the internal tides. The majority of the baroclinic energy (1.7 GW) is radiated out of the model domain and 0.45 GW is dissipated in the study region.

Tidal energy losses to turbulence were estimated by Klymak et al. (2006) based on turbulence measurements. Approximately 3 GW of tidal energy is lost to turbulence dissipation within 60 km of the ridge. An increase of diffusivity was found near the seafloor. Very high diffusivity was found over the ridge crests, $K > 10^{-3}$ m^2 s^{-1}.

Tidal dissipation over the Hawaiian Ridge was estimated by Zaron and Egbert (2006) on the basis of satellite altimetry. The authors estimated that the barotropic M_2 tide loses energy at a rate of 19 GW presumably by means of conversion to internal tide; 88% of this energy is lost within 250 km of the ridge.

Two mixing processes over the Hawaiian Ridge were found by Klymak et al. (2008) in the waters above the 1100-m-deep ridge crest. At the depths above 400 m, mixing is similar to the open ocean mixing. Nearer to the ridge internal tide wave breaking occurs during each baroclinic crest passage. Large-amplitude, small-scale internal waves are triggered by tidal forcing, consistent with lee-wave formation at the ridge break.

Beams of internal tide waves were observed by Cole et al. (2009) using the Doppler sonar in the upper 400–600 m of the ocean. These data returned a representative picture of the across-ridge structure of internal wave beams and energy density. Interactions between tidal beams were observed.

Observations from satellite altimetry and field measurements within the Far-field Program of the HOME experiments were reported by Rainville et al. (2010). The observations agree with a high-resolution primitive equation model, simulating the generation and propagation of internal tides. Four sites of intense generation were found on the Hawaiian Ridge. Waves from these sources reproduce the interference pattern of sea surface height. The authors identify two main sources: the Kauai Channel and Nihoa Island (each 80 km long), from which internal tide energy was radiated. The depth integrated energy fluxes were 4100 and 4500 W m^{-1} producing total radiated energies of 0.37 and 0.36 GW, respectively.

Long-range propagation of internal tides was studied from the mooring data and satellite altimetry by Zhao et al. (2010). Six moorings were deployed in a line northeast of the Hawaiian Ridge over a distance of 1400 km between 25° 30′ and 37° 06′N. Mode-1 internal tide dominated in the northeastward energy flux. Satellite data revealed interference between the northeastward waves radiated from Hawaii and southeastward waves from the Aleutian Ridge.

Internal waves generated over the slopes of the Hawaiian Ridge propagate off the slopes and reach the Line Islands Ridge. The scattering of these waves was examined with a primitive equation numerical model by Johnston et al. (2003). The authors found that more energy was removed from mode one by scattering than was generated locally.

3.11   Karin Ridge (17°N, 168°W)

Two moorings were deployed on the slopes of the Karin Ridge in 1990–1991: one at 17° 09′N, 168° 30′W (the temperature meter was set at 1550 m) and the second at 16° 38′N, 168° 16′W (the instrument was set at 1415 m). The experiment was organized by the Scripps Institution of Oceanography, USA. Large amplitudes of internal tide were recorded over the slopes of the ridge that reached 50–60 m.

3.12   Clipperton Ridge (10°N, 119°W)

Ten moorings were deployed in 1986 by the Russian R/V *Vityaz* in the region between the Clarion Ridge at 18°N and Clipperton Ridge at 8°N (Fig. 3.23). The amplitudes of the semidiurnal internal tide were quite low ranging between 20 and 30 m at a depth of 1000 m. The highest among them were recorded on moorings at 11° 40′N and 12° 10′N, which were deployed close to a group of seamounts. Two wave systems of internal tide with low amplitudes were recorded by the antenna of moorings arriving from the south and north from the slopes of bottom topography of the fractures at 8°N (Clipperton Fracture Zone) and 18°N (Clarion Fracture Zone) (Fig. 3.24). The wavelength of the waves propagating to the northeast was
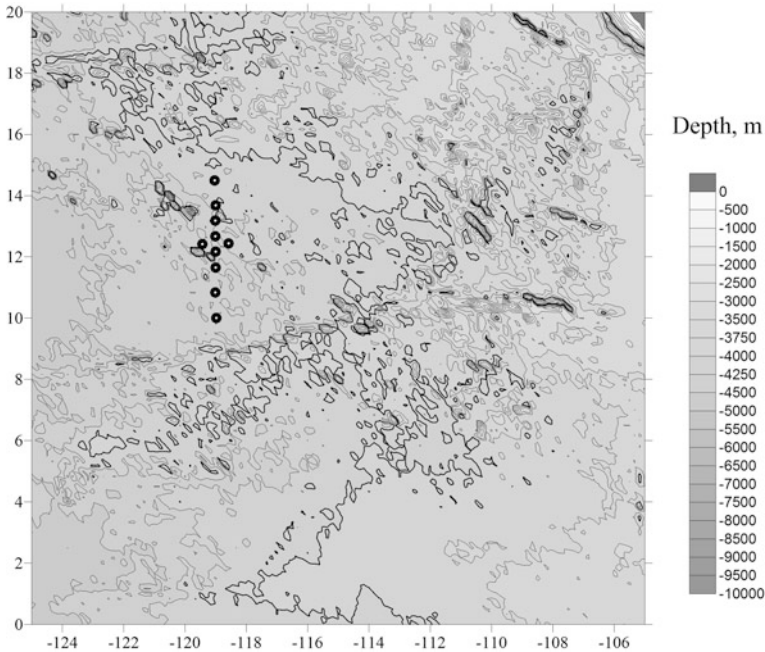
Fig. 3.23 Bottom topography in the region between the Clarion and Clipperton fracture zones. Depth contour lines are shown with an interval of 500 m. Additional isobaths at 3750 and 4250 are added. The 4000 m isobath is thicker. Locations of moorings are shown by black dots with a white dot in the middle. Land in the northeast is shown with gray color

117 km, and the wavelength of the other wave system was 93 km, which is related to the differences in the stratification, depth, and errors of estimates.

3.13 Kuroshio Current

During the WOCE PCM-5 experiment (ASUKA), nine moorings were deployed in 1993–1995 along the line from the continental slope of Shikoku Island to the deep ocean between 32° 28′N, 133° 09′E and 26° 32′N, 136° 25′E. The experiment was organized by Kyushu University. Another series of moorings replaced them in 1994–1995. The instruments were located in the depth range 500–600 and 1300–1500 m (Fig. 3.25). The line of moorings was located at a distance of 100 km north of a submarine ridge with crests at depths of 2500–3000 m. The amplitudes of internal tides in the depth range of measurements 1300–1500 m decreased with the distance from the continental slope from 62 m to 17 m. The energy of the internal tide also decreased with the distance from the slope. In the depth range 500–600 m, the amplitudes varied from 20 to 12 m. The amplitudes at the mooring located at
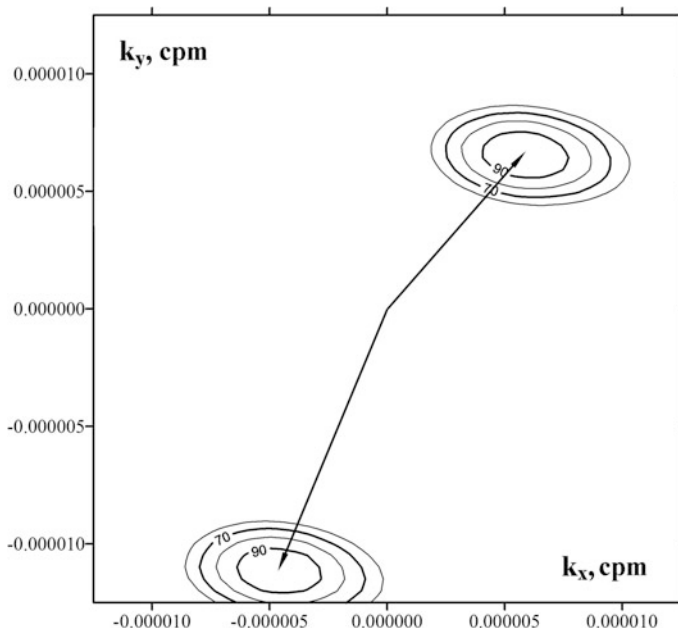
Fig. 3.24 Spatiotemporal spectrum at the semidiurnal frequency in the study site between the Clarion and Clipperton fracture zones in 1986 at a depth of 1000 m. The contour lines correspond to 90, 80, 70, and 60% of the main maximum. The arrows show the wave vectors corresponding to wavelengths of 117 km (propagating to the northeast) and 93 km (propagating to the southwest)

26° 32′N, 136° 25′E increased again (up to 25 m) because the mooring array reached the slope of a submarine rise.

We performed a procedure for estimating the energy density of internal tide similar to the one applied to the data collected in the Indian Ocean by Lozovatsky et al. (2003). The energy density of internal tides was plotted versus the distance normalized by the wave length of the first mode of internal tides (145 km). The energy decay was similar to the decay found previously in our work in the Indian Ocean, but the absolute values of the internal tide energy radiated from the slope were smaller. The energy densities in the region of the Kuroshio were one order of magnitude smaller than near the Mascarene Ridge in the Indian Ocean studied previously (Fig. 3.26).

The generation of internal tides over the shelf and continental slope of Japan off Fukushima was considered by Matsuno (1991). The author reports on beam propagation of the internal tides based on the moored observations. The generation of the internal tides on the continental slope and over the Izu Ridge in the southwestern part of Japan was reported by Kitade and Matsuyama (2002). The vertical displacement of the thermocline due to the semidiurnal internal tide reached 35 m. The beam structure of the internal tide was observed. The beams were generated from two peaks of the ridge near the critical slope.

Fig. 3.25 Bottom topography in the study site southwest of Japan. Depth contour lines are shown at depths of 500, 1000, 2000, 3000, 4000, and 5000 m. Locations of moorings of the PCM-5 (southwestern line) and PCM-7 (northeastern line) experiments are shown with black symbols. Land and islands are shown with gray color
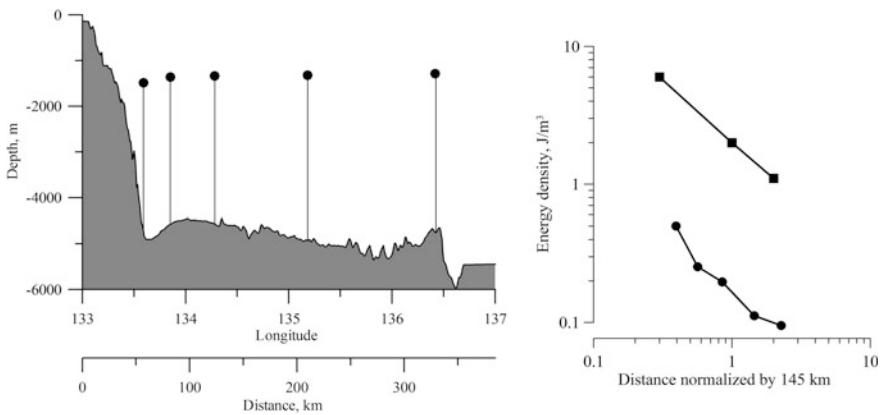
Fig. 3.26 Locations of the instruments in the PCM 5 experiment relative to the continental slope (left panel). Decay of the semidiurnal internal tide energy versus distance from the continental slope of Shikoku Island (Japan) (dots) (right panel). Decay of the internal tide energy based on the measurements near the Mascarene Ridge in the Indian Ocean (squares) (Lozovatsky et al. 2003) is shown for comparison

3.14   Kuroshio Extension, WOCE PCM-7, KERE Experiment

The WOCE PCM-7 Kuroshio Extension Regional Experiment (KERE) was conducted in the region of the Kuroshio extension: 34° 30′–36° 00′N, 142°–143°E. Four moorings were deployed in 1992–1994 (Fig. 3.25). The experiment was organized by the NASA Stennis Space Center, USA. The instruments on the moorings were set at 400–500 and 2000 m, while the ocean depth was 3000–6000 m. The amplitude of internal tide was estimated at 30–35 m at a depth of 2000 m.

3.15   Monterey Bay

The recorded internal wave field in Monterey Bay (36°N, 122°W) was almost an order of magnitude greater than in the open ocean (Kunze et al. 2002). A vertically integrated energy flux of 500 W m^{-1} at the mouth of the canyon decreased to 100 Wm^{-1} toward the shallow end of the canyon. Numerical model simulations reported by Carter (2010) and by Hall and Carter (2011) confirm these estimates.

A moored experiment was organized by Oregon State University and the Monterey Bay Research Institute. Seven moorings were deployed in 1993–1994 and two in 1989–1991. The amplitudes of internal tides at a depth of 1600 m were estimated at 15–20 m. A very diffuse peak on the spatiotemporal spectrum indicates that the waves were propagating from the continental slope in the southwestern direction. The wavelength was approximately 50 km, but the moorings were located too close to each other to estimate the wavelength more exactly. In addition the mooring array was elongated in the direction of the canyon (to the southwest) and it was narrow in the transversal direction.

More experiments were conducted in the region. Analysis of the energy distribution during energy transfer from the barotropic tide to internal tides and mixing was performed by Kang and Fringer (2012). Beams of the M_2 internal tide generated at the submarine ridge near Monterey Bay were found by Johnston et al. (2011). Propagation of the internal tide along the canyon was observed by Wain et al. (2013). Changes in the thalweg direction deflect baroclinic energy flux, but the bends in the measurement region are too sharp for the flux to follow the thalweg. Ridges that form the bends in the canyon act as obstacles to the flow, and turbulent dissipation increases over the flanks. Observations from moorings and ships in the bay by Petruncio et al. (1998) revealed semidiurnal internal displacements of isopycnals up to 50 m. The kinetic and potential energy was the greatest along paths following the characteristics calculated from the linear theory.

3.16   Central North Pacific (152°W, 175°W) (31°–41°N, 175°E)

Two lines of moorings were deployed in 1982–1985 in the Northeast Pacific: one along 175°W from 41°N to 31°N and the second along 152°W from 42°N to 28°N.

A chart of the region with locations of moorings is shown in Fig. 3.27.

The amplitude of internal tides at 42°N, 152°W varied between 18 and 25 m in the depth range 600–1200 m. This mooring was deployed north of the Mendocino Escarpment. The amplitudes of internal tides measured at 669 m on the mooring at 39°N located south of the Mendocino Escarpment were almost the same (22 m).

Two moorings were located at 35°N, 152°W and 28°N, 152°W southwest of the Mendocino Escarpment. The instruments at 665 and 723 m recorded internal tides with amplitudes of 22 and 35 m. The southern mooring was closer to the Hawaiian Ridge.

Four moorings were deployed in 1983–1985 along 175°W. Some of the moorings (33°N, 175° W) were closely located to the Hawaiian and Emperor ridges and the Hess Rise. The amplitudes of the internal tide on the closest mooring to the ridge located at 35°N, 175°W were estimated at 40 m at a depth of 643 m. The amplitudes decreased to the north to 23 m (depth 659 m) at 39°N and 18 m (depth 635 m) at 41°N; at the southern mooring (31°N) the amplitude was estimated at 22 m at a depth of 640 m.
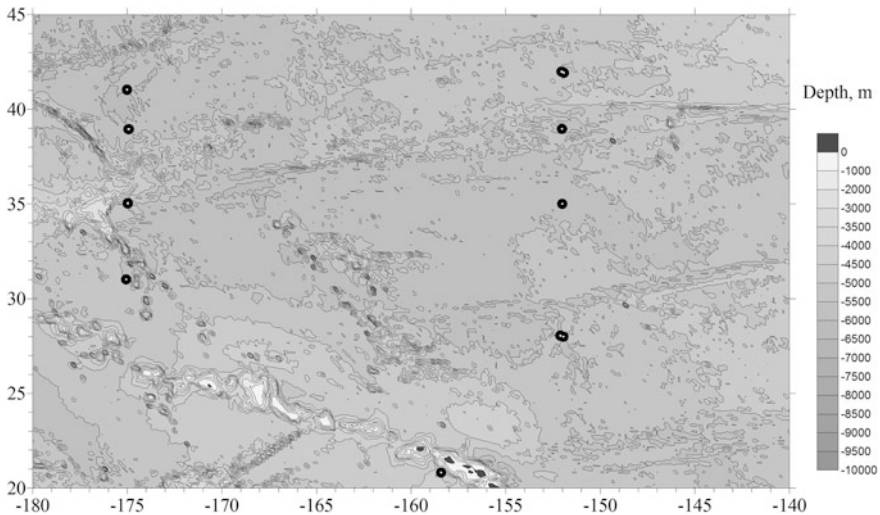
Fig. 3.27 Bottom topography in the Central North Pacific and locations of moorings. Depth contour lines are shown at depths of 500, 1000, 2000, 3000, 4000, and 5000 m. Locations of moorings are shown with black dots. Land and islands are shown with gray color

3.17   Bussol Strait, Sea of Okhotsk

Two moorings were deployed in 1998–2000 in the Bussol Strait connecting the Sea of Okhotsk and the Pacific Ocean at 46° 25′N, 151° 07′E and 46° 36′N, 151° 38′E. The experiment was organized by the University of Washington, USA. It was possible to estimate the amplitudes of internal tides only on the basis of measurements in autumn when the vertical temperature gradient is negative (cooler temperatures in the deeper layer). The amplitude varied from 30 to 120 m depending on the spring-neap periodicity. In the other seasons, the temperature increased with depth or the gradient was close to zero; thus, no amplitudes were estimated.

3.18   West of Peru

In 1981–1982 several repeated deployments of moorings were performed in the region of the continental slope and open ocean at a distance of 100–300 km from the slope at points: 2°01′ S, 82°29′ W; 4°10′ S, 84°58′ W; 10°14′ S, 79°28′ W. The experiment was organized by Oregon State University. The amplitudes of internal tide at a depth of 400 m were 30 m.

3.19   Southeast Australia, Australian Coastal Experiment (ACE)

In 1983–1984, the measurements southeast of Australia were conducted by Oregon State University (Beaver Line of moorings) and CSIRO Stanwell Park Line. The moorings were deployed on the continental slope of Southeastern Australia in three lines at 34° 20′S, and 37° 30′S along 151° E from the shelf up to the depths of 1000–2000 m. The amplitudes of internal tides were estimated at 30–32 m (Fig. 3.28).

This is a good example of the propagation of beams of internal waves down the slope. Figure 3.29 shows the characteristic line of the propagation of internal perturbations at the semidiurnal frequency and the spectra of the zonal velocity components. The spectral peak at the semidiurnal frequency is strong if the instrument is located on the characteristic line, while weak peaks are observed at the points far from the line.
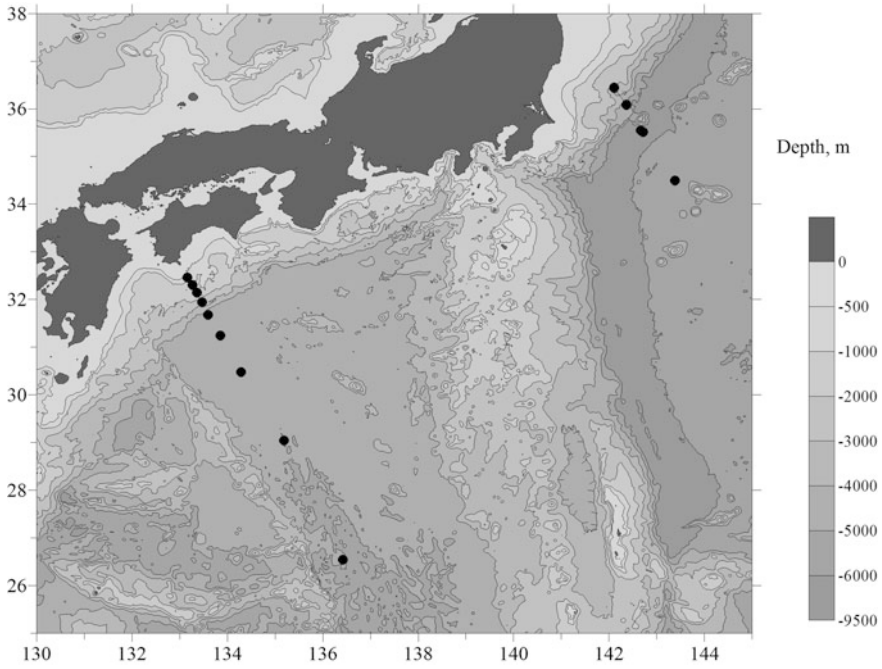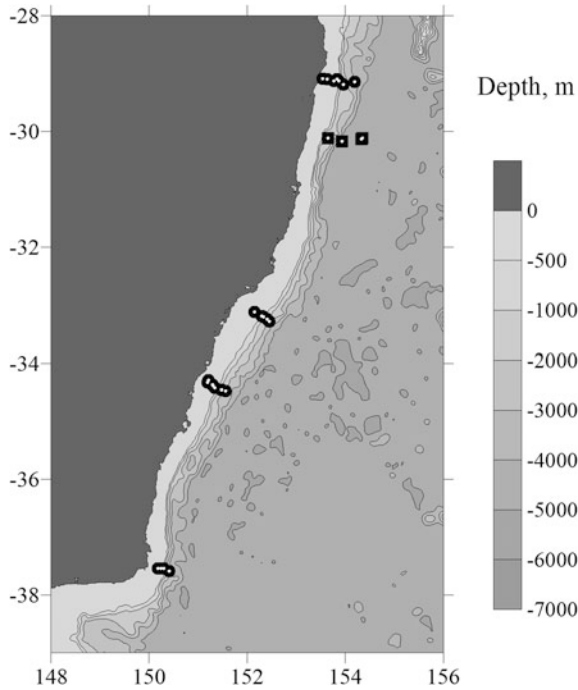
Fig. 3.28 Bottom topography near the east coast of Australia. Depth contour lines are shown at depths of 500, 1000, 2000, 3000, 4000, and 5000 m. Locations of moorings are shown with black symbols. The ACE moorings are shown with dots; the PCM-3 moorings are shown with squares
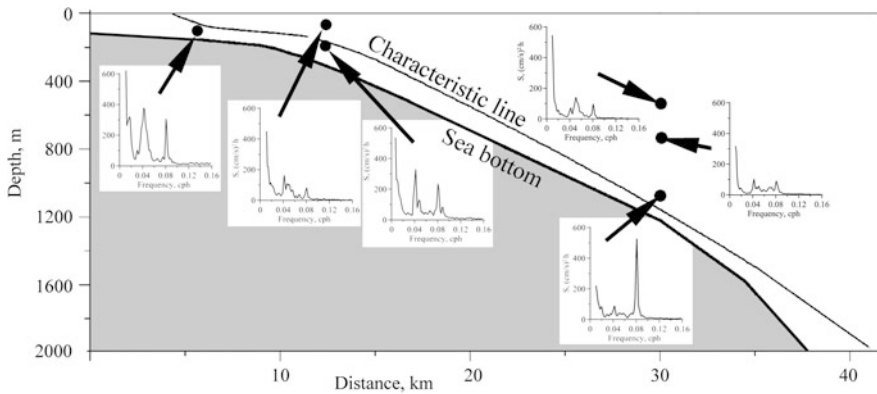
Fig. 3.29 Beams of internal tides, Southeastern Australia. The figure shows the bottom slope, locations of instruments (dots) relative to the bottom slope, characteristic line for internal tides, and spectra of velocity component fluctuations in units $(cm/s)^2 h$. Large dots show the locations of instruments on moorings relative to the bottom slope and characteristic line. Peaks at the semidiurnal frequency are high if the location of instruments is close to the characteristic line

3.20   East of Australia, WOCE PCM-3 Experiment

Six moorings were deployed in 1991–1993 in a line from the shelf to the continental slope and the slope foot east of Australia along 30°S over a distance of 50 miles (Fig. 3.28). The experiment was organized by CSIRO, Australia. Three of the moorings were located at depths greater than 2000 m. The amplitudes at 1500 m were estimated at 25–30 m.

3.21   Lord Howe Rise

Two moorings were deployed over the Lord Howe Rise in 1989–1990 at locations 28°S, 162°E and 37°S, 167°E. The experiment was organized by CSIRO, Australia. The depths of the locations were 1497 and 1014 m, respectively. The amplitudes of internal tides measured on the northern mooring at a depth of 515 m ranged from 25 to 50 m. The amplitudes at the southern mooring at a depth of 454 m were 35 m.

3.22   Storms Experiment

In 1987–1988, mooring C1 (47° 24′N, 139°W) with velocity and temperature meters at 15 depths from the upper layer to 4000 m operated over one year. The experiment was organized by Oregon State University, USA. The depth of the ocean at the mooring location was 4224 m. The amplitude of internal tides at a depth of 1000 m was 20 m.

3.23   Southeast of New Zealand, RIDGE Experiment

In 1978–1980, four moorings with velocity and temperature meters were deployed southeast of New Zealand in the region of 49° S, 170° W. The experiment was organized by the Woods Hole Oceanographic Institution, USA. The instruments were set at a depth of 1000 m. The depth of the ocean was 5100 m. The amplitude of internal tides at a depth of 1000 m was 40 m. On a mooring at 51° S, 175° W located closer to the underwater slope the amplitude was greater and reached 50 m.

Two mooring experiments were conducted on the Chatham Rise east of New Zealand in 1996 and 1997. The moorings were located at 43° 30′S, 178° 30′E (Chiswell 2000). The total estimated radiated energy was estimated at 1440 W m^{-1}. The length of the Chatham Rise is 795 km, thus the total radiated power was 1.2 GW.

3.24   Samoan Passage, WOCE PCM-11 Experiment

In 1992–1994, the WOCE PCM-11 experiment was conducted to analyze the flow of Antarctic Bottom Water through the Samoan Passage to the north at 10° S, 170° W. The experiment was organized by Oregon State University and Scripps Institution of Oceanography, USA. This abyssal channel forms the major pathway for deep interbasin exchange between the hemispheres in the Pacific (Johnson et al. 1994; Roemmich et al. 1996). A total of six moorings with 27 Aanderaa RCM8 current meters were deployed in the passage 100 km wide in the deepest (5000 m) part (Rudnick 1997). The moorings were located along a transect of the Samoan Passage. The shallowest instruments were located at a depth of 3000 m. Stratification is weak at these depths. The amplitudes of internal tides were estimated at 60 m at the western mooring. They decreased to 40 m with the distance from Tokelau Island slope over 200 km of the mooring array span.

3.25   British Columbia

Internal tides off British Columbia were studied by Cummins and Oey (1997) and by Cummins et al. (2000) on the basis of a 3D primitive equation numerical model. The tidal ellipses associated with internal tides measured on the moorings in the region agree well with the model simulations. The amplitudes of the M_2 internal tide exceeded 40 m over a steep continental slope. The offshore M_2 baroclinic energy flux was estimated at 0.5 GW, which gives an average flux of about 625 W m^{-1} with a model coastline 800 km long. This is significantly larger than an earlier estimate made by Baines (1982).

Mooring data southwest of Vancouver Island on the shelf and continental slope were analyzed by Drakopoulos and Marsden (1993). Clearly pronounced beams of internal tides were recorded. Tides penetrating deep into the Knight Inlet and tidally generated internal waves based on ADCP measurements in the inlet were analyzed by Marsden and Greenwood (1994). The observations show how strongly nonlinear internal waves develop on a bore propagating upstream of the sill crest. These waves propagate upstream. As the tide relaxes, the bore evolves into a group of upstream-propagating solitary-like internal waves (Cummins et al. 2003).

3.26   South China Sea

Several experiments have been carried out in the South China Sea to study internal waves. The Windy Islands Soliton Experiment/Variability Around the Northern South China Sea (WISE/VANS) in 2005–2006, the Nonlinear Internal Waves Initiative/South China Sea Ocean Prediction Experiment (NLIWI/SCOPE) in 2007,

and the Internal Waves in Straits Experiment (IWISE) in 2011 yielded much data on the dynamics of internal tides (Ramp and Tang 2011).

The Luzon Strait is known as a strong generation region of internal tides due to the existence of two steep submarine ridges (Heng Chun and Lan Yu ridges) along the north-south direction. Internal tides generated over this pair of ridges propagate in both directions to the South China and Philippine seas. Many field studies with moored thermistor strings and ADCPs, satellite and radar observations, and model simulations have been dedicated to this region of strong internal tides and they have also been the subject of theoretical research (Kuroda and Mitsudera 1995; Liu et al. 1998; Orr and Mignerey 2003; Niwa and Hibiya 2004; Duda et al. 2004; Ramp et al. 2004; Lien et al. 2005; Chang et al. 2006; Yuan et al. 2006; Alford et al. 2010, 2011; Farmer et al. 2009; Buijsman et al. 2010a, b; Ramp et al. 2010; Zhang et al. 2011; Li and Farmer 2011; Simmons et al. 2011; Lee et al. 2012; Xu et al. 2013; Ma et al. 2013; Mercier et al. 2013; Fang et al. 2015; Pickering et al. 2015; Kerry et al. 2016). Internal tides generated over the slopes of these two submarine ridges propagate both sides. Internal tides west of the strait are extremely intense. The role of each ridge was considered by Chao et al. (2007) using numerical modeling. The eastern ridge in the Luzon Strait seems most important in the generation of internal tides. Another analysis using a numerical model was performed by Jan et al. (2008). The authors report that strong baroclinic tides with a power of ∼19 GW for the diurnal tides and ∼11 GW for the semidiurnal tides are generated over the slopes of the eastern (70%) and western (30%) ridges. The average turbulence diffusivity over the Luzon Strait is 10^{-3} m^2/s. Model experiments by Wu et al. (2013) indicate that internal tides and mixing are stronger in winter than in summer. This conclusion is supported by field measurements reported by Liu et al. (2015) based on the moored ADCP measurements between 50 and 500 m at 19° 28′N, 119° 57′E near the Luzon Strait in the northeastern part of the South China Sea. The largest kinetic energy densities of diurnal and semidiurnal baroclinic tidal currents in winter are 2.81 and 0.83 kJ/m^2.

According to the measurements reported by Xu and Yin (2012) and by Xu et al. (2013), the amplitudes of the semidiurnal internal tides in the northern South China Sea were 30 m on average but the maximum values were as high as 45 m. This was supported by the field observations made in 2005 at Wenchang Station (19° 35′N, 112°E) on the northwestern shelf of the South China Sea. The water depth at the station is 117 m.

Another site of measurements in the South China Sea was located at a distance of 450 km west of the Luzon Strait on the continental slope south of China (21° 30′ N, 117° 00′E). The measurements were made during the Asian Seas International Acoustics Experiment (ASIAEX) in 2001 (Duda and Rainville 2008). Many moorings were deployed during this operation, with a full description by Ramp et al. (2004). The amplitudes of internal tides reached 50 m. Alford et al. (2015) report on the observations of internal tides at 20°30′N 119°00′ E. The measurements reveal the existence of high internal waves greater than 200-m in the region of generation. The observations from moorings, shipboard stations, and gliders over the Strait of Luzon and west of it reveal westward energy fluxes of 40,000 W m^{-1}.

Measurements with a string of thermistors from a boat at 20° 20′N, 119° 00′E at a distance of approximately 200 km from the ridge in the Luzon Strait presented by Chen et al. (2011) indicate that the amplitudes of internal tides reached 100 m. Horizontal coherence of internal tides based on moored measurements was significant (Pickering et al. 2015).

The analysis by Fang et al. (2015) was based on the moored ADCP measurements southwest of the Luzon Strait at (19° 30′N, 120°E). The ocean depth at this location is 4176 m. The authors reported that semidiurnal waves had a multimodal structure since the mooring was located at a distance less than 100 km from the ridge.

Guo et al. (2006) report on the measurements in 1998 during the SCSMEX experiment from an observational platform at 116° 51′E, 20° 21′N. The site was located over the continental shelf-break in the vicinity of southern Dongsha Island. The water depth is 500 m. The authors reported on the existence of diurnal and semidiurnal internal tides with mean amplitudes of 50 m reaching almost 100 m. Another paper by Guo et al. (2012) reports on moored ADCP measurements in the northern South China Sea at approximately 21°N, 115°E near Dongsha Island, which has a relatively flat slope and seafloor topography. The diurnal components of the internal tides were energetic with the highest diurnal kinetic energy exceeding 10 kJ/m^2. The two semidiurnal constituents (M_2 and S_2) were relatively weak. The highest kinetic energy of the baroclinic semidiurnal current was 2700 J/m^2.

Two main sources of internal ides exist in the South China Sea (Wang et al. 2016): remote generation in the Luzon Strait and local generation in the South China Sea. Internal tides radiated from the Luzon Strait are the dominant energy source. The authors estimate the diapycnal diffusivity at $\sim O(10^{-2})$ m^2/s. Intense turbulence was found in the deep-water basin of the sea with a diapycnal diffusivity of $O(10^{-3} \text{ to } 10^{-1})$ m^2/s in a 2000-m layer above the bottom and seafloor as well as in the shelf-break region with a dissipation rate of $O(10^{-7} \text{ to } 10^{-6})$ W kg^{-1} and diapycnal diffusivity of $O(10^{-4} \text{ to } 10^{-3})$ m^{2}s^{-1}.

The semidiurnal internal tide energy flux estimated by Rainville et al. (2013) over a vast area 600 × 800 km using gliders was 3.7 GW to the South China Sea and 2.7 GW to the Pacific Ocean. These values are close to the model estimates by Niwa and Hibiya (2004).

Model simulations by Wang et al. (2015) revealed internal wave attractors (Maas et al. 1997) in the Luzon Strait between two ridges that play the role of two walls separated approximately by 50 km.

A model study by Jan et al. (2012) shows that the influence of the Kuroshio on internal tides generation is quite strong. The current crosses the submarine ridges between Taiwan and Luzon islands and induces lee waves. The absence of the Kuroshio, which was modeled in their research, decreases the westward baroclinic energy flux by 30%. This conclusion was supported by Shaw et al. (2009). The authors reported that meandering of the current influences the generation of internal tides and solitons.

The study of surface manifestations of internal tides from satellites by Zhao (2014) shows that the K_1 and O_1 internal tides travel over 1600 km across the central deep basin of the South China Sea and arrive at the Vietnam coast. In the West Pacific, they propagate over 2500 km across the Philippine Sea, reaching the Mariana Ridge. The M_2 internal tides propagate shorter distances (1000 km) in both basins.

3.27   Tasman Sea

Internal waves in the Tasman Sea were studied during the TTIDE experiment (Johnston et al. 2015). Intense internal tides were generated over the Macquarie Ridge south of New Zealand. Then, they propagated to the northwest across the Tasman Sea to the Tasmanian slope and then reflected back into the Tasman Sea setting up a standing internal tide (Klymak et al. 2016). Spatial surveys by two autonomous underwater gliders showed that almost all of the incident energy flux reflected near 43°S. The gliders were piloted to form an antenna, over which internal plane-wave fits were made. The estimated energy flux of mode-1 internal tides was of the order of 1000–2000 W m^{-1}. The direction of the incident internal tides was consistent with altimetry and modeling. Standing internal tides were found within 150 km of the slope. The reflection of a low-mode internal tide on the Tasman continental slope was investigated by Klymak et al. (2016) using simulations of realistic and simplified topographies. The slope was supercritical to the internal tide; hence a large fraction of the energy was reflected. The existence of a beam of internal tides originating over the Macquarie Ridge was confirmed by the glider measurements reported by Boettger et al. (2015) east of Tasmania.

References

Alford MH, Lien R-C, Simmons H, Klymak J, Ramp SR, Yang Y-J, Tang T-Y, Farmer D, Chang M-H (2010) Speed and evolution of nonlinear internal waves transiting the South China Sea. J Phys Oceanogr 40:1338–1355

Alford MH, MacKinnon JA, Nash JD et al (2011) Energy flux and dissipation in Luzon Strait: two tales of two ridges. J Phys Oceanogr 41(11):2211–2222

Alford MH, Peacock T, MacKinnon JA, Nash JD, Buijsman MC, Centuroni LR, Chao SY, Chang MH, Farmer DM, Fringer OB, Fu KH, Gallacher PC, Graber HC, Helfrich KR, Jachec SM, Jackson CR, Klymak JM, Ko DS, Jan S, Johnston TM, Legg S, Lee IH, Lien RC, Mercier MJ, Moum JN, Musgrave R, Park JH, Pickering AI, Pinkel R, Rainville L, Ramp SR, Rudnick DL, Sarkar S, Scotti A, Simmons HL, St Laurent LC, Venayagamoorthy SK, Wang YH, Wang J, Yang YJ, Paluszkiewicz T, Tang TYD (2015) The formation and fate of internal waves in the South China Sea. Nature 521(7550):65–69. https://doi.org/10.1038/nature14399

Althaus AM, Kunze E, Sanford TB (2003) Internal tide radiation from Mendocino Escarpment. J Phys Oceanogr 33:1510–1527

Baines PG (1973) The generation of internal tides by flat-bump topography. Deep-Sea Res 20:179–205

Baines PG (1974) The generation of internal tides over steep continental slopes. Phil Trans Roy Soc London Ser A 277:27–58

Baines PG (1982) On internal tide generation models. Deep-Sea Res 29(3):307–338

Baines PG (1983) Tidal motion in submarine canyons—a laboratory experiment. J Phys Oceanogr 13(2):310–328

Baines PG (2007) Internal tide generation by seamounts. Deep Sea Res 54(9):1486–1508. https://doi.org/10.1016/j.dsr.2007.05.009

Barber NF (1963) The directional resolving power of an array of wave detectors. In: Ocean wave spectra. NY. Englewood Cliffs. Prentice Hall, pp 137–150

Boettger D, Robertson R, Rainville L (2015) Characterizing the semidiurnal internal tide off Tasmania using glider data. J Geophys Res 120:3730–3746

Bondur VG, Grebenyuk YV, Sabinin KD (2008) Variability of internal tides in the coastal water area of Oahu Island (Hawaii). Oceanology 48(5):611–621

Bracher C, Flatté SM (1997) A baroclinic tide in the Eastern North Pacific determined from 1000-km acoustic transmissions. J Phys Oceanogr 27(4):485–497

Buijsman MC, Kanarska Y, McWilliams JC (2010a) On the generation and evolution of nonlinear internal waves in the South China Sea. J Geophys Res 115:C02012. https://doi.org/10.1029/2009JC005275

Buijsman MC, McWilliams JC, Jackson CR (2010b) East-west asymmetry in nonlinear internal waves from Luzon Strait. J Geophys Res 115:C10057. https://doi.org/10.1029/2009JC006004

Carter GS, Merrifield MA, Becker JM, Katsumata K, Gregg MC, Luther DS, Levine MD, Boyd TJ, Firing YL (2008) Energetics of M_2 barotropic-to-baroclinic tidal conversion at the Hawaiian Islands. J Phys Oceanogr 38(10):2205–2223

Carter GS (2010) Barotropic and baroclinic M_2 tides in the Monterey Bay region. J Phys Oceanogr 40(8):1766–1783

Chang M-H, Lien R-C, Tang TY, D'Asaro EA, Yang YJ (2006) Energy flux of nonlinear internal waves in northern South China Sea. Geophys Res Lett 33:L03607

Chao S-Y, Ko D-S, Lien R-C, Shaw P-T (2007) Assessing the west ridge of Luzon Strait as an internal wave mediator. J Oceanogr 63:897–911

Chavanne C, Flament P, Carter G, Merrifield M, Luther D, Zaron E, Gurgel K-W (2010) The surface expression of semidiurnal internal tides near a strong source at Hawaii. Part I: observations and numerical predictions. J Phys Oceanogr 40(6):1155–1179

Chen G-Y, Su F-C, Wang C-M, Liu C-T (2011) Derivation of internal solitary wave amplitude in the South China Sea deep basin from satellite images. J Oceanogr 67(6):689–697

Chiswell SM (1994) Vertical structure of the baroclinic tides in the Central North Pacific Subtropical Gyre. J Phys Oceanogr 24(9):2032–2039

Chiswell SM, Moore MI (1999) Internal tides near the Kermadec Ridge. J Phys Oceanogr 29(5):1019–1035

Chiswell SM (2000) Tidal energetics over the Chatham Rise, New Zealand. J Phys Oceanogr 30(9):2452–2460

Chiswell SM (2002) Energy levels, phase, and amplitude modulation of the baroclinic tide off Hawaii. J Phys Oceanogr 32(9):2640–2651

Cole ST, Rudnick DL, Hodges BA, Martin JP (2009) Observations of tidal internal wave beams at Kauai Channel, Hawaii. J Phys Oceanogr 39(2):421–436

Cummins PF, Oey LY (1997) Simulation of barotropic and baroclinic tides off Northern British Columbia. J Phys Oceanogr 27(5):762–781

Cummins PF, Masson D, Foreman MG (2000) Stratification and mean flow effects on diurnal tidal currents off Vancouver Island. J Phys Oceanogr 30:15–30

Cummins PF, Cherniawsky JY, Foreman MG (2001) North Pacific internal tides from the Aleutian Ridge: altimeter observations and modeling. J Mar Res 59:167–191

Cummins PF, Vagle S, Armi L, Farmer DM (2003) Stratified flow over topography: upstream influence and generation of nonlinear internal waves. Proc Roy Soc Lond A 459:1467–1487

D'Asaro EA, Lien R-C, Henyey F (2007) High-frequency internal waves on the Oregon continental shelf. J Phys Oceanogr 37(7):1956–1967

Drakopoulos PG, Marsden RF (1993) The internal tide off the west coast of Vancouver Island. J Phys Oceanogr 23(4):758–775

Duda TF, Lynch JF, Irish JD, Beardsley RC, Ramp SR, Chiu C-S, Tang T-Y, Yang Y-J (2004) Internal tide and nonlinear internal wave behavior at the continental slope in the northern South China Sea. IEEE J Oceanic Eng 29:1105–1131. http://dx.doi.org/10.1109/JOE.2004.836998. Last accessed in Oct 2017

Duda TF, Rainville L (2008) Diurnal and semidiurnal internal tide energy flux at a continental slope in the South China Sea. J Geophys Res 113:C03025. https://doi.org/10.1029/2007JC004418

Dushaw BD, Cornuelle BD, Worcester PF, Howe BW, Luther DS (1995) Barotropic and baroclinic tides in the central North Pacific Ocean determined from long-range reciprocal acoustic transmissions. J Phys Oceanogr 25:631–647

Eich ML, Merrifield MA, Alford MH (2004) Structure and variability of semidiurnal internal tides in Mamala Bay, Hawaii. J Geophys Res 109(C5):C05010. https://doi.org/10.1029/2003JC002049

Egbert GD, Ray RD (2001) Estimates of M_2 tidal energy dissipation from TOPEX/poseidon altimeter data. J Geophys Res 106:22475–22502

Egbert GD, Erofeeva S (2002) Efficient inverse modeling of barotropic ocean tides. J Atmos Ocean Tech 19:183–204

Eriksen CC (1998) Internal wave reflection and mixing at Fieberling Guyot. J Geophys Res 103 (C2):2977–2994

Fang Y, Hou Y, Jing Z (2015) Seasonal characteristics of internal tides and their responses to background currents in the Luzon Strait. Acta Oceanol Sin 34(11):46–54. https://doi.org/10.1007/s13131-015-0747-z

Farmer D, Li Q, Park J-H (2009) Internal wave observations in the South China Sea: the role of rotation and nonlinearity. Atmos Ocean 47:267–280

Garrett CJR, Munk WH (1972) Space-time scales of internal waves. Geophys Fluid Dyn 3(3):225–264

Gourdeau L (1998) Internal tides observed at 2°S–156°E by in situ and TOPEX/POSEIDON data during the Coupled Ocean-Atmosphere Response Experiment (COARE). J Geophys Res 103 (C6):12629–12638

Guo P, Fang W, Gan Z, Chen R, Long X (2006) Internal tide characteristics over northern South China Sea continental slope. Chinese Sci Bull 51(Supp. II):17–25. https://doi.org/10.1007/s11434-006-9017-y

Guo P, Fang W, Liu C, Qiu F (2012) Seasonal characteristics of internal tides on the continental shelf in the northern South China Sea. J Geophys Res 117:C04023. https://doi.org/10.1029/2011JC007215

Hall RA, Carter GS (2011) Internal tides in Monterey submarine canyon. J Phys Oceanogr 41 (1):186–204

Holloway PE, Merrifield MA (1999) Internal tide generation by seamounts, ridges, and islands. J Geophys Res 104(C11):25937–25951

Holloway PE, Merrifield MA (2003) On the spring-neap variability and age of the internal tide at the Hawaiian Ridge. J Geophys Res 108(C4):3126. https://doi.org/10.1029/2002JC001486

Jan S, Lien R-C, Ting C-H (2008) Numerical study of baroclinic tides in Luzon Strait. J Oceanography 64(5):789–802

Jan S, Chern C-S, Wang J, Chiou M-D (2012) Generation and propagation of baroclinic tides modified by the Kuroshio in the Luzon Strait. J Geophys Res 117:C02019. https://doi.org/10.1029/2011JC007229

Johnson GC, Rudnick DL, Taft BA (1994) Bottom water variability in the Samoa Passage. J Mar Res 98:6883–6893

Johnston TMS, Merrifield MA, Holloway PE (2003) Internal tide scattering at the Line Islands Ridge. J Geophys Res 108(C11):3365. https://doi.org/10.1029/2003JC001844

Johnston TMS, Rudnick DL, Carter GS, Todd RE, Cole ST (2011) Internal tidal beams and mixing near Monterey Bay. J Geophys Res 116:03017. https://doi.org/10.1029/2010JC006592

Johnston TMS, Rudnick DL, Kelly SM (2015) Standing internal tides in the Tasman Sea observed by gliders. J Phys Oceanogr 45(11):2715–2737

Kang D, Fringer O (2012) Energetics of barotropic and baroclinic tides in the Monterey Bay area. J Phys Oceanogr 42(2):272–290

Kang SK, Foreman MG, Crawford WR, Cherniawsky JY (2000) Numerical modeling of internal tide generation along the Hawaiian Ridge. J Phys Oceanogr 30(5):1083–1098

Kerry CG, Powell BS, Carter GS (2016) Quantifying the incoherent M_2 internal tide in the Philippine Sea. J Phys Oceanogr 46(8):2483–2491

Kitade Y, Matsuyama M (2002) Semidiurnal internal tide observed over Ohmuro-Dashi, the northern part of the Izu Ridge. Deep-Sea Res 49(8):1309–1320

Klymak JM, Moum JN, Nash JD, Kunze E, Girton JB, Carter GS, Lee CM, Sanford TB, Gregg MC (2006) An estimate of tidal energy lost to turbulence at the Hawaiian Ridge. J Phys Oceanogr 36(6):1148–1164

Klymak JM, Pinkel R, Rainville L (2008) Direct breaking of the internal tide near topography: Kaena Ridge, Hawaii. J Phys Oceanogr 38(2):380–399

Klymak JM, Simmons HL, Braznikov D, Kelly S, MacKinnon JA, Alford MH, Pinkel R, Nash JD (2016) Reflection of linear internal tides from realistic topography: the Tasman continental slope. J Phys Oceanogr 46(11):3321–3337

Kunze E, Rosenfeld LK, Carter GS, Gregg MC (2002) Internal waves in Monterey submarine canyon. J Phys Oceanogr 32(6):1890–1913

Kurapov AL, Egbert GD, Allen JS, Miller RN, Erofeeva SY, Kosro PM (2003) The M_2 internal tide off Oregon: inferences from data assimilation. J Phys Oceanogr 33(8):1733–1757

Kuroda Y, Mitsudera H (1995) Observation of internal tides in the East China Sea with an underwater sliding vehicle. J Geophys Res 100(C6):10801–10816

Lee CM, Sanford TB, Kunze E, Nash JD, Merrifield MA, Holloway PE (2006) Internal tides and turbulence along the 3000-m isobath of the Hawaiian Ridge. J Phys Oceanogr 36(6):1165–1183

Lee I-H, Wang Y-H, Yang Y, Wang D-P (2012) Temporal variability of internal tides in the northeast South China Sea. J Geophys Res 117:C02013. https://doi.org/10.1029/2011JC007518

Levine MD, Richman JR (1989) Extracting the internal tide from data: methods and observations from the mixed layer dynamics experiments. J Geophys Res 94:8125–8135

Levine MD, Boyd TJ (2006) Tidally forced internal waves and overturns observed on a slope: results from HOME. J Phys Oceanogr 36(6):1184–1201

Li Q, Farmer DM (2011) The generation and evolution of nonlinear internal waves in the deep basin of the South China Sea. J Phys Oceanogr 41:1345–1363

Liang X (2014) Semidiurnal tidal currents in the deep ocean near the East Pacific Rise between 9° and 10°N. J Geophys Res 119(C7):4264–4277. https://doi.org/10.1002/2013JC009522

Lien R-C, D'Asaro EA, McPhaden MJ (2002) Internal waves and turbulence in the Upper Central Equatorial Pacific: Lagrangian and Eulerian observations. J Phys Oceanogr 32(9):2619–2639

Lien R-C, Tang TY, Chang MH, D'Asaro EA (2005) Energy of nonlinear internal waves in the South China Sea. Geophys Res Lett 32:L05615

Liu AK, Chang YS, Hsu M-K, Liang NK (1998) Evolution of nonlinear internal waves in the East and South China seas. J Geophys Res 103(C4):7995–8008

Liu J, He Y, Wang D, Liu T, Cai S (2015) Observed enhanced internal tides in winter near the Luzon Strait. J Geophys Res 120:6637–6652. https://doi.org/10.1002/2015JC011131

Lozovatsky ID, Morozov EG, Fernando HJS (2003) Spatial decay of energy density of tidal internal waves. J Geophys Res 108(C6):3201–3216

Ma BB, Lien R-C, Ko D-S (2013) The variability of internal tides in the Northern South China Sea. J Oceanogr 69(5):619–630

Maas LRM, Benielli D, Sommeria J, Lam FPA (1997) Observations of an internal wave attractor in a confined stably stratified fluid. Nature 388:557–561

Marsden RF, Greenwood KC (1994) Internal tides observed by an acoustic Doppler current profiler. J Phys Oceanogr 24(6):1097–1109

Martin JP, Rudnick DL, Pinkel R (2006) Spatially-broad observations of internal waves in the upper ocean at the Hawaiian Ridge. J Phys Oceanogr 36(6):1085–1103

Martini KI, Alford MH, Kunze E, Kelly SM, Nash JD (2011) Observations of internal tides on the Oregon continental slope. J Phys Oceanogr 41(9):1772–1794

Martini KI, Alford MH, Kunze E, Kelly SM, Nash JD (2013) Internal bores and breaking internal tides on the Oregon continental slope. J Phys Oceanogr 43(1):120–139

Matsuno T (1991) Propagation of semidiurnal internal tides observed off Fukushima along the East Coast of Japan. J Oceanogr Soc Japan 47(4):138–151

Maximenko NA, Koshlyakov MN, Ivanov YA, Yaremchuk MI, Panteleev GG (2001) Hydrophysical experiment "Megapolygon-87" in the northwestern Pacific Subarctic frontal zone. J Geophys Res 106:14143–14163

Melnikov VA, Morozov EG, Nikitin SV (1985) Investigation of internal gravity waves using expandable bathythermographs. Oceanol Res 37:69–76

Mercier MJ, Gostiaux L, Helfrich K, Sommeria J, Viboud S, Didelle H, Ghaemsaidi SJ, Dauxois T, Peacock T (2013) Large-scale, realistic laboratory modeling of M_2 internal tide generation at the Luzon Strait. Geophys Res Lett 40:5704–5709. https://doi.org/10.1002/2013GL058064

Merrifield MA, Holloway PE, Johnston TS (2001) The generation of internal tides at the Hawaiian Ridge. Geophys Res Lett 28:559–562

Merrifield MA, Holloway PE (2002) Model estimates of M_2 internal tide energetics at the Hawaiian Ridge. J Geophys Res 107(C8):3179. https://doi.org/10.1029/2001JC000996

Mitchum GT, Chiswell SM (2000) Coherence of internal tide modulations along the Hawaiian Ridge. J Geophys Res 105(C12):28653–28661

Morozov EG, Nikitin SV (1985) Spatiotemporal spectrum for semidiurnal internal waves in the Northwest Pacific. Oceanol Res 38:31–35

Morozov EG (1995) Semidiurnal internal wave global field. Deep-Sea Res 42(1):135–148

Morozov EG (2006) Internal tides. Global field of internal tides and mixing caused by internal tides. In: Waves in geophysical fluids. Springer, Wein, New York. pp 271–332

Morozov EG, Nechvolodov LV, Sabinin KD (2009) Beam propagation of tidal internal waves over a submarine slope of the Mascarene Ridge. Oceanology 49(6):745–752

Nakamura T, Awaji T, Hatayama T, Akitomo K, Takizawa T (2000) Tidal exchange through the Kuril Straits. J Phys Oceanogr 30(7):1622–1644

Nash JD, Kunze E, Lee CM, Sanford TB (2006) Structure of the baroclinic tide generated at Kaena Ridge, Hawaii. J Phys Oceanogr 36(6):1123–1135

Niwa Y, Hibiya T (2001) Numerical study of the spatial distribution of the M_2 internal tide in the Pacific Ocean. J Geophys Res 106:22441–22449

Niwa Y, Hibiya T (2004) Three-dimensional numerical simulation of the M_2 internal tides generated around the continental shelf edge in the East China Sea. J Geophys Res 109:C04027

Orr MH, Mignerey PC (2003) Nonlinear internal waves in the South China Sea: observation of the conversion of depression internal waves to elevation internal waves. J Geophys Res 108 (C3):3064. https://doi.org/10.1029/2001JC001163

Osborne JJ, Kurapov AL, Egbert GD, Kosro PM (2011) Spatial and temporal variability of the M_2 internal tide generation and propagation on the Oregon shelf. J Phys Oceanogr 41(11):2037–2062

Park J-H, Watts DR (2006) Internal tides in the Southwestern Japan/East Sea. J Phys Oceanogr 36 (1):22–34

Petruncio ET, Rosenfeld LK, Paduan JD (1998) Observations of the internal tide in Monterey Canyon. J Phys Oceanogr 28(10):1873–1903

Pickering A, Alford M, Nash J, Rainville L, Buijsman M, Ko D-S, Lim B (2015) Structure and variability of internal tides in Luzon Strait. J Phys Oceanogr 45(6):1574–1594

Pinkel R, Munk W, Worchester P, Cornuelle BD, Rudnick D, Sherman J, Filloux JH, Dushaw BD, Howe BM, Sanford TB, Lee CM, Kunze E, Gregg MC, Miller JB, Moum JM, Caldwell DR,

Levine MD, Boyd T, Egbert GD, Merrifield MA, Luther DS, Firing E, Brainard R, Flament PJ, Chave AD (2000) Ocean mixing studies near the Hawaiian Ridge. EOS Trans AGU 81 (46):545–553

Rainville L, Pinkel R (2006a) Baroclinic energy flux at the Hawaiian Ridge: observations from the R/P FLIP. J Phys Oceanogr 36(6):1104–1122

Rainville L, Pinkel R (2006b) Propagation of low-mode internal waves through the ocean. J Phys Oceanogr 36(6):1220–1236

Rainville L, Johnston TMS, Carter GS, Merrifield MA, Pinkel R, Worcester PF, Dushaw BD (2010) Interference pattern and propagation of the M_2 internal tide south of the Hawaiian Ridge. J Phys Oceanogr 40(2):311–325

Rainville L, Lee CM, Rudnick DL, Yang K-C (2013) Propagation of internal tides generated near Luzon Strait: observations from autonomous gliders. J Geophys Res 118(C9):4125–4138. https://doi.org/10.1002/jgrc.20293

Ramp SR, Tang TY, Duda TF, Lynch JF, Liu AK, Chiu C-S, Bahr FL, Kim H-R, Yang Y-J (2004) Internal solitons in the northeastern South China Sea. Part I: sources and deep water propagation. IEEE J Oceanic Eng 29:1157–1181

Ramp SR, Yang YJ, Bahr FL (2010) Characterizing the nonlinear internal wave climate in the northeastern South China Sea. Nonlinear Processes Geophys 17:481–498

Ramp SR, Tang TY (2011) A history of Taiwan/US oceanographic research in the South China Sea. Oceanography 24(4):16–23

Rattray M (1960) On the coastal generation of internal tides. Tellus 12:54–62

Ray RD, Mitchum GT (1996) Surface manifestation of internal tides generated near Hawaii. Geophys Res Lett 23(16):2101–2104

Ray RD, Mitchum GT (1997) Surface manifestation of internal tides in deep ocean: observations from altimetry and island gauges. Prog Oceanogr 40:135–162

Ray RD, Cartwright DE (2001) Estimates of internal tide energy-fluxes from TOPEX/Poseidon altimetry: Central North Pacific. Geophys Res Lett 28:1259–1262

Roemmich D, Hautala S, Rudnick D (1996) Northward abyssal transport through the Samoan Passage and adjacent regions. J Geophys Res 101:14039–14055

Rudnick DL (1997) Direct velocity measurements in the Samoan Passage. J Geophys Res 102:3293–3302

Shaw P-T, Ko DS, Chao S-Y (2009) Internal solitary waves induced by flow over a ridge: with applications to the northern South China Sea. J Geophys Res 114:C02019. https://doi.org/10.1029/2008JC005007

Simmons HL, Chang MH, Chang YT et al (2011) Modeling and prediction of internal waves in the South China Sea. Oceanography 24(4):88–99

Smith WHF, Sandwell DT (1997) Global sea floor topography from satellite altimetry and ship depth soundings. Science 277:1956–1962. http://topex.ucsd.edu/cgi-bin/get_data.cgi. Last accessed in Oct 2017

St. Laurent LS, Stringer S, Garrett C, Perrault-Joncas D (2003) The generation of internal tides at abrupt topography. Deep-Sea Res 50:987–1003

Tanaka Y, Hibiya T, Niwa Y (2008) Estimates of tidal energy dissipation and diapycnal diffusivity in the Kuril Straits using TOPEX/POSEIDON altimeter data. J Geophys Res 112:C10021. https://doi.org/10.1029/2007JC004172

Tanaka Y, Hibiya T, Niwa Y, Iwamae N (2010) Numerical study of K1 internal tides in the Kuril straits. J Geophys Res 115:C09016. https://doi.org/10.1029/2009JC005903

Torgrimson GM, Hickey BM (1979) Barotropic and baroclinic tides over the continental slope and shelf off Oregon. J Phys Oceanogr 9:945–961

Turner JS (1973) Buoyancy effects in fluids. Cambridge University Press, Cambridge

Vlasenko VI (1992) Nonlinear model for the generation of baroclinic tides over extensive inhomogeneities of bottom topography. Phys Oceanogr (Morskoy gidrofizicheskiy zhurnal) 3:417–424

Vlasenko V, Stashchuk N, Hutter K (2005) Baroclinic tides: theoretical modeling and observational evidence. Cambridge University Press, Cambridge, p 351

Wain DJ, Gregg MC, Alford MH, Lien R-C, Hall RA, Carter GS (2013) Propagation and dissipation of the internal tide in upper Monterey Canyon. J Geophys Res 118:4855–4877. https://doi.org/10.1002/jgrc.20368

Wang G, Zheng Q, Lin M, Qiao F (2015) Three dimensional simulation of internal wave attractors in the Luzon Strait. Acta Oceanol Sin 34:14–21. https://doi.org/10.1007/s13131-015-0744-2

Wang X, Peng S, Liu Z, Huang RX, Qian Y-K, Li Y (2016) Tidal mixing in the South China Sea: an estimate based on the internal tide energetic. J Phys Oceanogr 46(1):107–124

WOD13 (2013) World Ocean Database 2013. Geographically sorted data, https://www.nodc.noaa.gov/OC5/WOD/datageo.html. Last accessed in Oct 2017

Wu L, Miao C, Zhao W (2013) Patterns of K_1 and M_2 internal tides and their seasonal variations in the northern South China Sea. J Oceanogr 69(4):481–494. https://doi.org/10.1007/s10872-013-0183-7

Xu Z, Yin B (2012) Variability of internal solitary waves in the Northwest South China Sea. In: Marcelli M (ed) Oceanography. ISBN: 978-953-51-0301-1

Xu Z, Yin B, Hou Y, Xu Y (2013) Variability of internal tides and near-inertial waves on the continental slope of the northwestern South China Sea. J Geophys Res 118:197–211. https://doi.org/10.1029/2012JC008212

Yuan Y, Zheng Q, Dai D, Hu X, Qiao F, Meng J (2006) Mechanism of internal waves in the Luzon Strait. J Geophys Res 111:C11–S17. https://doi.org/10.1029/2005JC003198

Zaron ED, Egbert GD (2006) Estimating open-ocean barotropic tidal dissipation: the Hawaiian Ridge. J Phys Oceanogr 36(6):1019–1035

Zhang Z, Fringer OB, Ramp SR (2011) Three-dimensional, nonhydrostatic numerical simulation of nonlinear internal wave generation and propagation in the South China Sea. J Geophys Res 116:C05022. https://doi.org/10.1029/2010JC006424

Zhao Z (2014) Internal tide radiation from the Luzon Strait. J Geophys Res 119:5434–5448. https://doi.org/10.1002/2014JC010014

Zhao Z, Alford MH, MacKinnon JA, Pinkel R (2010) Long-range propagation of the semidiurnal internal tide from the Hawaiian Ridge. J Phys Oceanogr 40(4):713–736

Zilberman NV, Merrifield MA, Carter GS, Luther DS, Levine MD, Boyd TJ (2011) Incoherent nature of M_2 internal tides at the Hawaiian Ridge. J Phys Oceanogr 41(11):2021–2036

Chapter 4
Observations of Internal Tides in the Indian Ocean

Abstract This chapter describes the measurements of internal tides in the Indian Ocean together with modeling of the generation and propagation of internal tides in some important regions of the Indian Ocean. The generation of internal tides is associated with the interaction of the currents of the barotropic tide with the slopes of the bottom topography. One of the most important ideas presented here is the strong generation of internal tides over submarine ridges. The generation and propagation of strong internal tides over the Mascarene Ridge are analyzed. The generation and propagation of internal tides in the Bab el Mandeb Strait where very strong internal tides exist are described. Strong internal tides are also found in the Madagascar Strait. Measurements of internal tides on mooring clusters confirm the well known fact that internal tides are generated over the bottom slopes.

4.1 Mascarene Ridge

The Mascarene Ridge is one of the regions of the most intense internal tidal waves in the World Ocean (Morozov 2006). The general circulation in the region is described by New et al. (2007). The array of moorings for the investigation of internal tidal waves in March 1987 was planned on the Russian R/V *Vityaz* assuming that the internal tide is generated as a result of the interaction between the barotropic tidal currents and the Mascarene Ridge. After the generation, the internal tide propagates into the ocean (Garrett and Kunze 2007). While planning the mooring array, we considered that the barotropic tidal flow is generally concentrated in the underwater passage between the Saya de Malha and Nazareth banks (Morozov and Fomin 1989). Other experiments were conducted in 1987 and 1990 (Konyaev et al. 1995; Leontieva et al. 1992). The measurements confirmed large-amplitude internal tides. It follows from the theory that the maximum velocities of the tide and the most intense internal waves should be generated in this passage, which was confirmed by the experiment. No strong currents were observed over the bank with a depth of 40–50 m. In 1987, a mooring array of six moorings was extended in the direction to the southeast from the strait between the two banks.

A scheme of the experiment is shown in Fig. 4.1. The current and velocity meters were set on the moorings at depths of 100, 200, 500, 1000, 1200, 1800, and 2500 m.

The theoretical wavelength of the first mode of internal tidal wave was determined by the numerical integration of the equation for the vertical velocities of
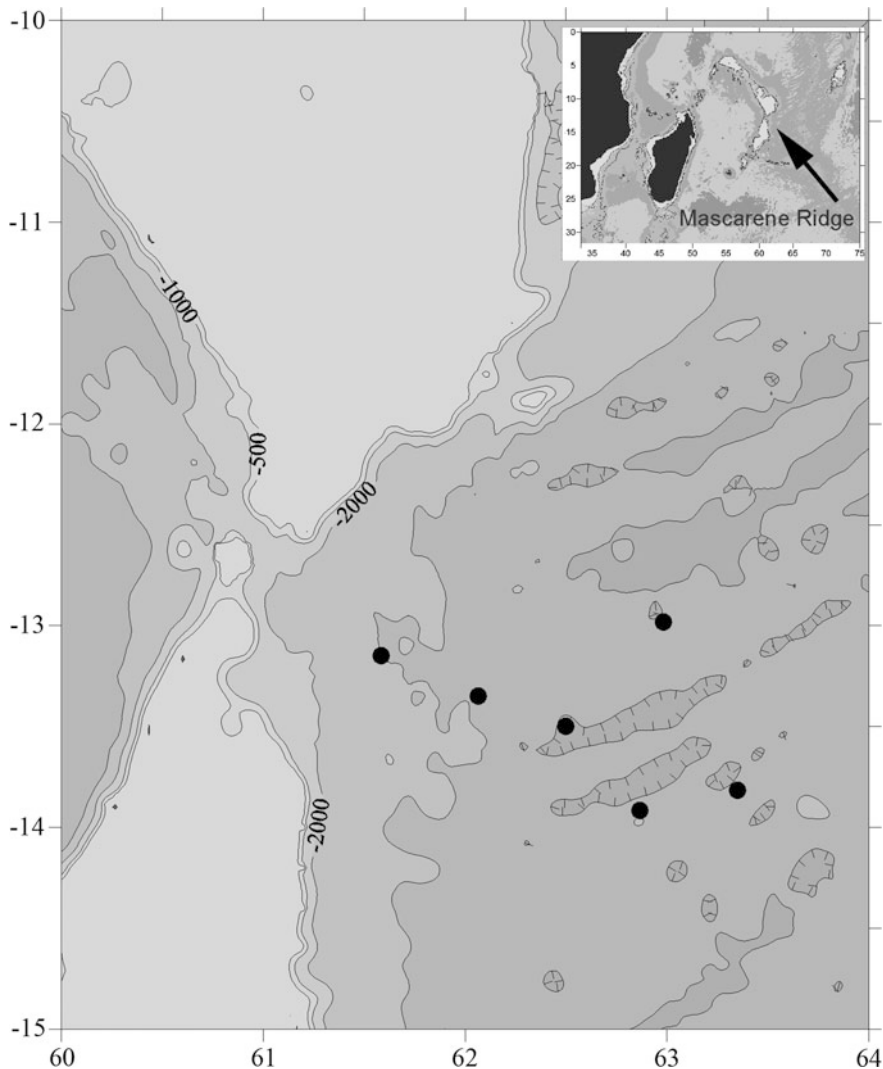
Fig. 4.1 Bottom topography (meters) and schematic location of moorings near the Mascarene Ridge. Depth contour lines are shown at depths of 500, 1000, 1500, 2000, 3000, 3500, and 4000 m. Locations of moorings are shown with black dots. Land and islands are shown with black color. A general chart is shown in the inset

internal waves with the realistic stratification and zero boundary conditions at the surface and bottom (see Sect. 1.4.3, Eq. 1.39). The wavelength was equal to 125 km, while the phase velocity was 2.8 m/s.

Let us consider temperature time series and calculate the vertical displacements caused by the internal tides (Fig. 4.2). One can easily distinguish from this figure the semidiurnal internal tide fluctuations in the temperature time series measured on the mooring. Their mean amplitude at a depth of 1200 m was 0.2 °C. If we recalculate this value to the vertical displacements given the measured vertical gradient of temperature, the vertical displacements of the water particles would be equal to 120 m and correspondingly the amplitude of the displacement from the mean position would be 60 m. The maximum displacements exceeded 150 m, while the minimum ones were approximately 65 m.

The amplitude variations are related to the phases of the Moon and have a time delay relative to the time moments of the spring and neap tides because time is needed for the internal wave to propagate from the generation region. Therefore, the minimum amplitudes on the eastern mooring appear later than on the western mooring. The moment of the smallest amplitudes on the eastern mooring occurs on March 26, and on the western mooring this moment is on March 25. The eastern mooring was located 200 km farther from the source over the slopes of the ridge. Knowing the distance between moorings it is possible to estimate the group velocity of internal tides:

$$C_g = \frac{200,000\,\text{m}}{24 \cdot 3600\,\text{s}} = 2.3\,\text{m/s}.$$

The spectral densities are characterized by a highly reliable peak at the semidiurnal frequency. A decrease in the energy of semidiurnal oscillations was found over the horizontal scales of the study region. We shall discuss the long-distance propagation of internal tides in Sect. 7.7 with the example of internal tides
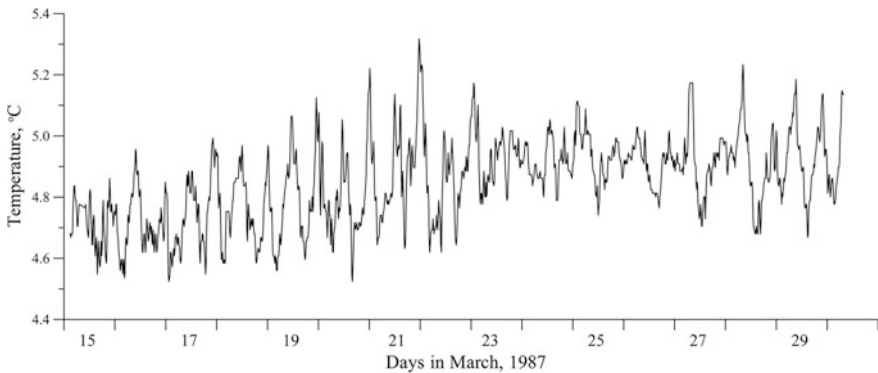
Fig. 4.2 Time series of temperature fluctuations on the western mooring east of the Mascarene Ridge at a depth of 1200 m

Table 4.1 Spectral densities of temperature fluctuations at the semidiurnal frequency (M_2) on different moorings at depths 1000 and 1200 m $(°C)^2$min

Depth (m)	Mooring 16, 13° 09′S, 61° 35′ E	Mooring 15, 13° 21′S, 62° 04′ E	Mooring 14, 13° 30′S, 62° 30′ E	Mooring 11, 13° 49′S, 63° 21′ E
1000	4.0	2.0	3.0	2.3
1200	3.2	4.3	1.1	2.1

generated over the Mascarene Ridge. A decrease in the spectral estimates was found over the scales of the study site. Variations in the spectral densities at the semidiurnal frequency on four moorings are shown in Table 4.1. We note that spectral densities decrease almost by a factor of two over a distance of 200 km.

Let us consider vertical variations in the spectral densities of temperature fluctuations at the semidiurnal frequency. A graph of the Eigen function for the oscillations of the first mode is shown in Fig. 4.3. This was calculated by the numerical integration of the equation for the vertical velocity of internal waves at realistic stratification (see Sect. 1.4.3, Eq. 1.39). The amplitudes of internal waves based on the spectral analysis of time series measured at different depths on the eastern mooring are also shown in the figure, which corresponds to the theoretical calculation assuming that the first mode dominates.

It is worth noting that the mode structure was formed at a close distance to the ridge (approximately at a distance of one wavelength). The measurements near a seamount (see Chap. 3, Sect. 3.1) did not reveal such a mode structure but a beam structure was observed there. A possible difference between the two processes is that a seamount is a non-ideal point source, while a submarine ridge is a non-ideal linear source of internal tides because the ridge crest is not a straight line. Many beams of internal waves with random phases and amplitudes are generated near the ridge. Therefore, random phase shifts in the beams arriving from different points of the ridge crest facilitate faster compensation of the vertical wavenumbers and formation of the mode structure. High vertical coherence between the time series confirms the fact that the fluctuations are well developed over the vertical direction and that the mode structure has been formed. Table 4.2 presents the vertical coherences for the measurements on the eastern mooring (13° 49′S, 63° 21′E).

High horizontal coherences are observed at all pairs of time series. A graph of the dependence of horizontal coherence on distance is shown in Fig. 4.4. All estimates are higher than the 95% confidence level (0.5).

Spatiotemporal spectra at the semidiurnal tidal frequency were calculated at various levels of measurements using the method suggested by Barber (1963) (see Sect. 1.4.2). Figure 4.5 shows an example of a spatiotemporal spectrum calculated from the temperature data at 1200 m. The spectra at other levels are similar. The wavelength of internal tide was 140–150 km, and its direction from the strait between the banks was 110°.

According to the towed measurements by Sabinin et al. (1992) the amplitudes of individual internal waves over the steep slopes of the Mascarene Ridge were as high

Fig. 4.3 Amplitudes of semidiurnal internal waves near the Mascarene Ridge. The curve corresponds to the calculation of the eigen function for the amplitude of internal waves normalized to fit the data of measurements; the circles show measurements at the easternmost mooring
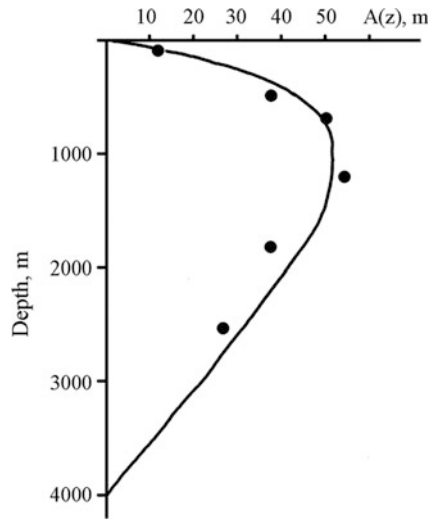
Table 4.2 Vertical coherences of temperature fluctuations at the semidiurnal frequency between various pairs of time series at different levels. Pairs of depths are determined by the crossing of lines and columns

Depth (m)	Depths (m)					
	200	500	1000	1200	1800	2500
100	0.90	0.93	0.96	0.92	0.91	0.86
200		0.89	0.94	0.93	0.97	0.92
500			0.96	0.95	0.93	0.92
1000				0.96	0.95	0.93
1200					0.96	0.92
1800						0.96

as 80 m. Analysis of the propagation of internal solitons was reported by da Silva et al. (2011, 2015) and by New et al. (2013) based on the satellite SAR images between the Saya de Malha and Nazareth banks. Schemes of the spreading of internal solitary waves to the northwest and southeast of the ridge show that leading waves were located with the intervals of approximately 100–120 km indicating that this is approximately the distance between the crests of internal tides of the first mode. The direction of their propagation was close to 120°. The waves propagated over at least 400 km to the west and 300 km to the east of the sill. The length of the crests was approximately 350 km, which exceeds the similar length in many other regions, except the South China Sea.

Model simulations of the internal tide by Morozov and Vlasenko (1996), Lozovatsky et al. (2003), Morozov et al. (2009), and da Silva et al. (2015) agree with the moored and SAR observations.
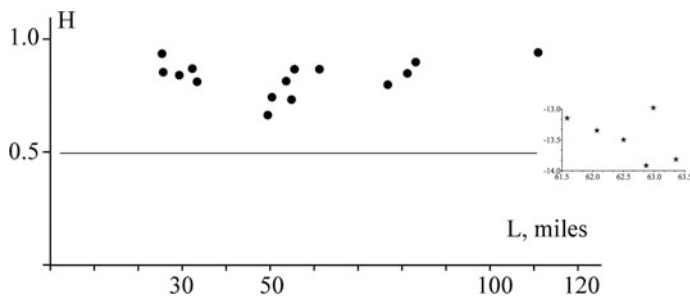
Fig. 4.4 Horizontal coherence at 1200 m versus distance between moorings. Line 0.5 shows the 95% confidence level. Scheme of the moorings (stars) is shown in the inset

4.2   Madagascar Basin

The experiment site in the Madagascar Basin in April 1987 was located far from the ridges at $28° 56'$S, $55° 17'$E (Fig. 4.12). The experiment was organized by the Shirshov Institute of Oceanology, Russia. The distance to the West Indian Ridge was greater than 300 km. It is important to note that in this region the barotropic tidal wave propagates parallel to the West Indian Ridge; hence only weak inter-action and generation of internal tide is possible. Six moorings with velocity and temperature meters at depths of 50, 100, 150, 200, 300, 400, 500, 600, 800, and 1000 m were deployed. The distance between the moorings was 10–11 km.

Extraordinary horizontal variability was recorded at six moorings 10 km apart from one another. Intense highly reliable peaks were recorded at different levels of each mooring. An almost complete absence of peaks was observed at the same level on neighboring moorings. A ray trajectory of the 12-hour oscillation can be traced from a seamount 1000 m above the bottom explaining the semidiurnal oscillations measured by several instruments located on this trajectory, while the other meters set out of the trajectory measured only the background spectra (Figs. 4.6 and 4.7). The experiment was very short, and the records of instruments on the moorings did not exceed 215 h. Thus, the resolution of the spectral functions appeared poor.

Vertical coherences are significant only over distances not exceeding 200–300 m. Horizontal coherences vary strongly from insignificant to high values, which appear between time series in sloping directions coinciding with the slopes of the characteristic curves.

Horizontal coherences are sometimes not significant even at distances of 10 km between moorings. Such a variation in spectral and coherence functions is possible if a beam structure of internal perturbations exists in the study site which has not transformed into modes. Many small submarine hills are located in the region, which makes them a prominent feature of bottom topography here. Their elevations over the seafloor are 1000–1500 m.

Propagation of a beam of the semidiurnal internal perturbation from a submarine hill is shown in Fig. 4.7. Spectral cross-analysis of the semidiurnal fluctuations of
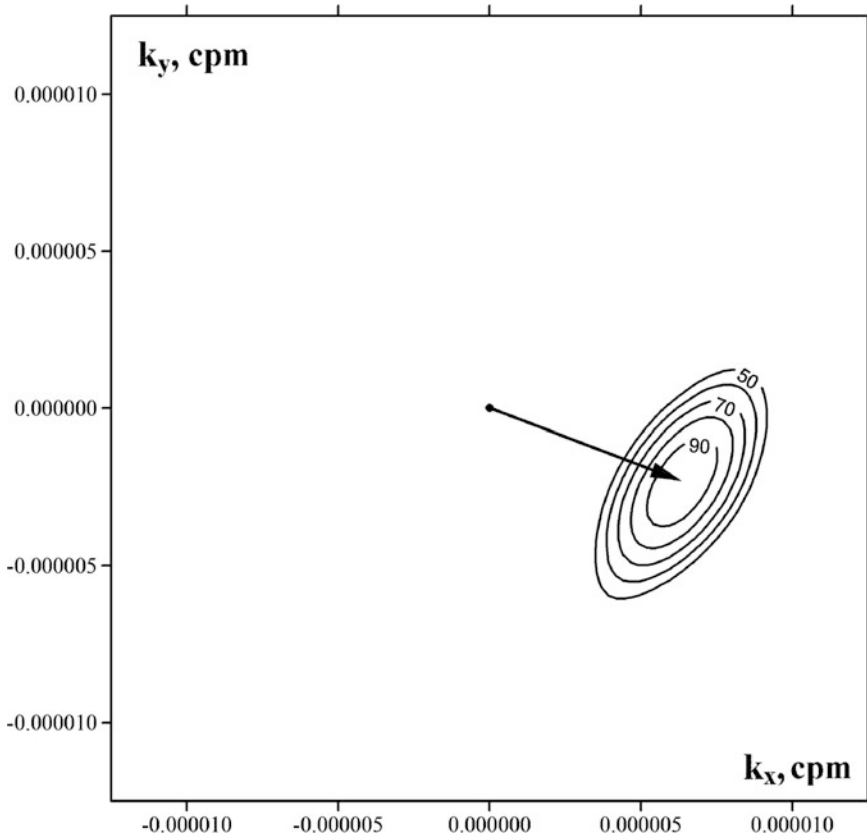
Fig. 4.5 Spatiotemporal spectrum at the semidiurnal frequency in the Mascarene region calculated from the temperature data at 1200 m. The contour lines correspond to 90, 80, 70, 60, and 50% of the main maximum. The arrow shows the wave vector. The internal tide propagates to the southeast (azimuth 110°, wavelength 145 km)

velocity components along a slant trajectory from mooring 2 (depth 500 m) to mooring 4 (depth 1000 m) showed that coherence between these two pairs of time series exceeds 0.65. The pairs were specially selected assuming that a beam of internal perturbations propagates in this direction. The spectra of these time series have reliable peaks at the semidiurnal frequency.

Thus, in the Madagascar Basin we observed a wave regime of the internal tides similar to that in the Polygon-70 and Mesopolygon-85. The barotropic tidal wave propagates parallel to the West Indian Ridge and does not induce significant internal tide generation over the ridge. The waves of internal tide generated over the ridge do not reach the study site.

Currents of the barotropic tide overflow numerous submarine hills and induce periodical perturbations to the density fields (Baines 2007), thus generating beams of the semidiurnal internal perturbations of low intensity. After a few reflections
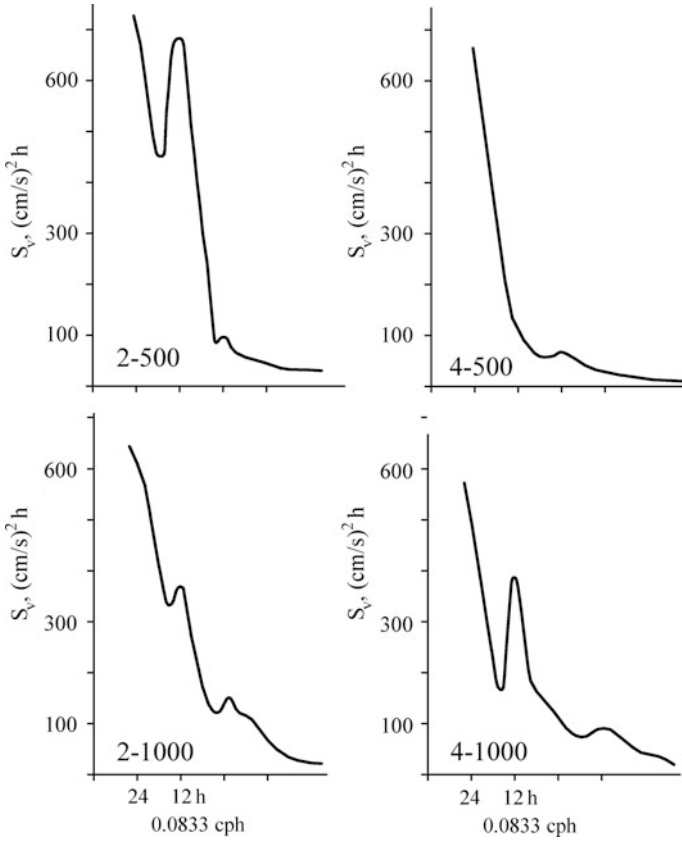
Fig. 4.6 Spectra of fluctuations of the meridional velocity component based on the data of measurements on moorings 2 and 4 in the Madagascar Basin (depths of velocity meters are 500 and 1000 m). Modified and redrawn from Morozov (1995)

from the surface and bottom they decay and do not form the mode structure of the internal tides. Neither have they formed a directed wave system. A similar generation of semidiurnal beams of perturbations was reported by Lyashenko and Sabinin (1979) on the basis of the Polygon-70 data.

4.3 Kerguelen Rise

Moored measurements north of Kerguelen Island were carried out in January 1983. The experiment was organized by the Shirshov Institute of Oceanology, Russia. The bottom topography and the scheme of moorings are shown in Fig. 4.8. Six moorings were deployed 300 km north of the island. The moorings were arranged
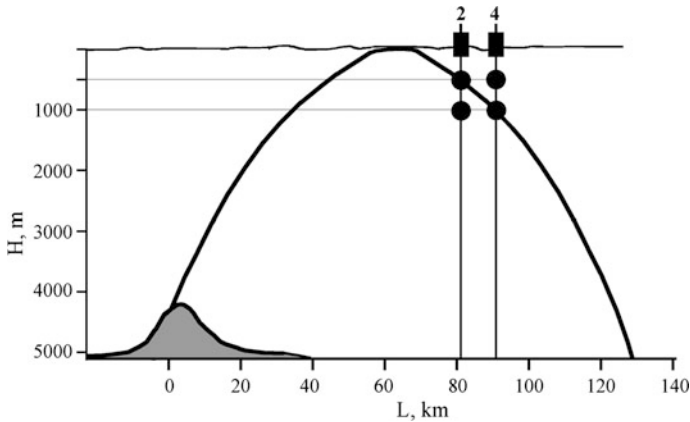
Fig. 4.7 Scheme of the propagation of internal perturbation beam from a submarine hill to the moorings in the Madagascar Basin. The numerals denote numbers of moorings. Modified and redrawn from Morozov (1995, 2006)

in a line normal to the Antarctic Circumpolar Current to measure the velocities of the current. Since the moorings were deployed in a line it was impossible to calculate the spatiotemporal spectra. The semidiurnal peaks on the spectra of temperature were weak. Most of the spectra do not have semidiurnal peaks. The coherences were insignificant. Barotropic tidal currents are parallel to the "flat" ridge; hence, they cannot cause significant generation of internal tides. The amplitudes of the semidiurnal tides were close to 10–15 m. The region is far from the intense sources of internal tides. The slopes of the Kerguelen Ridge located south of the study site are not strong generators of internal tides. In addition, the currents of the barotropic tide in this region flow in the direction along the submarine ridge; hence the recorded weak internal tides are poorly correlated.

Maraldi et al. (2011) analyzed internal tides based on satellite altimetry data in this region and numerical modeling. The generation of internal tides was found over the northern Kerguelen Plateau. According to the satellite altimetry, the internal tides were generated at the northern slope of the Kerguelen Plateau and propagated northward towards the southern front of the Antarctic Circumpolar Current. Here, coherence dropped rapidly. Maraldi et al. (2011) estimated that ~ 0.81 GW was converted from the barotropic to baroclinic tidal modes between Kerguelen and Heard islands.

Internal waves in the region were analyzed by Meyer et al. (2016) on the basis of high-resolution hydrographic profiles from electromagnetic profiling floats EM-APEX. The authors conclude that the internal wave field is composed of waves from several sources and the most energetic internal waves are close to inertial waves. The internal wave field in the Subantarctic zone is influenced by atmospheric forcing. They did not distinguish internal tides as internal waves of notable energy.
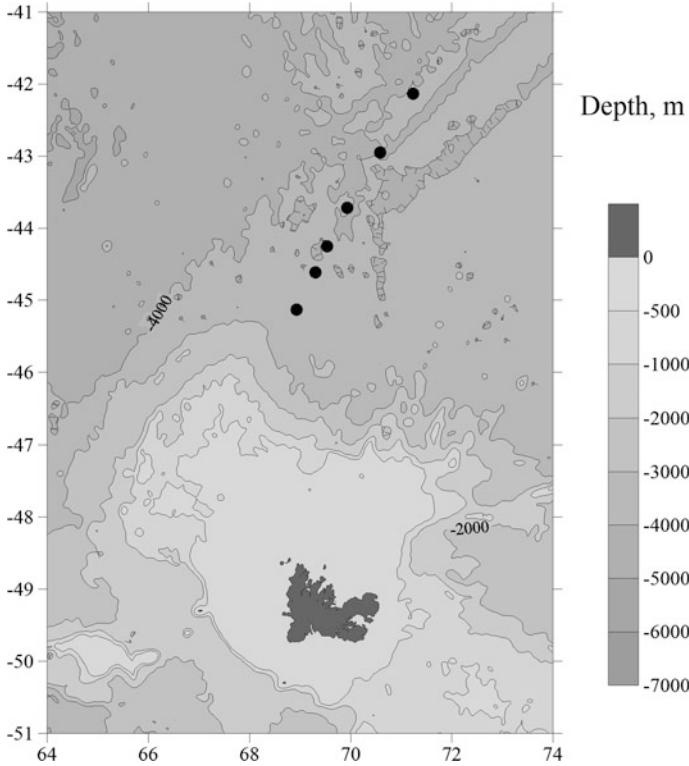
Fig. 4.8 Bottom topography (meters) in the study site near the Kerguelen Plateau. Depth contour lines are shown at depths of 500, 1000, 2000, 3000, and 4000 m. Locations of moorings are shown with black dots. Land and islands are shown with gray color

4.4   Bab el Mandeb Strait

The Bab el Mandeb Strait is located between Arabia and Africa. It connects the Red Sea with the Gulf of Aden and the Indian Ocean. The strait is divided into two channels by Perim Island; the western channel is 26 km wide, and the shallow eastern channel is 3 km wide. The strait has been named in Arabic the Gate of Tears due to the dangers associated with this region. The depth of the Hanish Sill in the strait is 180 m (Murray and Johns 1997). The currents in the strait are similar to those in the Strait of Gibraltar. There is a surface current into the Red Sea in both channels and a strong undercurrent from the Red Sea in the western channel. These currents are physically driven by the same causes as those in the Strait of Gibraltar. High evaporation and zero inflow of fresh water in the Red Sea require additional water supply from the Indian Ocean (Dietrich et al. 1980). The Bab el Mandeb Strait closed during the same periods in geological history (5 million years before the present) as the Strait of Gibraltar and the Red Sea dried to an empty, salt-floored
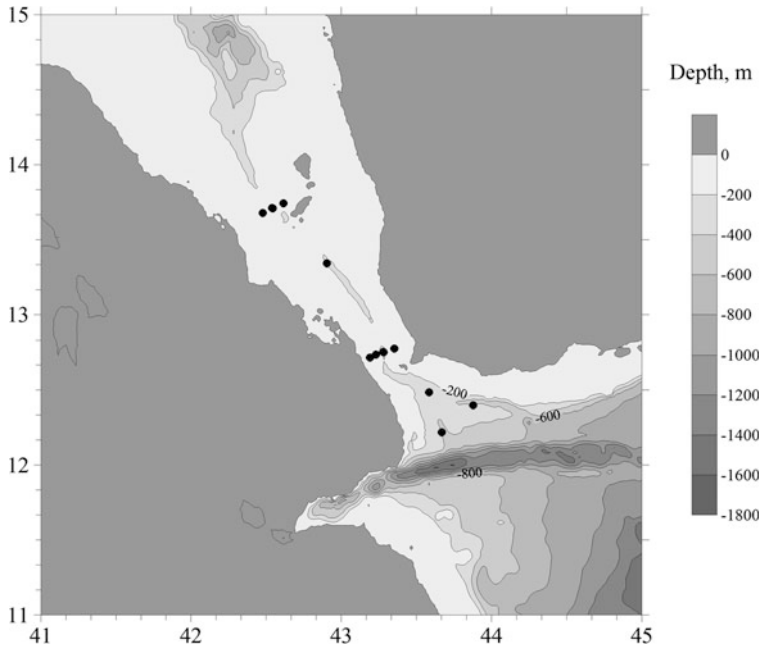
Fig. 4.9 Bottom topography (meters) and locations of moorings in the Bab el Mandeb Strait (black dots). Isobaths are shown with an interval of 200 m. Land and islands are shown with gray color

sink. A strong current with velocities exceeding 30 cm/s to the Red Sea compensating evaporation exists in the upper 100 m of the strait. An opposing current transporting high salinity (40 psu) water with velocities up to 50 cm/s flows to the ocean in the lower layer with the core at approximately 160 m. The width of the strait is narrower in the deep layers: its width at a depth of 150 m is 8 km. Hence, the velocity in the deep layers is greater. Lenses of high salinity from the Red Sea were also found in the Indian Ocean similar to those in the Atlantic Ocean. A barotropic tide wave with velocities up to 120 cm/s is superimposed on the existing system of mean currents in the strait generating internal tide while overflowing the slopes of the bottom topography especially over the sill in the region of Perim Island.

In 1995–1996, a mooring experiment was carried out in the strait. The experiment was organized by the Miami Rosenstiel School of Marine and Atmospheric Science (RSMAS) and Louisiana State University. A chart of the bottom topography and moorings is shown in Fig. 4.9. The velocity and temperature meters were set on submersible buoyancies and uplooking ADCP current meters were set on the bottom. Time sampling was set at one hour (Smeed 1997, 2004). The regime of currents in the strait was analyzed by Bower et al. (2000).

Both diurnal and semidiurnal tides exist in the strait. Hence diurnal and semidiurnal internal tides are generated over the slopes of topography (Jarosz et al. 2005).
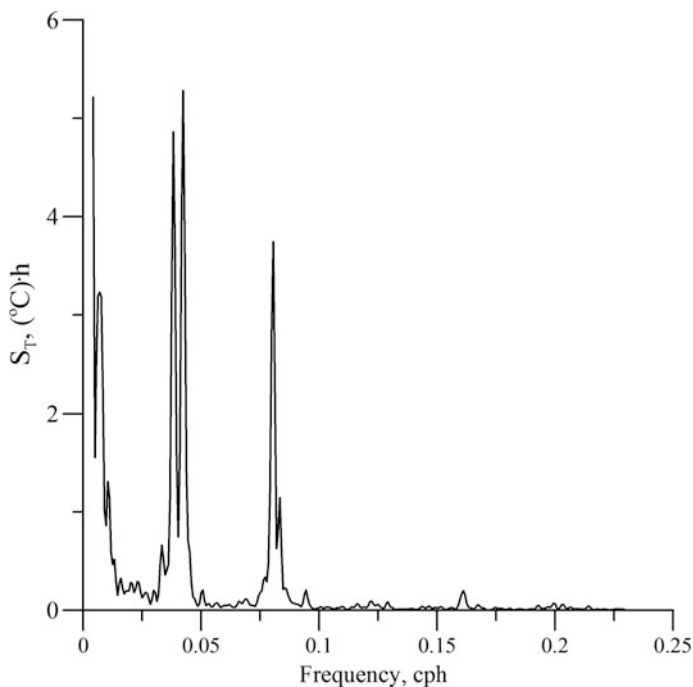
Fig. 4.10 Spectrum of temperature fluctuations in the Bab el Mandeb Strait from a mooring over the Hanish Ridge (latitude 12° 30′N, depth of the instrument is 117 m; depth of the location is 162 m)

The confidence level of the peaks is very high. The diurnal internal tides dominate. Overtones appear on the spectra at periods of 8.0 and 6.2 h.

The spectrum of temperature fluctuations measured at a depth of 117 m over the depth of the ocean equal to 162 m on a mooring deployed near the Perim Sill is shown in Fig. 4.10. Strong oscillations are associated with the internal waves of the diurnal and M_2 frequencies. The mean amplitude of the semidiurnal internal tides over the sill near Perim Island (latitude 12° 30′N) was 80 m. The maximum vertical displacements of water particles caused by the joint effect of the diurnal and semidiurnal internal tides reached 160 m. In the northern group of moorings (latitude 13° 30′N) the amplitude decreased to 20 m.

We estimated the direction and wavelength of the semidiurnal internal tide using the Barber's method (see Sect. 1.4.2) (Barber 1963). The calculation was performed on the basis of temperature data from three moorings in the southern part of the strait at a depth of 400 m, while the depth of the ocean was 500 m increasing to the southeast. The spatiotemporal spectrum is shown in Fig. 4.11. The wavelength was 80 km. The internal tide wave was directed to the southeast (150°). These waves can be interpreted as the semidiurnal internal tides generated over the sill in the strait close to Perim Island.
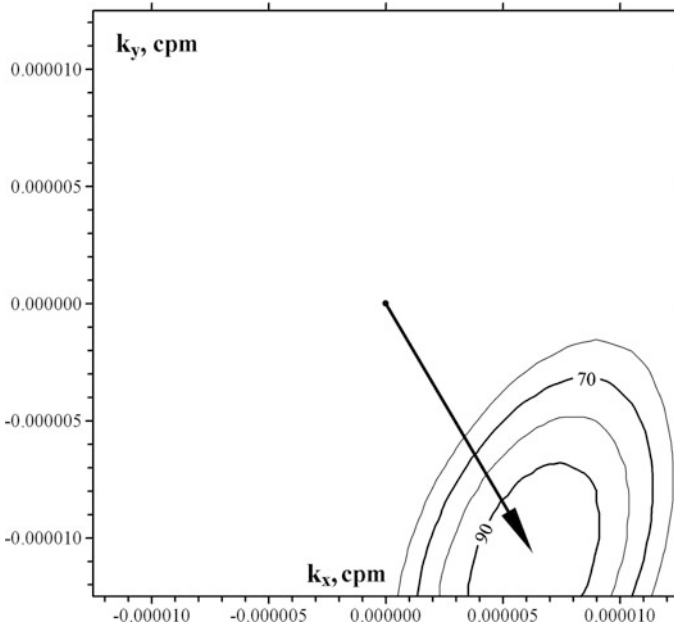
Fig. 4.11 Spatiotemporal spectrum at the semidiurnal frequency based on the temperature data from the moorings in the southern group at a depth of 400 m. The contour lines correspond to 90, 80, 70, and 60% of the main maximum. The arrow shows the wave vector corresponding to a wavelength of 80 km. The internal tide propagates to the southeast (azimuth 150°)

4.5   Southwest Indian Ocean (20°S; 50°E, 70°E, and 90°E), MAPSOON, WOCE ICM-3 Experiments

Three arrays of moorings in 1995–1997 were designed to describe the water characteristics, velocity structure, and transport of the three systems of deep western boundary currents in the Indian Ocean. This was the WOCE ICM-3 experiment (MAPSOON). The experiment was organized by the Woods Hole Oceanographic Institution, Texas A&M University, and Oregon State University. In these regions the boundary currents transport the water of Antarctic origin northward into the three major basins of the Indian Ocean. The three basins are the Mascarene Basin (West Array), the Central Indian Basin (Central Array) and the West Australian Basin (East Array). Three arrays of moorings were deployed in 1995–1997 along 20°S east of Madagascar. They were deployed from the R/V *Knorr* in 1995 and recovered in 1997 by the R/V *Melville* (Warren et al. 2002). Each of the three arrays was organized in a line. The upper level of measurements was at 2300–2500 m. The longitudes of the western line were 49° 30′–52° 30′E; the longitudes of the middle line were 69° 38′–74° 18′E; and the longitudes of the eastern line were 88° 21′–92° 35′E (Fig. 4.12).

Fig. 4.12 Bottom topography (meters) and schematic location of moorings in the South Indian Ocean. Depth contour lines are shown at depths of 500, 1000, 2000, 3000, 4000, and 5000 m. Locations of moorings are shown with black symbols. Land and islands are shown with gray color. The ICM-3 moorings are shown by dots with a white circle in the middle; the moorings of the Russian-Indian experiment in 1995 are shown with triangles; the Mascarene-87 moorings are shown with diamonds; the Madagascar study region with 6 moorings in 1987 is shown with a square; the Russian equator moorings in 1974 are shown with stars; the INDEX moorings in 1977–1980 are shown with crosses; the EQCM moorings are shown by squares with a white dot in the middle

The amplitudes of the internal tides at the western line of moorings were esti-mated at 40–50 m with a slight decay to the east over a length of 312 km. The second line of moorings was located near the Arabian-Indian Ridge; several moorings were deployed on the slopes of the ridge because the ridge is relatively wide. The ridge consists of many seamounts, the tops of which are quite deep approximately at a depth of 3800 m. The amplitudes of internal tides on the western mooring (69° 38′E) at a depth of 2000 m were estimated at 60 m. The amplitudes of the semidiurnal internal tides were 65 m at a longitude of 70° 04′E at a depth of 2500 m. The amplitudes on the third mooring at 70° 38′E at a depth of 2513 m were 65 m. The amplitudes on the fourth mooring at 71° 33′E at a depth of 2579 m were 50 m. The amplitudes on the fifth mooring at 72° 29′E at a depth of 3014 m were 50 m. The sixth mooring was deployed east of the ridge (73° 20′E) over a depth of 4883 m. The amplitudes at a depth of 3001 m were estimated at 40 m. The amplitudes on the seventh mooring east of the ridge at 74° 18′E at a depth of 3018 m were estimated at 35 m.

The third line of moorings was deployed east of the Ninetyeast Ridge and on its slopes. The amplitudes of the semidiurnal internal tides over the slopes of the ridge between longitudes 88° 21′E and 89° 15′E at depths of 2229–3067 m were within 35–40 m. The amplitudes over the slopes of the ridge (longitude 89° 43′E) at a

depth of 2985 m were estimated at 70 m; and at a distance from the ridge between 90° 33′E and 92° 35′E, the amplitudes at a depth of 3000 m decreased to 35 m.

Three moorings were deployed in 1995 during the Russian-Indian experiment in the southern tropical part of the Indian Ocean at a distance of 1000 km from the Mascarene Ridge at 9° 57′S, 74° 55′E; 14° 46′S, 71° 55′E; and 14° 55′S, 76° 58′E. The Central Indian (Arabian-Indian) Ridge located at 75°E is quite near. The amplitudes of the semidiurnal internal tides on these moorings at depths of 1200–1300 m were estimated at 35–40 m.

4.6   Arabian Sea

An array of four moorings was deployed from the Russian R/V *Vityaz* in the Arabian Sea in 1967. The study site was located within: 12° 04′N, 64° 37′E; 12° 23′N, 64° 32′E, 11° 58′N, 64° 56′E, 11° 58′N, 64° 32′E. The mean depth of the sea in the region is approximately 4000 m. The mooring measurements were carried out in the upper layer up to 200 m. Small amplitudes of internal tides were recorded within 15–20 m. In 1994, a mooring was deployed in this region within the Arabian Sea Mixed Layer Dynamics Experiment (WHOI) at 15° 30′N, 61° 30′E. The instruments recorded greater amplitudes of internal tides up to 25–30 m at a depth of 300 m.

4.7   Indonesian Throughflow, MALUKU, JADE, WOCE ICM-4, Arlindo, and Makassar Experiments

Two moorings were deployed in 1994–1995 in the Talaud-Morotai region north of Indonesia at 3° 11′N, 128° 27′E and 4° 01′N, 127° 31′E. The temperature meters at a depth of 1050 m over the oceanic depths of 2300–2500 m recorded the amplitudes of internal tides up to 70 m.

In 1989–1990, a mooring was deployed north of Timor Island at 11° 15′S, 122° 53′E with velocity and temperature meters at depths of 420 and 1020 m. This was the WOCE ICM-4 JADE experiment. The experiment was organized by the Laboratoire d'Océanographie Dynamique et de Climatologie (France). The depth of the ocean was 1850 m. The mooring was located on the continental slope. The amplitudes of the semidiurnal internal tides were within 25–30 m.

The Arlindo experiment was carried out by Indonesia (Agency for Marine and Fisheries Research) and the United States (Oregon State University). The name is an acronym for Arus Lintas Indonen, which means 'through flow' in Bahasa Indonesian. The goal of the experiment was to study the circulation and water mass properties in the Indonesian Seas and to estimate the transport and velocity fields across the central passages of the Indonesian Seas. The Arlindo experiment was

carried out in 1996–1998 in the Makassar Strait in Indonesia. Two moorings were deployed at a latitude of $2° 52'S$ at longitudes $118° 27'E$ and $118° 37'E$. Temperature meters were set at depths of 1611 and 2137 m. Spectra of temperature fluctuations have narrow reliable peaks at the M_2 and S_2 frequencies (periods 12.4 and 12.0 h) and also diurnal peaks at periods of 23.9 and 25.8 h, which correspond to tidal frequencies K_1 and O_1. The amplitudes of the semidiurnal internal tides at depths of 750 and 1500 m were estimated at 50 m.

Modeling of internal tides in the Indonesian straits was performed by Robertson and Ffield (2008). The results of modeling were compared with observations. The authors report on strong interactions in the internal tidal fields: between a beam and its own reflections, between internal tides generated at different locations, for example at different sides of a channel, and between the barotropic and baroclinic tidal beams.

Internal waves in the Strait of Lombok reported by Susanto et al. (2005) were as high as 100 m.

4.8   Mozambique Channel, Agulhas, WOCE ICM-1 Experiment

The Mozambique Channel is a region of strong internal tide generation over the continental slopes (Baines 1982). The WOCE ICM-1 experiment was conducted in 1995–1996. The experiment was organized by the National Oceanography Centre Southampton (NOCS), UK. Five moorings were deployed in a line normal to the continental slope of Africa in the Mozambique region from $31° 05'S$, $30° 26'E$ to $31° 55'S$, $31° 28'E$. The length of the mooring line was 134 km. The main goal of the experiment was to investigate the Agulhas boundary current. The bottom topography and locations of moorings are shown in Fig. 4.13. The location of instruments relative to the slope is shown in Fig. 4.14. The peak to peak temperature fluctuations at a depth of 750–800 m were 0.3–0.4 °C. On the northwestern mooring these fluctuations correspond to the amplitudes of internal tides of 40 m while on the southeastern mooring they are smaller and range between 25 and 30 m. The instruments shown in Fig. 4.14 were used to calculate the energy decay with the distance from the shore. The procedure was the same as we used previously (Lozovatsky et al. 2003). We found that the decay of internal wave energy in the Mozambique region was quite similar to that, which was found in the region of the Mascarene Ridge (Fig. 4.15).

Internal waves in the Mozambique Channel were studied by Manders et al. (2004). Seven current meter moorings were deployed for a year and a half in 2000–2001. The measurements were compared with the results of numerical simulations. The channel is 350 km wide; therefore, multiple reflections of internal wave beams were found across the channel. Wave attractors (Maas et al. 1997) were not found in the Mozambique Channel at the existing stratification despite the existence of two
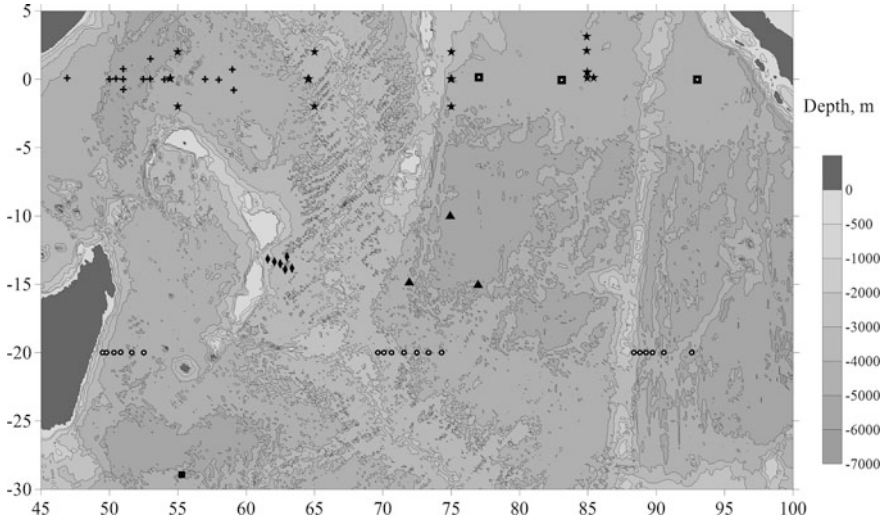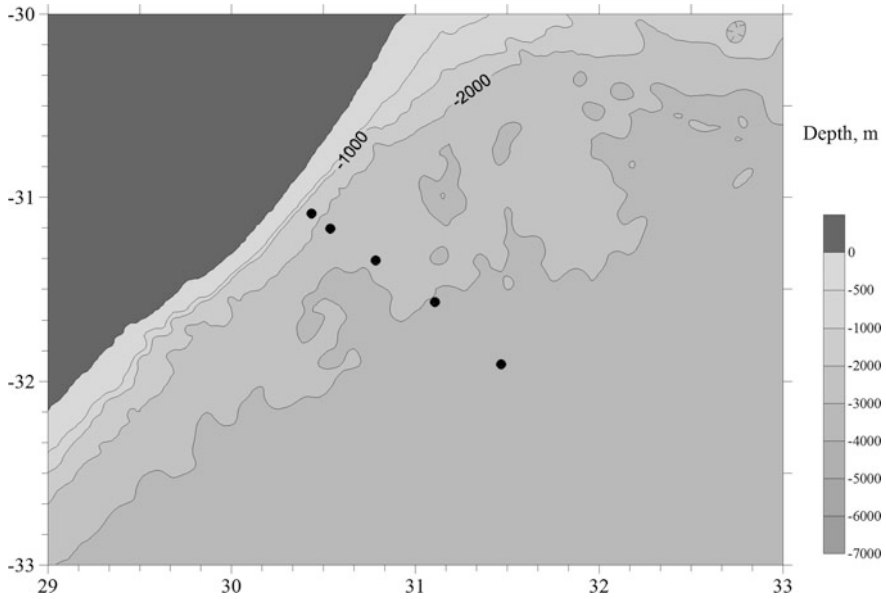
Fig. 4.13 Bottom topography (meters) and schematic location of moorings southeast of Africa. Depth contour lines are shown at depths of 500, 1000, 2000, and 3000 m. Locations of moorings are shown with black dots. Land is shown with gray color
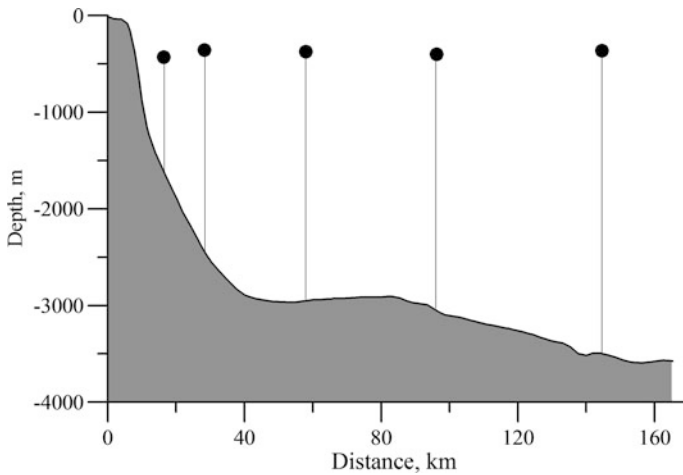
Fig. 4.14 Locations of moorings and instruments relative to the slope southeast of Africa

opposite slopes (African and Madagascar) located not very far from each other. The numerical results suggest that the energy may become largely concentrated in the western half of the basin. Strong internal tide generation in the western part of the
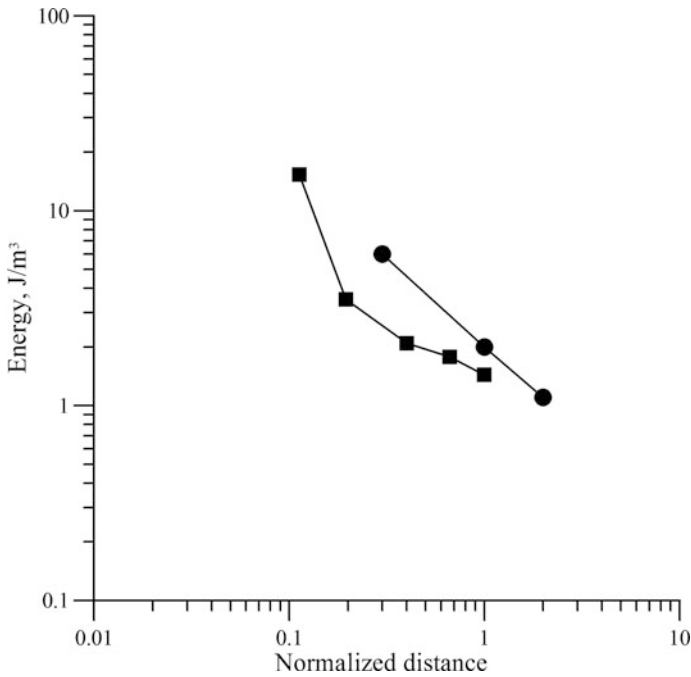
Fig. 4.15 Semidiurnal internal tide energy decay with the distance from the continental slope of Africa in the Mozambique Basin (squares). Decay of the internal tide energy based on the measurements near the Mascarene Ridge in the Indian Ocean (dots) by Lozovatsky et al. (2003) is shown for comparison

channel over the Sofala Bank at 20° 30′S 36° 00′E over critical topography was observed by da Silva et al. (2009) on the basis of the SAR satellite images. This region between 20° and 21°S is considered a hot spot for the generation of internal waves and internal tides that travel to the ocean away from the shelf break.

4.9 Western Australia, LEEUWIN, WOCE ICM-6 Experiments

Moored observations over the shelf break on the northwestern shelf of Australia at 20°S, 116°E using current meters and thermistor chains were analyzed by Holloway (1983, 1984, 1994). The experiment was organized by CSIRO, Australia. This is a region of very intense barotropic tides (Baines 1982).

The amplitudes of the internal tides reached 30 m. The author suggested that the internal tides were generated in the depth interval 400–1000 m over the continental slope. The observations over a broader region fall into three categories related to the ratio of the slope steepness and slope of internal tide characteristics (Holloway

1985). If the slope is critical relative to internal tides $\alpha/c \sim 1$ (where α is the slope of bathymetry and $c = \sqrt{\frac{\omega^2 - f^2}{N^2 - \omega^2}}$ is the slope of internal tide characteristic) strong generation of internal tide occurred. If the slope is supercritical ($\alpha/c \sim 2$), only weak generation occurred. At subcritical slopes ($\alpha/c \sim 0.2$) no intensification of semidiurnal currents was observed. The waves propagated onshore. The directions of the waves averaged over several months are consistent from year to year. The observations are also consistent with the author's numerical model (Holloway 1996). Packets of short-period internal waves generated from internal tides over the shelf break are described by the Korteweg-de Vries model by Holloway et al. (1997, 1999).

Observations of the internal tide in the region of the northwest Australian shelf are also described by Holloway et al. (2001). The data were collected from a line of moorings deployed over the continental shelf and slope on the Australian northwestern shelf to the depths of 1400 m between 19°–20°S and 115°–117°E. The data were supplemented with repeated CTD and ADCP profile measurements in 1995. The measurements recorded internal tide propagating to the shore. Generation sites were distinguished in the regions of bottom topography where the slopes are equal or steeper than the characteristics of the internal tides. The authors also distinguished beams of internal tides.

Moored measurements and numerical simulations show that propagation of a tropical cyclone over the study region modifies stratification and this results in significant changes to internal tide characteristic paths and hence the internal tide generation process on the continental slope (Davidson and Holloway 2003).

4.10 Equatorial Indian Ocean

In January–March, 1974, mooring measurements of velocity and temperature were carried out from the Russian R/V *Vityaz* at three sites located near the equator at longitudes 55°, 65°, 75°, and 85°E. The duration of measurements at each site was 7–8 days. The goal of the experiment was to study equatorial currents in the winter spring monsoon season (Koshlyakov et al. 2016). The moorings were generally deployed in lines normal to the equator from 4°S to 4°N (Fig. 4.12). The spectral functions are characterized by a peak at the semidiurnal frequency. Vertical displacements at the semidiurnal frequency were calculated from the time series of temperature and vertical temperature gradients.

The site at 55°E was located at a distance of 400 km north of the Mascarene Ridge. It is known that intense semidiurnal internal tides are generated over the slopes of the Mascarene Ridge. The measurements at the research site at 55°E show that the amplitudes of the semidiurnal internal tides reached 40 m.

The site at 65° E was located at a distance of 200 km west of the Arabian Indian Ridge (Central Indian Ridge). The instruments at a depth of 600 m recorded the semidiurnal internal tides with amplitudes of 25 m.

The site at 75° E was located at a distance of 200 km east of the Maldives. Semidiurnal internal tides with amplitudes of 50 m were recorded at a depth of 1000 m.

The site at 85° E was located at a distance of 500 km west of the Ninetyeast Ridge. The amplitudes of the semidiurnal internal tides were about 30 m.

Thus, these measurements showed that the Mascarene and Maldivian ridges are regions of intense generation of internal tides. The moorings were deployed in lines; unfortunately, it is impossible to estimate the wavelengths and directions of internal tides here. Only at 85° E three moorings were deployed in the form of a triangle. The estimated wavelength was 117 km and the waves were directed from the Ninetyeast Ridge.

In 2000–2004, several moorings were deployed near the equator by scientists from the National Institute of Oceanography (NIO), India. Mooring EQCM1 was deployed 300 km west of the Ninetyeast Ridge at 0°, 93° E. The mooring was replaced twice. The total time of its operation was three years. The amplitudes of the semidiurnal internal tides in the region at depths of 950–1050 were estimated at 60–80 m.

Mooring EQCM2 was located at 0°, 83° E at a distance of 700 km west of the Ninetyeast Ridge. The amplitudes of the semidiurnal internal tides at a depth of 1072 m were 30–35 m.

Mooring EQCM3 was located at 0°, 76° E at a distance of 300 km west of the Maldives. The amplitudes of the semidiurnal internal tides at a depth of 823 m were 60 m.

Mooring EQCM3A was located at 0°, 77° E at a distance of 400 km east of the Maldives. The amplitudes of the semidiurnal internal tides at a depth of 1059 m were 30–35 m.

During the INDEX experiment in 1976–1980 (WHOI), twelve moorings were deployed in the western part of the equatorial Indian Ocean (INDEX experiment, WHOI). In 1979, a mooring at 47° E (0° 05′N, 46° 54′E) recorded internal tides at a depth of 750 m with amplitudes ranging from 20 to 35 m. The amplitude of the semidiurnal internal tides recorded on moorings at 50°–51° E varied from 20 to 40 m. The spatiotemporal spectrum calculated from these data showed that the wavelength was 120–130 km. The direction of waves varied from 150° to 170°, which indicates that the generation of the semidiurnal internal tides occurred over a submarine cape of the continental slope located in the region of 4° N, 48° E. The amplitude of the internal tides at a longitude of 54° E decreased to 15–20 m and at a longitude of 59° E it decreased to 15–20 m.

4.11   South of Africa

In January–February, 1983, a cluster of moorings was deployed from the Russian R/V *Akademik Mstislav Keldysh* south of Africa to study the Antarctic Circumpolar Current. The cluster was located north and northwest of the African-Antarctic Ridge.
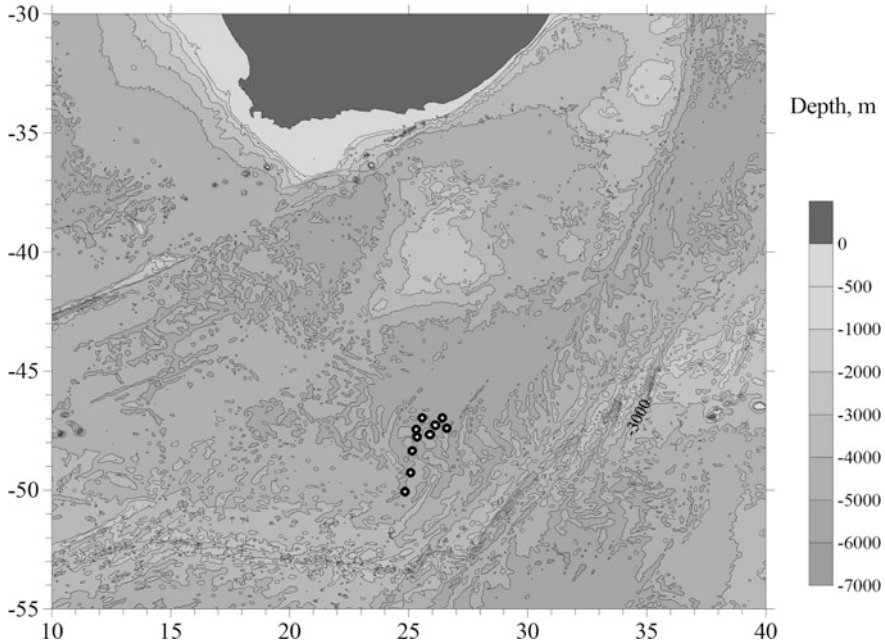
Fig. 4.16 Bottom topography (meters) and schematic location of moorings south of Africa. The experiment on R/V *Akademik Mstislav Keldysh* south of Africa in 1983. Depth contour lines are shown at depths of 500, 1000, 2000, 3000, 4000, and 5000 m. Locations of moorings are shown by black dots with a white circle in the middle. Land and islands are shown with gray color

Locations of moorings are shown in Fig. 4.16. The amplitudes of the semidiurnal internal waves at a depth of 300 m were estimated at 30 m and at the depths of 600 and 1700 m they were 40–50 m. The waves propagated almost to the north (340°) from the slopes of the African-Antarctic Ridge south of the mooring cluster. The wavelength was 90 km. Stratification at these latitudes is not as strong as it is at mid-latitudes; hence the wavelength is shorter. The spatiotemporal spectrum for the semidiurnal internal tides at a depth of 300 m is shown in Fig. 4.17.

4.12   Southwest of Australia, WOCE SCM-4 Experiment

In 1995–1996 a line of nine moorings was deployed southwest of Australia between 32° 21′S, 102° 07′E and 34° 10′S, 109° 37′E. (Figure 4.18). The experiment was organized by CSIRO Marine Research Department, Australia. The line of moorings crossed a deep channel between the Australian continental slope in the east and the Broken Plateau (Broken Ridge) in the west. The measurements were made below 3200 m. The amplitudes at 3200 m ranged from 28 to 56 m generally decreasing in the southeastern direction from the Australian continental slope. A graph of the
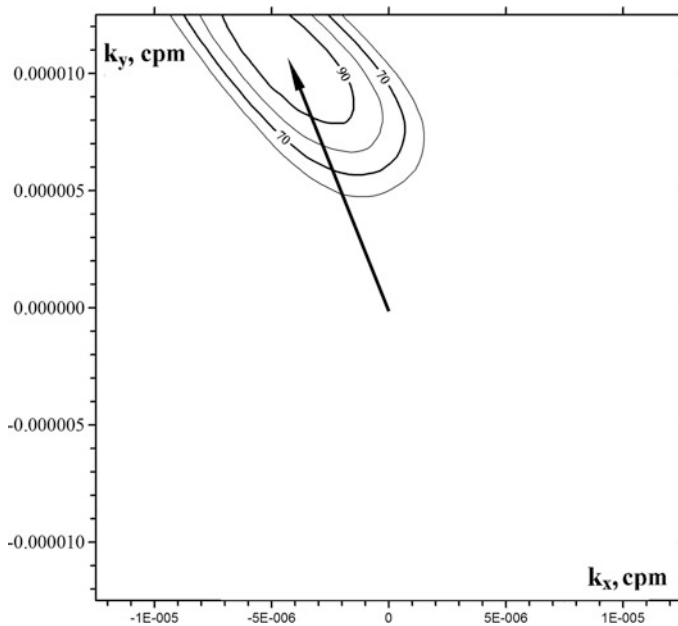
Fig. 4.17 Spatiotemporal spectrum at the semidiurnal frequency based on the data south of Africa in 1983 at a depth of 300 m. The contour lines correspond to 90, 80, 70, and 60% of the main maximum. The arrow shows the wave vector
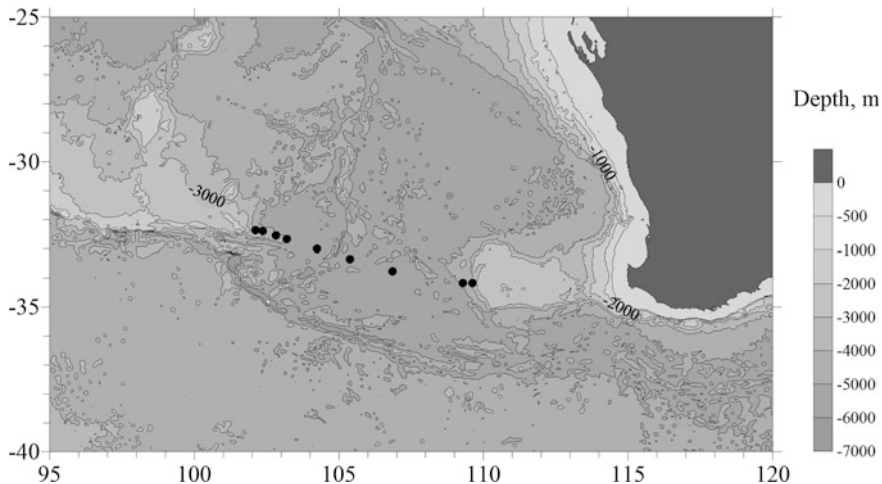
Fig. 4.18 Bottom topography southwest of Australia. The moorings are shown with black dots. Depth contour lines are shown at depths of 500, 1000, 2000, 3000, and 4000 m. Land and islands are shown with gray color
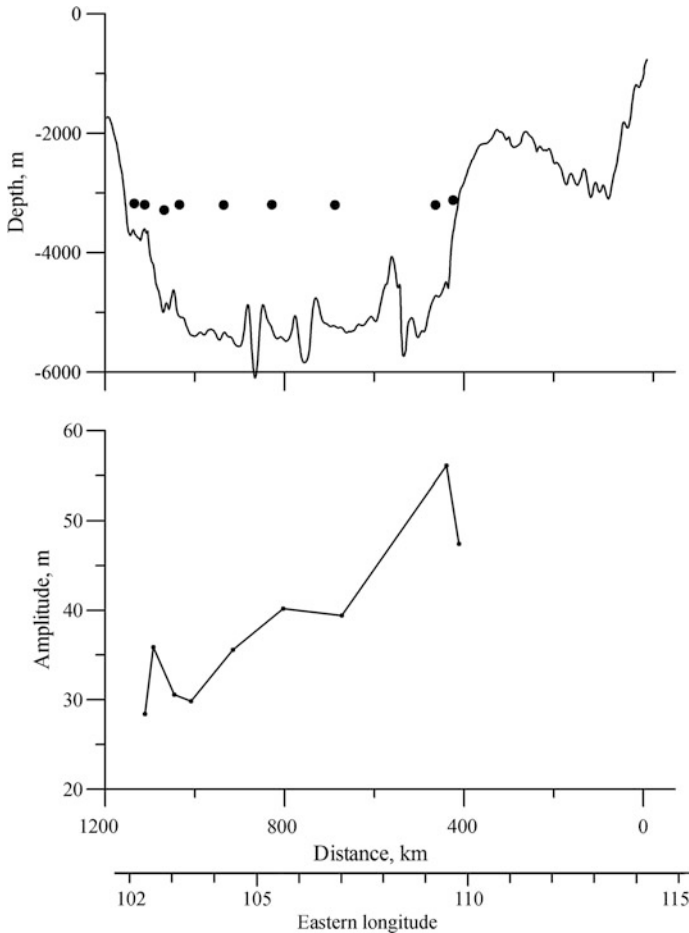
Fig. 4.19 Scheme of the locations of instruments over bottom topography of west Australia (2000 m isobath) (dots) (top panel); semidiurnal internal tide amplitude decay with the distance from the continental slope (bottom panel)

internal wave amplitudes at a depth of 3200 m versus longitude and distance from the 200 m isobath in the western direction is shown in Fig. 4.19. One can expect a gradual decrease with the distance from the continental slope, but the general trend is clearly seen. A topographic feature exists west of the mooring array. It is a ridge with the crest at 2000 m but it is oriented in the zonal direction as a continuation of the line of moorings. Therefore its effect as an internal tide generator should be seen north and south of the ridge but not on the moorings deployed here. Actually no increase in the internal tide amplitudes and energy was detected on the western moorings.

References

Baines PG (1982) On internal tide generation models. Deep-Sea Res 29(3):307–338

Baines PG (2007) Internal tide generation by seamounts. Deep Sea Res 54(9):1486–1508. https://doi.org/10.1016/j.dsr.2007.05.009

Barber NF (1963) The directional resolving power of an array of wave detectors. In: Ocean wave spectra. Prentice Hall, Englewood Cliffs, pp 137–150

Bower AS, Hunt HD, Price JF (2000) Character and dynamics of the Red Sea and Persian Gulf outflows. J Geophys Res 105:6387–6414

da Silva JCB, New AL, Magalhaes JM (2009) Internal solitary waves in the Mozambique channel: Observations and interpretation. J Geophys Res 114: C05001. https://doi.org/10.1029/2008JC005125

da Silva JCB, New AL, Magalhaes JM (2011) On the structure and propagation of internal solitary waves generated at the Mascarene Plateau in the Indian Ocean. Deep-Sea Res 58:229–240

da Silva JCB, Buijsman MC, Magalhaes JM (2015) Internal waves on the upstream side of a large sill of the Mascarene ridge: a comprehensive view of their generation mechanisms and evolution. Deep-Sea Res 99:87–104

Davidson FJM, Holloway PE (2003) A study of tropical cyclone influence on the generation of internal tides. J Geophys Res 108(C3):3082. https://doi.org/10.1029/2000JC000783

Dietrich GK, Kalle K, Krauss K, Siedler G (1980) General Oceanography. Willey, NY, p 626

Garrett C, Kunze E (2007) Internal tide generation in the deep ocean. Annu Rev Fluid Mech 39:57–87

Holloway PE (1983) Internal tides on the Australian northwest shelf. A preliminary investigation. J Phys Oceanogr 13(8):1357–1370

Holloway PE (1984) On the semidiurnal internal tide at a shelf-break region on the Australian North West Shelf. J Phys Oceanogr 14(11):1787–1799

Holloway PE (1985) A comparison of semidiurnal internal tides from different bathymetric locations on the Australian North West shelf. J Phys Oceanogr 15(3):240–251

Holloway PE (1994) Observations of internal tide propagation on the Australian North West shelf. J Phys Oceanogr 24(8):1706–1716

Holloway PE (1996) A numerical model of internal tides with application to the Australian North West shelf. J Phys Oceanogr 26(1):21–37

Holloway PE, Pelinovsky EN, Talipova TG, Barnes B (1997) A nonlinear model of internal tide transformation on the Australian North West shelf. J Phys Oceanogr 27:871–896

Holloway PE, Pelinovsky E, Talipova T (1999) A generalised Korteweg-de Vries model of internal tide transformation in the coastal zone. J Geophys Res 104:18333–18350

Holloway PE, Chatwin PG, Craig P (2001) Observations from the Australian North West shelf in Summer 1995. J Phys Oceanogr 31(5):1182–1199

Jarosz E, Blain CA, Murray SP, Inoue M (2005) Barotropic tides in the Bab el Mandab Strait, numerical simulations. Cont Shelf Res 25:1225–1247

Konyaev KV, Sabinin KD, Serebryany AN (1995) Large-amplitude internal waves at the Mascarene Ridge in the Indian Ocean. Deep-Sea Res 42(11–12):2075–2091

Koshlyakov MN, Morozov EG, Neiman VG (2016) Historical findings of the Russian physical oceanographers in the Indian Ocean. Geosci Lett 3(1):1–8. https://doi.org/10.1186/s40562-016-0051-6

Leontieva EA, Sabinin KD, Shulepov VA, Yampolsky AD (1992) Experimental data on internal tides at the Mascarene Ridge and their ray tracing. Oceanology 32(6):707–713

Lozovatsky ID, Morozov EG, Fernando HJS (2003) Spatial decay of energy density of tidal internal waves. J Geophys Res 108(C6):3201–3216

Lyashenko AF, Sabinin KD (1979) On the spatial structure of the internal tides on the 1970 hydrophysical test range in the Atlantic. Izv Acad Sci USSR, Ser Atmos Ocean Phys 15(8):595–601

Maas LRM, Benielli D, Sommeria J, Lam FPA (1997) Observations of an internal wave attractor in a confined stably stratified fluid. Nature 388:557–561

Manders AMM, Maas LRM, Gerkema T (2004) Observations of internal tides in the Mozambique Channel. J Geophys Res 109:C12034. https://doi:10.1029/2003JC002187

Maraldi C, Lyard F, Testut L, Coleman R (2011) Energetics of internal tides around the Kerguelen Plateau from modeling and altimetry. J Geophys Res 116:C06004. https://doi.org/10.1029/2010JC006515

Meyer A, Polzin KL, Sloyan BM, Phillips HE (2016) Internal waves and mixing near the Kerguelen Plateau. J Phys Oceanogr 46(2):417–437

Morozov EG (1995) Semidiurnal internal wave global field. Deep-Sea Res 42(1):135–148

Morozov EG (2006) Internal tides. Global field of internal tides and mixing caused by internal tides. In: Waves in Geophysical Fluids. Springer, Wein, New York, pp 271–332

Morozov EG, Fomin LM (1989) Extreme internal tidal waves measured in the Indian Ocean. Dokl Akad Nauk SSSR (Earth science sections) 305(2):241–244

Morozov E, Vlasenko V (1996) Extreme tidal internal waves near the Mascarene Ridge. J Mar Sys 9(3–4):203–210

Morozov EG, Nechvolodov LV, Sabinin KD (2009) Beam propagation of tidal internal waves over a submarine slope of the Mascarene Ridge. Oceanology 49(6):745–752

Murray SP, Johns W (1997) Direct observations of seasonal exchange through the Bab el Mandab Strait. Geophys Res Lett 24(21):2557–2560

New AL, Alderson SG, Smeed DA, Stansfield KL (2007) On the circulation of water masses across the Mascarene Plateau in the South Indian Ocean. Deep-Sea Res 54(1):42–74

New AL, Magalhaes JM, da Silva JCB (2013) Internal solitary waves on the Saya de Malha bank of the Mascarene Plateau: SAR observations and interpretation. Deep-Sea Res 79:50–61

Robertson R, Ffield A (2008) Baroclinic tides in the Indonesian seas: Tidal fields and comparisons to observations. J Geophys Res 113:C07031. https://doi.org/10.1029/2007JC004677

Sabinin KD, Nazarov AA, Filonov AY (1992) Internal-wave trains above the Mascarene Ridge. Izv Atmos Ocean Phys 28(6):473–479

Smeed DA (1997) Seasonal variation of the flow in the Strait of Bab el Mandeb. Oceanol Acta 20:773–781

Smeed DA (2004) Exchange through the Bab el Mandab. Deep-Sea Res II 51:455–474

Susanto RD, Mitnik L, Zheng Q (2005) Ocean internal waves observed in the Lombok Strait. Oceanography 18:80–87

Warren DA, Whitworth T, LaCasce JH (2002) Forced resonant undulation in the deep Mascarene Basin. Deep-Sea Res II 49:1513–1526

Chapter 5
Observations of Internal Tides in the Southern Ocean

Abstract This chapter describes the measurements of internal tides in the Southern Ocean. The generation of internal tides is associated with the interaction of the currents of the barotropic tide with the slopes of the bottom topography. One of the most important ideas presented here is the strong generation of internal tides over submarine ridges. There are not so many field measurements in the Southern Ocean as in the other oceans. Only the Drake Passage is well covered with measurements. No strong generators of internal tides exist here. Measurements of internal tides on mooring clusters confirm the well known fact that internal tides are generated over the bottom slopes. Some of the regions of field measurements are located south of the critical latitude (74° 30′S) so that semidiurnal internal tides rapidly decay with the distance from the bottom slopes.

5.1 Drake Passage

Clusters of moorings were deployed in the Drake Passage in 1977 and 1979. The study site was located between the Antarctic Peninsula and Tierra del Fuego Island. The experiment was organized by the Texas A&M University and Oregon State University. The Shackleton Ridge crosses the passage as a sill. In addition to the Shackleton Ridge many other elevations are located in the strait. A chart of the region with locations of moorings is shown in Fig. 5.1.

The measurements were carried out in the Antarctic Circumpolar Current in the zone of high velocities. Spectral functions reveal intense oscillations at the semidiurnal frequency. The amplitudes of internal tides at a depth of 500 m were 30 m and at a depth of 1000 m they were as high as 50 m. Two versions of spatiotemporal spectra were calculated from the data in 1977 (five moorings with temperature meters at 1000 m) and in 1979 (eight moorings with temperature measurements at 500 m). The horizontal scale of the mooring cluster in 1977 was smaller than the wavelength; thus the peak appeared very wide.

The estimates of the spatiotemporal spectrum at the semidiurnal frequency calculated from the data in 1977 and 1979 agree. The maximum on the spatiotemporal

Fig. 5.1 Bottom topography in the study site in the Drake Passage and locations of moorings in 1976–1977 (stars); 1977–1978 (diamonds); 1978–1979 (dots); and 1979–1980 (triangles). Depth contour lines are shown with an interval of 1000 m. The moorings used to calculate spatiotemporal spectra in 1977–1978 and 1979–1980 are shown with a white dot in the middle
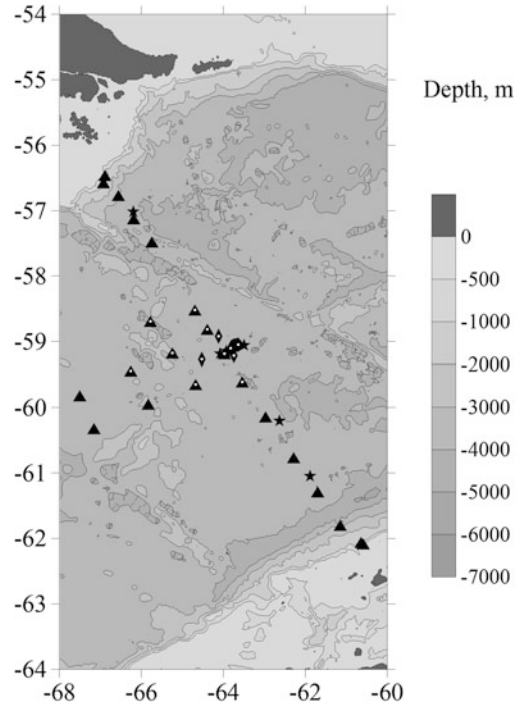
spectrum in 1977 is wider than in 1979 (Figs. 5.2 and 5.3). The characteristic scale of the mooring cluster in 1977 was 90 km and in 1979 it was larger (180 km). The peaks of the spatiotemporal spectra in 1977 and 1979 are closely located. Two peaks are seen on the spectrum in 1979 corresponding to the waves generated over the slopes of the Shackleton Ridge (the wave direction was 170° and the wavelength was 120 km) and to the waves generated at a submarine elevation southwest of the study site (the wave direction was 40° and the wavelength was 110 km).

An attempt to detect the internal tides in the Drake Passage using combinations of bottom pressure recorders and inverted echo sounders was described by Heywood et al. (2007). The bottom pressure recorders measured the barotropic tide; the inverted echo sounders measured the sea level (barotropic tide) and internal sound speed (internal tide). The authors separated the internal tide by subtracting one from the other. The measured amplitudes of internal tides ranged from 20 m in the southern part of the Drake Passage to 70 m in its northern part.

5.2 South of New Zealand, East of the Macquarie Ridge

Moored measurements were conducted in January 1983 in the Pacific sector of the Southern Ocean south of New Zealand and east of the Macquarie submarine ridge from the Russian R/V *Dmitry Mendeleev* (Morozov et al. 1985). The mooring array
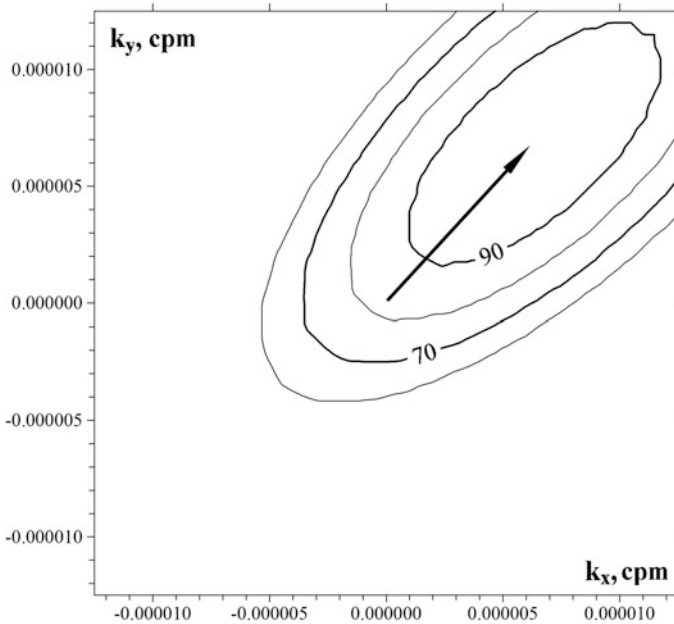
Fig. 5.2 Spatiotemporal spectrum at the semidiurnal frequency in the study site in the Drake Passage in 1977 based on the data at a depth of 1000 m. The contour lines correspond to 90, 80, 70, and 60% of the main maximum. The arrow shows the wave vector

was located among various forms of bottom topography. The mooring site was located 400 km east of the Macquarie Ridge. The moorings were deployed in a line north of the South Pacific Ridge (Fig. 5.4).

The measurements were carried out in the region of strong flows of the Antarctic Circumpolar Current. Spectral functions are characterized by significant peaks at the semidiurnal frequency. The amplitudes of the semidiurnal internal tides at a depth of 400 m were 15–20 m. Several versions of the spatiotemporal spectra were calculated over the time interval of measurements that covered 20 days. The estimates of spatiotemporal spectra show that the main wave system propagated from the northwest of the mooring cluster. It is likely that it was generated over the slopes of the Macquarie Ridge. The direction of the waves was 120°. The wavelength was 97 km. These waves were relatively stable and can be seen as peaks in all calculated spatiotemporal spectra. In some calculations one can see a weak wave propagating from the south Pacific Ridge. The spatiotemporal spectrum is shown in Fig. 5.5.

The direction of the wave can be also estimated from the cross-analysis of velocity components assuming that the currents of the barotropic tide are small. If the measurements of currents at several depths are available, it is possible to exclude the currents of the barotropic tide by filtration and vertical averaging (see Sect. 7.5). The wave direction can be derived from the major and minor axes of the tidal ellipses of semidiurnal oscillations. This method has been developed by
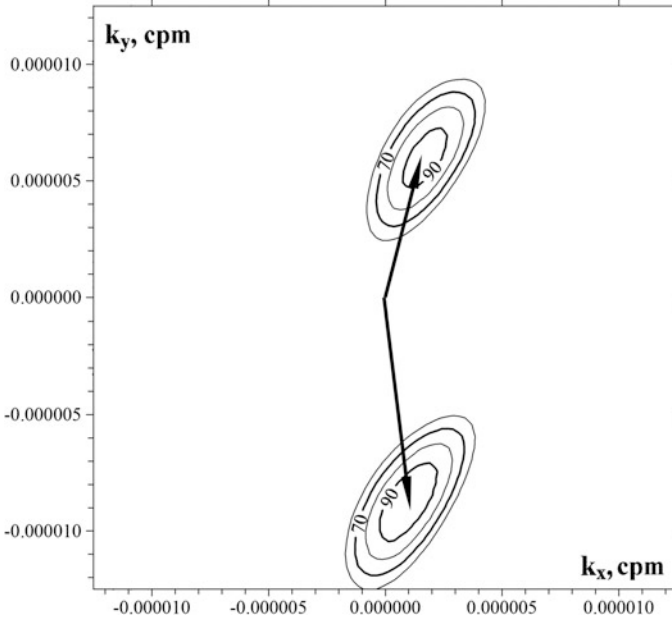
Fig. 5.3 Spatiotemporal spectrum at the semidiurnal frequency in the study site in the Drake Passage in 1979 based on the data at a depth of 500 m. The contour lines correspond to 90, 80, 70, and 60% of the main maximum. The arrows show the wave vectors

Fofonoff (1969). It allows us to determine the wave direction to an accuracy to 180°, and then determine the direction of the wave from the physical sense. The calculation was performed using the following formula:

$$\Theta = \frac{1}{2} arctg \frac{2Co_{uv}}{S_{vv} - S_{uu}}, \tag{5.1}$$

where Co_{uv} is cospectrum of the velocity components u and v; S_{uu} and S_{vv} are their spectra. The formula is based on the orientation of the main axes of tidal currents. The estimates from the data of velocities using this formula result in a wave direction close to 120°, which agrees with the previous result that internal tides were generated in the region of the Macquarie Ridge.

5.3 PRIZM Experiment, Ross Sea

Mooring clusters were deployed by Oregon State University in 1983–1987 in the Ross Sea close to 78°S, which is beyond the critical latitudes for the M_2 internal tide. The moorings were generally deployed in a line along the 78°S crossing a significant part of the Ross Sea. The depths of the sea at the locations are within
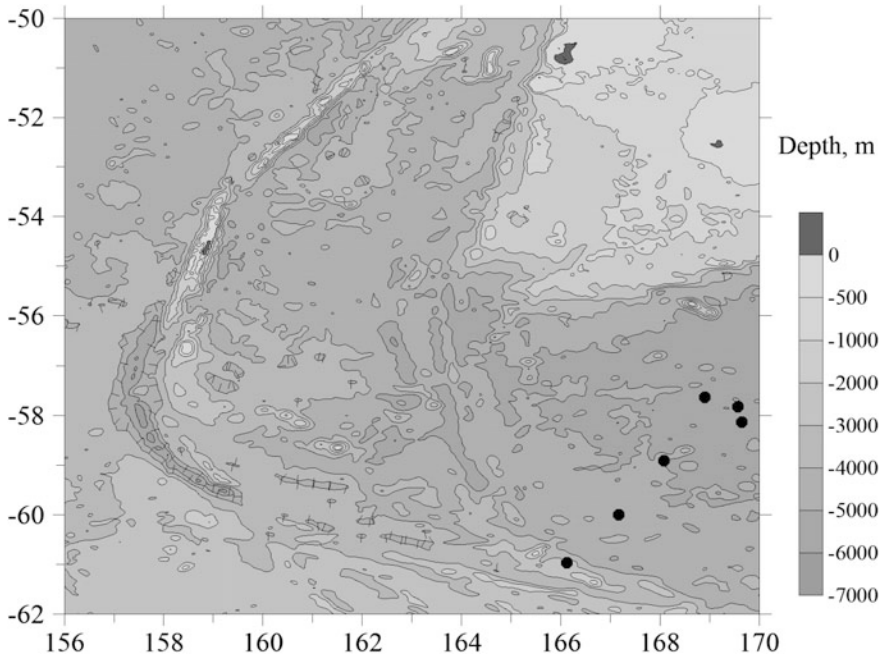
Fig. 5.4 Bottom topography south of New Zealand. The moorings are shown with black dots. Depth contour lines are shown at depths of 500, 1000, 2000, 3000, 4000, and 5000 m. Land and islands are shown with gray color

500–700 m. Two-three instruments were set on each mooring at depths of 175–400 m. Some of the instruments were set closer to the bottom. Stratification in the Ross Sea is weak. The amplitudes of the semidiurnal internal tides at depths of 170–250 m were 15–20 m on all moorings in the region.

Model simulations using the ROMS model reported by Robertson (2005a) indicate that the M_2 internal tides exist only over steep topography. Model simulations are supported by measurements on moorings, which did not reveal strong baroclinic tides even over steep slopes.

5.4 Antarctic Slope, Cape Adare

In 2003–2005 during the AnSlope experiment, a cluster of moorings was deployed on the Antarctic slope east of Cape Adare at 72° 00′S, 172° 00′E. The experiment was organized by the Lamont-Doherty Earth Observatory of Columbia University, Texas A&M University, and Oregon State University. The depth in the site of measurements varied from 500 to 1750 m. Intense semidiurnal internal tides were recorded at depths of 270–280 m with amplitudes exceeding 70 m.
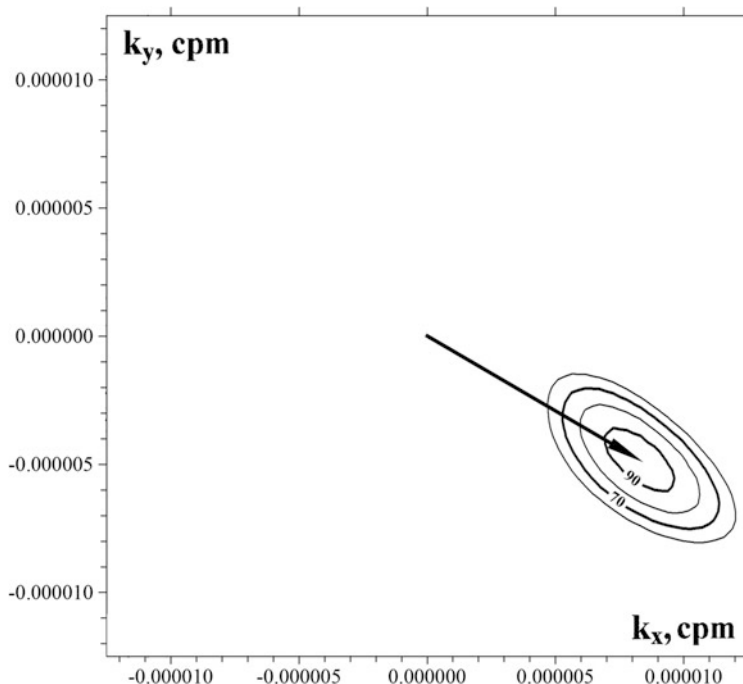
Fig. 5.5 Spatiotemporal spectrum at the semidiurnal frequency in the study site south of New Zealand in January 1983 at 200 m. The contour lines correspond to 90, 80, 70, and 60% of the main maximum. The arrow shows the wave vector

5.5 Greenwich Meridian, Bouvet Island, WOCE SCM-2 Experiment

Many moorings were deployed in 1986–2000 in the Southern Ocean close to the Greenwich meridian to study the Antarctic Circumpolar Current dynamics and the Polar Front (experiments SCM2 and PF). The experiment was organized by the Alfred Wegener Institute, Germany. Bouvet Island is located in this region (55°S, 4°E). In the zonal band between 50°S and 60°S, the amplitudes of the semidiurnal internal tides in the depth layer 400–800 m were in the range between 15 and 25 m. The exclusion is mooring AWI-228 (57° 00′S, 0° 01′E) with the instruments at 449 and 810 m, where the amplitudes reached 40 m. However, a submarine hill was located in this region up to 1000 m over the bottom at 4700 m. The ocean depth at the location of the mooring is 3900 m. Internal tides could be generated over the slopes of this hill.

Southern moorings (AWI-227, 59°S, 0° 05′E) recorded amplitudes reaching 30 m. The amplitudes recorded by the thermistor chains on the moorings located closer to the continent (AWI-229, 64°S, 0° 02′E, depths 490 and 725 m; AWI 230 66°S, 0° 02′E, depth 484 m) ranged within 10–20 m. The moorings at the bottom

of the continental slope (AWI-232, AWI-233) recorded amplitudes up to 30 m at a depth of 773 m.

5.6 Southwest of Tasmania, WOCE SCM-3 and SAZ Experiments

The WOCE SCM-3 experiment was conducted in 1993–2009. A cluster of four moorings was deployed southwest of Tasmania in the region 51°S, 144°E. In 1997–1999, four moorings were deployed approximately in this region during the Sub-Antarctic Zone (SAZ) experiment at 46° 26′S, 142° 04′E; 53° 45′S, 141° 45′E; 51° 00′S, 141° 45′E; 44° 47′S, 145° 38′E. The experiment was organized by the Antarctic Climate and Ecosystems Cooperative Research Centre and CSIRO Marine Research Department (Australia). The amplitudes of the semidiurnal internal tides at depths of 800–1000 m were within 20–25 m on all moorings in the region.

5.7 Southeast of the Crozet Islands, WOCE SCM-6, Antarctic Deep Outflow Experiment

In 1993–1994 during the WOCE SCM-6 Antarctic Deep Outflow Experiment (ADOX), a line of eight moorings was deployed south of the Crozet Islands in the southeastern direction at approximately 48°S, 66°E. The experiment was organized by the Centre for Environment, Fisheries and Aquaculture Science (UK). The line of moorings crossed a deep depression with depths up to 4400 m and reached the slopes of a rise around Kerguelen Island. The ends of the line were located at 45° 26′S, 48° 00′E, and 48° 35′S, 61° 18′E. The instruments were set at depths from 300 m to the bottom. Up to seven instruments were set on each of the moorings. The amplitudes of the semidiurnal internal tides at depths of 600 m reached 70 m over the slopes of the plateau with a depth of 1600 m. In the middle of the line, the amplitudes were 30–40 m and decreased to 25 m in the basin in the western part of the mooring line.

5.8 Weddell Sea, WOCE SCM-7 Experiment

In 1989–1995, several moorings were deployed by the Alfred Wegener Institute in the Weddell Sea. Most of the moorings were deployed in a line from the Neumayer Antarctic Station to the northwest (Fig. 5.6). The amplitudes of the internal tides were not reliably estimated owing to the low temperature gradient in the region.

However the estimates seem more or less reasonable. They ranged from 70 m near the continental slope to 10 m in the middle of the sea. A decrease in the amplitudes was observed over a distance of 200 km from the continental slope based on the measurements on the AWI moorings 204, 205, 211, and 210 from 70° 56′S, 11° 57′ W to 69° 39′N, 15° 44′W with the instruments in the depth range 700–1000 m (Fig. 5.7). In the deeper waters, the vertical temperature gradient was very low, which caused greater errors in the determination of the amplitudes.

Several moorings were deployed in the southern part of the Weddell Sea at depths of 600–700 m (moorings FR-1–FR-6). They were located between longitudes 31°W and 61°W. The instruments at depths of 200–300 m recorded the amplitudes in the range 15–20 m.

Measurements of high-frequency internal waves were carried out from ice in the western part of the sea over the continental slope. The ice station drifted about 600 km in January–June, 1992 northward from 52°W, 71° 30′S to 52°W, 66°S. However, the signal of internal tide was very low as reported by Levine et al. (1997).

Internal tides in the Weddell Sea were studied using the ROMS numerical model by Robertson (2005b). The simulations show that the M_2 internal tides south of the critical latitude 74° 28′S exist only over steep underwater slopes (Robertson 2001). North of the critical latitude (60° 57′S along 40°W) the internal tides propagated from the slopes as beams. The wavelength (distance between reflections of beams) was 60–80 km. According to the model simulation the direction of the propagation of M_2 internal tides turns to zonal as the waves approach the critical latitude.
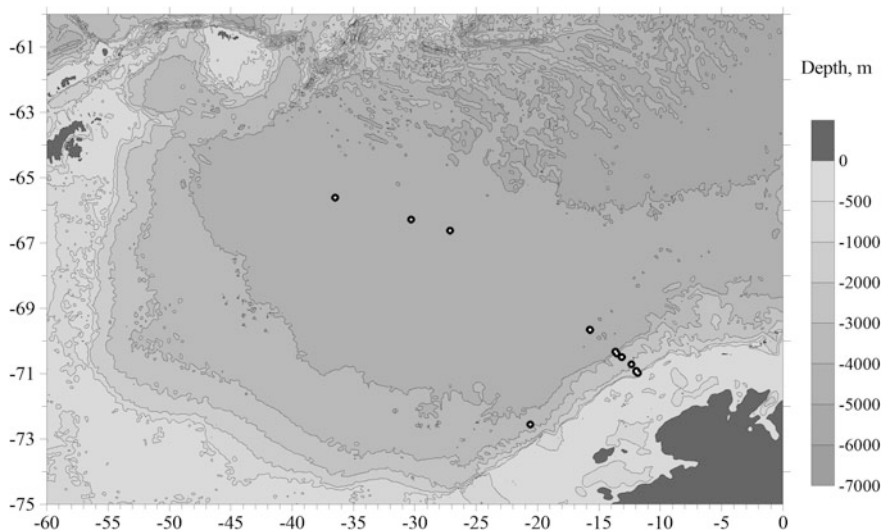
Fig. 5.6 Bottom topography in the Weddell Sea and locations of moorings. Depth contour lines are shown at depths of 500, 1000, 2000, 3000, 4000, 5000, and 6000 m. Locations of moorings are shown by black dots with a white circle in the middle. Land and islands are shown with gray color
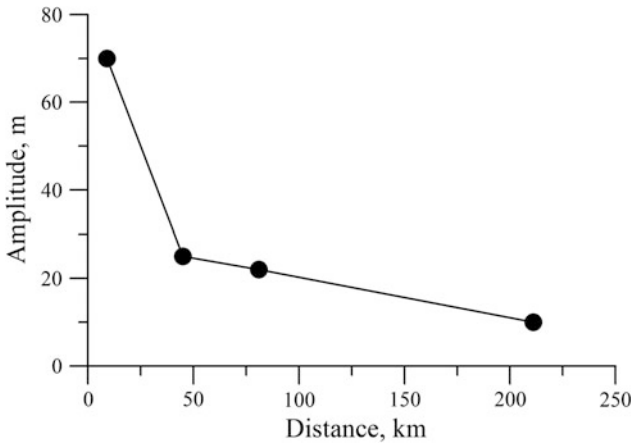
Fig. 5.7 Decay of the semidiurnal internal wave amplitudes over the continental slope of Antarctica in the northwestern direction from the coast

5.9   Prince Edward Islands

In 1993–1995, a line of five moorings was deployed north of the Prince Edward Islands. The WOCE SCM-9 Southwest Indian Ocean Experiment (SWINDEX) was organized by the Southampton Oceanographic Centre.

The eastern group of moorings was deployed on a deep plateau at depths of 1600–2800 m at 45° 25′S, 47° 50′E, 44° 44′S, 45° 44′E, 44° 33′S, 41° 19′E. Two western moorings were deployed at 43° 23′S, 36° 04′E and 41° 51′S, 32° 50′E in a deep basin at depths of 4200–5900 m. The amplitudes of internal tides did not exceed 20 m.

5.10   Antarctic Slope, SOGLOBEC Experiment West of the Antarctic Peninsula

In 2001–2003, the SOGLOBEC experiment was performed at 67°S, 70°W. The experiment was organized by the Woods Hole Oceanographic Institution (USA). Five moorings operated in 2001–2002 and three more in 2002–2003 west of the Antarctic Peninsula on the Antarctic shelf. Ten velocity and temperature meters were set on each mooring. The amplitudes of semidiurnal internal tides were within 10–15 m.

5.11   Ridge Experiment, Campbell Plateau

The Ridge experiment was conducted in 1978. Five moorings were deployed east of the Campbell Plateau at depths greater than 5000 m in the region with coordinates 49° 40′S, 170° 00′W and one mooring was deployed on the plateau at a depth

of 1090 m at 51° 10′S, 175° 00′E. The experiment was organized by the Woods Hole Oceanographic Institution (USA). The amplitudes of the semidiurnal internal tides east of the Campbell Plateau at depths of 1000 m were 20–25 m on all moorings in the region. The amplitudes of the internal tides on the mooring on the Campbell Plateau reached 40 m at a depth of 300 m.

5.12   South Orkney Islands

One mooring was deployed southwest of the South Orkney Islands in 1989–1990 and repeated in 1993–1995 at 63° 29′S, 52° 06′W. The experiment was organized by the Alfred Wegener Institute (Germany). The depth of the ocean was 950 m. The amplitudes of the semidiurnal internal tides at depths of 230 and 280 m were 20–25 m.

5.13   South Sandwich Islands

A mooring was deployed in 1989–1990 south of the South Sandwich Islands at 66°36′S, 27° 07′W. The experiment was organized by the Alfred Wegener Institute. The depth of the ocean at the location of the mooring was 4863 m. The amplitudes of semidiurnal internal tides at depths of 293 and 993 m were 20–30 m.

References

Fofonoff NP (1969) Spectral characteristics of internal waves in the ocean. Deep-Sea Res 16:58–71

Heywood KJ, Collins JL, Hughes CW, Vassie I (2007) On the detectability of internal tides in Drake Passage. Deep-Sea Res 54(11):1972–1984

Levine MD, Padman L, Muench RD, Morison JH (1997) Internal waves and tides in the western Weddell Sea: Observations from Ice Station Weddell. J Geophys Res 102(C1):1073–1089

Morozov EG, Nikitin SV, Shapovalov SM (1985) Mesoscale variability of the ocean based on moored measurements in the New Zealand region of the Southern Ocean. Oceanol Res 39:53–64

Robertson R (2001) Internal tides and baroclinicity in the southern Weddell Sea 2. Effects of the critical latitude and stratification. J Geophys Res 106(C11):27017–27034

Robertson R (2005a) Baroclinic and barotropic tides in the Ross Sea. Antarct Sci 17(1):107–120

Robertson R (2005b) Baroclinic and barotropic tides in the Weddell Sea. Antarct Sci 17(3):461–474

Chapter 6
Observations of Internal Tides
in the Arctic Ocean

Abstract This chapter describes the measurements of internal tides in the Arctic Ocean. Most of the regions of field measurements are located north of the critical latitude (74° 30′N) so that semidiurnal internal tides rapidly decay with the distance from the bottom slopes. The generation of internal tides is associated with the interaction of the currents of the barotropic tide with the slopes of the bottom topography. One of the most important ideas presented here is the strong generation of internal tides over submarine ridges. The chapter begins with general notes on internal tides in the Arctic region whose major part in located north of the critical latitude. Measurements of internal tides on mooring clusters confirm the well known fact that internal tides are generated over the bottom slopes. Internal tides rapidly decay with the distance from submarine slopes (74° 30′N). Strong generation of internal tides was found in the Strait of Kara Gates between the Barents and Kara seas. The existence of permanent polynyas in the Laptev Sea is associated with internal tides over the continental shelf. Properties of internal tides measured near the North Pole are described.

6.1 General Notes

Internal tides transform the velocity field of the barotropic tide so that relatively low tidal velocities form a velocity field with higher horizontal velocities and amplitudes of the vertical displacements confined to the regions of sharp changes in the bottom topography.

It is known that internal tide in the ocean is generated when tidal currents overflow submarine slopes. Vertical components of the tidal currents periodically displace isopycnals. The most energetic component of internal tide is generally the component corresponding to the barotropic tide M_2 with a period of 12.4 h. Many properties of internal tides depend on latitude. We shall show this with the example of a well-known equation for the vertical velocities associated with internal waves (Le Blond and Mysak 1978) (see Sect. 1.4.3):

$$\frac{d^2w}{dz^2} + \frac{N^2(z)}{g}\frac{dw}{dz} + \frac{N^2(z) - \omega^2}{\omega^2 - f^2}k^2w = 0. \qquad (6.1)$$

This is an equation with the boundary conditions for the vertical velocity, which we assume zero at the surface and bottom. Here, k is the wavenumber. The denominator in the third term of this equation is important for the problems we discuss here. As the latitude increases the difference between the M_2 tidal frequency and the Coriolis parameter decreases. At a latitude of approximately $\varphi = 74° 30'$, this difference becomes equal to zero, which excludes oscillatory solutions of the equation. This is true if we assume some simplifications, for example, a flat bottom.

Thus, latitudes close to $74° 30'$ are critical for the internal tides with a period of 12.4 h (M_2 frequency). However, other waves with the semidiurnal frequency can exist, for example Kelvin waves (Støilen 2014). A special case when the tidal frequency is smaller than the Coriolis frequency due to the low stratification in the Arctic region was considered by Falahat and Nycander (2015).

Free internal tides generally cannot exist north of the critical latitude ($74° 30'$) in the Arctic region over a flat bottom. However, the generation process of internal tides at the northern latitudes does not differ from the process at low and mid-latitudes. Namely, the currents of the barotropic tide flow over submarine slopes and periodically displace the isopycnals due to the existence of vertical components of tidal currents over slopes (Baines 1982; Konyaev and Sabinin 1992). The differences are related to the fact that in the region of supercritical latitudes the internal tide is a forced wave and cannot freely propagate from the slope as it does at lower latitudes.

Reports of field observations of internal tides in the Arctic are not numerous. Probably the first results of measurements of internal tides in the Arctic region close to the critical latitudes were published by Nansen (1902) and later by Zubov (1932). In the well-known monograph by Krauss (1966) the measurements over several days from an anchored ship at a station in the Barents Sea show an example of the existence of internal tides north of $75°$ N.

Despite the fact that it is impossible to explain the existence of the semidiurnal internal tide of the M_2 period (12.4 h) at polar latitudes north of $74° 30'$N within the linear theory of internal waves in the ocean of constant depth (Krauss 1966), internal waves of the M_2 period exist in the Arctic Ocean and can be observed in field studies. Reports on the existence of semidiurnal fluctuations of temperature, and salinity beyond the critical latitudes in the Arctic were given in Bannov-Baikov et al. (1989), Parsons et al. (1996), Plueddemann (1992), Levine et al. (1985), Pisarev (1996), Sabinin and Stanovoi (2002) and in the Weddell Sea by Robertson (2001). The measurements from an autonomous drifting buoy over the Nansen Basin, Yermak Plateau, and Greenland Sea in 1987–1988 yielded much data on the semidiurnal tides close to the critical latitudes (Padman et al. 1992; Plueddemann et al. 1998). In particular, this drift revealed spatially localized bursts of semidiurnal internal tides over sharp bottom elevations over the Yermak Plateau. An interpretation was suggested that diurnal barotropic tide provides negative (anticyclonic)

vorticity; thus, the location of the critical latitude changes and conditions are formed for the existence of the semidiurnal internal tide. The latter is generated by the semidiurnal barotropic tide over the bottom (Konyaev 2000).

If we consider not only free progressive internal gravity waves, we note that semidiurnal oscillations with the tidal periods can be determined by other processes, for example, internal coastal trapped waves (Allen 1975). The existence of such waves is not restricted by critical latitudes for the M_2 internal tide (north of 74° 30′ latitude). If the measurements are carried out only at one point (as frequently occurs in the severe Arctic conditions) it is impossible to identify and differentiate waves of different origin. The frequency of such waves is close to the semidiurnal and inertial frequencies at high latitudes.

A decrease in the effective Coriolis frequency is one of the possible mechanisms that make possible the existence of free semidiurnal internal tides of the M_2 period. This decrease can appear due to background negative (anticyclonic) vorticity. If the effective Coriolis frequency becomes smaller than the M_2 tidal frequency, the existence of internal tides north of the theoretical critical latitude becomes possible. It was shown by Kozubskaya et al. (1999) that negative vorticity up to 5.5×10^{-6} s^{-1} observed in the ocean can shift the efficient critical latitude up to the latitude of Spitsbergen (78° N).

One of the possible mechanisms for the generation of short-period internal wave packets is resonance. When the M_2 barotropic tide frequency is close to the local inertial frequency the resonance effect can induce energy transfer from the barotropic tide to the inertial oscillations. Instability can appear under specific conditions that will lead to the generation of short-period internal wave trains with a periodicity close to the tidal period, which is close to the inertial period.

It was shown by Vlasenko et al. (2003) that at high latitudes nonlinearity should be high to allow the generation of internal waves, otherwise nonlinear effects are suppressed by rotation. In the region of critical latitudes, the wavelength of internal tides and correspondingly the phase speed tend to infinity. However, elevations of isopycnals induced by the tidal currents overflowing the slopes can be significant and instability conditions of forced internal waves can appear. Since the existence of internal tide is prohibited, internal waves can break into packets of shorter internal waves, which have no restrictions on their existence.

Investigations by Furevik and Foldvik (1996) based on the moored current meters and 800 CTD stations in the Barents Sea between 70° N and 79° N reveal a stability minimum in the central part of the Barents Sea. The authors attribute this minimum to the enhanced tidal mixing near the critical latitude due to the breaking of internal tides.

A nonlinear model was suggested by Vlasenko et al. (2003), which allows the existence of internal tides at high latitudes. They do not introduce negative vorticity, but form a strong nonlinear baroclinic response of the ocean to the tidal perturbations. A dome-shaped elevation of the pycnocline is formed over a slope under the forcing of tidal currents. This elevation breaks, and two packets of progressive short-period waves are generated, which propagate in opposite directions. The wave form is significantly different from the sinusoidal one.

Semidiurnal internal tides are frequently observed over underwater slopes. Pisarev (1988, 1991, 1992), Kurkina and Talipova (2011) showed that semidiurnal oscillations are observed in the Arctic regions over underwater slopes, while only packets of short-period waves are observed far from the slopes over a relatively flat bottom. This is confirmed by a model presented by Kurkina and Talipova (2011) and by observations reported by Morozov and Paka (2010). D'Asaro and Morison (1992) found high shear over rough topography in the Fram Strait and Nansen Basin and attribute this fact to the generation of internal tide over underwater slopes.

Before presenting the results of simulations of internal tides in the Arctic seas let us consider the simulations of internal tides with variable input parameters. In order to do this, we use a numerical model developed by Vlasenko (see Sect. 1.4.1) (Vlasenko 1992; Vlasenko et al. 2002b, 2005).

Let us consider the results of modeling internal waves in the region of the Arctic shelf and discuss the numerical experiments with varying parameters reported by Morozov and Pisarev (2002). We shall choose certain basic parameters and change the parameters comparing the new solution with the basic solution. Let us specify a characteristic strong stratification corresponding to a warm and freshened upper layer with density $\sigma_t = 23.5$ and denser water at the bottom ($\sigma_t = 27.5$) with a sharp density interface at a depth of 10 m corresponding to the Brunt–Väisälä frequency $N = 0.06$ cycle/s. Such density values can appear when the values of temperature and salinity at the surface are equal to 7 °C and 30 psu, respectively, and the corresponding values at the bottom are equal to 1 °C and 34 psu, respectively. The tidal flow was specified so that the altitude of the surface elevation at the coast was equal to 1 m. The density contour lines obtained in the model calculation after eight periods of semidiurnal oscillations are shown in Fig. 6.1.

An analysis of the vertical structure of the generated waves shows that the vertical motion of water particles occurs in-phase, while the largest deviations of the isopycnals occur in the vicinity of the sharp pycnocline and near the sharp deepening of the bottom, where they can reach 10 m. In this numerical experiment, the latitude of the region was equal to 70° N (Fig. 6.1a).

We performed calculations of the perturbations of the density field by internal waves at the same parameters but at latitudes 5°, 40°, and 60°. The corresponding graphs are shown in Fig. 6.1b–d. The regions at 5°, 40°, and 60° are not close to the critical latitude; therefore, intense internal tides are developed here, which propagate from the slope with a lesser decay. Let us consider however, the results of the comparison. A clearly pronounced wave with a wavelength close to 25 km and a sharp wave front, which can lead to the generation of short-period wave packets, is seen at a latitude of 5°. A similar pattern is observed at a latitude of 40°, but the wavelength is somewhat greater: 27–28 km. The effect of the proximity to the critical latitude is seen already at a latitude of 60°, the wave is distinguishable and its wavelength exceeds 30 km. At a latitude of 70°, which is close to the critical latitude, the fluctuations practically do not propagate from the slope.

In the next step we shall consider the dependence of internal tide generation on stratification. Above, we considered internal tides generated in a strongly stratified
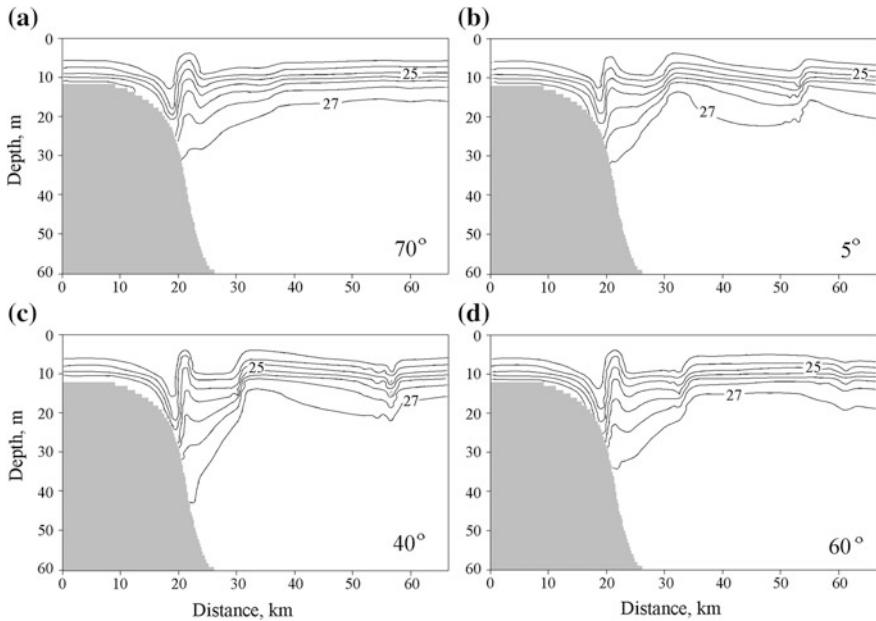
Fig. 6.1 Field of the isopycnal surfaces at different latitudes (all other parameters are the same). The slope of the bottom is 3×10^{-3}, and the Brunt–Väisälä frequency at the depth of the density interface is equal to 6×10^{-3} cps: **a** latitude 70°, **b** latitude 5°, **c** latitude 40°, and **d** latitude 60°. Reproduced from Morozov and Pisarev (2002) ©Pleiades Publishing, Ltd. Used with permission

water column in summer. The upper low saline water layer was formed due to the freshwater discharge from rivers or ice melting. The other extreme case of the summer stratification is a water layer with almost uniform salinity due to the lack of freshwater from rivers, so that the stratification is almost completely determined by temperature. In summer, the surface temperature can be as high as 7 °C, while at the bottom the temperature is close to 1 °C. If water salinity is 34 psu the corresponding density at the surface would be equal to 26.5 and increase to the bottom up to 27.5. The Brunt–Väisälä frequency at this density profile would be equal to 0.03 cps at a depth of 10 m.

In the case of weak stratification, the amplitude of fluctuations over the slope is approximately two times greater; at the interface, it is equal to 20 m. This can be easily explained, because at lesser stratification, the resistance of the buoyancy forces to the vertical displacement of the isopycnal surfaces caused by the currents of the barotropic tide becomes smaller. Let us now consider the form of the characteristic lines for internal waves in the case of different stratification.

Let us analyze how the conditions of internal tide generation would differ in these two cases. The results of calculations of the density field in the cases of strong and weak stratifications are shown in Fig. 6.2 for the locations at a latitude of 70°.

In the case of weak stratification the amplitudes of internal tide over the slope are approximately two times greater than in the case of strong stratification.

Let us consider the form of characteristic curves for internal tides at different stratifications. The curve of the characteristic line is determined by Eq. (6.2).

$$\frac{dz}{dx} = \pm\left(\frac{\omega^2 - f^2}{N^2 - \omega^2}\right)^{1/2}. \tag{6.2}$$

The characteristic curves for the bottom slope between 12 and 60 m over a length of 15 km are shown in Fig. 6.3 (the inclination of the slope is equal to 3×10^{-3}).

Lines 1 and 2 show the characteristic curves. A smaller inclination of the curve corresponds to strong stratification (the corresponding wavelength is greater than in the case of weak stratification); a greater inclination corresponds to weak stratification. The calculation was carried out for a latitude of 70°. In order to show the influence of the critical latitude, a characteristic curve for latitude 75.2° is drawn in the upper part of Fig. 6.3. It goes beyond the scale of the figure and reaches the bottom edge at a distance of approximately 400 km, which at this latitude corresponds to half of the wavelength scale.

The motion of the water particles caused by the internal waves occurs along the characteristic lines. The vector of the group velocity is also directed along these lines. Characteristic lines go from the surface to the bottom and reflect from them. One full horizontal distance between two contacts with the bottom or with the surface corresponds to the scale of the internal wavelength. When an ensemble of internal perturbations is generated, bundles of characteristic lines start from the irregularities of the bottom topography. An ensemble of such beamlike
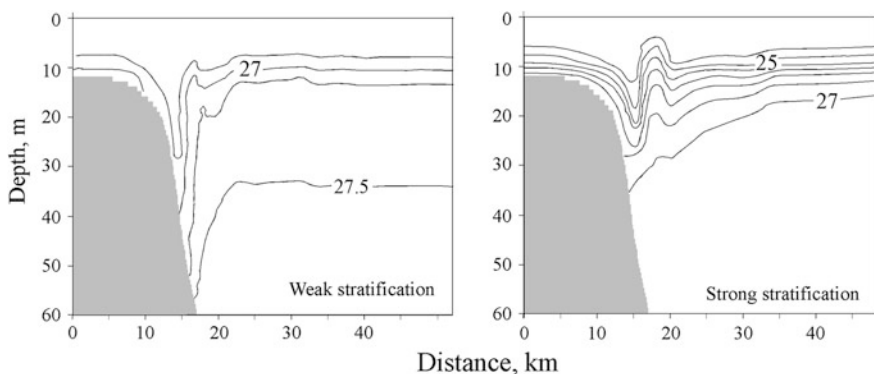
Fig. 6.2 Field of the isopycnal surfaces at two typical stratifications (the remaining characteristics are the same). Weak summer stratification (left panel), the Brunt–Väisälä frequency at the density interface is 3×10^{-3} cps and strong summer stratification, the Brunt–Väisälä frequency (right panel) is 6×10^{-3} cps. Reproduced from Morozov and Pisarev (2002) ©Pleiades Publishing, Ltd. Used with permission
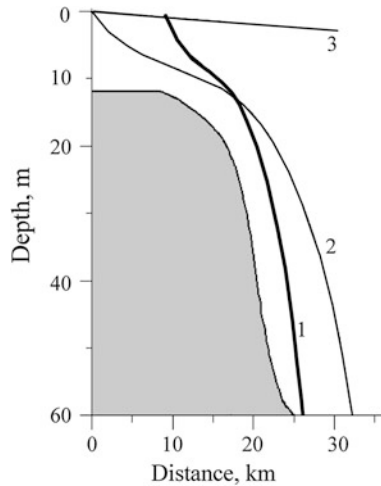
Fig. 6.3 Comparison of the inclination of the characteristic lines determined by Eq. 6.2 and the bottom slope. Sharply deepening characteristic line 1 corresponds to weak summer stratification. Line 2, which does not deepen so sharply, corresponds to strong summer stratification (latitude 70°). Line 3 corresponds to latitude 75.2°. The bottom slope is shown with gray color. Reproduced from Morozov and Pisarev (2002) ©Pleiades Publishing, Ltd. Used with permission

perturbations is generated over an uneven slope with a large number of sources. The vertical components of the wave vectors of perturbations propagating downward and upward compensate each other; thus, a standing wave by vertical or mode is formed.

It is seen in Fig. 6.3 that in the case of weak summer stratification, the slope of the bottom is close to the inclination of the characteristic line. Thus, the direction of the barotropic tidal currents along the slope is close to the natural inclination of the particle motion in an internal wave, which corresponds to the case of intense generation of oscillations.

Let us now consider the influence of the bottom slope on the generation of oscillations in the case of weak summer stratification. As can be seen from the previous figure showing the inclination of the characteristic lines, the bottom slope equal to 3×10^{-3} almost coincides with the inclination of the curve. In this case, intense generation of oscillations occurs in almost the entire water column along the slope. The pattern of the displacement of the density contour lines formed in this case is shown in Fig. 6.4b. A greater mean inclination equal to 6×10^{-3} provides for even better conditions of generation (Fig. 6.4a), since here, the coincidence with the inclination of the characteristic lines (3×10^{-3}) is found in the upper part of the slope at a depth of approximately 10 m, where the stratification is stronger. Here, the energy transferred by the barotropic tidal currents to the oscillations of the isopycnal surfaces is greater. The potential energy of the oscillations is determined by the squared product of the Brunt–Väisälä frequency and the amplitude of the vertical displacements. At smaller slopes of the bottom, the generation is weaker.
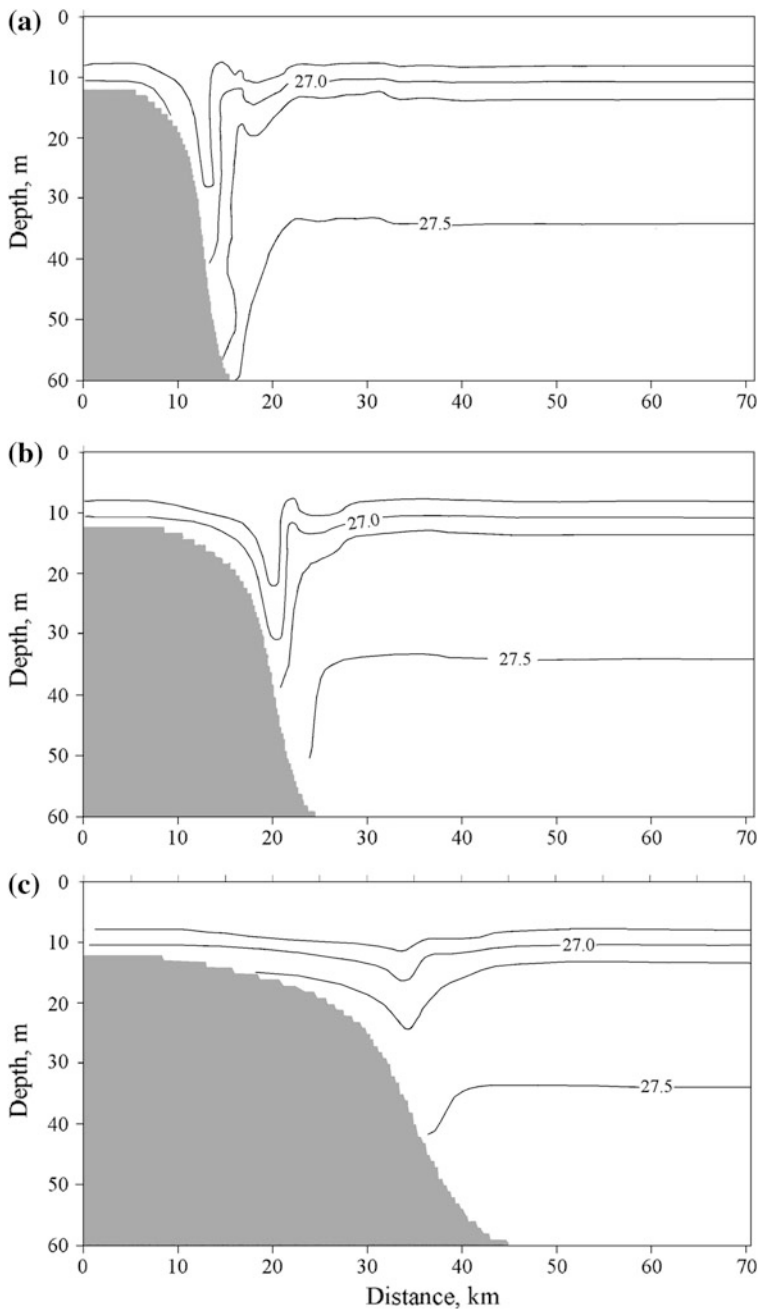
Fig. 6.4 Fields of the isopycnal surfaces at different bottom slopes (the remaining characteristics are the same). The Brunt–Väisälä frequency at the depth of the density interface is equal to 6×10^{-3} cph. The slopes of the bottom are equal to: **a** 6×10^{-3}; **b** 3×10^{-3}; **c** 1.5×10^{-3}. Reproduced from Morozov and Pisarev (2002) ©Pleiades Publishing, Ltd. Used with permission

This is shown in Fig. 6.4c, which shows the field of the isopycnal surfaces over the bottom slope equal to 1.5×10^{-3}.

Model calculations show that forced internal tide can be generated over usual bottom slopes characteristic of the study regions in the Arctic Ocean. Owing to the gentle slopes of the characteristic curves in high-latitude regions internal tides with relatively high amplitudes can be generated. Since stratification and slopes of topography are not regular the field of internal tides may have a patchy structure. The maximum amplitudes would be observed in random locations, where bottom slopes might coincide with the slopes of the characteristic curves for internal tides. In this case, the proximity of the critical latitude would play a significant role.

We also note an obvious fact: The greater the mass flux transported by the currents of the barotropic tide through a section parallel to the slope, the greater the amplitudes of the internal tide.

6.2   Internal Tides in the Arctic Seas of Russia

The objective of this section is to determine the spatial variability of the amplitudes of internal tides in the Arctic seas of Russia on the basis of the investigation of the generation, propagation, and decay of internal waves of the M_2 frequency and to plot a map of internal tide amplitudes in this region.

The geographical location of the Arctic seas on the continental shelf of Russia and beyond it at latitudes north of 70° N leads to the following physical phenomenon. It is known that the frequency range of the existence of internal waves is between the Brunt-Väisälä frequency and the inertial frequency. The latitudes of the Arctic shelf are close to the critical for the M_2 internal tide (74° 30′N). Therefore, internal tide cannot exist here as a progressive internal wave. However, internal tide should be generated over the continental shelf and exist in the vicinity of the generation region as a forced wave. The waves should break while propagating offshore and onshore.

The measurements of internal tides with temperature sensors were performed from the drifting ice in the Saint Anna Trough in 1983 and in the Franz-Victoria Trough in 1986–1989 (Pisarev 1988, 1996) at latitudes of 80°–81° N, over the depths of 200–500 m. The measurements of internal waves were accompanied by echo-sounding, CTD-profiling, and measurements of currents at several depths. Very short, spatially localized semidiurnal internal waves were recorded with a wavelength of 2000–4000 m. They propagated from the walls of the trough to the regions of the flat bottom. The amplitudes of these waves rapidly decreased with distance.

The Polar Front of the Barents Sea experiment was conducted in August 1992 east of Bear Island. Four surveys of velocity, temperature, and salinity fields over a study site 80 by 70 km were performed over 20 days. Three moorings with velocity and temperature meters at three depths were deployed for 10 days. The center of the study site was at a latitude of 74.3° N. Analysis of the data revealed the properties

of the internal tide close to the critical latitude (Kozubskaya et al. 1999). It was found that the vertically average amplitude of the semidiurnal tide currents was 3.5 cm/s; the wavelength was 200 km. The vertical structure of oscillations corresponded to the first mode. The internal tide propagated across the slope to the greater depths. The authors suggested that the internal tide generated over the slope could propagate down the slope due to the negative (anticyclonic) vorticity of the medium. In the case of positive vorticity, the internal tides cannot propagate. In the medium partly or completely closed for the internal tide, the amplitude of the wave decreased and it was subjected to significant horizontal refraction. Shorter internal waves of higher frequency were generated.

The effect of the critical behavior of internal waves should already be pronounced in the regions of the Arctic coasts of the Barents, Kara, and Laptev seas located partly south of the critical latitude. Accurate interpretation of the field data in the region of the critical latitudes can be performed using the numerical modeling approach, which will make it possible to determine the dependence of internal wave behavior on various parameters separately. It is not possible to do this using the field data, by which we obtain the non-separated influence of several factors such as latitude, stratification, slope of the bottom topography, geometry of the slope, and velocities of the barotropic tide.

We applied the numerical model developed by V. Vlasenko (see Sect. 1.4.1) (Vlasenko 1992; Vlasenko and Hutter 2002a; Morozov et al. 2003c) to study the generation and propagation of internal tidal waves in the Arctic seas. Characteristic hydrological parameters in the region were used as the input data for the model. Although the model is two-dimensional, we introduce the equation for the V-component of velocity normal to the x, z-plane to account for the effects of rotation. However, the V-component is considered constant. The internal wave is considered flat and propagating normal to the continental slope.

We specify the density field undisturbed by internal waves, which is characterized by the distribution of the Brunt–Väisälä frequency $N(z)$. A long barotropic tidal wave propagates from the open sea to the continental slope. The tidal currents flowing over the continental slope obtain a vertical component. The periodically changing vertical components of these currents stimulate vertical oscillations of isopycnal surfaces, and internal waves of the tidal period are generated due to this mechanism. Thus, the problem of calculating the parameters of the baroclinic wave perturbations is solved on the basis of specified parameters of the barotropic tide, stratification, and bottom topography. The model calculations allow us to estimate the amplitude of internal tidal waves.

In order to evaluate the 3D distribution of the amplitude, we used the approach based on the well-known strip theory (Rodden 1959). This theory is used in aerodynamics to calculate the airflow around the wing of an airplane. If the variations of properties along the transversal coordinate are significantly smaller than along the longitudinal coordinate, the study region is divided into strips with approximately equal properties across the strips and sharp changes along the strips. In our case, the strips for the study were located across the isobaths so that the entire basin of the sea was divided into strips 20–100 km wide and 100–300 km long.

Within each strip we specified the model topography of the bottom, characteristic stratification, and currents of the barotropic tide.

Water transport by the barotropic tidal currents in each zone (strip) was specified by recalculating them into the stream function. The currents of the barotropic tide were calculated from the TOPEX/POSEIDON satellite data from the NASA database at Oregon State University (USA). We used the TPXO.7.1 global inverse tidal model with the Ocean Tidal Prediction Software (OTPS) algorithm (http://volkov.oce.orst.edu/tides/otps.html; last accessed in October 2017) based on the satellite data assimilation. The model was developed on the basis of the OTIS software (Oregon State University Tidal Inversion Software Model) (Egbert and Erofeeva 2002). The ellipses of tidal currents in characteristic locations of the Arctic seas are shown in Fig. 6.5.
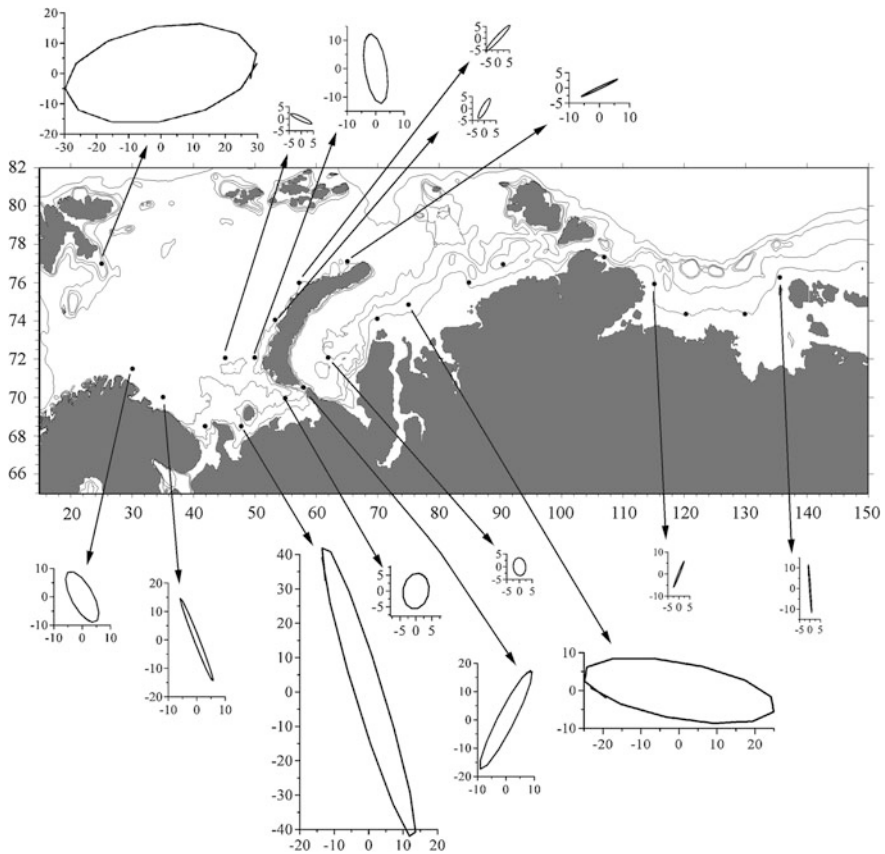
Fig. 6.5 Ellipses of the barotropic tide currents (cm/s) at some characteristic points of the Arctic seas based on the TOPEX/POSEIDON satellite data. The isobaths of 25, 50, 100, and 500 m are shown

In each of the zones for calculation, we specified the unperturbed density field by means of the Brunt–Väisälä frequency distribution. The density stratification was specified on the basis of the Russian–US Oceanographic Atlas of the Arctic Ocean (Atlas 1998). We used the climatic data averaged over approximately 50 years of observations. The sea bottom was specified on the basis of the ETOPO database (http://www.ngdc.noaa.gov/mgg/global/global.html; last accessed in October 2017).

The interaction of the barotropic tide with the bottom topography in the offshore part of the shelf is the main source of internal tide generation. The structure of the shelf and continental slope were modeled so that along the major portion of the shelf in the domain of calculation the mean depths increased smoothly from 10 to 50 m and in the seaward part the depths deepened sharply to 200 m and further.

Such shelf structure corresponds to the coastal region of the Arctic seas. The processes in the shelf zone at depths shallower than 10 m only slightly influence the structure of the open sea waters. Density stratification in the Arctic seas has a strong variation in the upper layer only up to a depth of 20 m.

In the model calculations, we used a work field 300 km long with a horizontal step of 50 m and 20 vertical levels. The time step was equal to 2 s. The coefficients of the horizontal eddy viscosity and density diffusivity were specified as 3–4 m^2 s^{-1}, and the corresponding vertical coefficients were equal to 0.0001 m^2 s^{-1}. Calculations of internal wave propagation in the Arctic basin near the critical latitude require that the rotation dispersion does not suppress the nonlinearity of the waves. Therefore, we had to choose such a small horizontal step.

After dividing the sea basin into a large number of calculation zones (strips) and using profiles of vertical density stratification and tidal currents in each of the zones, we obtained a pattern of the distribution of internal tide amplitudes in the region in the summer period. The calculations were corrected by individual measurements at moored stations in the open sea, Kara Gates Strait, near Bear Island, and near the northwestern coast of Novaya Zemlya. The analysis of the distribution of internal tide amplitudes in the Barents Sea, where we could select the coefficients of
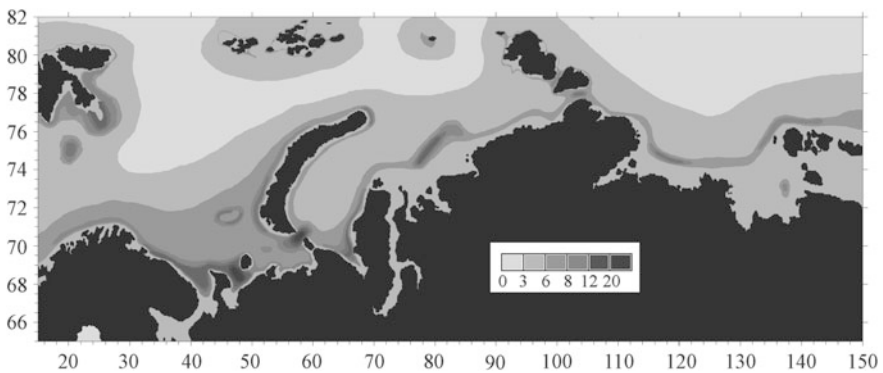
Fig. 6.6 Chart of amplitudes (meters) of internal tides in the Russian Arctic seas

viscosity based on the moored measurements was published by Morozov et al. (2003c). In the other Arctic seas east of the Barents Sea no data of moored measurements were available. Hence, we used the coefficients selected for the Barents Sea conditions. The calculated distribution in all Arctic seas is shown in Fig. 6.6. Different gray tones correspond to the amplitudes of vertical displacement associated with internal tides.

Stratification is significantly different in the summer and winter seasons. In winter, stratification is weaker; hence barotropic tide currents can generate internal tides of larger amplitudes.

A few regions with large amplitudes of internal tides were distinguished. The regions with the largest amplitudes were found in the Kara Gates Strait. Here, the depth of the sea in the fractures of the ridge crossing the strait is 120–160 m; while the wave amplitude reaches 40 m and the corresponding wave height (double amplitude or vertical displacement) is very close to the thickness of the water column from the surface to the bottom. This is an extraordinary effect observed only in some straits, for example, in the Strait of Gibraltar, where tidal currents concentrate in a narrow strait. This stimulates the intense generation of internal waves.

The amplitudes of the internal tides (about 10 m) along the northern slope of the Kola Peninsula (35–40° E) are related to the steep continental slopes along the coast and strong barotropic tide. The large amplitudes of internal tides between the Kola and Kanin peninsulas and around the Kanin Peninsula (44° E) are caused by significant currents of the barotropic tide in this region despite the fact that the continental slope is flatter than in the northern part of the Kola Peninsula.

Large amplitudes of the internal tide found in the Geese Bank (Gusinaya Banka) region (71° N, 46° E) and western coast of Novaya Zemlya are caused by the joint effect of strong barotropic currents and steep submarine slopes of the coastal shelf close to the inclination of internal tide characteristics. The large amplitudes in the northern parts of the Barents Sea over steep submarine slopes are caused by the physical mechanism of internal tide generation at supercritical latitudes, where a very steep slope is not necessary for the generation of internal tides as at southern latitudes.

Large amplitudes of the internal tide are observed in the Baydaratskaya Guba (Bay) (66° E) of the Kara Sea and northwest of the Taimyr Peninsula (78° E). This is determined by the strong currents of the barotropic tide directed normal to steep submarine slopes in these regions. Internal tides are weak in the eastern part of the Kara Sea. The amplitudes increase in the Vilkitsky Strait (102° E) and east of the Taimyr Peninsula.

Interesting results were found by comparing the chart of internal tide amplitudes and the chart of water turbidity in the surface layer based on the satellite SeaWiFS (Sea-viewing Wide Field-of-view Sensor) ocean color scanner data. A chart of water turbidity (Fig. 6.7) was constructed using a special algorithm for determining the concentration of suspension matter in the Barents Sea waters on the basis of the SeaWiFS data (Burenkov et al. 2001). A comparison of these charts shows similar features in the distribution of internal tide amplitudes and suspension matter concentration in shallow waters. The correlation between the internal tide amplitudes

with water turbidity at shallow depths is explained by the fact that strong bottom
currents induced by the internal waves facilitate the stirring up of bottom sediments
and their mixing in the entire water column (Gjevik et al. 1994). The general
features, which are clearly seen on the chart, are increased turbidity in the region of
the Kanin Peninsula, where the currents of the barotropic tide and the amplitudes of
the internal tide are large. In the shallow water regions close to the strait connecting
the Barents and White seas (Gorlo Strait) increased turbidity is caused only by the
strong currents of the barotropic tide over the shallow depths of the strait. The eigen
function for the horizontal velocities in the internal tides has maxima at the bottom
and at the surface; therefore, internal waves should cause relatively high bottom
currents over the shelf, thus increasing turbidity that raises suspended particles from
the bottom, which is seen in the satellite images of the shallow sea.

  Near the Kara Gates Strait the turbidity is high. However, the strait was covered
with ice at the time of the research and we could not get satellite data on turbidity.
High turbidity is also observed along the northwestern coast of Novaya Zemlya
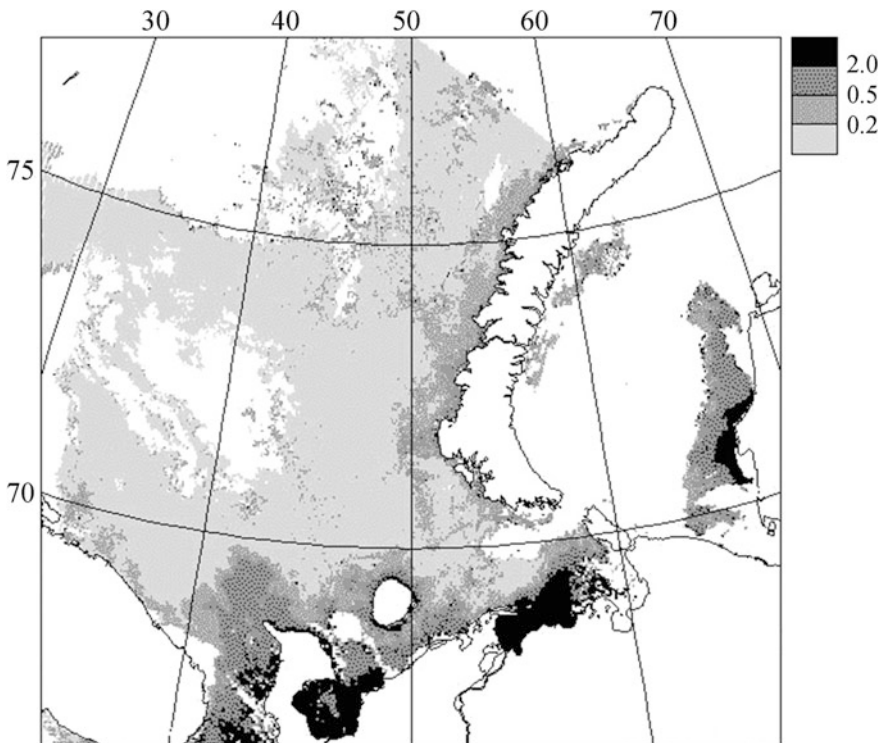
Fig. 6.7 Distribution of the suspended matter in the Barents Sea based on the satellite SeaWiFS
color scanner data in July–August 1998. Gradations of the suspended matter concentration (>2.0;
0.5, and 0.2 mg/l) are shown in the right panel. White color denotes missing data. ©Pleiades
Publishing Inc. Used with permission

where we estimated large amplitudes of the internal tide. The observed correlation between the charts is well proven in the shallow regions. In the center of the sea, both the suspended matter concentration and the amplitudes of internal tides are small. Here the concentration of suspension matter can be determined by the other factors.

Thus, the main conclusions of the numerical experiments are as follows. In the region of the Arctic coast, the barotropic tide generates an internal tide, whose influence most strongly manifests itself near the steep bottom topography. The internal tide, even in the regions located south of the critical latitude, practically does not develop into a free propagating internal wave. The fluctuations of the isopycnal surfaces with significant amplitudes are observed only near the bottom slopes. It is likely that here the internal tides lose their energy, which is transferred to the energy of short-period waves and to the potential energy of the mixed water column. This should be confirmed in the distribution of the hydrological properties. More mixed layers should be located near submarine slopes.

The calculations using the numerical model indicate that the bottom slopes characteristic of the region under study can lead to the generation of forced internal tide. Since the stratification and bottom slopes are irregular, the internal wave field should also have a patchy structure. The maximum amplitudes would be observed at the places where the inclination of the characteristic lines for the internal tides randomly coincides with the bottom slope. In order to form large amplitudes of the internal tide, the bottom slopes need not necessarily be as steep as they need to be in the regions of low and mid-latitudes. Due to the fact that the inclination of the curves of the characteristic equation for the internal waves in the Arctic latitudes is significantly smaller, large amplitudes of the internal tide can be generated even at small bottom inclinations. The proximity of the critical latitude for the internal tide, which is determined not only by the latitude of the place (approximately 74° 30′N) but also by the vorticity of the currents, will play a significant role here.

6.3   Great Siberian Polynya

The existence of polynyas in the Laptev Sea has been reported in numerous publications. Their location corresponds approximately to the 20-m isobath (Dobrovolsky and Zalogin 1982; Gukov 1999). As a rule, the conclusion has been drawn that the formation of polynyas is related to wind conditions (Smith et al. 1990). In relation to the Laptev Sea this conclusion seems doubtful. The wind is strong everywhere in the Arctic. Why does wind forcing break ice over the 20-m isobath and yet not break it over other depths? We do not exclude the role of wind forcing in the formation of polynyas, but suggest a mechanism that decreases the thickness of the ice cover, which later leads to its breaking under wind forcing and the formation of a polynya. This mechanism is related to the intensification of internal waves generated by the barotropic tide. Specific conditions of the

barotropic tide, stratification, and bottom topography lead to intense vertical motions related to internal tides, which eventually lead to the thinning of the ice cover.

In winter, sea ice covers the major part of the Arctic Ocean. In some regions of the ocean polynyas of open water exist almost permanently. These almost ice-free polynyas are surrounded by drifting ice or fast ice. The polynyas usually have an elliptic form. Their size ranges from hundreds of meters to tens of kilometers (Smith et al. 1990). The permanent existence of ice-free water at low winter air temperatures stimulates intense ice formation in polynyas, which is accompanied by the vertical mixing and formation of denser waters with higher salinity.

At the end of the polar night, solar irradiance is absorbed by the dark surface of the open water. Thus, in the relatively warm season, polynyas serve as sources of warming water and centers that clean the surface from the floating ice (Smith et al. 1990). The interest of researchers in the problem of formation and maintenance of polynyas emerged at the beginning of the high-latitude navigation period.

It is currently accepted that two main mechanisms are responsible for the existence of polynyas (Smith et al. 1990). The first mechanism is based on the amounts of oceanic heat sufficient for the maintenance of an ice-free surface due to the supply of warm waters. These polynyas are called polynyas of the explicit heat. According to the second mechanism, the ice that freezes in the region of the polynya can be permanently drawn away from the region by prevailing winds, currents, or a combination of these two processes. The heat needed to compensate for the heat losses of water to the atmosphere and maintain ice-free water is supplied due to the latent heat release during continuous and repeated ice formation. The polynyas of this type are called latent heat polynyas or wind polynyas (see, for example, Alexandrov et al. 2000).

Among the wind polynyas, the system of the Laptev Sea polynyas occupies a special place. This region is the main source of sea ice in the Eurasian Arctic sector (Alexandrov et al. 2000). In addition, the changes in the conditions of dense saline water formation in the polynyas of the Laptev Sea are considered one of the main causes of the present salinity variations in the Arctic basin (Johnson and Polyakov 2001).

The system of polynyas in the Laptev Sea is a band of ice-free water and young ice regularly formed beyond the outer edge of the fast ice as a result of the influence of prevailing winds. Usually, one can recognize the following polynyas in this band (from west to east): Eastern (located east of Severnaya Zemlya), Taimyr, Lena, and Novosibirsk polynyas (Klepikov et al. 1985). It is interesting that, from one year to another, despite significant interannual variability of hydrological and meteorological conditions preceding the beginning of ice formation and those accompanying this process, the northern boundary of the fast ice and, correspondingly, the southern boundary of the polynyas are located along the 20–25 m isobaths (Dobrovolsky and Zalogin 1982; Gukov 1999) (Fig. 6.8).
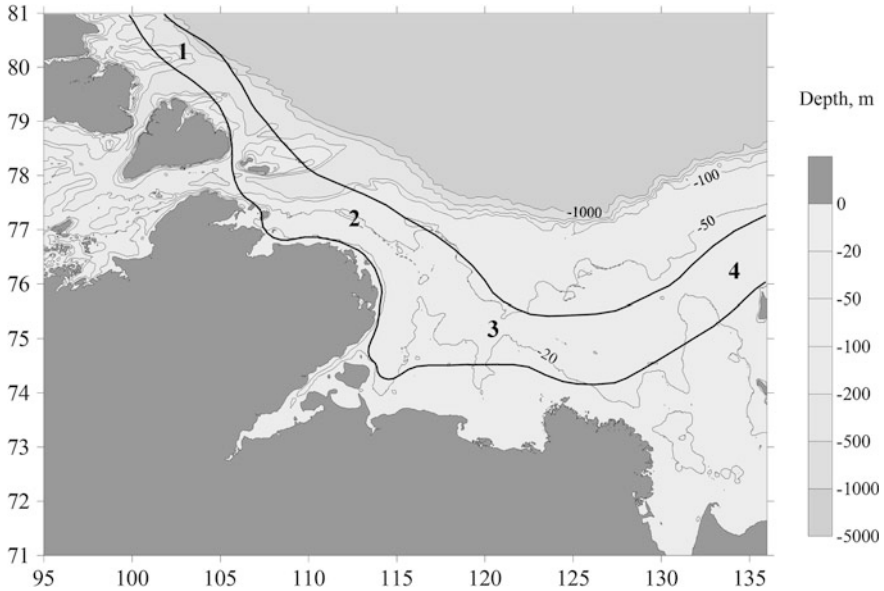
Fig. 6.8 Bottom topography of the Laptev Sea and quasi-stationary position of polynyas. Black lines show the 20, 50, 100, 200, and 500 m isobaths. The locations of polynyas are plotted according to the data from Gukov (1999). Thick lines show the borders of polynyas. Numerals correspond to polynyas: (1) Eastern (east of Novaya Zemlya), (2) Taimyr, (3) Lena, (4) Novosibirsk. Land and islands are shown with gray color

This suggests that a permanent mechanism preventing the formation of fast ice over steeper slopes of the bottom in the region of the 20–25 m isobaths exists in the Laptev Sea. On the one hand, this mechanism should be related to the bottom topography, and, on the other hand, it should not strongly depend on the variable stratification in the shallow part of the Laptev Sea. In a first approximation, the transformation of the barotropic tide into internal waves meets these requirements. The opinion that the existence of polynyas is related to the deformation of the barotropic tidal wave over the continental slope has already been put forward by Klepikov et al. (1985). Therefore, we carried out a number of numerical experiments to check whether internal waves correlate with the southern boundary of polynyas in the Laptev Sea (Morozov and Pisarev 2004).

We used a numerical model developed by Vlasenko (see Sect. 1.4.1) (Vlasenko 1992; Vlasenko et al. 2005). The initial data of sea bottom topography were taken from the IBCAO depths database (Jakobsson et al. 2000). Sea bottom topography was specified over the meridional sections approximately normal to the Lena polynya. The topography is rather flat; however, the bottom slope between 20 and 30-m isobaths is steeper than it is over smaller and larger depths. The density stratification was specified on the basis of the Joint US–Russian Atlas of the Arctic Ocean (Atlas 1998).

Water transport by the barotropic tidal currents was specified by recalculating them into a stream function. The currents of the barotropic tide at four points of the Laptev Sea at the 20-m isobath were taken from the TOPEX/POSEIDON satellite data from the NASA database at Oregon State University (USA). We used the TPXO.7.1 global inverse tidal model with satellite data assimilation (http://volkov. oce.orst.edu/tides/otps.html; last accessed in October 2017). The model was developed on the basis of the OTIS (Oregon State University Tidal Inversion Software Model) software package (Egbert and Erofeeva 2002). According to these data, the amplitude of the barotropic tide currents is 9–11 cm/s. The measurements of tides in the Laptev Sea were reported by Janout and Lenn (2014).

In the model calculations, we used a work field 300 km long with a horizontal step of 125 m and 30 vertical levels. The time step was 4.5 s. The coefficients of the horizontal eddy viscosity and density diffusivity were specified as 2 m^2/s, and the corresponding vertical coefficient was equal to 0.0005 m^2/s. Calculations of internal wave propagation in the Arctic basin near the critical latitude require that the rotation dispersion does not suppress the nonlinearity of the waves. Therefore, we had to choose such a small horizontal step.

Periodic changes in the horizontal flow due to the barotropic tide with velocity amplitudes of $\sim$10 cm/s induce an internal wave. Density contour lines corresponding to internal oscillations in the calculation area are shown in Fig. 6.9. This shows density distributions corresponding to two oscillation phases (the maximal deepening and maximum elevation of density contour lines over the slope).

According to the calculations, the amplitude of wave oscillations over the slope is approximately 10 m. Since the study region is located close to the critical latitude for the M_2 internal tide, i.e., the frequency of forcing is almost equal to the Coriolis parameter, an internal wave with this frequency cannot develop into a progressive wave, and intense oscillations are observed only over the slope near the generation region. Investigations reported by Dmitrenko et al. (2012) support the theory that
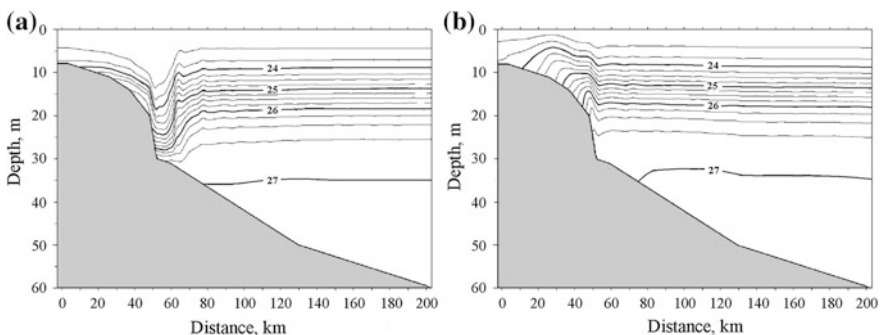
Fig. 6.9 Isopycnal surfaces (from 1.023 to 1.027 g/cm^3, with a 0.0025 g/cm^3 interval) corresponding to the model calculation of internal oscillations over the bottom slope. The ocean bottom is shown with gray color. **a** Maximum deepening of isopycnal surfaces over the slope; **b** maximum elevation of isopycnal surfaces over the slope
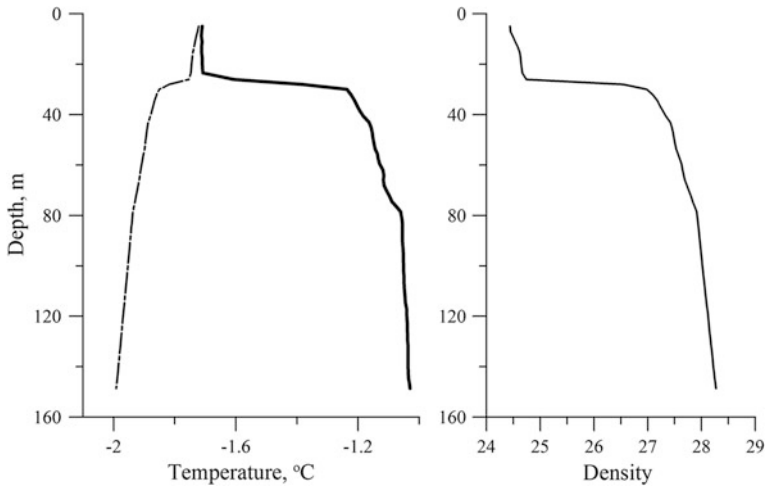
Fig. 6.10 Vertical profiles of temperature (thick solid line) and freezing temperature depending on salinity (thin dashed-dotted line) (left panel) and density (right panel) on October 19, 2008 in the Laptev Sea at 77° 04′N. 126° 05′E

the baroclinic semidiurnal tides influencing mixing can be generated only locally close to the locations of their measurements over underwater slopes. Partial wave breaking occurs after its generation, and waves with higher frequencies propagate into the open sea. Internal waves raise water from the deeper layers closer to the surface. Due to the intense vertical oscillations of density over the slope, the lower ice layer is washed out and becomes thinner. The mean temperature below 20–25 m increases with depth (Fig. 6.10). In addition, the freezing temperature of water located deeper than 20 m decreases due to higher salinity. The velocity of vertical motions is estimated at 0.2 mm/s. Periodical divergent and convergent currents caused by internal waves over the slope intensify the forcing. Finally, the cracking of thin ice occurs due to all external forcing, and further wind forcing forms a polynya.

6.4 Kara Gates

The Strait of Kara Gates connects the Barents and Kara seas. The Barents Sea is a relatively warm sea in Northern Europe due to the transport of warm water from the Atlantic Ocean. The southern part of sea never freezes. The Kara Sea is a very cold sea. It is ice-free only in August–October. A warm flow exists from the Barents Sea to the Kara Sea due to the density difference. A shallow sill crosses the strait. The minimal depth of the sill is 30 m, but there are fractures in the sill which are 100 m deep. The region has not been well investigated.
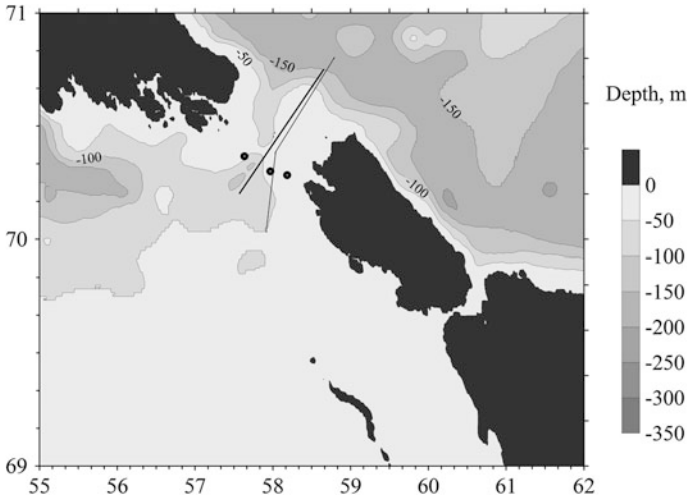
Fig. 6.11 Bottom topography in the Kara Gates based on the ETOPO database. This topography is significantly different from the depths measured by the echo sounders in the strait (Morozov et al. 2017) ©Pleiades Publishing Inc. Used with permission. Two ship tacks with towed CTD are shown: the thin line denotes the tack in 2007, and the thick line shows the tack in 2015. The moorings in 1997 are shown with black dots. Land and islands are shown with gray color

Moored measurements of currents and temperature in the Strait of Kara Gates were performed in September–October 1997. Three moorings with currents and temperature meters were deployed in the strait for a few days at 70° 22′N, 57° 38′E; 70° 18′N, 57° 58′E; 70° 17′N, 58° 11′E (Fig. 6.11). The fourth mooring was deployed at a distance of 200 km southwest of the strait at 69° 43′N, 51° 02′E.

Internal tides in the Kara Gates were analyzed by Morozov et al. (2003a, b, 2008, 2017) on the basis of moored measurements, numerical modeling, towed CTD, and satellite images. A current from the Barents Sea to the Kara Sea was recorded based on the mooring measurements with velocities ranging from 6 to 25 cm/s. The maximum velocity reached 50 cm/s. A bottom reverse flow from the Kara Sea with a mean velocity of 11 cm/s was recorded by a deep instrument in a fracture of the sill across the strait.

Moored temperature measurements in 1997 show that in the spring phase of the tide the vertical peak to peak displacement of isothermal surfaces reached 60 m, while the total depth at the measurement site is 230 m. The amplitude of internal tides on a mooring located 200 km southwest of the Strait was 12 m.

Based on the data of the previous studies (Morozov et al. 2003a, b, 2008, 2017), the structure of the internal tides in the Kara Gates is similar to that in the Strait of Gibraltar and Bab el Mandeb Strait. Internal tides are generated due to a strong barotropic tide on slopes of the sill that crosses the strait (Brandt et al. 1996; Hibiya 1990; Morozov et al. 2002). A warm current from the Barents Sea to the Kara Sea generated by sea level difference intensifies the internal tide propagating to the

southwest (Morozov et al. 2017). Superposition of the current and barotropic tide flow forms a complex dynamic situation in the Kara Gates. Interaction with the currents intensifies internal tides.

The field studies were continued in 2007, 2015, and 2016. The joint application of towed CTD measurements, radar imaging, and numerical modeling is a new approach to the investigation of internal tides. A scheme of the field works in the strait is shown in Fig. 6.11. Moon phases are important in the investigation of internal tides. The measurements in 2007 and 2015 coincided with the spring tide.

The ellipses of the baroclinic tides M_2 and S_2 on the dates of towed measurements across the strait were calculated on the basis of the data assimilation of satellite altimetry using the OTIS algorithm of Oregon State University (http://volkov.oce.orst.edu/tides/otps.html; last accessed in October 2017) (Egbert and Erofeeva 2002). The ellipses are shown in Fig. 6.12.

On August 28–29, 2015, towed measurements in the scanning regime were carried out in the strait with a towed CTD-profiler IDRONAUT 320 plus. The instrument was towed by the ship moving at a speed of 6 knots. The instrument was periodically lowered and raised so that the recordings were made almost from the surface to the bottom. The cycle from the appearance at the surface to the next one lasted approximately 5 min. The horizontal distance between the points where the instrument reached the surface was several hundred meters (Morozov et al. 2017). A scheme of the ship tacks is shown in Fig. 6.11.
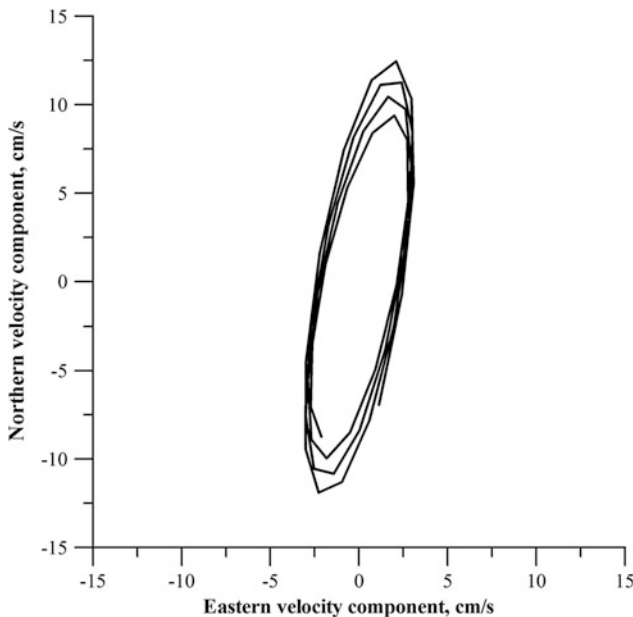
Fig. 6.12 Ellipses of barotropic tidal currents M_2 and S_2 on August 28–29, 2015 based on satellite altimetry with a time step of 1 h (Morozov et al. 2017) ©Pleiades Publishing Inc. Used with permission
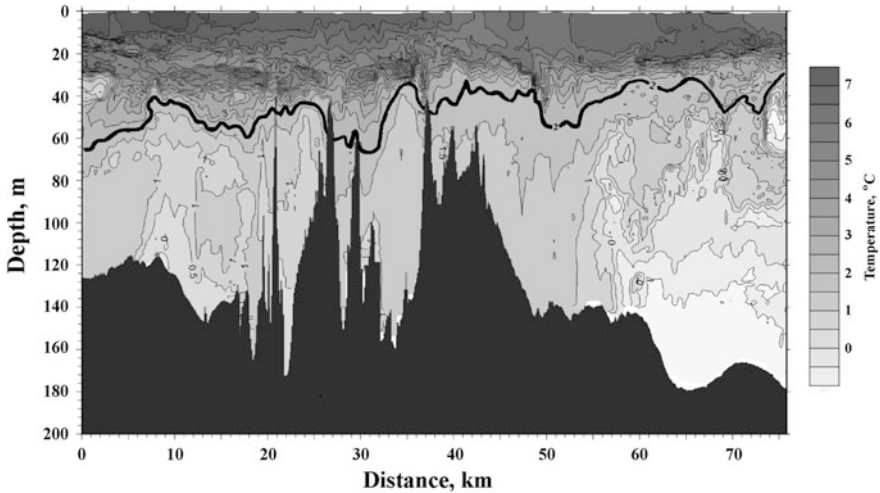
Fig. 6.13 Distribution of temperature over the towed CTD section during the ship's motion from the Barents to the Kara Sea. Isotherms are shown with an interval of 0.5 °C. The thicker line shows the 2 °C isotherm to emphasize the observed effect. Dark gray color shows the bottom profile (below) (Morozov et al. 2017) ©Pleiades Publishing Inc. Used with permission

A temperature section was plotted on the basis of towed measurements. Figure 6.13 shows a snapshot of the displacements of isotherms along the cruise tack. Fluctuations of the isotherms caused by internal waves are seen in the plots. The Barents Sea is on the left side. A hydraulic jump (deepening of isotherms by 70 m) is seen on the Kara Sea side. The 1.5 °C isotherm descends from 50–60 to 120 m. In the western part of the section one can see fluctuations of the isotherm typical for the internal tide. Internal tide is most pronounced in the fluctuations of isotherms 1.0–2.5 °C. Judging from the distances between the maximum depths of isotherms the wave nearest to the sill is 12 km long, the next is 15 km, and the third is 18 km. The internal tide wavelength increases because the ocean becomes deeper.

The ship was moving from the Barents Sea in the opposite direction to the propagation of internal tide in the Barents Sea. On the Kara Sea side the wavelengths are longer: 25–27 km. Their amplitudes are smaller than on the Barents Sea side.

Numerical modeling using a fully non-hydrostatic model developed by Vlasenko (see Sect. 1.4.1) (Vlasenko 1992; Vlasenko and Hutter 2002a) was used to study the influence of the currents on internal tides. In this calculation, we used the data of topography from the tacks of our towed measurements in the region. Stratification was taken from the CTD data. The amplitude of barotropic tidal currents was assumed equal to 12 cm/s on the basis of satellite altimetry (Egbert and Erofeeva 2002). Calculations were carried out using a domain 200 km long with a horizontal step of 75 m and 20 vertical levels. The time step was approximately equal to 1.5 s. In the model we specified the coefficients of horizontal eddy viscosity and density diffusivity as 8 m²/s over the ridge and 2 m²/s beyond the ridge over the flat

bottom. The coefficients of vertical turbulent viscosity and density diffusion were set at 0.001 m^2/s over the ridge and 0.0001 m^2/s beyond the ridge. A small horizontal step in these calculations allows us to increase the nonlinearity, which suppresses the dispersion due to strong rotation at high latitudes.

In the model we introduced a mean flow from the Barents Sea with a velocity of 12 cm/s, which is directed to the northeast and occupies the entire depth; the direction of the flow is from left to right. A periodical barotropic tidal flow was superimposed on this current. Periodical changes in the tidal horizontal flow with an amplitude of 9 cm/s induce an internal wave propagating in both directions from the sill. The estimates of barotropic tide current velocities were calculated from the satellite data on the day of the towed CTD section. Close values of tidal velocities were calculated using model simulations by Kagan and Timofeev (2015).

The perturbations of the density field induced by the propagating internal tide after three tidal periods (36 h) of calculation are shown in Fig. 6.14. The fluctuations of the density field are not symmetrical relative to the sill that crosses the strait.

It is clear from the physical considerations that a stronger internal tide should be observed in the Barents Sea because the southwestern direction of the wave propagating from the sill in the strait is opposite to the current. This is confirmed by the numerical simulation. When internal tide propagates opposite to the current its amplitude increases due to the decrease in the wavelength and conservation of energy over one period. The leading edge of the wave is flat and the trailing edge is steep. Owing to strong nonlinear effects and the mean current opposite to the wave propagation an internal bore is formed east and west of the sill. The isopycnals deepen sharply to 10–15 m forming a bore. A packet of short-period waves follows the bore. These smaller scale waves and the bore induce vertical motions, which manifest themselves at the surface. These high-frequency waves cause spatial inhomogeneities in the vertical motions, which manifest themselves at the surface
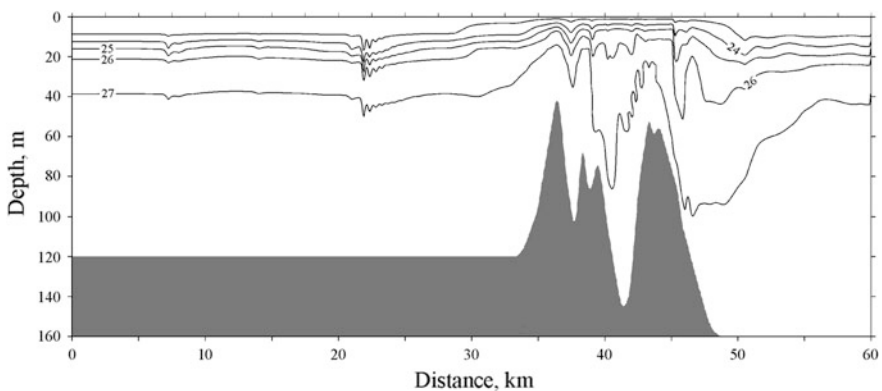
Fig. 6.14 Numerical calculation density field perturbed by internal waves in the Kara Gates Strait. The contour lines of density from 1.023 to 1.027 g/cm^3 (23–27 in the figure) perturbed by the current in the flow and internal waves are shown based on the numerical simulations. The bottom is shown with gray color

as bands of ripples in the convergence zones and bands without ripples in the divergence zones. The cycle of the internal bore is seen left of the bore. The wavelength is approximately 17–18 km. Calculation of the wavelength from the dispersion relation indicates that the wavelength is 23 km. The difference appears due to the Doppler effect.

A sharp deepening of isopycnals is observed on the Kara Sea side. This is a hydraulic jump that appears on the lee side of a flow beyond an obstacle. According to the numerical simulations the 1.027 g/cm^3 isopycnal deepens from 40 to 100 m. A similar pattern is observed in the data of towed measurements (Figs. 6.13, and 6.14).

Wave packets of short-period internal waves directed to the Barents Sea are seen on a satellite image in Fig. 6.15. The length of the wave packets is 1–2 m. The distance between packets is 4–6 km. High contrasts on the images are caused by the formation of an intense convergence of vertical flows, in which backscattering is strongly enhanced over wind ripples and wave breaking (Kudryavtsev et al. 2014; Morozov et al. 2017).
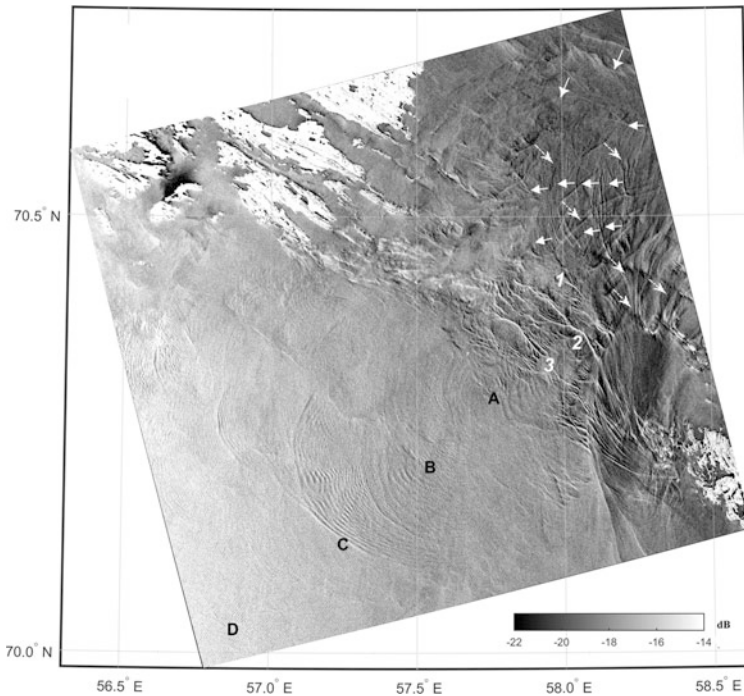
Fig. 6.15 A satellite radar image ALOS-2 PALSAR-2 of internal waves in the Kara Gates on October 1, 2015. Letters A–D and numerals 1–3 indicate internal wave packets; the arrows denote the direction of their propagation. The data were obtained from the Japanese JAXA agency within projects PI No 1193, PI No 3395 (4th & 6th ALOSRA for ALOS-2). Reproduced with permission

6.5 Beaufort Sea

Four moorings were deployed in the Beaufort Sea in 1992–1994 at depths ranging from 700 to 3370 m. The instruments were located at different depths from 50 to 1500 m. The experiment was organized by the University of Washington, USA. No significant semidiurnal fluctuations were found in the temperature records. Judging from the vertical temperature gradient the vertical amplitudes of the semidiurnal fluctuations were only a few meters and did not exceed 10 m.

The AIWEX experiment was carried out in March–May, 1985 (Levine 1990; D'Asaro and Morehead 1991). The horizontal and vertical arrays of temperature and conductivity sensors were lowered from ice at 74° N, 143° W and drifted with the ice for nearly 120 km. The internal wave field was significantly less energetic than the lower-latitude observations by a factor of 0.03–0.07. The shape of the frequency spectrum was significantly different from any previous observations. The spectral slope was close to −1. The spectral bandwidth was 10 times larger than GM-75.

A mooring was deployed in 2002 in the Canada Basin at 73° 30′N, 137° W (Timmermans et al. 2007). Vertical motions with periods close to f and M_2 with amplitudes 10–20 m were recorded at a depth of 2500 m.

A comparison of internal waves in the Beaufort Sea measured in the 1980s and in 2007 was carried out by Guthrie et al. (2013). The authors found that mixing and internal wave energy in the Beaufort Sea are lower compared to the central and eastern Arctic Ocean. They did not find significant changes between the historical results from the Arctic Internal Wave Experiment in the 1980s and measurements in 2007. They suggest that internal wave energy remains lowest in the Beaufort Sea despite the decline in sea ice there, because increased stratification amplifies the negative effect of boundary layer dissipation on internal wave energy.

Halle and Pinkel (2003) found strong internal wave variability in the Beaufort Sea on the basis of measurements from the drifting ice. The internal motion was close to the inertial and correlated with the atmospheric forcing and drift of the ice camp through anticyclonic eddies.

6.6 Lomonosov Ridge

Moored measurements were carried out from August 1995 to August 1996. The experiment was organized by the University of Washington, USA. Three moorings were deployed in the Arctic Ocean in the region of the underwater Lomonosov Ridge at 78° 30′N, 133° 57′E; 81° 04′N, 138° 54′E; and 80° 19′N, 150° 03′E. Measurements of temperature, salinity and velocity were carried out with time sampling of 30 and 60 min at depths of 114, 272, 712, 1112, 1162, and 1693 m. The depths of the ocean over the slope were 1700 m.

Internal tides of the M_2 frequency (12.42 h) cannot exist at these latitudes; however, this restriction is not related to the internal tides of the S_2 frequency (12.0 h). The measurements on the northern mooring (81° N) confirm this fact. The spectra of velocity and temperature fluctuations at a depth of 712 m are shown in Fig. 6.16. Two peaks at frequencies of M_2 and S_2 related to the currents of the barotropic tide are found on the velocity spectra. Only the peak at the S_2 frequency was found on the temperature spectra. Insignificant peaks were found on the temperature spectra at several deep levels of the measurements because the moorings were deployed on the slopes but not on a flat bottom. However, the amplitudes of the semidiurnal internal tide M_2 over the slopes of the Lomonosov Ridge reached 30 m at a depth of 700 m.

6.7   North Pole

Moored measurements were carried out almost exactly at the North Pole from April 2001 to April 2008. The experiment was organized by the University of Washington, USA. The moorings were replaced every year. The measurements were carried out at depths from 61 to 2500 m. As expected, peaks at the M_2
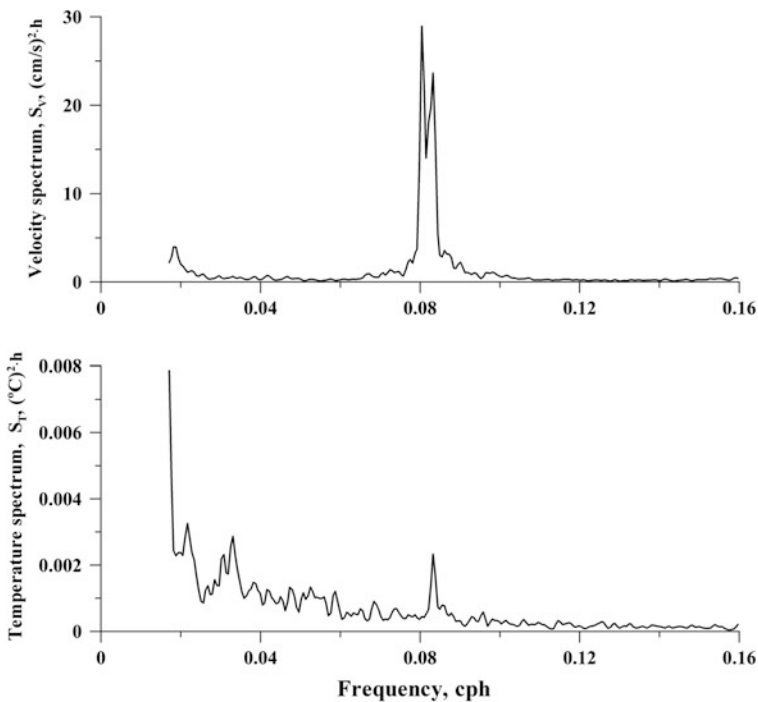
Fig. 6.16 Velocity (top panel) and temperature (bottom panel) spectra from a mooring deployed near the Lomonosov Ridge (81° 04′N, 138° 54′E). Measurements at a depth of 114 m over the ocean depth 1700 m

Fig. 6.17 Temperature
spectra from a mooring near
the North Pole (89° 28′N, 53°
31′E). Measurements at
depths of 61 m (black solid
line) and 608 m (gray dashed
line)
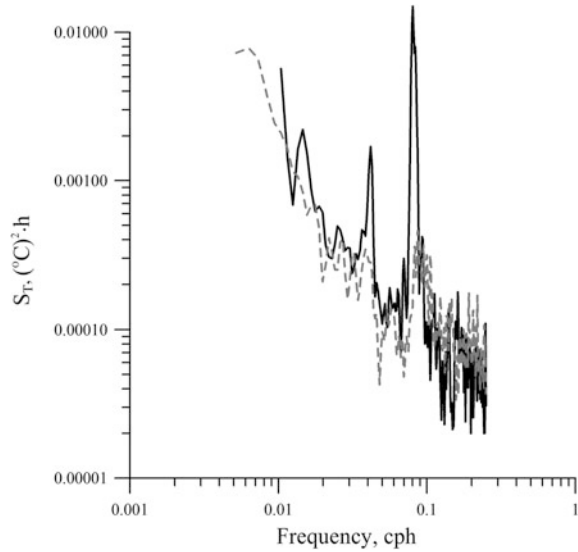
frequency were almost absent. Possible generation of internal tides occurred close
to the ice surface owing to uneven ice surface at the boundary with water. Peaks at
the M_2 frequency were recorded in the spectra calculated from the temperature data.
The amplitudes of internal tides were of the order of 10 m. However, the internal
waves decreased with the distance from ice. Peaks at the S_2 frequency were also
found, but they were not very reliable. Spectra of temperature fluctuations at depths
of 61 and 608 m are shown in Fig. 6.17. The M_2 peak exists only at a depth of
61 m. At 608 m a reliable peak cannot be found at the S_2 frequency.

6.8   Greenland Sea

Twelve moorings were deployed at the eastern coast of Greenland in 1987–1989.
The experiment was organized by NOAA/PMEL, USA. Some of the moorings
were located over the continental slope, while the others were in the open sea. At
the slope the amplitudes of internal tides at depths of 359 and 495 m over the ocean
bottom at 1312 and 1794 m, respectively were estimated at 35–40 m. In the open
sea, the amplitudes at 200–215 m over the oceanic depth of 3600–3700 m were in
the range 15–20 m. The peaks near the slope were at the M_2 and S_2 frequencies,
while only the S_2 peaks were found over the flat bottom. Peaks at the S_2 frequency
exist on the temperature spectra in the Greenland Sea on a mooring close to Jan
Mayen Island.

References

Alexandrov VY, Martin T, Kolatshek J, Eicken H, Kreyscher M, Makshtas AP (2000) Sea ice circulation in the Laptev Sea and ice export to the Arctic Ocean: results from satellite remote sensing and numerical modeling. J Geophys Res 105(C7):17143–17159

Allen JS (1975) Coastal trapped waves in a stratified ocean. J Phys Oceanogr 5(4):300–326

Atlas (1998) Joint U.S.-Russian Atlas of the Arctic Ocean: oceanography atlas for the winter and summer period (CD-ROM), Environmental Working Group. National Snow and Ice Data Center (NSIDC), Boulder, Colorado

Baines PG (1982) On internal tide generation models. Deep-Sea Res 29(3):307–338

Bannov-Baikov YL, Totubakin YY, Yakovleva AB (1989) Intra-diurnal variations in the temperature, salinity, and density of waters in the American-Asian sub-basin of the Arctic Ocean. Proc Arctic Antarct Res Inst 414:101–105

Brandt P, Alpers W, Backhaus JO (1996) Study of the generation and propagation of internal waves in the Strait of Gibraltar using a numerical model and synthetic aperture radar images of the European ERS 1 satellite. J Geophys Res 101:14,237–14,252

Burenkov VI, Ershova SV, Kopelevich OV, Sheberstov SV, Shevchenko VP (2001) An estimate of the distribution of suspended matter in the Barents Sea waters on the basis of the SeaWiFS satellite ocean color scanner. Oceanology 41(5):622–628

D'Azaro EA, Morehead MD (1991) Internal waves and velocity fine structure. Internal waves and velocity fine structure in the Arctic Ocean. J Geophys Res 96:12725–12738. https://doi.org/10.1029/91JC0107

D'Asaro EA, Morison JH (1992) Internal waves and mixing in the Arctic Ocean. Deep-Sea Res 39 (Suppl. 2):S459–S484

Dmitrenko IA, Kirillov SA, Bloshkina E, Lenn Y-D (2012) Tide-induced vertical mixing in the Laptev Sea coastal polynya. J Geophys Res 117:C00G14. https://doi.org/10.1029/2011JC006966

Dobrovolsky AD, Zalogin BS (1982) Seas of the USSR. Moscow State University, Moscow [in Russian]

Egbert GD, Erofeeva S (2002) Efficient inverse modeling of barotropic ocean tides. J Atmos Ocean Tech 19:183–204

Falahat S, Nycander J (2015) On the generation of bottom-trapped internal tides. J Phys Oceanogr 45(2):526–545

Furevik T, Foldvik A (1996) Stability at M_2 critical latitude in the Barents Sea. J Geophys Res 101 (C4):8823–8837

Gjevik B, Nøst E, Straume T (1994) Model simulations of the tides in the Barents Sea. J Geophys Res 99(C2):3337–3350

Gukov AY (1999) Ecosystem of the Siberian Polynya. Nauchnyi Mir, Moscow [in Russian]

Guthrie JD, Morison JH, Fer I (2013) Revisiting internal waves and mixing in the Arctic Ocean. J Geophys Res 118:3966–3977. https://doi.org/10.1002/jgrc.20294

Halle C, Pinkel R (2003) Internal wave variability in the Beaufort Sea during the winter of 1993/1994. J Geophys Res 108(C7):3210. https://doi.org/10.1029/2000JC000703

Hibiya T (1990) Generation mechanism of internal waves by a vertically sheared tidal flow over a sill. J Geophys Res 95:1757–1764. https://doi.org/10.1029/JC095iC02p01757

Jakobsson M, Cherkis NZ, Woodward J, Macnab R, Coakley B (2000) New grid of Arctic bathymetry aids scientists and mapmakers. EOS Trans AGU 81(9):89–96

Janout MA, Lenn Y-D (2014) Semidiurnal tides on the Laptev Sea shelf with implications for shear and vertical mixing. J Phys Oceanogr 44(1):202–219

Johnson MA, Polyakov IV (2001) The Laptev Sea as a source for recent Arctic Ocean salinity changes. Geophys Res Lett 28(10):2017–2020

Kagan BA, Timofeev AA (2015) Modeling of the stationary circulation and semidiurnal surface and internal tides in the Strait of Kara Gates. Fundam Appl Hydrophys 8(3):72–79

Klepikov VV, Sarukhanyan EI, Smirnov NP (1985) Specific features of hydrology: the Arctic and Southern Oceans. Nauka, Leningrad, pp 29–33 [in Russian]

Konyaev KV (2000) Internal tide at the critical latitude. Izv Atmos Ocean Phys 36(3):363–375

Konyaev KV, Sabinin KD (1992) Waves inside the Ocean. S.-Petersburg, Gidrometeoizdat, 272 pp [in Russian]

Kozubskaya GI, Konyaev KV, Plueddemann A, Sabinin KD (1999) Internal waves at the slope of Bear Island from the data of the barents sea polar front experiment (BSPF-92). Oceanology 39 (2):147–154

Krauss W (1966) Interne Wellen. Gebrüder Borntraeger, Berlin-Nikolasee

Kudryavtsev V, Kozlov I, Chapron B, Johannessen JA (2014) Quad-polarization SAR features of ocean currents. J Geophys Res 119(9): 6046–6065. https://doi.org/10.1002/2014JC010173

Kurkina OE, Talipova TG (2011) Huge internal waves in the vicinity of the Spitsbergen Island (Barents Sea). Natural Hazards Earth System Studies, pp 981–986

LeBlond PH, Mysak LA (1978) Waves in the Ocean. Elsevier Oceanographic Series. Elsevier, Amsterdam, p 602

Levine MD (1990) Internal waves under the Arctic pack ice during the Arctic Internal Wave Experiment: the coherence structure. J Geophys Res 95:7347–7357. https://doi.org/10.1029/JC095iC05p07347

Levine MD, Paulson CA, Morison JH (1985) Internal waves in the Arctic Ocean: comparison with lower latitude observations. J Phys Oceanogr 15:800–809

Morozov EG, Paka VT (2010) Internal waves in a high-latitude region. Oceanology 50(5):668–674

Morozov EG, Pisarev SV (2002) Internal tides at the Arctic latitudes (numerical experiments). Oceanology 42(2):153–161

Morozov EG, Pisarev SV (2004) Internal waves and polynya formation in the Laptev Sea. Dokl Earth Sci 398(7):983–986

Morozov EG, Trulsen K, Velarde MG, Vlasenko VI (2002) Internal tides in the strait of Gibraltar. J Phys Oceanogr 32:3193–3206

Morozov EG, Neiman VG, Shcherbinin AD (2003a) Internal tide in the Kara Strait. Dokl Earth Sci 393(9):1312–1314

Morozov EG, Parrilla-Barrera G, Velarde MG, Scherbinin AD (2003b) The Straits of Gibraltar and Kara Gates: a comparison of internal tides. Oceanol Acta 26(3):231–241

Morozov EG, Pisarev SV, Neiman VG, Erofeeva SY (2003c) Internal tidal waves in the Barents Sea. Dokl Earth Sci 393(8):1124–1126

Morozov EG, Paka VT, Bakhanov VV (2008) Strong internal tides in the Kara Gates Strait. Geophys Res Lett 35:L16603

Morozov EG, Kozlov IE, Shchuka SA, Frey DI (2017) Internal tide in the Kara Gates Strait. Oceanology 57(1):8–18

Nansen F (1902) Oceanography of the North Pole basin: Norwegian North Pole expedition, 1893–1896. Scientific Results, vol 3(9). Longmans and Green, Toronto, 1–427 p

Padman L, Plueddemann A, Muench R, Pinkel R (1992) Diurnal tides near the Yermak Plateau. J Geophys Res 97:12639–12652

Parsons AR, Bourke RH, Muench RD, Chiu C-S, Lynch JF, Miller JH, Plueddemann AJ, Pawlowicz R (1996) The Barents Sea polar front in summer. J Geophys Res 101(C6):14201–14221

Pisarev SV (1988) Experimental frequency spectra of internal waves in an ice-covered high-latitude basin. Oceanology 28(5):577–580

Pisarev SV (1991) Some measurements of the spatial and temporal characteristics of internal waves in an ice-covered high-latitude basin. Oceanology 31(1):42–46

Pisarev SV (1992) Spatial and temporal characteristics of internal waves at the edge of the continental shelf in the Arctic basin. Oceanology 32(5):579–583

Pisarev SV (1996) Low-frequency internal waves near the shelf edge of the Arctic basin. Oceanology 36(6):771–778

Plueddemann AJ (1992) Internal wave observations from the Arctic Environmental Drifting Buoy. J Geophys Res 97:12619–12638

Plueddemannn AJ, Krishfield R, Takizawa T, Hatakeyama K, Honjo S (1998) Upper ocean velocities in the Beaufort Gyre. Geophys Res Lett 25(2):183–186

Robertson R (2001) Internal tides and baroclinicity in the southern Weddell Sea 2. Effects of the critical latitude and stratification. J Geophys Res 106(C11):27017–27034

Rodden WP (1959) Aerodynamic influence coefficients from strip theory. J Aerospace Sci 26 (12):833–834

Sabinin KD, Stanovoi VV (2002) Intense semidiurnal internal waves in the Kara Sea. In: Surface and Internal Waves in the Arctic Seas. Gidrometeoizdat, St. Petersburg, pp 265–279 [in Russian]

Smith SD, Muench RD, Pease CJ (1990) Polynyas and leads: an overview of physical processes and environment. J Geophys Res 95(C6):9461–9479

Støylen E, Fer I (2014) Tidally induced internal motion in an Arctic fjord, Nonlin. Process Geophys 21:87–100. https://doi.org/10.5194/npg-21-87-2014

Timmermans M-L, Melling H, Rainville L (2007) Dynamics in the deep Canada Basin, Arctic Ocean, inferred by thermistor-chain time series. J Phys Oceanogr 37(4):1066–1076

Vlasenko VI (1992) Nonlinear model for the generation of baroclinic tides over extensive inhomogeneities of bottom topography. Phys Oceanogr (Morskoy gidrofizicheskiy zhurnal) 3:417–424

Vlasenko V, Hutter K (2002) Numerical experiments on the breaking of solitary internal waves over a slope-shelf topography. J Phys Oceanogr 32:1779–1793

Vlasenko V, Stashchuk N, Hutter K (2002) Water exchange in fjords induced by tidally generated internal lee waves. Dyn Atmos Oceans 35(1):63–83

Vlasenko V, Stashchuk N, Hutter K, Sabinin K (2003) Nonlinear internal waves forced by tides near the critical latitude. Deep-Sea Res 50:317–338

Vlasenko V, Stashchuk N, Hutter K (2005) Baroclinic Tides: Theoretical Modeling and Observational Evidence. Cambridge University Press, Cambridge, 351 pp

Zubov NN (1932) Hydrological studies of the Marine Scientific Institute in the southwestern part of the Barents Sea in summer 1928 on board the R/V "Persey". Proc State Oceanogr Inst 2 (4):3–80 [in Russian]

Chapter 7
Properties of Internal Tides

Abstract This chapter describes some important properties of internal tides. The diurnal and semidiurnal spectral peaks related to the internal tides consist of separate waves with close frequencies. Internal tides are modulated due to the spring-neap variability of the barotropic tide that generates them. Strong internal tides usually have mode structure, which is considered here on the basis of field measurements. Fluctuations of currents at a semidiurnal frequency consist of the currents induced by the barotropic tide and internal tide. The methods for separating them are considered. The beam propagation of internal tides near the generation regions of submarine slopes is considered. The long distance propagation of internal tides and decay of their energy are analyzed based on observations and modeling. Mixing induced by internal tides influences the propagation of Antarctic Bottom Water to the north in the Atlantic Ocean.

7.1 Spectral Composition of Internal Tides

The diurnal and semidiurnal barotropic tides are composed of several harmonics, whose frequencies are slightly different. Each of these components should separately interact with the bottom topography and generate baroclinic internal waves of the same frequency. The separation of these components requires very long continuous time series without changing moorings and instruments. Many of such time series are available.

For example, the data of the Array-1 and Array-2 in the Sargasso Sea are nine months long with a time sampling of 15 min. During the Array-2 experiment, the moorings were replaced twice, so that the total duration of time series was two years. Spectral functions were calculated from these data to study the frequency distribution of energy over a wide range (Morozov 1983). Characteristic spectral densities of temperature fluctuations from the Array-2 experiment are shown in Fig. 7.1.

The spectra calculated from the data of the two-year long time series with two replacements of moorings reflect the characteristic properties of mesoscale
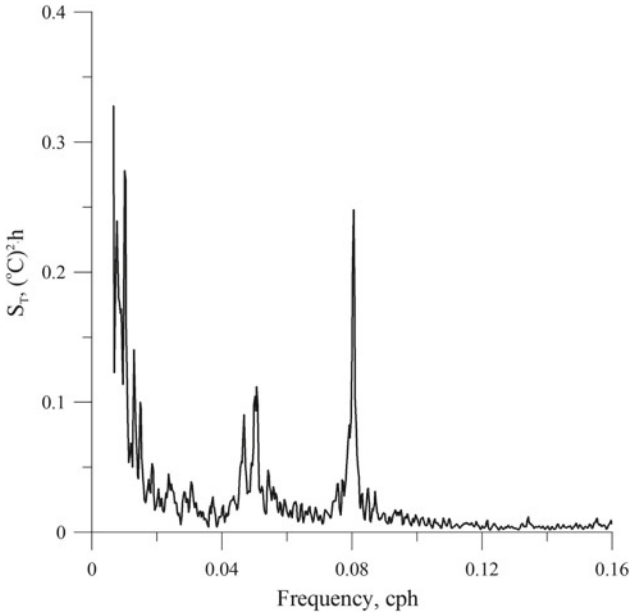
Fig. 7.1 Characteristic frequency spectra of temperature fluctuations based on the Array-2 experiment data. The data are from a mooring at 34° 53′N, 55° 02′W at a depth of 1002 m

processes. A wide prominent maximum exists on the spectra of velocity at a period of 90 days. This peak is related to strong mesoscale eddies existing in the Sargasso Sea. A deep wide minimum is found in the frequency range between the maximum related to the mesoscale eddies and the diurnal frequency (Wunsch 1972).

The inertial period in the region of the Array-2 experiment varies between 25.7 and 21.4 h. The diurnal tides are also within this range of periods. Among the multitude of spectral peaks we distinguish the peaks at 23.9 and 25.8 h, which correspond to tidal waves K_1 and O_1.

Several separate peaks exist in the semidiurnal frequency range. The maximum energy is associated with the M_2 and S_2 waves with periods of 12.42 and 12.00 h. However, the S_2 peak is very low.

High spectral peaks in the velocity spectra can be associated with the following physical processes: barotropic tidal waves M_2, S_2, K_1, O_1 (Marchuk and Kagan 1989), inertial currents, and baroclinic (internal) tides generated as a result of the interaction between the barotropic tides and bottom topography. The barotropic tide is not seen in the temperature spectra because the barotropic tide does not cause significant vertical displacements of water particles in the water column.

Many moorings of the Array-2 experiment were deployed at latitudes where the periods of inertial oscillations and diurnal tides are close. The inertial peaks are slightly displaced to higher frequencies (Munk and Phillips 1968) relative to the local inertial frequency; hence identification of each peak is difficult. Sometimes the inertial and diurnal tide peaks merge into one. The Doppler effect caused by the strong currents of mesoscale eddies makes identification and separation of the peaks

even more difficult (Morozov et al. 1979a; Morozov and Nikitin 1984a). The Doppler effect can displace the peaks to either side. If the spectrum is calculated from data measured over several months, the Doppler effect of both signs not only displaces the peak but also makes it wider.

However, despite the fact that the inertial and tidal peaks frequently merge we can conclude that the inertial oscillations make a greater contribution to the energy of fluctuations in the vicinity of the diurnal frequency. This conclusion follows from the analysis of spectra calculated from the data of measurements at different latitudes with different frequencies of the inertial oscillations. As the latitude changes, the maximum peak of the spectral density displaces following the inertial frequency.

It is clear that the peaks corresponding to the baroclinic waves K_1 and O_1 should not displace or change their position on the spectra depending on latitude. By varying the frequency we can separate the inertial and tidal peaks. In the case when the Array-2 moorings are located, for example at a latitude of $38°$ $30'$N, the frequencies of waves K_1 and O_1 are at the maximum distance on the frequency axis from the inertial peak. One can see that the peaks corresponding to waves K_1 and O_1 are not high and much lower than the inertial peak (Fig. 7.2). Furthermore, the O_1 wave is almost not manifested on the spectra, whereas the peak corresponding to wave K_1 is found on almost all spectra.
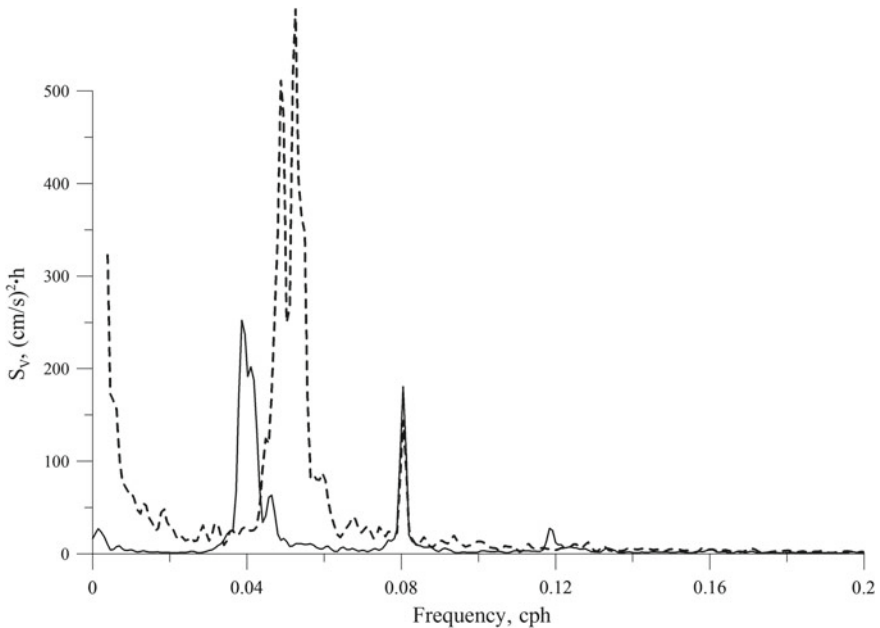
Fig. 7.2 Spectra of velocity fluctuations illustrating the displacement of the inertial peak depending on latitude. The solid line shows mooring 7 (latitude $31°$ $35'$N), the dashed line shows mooring 9 (latitude $38°$ $29'$N). Both time series were measured at a depth of 1500 m, the Array-2 experiment

The peak at the inertial frequency is frequently found on the temperature spectra. It is caused by the vertical components of the inertial oscillations. A significant peak on many spectra exists at a period of 23.9 h, which corresponds to the internal tide generated by wave K_1 of the barotropic tide.

The peak corresponding to the M_2 tidal wave is the most pronounced in the semidiurnal range of the velocity spectra. In addition, baroclinic waves also contribute to the spectral density at this period. The S_2 tidal wave has a smaller peak. No manifestations of other waves (N_2, K_2) were observed.

The peak at a period of 12.42 h always dominates on the temperature spectra. Temperature fluctuations reflect the motions associated with the internal tides; hence, this is the cause of the domination of this peak. Another peak of smaller amplitude always exists close to the M_2 peak. This peak is caused by the internal tide with a period of 12.0 h generated by the S_2 tidal wave interacting with the bottom topography.

The locations of peaks corresponding to the semidiurnal waves are sometimes displaced relative to the M_2 frequency. This displacement is explained by the influence of the Doppler effect on the internal tide. The phase velocity of the barotropic wave is too high to be influenced by the Doppler effect (Morozov et al. 1979a).

The spectral composition of internal tides, which depend on the barotropic tide, varies from region to region similar to the barotropic tide. We shall consider a few examples. In the Sargasso Sea (the Array experiment; 34° 55′N, 55° 05′W, instrument at 1000 m over a depth of 4712), the strongest peak is related to the M_2 (12.42 h) internal tide, while the S_2 (12.0 h) peak is low. The peaks related to the O_1 (25.8 h) and K_1 (23.9 h) waves are slightly lower than the M_2 peak (Fig. 7.1). In the Hunter Channel (34° 23′S, 27° 43′W; instrument at 905 m over a depth of 4550) (Fig. 7.3) the M_2 peak is prominent, while all the others are very low. In the Brazil Basin (28° 17′S, 45° 13′W, instrument at 915 m over a depth of 3280) (Fig. 7.4), the diurnal peaks are only two times smaller than the M_2 peak, while the S_2 peak is low. In Biscay Bay (49° 07′N, 12° 11′W, instrument at 496 m over a depth of 996 m) (Fig. 7.5), the S_2 peak is only two times lower than the M_2 peak, while the diurnal peaks are not seen. The diurnal and semidiurnal peaks in the Bab el Mandeb Strait are of almost the same height (Fig. 4.10).

The width of the spectral peak corresponding to the M_2 internal tide (at half-height of the peak) is usually 3–4 times greater than the resolution of the spectrum. For example, if the time series is 400 days long and the spectral resolution is $\Delta\omega = 0.0005$ cph, the width of the spectral peak at its half height is $\Delta\omega = 0.0015$ cph. The width of the spectrum peak does not depend on the resolution provided that the resolution is sufficient to resolve the peak. However, the existing time series do not provide the resolution much better than $\Delta\omega = 0.0005$ cph.
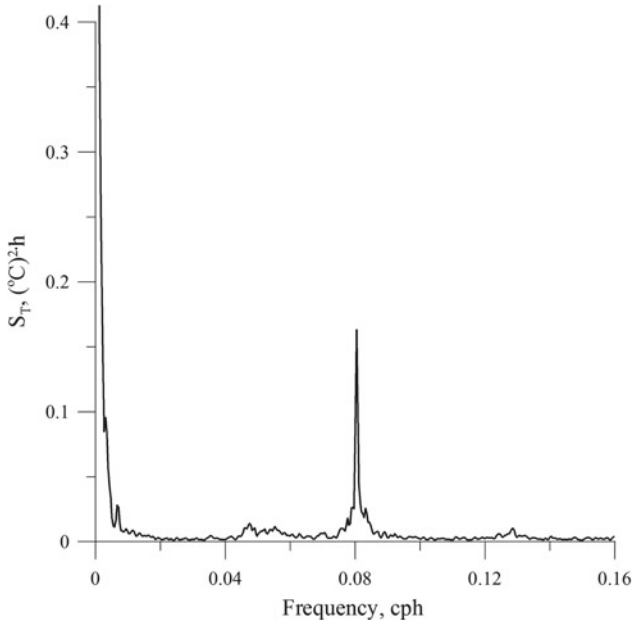
Fig. 7.3 Frequency spectra of temperature fluctuations based on the data in the Hunter Channel (34° 23′S, 27° 43′W; instrument at 905 m over a depth of 4550)
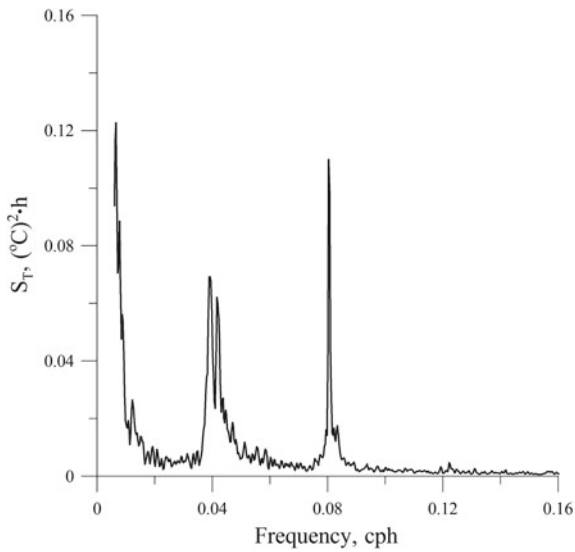
Fig. 7.4 Frequency spectra of temperature fluctuations based on the data in the Brazil Basin (28° 17′S, 45° 13′W, instrument at 915 m over a depth of 3280)
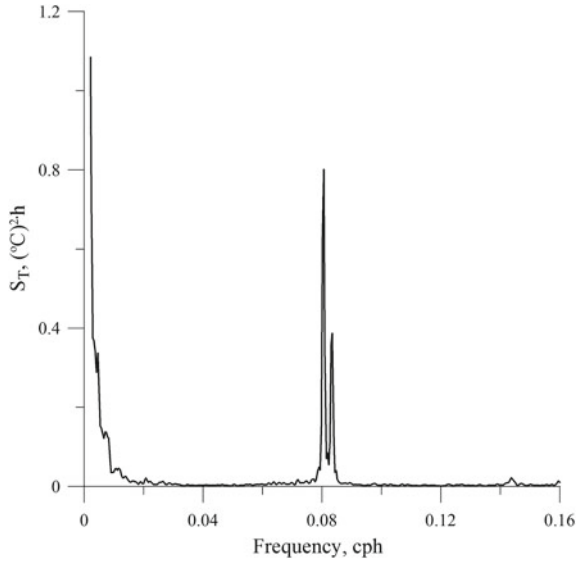
Fig. 7.5 Frequency spectra of temperature fluctuations based on the data in Biscay Bay (49° 07′ N, 12° 11′W, instrument at 496 m over a depth of 996 m)

7.2   Modulation of Semidiurnal Internal Tide

Numerous moored measurements in the ocean show that the semidiurnal peak is well pronounced and dominates over the other peaks on the spectra of temperature and velocity fluctuations. Since internal tides are generated as a result of the interaction between the tidal currents and bottom topography one can expect that the energy of the internal tides is determined by the energy of the barotropic tide. The bottom topography in the ocean is stationary, and tidal currents are quasi-stationary. The main period of tide variability (spring-neap variations) is related to the phases of the Moon. It is approximately 14 days long. Clearly pronounced half-month variations in the barotropic tide should cause similar variability in the internal tides, at least in the regions close to their generation.

The investigation of such variability and its statistical description requires long time series, at least 10 times longer than the spring-neap period. Moored temperature data are more applicable for this study because they are almost completely determined by the internal waves unlike the velocity data, in which the signal of the barotropic tide may be significant.

The first time series that satisfied this requirement were the data of the Polygon-70 (Ivanov and Morozov 1977). The time series were filtered with a band filter tuned to a central frequency corresponding to the M_2 wave (period 12.4 h). A time series of the envelope curve of the filtered data was constructed from the amplitudes of the filtered time series. The time sampling of such time series was 12.4 h. The duration of this time series was 4464 h (186 days) or 360 elements of
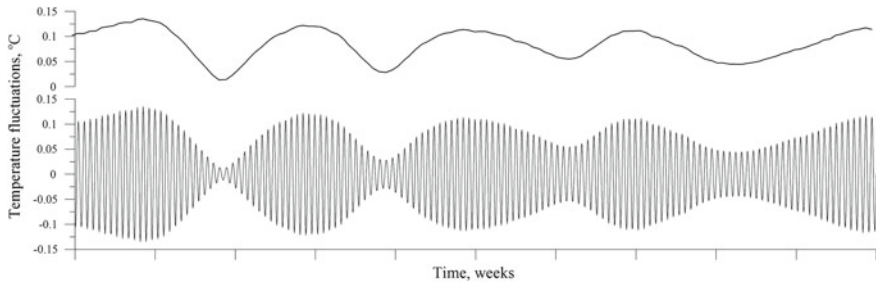
Fig. 7.6 Band filtered temperature fluctuations from time series (CMDAC no. acc07000) of the OMEX experiment (49° 07′N, 12° 11′W). The instrument depth was 496 m. The period covers the time period from October 10 to December 23, 1994

the time series. The region was far from the submarine ridges and continental slope. The peak at a period of 14 days appeared low, but nonetheless, it confirmed the existence of the spring-neap variability. The theoretical period of this variability is 14.76 days.

We selected another region in the northern part of Biscay Bay to test whether the spring neap variability is a characteristic feature of the semidiurnal internal tide. Actually, this occurs due to the beating of two oscillations: the M_2 with a period of 12.4 h and S_2 with a period of 12.0 h. A mooring was deployed on the northern slope of Biscay Bay at 49° 07′N, 12° 11′W. The temperature meter was set at 496 m over a depth of 996 m. The spectrum of temperature fluctuations is shown in Fig. 7.5. The peaks at the M_2 and S_2 frequencies differ by approximately a factor of two. The time series of temperature were band filtered tuned to the central frequency corresponding to a period of 12.2 h (12.0/2 + 12.4/2). The boundary frequencies of the band filter corresponded to periods of 11.0 and 13.6 h. The filtered time series shows clear spring-neap variation. A graph of filtered temperature fluctuations is shown in Fig. 7.6. The time period shown in the graph covers 10 weeks from October 10 to December 23, 1994. The ticks correspond to week periods. The positive envelope curve is shown in the top panel. It was later used to calculate the power spectrum of the envelope curve.

A spectrum of the fluctuations of the envelope curve was calculated. A clearly pronounced peak at the fortnight frequency is seen. A similar spectrum was calculated from the data measured at a depth of 580 m on a mooring located at 49° 05′N, 13° 26′W approximately 100 km west of the previous mooring downslope over the ocean depth 3651 m. The fortnight peak is significantly smaller (Fig. 7.7).

Thus, we can conclude that the spring neap (fortnight) modulation of the semidiurnal internal tides can be found in the regions where the S_2 peak is not negligible. In addition, this effect is observed only in the close vicinity of the generation region. At a distance of 100 km, this effect becomes significantly weaker. The peak becomes almost not significant.

Fig. 7.7 Spectral density of
the amplitude of semidiurnal
temperature fluctuations on
two moorings in Biscay Bay at
49° 07′N, 12° 11′W (thin line)
and at 49° 05′N, 13° 26′W 5
(thick line)
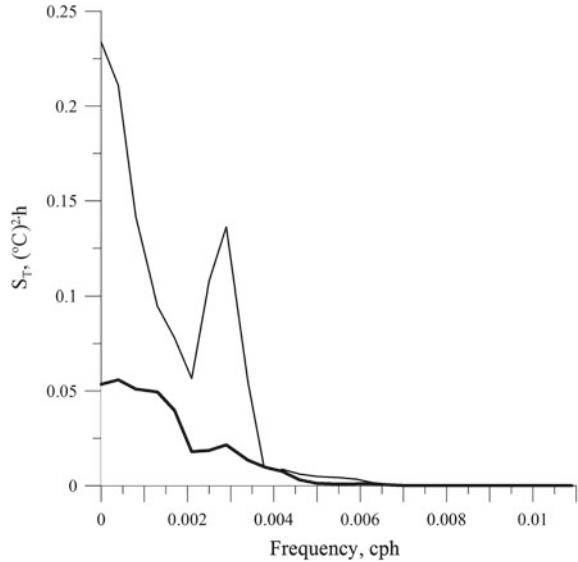
7.3 Eigen Functions for the Internal Wave Equation

The estimates of wavelengths of internal tides can be obtained theoretically from the
known depth and stratification (see Sect. 1.4.3). These estimates can be calculated
by solving the equation for the vertical velocity induced by internal waves
(Sect. 1.4.3). The authors of many publications have suggested various model
vertical distributions of density and solved the problem analytically (Groen 1948;
Krauss 1966; Tareev 1966; Lozovatsky and Shapovalov 1973). However, all models
give only a rough vertical density profile in the ocean, while the analytical solutions
for even very simple distributions are cumbersome. It is possible to obtain more
exact wave parameters using the methods of numerical integration of the equation
with the arbitrary vertical profile of density or the Brunt-Väisälä frequency. Such a
method is known as the Fjelstad method (Fjelstad 1933). The idea of the method is
integration of the equation for the vertical velocity at the given boundary conditions
and stratification. This method was developed to perform calculations without
computers, when only old types of calculators were available. There is no longer any
need for such laborious calculations or for the previous simplifications, which only
decreased the accuracy of the results (Morozov and Nikitin 1981a, b).

   The equation for the vertical velocity is written as (Krauss 1966; LeBlond and
Mysak 1978) (see Sect. 1.4.3):

$$\frac{d^2w}{dz^2} + \frac{N^2(z)}{g}\frac{dw}{dz} + \frac{N^2(z) - \omega^2}{\omega^2 - f^2} = 0, \qquad (7.1)$$

where $N^2(z)$ is the squared Brunt-Väisälä frequency based on the CTD data, ω is the
semidiurnal frequency, f is the Coriolis parameter, and k is the horizontal
wavenumber.

This equation is integrated at the given distribution of the Brunt-Väisälä frequency with depth. The data of density is taken from the CTD profiles. Usually the boundary conditions are assumed zero at the surface and bottom: $w = 0$ at $z = 0$ and $z = H$. The depth of the ocean is introduced through the boundary conditions. Since Eq. (7.1) is not applicable for the frequencies close to N and f, the dispersion relation close to these frequencies has to be studied separately. The equation for the vertical velocity has been integrated using various approaches (Kulakov 1977; Fliegel and Hunkins 1975).

Numerical integration requires that the equation is transformed to finite differences. The vertical step is usually taken equal to 10 m ($h = 10$ m). We find the vertical velocity at each step w_{n+1} as a function of its value at the previous two steps w_n and w_{n-1}:

$$w_{n+1} = 2w_n - w_{n-1} - \frac{N_n^2 \cdot h}{g}(w_n - w_{n-1}) - \frac{N_n^2 - \omega^2}{\omega^2 - f^2} h^2 k^2 w_n. \qquad (7.2)$$

At the beginning we specify initial approximation for wavenumber k. We specify its value at the surface as $w_0 = 0$. We use recurrence function (7.2) to find sequentially all w_n. If the value of velocity at the bottom w_M is not zero to the accuracy initially specified, we vary wavenumber k, and find such a value of the wavenumber that suits the solution. Thus, we find the eigen values and eigen functions of the equation. The latter are normalized by the maximum values over vertical for each mode.

Transition from the eigen functions of the equation for the vertical velocity to the eigen functions for the horizontal velocity is quite easy. The eigen functions for the horizontal velocity are proportional to the derivative of the eigen function for the vertical velocity with respect to depth.

Let us consider the results of numerical modeling of Eq. (7.1) on the example of the density distribution in the Sargasso Sea. The density distributions in summer and winter were taken from the CTD data in the region averaged over 23 profiles in a one degree square at a latitude of 29°N. The depth of the ocean was assumed equal to 5400 m.

Results of the calculation of the dispersion curve show that it is almost linear in the range of frequencies corresponding to periods from 2 to 22 h. We performed calculations of the dispersion curve for the first mode setting the Coriolis parameter equal to zero to show the effect of the Earth's rotation on internal waves. The effect of the Earth's rotation becomes notable for the waves with periods greater than 6 h. The effect is manifested in the increase of the wavelength.

Results of the calculation of wavelengths as a function of latitude (all other parameters remain the same) are shown in Table 7.1. The wavelengths increase with latitude. Variations in latitude on a horizontal scale of one wavelength almost do not influence the value of the wavelength. The increase is within 1%. The form of the eigen function curve does not depend on the latitude variation.

Table 7.1 Wavelengths of mode 1 internal waves with periods of 12.4 h versus latitude

Latitude (°)	Wavelength (km)
27	142.6
29	145.5
31	148.8

Figure 7.8 shows the graphs of the eigen functions for the vertical velocity of two lower modes of the internal tide of semidiurnal frequency. The graphs of the eigen function for the horizontal velocity are also shown in the graph.

The maxima of the eigen function for the horizontal velocity are at the surface and bottom. The eigen functions for the horizontal velocity are proportional to the vertical gradients of the functions for the vertical velocity. Let us analyze the functions for the vertical velocity and discuss the peculiarities of their variation.

The maximum of the vertical profile of amplitudes displaces down, as the number of mode increases. Since the amplitudes of vertical displacements of water particles are maximal in the main pycnocline at depths of 1000–1500 m we think that the mode composition of internal tides in the ocean generally consists of the lower modes and the higher modes are weak.

The next step of our analysis is the investigation of the dependence of wavelength on the ocean depth. The wavelengths were calculated for the depth range between 4400 and 5400 m with a step of 100 m, while stratification and latitude were conserved. Stratification in the bottom layer was assumed linear. The latitude was specified as 29°N. The results of this calculation are shown in Table 7.2. The
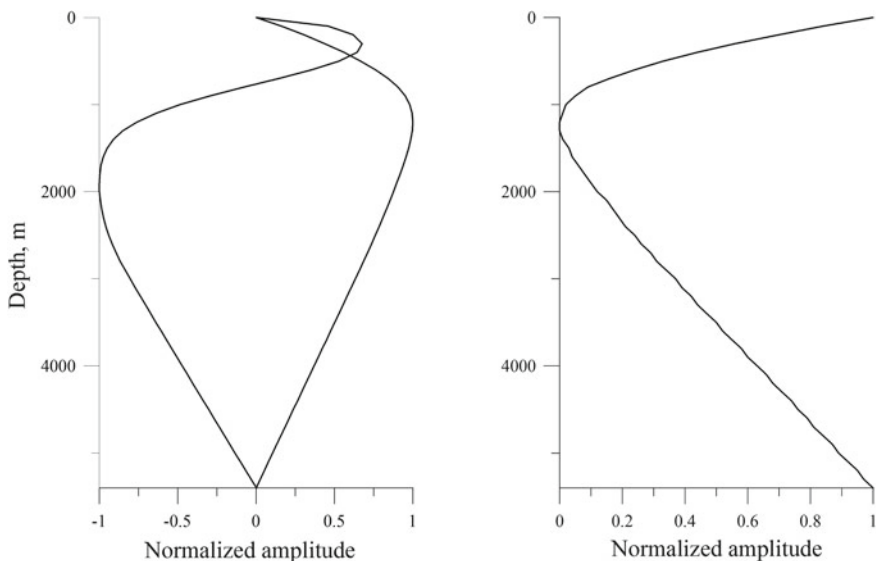
Fig. 7.8 Eigen functions for two lower modes of internal tides (M_2) with a period of 12.4 h. The eigen functions for the vertical velocity (modes 1 and 2) (left panel); the eigen function for the horizontal velocity (mode 1) (right panel). The density distribution was taken from the CTD data in the Sargasso Sea

Table 7.2 Dependence of the M_2 internal tide wavelength on the ocean depth

Depth (m)	4400	4600	4900	5100	5400
Wavelength (m)	140,985	142,041	143,482	144,336	145,500

dependence of the wavelength on depth is almost linear for the semidiurnal internal tides. It is important that a 25% increase in the depth leads to only a 3% increase in the wavelength and the maxima of eigen functions displace slightly deeper. We made similar calculations for the internal waves of shorter periods up to 2 h. The wavelengths of short-period waves almost do not depend on the depth variations.

We studied the dependence of the M_2 internal tide wavelength on stratification in the Sargasso Sea, which significantly changes from summer to winter. The density profiles also change when intense mesoscale eddies pass the point of observations. We selected the vertical distributions of density corresponding to the summer and winter profiles and also the distributions corresponding to the profiles in mesoscale cyclones and anticyclones. The depth and latitude in each calculation were specified as 5400 m and 29°N, respectively. The results of the calculations are presented in Table 7.3.

It is seen from the table that the dependence of wavelength on stratification is notable for long waves and almost negligible for short waves. The wavelength in cyclones is smaller than in anticyclones regardless of the season. This occurs because isopycnals are deeper in anticyclones compared to cyclones; hence mean stratification is greater in the layers, in which the amplitudes are maximal. This also explains the fact that the depths of the maximum vertical velocities in cyclonic eddies are higher than in anticyclones. Since the wavelengths in cyclones and anticyclones are different, internal tides should be subjected to refraction on intense eddies and the plane front of their propagation would bend.

In winter, the depths of the maximum velocities are higher. This agrees with the seasonal oscillation of the pycnocline. Thus, we can conclude that the wavelength of internal tides is a stable characteristic of the region. It is only slightly influenced by the depth and stratification. The wavelength of short-period waves almost does not depend on the depth, but strongly depends on stratification.

7.4 Mode Composition of Internal Tides

The problem of the mode composition of internal waves, and internal tides in particular, is important. In other words, we should investigate the energy ratio between modes. It is generally accepted that many modes exist close to the generation regions over the slopes of the bottom topography forming the beam structure of internal tides. As the distance from the generation region increases, higher modes decay, and only a few lower modes remain.

It is likely that mode structure, i.e., formation of a vertical standing wave is characteristic only of long waves of low frequency and high energy, which are internal tides. High-frequency internal waves can form modes in narrow waveguides of the seasonal thermocline; but we will not discuss that problem here.

Table 7.3 Dependence of the wavelength on stratification

Period	Stratification type					
	Summer			Winter		
	Cyclone	Beyond eddies	Anticyclone	Cyclone	Beyond eddies	Anticyclone
	Wavelength (km)/depth of the maximum (m)					
12.4	137/1130	147/1200	148/1190	142/1560	146/1170	151/1180
2.0	17/101	19/1120	19/1100	18/1060	19/1080	20/1120

We shall confine this section to the mode structure of internal tides, which can develop in the entire water column of the deep ocean. The energy of semidiurnal internal tides is high compared to the energy of internal waves of other frequencies. It is important that the energy of internal tides should be high enough to develop into the mode structure in the entire water column.

Before determining the ratio between modes in the water column we must be sure that the oscillations we study are well developed over the vertical from the surface to the bottom. If the measurements of temperature fluctuations span over the entire vertical water column in the ocean, for example on a mooring, we must be sure that the oscillations are correlated and high coherence is observed between various pairs of time series. The presence of many modes decreases coherence. Such high energy internal tides with high vertical coherence have been measured in the central Atlantic near the Mid-Atlantic Ridge, in the region of the Mascarene Ridge, near the Aleutian Ridge, and in some other places located close to the generation regions.

If the vertical coherences exceed the 95% confidence level we shall try to determine the ratio between the amplitudes and energies of different modes on the example of measurements near the Mid-Atlantic Ridge south of the Azores.

We applied decomposition of amplitude functions with respect to the eigen functions to determine the mode composition of internal tides (Morozov 1988a). The amplitudes of the internal tides at each depth of measurements are composed from the amplitudes of individual modes with the corresponding coefficients. Therefore, the amplitudes of vertical oscillations measured by the instruments at each depth of measurements are presented as sums of the theoretically calculated values of mode superposition. The amplitudes of vertical oscillations were calculated from the amplitudes of temperature fluctuations at semidiurnal frequencies after filtering out all other frequencies of oscillations. Then, they were transferred to the vertical displacements in meters by dividing the temperature amplitudes by the vertical temperature gradient. The eigen functions for each of the modes were obtained by integration of Eq. (7.1) for the vertical velocity at zero boundary conditions. The vertical distribution of the Brunt-Väisälä frequency and the vertical temperature gradients were taken from the CTD profiles. Then, the measured amplitude of vertical displacements was presented as a sum of the calculated values of eigen function at the same depth with unknown coefficients.

Thus, we obtained a system of linear algebraic equations. Their number is determined by the number of depths of measurements. Correspondingly, this number determines the number of modes, whose energy we wished to compare. The equation system is written as follows:

$$\begin{cases} k_1 A_{H_1}^1 + k_2 A_{H_1}^2 + \cdots + k_M A_{H_1}^M = \zeta_{H_2} \\ k_1 A_{H_2}^1 + k_2 A_{H_2}^2 + \cdots + k_M A_{H_2}^M = \zeta_{H_M} \\ \ldots\ldots \\ k_1 A_{H_M}^1 + k_2 A_{H_M}^2 + \cdots + k_M A_{H_M}^M \cdots = \zeta_{H_2} \end{cases}.$$

Here, k_i are sought coefficients, $A_{H_i}^j$ are values of the eigen function of mode j at depth H_i. We analyze M depths; ζ_{H_i} are measured amplitudes of vertical displacements at depth H_i in meters. Thus, we obtained the following equation system for the measurements close to the Mid-Atlantic Ridge:

at 200 m $0.29k_1 + 0.56k_2 + 0.49k_3 + 0.45k_4 + 0.30k_5 = 13.9$

at 300 m $0.42k_1 + 0.71k_2 + 0.49k_3 + 0.25k_4 - 0.01k_5 = 14.2$

at 500 m $0.66k_1 + 0.73k_2 + 0.13k_3 - 0.36k_4 - 0.39k_5 = 22.5$

at 700 m $0.85k_1 + 0.40k_2 - 0.37k_3 - 0.38k_4 + 0.14k_5 = 33.1$

at 2000 m $0.73k_1 - 0.93k_2 + 0.99k_3 - 0.99k_4 + 0.90k_5 = 36.5$.

The right parts of equations in this system are amplitudes of oscillations in meters based on the observations on a mooring. The formal solution of this system is easy. Reliable measurements were obtained at five depths; therefore, in principle, we can estimate the energies of five modes. However, some difficulties appear in the solution of this system. The first one is inexact knowledge of the vertical temperature gradient; hence we cannot calculate exact values of displacements in the right parts of equations, which influence the solution.

The quality of analysis was tested in several stages. In the first stage we assumed that only two lower modes are significant. In this case, the solution is clearly seen on the graph. We have measurements at five depths, hence we can write five equations for dependences between coefficients k_1 and k_2. These dependences are clearly seen in Fig. 7.9 as the straight lines. The intersections between two straight lines correspond to the solution of the equation system. Each pair of lines has its own intersection point, but a small region of intersections between four straight lines is important.

It is seen from the figure that the scatter of intersections is not very wide. All intersection points indicate that the amplitudes of the first mode are 6–7 times larger than the amplitudes of the second mode. The intersection points corresponding to the equation for 200 m are not close to the other points of intersection. This makes us think that the vertical temperature gradient was not introduced correctly.

Small errors in the initial data at close depths can introduce significant errors to the solution. If we select four equations from the five excluding one of the closely located depths (either 200 or 300 m) we find that the solution only slightly depends on the small variations of values in the right parts, which are the initial data of vertical displacements at each of the depths.

Dependence of the eigen function of the first mode of internal tide on the variation of amplitude at one of the depths is shown in Fig. 7.10. The curves of dependence are calculated for the variation of amplitude at one of the depths with a step of 0.25 m. The figure shows low variations in the contribution of the first mode to the total energy and a maximum at the value close to the measured amplitude.

Fig. 7.9 Solution of
algebraic equations. Graphs
of dependences of the
contribution of the first and
second modes to the total
energy of oscillations
provided that the contribution
of the other modes is zero.
Numerals 200, 300, 500, 700,
and 2000 indicate the depths
(m), for which we find
solutions
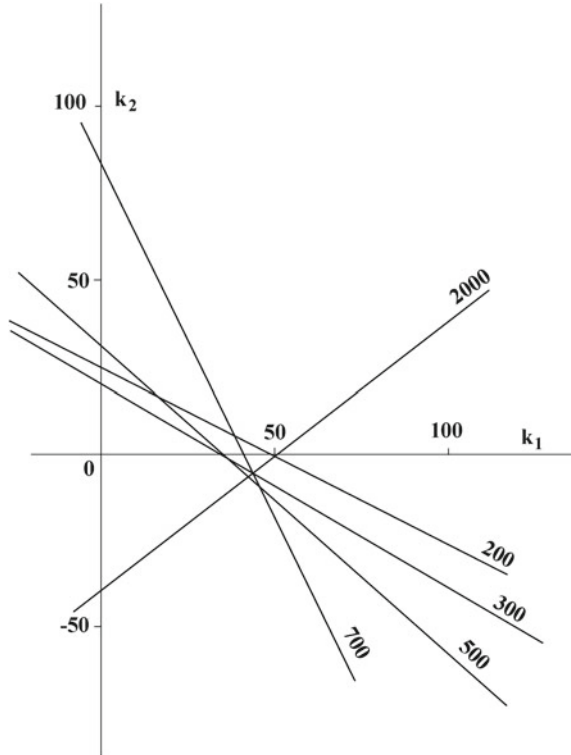
The solution of the system of five equations leads to the result that the first mode
dominates. Its energy is approximately 90% of the total energy of five modes. Each
of the highest modes gives approximately a 2–3% contribution to the energy, which
is within the error of the determination caused by inexact specification of the
amplitude values at each of the depths. It is important that the study site was located
close to the Mid-Atlantic Ridge and the Great Meteor Bank; hence the observations
were made very close to the generation region.

7.5 Separation of Semidiurnal Fluctuations of Currents Caused by the Barotropic and Internal Tides

Two types of semidiurnal oscillations of the same time scale exist in the ocean:
semidiurnal barotropic tide and internal tide with the same period. The spatial scales
of these processes differ by one-two orders of magnitude. However, if we study
fluctuations of properties of seawater such as temperature, salinity, and velocity
with a 12-h period on the basis of time series from moorings at one point, the spatial
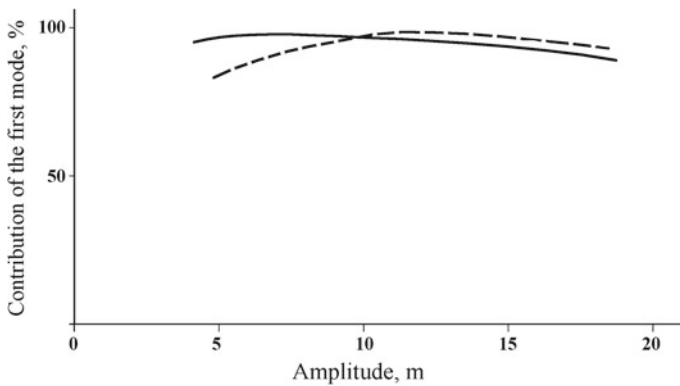
Fig. 7.10 Dependence of the contribution of the first mode to the total energy of oscillations as function of the variations in the measured amplitudes at one of the depths laid off at the x-axis (the other amplitudes remain constant). The contribution is shown in %. The solid line shows the variation in the amplitude at 200 m; the amplitudes at 500, 700, and 2000 m remain constant. The dashed line shows the same for the variation in the amplitude at 300 m

scale of these processes cannot manifest itself. Therefore, both processes are recognized as one whole if we analyze moored measurements with one instrument.

Since the barotropic tide almost does not cause any vertical displacements of water particles in the open ocean, the temperature fluctuations caused by the barotropic tide are negligible. The amplitudes of the horizontal currents induced by each of these processes are comparable. In many publications the authors report that horizontal coherence between velocity components at a period of 12 h is not significant. This is explained by the fact that both processes with different spatial scales contribute to the fluctuations of currents. Each of them is noise relative to the other process. However, it is clear from the physical considerations that coherence between each of the fluctuations separately measured on two moorings should be relatively high.

Fahrbach (1976) averaged Fourier coefficients over vertical and made an attempt to divide the velocity field into the barotropic and baroclinic tides. In this chapter, we suggest another method to separate these processes. We used the property of the barotropic tide of constant horizontal velocity of the barotropic tide currents over vertical (Morozov et al. 1979b).

If the velocity measurements are available along the entire water column from the surface to the bottom we can apply a band filter to separate the semidiurnal oscillations from each of the time series at different depths. Each of the filtered time series includes the barotropic tide and internal wave fluctuations. If we average these time series over vertical at each moment of measurements the resulting time series would be determined by the barotropic tide. The difference between each of the time series and the time series of the barotropic tide would represent the fluctuations caused by the internal tide. The necessary requirement for this method is a sufficient number of time series covering the entire depth of measurements.

Our calculations showed that if we take an integral of the eigen function for the horizontal velocity with respect to depth, this integral would be equal to zero to a high degree of accuracy. Hence, the calculations to separate the barotropic tide require the maximum possible number of current meters more or less uniformly distributed by depth. Usually, the instruments are not located uniformly: more instruments are set in the upper layers of the ocean. However, the above described averaging of data is possible. One of the options is to perform averaging with different weight coefficients.

We shall test this method on the example of data from a mooring in the Sargasso Sea with current meters set at 100, 700, 1400, 3000, and 4500 m. We used band filtering to separate a band of oscillations of velocity components (u and v) with periods 12.4 ± 2 h. After separation of this narrow band of oscillations with time sampling of one hour we performed averaging the data over vertical. Five values of velocity over the vertical measured every hour were averaged by dividing their sum by five. We assumed that the averaged time series of two components were caused by the barotropic tide. We interpret this time series as velocities of the barotropic tide. This time series has a clearly pronounced period of 12.4 h and the variation in its amplitude is almost sinusoidal.

The difference between the filtered time series at each depth and the time series of the barotropic tide is interpreted as fluctuations caused by internal tide. Time series of the zonal and meridional components of the barotropic and baroclinic tides present the orbital velocities of the particles determined by the barotropic and baroclinic tides.

Let us denote the sum time series of the barotropic and baroclinic velocity perturbations as U_Σ, the perturbations of the barotropic tide as U_{bt}, and the perturbations caused by internal tidal waves as U_{iw}. The U_{iw} time series at each depth are characterized by fluctuations with a period of 12.4 h. The amplitudes of velocities at depths shallower than 1000 m of the time series U_Σ are 6–10 cm/s; the velocities of time series U_{bt} are close to 1–2 cm/s and the velocities of the time series U_{iw} are 5–6 cm/s. At depths greater than 1000 m the velocities of time series U_Σ are 4–6 cm/s, time series U_{bt} are the same close to 1–2 cm/s, and the amplitudes of internal tide U_{iw} are 2–3 cm/s.

The energy of the semidiurnal baroclinic tide was estimated by Wunsch (1975a, b) as 10–50% of the semidiurnal barotropic tide. We can use our data to estimate the ratio of the internal tide energy to the barotropic tide energy using the following relation:

$$k = \frac{\Delta_{iw100}h_1 + \Delta_{iw700}h_2 + \Delta_{iw1400}h_3 + \Delta_{iw3000}h_4 + \Delta_{iw4500}h_5}{\Delta_{bt}H}$$

where Δ_{iw} is the dispersion of the semidiurnal velocity fluctuations caused by the internal tide at each of the depths with current meters; Δ_{bt} is the dispersion of the semidiurnal velocity fluctuations caused by the barotropic tide; h_i is the thickness of the layer; H is the ocean depth ($H = \Sigma h_i$). In this context, dispersion (σ) is the dispersion of time series of velocity components, which is the second central

moment: root-mean-square deviation of current fluctuations (actually the energy of fluctuations, but not the energy losses):

$$\sigma = \sum_k (x_k - \overline{x})^2.$$

Such an estimate of the internal tide energy shows that it is greater than the energy of the barotropic tide by 20%, which is greater than the estimate by Wunsch (1975a). This estimate characterizes semidiurnal oscillations in the Sargasso Sea, where intensity of internal tides is far from the highest levels in the ocean because unlike submarine ridges and continental slopes no intense generation of internal tides occurs here. The direction of the barotropic tidal wave was estimated from relation (5.1) based on the relative position of the axes of the ellipse of the barotropic tide currents. It follows from this equation that the direction of the barotropic tide is 8°, which is very close to the estimates from satellite altimetry by Egbert and Erofeeva (2002) and calculations of the M_2 tidal wave by Bogdanov and Magarik (1967). The estimates of the direction of the internal tide at different depths were as follows: 270° at 100 m, 263° at 700 m, 261° at 1400 m, 290° at 3000 m, and 213° at 4500 m. It is clear that the directions of the internal wave at different depths do not differ significantly, because the internal tide wave propagates in the entire water column.

Let us consider vertical spectral cross-analysis between velocity components and absolute velocity. As was expected, vertical coherence between time series U_Σ is below the significance level. For example, coherence between the pair of time series U_Σ 100–700 m is 0.32. Coherence between the pair of time series U_{iw} from the same depths is much higher; it is equal to 0.69. An opposite effect is found in the deep layers. Coherence between pairs of time series U_Σ 3000–4500 m is 0.96. The phase shift between fluctuations is close to zero. Coherence between pairs of time series U_{iw} is equal to 0.29.

Thus, in the upper layers of the ocean (up to 700 m), in which internal tide is strong, superposition of the barotropic and internal tide leads to a decrease in the vertical coherence between pairs of velocity time series. The internal tide separated from the barotropic tide is well correlated by the vertical. In the deep layers, in which the amplitudes of velocities of internal tides are smaller, correlation at the semidiurnal frequency is almost completely determined by the correlation of the barotropic tide.

This approach was also employed in the central Atlantic south of the Azores and southwest of the shallow Great Meteor Banks by Morozov and Nikitin (1984b). One of the moorings deployed at 32° 41′N, 32° 08′W was equipped with current meters at depths of 30, 200, 300, 500, 700, 1500, 2000, 2500, 3000, and 3500 m. The depth of the ocean at the location of the mooring was 3700 m. The measurements were processed with a band filter that separates the fluctuations in the band with periods 12.4 ± 2 h. Then, we calculated the ratio of the internal tide energy to the barotropic tide energy, which appeared equal to 1.5. The energy of internal waves exceeds the energy of the barotropic tide because the moored

measurements were carried out close to the region of internal tide generation over the slopes of the Mid-Atlantic Ridge.

Let us use the data of currents from this mooring and consider the vertical distribution of the dispersion of velocity components to estimate the modal composition of the semidiurnal internal tides. The distribution of the dispersion of velocity fluctuations over depth is shown in Fig. 7.11. High dispersions are found in the upper layer of the ocean. This was expected because the maximum of the eigen function for velocity fluctuations of the internal tide is at the surface. Another maximum is found at the bottom. The minimum was found at a depth of 1600 m. Since the minimum at 1600 m coincides with the zero of the eigen function for the horizontal velocity we can conclude that the first mode of internal tide dominates. This fact was previously (see Sect. 7.4) found from the other considerations.

After the time series were separated into the barotropic and baroclinic time series we performed spectral cross-analysis between baroclinic time series at different depths. The results of this calculation are shown in Table 7.4 in the second line of each cell. Coherences between unseparated time series U_Σ are presented in the first line of each cell. It is clearly seen from the table that after removing the barotropic time series U_{bt} the coherence between oscillations determined only by the internal tide increased and became greater than the confidence level (0.5). High coherence was also found between the time series of temperature and velocity (baroclinic component) measured at one depth, which provides evidence that the fluctuations were caused by one and the same wave process because they are functionally related.

Fig. 7.11 Vertical variation in the dispersion of the semidiurnal baroclinic currents in the region south of the Azores (solid line). The dashed line shows squared eigen function of the horizontal velocity for the semidiurnal internal tides of the first mode
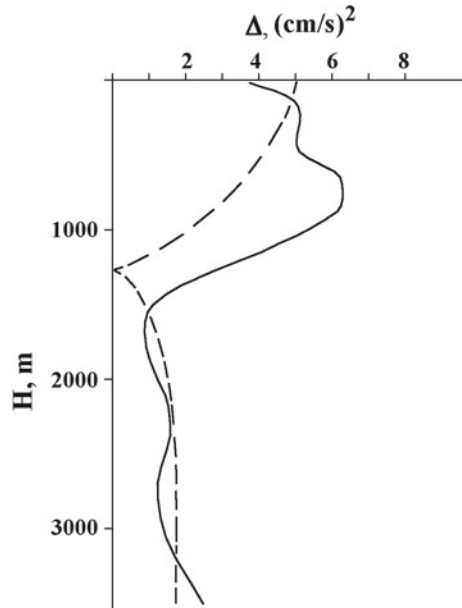
We performed a similar procedure of separation between semidiurnal oscilla-
tions caused by the barotropic and baroclinic tides in the Kara Gates Strait (see
Sect. 6.4). Four current meters were set on a mooring deployed in the strait over a
depth of 230 m. The ellipses of the currents induced by the barotropic tide were
calculated from the satellite altimetry data using the OTIS algorithm (Egbert and
Erofeeva 2002). The ellipses of the barotropic tide obtained by averaging the data
of current meters on the mooring and similar ellipses calculated from the altimetry
are shown in Fig. 7.12.

It is possible to separate the barotropic and baroclinic tidal currents using the
property that the wavelength of the barotropic tide is much longer than the
wavelength of internal tide. Usually the oceanographic study sites are small com-
pared with the scale of the barotropic tide wave, while the wavelength of internal
tide is comparable with the scale of the study sites. If the semidiurnal oscillations
are averaged over the scale of internal tide wavelength, we can calculate the
oscillations caused by the barotropic tide. The fluctuations averaged over spatial
distribution can be identified as the barotropic tide. Such practice is justified by the
property of linear waves that mean transport by the currents in the waves is zero.

Such averaging in the Sargasso Sea was performed using the measurements at
one depth over eight moorings of the Array-2 experiment. The semidiurnal fluc-
tuations of velocity were averaged at depths of 600, 1000, 1500, and 4000 m. The
time series of currents 10 and 40 days long were averaged. The ratio of the mean

Table 7.4 Coherence between time series of velocity

Depths of measurements (m)	Depths of measurements (m)								
	200	300	500	700	1500	2000	2500	3000	3500
30	0.62	0.41	0.80	0.50	0.66	0.32	0.58	0.74	0.53
	0.87	0.56	0.97	0.74	0.86	0.71	0.95	0.69	0.96
200		0.20	0.72	0.56	0.55	0.32	0.48	0.64	0.34
		0.46	0.88	0.84	0.96	0.91	0.92	0.87	0.92
300			0.24	0.22	0.25	0.31	0.49	0.42	0.23
			0.66	0.75	0.43	0.49	0.58	0.57	0.63
500				0.72	0.67	0.41	0.36	0.74	0.79
				0.80	0.86	0.74	0.92	0.77	0.98
700					0.70	0.35	0.49	0.78	0.47
					0.77	0.78	0.86	0.77	0.85
1500						0.39	0.34	0.73	0.54
						0.92	0.87	0.84	0.88
2000							0.08	0.20	0.18
							0.79	0.92	0.79
2500								0.29	0.55
								0.73	0.96
3000									0.45
									0.82

Coherences between unseparated time series U_{Σ} are presented in the first line of each cell.
Coherences between separated time series U_{iw} are presented in the second line of each cell

Fig. 7.12 Ellipse of tidal currents at the M_2 frequency on a mooring in the Kara Gates at 70° 17′N, 58° 11′E calculated from the measurements is shown with a thick line. The ellipse of tidal currents calculated on the basis of the TOPEX/POSEIDON data is shown with a thin line
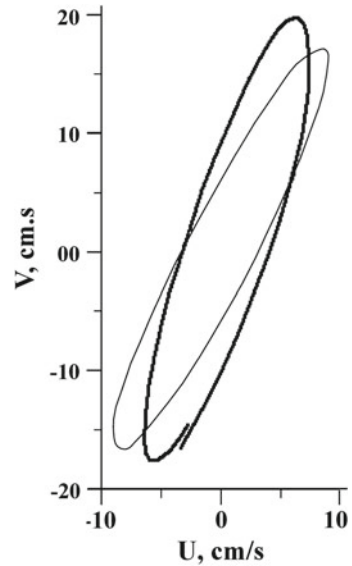
dispersion of internal tide to the dispersion of the barotropic tide was close to unity. This fact means that the energies of the barotropic tide and internal tide are approximately the same in the Sargasso Sea. When this ratio is close to unity it means that the internal tide energy has been decayed over a long distance of propagation from the generation regions over slopes of topography.

A similar approach to separate the currents of the barotropic tide was applied to the Megapolygon data in 1987. Current measurements on 51 moorings in the Northwest Pacific were averaged. This was the approach used to average the data over the spatial distribution of measurements (see Chap. 3, Sect. 3.3).

7.6 Beam Propagation of Internal Tides

We shall analyze the beam propagation of internal wave perturbations over the slopes of submarine ridges or continental slopes. Strong internal tides are generated over the slopes of the Mascarene Ridge in the Indian Ocean. We shall perform our analysis of beam propagation of internal tides in the neighborhood of their source on the basis of numerical modeling. We shall analyze the semidiurnal internal tides.

Internal tides are generated over the slopes of submarine ridges due to the interaction between the barotropic tide currents and the submarine slope. Barotropic tide currents flow over the slope and obtain a vertical component. These periodic vertical components cause the vertical displacement of isopycnals, thus generating internal waves. Internal tides propagate to the ocean normal to the slope regardless of the incident angle of the barotropic tide wave (Weigand et al. 1969).

In March 1987, a mooring array of six buoys was deployed near the Mascarene Ridge. Measurements at eight depths up to 1800 m were carried out over 15 days

(see Sect. 4.1). The planning of the location of the moorings presumed that the main tidal flow is confined in the channel (over the sill) between the Saya de Malha and Nazareth banks. The maximum tidal currents and intense internal waves should be generated in the channel. Therefore, the mooring array was extended in the direction from the channel. A scheme of the array and the bottom topography is shown in Fig. 4.1. The recalculation of the temperature fluctuations to the vertical displacements yields the amplitude of the waves equal to 60 m (and the wave height was correspondingly 120 m). The maximum wave heights exceeded 150 m, while the minimum were 65 m. The calculations of the spectral densities of the fluctuations of the temperature and currents based on the data of the measurements demonstrate the existence of a clearly manifested peak in the semidiurnal period that corresponds to the M_2 tidal period.

The beam trajectory was calculated from the given density distribution. Packets of semidiurnal internal oscillations propagate along the beam. In this section, we study the generation and propagation of tidal internal waves over the bottom slope on the basis of numerical modeling. We used a two-dimensional model of the generation and propagation of the internal waves in coordinates normal to the submarine ridge and along the depth. The original model was developed by Vlasenko (Vlasenko 1992; Vlasenko et al. 2005). The internal waves are considered plane and propagating normal to the ridge. We specified a density field not perturbed by internal waves that corresponds to the distribution of the Brunt–Väisälä frequency $N(z)$. The density distribution was taken from the available data of observations characteristic of this region in the tropical part of the Indian Ocean. The surface density was specified as 1.02275 g/cm^3.

When we analyzed the dependence of the beam propagation of the waves on the stratification, we did not change the deep part of the profile, but the variations were introduced only in the upper layer (Morozov et al. 2009). In the numerical experiments we used a work field 560 km long with a horizontal step of 100 m and 30 vertical levels. The time step was equal to 7 s according to the Courant–Friedrichs-Lewy condition (Richtmyer 1957). The coefficients of the horizontal eddy viscosity and the density diffusivity were specified equal to 200 m^2/s, and the corresponding vertical coefficients were equal to 0.0001 m^2/s. The water transport by the barotropic tidal wave was 174 m^2/s (Morozov and Vlasenko 1996). We performed several versions of calculations with different topography and the sill depth between the Saya de Malha and Nazareth banks. We also varied the bottom slope to study the dependence of the generation intensity on its inclination. The inclination of the internal wave characteristic line did not always coincide with the bottom slope inclination. These inclinations coincided at a specific depth either in the region of the upper thermocline or at a greater depth.

We also considered a version of the bottom slope in the case if the slope corresponded exactly to the internal wave characteristic line. Special attention was focused on the depth of the upper part of the submarine ridge, which varied in the numerical experiments from 100 to 400 m.

The perturbations of the stream function Ψ related to the internal waves at zero viscosity are described by the following equation (Prinsenberg and Rattray 1975):

$$(N^2 - \omega^2)\Psi_{zz} - (\omega^2 - f^2)\Psi_{xx} = 0 \qquad (7.2)$$

where, N is the Brunt–Väisälä frequency, f is the inertial frequency, and ω is the semidiurnal tidal frequency. From this equation, we get the characteristic curve for the internal waves, which is described by the following equation:

$$\frac{dz}{dx} = \pm \left(\frac{\omega^2 - f^2}{N^2 - \omega^2} \right)^{1/2}. \qquad (7.3)$$

The direction of the characteristic curve coincides with the direction of the group velocity; hence, it coincides with the direction of the energy transport by the internal waves. The internal wave energy propagates along the characteristic curves similar to the propagation along beams. The characteristic curves are lines with equal phase of the internal waves. Let us consider the perturbation pattern of the isopycnals by internal tide based on the results of the modeling. Figure 7.13 shows the density field near the Mascarene Ridge perturbed by the internal tide.

Propagation of an internal tidal wave with an amplitude exceeding 100 m is shown in Fig. 7.13; its wavelength is approximately equal to 130 km. Three characteristic curves start over the slopes of the ridge. One is directed to the deep ocean and the other to the surface. After reflecting from the surface, the second characteristic curve and the energy flux of the internal waves turn to the bottom. The first characteristic curve reflects from the bottom and turns to the surface. We emphasize that the law of equal incidence and reflection angles is not true here. The
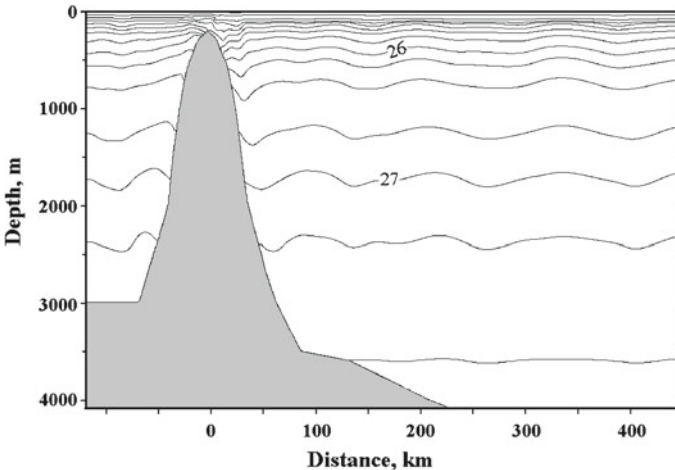
Fig. 7.13 Density field near the Mascarene Ridge generated by the internal tide. The density contour lines are shown with an interval of 0.00025 g/cm³. The bottom is shown in gray color. Numerals 26 and 27 indicate isopycnals 1.026 and 1.027 g/cm³. Reproduced from Morozov et al. (2009) ©Pleiades Publishing, Ltd. Used with permission

inclination of the characteristic curve is determined only by the ocean stratification, the wave frequency, and the latitude. The third characteristic line corresponds to the wave group (perturbation beam) propagating over the ridge in the opposite direction.

By numerical simulation, we obtained a section of the horizontal velocity field at a specific phase of the M_2 tide with a period of 12.4 h. Let us consider the case when the deep part of the characteristic line reaches the inclined bottom. The reflection angle is determined by the equations for the inclination of the characteristic curve (Eq. 7.3). This angle is determined by stratification N, latitude f, and frequency ω of the wave generation (M_2). The results of the model calculations are presented below. The velocities induced by the internal waves are shown in Fig. 7.14 and all the subsequent figures for the phase of the barotropic tide, at which all the tidal velocities are zero.

Let us analyze the velocity field generated by the internal tide over the submarine ridge. The specified depth of the submarine crest is 200 m. The total depth of the ocean is 4080 m. We select the moment of the velocity distribution in space when the barotropic tide velocities are zero. Figure 7.14 shows the spatial distribution of the horizontal velocities induced by the internal tide. Two systems of beams are developed. One beam is close to the slope of the bottom and the second is directed to the surface along the characteristic curve from the sharp deepening of the bottom. The thick lines show the characteristic curve according to Eq. (7.3).

The two beams generated at the ridge crest are related to the peculiarities of the interaction between the barotropic flow and the bottom topography. When the
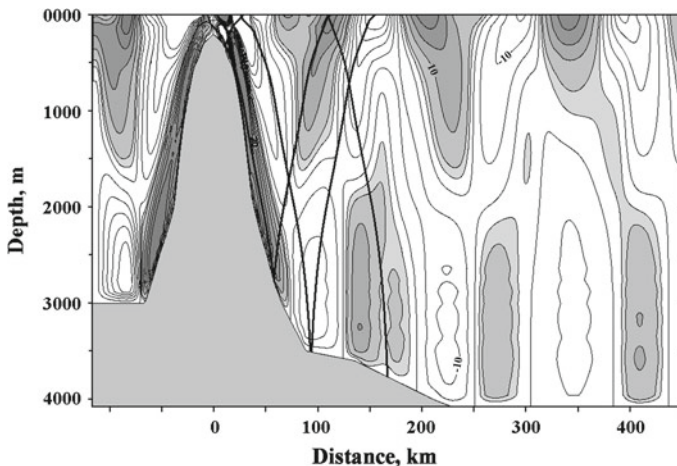
Fig. 7.14 Distribution of the horizontal velocities near the slope. The contour lines of the velocities (0, 5, 10, 15, 20, and 25 cm/s) are shown. The velocity distribution is given at the barotropic tide phase when the barotropic tide velocities are zero. Positive velocities are shown in gray color. The heavy black lines show the characteristic curves. Reproduced from Morozov et al. (2009) ©Pleiades Publishing, Ltd. Used with permission

barotropic tide currents from the entire water column are directed across the slope, the whole water mass cannot be transported by the flow to shallow depths over the threshold. Therefore, the flow splits, and part of the water in the upper layer turns into the opposite flow.

A similar effect is observed when the direction of the barotropic current changes. The mass flux along the slope to the ocean depth is quite high. The water mass that flows over the ridge is not enough to fill the entire flow. Thus, water from the upper layer over the slope is entrained into the flow. Circulation cells are formed in the space between the beams of intense water motion as a result of such water transport. Thus, the flow transforms from a barotropic to a baroclinic one with the dominating motion along the characteristics. Such a process occurs in alternating directions and at variable velocities of the currents. This process is similar to the blocking of the atmospheric flow over a ridge (Epifano and Rotunno 2005). In the case of a permanent barotropic flow when it is directed from the deep ocean over the threshold, the streamlines just converge and the flow accelerates without reversible motion of part of the flow.

We performed special numerical experiments to study the peculiarities of the internal wave perturbation field if the bottom slope coincides exactly with the characteristics of the internal waves at the given stratification. An example of such calculations is shown in Fig. 7.15. This is the case of the exact coincidence of the bottom slope and the characteristic curve. In this case, the second beam directed from the ridge crest to the surface is almost not developed. This confirms the previous qualitative consideration that, if the most intense generation occurs over the slope (where the greatest vertical density gradient coincides at a specific depth
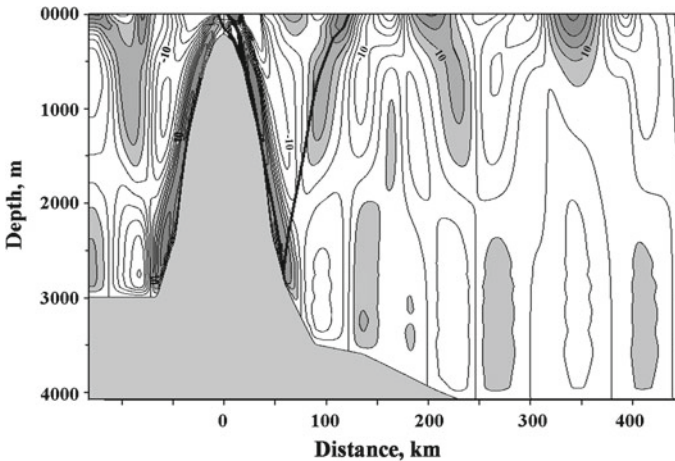
Fig. 7.15 Distribution of the horizontal velocities in the case of the exact coincidence of the bottom slope and the characteristic line of the equation for the internal tides. The ridge crest depth is 400 m. The thick lines show the characteristic curves as given by relation (7.3). Reproduced from Morozov et al. (2009) ©Pleiades Publishing, Ltd. Used with permission

with the region of equal inclinations of the bottom slope and the characteristic line), then two characteristics are directed approximately from this point: one to the surface and the other to the bottom. In the case considered here, the inclination of the characteristic lines always coincides with the bottom slope and there is no point of dominating generation on the slope.

The generation of internal tide becomes weak if the slope of the submarine ridge is flatter than the inclination of the characteristic line of the internal tidal wave. When the bottom slope coincides with the inclination of the characteristic line only at a large depth, the most intense generation occurs at larger depths where the stratification is weak. Such a bottom inclination was specified for the calculation of the velocity field shown in Fig. 7.16. It can occur that no depth layer exists in which the bottom slope and the inclination of the characteristic line coincide.

In the next step we shall consider the dependence of the beam (characteristics) pattern on the stratification. The intensity of the internal tide generation decreases at weaker stratification. If the stratification decreases so that the bottom slopes become flatter than the inclination of the internal tide characteristic line, the generation decreases even more. At weak stratification, the beam reaches the bottom at a smaller distance from the ridge crest and reflects from the inclined bottom (Fig. 7.17).

It is clear that the stronger the fluid flow transported by the barotropic tide, the stronger the generation of the internal tide. When the amplitude of the flow transported by the barotropic tide increases, the second characteristic line, which is
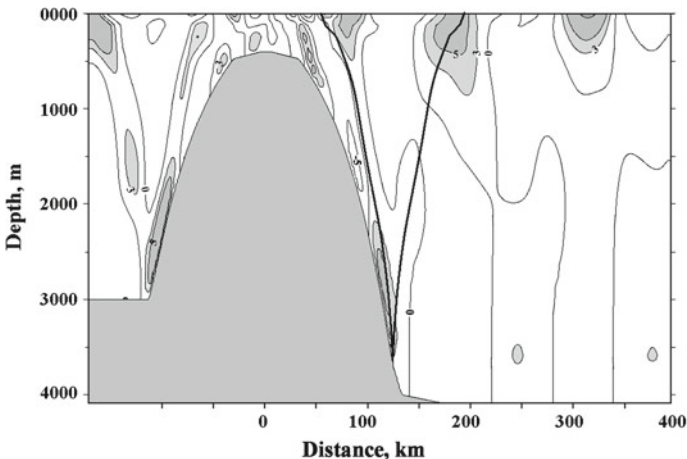
Fig. 7.16 Distribution of the horizontal velocities in the case of a flatter slope inclination than the characteristics of the equation for the internal tidal waves. The threshold depth is 400 m. The thick lines show the characteristic curves as given by relation (7.3). Reproduced from Morozov et al. (2009) ©Pleiades Publishing, Ltd. Used with permission
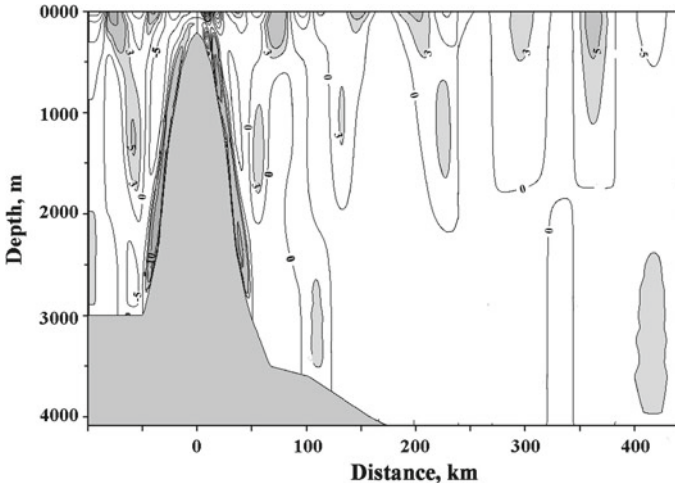
Fig. 7.17 Distribution of the horizontal velocities in the case of weak stratification. The threshold depth is 400 m. The thick lines show the characteristic curves as given by relation (7.3). Reproduced from Morozov et al. (2009) ©Pleiades Publishing, Ltd. Used with permission

directed from the threshold to the surface, becomes weaker compared to the one directed to the bottom. The currents are intensified everywhere including the circulation cells, in which the motion is directed opposite to the current in the main characteristic line.

Thus, we have shown that the most intense generation occurs in the region of the bottom, where its slope coincides with the inclination of the characteristic line for the internal wave equation. The radiated energy increases as the water density stratification increases in the region. The generation becomes weaker if the inclination of the submarine ridge slope is smaller than the inclination of the characteristic line of the internal tidal wave.

Three beams of high internal wave energy start from the generation region (at the ridge crest). The first beam is directed from the threshold to the deep ocean, the second is directed to the surface, and the third beam is also directed to the surface but in the opposite direction (in the direction of the threshold). After the reflection of the first beam from the surface, the energy flux of the internal waves turns to the bottom. The second beam (usually more intense) is reflected from the bottom and turns to the ocean surface. The spectra of the tidal currents as function of the vertical wavelength calculated from the data of the measurements in the region considered here agree well with the results of the numerical modeling.

7.7 Long Distance Propagation of Internal Tides and Their Energy Decay with Distance

In this section we shall consider the propagation of internal tides over long distances in the ocean and their decay in the course of propagation. Tidal energy is the main cause of mixing in the ocean. Tidal energy is transformed to internal tides, shorter internal waves, and then to mixing. Internal tides generated by the barotropic tide decay as they propagate; this leads to the formation of short-period internal waves, turbulence, and mixing, which influences the balance of mass and heat in the ocean (Munk and Wunsch 1998). The energy of internal tides gradually transforms to heat and potential energy of dense water from the deep layers mixing with lighter water in the upper layers. These processes are manifested most strongly in the generation regions over the slopes of the bottom topography where internal tides are most intense. Many publications indicate that a significant part of the energy of tidal internal waves dissipates near the source of their generation above submarine slopes (Thorpe 1999; Egbert and Ray 2000; St. Laurent et al. 2003; Zaron and Egbert 2006). However, internal tides can propagate over long distances. For example, it was found from altimetry measurements (Dushaw et al. 1995) that internal tide generated near the Hawaii Islands propagates over more than 2000 km.

Field studies of internal tides are generally carried out in study sites in the ocean. The horizontal scales of study sites seldom exceed 100–200 km, which is approximately a distance of one wavelength of the internal tide. Among the experiments known to us, the largest study site to date was in the Megapolygon experiment in the Northwest Pacific in 1987. Its horizontal size was approximately 500 km. The Array-2 experiment was located on a larger basin, but the moorings were deployed at large distances from each other. We have to use other approaches to study the longer propagation of internal tides and to analyze the behavior of the wave on larger horizontal scales over distances of several wavelengths. We assume that internal tides are generated over submarine ridges and propagate in the ocean decreasing its amplitude and energy with distance. This phenomenon was shown in the previous chapters on the examples of several study sites. While the wave propagates over the regions with variable topography and horizontally non-uniform fields of temperature, salinity, and currents it transforms and refracts. New waves with different phases and amplitudes generated over uneven bottom topography are added causing interference. Plane waves of tidal frequency generated at a remote source are not found at large distances from the ridges in the deep basins with flat bottoms. The entire wave field presents a background state with numerous waves of variable phases and amplitudes.

The horizontal variability of internal tides over large scales was analyzed by Morozov et al. (1976) on the basis of moored measurements in the equatorial zone of the Indian Ocean. The authors analyzed the amplitudes of vertical displacements caused by internal tides. They did not make any assumptions that these waves were generated at one source. Furthermore, this work was conducted before the appearance of the paper by P. Baines on the models of internal tide generation

(Baines 1982) and the review by Garrett and Munk (1979). At this time the main sources of internal tides in the ocean had not been clearly determined. The propagation of internal tides from a single source was investigated by Morozov and Vlasenko (1996). They studied internal tides near the Mascarene Ridge, which is one of the strongest sources of internal tides in the Indian Ocean. The authors determined parameters of the internal tides and demonstrated their propagation from the ridge on the basis of moored measurements and numerical modeling. Decay of the amplitude of internal tides was investigated over a distance of one and a half wavelengths. Similar results were obtained near a strong source of internal tides over the Great Meteor Banks in the Atlantic (Morozov et al. 1990). The quasi-stationary property of internal tides was demonstrated by Ivanov and Morozov (1983). The authors concluded that since the sources of internal tides are tidal currents, which are quasi-stationary, and bottom topography, which is stationary, the regime of internal tides should be quasi-stationary. The dominating period of their variations is spring-neap periodicity equal to 14 days. This conclusion was reached on the basis of six-month measurements in the Polygon-70 experiment. It was confirmed on the basis of data collected in other regions of the ocean by Morozov (1985) (see also Sect. 7.2). However, this property is characteristic of internal tides only in the regions close to their generation.

We understand the significance of the results presented above, and set ourselves the goal of analyzing the behavior of internal tide propagating from such a powerful source as the Mascarene Ridge in the eastern direction to the central part of the Indian Ocean. The moorings east of the Mascarene Ridge in 1987 were deployed as an antenna at distances of 90, 140, 185, 230, 245, and 285 km from the ridge (Morozov and Fomin 1989) (see Sect. 4.1). We also applied the 9-month data of two moorings in 1995 and 1996 with temperature records at 500 and 1200 m at distances of 1100 and 1745 km to the east from the ridge (Fig. 4.12) (Morozov et al. 1999; Lozovatsky et al. 2003).

Since the data we used in the analysis had been collected over a large basin at different depths and times, we had to assume that the oscillations determined by the propagation of internal tide are quasi-stationary. Above, we noted that internal tides possess this property. It is likely that the amplitudes of internal tides are subjected to spring-neap half-month variability due to the same variability of the barotropic tide. Generally, the amplitudes differ by ±25%. Long-term moored measurements demonstrate similar variations without seasonal variability. The depths of measurements on different moorings were not the same; hence, in our analysis we accepted only the measurements in the main pycnocline (700–1200 m), which correspond to the amplitudes of vertical displacements related to the first vertical mode of internal tides.

Analysis of temperature time series and spectra shows that as the wave propagates from the source its amplitude decreases. In our analysis we assumed that the wave was generated over the slopes of the Mascarene Ridge and propagated to the southeast. We neglect additional generation of internal tide in the bottom region of the abyssal basins, which is not absolutely correct because such generation occurs. However, we assume this because no significant topographic forms exist on the
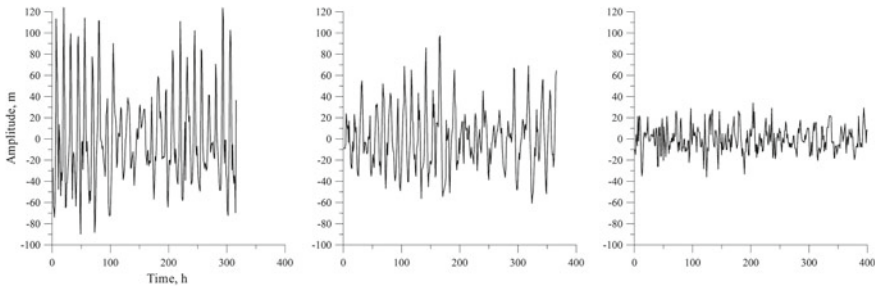
Fig. 7.18 Time series of vertical displacements on three moorings: mooring at 13° 09′S, 61° 35′E (depth 1200 m) (left panel), mooring at 13° 49′S, 63° 21′E (depth 1200 m (middle panel); mooring at 14° 05′S, 71° 05′E (depth 1300 m) (right panel)

pathway of the internal tide from the Mascarene Ridge to the central part of the Indian Ocean. Of course, waves can arrive at the locations of our moorings in the central part of the ocean from different sources. The closest of them is the Ninetyeast Ridge. According to the data presented by Morozov (1995) the waves generated there have significantly smaller amplitudes than those propagating from the Mascarene Ridge. In addition, generation also occurs in the abyssal depths due to the tidal currents flowing over small irregularities of the bottom topography (Bell 1975; Morozov 1991). All these factors introduce noise in our measurements.

Graphs of the time series of vertical displacements and their spectra were analyzed to reveal the decay law of the internal tide with distance. The temperature measurements on moorings were first subjected to the procedure of removing the existing trend. Then, the temperature measurements on moorings were recalculated into vertical displacements by means of dividing the temperature fluctuations by the vertical temperature gradients. Graphs of the time series of vertical displacements at depths of 1200–1300 m on three moorings near the Mascarene Ridge and distant from it are shown in Fig. 7.18. Their spectra are shown in Fig. 7.19. A decrease in the semidiurnal spectral peak as the distance from the source increases is clearly seen.

A graph of the decay of internal tide amplitudes based on these data with distance is shown in Fig. 7.20. These data show how wave amplitudes decrease as the wave propagates from the ridge. At small distances from the source where the amplitudes are high they decrease faster than at longer distances. Of course, this decay is influenced by the nonlinear effects characteristic of large amplitude waves. In the generation region the amplitudes of internal tides reach 75 m on the mooring located at a distance of 90 km from the ridge, while the mean amplitudes are 60 m. At a distance of 285 km the mean amplitudes decrease to 45 m. The amplitudes of internal tides are 25 m on the distant mooring located at 1100 km, while at 1745 km they do not exceed 20 m.

The mooring at 14° 58′S, 76° 59′E deployed at a distance of 1745 km from the Mascarene Ridge is closer to the Ninetyeast Ridge. The results of measurements show that the amplitudes on this mooring are small. Even if the waves from the

Fig. 7.19 Spectra of vertical
displacements on mooring at
13° 09′S, 61° 35′E (thick
line), at 13° 49′S, 63° 21′E
(dashed line), and at 14° 05′S,
71° 05′E (thin line)
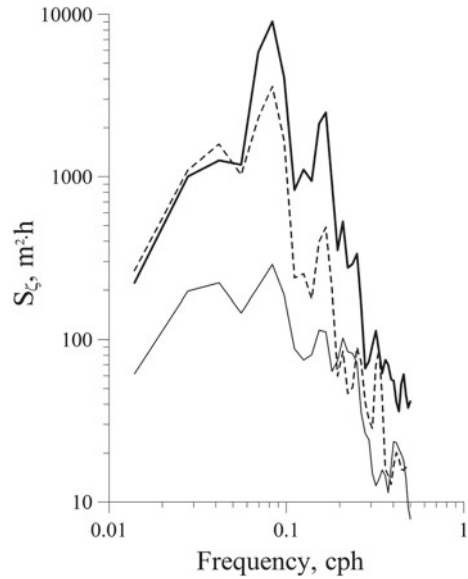
Fig. 7.20 Combined graph
of the semidiurnal internal
tide amplitude decay with the
distance from the Mascarene
Ridge based on the data of
moorings at 1200 m
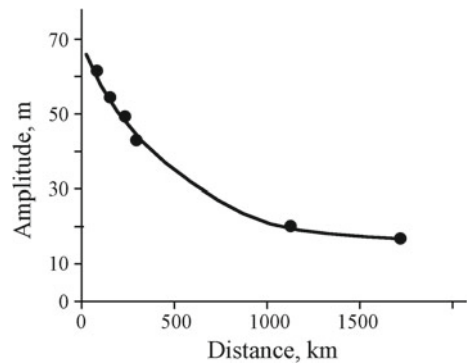
Ninetyeast Ridge contribute to the energy of internal tides measured on this
mooring, their contribution is low and the waves from both sources together form
the internal tides, which are only slightly higher than the background level. These
data indicate that the amplitudes of internal tides decrease by approximately 10%
over one wavelength. In addition, the moored measurements in the Crozet Basin far
from the regions of generation show that the amplitudes of the semidiurnal fluc-
tuations are extremely small (10–15 m), which is close to the background level
determined by the Garrett-Munk model (Garrett and Munk 1972). On several
spectral functions the spectral peak is either very weak or even lacking. This fact
indicates that only the background field of the internal wave exists here, because the
region is located far from the generation sources. Such measurements allow us to

estimate the limiting distance for the propagation of internal tides, which is equal to 2000–2500 km or 12–15 wavelengths.

We shall continue our research by analyzing the decrease in the energy of internal tide in the course of the wave propagation. The energy densities of internal tide (E_{IT}) were averaged over the wave period according to Torgrimson and Hickey (1979), Holloway and Merrifield (1999), and Lozovatsky et al. (2003). We used a band-pass filter to separate semidiurnal tidal components from the velocity and temperature time series. The density of the kinetic energy of the horizontal components of internal tide was determined as the sum of squared amplitudes of velocity. The total energy density of internal tide was calculated using the following formula:

$$E_{IT}(z) = 0.25\rho\left(\overline{u_{IT}^2(z)} + \overline{v_{IT}^2(z)} + N^2(z)\overline{\varsigma_{IT}^2(z)}\right) = E_H + E_\zeta. \qquad (7.4)$$

Here, u_{IT}, v_{IT} are the amplitudes of the semidiurnal internal tide velocity components, ς_{IT} are vertical displacements (Lozovatsky et al. 2003). Internal tide velocity components were calculated from the mooring data subtracting the barotropic tide velocities.

Horizontal velocities of the barotropic tide in the region were calculated using the OTIS tidal inversion software based on satellite data assimilation (Egbert and Erofeeva 2002). The barotropic tide velocities over the slopes of the ridge exceed 40 cm/s, while away from the ridge they decrease to 1–2 cm/s.

The energy density of internal tides was calculated from the time series at least 14 days long to exclude the spring-neap variability. The calculations show that the mean amplitudes of internal tides in the main pycnocline decreased from 60 to 18 m on the moorings located at distances from 90 to 1745 km from the ridge.

We normalized the distances by the scale equal to the wavelength of the first mode $\lambda = 145$ km. At a distance of one wavelength from the ridge ($x/\lambda = 0.97$) the energy density of the internal tide at a depth of 1000 m is $E_{IT} = 2.65$ J/m³. At a distance of 1745 km ($x/\lambda = 12.0$) from the ridge at a depth of 1200 m, the energy density decreases by a factor of 10 ($E_{IT} = 0.23$ J/m³) (Fig. 7.21). This is approximately 15% loss of energy over one wavelength.

Its total energy decreased by a factor of 10 over a distance of 1745 km compared to the energy at a distance of 145 km; hence a 10-fold energy decrease occurs over a distance of 12 wavelengths.

We compared the energy decay of the internal tide in the Mascarene region with some other regions. The graphs of energy decay in the Kuroshio, Aleutian, Kermadec, Mozambique, and Iberia regions are also shown in Fig. 7.21. The energy level in each of the regions is different but the rate of energy decay is very similar to the one analyzed near the Mascarene Ridge.

We shall apply model calculations to compare the experimental field results with numerical calculations using the Vlasenko model (see Sect. 1.4.1) (Vlasenko 1992; Morozov and Vlasenko 1996; Vlasenko et al. 2005; Morozov et al. 2002).
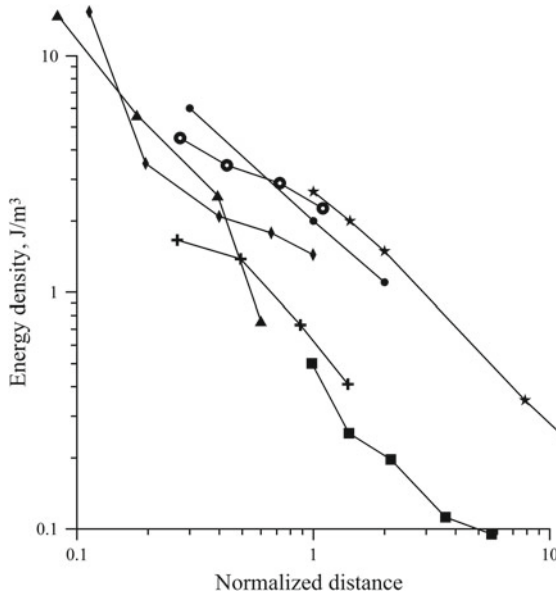
Fig. 7.21 Total energy density $E_{IT} = E_H + E_\zeta$ of the semidiurnal internal tide east of the Mascarene Ridge. The distance from the ridge is normalized by the wavelength of the first mode λ = 145 km. The measurement depth is in the interval 1000–1200 m. Energy density at 1000 m is shown with small dots; and that at 1200 m is shown with stars. Graphs of energy decay in the other regions are shown with different symbols: diamonds show energy decay in the Mozambique region (Fig. 4.15); squares show energy decay in the Kuroshio region (Fig. 3.26); triangles show energy decay from the Aleutian Islands (Fig. 3.22); crosses show energy decay from the Kermadec Ridge; large circles with a white dot in the middle show energy decay west of the Iberian Peninsula

The bottom topography was specified in the model as follows. The ridge crest was set at 500 m. The slopes were specified according to the ETOPO digital database. The ocean depth east of the ridge at distances greater than 230 km was assumed constant H = 5100 m. The total number of vertical layers was 34. The time step was 7.2 s, and the horizontal step was 900 m. The coefficients of horizontal viscosity and density diffusion near the ridge were 250 m^2/s and they gradually decreased to 200 m^2/s over 100 km. At greater distances they were specified constant. The vertical diffusion was specified equal to 0.01 m^2/s in the entire water column over the slopes and then it reduced to 0.0001 m^2/s over the flat bottom. The stream function amplitude (water transport) related to the barotropic tide forcing was specified equal to 174 m^2/s at the bottom and zero at the ocean surface.

In order to calculate the energy density of internal tide we subtracted the model barotropic velocities from the model simulated velocities to obtain only the perturbations related to internal tide. The density fluctuations were recalculated to the vertical displacements by means of dividing by the vertical density gradient.

Fig. 7.22 Model calculation of internal tide energy decay versus distance normalized by the length of the first mode, 145 km (dots). Internal tide energy densities calculated from the field data in the depth range 1000–1300 m are shown with stars
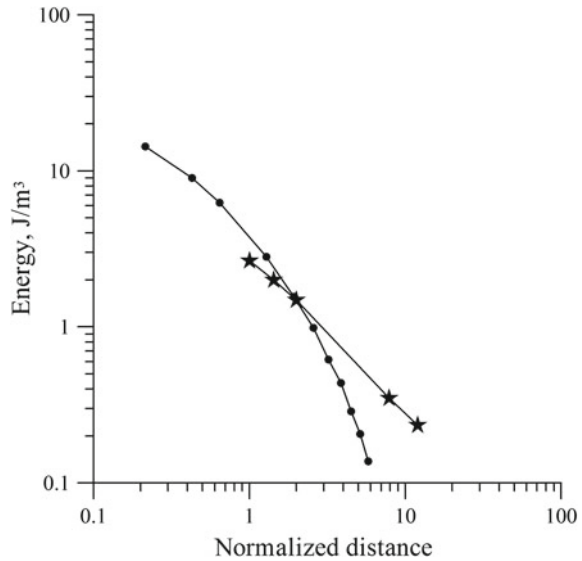
Vertical displacements and horizontal velocities were band filtered using the same algorithm as the measured values.

The model simulated energy densities induced by the internal tide at 1200 m are shown in Fig. 7.22 (black dots). The field data in the range 1000–1300 m are shown with stars. At distances $x/\lambda < 2$, model simulations are close to the observations.

The modeling result indicates that at distance greater than three wavelengths internal wave energy decreases faster than it follows from the field measurements. Approximately at this distance from the ridge the bottom in the model was specified flat. The real bottom topography is characterized by moderate roughness. We suppose that additional generation of internal tide over irregularities of the bottom topography occurred in the regions where we specified a flat bottom in the model. Hence, the field data show a smaller rate of decay.

Thus, analysis of the measurements of internal tides over the basin of the Indian Ocean shows that strong internal tides generated over the slopes of the Mascarene Ridge can propagate over long distances in the ocean at least up to 2000 km. In the course of internal tide propagation the amplitudes of the waves decrease. At small distances from the source, the energy losses are stronger than at larger distances when the amplitudes become smaller and the role of nonlinear terms decreases. A decrease in the amplitude can be estimated as 10% over one wavelength. The energy losses are about 15% over one wavelength. Some other estimates in other regions of the ocean indicate that the losses of amplitudes are 5–10% and the energy losses are 10–20% over one wavelength. The losses naturally depend on the initial amplitude and energy of internal tides.

At distances of 1500–1700 km from the source of generation, which is approximately 10–12 wavelengths, the influence of internal tides becomes insignificant. Their contribution to the total energy of internal waves is of the order of 10% over the background level determined by the Garrett-Munk model (1972).

According to the model simulations by Holloway and Merrifield (1999) of the propagation of internal tides from the Hawaiian Ridge, their energy becomes smaller than the energy of the barotropic tide at distances greater than 3 wavelengths.

Our model calculation indicates that the ratio of the internal tide energy to the energy of the barotropic tide becomes equal to unity at distances of five wavelengths, which is close to the estimates of Holloway and Merrifield (1999). Faster decay of internal tide energy in the model can be explained by the fact that unlike natural conditions the model has no additional sources over the uneven bottom. Divergence of energy is another mechanism of losses. In the case of a linear source like a submarine ridge radial divergence should not be strong at distances smaller than the characteristic length of the topographic formation (of the order of 1000 km).

The study of surface manifestations of internal tides from satellites by Zhao (2014) shows that the K_1 and O_1 internal tides travel over 1600 km across the central deep basin of the South China Sea and arrive at the Vietnam coast. In the West Pacific, they propagate over 2500 km across the Philippine Sea, reaching the Mariana Ridge. The M_2 internal tides propagate shorter distances (1000 km) in both basins.

Modeling of internal tides generated over the Hawaiian Ridge was reported by Kang et al. (2000). The M_2 baroclinic energy flux exceeds 10,000 W m^{-1} for the strongest energy beam propagating to the northeast. Tidal energy is transformed into the internal tides that propagate in both directions from the ridge over distances exceeding 1000 km.

Intense semidiurnal internal tide generated in the Gulf of Alaska was analyzed by Bracher and Flatté (1997) on the basis of acoustic experiments in the Central Pacific at 32°–33°N. They recorded the M_2 internal tide signal after the waves propagated over more than 3000 km. The maximum energy flux was estimated at 7000 W m^{-1}.

Altimetric estimates of internal tides in the North Pacific were analyzed by Zhao and Alford (2009). They recorded internal tidal beams emanating from the Hawaiian Ridge and Aleutian Islands propagating more than 3500 km across the North Pacific Ocean.

Energy losses of internal tides after propagating over long distances in the ocean were studied by Kelly et al. (2013). The authors study bottom scattering of energy when mode-1 internal tides propagate across the ocean. The waves interact with the irregularities of the bottom topography and scatter energy to higher-mode internal tides. The authors use near-bottom velocities in the model to estimate mode-1 scattering. The major part of internal tide energy dissipates at large topographic features. Internal tides lose about 60% of their energy upon impacting the continental margins: 20% transmits onto the continental shelf, 40% scatters to higher

modes, and 40% reflects back to the ocean. These mechanisms of energy dissipation of remotely generated internal tides over the continental slope of Virginia in the North Atlantic were studied by Nash et al. (2004). The authors report that the energy flux of the internal tides on the continental slope off Virginia reaches 1000 W m^{-1}.

Alford and Zhao (2007) analyzed 2200 historical moorings and selected 80 of them to understand the long-range propagation of internal waves. They computed energy and horizontal energy flux for the two gravest baroclinic modes around the globe emphasizing the M$_2$ internal tides generated by the flows over sloping topography. They also used altimetry in their study. Their results indicate that the internal tide propagates over long distances, at least 2400 km northeast from Hawaii taking ~ 10 days to cover this distance. The wave field is strongly refracted by the mesoscale currents and stratification. The authors distinguish several regions of strong internal tide generation: Biscay Bay, Canary Basin, Mid-Atlantic Ridge, Kyushu-Palau Ridge, Mascarene Ridge, and Madagascar Basin. The authors introduce a criterion for the initial energy flux of the order of $O(1000$ W m$^{-1})$, which is sufficient for internal tide to propagate far from the source.

The influence of abyssal hills with a horizontal scale of 10 km on the generation of internal tides was studied by Melet et al. (2013) based on the analytical theory and a global map of topography with a resolution of 1/120°. The authors estimate the global energy spent on the generation of the internal tide over abyssal hills at 0.1 TW, which is 10% of the energy flux due to larger topographic scales. These estimates are consistent with the previous estimates by Bell (1975).

7.8 Influence of Internal Tides on Antarctic Bottom Water Flow

The spreading of Antarctic Bottom Water in the Atlantic Ocean can be seen from the temperature at the bottom. Figure 7.23 shows the topography of the Atlantic Ocean and the distribution of potential temperature at the bottom, which characterizes the spreading of Antarctic Bottom Water. The potential temperature increases significantly after passage of the narrow abyssal channels: Vema Channel (31°S, 39°W), Vema Fracture Zone (11°N, 41°W), Romanche and Chain fracture zones (equator, 16°W).

Orographic peculiarities have a determining influence on the propagation of abyssal waters of Antarctic origin. The deepest part of the Atlantic Ocean is a series of alternating depressions and elevations of the ocean bottom in the western and eastern parts of the ocean divided by the Mid-Atlantic Ridge. The publications by Wüst (1936), Hogg and Zenk (1997), Saunders (1994), Koltermann et al. (1999), Friedrichs and Hall (1993), Harvey and Arhan (1988) demonstrate the significant role of fractures in the Mid-Atlantic Ridge, such as Romanche (0°), Vema (11°N), and Charlie Gibbs (53°N) in the propagation of the deep and especially bottom
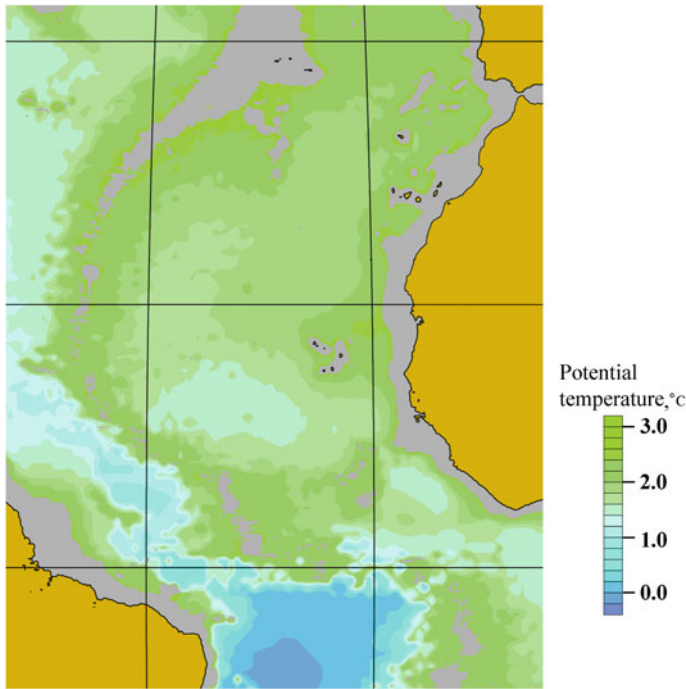
Fig. 7.23 Distribution of potential temperature (°C) at the bottom in the tropical Atlantic Ocean that gives an idea of Antarctic Bottom Water spreading in the North Atlantic Ocean. Gray color shows the depths not related to the bottom water spreading

waters. In the eastern parts of the ocean, their propagation is limited by the Walvis Ridge crossing the entire eastern basin. Although Connary and Ewing (1974) report that a small portion of Antarctic Bottom Water propagates to the Angola Basin through a channel in the Walvis Ridge, the main role in the water exchange between the western and eastern parts of the ocean belongs to the deep fractures in the Mid-Atlantic Ridge.

It is commonly accepted that the main pathway for Antarctic Bottom Water to the East Atlantic is the Vema Fracture Zone in the Mid-Atlantic Ridge at 11°N. This concept was first time suggested by Mantyla and Reid (1983). They proposed that bottom waters propagating through the Romanche Fracture Zone influence only the equatorial and southeastern part of the Atlantic Ocean and do not spread to the north through the Kane Gap, whereas the Vema Fracture Zone is the main pathway for bottom waters into the northeastern Atlantic. This idea was later supported by McCartney et al. (1991) and by Morozov et al. (2010).

Munk and Wunsch (1998) estimated that without mixing, Antarctic Bottom Water would fill the entire ocean within a few thousand years and turn it into a stagnant pool of cold water. Only a thin upper layer of warm water would remain at the surface. Internal tide is the main source of ocean mixing, especially at the

mixing hot spots over slopes of bottom topography. Impressive laboratory experiments by Whitehead and Wang (2008) demonstrate this.

Here, we will attempt to give a physical explanation as to why strong mixing occurs in the Romanche and Chain fracture zones, which results in the isolation of different basins east of the Mid-Atlantic Ridge. We believe that this fact is explained by different intensities of mixing of Antarctic waters with the overlying North Atlantic Deep Water due to internal tides generated over the slopes of the Mid-Atlantic Ridge.

Morozov (1995) calculated the amplitudes of internal tidal waves in the World Ocean based on the integrated results of measurements and model calculations. According to these estimates, the amplitude of internal tidal waves reaches almost 50 m in the Romanche Fracture Zone region at the equator and only slightly exceeds 20 m in the Vema Fracture Zone region at 11°N.

Figure 7.24 shows a chart of amplitudes of internal tides in the tropical region of the Atlantic Ocean. Due to such a significant difference in the amplitudes of waves in these regions, mixing of deep water masses also differs significantly. The main mixing occurs over the slopes of the submarine ridge, where amplitudes of internal waves are the greatest. Internal tides are intensely generated in the regions of strong barotropic tides if the currents are normal to the ridge. Generation is intensified if the inclination of the bottom coincides with the inclinations of characteristic curves of internal tides, which depend on stratification (Morozov 1995). The conditions that favor the strong generation of internal tides are much better in the region of equatorial channels than in the Vema Fracture Zone.
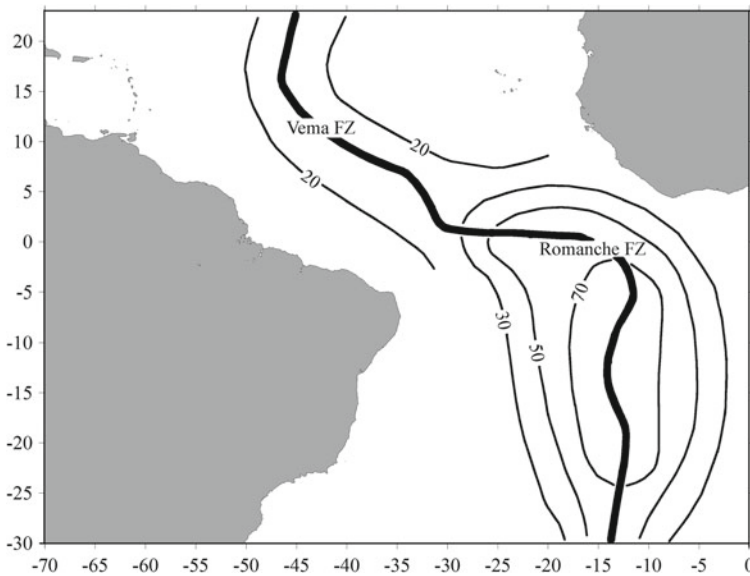
Fig. 7.24 Contour lines of amplitudes of internal tide in meters based on Morozov (1995). Thick lines show the Mid-Atlantic Ridge. The internal tide amplitude exceeds 50 m in the Romanche Fracture Zone region and only slightly exceeds 20 m in the Vema Fracture Zone region

Velocity ellipses of the barotropic tide currents in the region of the bottom water outflow from the Romanche and Chain fracture zones were calculated from the TOPEX/POSEIDON satellite data by S. Erofeeva (Oregon State University) upon our request. Ellipses in Fig. 7.25 show two remarkable properties: (i) the velocities are quite high (5 cm s^{-1}) compared to the usual 1–2 cm s^{-1} in the open ocean; (ii) the ellipse is strongly elongated in the E-W direction, which is close to the direction of the Romanche and Chain fracture zones. It is essential that the ellipses were calculated from the data of surface elevations and they represent the entire tidal structure in the water column, the largest part of which is located above the deep channel. Thus, such barotropic tides can induce the strong generation of internal tides.

Characteristic curves for internal tides, where amplitudes of internal waves are maximal, are inclined near the slopes of the ridges. The results of numerical calculation of the field of horizontal velocities of particle motion in the internal tidal waves over the slopes of the Mid-Atlantic Ridge in the Romanche Fracture Zone region are shown in Fig. 7.26. The results of numerical calculation are presented for the phase of the barotropic tide when the velocities of the barotropic tide currents are zero. The calculation was made using the numerical model described by Vlasenko (1992) and by Vlasenko et al. (2005). Strong mixing in the Romanche Fracture Zone region transforms the properties of the Antarctic water.

A similar calculation was performed for the Vema Fracture Zone region (Fig. 7.27). Velocities of internal tide are lower. Hence, internal waves provoke lesser mixing in this region.

We summarize that mixing in the equatorial region of the East Atlantic is greater than in the region of the Vema Fracture Zone. This strong mixing is caused by a strong barotropic tide in the equatorial region of the East Atlantic compared to the region of the Mid-Atlantic Ridge near the Vema Fracture Zone.

Fig. 7.25 Ellipses of M$_2$ barotropic tide (cm s^{-1}) in the region east of the Romanche and Chain fracture zones based on TOPEX/ POSEIDON data. The ellipses are calculated for the time of measurements in the region (April, 2009)
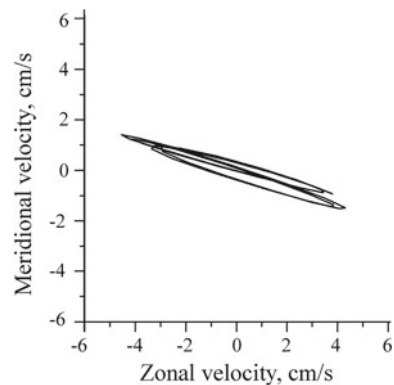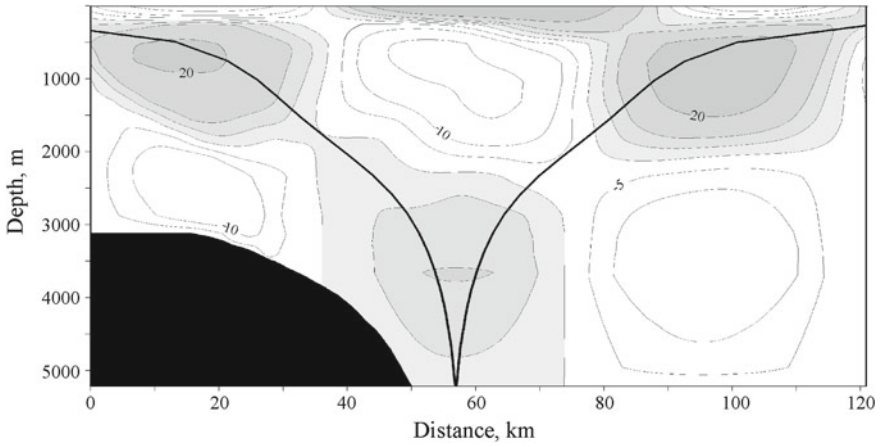
Fig. 7.26 Distribution of velocities during generation of internal tide over the slope of the Mid-Atlantic Ridge in the Romanche Fracture Zone region. Contour lines of velocities are given in cm s^{-1}. The black color denotes the ocean bottom. The thick black line shows the characteristic curve for internal tide M_2
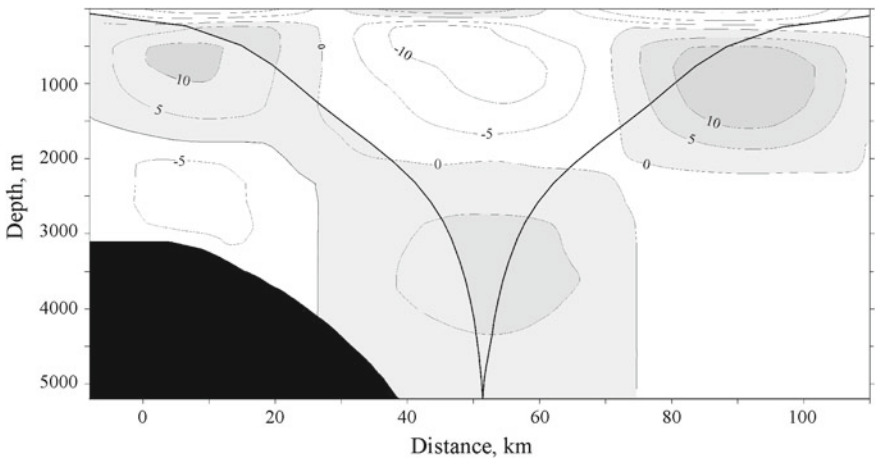
Fig. 7.27 Distribution of velocities during the generation of internal tide over the slope of the Mid-Atlantic Ridge in the Vema Fracture Zone region. Contour lines of velocities are given in cm s^{-1}. The black color denotes the ocean bottom. The thick black line shows the characteristic curve for internal tide M_2

Strong mixing explains the difference in the contribution of the equatorial channels and Vema Fracture Zone to the bottom water mass composition in the Northeast Atlantic. Without strong mixing in the equatorial region, the influence of the Romanche and Vema fracture zones on the Northeast Atlantic seems to be equal:

(1) Antarctic Bottom Water transports through the Romanche and Chain fracture zones are of the order of 1 Sv, which is almost the same as the water transport through the Vema Fracture Zone.

(2) The difference between the smallest values of potential temperature of bottom water is insignificant after the water outflows to the East Atlantic: θ = 1.66°C (in Romanche) and θ = 1.69°C (in Vema).

(3) The depths of the main sills in the channels do not differ greatly: 4359 m (Romanche FZ) and 4571 m (Vema FZ).

Despite the fact that the depths of the Kane Gap (9°N, 19°W) allow propagation of Antarctic Bottom Water and only 1.8°C isotherm is separated over the passage, the transport of bottom water through this channel is not high (0.5 Sv) (Morozov et al. 2013).

Strong mixing with overlying waters results in the strong transformation of properties of Antarctic Bottom Water after its outflow from the equatorial channels. In addition, the region of strong mixing also includes the Kane Gap, which makes this passage almost impossible for the strong northerly flow of bottom waters. The amplitudes of the internal tide at the bottom based on measurements with a string of thermistors reach 70 m (van Haren et al. 2014). Strong mixing closes this pathway for the flow of bottom water transported through the equatorial fracture zones. On the other hand, mixing conditions in the Vema Fracture Zone region are not as strong as in the equatorial East Atlantic and the bottom water that is transported to the east is less transformed in the Vema Fracture Zone; hence, it fills the entire Northeast Atlantic abyssal depths.

Different intensity of mixing results in different stratification at the outflow from the channels. The Brunt-Väisälä frequency east of the Romanche Fracture Zone is $N = 0.14 \times 10^{-3}$ s^{-1}, while east of the Vema Fracture Zone it is equal to $N = 0.80 \times 10^{-3}$ s^{-1}. A simple relation in Gargett (1984) gives the dependence of vertical diffusivity k_z on stratification:

$$k_z = \frac{10^7 \; m^2 \, s^2}{N(z)}.$$

According to this relation diffusivity in the deep layers of the Mid-Atlantic Ridge east of the Vema Fracture Zone is $k_z = 1.2 \times 10^{-4}$ m^2/s, and east of the Romanche Fracture Zone it is 6 times greater ($k_z = 7.1 \times 10^{-4}$ m^2/s).

References

Alford MH, Zhao Z (2007) Global patterns of low-mode internal-wave propagation. Part I: energy and energy flux. J Phys Oceanogr 37(7):1829–1848

Baines PG (1982) On internal tide generation models. Deep-Sea Res 29(3):307–338

Bell TH (1975) Topographically generated internal waves in the open ocean. J Geophys Res 80 (3):320–327

Bogdanov KT, Magarik VA (1967) Numerical solution of the problem of tidal wave propagation (M_2 and S_2) in the World Ocean. Dokl Akad Nauk SSSR 172(6):1315–1317

Bracher C, Flatté SM (1997) A baroclinic tide in the Eastern North Pacific determined from 1000-km acoustic transmissions. J Phys Oceanogr 27(4):485–497

Connary SD, Ewing M (1974) Penetration of Antarctic bottom water from the Cape Basin into the Angola Basin. J Geophys Res 79:463–469

Dushaw BD, Cornuelle BD, Worcester PF, Howe BW, Luther DS (1995) Barotropic and baroclinic tides in the central North Pacific Ocean determined from long-range reciprocal acoustic transmissions. J Phys Oceanogr 25:631–647

Egbert GD, Erofeeva S (2002) Efficient inverse modeling of barotropic ocean tides. J Atmos Ocean Tech 19:183–204

Egbert GD, Ray RD (2000) Significant dissipation of tidal energy in the deep ocean inferred from satellite altimeter data. Nature 405:775–778

Epifano CC, Rotunno R (2005) The dynamic of orographic wake formation in flows with upstream bloking. J Atmos Sci 62:3127–3150

Fahrbach E (1976) Einige Beobachtungen sur Erseugung und Ausbreitung interner Gereiten wellen am Kontinentalabhang vor Sierre Leone "Meteor" Freschungsegeb No 18:64–77

Fjelstad JE (1933) Interne Wellen. Geophys Publ Oslo 10(6):1–35

Fliegel M, Hunkins K (1975) Internal wave dispersion calculated using the Thomson-Haskel method. J Phys Oceanogr 5(3):541–548

Friedrichs MA, Hall MM (1993) Deep circulation in the tropical North Atlantic. J Mar Res 51 (4):697–736

Gargett AE (1984) Vertical eddy diffusivity in the ocean interior. J Mar Res 42:359–393

Garrett CJR, Munk WH (1972) Space-time scales of internal waves. Geophys Fluid Dyn 3(3):225–264

Garrett C, Munk W (1979) Internal waves in the ocean. Ann Rev Fluid Mech 11:339–369

Groen P (1948) Contributions to the theory of internal waves. Mededelinger en Verhandelingen, Serie B Deel 11, No. 11, Koninkijk Nederlandsch Meterologisch Imtitut de Bilt

Harvey J, Arhan M (1988) The water masses of the Central North Atlantic in 1983–1984. J Phys Oceanogr 18(12):1855–1874

Hogg NG, Zenk W (1997) Long-period changes in the bottom water flowing through Vema Channel. J Geophys Res 102(C7):15639–15646

Holloway PE, Merrifield MA (1999) Internal tide generation by seamounts, ridges, and islands. J Geophys Res 104(C11):25937–25951

Ivanov YA, Morozov EG (1977) Half-month inequality of internal waves of tidal period. Dokl Akad Nauk SSSR 236(3):733–735

Ivanov YA, Morozov EG (1983) Investigations of temperature fluctuations at tidal and inertial periods. In: Atlantic hydrophysical polygon-70. Amerind Co. Oxonian Press Ltd., New Delhi, pp 289–299

Kang SK, Foreman MG, Crawford WR, Cherniawsky JY (2000) Numerical modeling of internal tide generation along the Hawaiian Ridge. J Phys Oceanogr 30(5):1083–1098

Kelly SM, Jones NL, Nash JD, Waterhouse AF (2013) The geography of semidiurnal mode-1 internal-tide energy loss. Geophys Res Lett 40:4689–4693. https://doi.org/10.1002/grl.50872

Koltermann KP, Sokov AV, Tereschenkov VP, Dobroliubov SA, Lorbacher K, Sy A (1999) Decadal changes in the thermohaline circulation of the North Atlantic. Deep-Sea Res II 46:109–138

Krauss W (1966) Interne Wellen. Gebrüder Borntraeger, Berlin-Nikolasee

Kulakov AV (1977) Numerical methods for calculating the vertical structure of oscillations in the ocean. Oceanology 17(5):525–528

St. Laurent LS, Stringer S, Garrett C, Perrault-Joncas D (2003) The generation of internal tides at abrupt topography. Deep-Sea Res 50:987–1003

LeBlond PH, Mysak LA (1978) Waves in the Ocean. Elsevier oceanographic series. Elsevier, Amsterdam, p 602

Lozovatsky ID, Shapovalov SM (1973) Determination of certain characteristics of internal waves at a given Väisälä-Brunt frequency. Izv Acad Sci USSR, Ser Atmos Ocean Phys 9(4):248–249

Lozovatsky ID, Morozov EG, Fernando HJS (2003) Spatial decay of energy density of tidal internal waves. J Geophys Res 108(C6):3201–3216

Mantyla AW, Reid JL (1983) Abyssal characteristics of the World Ocean waters. Deep-Sea Res 30 (8):805–833

Marchuk GI, Kagan BA (1989) Dynamics of Ocean tides. Kluwer Academic Publishers, Dordrecht

McCartney MS, Bennet SL, Woodgate-Jones ME (1991) Eastward flow through the Mid-Atlantic ridge at 11°N and its influence on the abyss of the Eastern basin. J Phys Oceanogr 21(8):1089–1121

Melet A, Nikurashin M, Muller C, Falahat S, Nycander J, Timko PG, Arbic BK, Goff JA (2013) Internal tide generation by abyssal hills using analytical theory. J Geophys Res 118:6303–6318. https://doi.org/10.1002/2013JC009212

Morozov EG (1983) Investigation of 9-month temperature and velocity spectra in the Western Atlantic. Izv Acad Sci USSR Ser Atmos Ocean Phys 19(10):166–168

Morozov EG (1985) Oceanic internal waves. Nauka Moscow 151 p. [in Russian]

Morozov EG (1988a) Studies of the mode structure of semidiurnal internal waves. Ocean Res 41:68–72

Morozov EG (1991) Tidal fluctuations in the ocean bottom layer. Oceanology 31(2):140–142

Morozov EG (1995) Semidiurnal internal wave global field. Deep-Sea Res 42(1):135–148

Morozov EG, Fomin LM (1989) Extreme internal tidal waves measured in the Indian Ocean. Dokl Akad Nauk SSSR (Earth Sci Sect) 305(2):241–244

Morozov EG, Nikitin SV (1981a) Investigation of the direction of internal waves of tidal period in study area 70. Oceanology 21(2):168–171

Morozov EG, Nikitin SV (1981b) Dispersion relation for internal gravity waves and their vertical structure in the POLYMODE region. Ocean Res 34:78–84

Morozov EG, Nikitin SV (1984a) Propagation of semidiurnal internal waves in a region with varying bottom topography. Ocean Res 36:44–49

Morozov EG, Nikitin SV (1984b) Separation and analysis of the baroclinic component of semidiurnal temperature fluctuations. Ocean Res 36:55–61

Morozov E, Vlasenko V (1996) Extreme tidal internal waves near the Mascarene Ridge. J Mar Syst 9(3–4):203–210

Morozov EG, Plakhin EA, Shapovalov SM (1976) Time and space variability of the temperature field in the equatorial zone of the Indian Ocean. Izv Acad Sci USSR Ser Atmos Ocean Phys 12 (3):179–184

Morozov EG, Samodurov AS, Limanskaya LI, Filatova LP (1979a) Investigations of the diurnal and semidiurnal temperature fluctuations. Ocean Res 30:63–73

Morozov EG, Samodurov AS, Filatova LP (1979b) Separation of semidiurnal temperature fluctuations determined by the barotropic tide and internal waves. Ocean Res 30:78–81

Morozov EG, Nikitin SV, Filyushkin BN (1990) Generation of internal tidal waves in the vicinity of seamounts in the Western Canary Basin. Doklady AN SSSR (Earth Sci Sect). 315(6):321–323

Morozov EG, Vlasenko VI, Demidova TA, Ledenev VV (1999) Tidal internal wave propagation over large distances in the Indian Ocean. Oceanology 39(1):42–46

Morozov EG, Trulsen K, Velarde MG, Vlasenko VI (2002) Internal tides in the Strait of Gibraltar. J Phys Oceanogr 32:3193–3206

Morozov EG, Nechvolodov LV, Sabinin KD (2009) Beam propagation of tidal internal waves over a submarine slope of the Mascarene Ridge. Oceanology 49(6):745–752

Morozov E, Demidov A, Tarakanov R, Zenk W (2010) Abyssal channels in the Atlantic Ocean: water structure and flows. Springer, Dordrecht

Morozov EG, Tarakanov RY, van Haren H (2013) Transport of AABW through the Kane Gap, tropical NE Atlantic Ocean. Ocean Sci 9:825–835. https://doi.org/10.5194/os-9-825-2013

Munk W, Phillips N (1968) Coherence and band structure of inertial motion in the sea. Rev Geophys 6:447–472

Munk WH, Wunsch C (1998) Abyssal recipes II: energetics of tidal and wind mixing. Deep-Sea Res 45:1977–2010

Nash JD, Kunze E, Toole JM, Schmitt RW (2004) Internal tide reflection and turbulent mixing on the continental slope. J Phys Oceanogr 34(5):1117–1134

Prinsenberg S, Rattray M (1975) Effects of continental slope and variable Brunt-Väisälä frequency on the coastal generation of internal tides. Deep-Sea Res 22:251–263

Richtmyer RD (1957) Difference methods for initial-value problems. Interscience, NY, p 238

Saunders PM (1994) The flux of overflow water through the Charlie-Gibbs fracture zone. J Geophys Res 99(C6):12343–12355

Tareev BA (1966) Dynamics of internal gravity waves in a continuously stratified ocean. Izv Acad Sci USSR Ser Atmos Ocean Phys 2(10):1064–1075

Thorpe SA (1999) Fronts formed by obliquely reflecting internal waves at a sloping boundary. J Phys Oceanogr 29:2462–2467

Torgrimson GM, Hickey BM (1979) Barotropic and baroclinic tides over the continental slope and shelf off Oregon. J Phys Oceanogr 9:945–961

van Haren H, Gostiaux L, Morozov E, Tarakanov R (2014) Extremely long Kelvin-Helmholtz billow trains in the Romanche Fracture Zone. Geophys Res Lett 41:8445–8451

Vlasenko VI (1992) Nonlinear model for the generation of baroclinic tides over extensive inhomogeneities of bottom topography. Phys Oceanogr (Morskoy gidrofizicheskiy zhurnal) 3:417–424

Vlasenko V, Stashchuk N, Hutter K (2005) Baroclinic tides: theoretical modeling and observational evidence. Cambridge University Press, Cambridge, 351 pp

Weigand JG, Farmer H, Prinsenberg S, Rattray M (1969) Effects of friction and surface tide angle of incidence on the coastal generation of internal tides. J Mar Res 27:241–259

Whitehead JA, Wang W (2008) A laboratory model of vertical ocean circulation driven by mixing. J Phys Oceanogr 38(5):1091–1106

Wunsch C (1972) The spectrum from two years to two minutes of temperature fluctuations in the main thermocline at Bermuda. Deep-Sea Res 19(8):577–594

Wunsch C (1975a) Deep ocean internal waves: what do we really know? J Geophys Res 80 (3):339–343

Wunsch C (1975b) Internal tides in the ocean. Rev Geophys Space Phys 13(1):167–182

Wüst G (1936) Schichtung und Zirkulation des Atlantischen Ozeans, Das Bodenwasser und die Stratosphäre. In: Defant A (ed) Wissenschaftliche Ergebnisse, Deutsche Atlantische Expedition auf dem Forschungs - und Vermessungsschiff "Meteor" 1925–1927, vol 6(1). Walter de Gruyter & Co. Berlin. 411 pp

Zaron ED, Egbert GD (2006) Estimating open-ocean barotropic tidal dissipation: the Hawaiian Ridge. J Phys Oceanogr 36(6):1019–1035

Zhao Z (2014) Internal tide radiation from the Luzon Strait. J Geophys Res 119:5434–5448. https://doi.org/10.1002/2014JC010014

Zhao Z, Alford MH (2009) New altimetric estimates of mode-1 M_2 internal tides in the Central North Pacific Ocean. J Phys Oceanogr 39(7):1669–1684

Chapter 8
Semidiurnal Internal Wave Global Field; Global Estimates of Internal Tide Energy

Abstract This chapter describes the semidiurnal internal wave global field and global estimates of internal tide energy. One of the most important ideas presented here is the strong generation of internal tides over submarine ridges. Energy fluxes from submarine ridges related to tidal internal waves exceed many times the fluxes from continental slopes. Submarine ridges form an obstacle to the propagation of tidal currents that provides internal tide generation because tidal currents obtain a vertical component over the ridge slopes. Energy fluxes from submarine ridges account for approximately one fourth of the total energy dissipation of the barotropic tides. Combined model simulations and moored measurements result in a map of the global distribution of internal tide amplitudes.

The problems of internal tide generation and the distribution of energy over the entire ocean are maybe the most important in the investigation of internal waves. It is currently accepted that the most efficient generation of internal tides occurs when the currents of the barotropic tide overflow various bottom slopes. It is likely that the first publications, in which the linear theory of internal wave generation by tides over submarine slopes was developed, were the papers by Rattray (Rattray et al. 1969; Rattray 1960). Vertical components of velocity that appear when the currents flow over slopes displace isopycnal surfaces. Since these vertical velocities are tidal, their frequency is also tidal. These components initiate oscillations of isopycnal surfaces, and as a result, internal perturbations develop. The problem of such a mechanism of internal tide generation over continental slopes was considered by Niiler (1968), Weigand et al. (1969), and Prinsenberg et al. (1974).

Cox and Sandström (1962) considered the problem of energy transfer from the barotropic tide to the internal tide due to the flow of tidal currents over the bottom irregularities. This problem was further developed by Mork (1968), Hendershott (1973), and Bell (1975). Different approaches to the problem are possible. Topography variations were considered by Cox and Sandström (1962) and (Bell 1975) as small perturbations of the horizontal bottom so that the internal tide is generated by the barotropic tide within a linear problem.

The second approach was used by Rattray et al. (1969) and Prinsenberg et al. (1974). The authors sought the solution of the problem in the form of modes on the steps of stepwise topography with further suing of the solutions at the boundaries between the steps.

A very promising approach was applied by Baines (1973, 1974, 1982, 1983, 2007). He used a solution of the problem in the form of beams of perturbations and the generation of internal tide by a mass force. Baines obtained the estimates of the energy flux of the semidiurnal internal tide generated over various parts of the continental slope in the global ocean. Numerical solutions of the problem of internal tide generation at arbitrary stratification and arbitrary bottom topography developed in the papers by Vlasenko (1992) and Gerkema and Zimmerman (1995) were important steps in our understanding of the problem of the generation and propagation of internal tides.

A model and estimates of energy conversion by the seamounts in the deep ocean were suggested by Llewellyn Smith and Young (2002). They estimated the barotropic tide energy conversion produced by the global inventory of over 1.4 million seamounts (Yesson et al. 2011; Smith and Jordan 1988). Llewellyn Smith and Young (2002) considered an "average" seamount with a radius of 1.6 km and a height of 320 m. The seamounts cover approximately 6% of the seafloor. An average seamount produces 10^4 W of power. The authors estimated 1/4 GW of conversion over a square of the ocean floor with a side of 1000 km. This is not very high but not negligible. Baines (2007) suggested that in a barotropic tidal flow of 1 cm/s amplitude, the energy fluxes from an individual seamount are of the order of 10^6 W. The sum of this energy over all seamounts higher than 1 km gives baroclinic energy generation of the order of 5×10^9 W. This is less than the estimates of the baroclinic energy flux from the continental slopes, but not negligible.

Along with the continental slope, submarine ridges are important regions of internal tide generation (Sjöberg and Stigebrandt 1992; Morozov 1995). Let us use Baines' model (1982) to estimate the energy contribution of the interaction between the barotropic tide and submarine ridges to the energy balance of the semidiurnal internal tides (Morozov 1995). This research was initially carried out and published by Morozov (1995, 2006). Since then, many of the results have been revised and improved. Below is a progressive report on the geographical distribution of the internal tide in the ocean.

Following Baines (1974, 1982) we shall write linearized equations describing small perturbations in a layer of stratified fluid limited by the surface $z = 0$ and bottom $z = h(r)$. We apply the approximations of Boussinesq and constant Coriolis parameter. Here, $r = r(x, y)$ is the horizontal radius vector; the z-axis is directed upwards:

$$\frac{\partial \vec{u}}{\partial t} + f \times \vec{u} + \frac{\nabla p}{\rho_0} + \frac{\rho g \vec{z}}{\rho_0} = 0$$
$$\frac{\partial \rho}{\partial t} + w \frac{d\rho_0}{dz} = 0$$
$$(\nabla \vec{u}) = 0$$

(8.1)

In this system, $\vec{u} = (u, v, w)$ is the velocity of fluid; $\vec{z}$ is the unit vector directed upwards; p is pressure; $\rho_0 = \rho_0(z)$ is the mean vertical profile of potential density; $\rho = \rho(x, y, z, t)$ are density perturbations.

Let us define $\vec{u}$ and p as the sums $\vec{u} = \vec{u}_1 + \vec{u}_i$, $p = p_1 + p_i$ so that $\vec{u}_1$ and p_1 determine the velocity field in a homogeneous ocean of mean density $\bar{\rho}_0$ over the vertical profile $\rho_0(z)$; hence, they describe the barotropic tide, then $\vec{u}_i$ and p_i describe the internal tide.

The problem of determining the internal tide generated from the interaction of the barotropic tide with uneven bottom topography is divided into two parts. The first one is determination of the barotropic tide $\vec{u}_1$, ρ_1 in the "equivalent" homogeneous ocean, and the second is determination of additional motion in the stratified ocean, which should satisfy the equations and boundary conditions.

We write the following equations for the barotropic tide:

$$\frac{\partial \vec{u}_1}{\partial t} + f \times \vec{u}_1 + \frac{\nabla p_1}{\bar{\rho}_0} + g\vec{z} = \vec{F}_0$$
$$(\nabla \vec{u}_1) = 0$$

(8.2)

with the boundary conditions:

$$\vec{u}_1 \cdot \nabla(z + h(x)) = 0 \text{ at } z = -h(x),$$

$$(D/Dt)(z - \eta(x, t)) = 0 \text{ at } z = \eta(x, t)$$

where $\vec{F}_0$ is the tidal mass force, $\eta = \eta(x, t)$ is the surface elevation determined by the barotropic tide, $z = -h(x)$ is the ocean bottom.

Baines (1982) showed that the following condition is true for the gentle slopes of bottom topography

$$\partial(hu_1)/\partial x = 0,$$

hence, we can write:

$$hu_1 = Q \cdot \cos \omega t,$$

where Q is the water transport determined by the barotropic tide, ω is the tidal frequency.

Then, we get an equation system for internal oscillations, the system for $\vec{u}_i$ and p_i:

$$\frac{\partial \vec{u}_i}{\partial t} + f \times \vec{u}_i + \frac{\nabla p_i}{\bar{\rho}_0} + \frac{\rho g \vec{z}}{\rho_0} = \vec{F}_0$$
$$(\nabla \vec{u}_i) = 0 \tag{8.3}$$
$$\frac{\partial \rho}{\partial t} + (w_1 + w_i) \frac{d\rho_0}{dz} = 0.$$

Baines (1982) showed that if we present ρ as $\rho = \rho_1 + \tilde{\rho}$, where ρ_1 are density perturbations caused by the barotropic motions u_1 and w_1 supported by the mean density field $\rho_0(z)$; then the equation system for internal waves may be rewritten so that the internal tide would be forced by mass force F:

$$\frac{\partial \vec{u}_i}{\partial t} + f \times \vec{u}_i + \frac{\nabla p_i}{\bar{\rho}_0} + \frac{\tilde{\rho} g \vec{z}}{\bar{\rho}_0} = \vec{F} = -\frac{g \rho_1 \hat{z}}{\bar{\rho}_0}$$
$$(\nabla \vec{u}_i) = 0$$

and

$$\frac{\partial \rho_1}{\partial t} = -w_1 \frac{d\rho_0}{dz}. \tag{8.4}$$

Since the barotropic tide is described by hydrostatic equations, it is possible to express w_1 in the terms of the mass flux or more exactly volume flux $\vec{Q}(x, y)$, i.e. by the value of water transport determined by the barotropic tide:

$$w_1(x, y, z, t) = -z\vec{Q}\nabla(\frac{1}{h}) \cdot e^{i\omega t}. \tag{8.5}$$

We get from Eq. (8.4):

$$\rho_1 = \int w_1 \frac{d\rho_0}{dz} dt = zQ \frac{\partial h}{\partial x} \frac{1}{h^2} \frac{\sin \omega t}{\omega} \frac{d\rho_0}{dz},$$

then:

$$\vec{F} = -\frac{g \rho_1 \hat{z}}{\bar{\rho}_0} = -\frac{QN^2}{\omega} z\hat{z} \frac{\partial h}{\partial x} \frac{1}{h^2} \sin \omega t,$$

where:

$N^2 = \frac{g}{\rho_0} \frac{d\rho_0}{dz}$ is squared Brunt-Väisälä frequency.

Water transport by the barotropic tide Q over the continental slope and shelf was determined by Baines (1982) as:

$$Q = \omega a_0 l_0,$$

where ω is the tidal frequency, a_0 is the amplitude of the surface elevation by tide measured on the shore, l_0 is the width of the shelf.

We introduce the stream function Ψ for internal tide motion:

$$u_i = -\Psi_z, w_i = -\Psi_x$$

then, we get from the previous expressions:

$$\nabla^2 \Psi_{tt} + N^2 \Psi_{xx} + f^2 \Psi_{zz} = -N^2 w_{1x}. \tag{8.6}$$

The boundary conditions for this equation are deduced from the condition of zero mass flux through the surface and bottom:

$\Psi = 0$ at $z = 0$ and $z = -h(x)$.
We take (8.5) into account and rewrite Eq. (8.6) in the following form:

$$\nabla^2 \Psi_{tt} + N^2 \Psi_{xx} + f^2 \Psi_{zz} = QN^2(z)z\left(\frac{1}{h}\right)_{xx}.$$

Since all variables we are interested in oscillate in time with frequency ω it is possible to introduce the following dependence:

$$\Psi = \Psi(x, z) \cdot e^{i\omega t},$$

then:

$$\Psi_{xx} - c^2(z)\Psi_{zz} = \frac{QN^2}{N^2 - \omega^2} z\left(\frac{1}{h}\right)_{xx}, \tag{8.7}$$

where

$$c^2(z) = \frac{\omega^2 - f^2}{N^2 - \omega^2}.$$

The boundary conditions are transformed correspondingly as:

$$\Psi = 0 \text{ at } z = 0 \text{ and } z = -h(x). \tag{8.8}$$

Before finding the general solution of this equation we find its particular solution, which is exact at constant N:

$$\Psi_1 = \frac{QzN^2}{N^2 - \omega^2} \frac{1}{h(x)}.$$

The general solution is presented as a sum:

$$\Psi = \Psi_1 + \Psi_2,$$

where Ψ_2 is the solution of the homogenous part of Eq. (8.7); and boundary conditions (8) for Ψ_2 are transformed as:

$\Psi_2 = 0$ at $z = 0$

$\Psi_2 = Q\left(1 + \frac{c^2}{1 - f^2/\omega^2}\right)$ at $z = -h(x)$.

Equations (8.7) are related to the hyperbolic type. The fundamental solution of the corresponding homogeneous equation can be found using the method of characteristics:

$$\Psi_2 = c(z)^{1/2}[f(\xi) + g(\eta)], \tag{8.9}$$

where $\xi = x + \int_0^z \frac{dz'}{c(z')}$, $\eta = -x + \int_0^z \frac{dz'}{c(z')}$.

We interpret solution (8.9) as follows. Generally, the generation of internal tides occurs over the slopes of submarine ridges or continental slopes. Then, the perturbations induced by the internal tide propagate along the characteristic lines (beams). The slope of characteristics is determined by the value of $c(z)$ and corresponds to the inclination of the vector of group velocity. The equation for the slope of characteristics is as follows:

$$\frac{dx}{dz} = \pm c^{-1}(z).$$

As the sloping beams propagate in the ocean they repeatedly reflect from the bottom and surface and eventually form the mode structure. Distance l from the topography, after which the mode structure is formed, is determined by the mean ocean depth H and characteristic value of $c(z)$:

$$l \sim \frac{H}{c}. \tag{8.10}$$

Indeed, the value of l coincides by the order of magnitude with half of the length of one beam cycle (the distance between nearest reflections from the surface and bottom). It is clear from the general considerations that formation of the mode structure requires several reflections of the beams. Thus, the sought estimate (8.10) appears underestimated. The distance, over which the mode structure is formed,

depends on the properties of the ridge (whether its form is close to the straight line) and also depends on the degree of roughness of the bottom topography, from which the beams are reflected.

Baines (1982) found solutions to estimate the flux of internal tide energy in the stratified water column. The energy flux:

$$E_f = \int\limits_0^z pu \cdot dz \qquad (8.11)$$

is determined by the following expression:

$$E_f = K_1 \rho_0 Q^2 N_0 \left(1 - \frac{f^2}{\omega^2}\right)^{1/2} K_2.$$

Stratification is presented in the form of the upper homogeneous layer:

$N^2 = N_0^2 + \frac{g\Delta\rho}{\rho_0}\delta(z+d)$ at $-h < z \leq -d$,

where δ is the Dirac delta function, $\Delta\rho$ is the density difference across the interface layer, N_0 is a constant in the expression for the Brunt-Väisälä frequency.

The coefficients in expression (8.11) are as follows:

K_1 is a dimensionless coefficient obtained from the integration of velocity with respect to depth. Under various conditions it ranges between 0.070 and 0.075; in our calculations we assume that $K_1 = 0.072$.

K_2 is a coefficient, which includes parameters of stratification and geometric forms of topography, over which internal tide is generated:

$$K_2 = (1 - R)^2 + \frac{R^2(1 - R)\gamma_1}{(1 + \sqrt{1 - R})^2} + 2(1 - R)\gamma_1\gamma_2,$$

here:

$$R = \frac{d}{h_1},$$

d is the depth of the upper homogeneous layer, h_L is the depth of the shelf or the depth of the ridge crest, α is the slope of the bottom. Functions γ_1 and γ_2 depending on R and T

$$T = \frac{h_L (\omega^2 - f^2)^{1/2}}{(g' \cdot d)^{1/2} \alpha}$$

were calculated and plotted by Baines (1982).

The most important parameter for the calculation of energy fluxes is water transport Q in the tidal flow. Baines (1982) estimated the water transport for the calculation of internal tide energy at the continental slopes from the data of the tide elevations measured at the shores. No such data are available for the calculation of internal tide energy over submarine ridges. Therefore, we estimated the currents of the barotropic tide from the TOPEX/POSEIDON satellite data from the NASA database at Oregon State University (USA). We used the TPXO.7.1 global inverse tidal model with the Ocean Tidal Prediction Software (OTPS) algorithm (http:// volkov.oce.orst.edu/tides/otps.html; last accessed in October 2017) (Egbert and Erofeeva 2002). We also used the available data of tidal velocities based on the velocity measurements at the closest possible distance to the ridges. We estimated the water transport in the open ocean as follows:

$$Q = \omega H S,$$

where, H is the ocean depth, S is the horizontal displacement of water particles in the tidal flow during half of the tidal period.

Therefore:

$$S = \frac{2u_0}{\omega} \sin \theta,$$

where u_0 is the mean amplitude of the horizontal barotropic tidal currents, θ is the angle between the direction of the barotropic currents and the ridge crest.

The estimates of u_0 were taken either from the calculations that make possible the separation of the barotropic and baroclinic velocities (see Sect. 7.5) or from the satellite altimetry (Egbert 1997; Egbert and Erofeeva 2002). In the previous estimates (Morozov 1995), the data of tidal velocities were calculated from the publications of numerical calculations of tidal wave M_2 spreading (Bogdanov and Magarik 1967; Gordeev et al. 1974; Accad and Pekeris 1978; Schwiderski 1979, 1980a, b; Ray 1999). The cotidal charts in the ocean based on three publications are shown in Fig. 8.1. Cotidal lines join the points at which high tide occurs simultaneously. The charts are not identical, but the general features of the tide can be seen in all versions. We consider that the newest charts are more exact.

In the first stage of our research we used the estimates of the internal tide energy fluxes from five submarine ridges, near which we had measurements of currents: these are the Emperor Ridge in the Northwest Pacific, Mendocino Escarpment in the Northeast Pacific, Macquarie Ridge south of Australia, Mid-Atlantic Ridge south of the Azores, and Mascarene Ridge in the western part of the Indian Ocean.
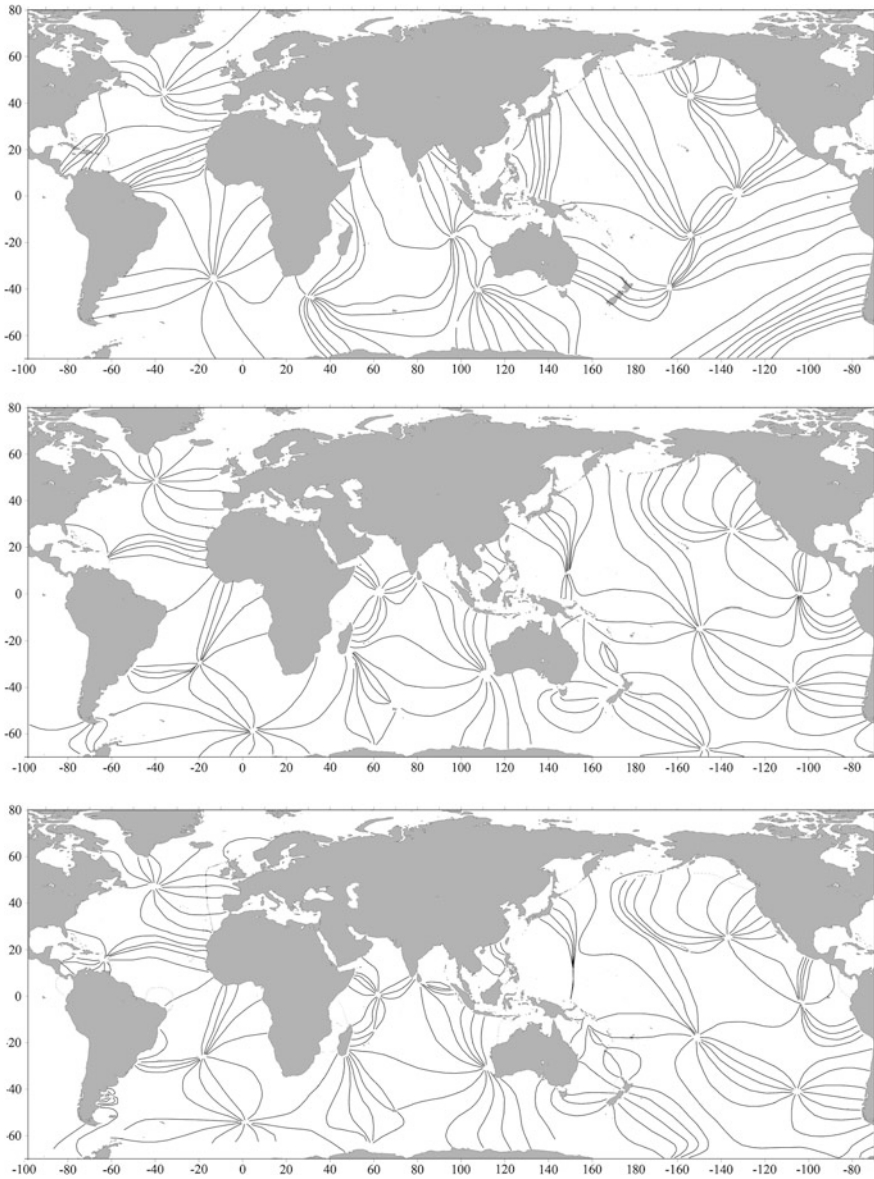
Fig. 8.1 Charts of barotropic tidal wave M_2 cotidal lines based on Gordeev et al. (1974) (**a**), Schwiderski (1979) (**b**), and Ray (1999) (**c**). The charts were redrawn from the publications and modified using the same background chart for better comparison

The mean amplitudes of the barotropic tidal currents M_2 separated from the internal tide based on the data in Morozov (1985), Morozov and Nikitin (1984a, b) in all regions of measurements were estimated at 1–2 cm/s. We assume that in these

five regions the values are 1.5 cm/s for definiteness. The same estimates were obtained from the satellite altimetry. Furthermore, based on the data of tidal amplitudes from Bogdanov and Magarik (1967), Gordeev et al. (1974), and Ray (1999) the surface elevations in three regions are the same and equal to 0.25 m/s. The results of the calculations are given in Table 8.1.

In the next step, we used the same approach to calculate energy fluxes from all major submarine ridges of the Atlantic, Pacific, and Indian oceans. Here, the ridges in the Southern Ocean were related to the respective three oceans. We used the satellite altimetry data to estimate the mean amplitudes of the barotropic tide velocities. The characteristics of bottom topography were taken from the digital databases ETOPO (http://www.ngdc.noaa.gov/mgg/global/global.html; last accessed in October 2017) and Smith and Sandwell (1997). Stratification of the ocean was calculated from the CTD World Ocean Database 2013 (WOD13 2013). The results of the calculations are given in Table 8.2.

The maximum energy fluxes are related to the ridges located normal to the propagation of the barotropic tidal waves. The geomorphological characteristics of the ridges facilitating generation of the strongest internal tides are high elevation of their crests over the bottom surrounded by deep waters around the ridges. Examples of such ridges include the Mid-Atlantic Ridge, Aleutian, Mascarene, and Hawaiian ridges and those in the Luzon Strait.

Table 8.2 presents the energy fluxes at one side of the ridge. Since internal tide is generated at both sides the values should be doubled. Then, the total energy fluxes for the World Ocean calculated from Table 8.2 are as follows: 3.48×10^{11} W in the Atlantic, 3.66×10^{11} W in the Pacific, and 2.74×10^{11} in the Indian Ocean.

The total amount $\sim 1.0 \times 10^{12}$ W is approximately one quarter of the total barotropic tide energy dissipation 4.3×10^{12} W (4.3 TW, terawatts or 4300 GW, gigawatts) obtained from the astronomical data. Cartwright (1977), Kaula and Harris (1975), and Munk and Wunsch (1998) report that tidal dissipation is even lower: 3.4–3.7 TW.

Table 8.1 Semidiurnal internal tide (M_2) energy fluxes over five submarine ridges: f is the Coriolis frequency, N_0 is the Brunt-Väisälä frequency at the depth of the mixed layer (~ 100 m), h_L is the depth of the ridge crest, H is the depth of the surrounding ocean, Θ is the angle between the incident currents of the barotropic tide and the ridge crest, Q is the water transport by the barotropic tide, E_f is the energy flux of internal tide per meter of the ridge length (J/m s or W m^{-1})

Submarine ridges	f (s^{-1})	N_0 (s^{-1})	h_L (m)	H (m)	Θ (°)	Q (m^3/s)	E_f (J/m s)
						Per 1 m of the ridge length	
Mid-Atlantic Ridge, near Great Meteor Bank	7.3×10^{-5}	5.5×10^{-3}	1500	3800	60	130	6550
Mendocino	8.3×10^{-5}	5.0×10^{-3}	1500	4500	60	115	4740
Macquarie	1.2×10^{-4}	3.0×10^{-3}	1200	4000	60	126	3000
Emperor	8.9×10^{-5}	5.0×10^{-3}	2000	4800	75	134	5400
Mascarene	2.5×10^{-5}	5.5×10^{-3}	400	4000	90	174	16,500

Table 8.2 Energy fluxes of the semidiurnal internal tide M_2 over major submarine ridges of the World ocean

Atlantic Ocean						
Ridges	L	Θ	E_f	E_{tot}	ζ, m	A, m
Reykjanes	1650	90	1940	3.20×10^9	36	40
N. Mid-Atl. mid-latitudes 40°N–50°N	1200	60	2940	3.53×10^9	30	
N. Mid-Atl. mid-latitudes 25°N–40°N	2800	60	6550	1.83×10^{10}	38	36
Great Meteor Banks	600	80	2800	1.68×10^9	55	60
N. Mid-Atl. tropical latitudes 5°N–25°N	2200	30	1520	3.34×10^9	18	
N. Mid-Atl. equatorial latitudes 0°–5°N	900	45	14,080	1.27×10^{10}	54	60
S. Mid-Atl. tropical latitudes 0°–25°S	2800	90	26,320	7.37×10^{10}	62	
S. Mid-Atl. mid-latitudes 25°–35°S	1100	90	10,290	1.13×10^{10}	44	
S. Mid-Atl. mid-latitudes 35°–55°S	2200	90	4900	1.08×10^{10}	36	
South Antilles	1000	90	5800	5.80×10^9	45	
Walvis	1700	60	11,400	1.94×10^{10}	54	
African-Antarctic	2250	15	340	7.65×10^8	10	
Trindadi, Martin Vas	700	80	10,520	7.30×10^9	52	50
Rio Grande Rise	300	80	6800	2.04×10^9	41	30
Pacific Ocean						
Ridges	L	Θ	E_f	E_{tot}		
Emperor	1650	75	5400	8.91×10^9	36	24
Hawaiian	2800	60	4320	1.21×10^{10}	40	40
Aleutian Islands	500	90	21,300	1.07×10^{10}	80	100
Luzon Strait	300	90	13,450	4.04×10^9	90	100
Mariana Islands	1600	75	8980	1.43×10^{10}	45	
Lord Howe	1600	45	4070	6.51×10^9	31	
South Pacific 180°–140°W	2800	15	190	5.32×10^8	10	
East Pacific 30°–55°S	3350	45	2120	7.10×10^9	25	
East Pacific 0°–30°S	3300	45	2860	9.43×10^9	29	20
Sala y Gomez, Nasca	2800	75	5840	1.63×10^{10}	41	
Mendocino	650	60	4740	3.08×10^9	28	14
Marshall, Gilbert islands	2800	90	9720	2.72×10^{10}	48	
Line, Tuamotu	2250	45	4230	9.52×10^9	33	
Kermadec	2500		330	8.25×10^8	35	33
Marcus-Nekker	3350	15	640	2.14×10^9	12	
Kyushu-Palau	2300	90	17,500	4.02×10^{10}	68	60
Kolwill-Lau	2200	30	1520	3.34×10^9	19	
Kuril Islands	1100	45	5920	6.51×10^9	21	20
Indian Ocean						
Ridges	L	Θ	E_f	E_{tot}		
West Indian 30°–50°S	3400	30	5250	1.78×10^{10}	38	
Maldives	1600	90	7460	1.19×10^{10}	46	50

(continued)

Table 8.2 (continued)

Indian Ocean						
Ridges	L	Θ	E_f	E_{tot}		
Arabian-Indian	3350	75	6250	2.09×10^{10}	43	
Mascarene	2150	90	16,500	3.54×10^{10}	60	70
Madagascar	1050	30	1820	1.91×10^{9}	21	20
Ninetyeast 5°N–15°S	2200	90	7350	1.62×10^{10}	43	30
Ninetyeast 15°S–35°S	2200	90	7530	1.66×10^{10}	44	30
West Australian	1300	30	1440	1.87×10^{9}	20	
Central Indian	2200	45	3360	7.39×10^{9}	29	
Kerguelen	1650	45	1880	3.10×10^{9}	25	15
Macquarie	1100	60	3000	3.30×10^{9}	34	15
Australian-Antarctic	3300	15	290	9.57×10^{8}	15	

Here: L is the ridge length in km, Θ is the incident angle of the tidal currents at the ridge, E_f is the energy flux from a linear meter in W m^{-1} or J/m s, E_{tot} is the total energy flux from the entire ridge length in Watts (J/s), $E_{tot} = E_f \cdot L \cdot 1000$. Amplitude ζ was calculated, amplitude A was measured on moorings at a distance of 100–200 km from the ridge

According to the estimates of Baines (1982), the calculated total global barotropic to baroclinic tidal energy conversions for the M_2 tide is 1.45×10^{10} W, which is no more than 1% of the tidal energy dissipation transferred to the energy of internal tides over continental slopes. Bell (1975) estimated that approximately 10% of the tidal energy is spent on internal tide generation in the abyssal depths over uneven topography of deep oceanic basins. Bell (1975) also estimated that the flux of energy in this process is of the order of 1 erg/cm^2 s (10^{-3} W/m^2).

We also present a table of energy fluxes from those continental slopes, which make a significant contribution to the generation of internal tides. This table is based on a review of the publications (Table 8.3).

Thus, the energy fluxes of internal tides from submarine ridges are very high and exceed the energy fluxes from the continental slopes. Baines (1982) estimated the highest characteristic values of the energy fluxes from the continental slopes, which are of the order of 1000 W m^{-1}. The fluxes from submarine ridges are usually several times greater. Greater fluxes from the submarine ridges can be explained as follows. The currents of the barotropic tidal wave M_2 are generally directed along the slopes normal to the cotidal lines (Fig. 8.1). The wave is very long (its length is of the order of 5000 km); thus its refraction to the coast is not significant. The cross-slope velocity components of the tidal wave are related to the generation of trapped Kelvin wave (Schwiderski 1979). Thus, only a small part of the mass flux associated with the barotropic tide is directed to the coast and crosses the slope line. Only this small portion of the mass flux generates tidal currents normal to the shore. These currents are responsible for the tidal sea level elevations on the shore and the generation of internal tides over the continental slope.

Table 8.3 Energy fluxes of the semidiurnal internal tide M_2 over major continental slopes based on the publications

Atlantic Ocean				
Continental slopes	L	E_f	E_{tot}	Source
Caribbean Islands	1100	70	0.08×10^9	Dushaw (2006)
North British Islands, Ireland Malin shelf	830	109 104	0.09×10^9	Baines (1982) Sherwin (1988)
South of Ireland	400	3390	1.34×10^9	Baines 1982
English Channel	150	4170	0.62×10^9	Baines (1982)
Bay of Biscay	500	634	0.30×10^9	Baines (1982)
Northwest Atlantic shelf		24		Hallock and Field (2005)
South America (north of equator)	1065	224	0.23×10^9	Baines (1982)
Nova Scotia	400	1300	0.52×10^9	Sandström and Elliott (2011)
Great Banks	500	200	0.10×10^9	Sandström and Elliott (2011)
Virginia, USA		1000		Nash et al. (2004)
Portuguese shelf	700	2000	1.40×10^9	Jeans and Sherwin (2001)
Georges Bank		195		Brickman and Loder (1993)
South Africa; Cape Point Valley.		40		Largier (1994)
Pacific Ocean				
Oregon shelf	400	100	0.04×10^9	Moum et al. (2007)
East China Sea (South)	476	1008	0.48×10^9	Baines (1982)
East China Sea (North)	423	283	0.12×10^9	Baines (1982)
Chatham Rise	795	1440	1.20×10^9	Chiswell (2000)
Monterey Bay		100		Kunze and Boss (1998)
British Columbia	800	625	0.50×10^9	Cummins et al. (2000)
Gulf of Alaska		max 7000		Bracher and Flatté (1997)
Indian Ocean				
Australian NW	1405	380 500 2000	0.01×10^9	Baines (1982) Holloway et al. (2001) Rayson et al. (2011)
Northwestern India-Pakistan	850	124	1.05×10^9	Baines (1982)
Mozambique	1170	68	0.08×10^9	Baines (1982)
Andaman Islands	489	202	0.10×10^9	Baines (1982)

Here: L is the length of the continental slope in km, E_f is the energy flux from a linear meter in J/m s or W m^{-1}, E_{tot} is the total energy flux from the entire continental slope length in Watts (J/s), $E_{tot} = E_f \cdot L \cdot 1000$. The energy flux per meter is based on publications in the literature. The references are given. The total flux from each of the continental slopes was calculated only in cases when it appeared reasonable

Many of the submarine ridges are normal or almost normal to the direction of the tidal currents and form an obstacle that provides intense internal tide generation because tidal currents obtain a significant vertical component.

We shall estimate the amplitudes of internal tides generated by the energy fluxes from submarine ridges. The energy flux for a wide class of waves is given by Gill (1982):

$$E_f = \int\limits_0^z pu \cdot dz.$$

In the case of the energy flux from the barotropic tide the energy flux per meter of the continental slope or ridge is given by:

$$E_f = \tilde{E} \cdot c_g,$$

where E_f is the energy flux vector from a linear meter (W m^{-1} or J/m s), $\tilde{E}$ is the vertically integrated energy density, c_g is the group velocity. Actually, the group velocity is the partial derivative of the frequency with respect to the wavenumber. It can be estimated from the following equation (Garrett and Munk 1979):

$$c_g = \frac{k k_z^2 (N^2 - f^2)}{\omega (k^2 + k_z^2)^2},$$

where k is the horizontal wavenumber, k_z is the vertical wavenumber. Since $N \gg f$ and $k_z \gg k$, we write the following expression leaving only the significant terms:

$$c_g = \frac{k N^2}{\omega k_z^2}.$$

We used the wavelengths estimated from the spatiotemporal spectra in various study sites to determine k and correspondingly k_z (Morozov 2006). The energy density according to Gill (1982) is as follows:

$$\tilde{E} = \frac{1}{2} \rho_0 \left(\frac{\tilde{w}_0}{\cos \varphi} \right)^2,$$

where $\cos \phi$ is found from the dispersion relation for internal gravity waves (Phillips 1977):

$$\frac{\omega}{N} = \cos \varphi.$$

A more general relation is as follows:

$$\omega^2 = \frac{N^2 k^2 + f^2 k_z^2}{k^2 + k_z^2} = N^2 \cos^2 \theta + f^2 \sin^2 \theta.$$

Here, ϕ is the angle between the wave vector and horizontal plane

$\frac{k}{k_z} = \sin \chi$, where $\chi = 90° - \varphi$.

Here, we introduced the following notations:

$\frac{\tilde{w}_0}{\cos \varphi}$ is the amplitude of velocity fluctuations,

$\tilde{w}_0$ is the amplitude of the vertical velocity.

We integrate over the vertical and obtain:

$$E = \frac{\rho V^2}{2} H,$$

where V is the vertically averaged amplitude of the orbital velocities of water particles. Then, the mean amplitude of the vertical velocity would be written as follows:

$$w_0 = V \cdot \cos \varphi,$$

and the vertical displacements during a half period are:

$$\zeta = \frac{2 w_0}{\omega}.$$

The results of calculations of amplitudes for the major submarine ridges are given in Table 8.2. The data of moored measurements of internal tide amplitudes are also given in the table if they are available.

It is worth noting that vertically mean displacements are shown in the column of calculated amplitudes (ζ), while maximum measured amplitudes at a distance from the ridge are shown in the column of measured amplitudes (A). The distances from the ridge vary between different ridges depending on the locations of moorings relative to the ridge; hence the amplitudes decrease due to dissipation. Thus, many of the input parameters were approximate; however, we see that the calculated and measured amplitudes agree quite well.

Let us summarize the estimates of energy flux from various locations of internal tide generation described on the basis of literature data in the previous chapters.

Depth integrated energy flux from the Great Meteor Banks was estimated by Gerkema and van Haren (2007) at 2300 W m^{-1} for the semidiurnal internal tide based on the observations using CTD/LADCP yo-yo casts; the model simulations result in an estimate of 2600 W m^{-1}.

Internal tides radiated from the Aleutian Ridge were studied by Cummins et al. (2001) using satellite altimetry and modeling. The strongest energy fluxes occur in

the vicinity of the Amukta Pass (52°N, 172°W). The model results suggest that near the Amukta Pass the rate of conversion of barotropic to baroclinic energy is about 1.8 GW. Generation of the internal tide in the Gulf of Alaska was analyzed by Bracher and Flatté (1997) on the basis of acoustic experiments in the Central Pacific at 32°–33°N. They studied the effect of the M_2 by ray tracing and found that the internal tide arrives from the Gulf of Alaska after propagating over more than 3000 km. The maximum energy flux was estimated at 7000 W m^{-1}.

According to Ray and Cartwright (2001), the generation of internal tides along the Aleutian Trench is primarily limited to a small region in the vicinity of 51°N, 170°–176°W. The waves form a narrow beam directed to the south that reaches a latitude of 35°N. The integrated flux along the 51°N parallel is only 0.6 GW.

Internal tides 100 km north of Oahu Island were studied by Chiswell (1994) at the ALOHA deep-water station (22° 45′N, 158° 00′W). Internal tides with amplitudes up to 30 m were recorded. Measurements using inverted echo sounders at the ALOHA station (Chiswell 2002) resulted in a semidiurnal energy flux equal to 4400 W m^{-1}. The depth average semidiurnal energy flux in the southern direction in the Far-field was estimated at 1700 W m^{-1}.

Model results of internal tide generation over the Hawaiian Ridge were reported by Holloway and Merrifield (1999). The maximum conversion of barotropic to baroclinic energy occurred over the 500 m submerged ridge with baroclinic energy fluxes reaching 1200 W m^{-1}. After propagating one wavelength, the energy flux reduced to 300 W m^{-1}. The maximum energy flux of the M_2 internal tide from the ridge in the channel between the Oahu and Kauai islands was as high as 13,700 W m^{-1}.

Velocity and density profiles along the 3000-m isobath were analyzed by Lee et al. (2006). Baroclinic energy fluxes radiating from different regions of the Hawaiian Ridge range from 21,000 to 13,000 W m^{-1}. The authors estimated the dissipative length scales of internal tides at 1000 km. Model simulations revealed a tide loss of 15 GW. Egbert and Ray (2001) estimated tidal losses near the ridge at 20 GW. Model simulations of Niwa and Hibiya (2001) result in 15 GW for M_2, and Morozov (1995) gives an estimate of 8 GW (this estimate increased from 8 GW up to 12 GW after recalculation to be reported in this book) based on the Baines model (1982). The model suggested by St. Laurent et al. (2003) estimated the tidal losses at 22 GW. An estimate of 6 GW along the entire ridge was given by Ray and Cartwright (2001).

Internal-tide energy fluxes of the order of 10000 W m^{-1} were found at various locations of the Hawaiian Ridge (Rainville and Pinkel 2006a, b; Nash et al. 2006). The total losses of barotropic tidal energy (over all the tidal constituents together) along the Hawaiian Ridge were estimated at 25 GW by Zaron and Egbert (2006). Integrated fluxes from the entire Hawaiian Ridge estimated by Ray and Mitchum (1997) were lower (15 GW).

Modeling of internal tides over the Hawaiian Ridge was reported by Kang et al. (2000). The M_2 baroclinic energy flux for the strongest energy beam propagating to the northeast exceeded 10,000 W m^{-1}. Tidal energy was transformed into internal tides that propagate in both directions from the ridge over distances exceeding

1000 km. The authors assume that on the average 2700 W m^{-1} energy was radiated from the ridge in both directions; then a total of 5.4 GW was radiated from the 2000 km long Hawaiian Ridge.

Modeling of the M$_2$ semidiurnal tidal energy conversion over the Hawaiian Ridge was performed by Carter et al. (2008) using a high-resolution primitive equation model over a region of the Hawaiian Ridge from Niihau to Maui approximately 800 km long. This region includes the Kaena Ridge, one of the three main internal tide generation sites along the Hawaiian Ridge. The M$_2$ barotropic tide loses 2.7 GW of energy over the study region. The major part of this energy (2.3 GW) is converted into internal tides. The majority of the baroclinic energy (1.7 GW) is radiated out of the model domain and 0.45 GW is dissipated in the study region.

Model simulations of internal tide generation in the region of the Mid-Atlantic Ridge over the axis of the ridge between 33° 35′S, 34° 17′S and 13° 40′, 15° 40′W were performed by Zilberman et al. (2009). Internal tides propagated from the Mid-Atlantic Ridge with peak depth-integrated baroclinic energy fluxes of 1100–1500 W m^{-1}.

Energy flux of internal waves from the shelf-edge of Nova Scotia and Grand Banks were studied by Sandström and Oakey (1995) and by Sandström and Elliott (1984, 2011). The energy flux from Nova Scotia shelf was within 1300–4700 W m^{-1}, whereas it was smaller from the Grand Banks (200 W m^{-1}).

Studies of internal tides on the basis of modeling and moored observations in the region of the Georges Bank in the outer Gulf of Maine were reported by Brickman and Loder (1993) based on measurements with moored thermistors at 42° 00′N, 66° 50′W. This is a region of strong tidal flow. However, the estimated energy flux of internal tides was quite low due to the shallow depths: 195 W m^{-1}.

Internal tides west of Scotland were analyzed by Sherwin (1988) (Malin shelf). Investigations were also carried out in the Rockall Deep. A numerical model was applied by Sherwin and Taylor (1990) to study internal wave generation over the Malin shelf. The energy flux was of the order of 100 W m^{-1}.

Moored measurements with thermistor chains were carried out on the shelf break west of Portugal at 41°N by Jeans and Sherwin (2001). The authors recorded high-frequency internal waves generated by internal tide with an amplitude of 45 m. The estimated energy fluxes were 2000 W m^{-1}.

Internal tides in the Faroe-Shetland Channel were studied by Hall et al. (2011). The authors applied moored ADCP and thermistors to study internal tides and also used a numerical model. The estimates of the energy fluxes over the flanks of the Wyville Thomson Ridge exceeded 5000 W m^{-1}.

Analysis of internal tide generation over the Mendocino Escarpment by Althaus et al. (2003) yields that the critical slopes for internal tide generation along the escarpment are 400 km long and the total integrated energy flux radiating from the Mendocino Escarpment (north plus south) was ∼3 GW. They estimated the semidiurnal internal tidal fluxes of 5000 W m^{-1} directed away from the escarpment (northward and southward) (Althaus et al. 2003). The authors report that this may

be an overestimate. Our estimates of the total flux are almost the same, but we assume that the escarpment is 650 km long (see Sect. 3.2).

Analysis of the data collected on the moorings near the Kermadec Ridge was presented by Chiswell and Moore (1999). The authors estimated the energy flux from the ridge and found it quite low: 264 W m^{-1}. Taking into account that the length of the ridge is 2500 km, the total radiated energy was approximately 0.8 GW.

The recorded internal wave field in Monterey Bay was almost an order of magnitude greater than in the open ocean (Kunze and Boss 1998; Kunze et al. 2002). A vertically integrated energy flux of 5000 W m^{-1} at the mouth of the canyon decreased to 1000 W m^{-1} toward the shallow end of the canyon.

Mooring experiments were carried out on the Chatham Rise east of New Zealand in 1996 and 1997 by Chiswell (2000). The total estimated radiated energy was estimated at 1440 W m^{-1}. The length of the Chatham Rise is 795 km, thus the total radiated power was 1.2 GW.

Internal tides off British Columbia were studied by Cummins and Oey (1997) and by Cummins et al. (2000) on the basis of a numerical model. The amplitudes of the M$_2$ internal tide exceed 40 m over a steep continental slope. The offshore M$_2$ baroclinic energy flux was estimated at 0.5 GW, which gives an average flux of about 625 W m^{-1} with a model coastline of 800 km.

In the Luzon Strait of the South China Sea, the semidiurnal internal tide energy flux estimated using gliders over a vast area 600×800 km by Rainville et al. (2013) was 3.7 GW to the South China Sea and 2.7 GW to the Pacific Ocean. Alford et al. (2015) report on the observations of internal tides at 20° 30′N, 119° 00′E. The measurements revealed the existence of breaking internal waves greater than 200-m high in the region of generation. The observations from moorings, shipboard stations, and gliders over the Strait of Luzon and west of it revealed westward energy fluxes of 40,000 W m^{-1}.

Internal waves in the Tasman Sea were studied during the TTIDE experiment by Johnston et al. (2015). Intense internal tides were generated over the Macquarie Ridge south of New Zealand. Then, they propagated to the northwest across the Tasman Sea to the Tasmanian slope and then reflected back into the Tasman Sea setting up a standing internal tide (Klymak et al. 2016). The estimated energy flux of mode-1 internal tides was of the order of 1000–2000 W m^{-1}.

The generation of internal tides was investigated over the northern Kerguelen Plateau by Maraldi et al. (2011). The authors studied the internal tides based on satellite altimetry data and numerical modeling. Internal tides were generated at the northern slope of the Kerguelen Plateau and propagated northward towards the southern front of the Antarctic Circumpolar Current. The authors estimated that ~ 0.81 GW was converted from the barotropic to the baroclinic tidal modes between Kerguelen and Heard Islands.

Let us discuss the problem of at what distance from the source the mode structure of oscillations is formed. Experiments that provided the determination of well-pronounced mode structure were conducted in the Central Atlantic, in the

Northeast Pacific 700 km south of the Mendocino Escarpment, and in the western part of the Indian Ocean 200 km southeast of the Mascarene Ridge.

These distances are slightly greater than the estimated scale using formula $l = H/c$. This is the distance from the source of internal tides, at which the mode structure of oscillations should be formed. If we assume that two-three reflections from the bottom and surface are enough to form the mode structure, then scale l is estimated at 500 km. Beam structure or its remains should be observed at shorter distances.

Such a structure at a close distance from seamounts was found by Torgrimson and Hickey (1979) and also in our measurements near Henderson Seamount in the East Pacific and Madagascar Basin.

Let us discuss the measurements in the regions of high energy fluxes from the ridges. It is clear that the amplitudes of internal tides in such regions are high. These regions include the equatorial part of the Mid-Atlantic Ridge and almost the entire Mid-Atlantic Ridge in the Southern Hemisphere, the Walvis Ridge, the Mascarene Ridge, the Aleutian Islands, the Southern China Sea, and the Kyushu-Palau Ridge.

Let us consider the previous results in the light of the energetic estimates of internal tide generation over the slopes of submarine ridges. Intense internal tides are found in the study sites located near submarine ridges if the currents of the barotropic tide are directed more or less normal to the ridge crest. Of course the ridges in the South China Sea in the Luzon Strait, the Aleutian Ridge, and the Mascarene Ridge are the most significant. The geometry of these ridges facilitates internal tide generation with extreme amplitudes. The amplitudes of the barotropic tide near the ridges are high. The crests of the ridges are located close to the surface and sometimes form shallow banks at the depths of strong stratification in the upper pycnocline. Slightly smaller amplitudes were recorded in the South Atlantic, near the Maldives in the Indian Ocean, and near the Kyushu-Palau Ridge in the Pacific. The measurements on a mooring near the Kyushu-Palau Ridge, which were carried out after the model was developed and predicted high amplitudes near this ridge, confirmed the theoretical estimates.

The most intense generation of internal tide occurs when characteristic surfaces of internal tides have the same slopes as the slopes of the bottom topography at the depth of the maximum stratification (New 1988). If an arc of islands (for example, Aleutian Islands or Hawaii) separated by deep straits is located normal to the direction of the barotropic tide currents, intense internal tides are generated similar to the mechanism of the generation of intense internal tides over the slopes of submarine ridges (Merrifield et al. 2001).

Large internal tides are generated in the Strait of Gibraltar, Bab el Mandeb Strait, and Kara Gates Strait. However, these waves have little influence on the energy budget of the ocean because they can be considered point sources, and the energy of internal tides dissipates in close vicinity within the straits.

Large but not extreme amplitudes of internal tides were recorded in the study sites near the Macquarie Ridge, Mendocino Escarpment, Emperor Mountains, Arabian-Indian Ridge, and Hawaii. The calculations indicate that estimates of energy fluxes over these ridges are smaller than over the ridges listed first as the

regions of extreme internal tides. This occurs because the amplitudes of the baro-tropic tide are smaller than in the regions with extremely strong internal tides, and the currents of the barotropic tide are not directed normally to the ridges. In addition, the geometry of these ridges is not so favorable for internal tide genera-tion; for example, the ridge crests of the sills between islands are not close to the ocean surface or what is even more important they are not close to the pycnocline.

In the regions of the Gambia Abyssal Plain far from the ridges and continental slopes (Polygon-70 and Mesopolygon-85) and also in the Madagascar Basin the internal tide signal generated by remote intense sources sometimes does not reach the study sites. Local generation of internal perturbations occurs over smaller forms of bottom topography in the deep ocean.

Internal tides are even less intense in the Sargasso Sea and north of Kerguelen Island. In the Sargasso Sea large topographic formations are distant from the regions of measurements. The bottom is flat. The signal from remote sensors does not reach the moorings. Relatively weak internal tides were found in the Sargasso Sea by Dushaw (2006). The research was based on an ocean acoustic tomography array deployed in 1991–1992 centered at 25°N, 66°W. It was a pentagonal array, 700-km across for mode-1 internal-tides. The M_2 internal-tide energy flux was estimated at 70 W m^{-1} radiating from the Caribbean Islands.

The wave of the barotropic tide north of Kerguelen Island propagates parallel to the closest submarine slopes. The generated internal tides are weak and the instruments almost do not record the signal. The local generation is also weak because the bottom in the region of the moorings is flat.

The differences between regions of strong and weak internal tides are clearly seen when one compares the power spectra of vertical displacements. Figure 8.2 shows the power spectra of vertical displacements in three regions: the Aleutian Islands (extremely strong internal tides); the Benguela region (moderate internal tides); and the Sargasso Sea (weak internal tides).

Horizontal and vertical coherences also differ significantly. In the region of intense internal tides vertical and horizontal coherences exceed the 95% confidence level (Fig. 3.4, Mendocino Escarpment; Fig. 4.4, Mascarene Ridge). In the region of internal tide generation over rough bottom topography in a deep basin such as the Gambia abyssal plain (Polygon-70 experiment) coherences are random (Fig. 2.11). In a region of weak internal tide such as the Sargasso Sea horizontal coherences are low (Fig. 2.14).

A chart of internal tide amplitudes can be constructed on the basis of calculations of energy fluxes from the submarine ridges and further estimation of wave amplitude near the ridges. Then, taking into account the energy dissipation in the course of internal tide propagation it is possible to extend the chart from the regions near ridges to the entire ocean. We need to estimate how amplitudes of internal tides decrease with the distance from the generating source.

Let us estimate the decay in the amplitudes and energy of internal tide in the course of its propagation from the ridge. Unfortunately not so many data are available that could be used to get the estimates of amplitude decay. The data we shall use were collected near the Mascarene Ridge, in the Megapolygon test site in the Northwest Pacific, near the Great Meteor Banks in the East Atlantic, near the

Fig. 8.2 Spectral densities of vertical displacements at a depth of 500 m in three regions: Aleutian Islands (**a**); Benguela (**b**), and Sargasso Sea (**c**)
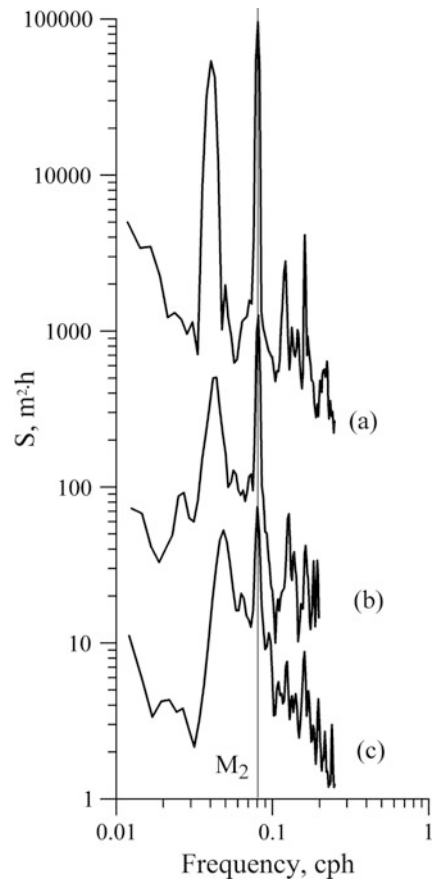
Aleutian Ridge, east of South America, in the Madagascar Strait, west of the Iberian Peninsula, and a few more study sites. The moorings in these sites were located in a line approximately normal to the ridge. Several moorings were closely located over a distance of one wavelength. These data were analyzed in the previous chapter when we discussed the long distance propagation of internal tides (see Sect. 7.7).

At small distances from the source, the energy losses are greater than at larger distances when the amplitudes become smaller and the role of the nonlinear terms decreases. A decrease in the amplitude can be estimated as 10% over one wavelength. The energy losses are about 15% over one wavelength.

The decay of the energy density in several regions combined on one graph is shown in Fig. 7.21. The graphs of the decay of amplitude and energy with distance are shown in Figs. 2.16, 2.18, 2.36, 3.17, 3.20, 3.21, 3.25, 4.15, 5.7, 5.9, 7.20, and 7.22. Detailed analysis of amplitude and energy decay over distance is given in Sect. 7.7 based on the data in several regions.

However, there are estimates that the decay of internal tide amplitudes is much lower (Dushaw et al. 2011). The authors report on the basis of satellite altimetry that the amplitude of the mode-1 internal tide decreases by less than 20% over the 2000 km path between the Hawaiian Ridge and 40°N.

A chart of the amplitudes of semidiurnal internal tides over the entire ocean was constructed as a result of analyzing the influence of various factors on wave amplitude: energy fluxes, barotropic tide currents, stratification, and geometry of the ridges with further comparison of calculations with the reference amplitudes measured on moorings (Fig. 8.3).

High amplitudes of internal tides are confined to the regions of submarine ridges. In the deep ocean basins far from submarine slopes and rough topography, internal tides decay to the background level (with amplitudes close to 10 m). The measurements of the semidiurnal internal tides on moorings in all study sites confirm the geographical distribution based on calculations.

The chart in Fig. 8.3 is still very rough despite the fact that it has been improved many times since its first publication by Morozov (1995). The author does not claim that this chart contains details. It reflects a qualitative pattern of the amplitude distribution in the ocean, which should be understood as regions of "large", "moderate", and "small" internal tide amplitudes. The amplitudes are "temporally averaged" with a half-month (spring-neap) time scale.

We shall now review some publications that consider the global distribution of internal tides in the ocean and global estimates of internal tide energy.

Nikurashin and Ferrari (2011) report that globally, the flow of the barotropic tide over continental slopes, shelf breaks, sills, abyssal hills, and seamounts generates more internal waves than geostrophic currents do. They estimated the global tidal energy input into internal tidal waves at 1 TW, while the global energy conversion from geostrophic currents into internal waves is 0.2 TW, which is most efficient in the region of the Antarctic Circumpolar Current (Nikurashin and Ferrari 2011).

The energy of the first mode M_2 baroclinic tide estimates were obtained from satellite observations by Kantha and Tierney (1997) based on the TOPEX/POSEIDON (T/P) altimetry. Internal tide patterns were associated with the generation over mid-ocean topographic features. The total energy in the global M_2 baroclinic tide is approximately 50 PJ (petajoule, 10^{15}). The authors indicate that M_2 is the only component of internal tide that can be obtained reliably from the altimetric measurements. The energy of the S_2 component is 8 PJ and the energy of the K_1 wave is 15 PJ. The total energy in all baroclinic tides of the first mode is 90 PJ. The model results indicate that approximately 360 GW of tidal energy are dissipated in the M_2 baroclinic tides and 520 GW are dissipated in all first mode baroclinic tides. The latter value is approximately 15% of the power input into barotropic ocean tides (3490 GW) from the tidal forces. The estimates of errors indicate that the dissipation rate could range from 400 GW–800 GW, the most likely value being about 600 GW.

Sjöberg and Stigebrandt (1992) used a numerical model and calculated that the global mean energy flux to internal tides per horizontal square unit is 44×10^{-4} W m^{-2}. This corresponds to a global energy flux of 1.3×10^{12} W, which amounts to approximately 25% of the tidal energy dissipation estimated from astronomical observations (Cartwright 1977).

A global chart of the surface elevations associated with the M_2 internal tide was constructed by Ray and Zaron (2016) from satellite altimeter data. The tidal fields
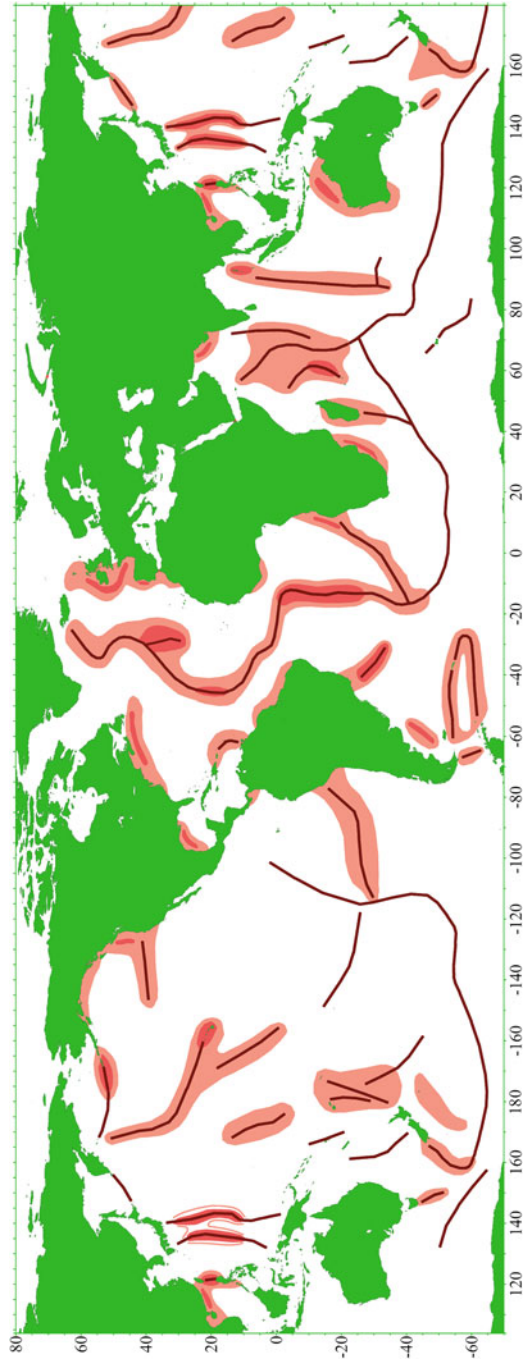
Fig. 8.3 World map of the amplitudes of semidiurnal internal tides (meters). Submarine ridges are shown with heavy brown lines. The regions of the semidiurnal internal tide amplitudes exceeding 50 and 30 m (peak-to-peak) are shown in dark and light red colors, respectively

were calculated on the basis of two-dimensional wavenumber spectral analysis, which results in an empirical map of modal wavelengths.

Satellite altimetry was used to construct a global map of open-ocean mode-1 M_2 internal tides by Zhao et al. (2016) based on sea surface height (SSH) measurements in 1992–2012. The authors constructed global maps of the amplitude and energy of the M_2 internal tides. The generation of internal tides was associated with topographic features such as continental slopes, submarine ridges, and seamounts. The authors indicated that the losses of internal tide energy during propagation are not directly related to the distance travelled. The authors estimated the total energy of the M_2 internal tide at 36 PJ (1 PJ = 10^{15} J).

The dissipation of the barotropic tide was estimated by Le Provost and Lyard (1997) based on the CEFMO hydrodynamic tidal model solution. The global energy input by astronomical forcing based on the M_2 sea surface elevation solution is 2.35 TW. An important conclusion is that a quarter of this energy input takes place over the South Atlantic Ocean. Approximately 40% of the tidal energy is dissipated over the North Atlantic Ocean. Energy is thus redistributed from the areas of energy input to feed the areas of dissipation. The Pacific Ocean, the Indian Ocean, and the South Atlantic Ocean receive more energy in total than they dissipate, in contrast with the North Atlantic Ocean and the Arctic Ocean. Detailed energy dissipation is estimated over different areas.

Generally, the calculated energy conversion from the M_2 barotropic tide to the M_2 internal tide in the deep ocean varies between 0.7 and 1.3 TW (Sjöberg and Stigebrandt 1992; Morozov 1995; Egbert and Ray 2001; Niwa and Hibiya 2001).

A model calculation of the barotropic tide energy conversion into internal waves was performed by Simmons et al. (2004) using a global domain multi-layer numerical model. The authors distinguish a few sites where intense internal wave generation occurs. The globally integrated conversion of the M_2 barotropic tide is 891 GW (gigawatts) (891×10^9 W) and the globally integrated dissipation of the barotropic tide is 2.94 TW (terawatts) (2.94×10^{12} W). These values agree with the estimates in other publications: 700 GW by Egbert and Ray (2001); 1100 GW by Morozov (1995); 1300 GW by Jayne and St. Laurent (2001); 1070 GW by Sjöberg and Stigebrandt (1992). Simmons et al. (2004) give the following depth integrated energy flux of internal tides in some important regions: 15 GW from the Aleutian Islands, 9 GW from the Antilles, 20 GW from the Azores, 11 GW from Bay of Biscay, 44 GW from the Drake Passage, 3 GW from the Emperor Seamounts, 17 GW from the Galapagos, 30 GW from the Hawaiian Islands, 78 GW from Indonesia, 9 GW from the Kerguelen Plateau, 5 GW from the Kuril Islands, 41 GW from the Kyushu-Palau Ridge, 22 GW from the Luzon Strait, 29 GW from the Macquarie Ridge, 56 GW from Madagascar, 79 GW from the North Fiji Basin, 53 GW from the South Fiji Basin, 66 GW from Tuamotu, 20 GW from the Walvis Ridge, 1 GW from the Fram Strait, 36 GW from the entire Mid-Atlantic Ridge. Not all of the energy fluxes agree with the above calculations, but all of them are important because the estimates are based on independent sources. We have to make the important comment that intense internal tides are generated in several small regions such as, for example, the Strait of Gibraltar.

However, owing to the small size of the source, its contribution to the energy balance can be negligible unlike the case of moderate energy internal tide generated over long submarine ridges.

A numerical model was applied by Nycander (2005) to calculate the tidal generation of internal tides on a global scale. The total flux over the area with a depth greater than 500 m was found to be 1.2 TW. The author distinguished the regions with high energy flux from the diurnal M_2 tidal component to internal waves. The regions with the strongest flux are: the Mascarene Ridge, the South China Sea, Hawaii, Kyushu-Palau Ridge, the Aleutian Islands, and the region south of New Zealand.

Similar results were reported by Li et al. (2015) on the basis of $1/10°$ model of the general ocean circulation. The authors found strong generation of internal tides in the regions of Hawaii, the Aleutian Islands, Mascarene Ridge, the South China Sea, the Andaman Islands, and the Kyushu-Palau Ridge.

Internal tides and sea surface elevations associated with internal tides were simulated in a high-resolution version of the HYbrid Coordinate Ocean Model (HYCOM) by Arbic et al. (2012). The results of their model were compared with the satellite altimetry and measurements on moorings. Their simulations confirmed strong internal tides in the Mascarene region, the South China Sea, Hawaii, and the Aleutian Islands, and also confirmed the existence of a beam of internal tides radiated south of New Zealand to the Tasman Sea.

The global ocean tide dissipates 25–30% of its total power loss (~ 1 TW) near large bathymetric features in the open sea. This is the conclusion of a recent study of global cotidal charts deduced from the TOPEX/POSEIDON satellite altimeter data by Egbert and Ray (2000). The physical mechanism responsible for this dissipation is apparently the scattering of energy into internal tides and other baroclinic motions and turbulence. Such scattering complements dissipation by turbulent friction in the bottom boundary layer of shallow seas, which is the traditional tidal energy sink.

Ray and Cartwright (2001) reported that in the Tuamotu Archipelago in the South Pacific the integrated energy flux is as high as 11 GW. The generation of internal tides along the Aleutian Trench is generally limited to a small region in the vicinity of 51°N, 170°–176°W. The waves follow a narrow beam southwards, spreading slightly, and reaching at least latitude 35°N. The integrated flux along the 51°N latitude is only 0.6 GW. The total integrated energy flux into the internal tides along the Hawaiian Ridge is 6 GW. Almost the same amount of the energy flux (5 GW) was reported by Kang et al. (2000). Merrifield and Holloway (2002) computed 9.7 GW from their 3-D model. A rough estimate of 15 GW by Ray and Mitchum (1997) was based on altimeter amplitudes averaged along the Hawaiian Ridge and could easily be two times smaller. They noted "not unreasonable" agreement with the figure of 8 GW obtained by Morozov (1995). Egbert and Ray (2000) estimate that the barotropic tide loses 20 GW over the Hawaiian Ridge.

References

Accad Y, Pekeris CL (1978) Solution of the tidal equations for the M_2 and S_2 tides in the world oceans from a knowledge of the tidal potential alone. Phil Trans Roy Soc A 290(1368):235–266

Alford MH, Peacock T, MacKinnon JA, Nash JD, Buijsman MC, Centuroni LR, … & Tang TYD (2015) The formation and fate of internal waves in the South China Sea. Nature 521(7550):65–69. https://doi.org/10.1038/nature14399

Althaus AM, Kunze E, Sanford TB (2003) Internal tide radiation from Mendocino Escarpment. J Phys Oceanogr 33:1510–1527

Arbic BK, Richman JG, Shriver JF, Timko PG, Metzger EJ, Wallcraft AJ (2012) Global modeling of internal tides within an eddying ocean general circulation model. Oceanography 25(2):20–29

Baines PG (1973) The generation of internal tides by flat-bump topography. Deep-Sea Res 20:179–205

Baines PG (1974) The generation of internal tides over steep continental slopes. Phil Trans Roy Soc London Ser A 277:27–58

Baines PG (1982) On internal tide generation models. Deep-Sea Res 29(3):307–338

Baines PG (1983) Tidal motion in submarine canyons—a laboratory experiment. J Phys Oceanogr 13(2):310–328

Baines PG (2007) Internal tide generation by seamounts. Deep Sea Res 54(9):1486–1508. https://doi.org/10.1016/j.dsr.2007.05.009

Bell TH (1975) Topographically generated internal waves in the open ocean. J Geophys Res 80(3):320–327

Bogdanov KT, Magarik VA (1967) Numerical solution of the problem of tidal wave propagation (M_2 and S_2) in the World Ocean. Dokl Akad Nauk SSSR 172(6):1315–1317

Bracher C, Flatté SM (1997) A baroclinic tide in the Eastern North Pacific determined from 1000-km acoustic transmissions. J Phys Oceanogr 27(4):485–497

Brickman D, Loder JW (1993) Energetics of the internal tide on northern Georges Bank. J Phys Oceanogr 23(3):409–424

Carter GS, Merrifield MA, Becker JM, Katsumata K, Gregg MC, Luther DS, Levine MD, Boyd TJ, Firing YL (2008) Energetics of M_2 barotropic-to-baroclinic tidal conversion at the Hawaiian Islands. J Phys Oceanogr 38(10):2205–2223

Cartwright DE (1977) Oceanic tides. Reports on progress in physics 40:665–708

Chiswell SM (1994) Vertical structure of the baroclinic tides in the Central North Pacific Subtropical Gyre. J Phys Oceanogr 24(9):2032–2039

Chiswell SM, Moore MI (1999) Internal tides near the Kermadec ridge. J Phys Oceanogr 29(5):1019–1035

Chiswell SM (2000) Tidal energetics over the Chatham rise, New Zealand. J Phys Oceanogr 30(9):2452–2460

Chiswell SM (2002) Energy levels, phase, and amplitude modulation of the baroclinic tide off Hawaii. J Phys Oceanogr 32(9):2640–2651

Cox CS, Sandström H (1962) Coupling of internal and surface waves in water of variable depth. J Oceanogr Soc Japan, 20-th anniversary 499–513

Cummins PF, Oey LY (1997) Simulation of barotropic and baroclinic tides off Northern British Columbia. J Phys Oceanogr 27(5):762–781

Cummins PF, Masson D, Foreman MG (2000) Stratification and mean flow effects on diurnal tidal currents off Vancouver Island. J Phys Oceanogr 30:15–30

Cummins PF, Cherniawsky JY, Foreman MG (2001) North Pacific internal tides from the Aleutian ridge: altimeter observations and modeling. J Mar Res 59:167–191

Dushaw BD (2006) Mode-1 internal tides in the western North Atlantic Ocean. Deep-Sea Res 53(3):449–473

Dushaw BD, Worcester PF, Dzieciuch MA (2011) On the predictability of mode-1 internal tides. Deep-Sea Res 58(6):677–698

Egbert GD (1997) Tidal data inversion: interpolation and inference. Prog Oceanogr 40:53–80

Egbert GD, Ray RD (2000) Significant dissipation of tidal energy in the deep ocean inferred from satellite altimeter data. Nature 405:775–778

Egbert GD, Ray RD (2001) Estimates of M_2 tidal energy dissipation from TOPEX/Poseidon altimeter data. J Geophys Res 106:22475–22502

Egbert GD, Erofeeva S (2002) Efficient inverse modeling of barotropic ocean tides. J Atmos Ocean Tech 19:183–204

Garrett C, Munk W (1979) Internal waves in the ocean. Ann Rev Fluid Mech 11:339–369

Gerkema T, van Haren H (2007) Internal tides and energy fluxes over Great Meteor Seamount. Ocean Sci 3:441–449. https://doi.org/10.5194/os-3-441-2007

Gerkema T, Zimmerman JTF (1995) Generation of nonlinear internal tides and solitary waves. J Phys Oceanogr 25(6):1081–1094

Gill AE (1982) Atmosphere-ocean dynamics. Academic Press, NY

Gordeev RG, Kagan BA, Rivkind VY (1974) Modeling of semidiurnal tides in the global ocean. Izv Acad Sci USSR, Ser Atmosph Oceanic Phys 10(7):497–498

Hall RA, Huthnance JM, Williams RG (2011) Internal tides, nonlinear internal wave trains, and mixing in the Faroe-Shetland Channel. J Geophys Res 116:C03008. https://doi.org/10.1029/2010JC006213

Hallock ZR, Field RL (2005) Internal-wave energy fluxes on the New Jersey shelf. J Phys Oceanogr 35(1):3–12

Hendershott MC (1973) Inertial oscillations of tidal period. Prog Oceanogr 6:1–27

Holloway PE, Merrifield MA (1999) Internal tide generation by seamounts, ridges, and islands. J Geophys Res 104(C11):25937–25951

Holloway PE, Chatwin PG, Craig P (2001) Observations from the Australian North West shelf in Summer 1995. J Phys Oceanogr 31(5):1182–1199

Jayne SR, St. Laurent LC (2001) Parameterizing tidal dissipation over rough topography. Geophys Res Lett 28:811–814

Jeans DRG, Sherwin TJ (2001) The evolution and energetics of large amplitude nonlinear internal waves on the Portuguese shelf. J Mar Res 59:327–353. https://doi.org/10.1357/002224001762842235

Johnston TMS, Rudnick DL, Kelly SM (2015) Standing internal tides in the Tasman Sea observed by gliders. J Phys Oceanogr 45(11):2715–2737

Kang SK, Foreman MG, Crawford WR, Cherniawsky JY (2000) Numerical modeling of internal tide generation along the Hawaiian Ridge. J Phys Oceanogr 30(5):1083–1098

Kantha LH, Tierney CC (1997) Global baroclinic tides. Prog Oceanogr 40:163–178. https://doi.org/10.1016/S0079-6611(97)00028-1

Kaula WM, Harris AW (1975) Dynamics of Lunar origin and orbital evolution. Rev Geophys Space Phys 13(2):363–371. https://doi.org/10.1029/RG013i002p00363

Klymak JM, Simmons HL, Braznikov D, Kelly S, MacKinnon JA, Alford MH, Pinkel R, Nash JD (2016) Reflection of linear internal tides from realistic topography: the Tasman continental slope. J Phys Oceanogr 46(11):3321–3337

Kunze E, Boss E (1998) A model for vortex-trapped internal waves. J Phys Oceanogr 28 (10):2104–2115

Kunze E, Rosenfeld LK, Carter GS, Gregg MC (2002) Internal waves in Monterey submarine canyon. J Phys Oceanogr 32(6):1890–1913

Largier JL (1994) The internal tide over the shelf inshore of Cape Point Valley South Africa. J Geophys Res 99:10023–10034

Le Provost C, Lyard F (1997) Energetics of the M_2 barotropic ocean tides: an estimate of bottom friction dissipation from a hydrodynamic model. Prog Oceanogr 40(1–4):37–52

Lee CM, Sanford TB, Kunze E, Nash JD, Merrifield MA, Holloway PE (2006) Internal tides and turbulence along the 3000-m isobath of the Hawaiian ridge. J Phys Oceanogr 36(6):1165–1183

Li Z, von Storch J-S, Müller M (2015) The M_2 internal tide simulated by a 1/10° OGCM. J Phys Oceanogr 45(12):3119–3135

Llewellyn Smith SG, Young WR (2002) Conversion of the barotropic tide. J Phys Oceanogr 32 (5):1554–1566

Maraldi C, Lyard F, Testut L, Coleman R (2011) Energetics of internal tides around the Kerguelen plateau from modeling and altimetry. J Geophys Res 116:C06004. https://doi.org/10.1029/2010JC006515

Merrifield MA, Holloway PE, Johnston TS (2001) The generation of internal tides at the Hawaiian Ridge. Geophys Res Lett 28:559–562

Merrifield MA, Holloway PE (2002) Model estimates of M_2 internal tide energetics at the Hawaiian ridge. J Geophys Res 107(C8):3179. https://doi.org/10.1029/2001JC000996

Mork M (1968) On the formation of internal waves caused by tidal flow over a bottom irregularity. Rep Geophys Inst Univ, Bergen, Norway, p 28

Morozov EG, Nikitin SV (1984a) Propagation of semidiurnal internal waves in a region with varying bottom topography. Oceanol Res (36):44–49

Morozov EG, Nikitin SV (1984b) Separation and analysis of the baroclinic component of semidiurnal temperature fluctuations. Oceanol Res (36):55–61

Morozov EG (1985) Oceanic internal waves. Nauka, Moscow. 151 [in Russian]

Morozov EG (1995) Semidiurnal internal wave global field. Deep-Sea Res 42(1):135–148

Morozov EG (2006) Internal tides. Global field of internal tides and mixing caused by internal tides. In: Waves in geophysical fluids. Springer, Wein, New York, pp 271–332

Moum JN, Klymak JM, Nash JD, Perlin A, Smyth WD (2007) Energy transport by nonlinear internal waves. J Phys Oceanogr 37:1968–1988. https://doi.org/10.1175/JPO3094.1

Munk WH, Wunsch C (1998) Abyssal recipes II: energetics of tidal and wind mixing. Deep-Sea Res 45:1977–2010

Nash JD, Kunze E, Toole JM, Schmitt RW (2004) Internal tide reflection and turbulent mixing on the continental slope. J Phys Oceanogr 34(5):1117–1134

Nash JD, Kunze E, Lee CM, Sanford TB (2006) Structure of the baroclinic tide generated at Kaena ridge, Hawaii. J Phys Oceanogr 36(6):1123–1135

New AL (1988) Internal tidal mixing in the Bay of Biscay. Deep-Sea Res 35:691–709

Niiler PP (1968) On the internal tidal motions in the Florida straits. Deep-Sea Res 15(1):113–123

Nikurashin M, Ferrari R (2011) Global energy conversion rate from geostrophic flows into internal lee waves in the deep ocean. Geophys Res Lett 38:L08610. https://doi.org/10.1029/2011GL046576

Niwa Y, Hibiya T (2001) Numerical study of the spatial distribution of the M_2 internal tide in the Pacific ocean. J Geophys Res 106:22441–22449

Nycander J (2005) Generation of internal waves in the deep ocean by tides. J Geophys Res 110: C10028. https://doi.org/10.1029/2004JC002487

Phillips OM (1977) The dynamics of the upper ocean, 2nd edn. Cambridge Univ. Press, NY, p 336

Prinsenberg SJ, Wilmot WL, Rattray M (1974) Generation and dissipation of coastal internal tides. Deep-Sea Res 21(4):263–281

Rainville L, Pinkel R (2006a) Baroclinic energy flux at the Hawaiian ridge: observations from the R/P FLIP. J Phys Oceanogr 36(6):1104–1122

Rainville L, Pinkel R (2006b) Propagation of low-mode internal waves through the ocean. J Phys Oceanogr 36(6):1220–1236

Rainville L, Lee CM, Rudnick DL, Yang K-C (2013) Propagation of internal tides generated near Luzon Strait: observations from autonomous gliders. J Geophys Res 118(C9):4125–4138. https://doi.org/10.1002/jgrc.20293

Rattray M (1960) On the coastal generation of internal tides. Tellus 12:54–62

Rattray M, Dworsky J, Kovala P (1969) Generation of long internal waves at the continental slope. Deep-Sea Res 16(Suppl.):179–195

Ray RD, Mitchum GT (1997) Surface manifestation of internal tides in deep ocean: observations from altimetry and island gauges. Prog Oceanogr 40:135–162

Ray RD (1999) A global ocean tide model from TOPEX/Poseison altimetry: GOT 99.2. NASA/ Tech Memo 209478

Ray RD, Cartwright DE (2001) Estimates of internal tide energy-fluxes from TOPEX/Poseidon altimetry: Central North Pacific. Geophys Res Lett 28:1259–1262

Ray RD, Zaron ED (2016) M_2 Internal tides and their observed wavenumber spectra from satellite altimetry. J Phys Oceanogr 46(1):3–22

Rayson MD, Ivey GN, Jones NL, Meuleners MJ, Wake GW (2011) Internal tide dynamics in a topographically complex region: browse basin, Australian North West shelf. J Geophys Res 116:C01016. https://doi.org/10.1029/2009JC005881

Sandström H, Oakey NS (1995) Dissipation in internal tides and solitary waves. J Phys Oceanogr 25(4):604–614

Sandström H, Elliott JA (1984) Internal tide and solitons on the Scotian shelf: a nutrient pump at work. J Geophys Res 89(C4):6415–6426. https://doi.org/10.1029/JC089iC04p06415

Sandström H, Elliott JA (2011) Production, transformation, and dissipation of energy in internal tides near the continental shelf edge. J Geophys Res 116:C04004. https://doi.org/10.1029/2010JC006296

Schwiderski EW (1979) Global ocean tides. Part II: the semidiurnal principal lunar tide (M_2), Atlas of tidal charts and maps. Naval Surface Weapons Center Report. NSWC TR 79–414, 15 pp

Schwiderski EW (1980a) Ocean tides, I, Global ocean tidal equations. Mar Geod 3:161–217

Schwiderski EW (1980b) On charting global ocean tides. Reviews Geoph Space Phys 18:243–268

Sherwin T (1988) Analysis of an internal tide observed on the Marlin Shelf north of Ireland. J Phys Oceanogr 18:1035–1050

Sherwin TJ, Taylor NK (1990) Numerical investigations of linear internal tide generation in the Rockall Trough. Deep-Sea Res 37(10):1595–1618

Simmons HL, Hallberg RW, Arbic BK (2004) Internal wave generation in a global baroclinic tide model. Deep-Sea Res Part II 51:3043–3068

Sjöberg B, Stigebrandt A (1992) Computations of the geographical distribution of the energy flux to mixing process via internal tides and the associated vertical circulation in the ocean. Deep-Sea Res 39:269–291

Smith WHF, Sandwell DT (1997) Global sea floor topography from satellite altimetry and ship depth soundings. Science. 277:1956–1962. http://topex.ucsd.edu/cgi-bin/get_data.cgi; last accessed in October 2017

Smith DK, Jordan TH (1988) Seamount statistics in the Pacific ocean. J Geophys Res 93 (B4):2899–2918

St. Laurent LS, Stringer S, Garrett C, Perrault-Joncas D (2003) The generation of internal tides at abrupt topography. Deep-Sea Res 50:987–1003

Torgrimson GM, Hickey BM (1979) Barotropic and baroclinic tides over the continental slope and shelf off Oregon. J Phys Oceanogr 9:945–961

Vlasenko VI (1992) Nonlinear model for the generation of baroclinic tides over extensive inhomogeneities of bottom topography. Phys Oceanogr (Morskoy gidrofizicheskiy zhurnal) 3:417–424

Weigand JG, Farmer H, Prinsenberg S, Rattray M (1969) Effects of friction and surface tide angle of incidence on the coastal generation of internal tides. J Mar Res 27:241–259

WOD13 (2013) World ocean database 2013, Geographically sorted data. https://www.nodc.noaa.gov/OC5/WOD/datageo.html. Last updated 26 October 2013; last accessed in October 2017

Yesson C, Clark MR, Taylor ML, Rogers AD (2011) The global distribution of seamounts based on 30 arc seconds bathymetry data. Deep-Sea Res 58(4):442–453

Zaron ED, Egbert GD (2006) Estimating open-ocean barotropic tidal dissipation: the Hawaiian ridge. J Phys Oceanogr 36(6):1019–1035

Zhao Z, Alford MH, Girton JB, Rainville L, Simmons HL (2016) Global observations of open-ocean mode-1 M_2 internal tides. J Phys Oceanogr 46(6):1657–1684

Zilberman NV, Becker JM, Merrifield MA, Carter GS (2009) Model estimates of M_2 internal tide generation over Mid-Atlantic Ridge topography. J Phys Oceanogr 39(10):2635–2651

Conclusions

Internal tides (internal waves of tidal period, baroclinic tides) are internal waves with tidal frequency, which are distinguished over the background internal waves as waves with fixed frequency, high amplitude, and energy. The measurements in various regions of the World Ocean analyzed in this book were carried out by the global oceanographic community over many years. These data allowed us to reveal many characteristic properties of the oceanic internal tides. Analysis of numerous measurements in different regions of the ocean shows that the properties of tidal internal waves vary from one region to another but their general features remain the same. This fact makes it possible to consider them as a process characteristic of the entire ocean. All the measurements indicate that internal tides are characterized by high energy. They dominate over the other internal waves in the entire range of their existence. The semidiurnal internal tides are usually stronger than the diurnal internal tides.

Large topographic formations such as submarine ridges and continental slopes are the main regions of internal tide generation. Generation of internal tidal oscillations occurs as a result of the interaction between the barotropic tidal currents and irregularities of the bottom topography. When barotropic tidal currents flow over sloping topography the streamlines are no longer horizontal. The currents obtain a vertical component and vertical perturbations of density field appear with the tidal frequency; thus the generation of internal tide occurs.

Since the frequency of the internal tides is always smaller than the buoyancy frequency, the trajectories of water particles are inclined. The relation between the slope angle α, wave frequency ω, Coriolis parameter f, and Brunt-Väisälä frequency N is well known (Phillips 1977):

$$\omega^2 = N^2 \cos^2 \alpha + f^2 \sin^2 \alpha.$$

Angle α is the angle between the wave vector and the horizontal plane. Such sloping (beam) propagation of internal tides unites them with the other internal wave perturbations in the ocean. In the close vicinity of the topographic formations, where the generation of internal tide occurs, the beam type of internal wave propagation dominates. The beam is a region of significant amplitudes of

oscillations oriented along characteristic lines. In the remaining domain the fluc-
tuations are small. The indications of the beam structure of internal tides were
revealed near submarine ridges, seamounts, and continental slopes. The beam starts
from the depths close to the top of the slope where the inclination of the slope is the
same as the inclination of the characteristic line. It can be traced over 50–100 km
from the topographic feature over which the perturbation was generated.

As the beam propagates from the ridge to the ocean it becomes wider and reflects
from the surface and bottom. After multiple reflections the mode structure is formed
when the vertical components of the wave vector directed from the bottom and from
the surface compensate each other. Wave packets propagating upwards and
downwards should have approximately the same intensity due to moderate energy
losses when they reflect from the surface and bottom. Vertical wavenumbers k_z in
the perturbations propagating up and down along sloping surfaces compensate each
other, thus a vertically standing wave is formed.

It was found that the mode structure is formed at closer distances from the ridges
than from seamounts. Clearly pronounced beam structure exits at a distance of
50 km from a seamount, while the mode structure starts to dominate over the beam
structure at this distance from a ridge. This is explained by the fact that a seamount
can be considered a point source. A single beam of maximum intensity is radiated
from the top of a seamount. A ridge crest is actually a line of seamounts located not
strictly along a straight line. Therefore, beams with different phases are radiated
from different points of the crest. However, their intensity is approximately the
same if the tops are located at the same depth. Unlike only one beam from the top of
a seamount, the semidiurnal internal perturbations from different points of the ridge
are superimposed and form the mode structure at closer distances than from a
solitary seamount. Thus, a submarine ridge can be considered a quasi-linear source
of internal tides.

The domination of the first mode at distances exceeding 50–100 km from the
ridge is confirmed by observations near the Mid-Atlantic Ridge, Mascarene Ridge,
Aleutian Ridge, south of the Mendocino Escarpment, and in many more regions.
The study sites were usually located at distances of 100–700 km from submarine
ridges. The internal tides generated over the slopes of these ridges were recorded by
the temperature meters on moorings. The estimates obtained from these mooring
clusters, which are antennas for internal tides, showed that the wavelength of the
dominating wave corresponds to the first mode of oscillations. These estimates were
always close to the theoretical wavelengths calculated by the numerical integration
of the equation for the vertical velocity in internal waves. The stratification was
taken from CTD casts near the ridges. The scale of the vertical coherence in these
sites located close to the submarine ridges always exceeded 1000 m. Horizontal
coherence in these regions over the scales of the sites (~ 100 km) was always
significant. The direction of the internal tide corresponded to the generation of
waves over the ridge and did not change significantly in time.

Internal tides are characterized by high energy; thus, they can propagate over
large distances from the regions of their generation. Beams forming the wave reflect
many times from the surface and bottom. High energy and ability for multiple

reflections make internal tides significantly different from waves of smaller scale, which lose part of their energy without even a single reflection.

Internal tides get additional energy supply from the interaction between the barotropic tide and the irregularities of smaller scale rather than large topographic formations. It is likely that this mechanism facilitates the excitation of higher modes at distances far from the slopes of the ridges and continental slopes.

Moored measurements in some of the study sites located at distances exceeding 1000 km from submarine ridges, for example, Polygon-70, and Mesopolygon-85 reveal several oscillation modes. In the case that two or more modes exist, the vertical coherence scale decreases to one hundred meters. Horizontal coherence decreases compared to the values recorded in the study sites close to the submarine ridges. However, the direction of the waves is quasi-stationary even in such regions. Observations indicate that the waves do not change direction within a few months. This may happen in such regions where the wave systems generated locally over the irregularities of the bottom topography on the deep bottom in the region of the study site can play a significant role.

At even larger distances from the generation sources, the internal tide loses its property of a deterministic process as it propagates through the oceanic fields with variable buoyancy frequency and vertical and horizontal shears of velocity. Owing to the fact that the ocean bottom is far from being flat, reflections and refractions occur over the bottom irregularities and the generation of new waves occurs.

Loss of the property of a deterministic process was found in the Array and POLYMODE experiments in the Sargasso Sea at far distances from the continental slopes and the Mid-Atlantic Ridge. This effect was found to an even greater degree in the southern part of the Indian Ocean north of Kerguelen Island and in the Madagascar Basin. The semidiurnal peaks on the temperature spectra in these regions are variable in time. Their confidence level is not high. Horizontal coherence on the scales of the study site is always below the confidence level.

In this study, the author attempted to reveal the regularities of internal tide dissipation in the course of its propagation. There are not many moored measurements over long lines of moorings extended in the direction of internal tide propagation that would allow us to estimate the energy losses. Moored measurements east of the Mascarene Ridge and in some other regions indicate that wave energy decreases by approximately 10–15% over one wavelength (120–150 km).

The measurements in the study sites located at distances greater than 1000 km from the sources indicate that the energy level of internal tides at such long distances from the sources is close to the background level. This estimate (1000 km) is not very reliable because only a few measurements were conducted when the tidal peak of temperature spectra is completely lacking. Local generation of internal tides over small irregularities of the bottom topography occurs everywhere in the deep basins. Exact estimates of the energy contribution from this mechanism to the total energy balance are only approximate.

The major part of the energy of internal tides is transferred from the energy of the barotropic tide in the regions of large underwater topographic formations: slopes of submarine ridges and continental slopes. Numerous islands and solitary

seamounts also make a contribution to the energy balance of the internal tide. It becomes clear from the previous results that submarine ridges are the main sources of energy for internal tide generation in the open ocean. We applied the Baines model (1982) to estimate the energy fluxes of internal tides generated over submarine ridges. The energy fluxes depend on the geometry of the slope, stratification, and water transport by the currents of the barotropic tide. The direction of tidal currents relative to the ridge is an important factor of internal tide generation. If the inclination of the slope is close to the characteristic curve of internal tides, which depends on stratification, the energy fluxes reach the maximum level.

Our estimates indicate that the energy fluxes of internal tides generated over the slopes of submarine ridges are higher than the energy fluxes from the continental slopes. This is explained by the fact that the currents of the barotropic tide are generally parallel to the continental slopes and shores (Accad and Pekeris 1978; Gordeev et al. 1974; Schwiderski 1979; Ray 1999). Therefore, the transport of water by the tidal currents in the direction across the continental slopes is not high. Only a small portion of the barotropic tide energy is transported to the shelf. Very frequently underwater ridges are normal to the propagation of the barotropic tide currents. Therefore, the entire tidal flow in the water column overflows the ridge and induces stronger generation of internal tide than over the continental slope.

The maximum energy fluxes and hence, the maximum amplitudes of internal tide are formed in the regions in which the currents of the barotropic tide are normal to the crests of the ridges. One of the typical regions is the southern part of the Mid-Atlantic Ridge in the Southern Hemisphere. In addition, the amplitudes of the barotropic tide and tidal currents are high in this region. The energy fluxes are maximal when the crest of the ridge is close to the maximum stratification and the surrounding depths of the ocean are deep. Typical examples are the Mascarene Ridge, the Aleutian Islands, and the ridges in the Luzon Strait. High amplitudes of the internal tides were found in these regions.

Tidal dissipation based on the astronomical data of the length of the day was estimated by Cartwright (1977) at 4.3×10^{12} J/s (10^{12} J/s are terawatts: TW). Recent estimates are smaller. Munk and Wunsch (1998) report that tidal dissipation is 3.7 TW. The dissipation of M_2 tide only is 2.5 TW. Le Provost and Lyard (1997) estimate the tidal dissipation at 2.35 TW. However, they consider only the bottom friction. Close values of tidal dissipation were reported by Le Provost et al. (1998), Kantha and Tierney (1997), and by Schrama and Ray (1994).

Previously, tidal dissipation was thought to occur in the bottom layers of shallow seas due to turbulent mixing. However, the balance of tidal dissipation remained not closed. Our estimates based on the sum of the energy fluxes of internal tides from the major underwater ridges account for approximately 25% of the tidal dissipation. This estimate has been supported by many authors (Sjöberg and Stigebrandt 1992; Morozov 1995; Egbert and Ray 2000).

Thus, the energy balance of the barotropic tide dissipation becomes clearer because the energy of the barotropic tide dissipation that was transferred to internal waves had not previously been estimated (Olbers 1983). Bell (1975) estimated the energy transfer from the barotropic tide to internal waves due to the interaction of

the tidal currents with rough topography at the abyssal depths at 10%. The estimate of Baines (1982) of the energy transfer over continental slopes is smaller than 1%. However, all estimates are approximate.

Numerous spectra calculations performed in this work and other studies indicate that the spectral peak corresponding to the semidiurnal internal tides is very narrow. The peak is clearly distinguished over the background spectra of internal waves in the frequency range of internal wave existence. The width of the semidiurnal spectral peak changes only slightly from one region of measurements to another.

The bandwidth corresponding to the semidiurnal internal tides is very narrow. The width of the spectral peak corresponding to the M_2 internal tide (at half-height of the peak) is usually 3–4 times greater than the resolution of the spectrum. For example, if the time series is 400 days long and the spectral resolution is $\Delta\omega = 0.0005$ cph, the width of the spectral peak at its half height is $\Delta\omega = 0.0015$ cph. Unfortunately, the current data from moorings do not provide a better resolution. Longer time series are needed.

The strong elevation of such a narrowband semidiurnal peak over the background spectra and many other properties of internal tides indicate that they cannot be described by the Garrett-Munk models (1972, 1975). However it should be noted that the authors never stated that the model describes internal tides. Such distinguishing properties of internal tides are related to the existence of a source corresponding to the range of existence of internal waves between the inertial and buoyancy frequencies. The existence of such a source has not been assumed in the model.

Long time series with a duration of one-two years allowed us to calculate spectra with high resolution. This made it possible to study detailed structure of spectra in the semidiurnal frequency band. It is known that diurnal and semidiurnal tides are divided into a number of individual constituents (Doodson 1921). Thus, the existence of individual internal tidal constituents is expected. Spectra with high frequency resolution allowed us to reveal the fine structure of spectra in the vicinity of the semidiurnal and diurnal frequencies.

The M_2 internal tide dominates in the semidiurnal frequency range. The oscillations of this frequency dominate both in the spectra of velocity components and temperature. The latter provide evidence that among the internal waves the M_2 wave (period 12.42 h) has the maximum energy. The S_2 wave (period 12.00 h) is less intense but it is still sufficiently strong. Almost no manifestations of the N_2 and K_2 waves were observed.

The maximum energy in the diurnal range is associated with the K_1 internal wave (period 23.9 h). The energy of the O_1 wave (period 25.8 h) is smaller. These estimates were obtained from the measurements in the Sargasso Sea. The inertial frequency at these latitudes is close to the diurnal and the peaks sometimes merge. In several regions, the amplitudes of the diurnal and semidiurnal peaks are almost the same, for example in: the Bab el Mandeb Strait, and Bay of Biscay.

Vertical variations in the amplitudes of internal tides are found everywhere in the ocean. Near the generation sources, the amplitudes of maximum vertical displacements are in the main pycnocline at depths of 700–1200 m. These are exactly

the depths of the maximum of the eigen function for the vertical velocities in internal tides of the first mode. This fact provides evidence that the first mode dominates in the major part of the regions where the measurements were conducted.

If several low modes exist, vertical variability is determined by the sum of their contributions. Vertical variation of each mode is determined by the eigen function of this mode. If the beam structure dominates in a close vicinity to the generation region the amplitudes are maximum on the beam line and low outside the beam.

Usually, the vertical displacements associated with internal tides are 15–25 m. The maximum amplitudes are found near large topographic features. For example, near the North Mid-Atlantic Ridge south of the Great Meteor Banks, the amplitude of vertical displacements was 36 m. East of the Meteor Banks the amplitudes reached 50 m. Near the Mascarene Ridge in the Indian Ocean, the maximum amplitudes were as high as 160 m. In the South China Sea and near the Aleutian Islands the amplitudes were even greater. Amplitudes up to 200 m were reported in the South China Sea. However, the record belongs to the Strait of Gibraltar, where vertical displacements up to 300 m were found.

The regions of the Polygon-70 and Megapolygon-87 experiments located at distances of many hundred kilometers from submarine ridges are characterized by moderate internal tide amplitudes within 15–20 m.

In the regions of the Sargasso Sea and the Indian sector of the Southern Ocean located very far from large topographic formations, the amplitudes of internal tides are even smaller. Such a distribution of the amplitudes of semidiurnal oscillations over the ocean basin confirms the concept that internal tides are generated over the slopes of topography and then propagate to the other regions of the ocean as free internal waves. In the course of their propagation they lose energy and also obtain new portions of energy from the generation over bottom irregularities at abyssal depths.

Our temperature meters set on the moorings recorded temperature time series. The amplitudes of temperature fluctuations caused by the propagation of internal tide and vertical displacements of water particles are determined by the product of vertical displacement and vertical temperature gradient. The variations of temperature fluctuations by vertical are very complex. It is impossible to judge about wave amplitudes from temperature fluctuations only. The maximum temperature fluctuations are usually found in the seasonal thermocline mainly due to the high vertical temperature gradient. Sometimes temperature fluctuations may be as much as a few degrees especially in the seasonal thermocline. At the same time, the amplitudes of vertical displacements caused by internal tide in the seasonal thermocline may not be very high because this layer is close to the surface. It is known that owing to the structure of the eigen function for the vertical displacements in internal waves, the maximum of amplitudes is approximately at mid-depth, while close to the surface and bottom the vertical displacements in the internal tide are not large. Analysis of internal tides based on the temperature fluctuations in the seasonal thermocline, and in particular, comparison of wave intensity at different points can lead to wrong conclusions if the variations in the temperature fluctuations are interpreted as variability associated with internal waves. In such a formulation of the problem it is

important to know the vertical temperature gradient, which eventually determines the variations in the intensity of fluctuations.

Internal tide amplitudes are not high in the seasonal thermocline in the upper layer and their measured signal may be even lower than noise. This fact could explain why internal tides in the upper layer are sometimes not recorded.

Horizontal variations in the spectral functions can be determined by the bottom topography influencing the conditions of internal tide generation. If the bottom topography is rough and the generation of internal tides occurs in the bottom layer, significant horizontal variations in the semidiurnal fluctuations are observed. This variability is related to the fact that the beam character of fluctuations did not transfer to the mode structure, and large amplitudes of fluctuations are observed only along the characteristic lines. A typical example of such variations was observed in the Madagascar Basin. To some extent this effect was also observed during the Polygon-70, Mesopolygon-85 experiments, and in some experiments in the Sargasso Sea.

Analysis of the variations in the semidiurnal spectral peaks in different study sites demonstrated that the greater the variations in the mean state of the ocean over the scales of the study region, the greater differences found in the spectral functions. In the regions with moderate variations in temperature, salinity, and velocity fields located far from clearly pronounced frontal zones, the spectral functions do not significantly differ over the scales of the order of 100 miles. In the layer of the main pycnocline, where horizontal differences in the mean conditions are small, we observed low variations in the spectral characteristics of the semidiurnal internal tides. Typical examples of such low variations are Polygon-70 and Mesopolygon-85 experiments located far from the jet currents, in which the eddy activity does not gain high levels.

In the Sargasso Sea, the mean state of the ocean changes significantly over the horizontal scales of the order of 100 miles because of the intense mesoscale eddies existing in this region. Despite the fact that the wavelength within the POLYMODE study site changed by no more than 10%, this variation was sufficient to influence the internal tide waves and cause notable variations in the spectral functions over horizontal scales of 100 miles. Strong currents with powerful mesoscale eddies displace the spectral peaks from their theoretical frequency owing to the strongly pronounced Doppler effect. The frequency shift of the peaks can be as high as $\Delta f = 0.015$ cph. In other regions of the ocean, in which currents are not so strong, the shift of the semidiurnal peak does not exceed $\Delta f = 0.005$ cph.

It is important to note that such frequency shifts are observed only if the duration of the time series is close to the interval of constant currents associated with a mesoscale eddy, during which the currents have approximately the same direction. In the region of the POLYMODE experiment in the Sargasso Sea, in which detailed observations of eddies were available, this time period is approximately 15–20 days. The westward drift of the eddies during this time is not significant. If longer time series are used to calculate spectra the shifts of different sign compensate each other because the spectral functions are averaged over the duration of the time series.

Numerous calculations of spectral functions show that the frequency shifts of the semidiurnal spectral peaks from the M_2 frequency decrease when the duration of the time series for spectrum calculation increases. Frequency shifts with variable signs caused by the Doppler effect lead to widening of the spectral peak if the spectrum is calculated from the data of a long time series.

Since internal tides are generated by the barotropic tide they should inherit the property of the spring-neap (half-month) variability. Analysis of long time series confirmed this theory. Long time series from the Sargasso Sea, the Bay of Biscay, and the Polygon-70 experiment allowed us to distinguish half-month (spring-neap) variations in the amplitudes of semidiurnal internal tides.

Since the direction of internal tides is quasi-stationary, the revealed half-month variability of amplitudes becomes very important. A basis for forecasting semidiurnal internal waves appears on the basis of these two properties. The sources of internal tides are stationary in space (bottom topography) and quasi-stationary in time with a half-month variability, which is determined by the spring-neap variability of the barotropic tide. Therefore, in principle if the internal tide regime is known in a given region, it is possible to forecast the amplitude of internal tide knowing the prediction results of the barotropic tide. The forecast is complicated by the fact that internal waves pass a distance from the region of generation through variable oceanographic medium. The state of this medium is variable, which influences the propagation and properties of internal tide.

The velocity of wave propagation on the pathway from the generation region to the place in which they are measured depends on the complex character of the distribution of temperature, salinity, and currents, which form the conditions of the mean state of the ocean. Irregular types of variation in the velocity field over the ocean basin and variable topography and stratification that lead to variable wavelength should cause variations in the direction of internal tide propagation relative to the mean direction. Variable directions and amplitudes make the forecast of internal tides difficult. The forecast of internal tides requires knowledge of the mean state of the ocean (temperature, salinity, and velocity fields) not only at the location of recording but also on the pathway of the internal tide propagation from the generation region.

It follows from the equation for internal waves that the wavelength of the internal tide and its phase velocity for each mode is determined by the ocean stratification, depth, and latitude of the location. The wavelength is quite stable within the usual study sites despite variations in the stratification and other local conditions of the ocean mean state. This conclusion was drawn on the basis of the numerical integration of the equation for internal waves with variations of different parameters. Seasonal variations in stratification or changes in the temperature, salinity, and velocity fields associated with the propagation of powerful mesoscale eddies and also depth variations within the study sites over the deep ocean lead to variations in the semidiurnal internal tide wavelength not exceeding 10%.

The form of the eigen functions of the equation for the vertical velocity of internal tides shows that the maximum vertical displacements approximately correspond to the middle part of the water column. The maximum displacements

related to the first mode are in the main thermocline (700–1200 m). Despite the fact that temperature fluctuations associated with internal waves can be high, the vertical displacements in the upper 50–200 m are not large. This is exactly the layer, in which the seasonal thermocline is usually located. Such a form of the eigen function agrees well with the previous conclusions about the maximum vertical displacements in the main thermocline.

The maxima of horizontal velocities of internal tides are in the upper layer at the surface and at the bottom. This follows from the form of the eigen functions for horizontal velocities in the internal tide. This may lead to additional distortions of the temperature spectra in the upper layer caused by advection of horizontal temperature inhomogeneities by the tidal currents and by the Doppler effect. Horizontal displacements of water particles by the internal tide may be as high as a few kilometers; therefore, advection of temperature inhomogeneities, which are in abundance in the upper layer, may cause the appearance of additional non-realistic peaks sometimes found on the spectra. The opinion that no internal waves exist in the surface layer is incorrect. Vertical velocities are actually small. Horizontal velocities caused by internal waves in the upper and bottom layers may be high. Horizontal velocities at the surface lead to the surface manifestations of internal waves that cause alternating convergence and divergence zones at the surface. They can be observed by remote methods as regions of different intensity of ripples. In the upper and bottom layers of the ocean internal tides manifest themselves as strong periodical horizontal currents.

A method has been suggested, by which one can separate the velocity fluctuations caused by the barotropic and internal tide of the same periods. The method was tested on the data from the Sargasso Sea and a region near the Mid-Atlantic Ridge. The calculations showed that in the Sargasso Sea the energies of the internal and barotropic tides were approximately the same. Near the Mid-Atlantic Ridge, the energy of the internal tide was 1.5–2.0 times greater than the energy of the barotropic tide. This may be explained by the energy losses of the internal tide in the course of its propagation from the region of generation. In the Sargasso Sea, the study site was located at a greater distance from the generation region than in the experiment near the ridges.

At present, it is generally accepted that internal tides are stable fluctuations of water particles and correspondingly temperature, salinity, and velocity. The spectral peak that corresponds to the internal tides is high above the background spectra of internal waves as a peak close to the delta-function, whereas the background spectrum is described by the Garrett-Munk model.

Unlike the other internal waves of the entire frequency range the direction of internal tides is quasi-stationary; they conserve their properties and energy over spatial scales exceeding the scales of one wavelength. Their generation generally occurs over the slopes of submarine ridges. This presents an important principal opportunity to forecast internal tides.

The highest energies in the frequency spectra of internal waves correspond to the inertial and tidal internal waves. These two processes occupy special places in the spectra of internal waves. Internal tides are distinguished by their clearly pronounced anisotropy, stability, and high amplitudes. These properties of internal waves are related to the existence of the source of internal tides. Variations in the internal tide are related to the variations in the barotropic tide that generates them.

The construction of the general model of internal waves describing the energy transfer to the internal wave frequency range, dissipations of this energy, energy cascade over the spectrum, and joint behavior of internal waves of the entire spectrum is possible only after the models of particular behavior of internal waves of different scale have been developed.

Our lack of detailed knowledge of internal waves is caused by the limited data of observations. Special experiments are needed to study various frequency ranges and interaction between internal waves of different scales. Unfortunately, our level of knowledge of the processes related to internal waves is not sufficient to contrive a model that could satisfy the practical needs of an internal tide forecast.

Concise Conclusions

1. We determined the properties of oceanic internal tides on the basis of numerous moored measurements in various regions of the ocean.
2. Moored measurements of internal waves showed that submarine ridges are the regions of intense generation of internal tides. The waves propagate from the ridges, and their direction does not change significantly over time. The energy fluxes from the barotropic tide to the internal tide over submarine ridges were calculated. These fluxes exceed the fluxes to the internal tides from the continental slopes. This occurs because the currents of the barotropic tide are generally parallel to the continental slopes; hence they do not transport much water across the slope. In the case of submarine ridges, the situation is different because tidal currents can flow normal to the ridge and overflow it. The sum of energy fluxes transferred to internal tides over all submarine ridges in the World Ocean is approximately 25% of the barotropic tide energy dissipation.
3. Moored measurements near large topographic formations such as submarine ridges showed that wave propagation in the close vicinity of submarine slopes has a beam character. Mode structure is formed at a distance from the slopes of the order of one wavelength of the internal tide (~ 100 km). Usually, the first mode dominates in this structure.
4. As the internal tide propagates over the ocean basins it loses its energy and at the same time more waves are generated over irregularities of the bottom topography. At large distances from the sources (of the order of 1000–1500 km) the internal tide loses its property of a deterministic process.

5. A chart of the distribution of internal tide amplitudes was constructed on the basis of calculations and measurements. Usually internal tide amplitudes are within 10–30 m, but the maximum amplitudes exceed 100 m.

6. The amplitudes of the semidiurnal internal tides are subjected to the variations with a spring-neap cycle equal to 14 days related to the variations in the semidiurnal barotropic tide.

7. Internal tides in the vicinities of the diurnal and semidiurnal frequencies are characterized by fine structure. The maximum energy is usually associated with the M_2 frequency; the energy of the waves of the S_2 frequency is smaller. The sources of internal tides are stationary in space and their time variation is close to the half-month periodicity; hence a possibility of predicting internal wave amplitudes and direction in some regions of strong internal tides appears.

References

Accad Y, Pekeris CL (1978) Solution of the tidal equations for the M_2 and S_2 tides in the world oceans from a knowledge of the tidal potential alone. Phil Trans Roy Soc A 290(1368): 235–266

Baines PG (1982) On internal tide generation models. Deep-Sea Res 29(3):307–338

Bell TH (1975) Topographically generated internal waves in the open ocean. J Geophys Res 80(3):320–327

Cartwright DE (1977) Oceanic tides. Rep Progr Phys 40:665–708

Doodson AT (1921) The harmonic development of the tide-generating potential. Proc R Soc Lond Ser A 100(704):305–329

Egbert GD, Ray RD (2000) Significant dissipation of tidal energy in the deep ocean inferred from satellite altimeter data. Nature 405:775–778

Garrett CJR, Munk WH (1972) Space-time scales of internal waves. Geophys Fluid Dyn 3(3): 225–264

Garrett C, Munk W (1975) Space-time scales of internal waves: a progress report. J Geophys Res 80(3):291–297

Gordeev RG, Kagan BA, Rivkind VY (1974) Modeling of semidiurnal tides in the global ocean. Izv Acad Sci USSR Ser Atmos Ocean Phys 10(7):497, 498

Kantha LH, Tierney CC (1997) Global baroclinic tides. Prog Oceanogr 40:163–178. https://doi.org/10.1016/S0079-6611(97)00028-1

Le Provost C, Lyard F (1997) Energetics of the M_2 barotropic ocean tides: an estimate of bottom friction dissipation from a hydrodynamic model. Prog Oceanogr 40(1–4):37–52

Le Provost C, Lyard F, Molines JM, Genco ML, Rabilloud F (1998) A hydrodynamic ocean tide model improved by assimilating a satellite altimeter-derived data set. J Geophys Res 103(C3):5513–5529

Morozov EG (1995) Semidiurnal internal wave global field. Deep-Sea Res 42(1):135–148

Munk WH, Wunsch C (1998) Abyssal recipes II: energetics of tidal and wind mixing. Deep-Sea Res 45:1977–2010

Olbers DJ (1983) Models of the oceanic internal wave field. Rev. Geophys Space Phys 21(7):1567–1606

Phillips OM (1977) The dynamics of the upper ocean, 2nd edn. Cambridge University Press, New York, 336 p

Ray RD (1999) A global ocean tide model from TOPEX/Poseison altimetry: GOT 99.2 NASA/Technical Memorandum, 209478

Schrama EJO, Ray RD (1994) A preliminary tidal analysis of TOPEX/POSEIDON altimetry. J Geophys Res 99(C12):24799–24808

Schwiderski EW (1979) Global ocean tides. Part II: the semidiurnal principal lunar tide (M_2), atlas of tidal charts and maps. Naval Surface Weapons Center Report. NSWC TR 79-414, 15 pp

Sjöberg B, Stigebrandt A (1992) Computations of the geographical distribution of the energy flux to mixing process via internal tides and the associated vertical circulation in the ocean. Deep-Sea Res 39:269–291